



TRANSPORT OF NUTRIENTS, METABOLITES AND IONS LINKED TO BIOENERGETICS: RELEVANCE TO HUMAN PATHOLOGY

EDITED BY: Cesare Indiveri, Mariafrancesca Scalise and Piotr Koprowski
PUBLISHED IN: *Frontiers in Molecular Biosciences* and
Frontiers in Cell and Developmental Biology



frontiers

Frontiers eBook Copyright Statement

The copyright in the text of individual articles in this eBook is the property of their respective authors or their respective institutions or funders. The copyright in graphics and images within each article may be subject to copyright of other parties. In both cases this is subject to a license granted to Frontiers.

The compilation of articles constituting this eBook is the property of Frontiers.

Each article within this eBook, and the eBook itself, are published under the most recent version of the Creative Commons CC-BY licence.

The version current at the date of publication of this eBook is CC-BY 4.0. If the CC-BY licence is updated, the licence granted by Frontiers is automatically updated to the new version.

When exercising any right under the CC-BY licence, Frontiers must be attributed as the original publisher of the article or eBook, as applicable.

Authors have the responsibility of ensuring that any graphics or other materials which are the property of others may be included in the CC-BY licence, but this should be checked before relying on the CC-BY licence to reproduce those materials. Any copyright notices relating to those materials must be complied with.

Copyright and source acknowledgement notices may not be removed and must be displayed in any copy, derivative work or partial copy which includes the elements in question.

All copyright, and all rights therein, are protected by national and international copyright laws. The above represents a summary only. For further information please read Frontiers' Conditions for Website Use and Copyright Statement, and the applicable CC-BY licence.

ISSN 1664-8714

ISBN 978-2-88971-632-6

DOI 10.3389/978-2-88971-632-6

About Frontiers

Frontiers is more than just an open-access publisher of scholarly articles: it is a pioneering approach to the world of academia, radically improving the way scholarly research is managed. The grand vision of Frontiers is a world where all people have an equal opportunity to seek, share and generate knowledge. Frontiers provides immediate and permanent online open access to all its publications, but this alone is not enough to realize our grand goals.

Frontiers Journal Series

The Frontiers Journal Series is a multi-tier and interdisciplinary set of open-access, online journals, promising a paradigm shift from the current review, selection and dissemination processes in academic publishing. All Frontiers journals are driven by researchers for researchers; therefore, they constitute a service to the scholarly community. At the same time, the Frontiers Journal Series operates on a revolutionary invention, the tiered publishing system, initially addressing specific communities of scholars, and gradually climbing up to broader public understanding, thus serving the interests of the lay society, too.

Dedication to Quality

Each Frontiers article is a landmark of the highest quality, thanks to genuinely collaborative interactions between authors and review editors, who include some of the world's best academicians. Research must be certified by peers before entering a stream of knowledge that may eventually reach the public - and shape society; therefore, Frontiers only applies the most rigorous and unbiased reviews. Frontiers revolutionizes research publishing by freely delivering the most outstanding research, evaluated with no bias from both the academic and social point of view. By applying the most advanced information technologies, Frontiers is catapulting scholarly publishing into a new generation.

What are Frontiers Research Topics?

Frontiers Research Topics are very popular trademarks of the Frontiers Journals Series: they are collections of at least ten articles, all centered on a particular subject. With their unique mix of varied contributions from Original Research to Review Articles, Frontiers Research Topics unify the most influential researchers, the latest key findings and historical advances in a hot research area! Find out more on how to host your own Frontiers Research Topic or contribute to one as an author by contacting the Frontiers Editorial Office: frontiersin.org/about/contact

TRANSPORT OF NUTRIENTS, METABOLITES AND IONS LINKED TO BIOENERGETICS: RELEVANCE TO HUMAN PATHOLOGY

Topic Editors:

Cesare Indiveri, University of Calabria, Italy

Mariafrancesca Scalise, University of Calabria, Italy

Piotr Koprowski, Nencki Institute of Experimental Biology (PAS), Poland

Citation: Indiveri, C., Scalise, M., Koprowski, P., eds. (2021). Transport of Nutrients, Metabolites and Ions Linked to Bioenergetics: Relevance to Human Pathology. Lausanne: Frontiers Media SA. doi: 10.3389/978-2-88971-632-6

Table of Contents

- 05** ***Editorial: Transport of Nutrients, Metabolites and Ions Linked to Bioenergetics: Relevance to Human Pathology***
Mariafrancesca Scalise, Piotr Koprowski and Cesare Indiveri
- 08** ***The Human SLC1A5 Neutral Amino Acid Transporter Catalyzes a pH-Dependent Glutamate/Glutamine Antiport, as Well***
Mariafrancesca Scalise, Tiziano Mazza, Gilda Pappacoda, Lorena Pochini, Jessica Cosco, Filomena Rovella and Cesare Indiveri
- 24** ***CG4928 is Vital for Renal Function in Fruit Flies and Membrane Potential in Cells: A First In-Depth Characterization of the Putative Solute Carrier UNC93A***
Mikaela M. Ceder, Tanya Aggarwal, Kimia Hosseini, Varun Maturi, Sourabh Patil, Emelie Perland, Michael J. Williams and Robert Fredriksson
- 47** ***Transferrin Receptor Functionally Marks Thermogenic Adipocytes***
Jin Qiu, Zhiyin Zhang, Sainan Wang, Yanru Chen, Caizhi Liu, Sainan Xu, Dongmei Wang, Junlei Su, Mengshan Ni, Jian Yu, Xiangdi Cui, Lu Ma, Tianhui Hu, Yepeng Hu, Xuejiang Gu, Xinran Ma, Jiqiu Wang and Lingyan Xu
- 64** ***Extracellular Citrate is a Trojan Horse for Cancer Cells***
Agata Petillo, Vittorio Abruzzese, Prashant Koshal, Angela Ostuni and Faustino Bisaccia
- 73** ***CFTR Deficiency Affects Glucose Homeostasis via Regulating GLUT4 Plasma Membrane Transportation***
Junzhong Gu, Weiwei Zhang, Lida Wu and Yuchun Gu
- 83** ***Functional Expression of the Human Glucose Transporters GLUT2 and GLUT3 in Yeast Offers Novel Screening Systems for GLUT-Targeting Drugs***
Sina Schmidl, Sebastian A. Tamayo Rojas, Cristina V. Iancu, Jun-Yong Choe and Mislav Oreb
- 96** ***A GC-MS/Single-Cell Method to Evaluate Membrane Transporter Substrate Specificity and Signaling***
Stephen J. Fairweather, Shoko Okada, Gregory Gauthier-Coles, Kiran Javed, Angelika Bröer and Stefan Bröer
- 117** ***SLC38A10 Transporter Plays a Role in Cell Survival Under Oxidative Stress and Glutamate Toxicity***
Rekha Tripathi, Tanya Aggarwal and Robert Fredriksson
- 127** ***Substrate Specificities and Inhibition Pattern of the Solute Carrier Family 10 Members NTCP, ASBT and SOAT***
Gary Grosser, Simon Franz Müller, Michael Kirstgen, Barbara Döring and Joachim Geyer
- 146** ***Vitamin K Vitamers Differently Affect Energy Metabolism in IPEC-J2 Cells***
Chiara Bernardini, Cristina Algieri, Debora La Mantia, Fabiana Trombetti, Alessandra Pagliarani, Monica Forni and Salvatore Nesci
- 157** ***Yeast Cell-Based Transport Assay for the Functional Characterization of Human 4F2hc-LAT1 and -LAT2, and LAT1 and LAT2 Substrates and Inhibitors***
Satish Kantipudi and Dimitrios Fotiadis

- 168** *Expression and Function of Organic Cation Transporter 2 in Pancreas*
Sandra Schorn, Ann-Kristin Dicke, Ute Neugebauer, Rita Schröter,
Maren Friedrich, Stefan Reuter and Giuliano Ciarimboli
- 176** *Mutational Analysis of the GXXXG/A Motifs in the Human
Na⁺/Taurocholate Co-Transporting Polypeptide NTCP on Its Bile Acid
Transport Function and Hepatitis B/D Virus Receptor Function*
Massimo Palatini, Simon Franz Müller, Kira Alessandra Alicia Theresa Lowjaga,
Saskia Noppes, Jörg Alber, Felix Lehmann, Nora Goldmann, Dieter Glebe
and Joachim Geyer
- 191** *Selective Nutrient Transport in Bacteria: Multicomponent Transporter
Systems Reign Supreme*
James S. Davies, Michael J. Currie, Joshua D. Wright,
Michael C. Newton-Vesty, Rachel A. North, Peter D. Mace, Jane R. Allison
and Renwick C.J. Dobson
- 201** *Role of Flavonoids in the Treatment of Iron Overload*
Xiaomin Wang, Ye Li, Li Han, Jie Li, Cun Liu and Changgang Sun



Editorial: Transport of Nutrients, Metabolites and Ions Linked to Bioenergetics: Relevance to Human Pathology

Mariafrancesca Scalise¹, Piotr Koprowski² and Cesare Indiveri^{1*}

¹Department DiBEST (Biologia, Ecologia, Scienze della Terra) Unit of Biochemistry and Molecular Biotechnology, University of Calabria, Rende, Italy, ²Nencki Institute of Experimental Biology (PAS), Warsaw, Poland

Keywords: transporter, pathology, metabolism, nutrients, bioenergetics

Editorial on the Research Topic

Transport of Nutrients, Metabolites and Ions Linked to Bioenergetics: Relevance to Human Pathology

The Research Topic on “*Transport of Nutrients, Metabolites and Ions linked to Bioenergetics: Relevance to Human Pathology*” volume 1, includes 15 contributions among which are 13 original articles and two reviews. This Research Topic aimed to shed further lights on the role of membrane transporters in bioenergetics, a forefront area in both basic and applied research. The number of genes coding for transport proteins increased across evolution from prokaryotes to eukaryotes: several hundreds of membrane transporters are now considered crucial in ensuring cell homeostasis and, hence, life. Indeed, these proteins allow for the flux of molecules that cannot freely cross biological membranes such as nutrients, ions, metabolites, and, last but not least, several xenobiotics including drugs (Nakanishi and Tamai, 2011; Rask-Andersen et al., 2013). In line with this fundamental role, the number of pathologies, which are recognized to be linked with inherited or acquired defects of function/expression/regulation of transporters is continuously increasing (Cesar-Razquin et al., 2015). Since molecular identification of membrane transporters is a relatively novel field of investigation, several gaps still exist in their knowledge. Accordingly, many genes encoding membrane transporters are still classified as orphans, i.e., the gene/protein is known but the functional characterization is not available yet. Some others, which display a longer scientific history, are at an advanced stage of investigation, including the resolution of 3D structures. However, most of the transporters are at an intermediate state of knowledge, thus needing further efforts to complete their characterization (Saier et al., 2021).

The original articles included in the Research Topic describe studies performed with various experimental models and updated technical approaches revealing novel aspects of membrane transporter biology and link with human pathologies.

Regarding the characterization of unknown transporters, Fredriksson’s group performed a study employing a *Drosophila melanogaster* model together with human cell lines revealing that the protein UNC93A is responsible for the regulation of potassium flow through the membrane of renal cells triggering edema development (Ceder et al.).

Regarding membrane proteins whose knowledge is at a more advanced stage, six articles have been included in the Research Topic. In the first one, novel roles for vitamin K (VK) acting on membrane features and bioenergetics have been proposed by Nesci’s group: the article pointed out that the diverse structures of VK vitamers can differently modulate gut functions, via mitochondrial OXPHOS, ranging from osmotic balance to nitrogen recycling (Bernardini et al.). In the next article,

OPEN ACCESS

Edited and reviewed by:

Cecilia Giulivi,
University of California, Davis,
United States

*Correspondence:

Cesare Indiveri
cesare.indiveri@unical.it

Specialty section:

This article was submitted to
Cellular Biochemistry,
a section of the journal
Frontiers in Molecular Biosciences

Received: 04 September 2021

Accepted: 14 September 2021

Published: 27 September 2021

Citation:

Scalise M, Koprowski P and Indiveri C
(2021) Editorial: Transport of Nutrients,
Metabolites and Ions Linked to
Bioenergetics: Relevance to
Human Pathology.
Front. Mol. Biosci. 8:770797.
doi: 10.3389/fmolb.2021.770797

Ciarimboli's group described the expression and function of the Organic Cation Transporter 2 (OCT2) in the pancreas. This protein is a well-known transporter involved in the uptake of several drugs currently employed in the therapy of human pathologies including diabetes and cancers. The presence of OCT2 in the pancreas along with the glucose transporter GLUT2, indicates a functional relationship of the two transporters under high glucose, suggesting that a mutual regulation of the two proteins may affect also the drug disposition in pancreatic cells (Schorn et al.).

The Xu's group achieved an important milestone in the study of energy homeostasis in thermogenic adipocytes; the article reveals an intriguing role for transferrin receptor Trf1 in monitoring the activation or inhibition of these cells upon external stimuli. The receptor can be considered a novel marker of functional adipocytes in terms of thermogenic program activation and mitochondrial integrity (Qiu et al.). Geyer's group described the actual substrate specificity of three transporters belonging to the SLC10 family, namely NTCP (SLC10A1), ASBT (SLC10A2), and SOAT (SLC10A6). These proteins are known as hepatic bile acid and steroid transporters, as well as hepatic virus receptors. By employing human cell lines stably overexpressing the three proteins the authors showed that some features, in terms of substrate specificity and inhibition pattern, among the three proteins are overlapping even though differences in active binding sites have been reported. As an example, Troglitazone, BSP, and erythrosine B were revealed to be common inhibitors, while cyclosporine A, irbesartan, ginkgolic acid 17:1, and betulinic acid only inhibited NTCP and SOAT, but not ASBT (Grosser et al.). Another article by Fredriksson's group suggested a new role for the recently orphanized SLC38A10 transporter, an ER/Golgi protein involved in the glutamate/GABA/glutamine cycle. In this article, a role for SLC38A10 in cortical astrocytes in sensing glutamate neurotoxicity and oxidative stress has been proposed, which is linked to the p53 action mechanism (Tripathi et al.). The Indiveri's group highlighted an unexpected function of the amino acid transporter ASCT2. This protein has been functionally and structurally characterized over the years and its function as neutral amino acid transporter is well assessed. In this article, using the proteoliposome model, the authors showed that ASCT2 mediates the transport of glutamate, as well. The transport of the acidic amino acid occurs by a more complex mechanism involving co-transport of proton besides Na^+ , in exchange with glutamine. These data underlie an additional role for ASCT2 in those tissues in which a glutamate/glutamine cycle occurs. The article also introduced a spectroscopic methodology for measuring transport, based on the use of a fluorescent probe entrapped into the proteoliposomes (Scalise et al.).

An important challenge in the study and characterization of membrane transporters is the use of adequate experimental techniques (Cesar-Razquin et al., 2015). It is not trivial to think that the relatively slow advancement in the knowledge of membrane transporters is mainly due to technical limitations of the classical biochemistry approaches employed in the studies of these highly hydrophobic

proteins. Therefore, the research of the most suitable model/method is still a hot spot in this field.

In line with this, the Research Topic hosts three articles dealing with technical advancements. The article by Broer's group described a GC-MS/Single-Cell method settled up for deciphering substrate specificities and signalling of amino acid transporters, whose redundancy and promiscuity is well recognized. Interestingly, the developed technique is based on the expression of every single transporter in *Xenopus laevis* oocytes, followed by GC-MS analysis of the whole content of single cells after the transport phenomenon. This approach revealed importance in updating the knowledge on some amino acid transporters: indeed, overlapping specificities but also some discrepancies with the published literature data have been described for the analysed proteins. As an example, in contrast to previous data, no substantial accumulation of cationic amino acids seems to be linked to $\text{ATB}^{0,+}$ (SLC6A14) and SNAT4 (SLC38A4) expression. In addition, SNAT2 (SLC38A2) was revealed to be a good leucine accumulator (Fairweather et al.). In the same frame, the article by Fotiadis's group deals with a yeast cell-based assay to search for substrates and inhibitors of two heterodimeric transporters, namely 4F2hc-LAT1 (SLC7A5) and 4F2hc-LAT2 (SLC7A8). These proteins are of great interest in the pharma field due to their involvement in human diseases, including cancers. The technique has been optimized using [^3H]-L-leucine as the main substrate, and triiodothyronine (T3) and thyroxine (T4) as well BCH and JPH203 (KYT-0353) as inhibitors. This validation opens novel perspectives also for other heterodimeric transporters of interest (Kantipudi and Fotiadis). Finally, Oreb's group set up a screening system for drugs targeting GLUT based on overexpression of functional GLUT2 and GLUT3 in yeast. This whole-cell system employs yeasts with defects in the glucose uptake, which are rescued upon human transporter expression. The simplicity of handling yeast makes this system a very powerful resource for screening anti-diabetic drugs candidates (Schmidl et al.).

The last corpus of three articles included in the Research Topic is mainly focused on membrane proteins linked to human diseases. In particular, the Bisaccias's group investigated the effects of citrate in hepatic tumour cells. Very interestingly, the treatment with low or high concentrations of citrate triggered opposite effects on cancer cell proliferation: at low doses, citrate has been reported as a promoter of cancer cell growth, while at high doses, citrate behaved as a Trojan horse for oxaloacetate inside cells with suppression of cell metabolism and consequently inhibition of cancer cell growth (Petillo et al.). Furthermore, a second paper by Geyer's group analysed the double function of the Na^+ -Taurocholate Co-transporting Polypeptide (NCPT) as both bile acid transporter and hepatitis B/D virus receptor. The authors employed a combined approach of mutational analysis, membrane-based yeast-two hybrid system, and co-immunoprecipitation to unveil structural/functional properties of the NCPT protein overexpressed in hepatic human cell lines. In particular, the authors identified the GXXXG/A motifs in TMD2 and TMD7 as important for proper folding and sorting of NTCP with indirect effects on glycosylation, homodimerization, and bile acid transport of NTCP, as well as its HBV/HDV receptor

function (Palatini et al.). Finally, the article of Gu's group proposed the molecular mechanism underlying Cystic Fibrosis (CF)-related diabetes. The authors demonstrated that this comorbidity in CF patients is due to a short-circuit of the communication between CFTR and the second messenger PI(4,5)P₂, responsible for GLUT4 translocation at the plasma membrane (Gu et al.).

The Research Topic includes also two reviews dealing with transporters involved in bacterial nutrient disposition and with detoxification by iron overload. The first one, by Dobson's group, is a systematic review on membrane transporters responsible for distributing a large variety of nutrients to pathogenic bacteria. This deep examination, in terms of protein-protein interactions and regulation by membrane lipids, has significant outlooks in the identification of novel antimicrobial targets (Davies et al.). The second review, by Sun's group deals with a high-risk factor, common to different human diseases, i.e., iron overload. The most common alteration of iron metabolism is iron deficiency and then, less attention is paid to iron overload that is detrimental for the body's homeostasis due to macromolecule peroxidation exerted by iron ions. The review focuses on the chelating properties of several plant-derived flavonoids and their

functions as a complementary therapy to treat iron overload. This analysis draws conclusion relevant to studies of flavonoid-delivering molecules to overcome some intrinsic difficulties linked to flavonoid absorption, such as their low water solubility (Wang et al.).

CONCLUDING REMARKS

This Research Topic added important missing pieces to the very large puzzle of the membrane transporter field. However, a systematic description of membrane transporters and channels and their actual role in cell homeostasis is far from being completed and is a long-term objective still requiring consistent efforts both in terms of experimentation, collection, and data analysis, due to the sizable number of players and the heterogeneity of their state of knowledge.

AUTHOR CONTRIBUTIONS

MS and PK wrote the editorial under the supervision of CI.

Conflict of Interest: The authors declare that the research was conducted in the absence of any commercial or financial relationships that could be construed as a potential conflict of interest.

Publisher's Note: All claims expressed in this article are solely those of the authors and do not necessarily represent those of their affiliated organizations, or those of the publisher, the editors and the reviewers. Any product that may be evaluated in this article, or claim that may be made by its manufacturer, is not guaranteed or endorsed by the publisher.

Copyright © 2021 Scalise, Koprowski and Indiveri. This is an open-access article distributed under the terms of the Creative Commons Attribution License (CC BY). The use, distribution or reproduction in other forums is permitted, provided the original author(s) and the copyright owner(s) are credited and that the original publication in this journal is cited, in accordance with accepted academic practice. No use, distribution or reproduction is permitted which does not comply with these terms.

REFERENCES

- César-Razquin, A., Snijder, B., Frappier-Brinton, T., Isserlin, R., Gyimesi, G., Bai, X., et al. (2015). A Call for Systematic Research on Solute Carriers. *Cell* 162, 478–487. doi:10.1016/j.cell.2015.07.022
- Nakanishi, T., and Tamai, I. (2011). Solute Carrier Transporters as Targets for Drug Delivery and Pharmacological Intervention for Chemotherapy. *J. Pharm. Sci.* 100, 3731–3750. doi:10.1002/jps.22576
- Rask-Andersen, M., Masuram, S., Fredriksson, R., and Schiöth, H. B. (2013). Solute Carriers as Drug Targets: Current Use, Clinical Trials and Prospective. *Mol. Aspects Med.* 34, 702–710. doi:10.1016/j.mam.2012.07.015
- Saier, M. H., Reddy, V. S., Moreno-Hagelsieb, G., Hendargo, K. J., Zhang, Y., Iddamsetty, V., et al. (2021). The Transporter Classification Database (TCDB): 2021 Update. *Nucleic Acids Res.* 49, D461–D467. doi:10.1093/nar/gkaa1004



The Human SLC1A5 Neutral Amino Acid Transporter Catalyzes a pH-Dependent Glutamate/Glutamine Antiport, as Well

Mariafrancesca Scalise^{1†}, Tiziano Mazza^{1†}, Gilda Pappacoda¹, Lorena Pochini¹, Jessica Cosco¹, Filomena Rovella¹ and Cesare Indiveri^{1,2*}

¹ Department DIBEST (Biologia, Ecologia, Scienze della Terra), Unit of Biochemistry and Molecular Biotechnology, University of Calabria, Arcavacata, Italy, ² CNR Institute of Biomembranes, Bioenergetics and Molecular Biotechnologies (IBIOM), Bari, Italy

OPEN ACCESS

Edited by:

Graça Soveral,
University of Lisbon, Portugal

Reviewed by:

Stefan Broer,
Australian National University,
Australia
Piero Pingitore,
University of Gothenburg, Sweden
Christof Grewer,
Binghamton University, United States

*Correspondence:

Cesare Indiveri
cesare.indiveri@unical.it

[†]These authors have contributed
equally to this work

Specialty section:

This article was submitted to
Cellular Biochemistry,
a section of the journal
Frontiers in Cell and Developmental
Biology

Received: 17 May 2020

Accepted: 19 June 2020

Published: 08 July 2020

Citation:

Scalise M, Mazza T,
Pappacoda G, Pochini L, Cosco J,
Rovella F and Indiveri C (2020) The
Human SLC1A5 Neutral Amino Acid
Transporter Catalyzes
a pH-Dependent
Glutamate/Glutamine Antiport, as
Well. *Front. Cell Dev. Biol.* 8:603.
doi: 10.3389/fcell.2020.00603

ASCT2 is a neutral amino acid transporter, which catalyzes a sodium-dependent obligatory antiport among glutamine and other neutral amino acids. The human ASCT2 over-expressed in *Pichia pastoris* and reconstituted in proteoliposomes has been employed for identifying alternative substrates of the transporter. The experimental data highlighted that hASCT2 also catalyzes a sodium-dependent antiport of glutamate with glutamine. This unconventional antiport shows a preferred sidedness: glutamate is inwardly transported in exchange for glutamine transported in the counter direction. The orientation of the transport protein in proteoliposomes is the same as in the cell membrane; then, the observed sidedness corresponds to the transport of glutamate from the extracellular to the intracellular compartment. The competitive inhibition exerted by glutamate on the glutamine transport together with the docking analysis indicates that the glutamate binding site is the same as that of glutamine. The affinity for glutamate is lower than that for neutral amino acids, while the transport rate is comparable to that measured for the asparagine/glutamine antiport. Differently from the neutral amino acid antiport that is insensitive to pH, the glutamate/glutamine antiport is pH-dependent with optimal activity at acidic pH on the external (extracellular) side. The stimulation of glutamate transport by a pH gradient suggests the occurrence of a proton flux coupled to the glutamate transport. The proton transport has been detected by a spectrofluorometric method. The rate of proton transport correlates well with the rate of glutamate transport indicating a 1:1 stoichiometry H⁺: glutamate. The glutamate/glutamine antiport is also active in intact HeLa cells. On a physiological point of view, the described antiport could have relevance in some districts in which a glutamate/glutamine cycling is necessary, such as in placenta.

Keywords: amino acid, SLC, glutamine, glutamate, membrane, transport, proteoliposome

Abbreviations: BBB, Blood Brain Barrier; BMGY, Buffered Glycerol-complex Medium; BMMY, Buffered Methanol-complex Medium; C₁₂E₈, Octaethylene glycol monododecyl ether; CNS, Central Nervous System; CryoEM, CryoElectron Microscopy; DEPC, diethyl pyrocarbonate; DMEM, Dulbecco's Modified Eagle Medium; DTE, DiThioErythritol; SLC, SoLute Carrier; YPDS, Yeast Extract Peptone Dextrose Sorbitol.

INTRODUCTION

The fifth member of the SLC1 family, ASCT2 (SLC1A5), attracted the attention of the membrane transport scientific community in the last years for its link with the metabolic rewiring occurring in cancer cells. The increased efforts in studying this transporter revealed novel physiological roles in the regulation of the amino acid homeostasis (Scalise et al., 2018a; Freidman et al., 2020) and brought to the resolution of the 3D structure (Garaeva et al., 2018). Since its first isolation in mice and human cells, ASCT2 was described as a sodium-dependent obligatory antiporter of neutral amino acids with specificity toward Ala, Ser, and Cys as indicated by the acronym ASCT2. Soon after its basic functional characterization, glutamine revealed to be the preferred substrate of the protein. This data was obtained in studies conducted in intact cell systems as well as in proteoliposomes using the murine and the human isoforms of ASCT2 either in native form or obtained by over-production in *P. pastoris* (Utsunomiya-Tate et al., 1996; Torres-Zamorano et al., 1998; Oppedisano et al., 2007; Pingitore et al., 2013). Interestingly, the availability of the recombinant hASCT2 together with its reconstitution in proteoliposomes allowed solving some controversies around this protein. As an example, it was demonstrated that the antiport of neutral amino acids, coupled to the movement of at least one sodium ion, is electrogenic in contrast with the previous believing describing an electroneutral exchange of amino acids and sodium. The intracellular sodium is an allosteric regulator of the hASCT2 transport function (Scalise et al., 2014). The kinetics of transport reaction obeys to a random simultaneous mechanism in which the three substrates do not influence the affinity of the transporter toward each other. A trimeric assembly of hASCT2 was proposed by cross-linking experiments. In this quaternary structure, the monomers work independently from each other (Scalise et al., 2014). Later on, the 3D structure of ASCT2 was solved by CryoEM employing the protein over-produced in *P. pastoris* (Pingitore et al., 2013; Garaeva et al., 2018, 2019), confirmed that the protein is organized as a trimer in the plasma membrane. The high affinity of hASCT2 toward glutamine underlies its role in cancer (Bhutia et al., 2015; Scalise et al., 2018a). Indeed, cancer cells are glutamine addicted and require a great supply of this amino acid to sustain their high proliferation rate both in terms of biomass and energy production. Interestingly, ASCT2 is overexpressed in virtually all human cancers, thus, it is not a surprise that this protein became a hot target for drug design (Bhutia et al., 2015; Scalise et al., 2018a). Therefore, one of the most attractive topics around hASCT2 is defining the molecular determinants for the substrate specificity. Understanding this basic aspect is, indeed, fundamental in either physiological studies and pharmacological applications. In this respect, it was recently described that cysteine is not a substrate of ASCT2 but acts as an allosteric regulator driving a glutamine efflux in intact cells as well as in proteoliposomes (Scalise et al., 2015). Then, data on the substrate-binding site were obtained by site-directed mutagenesis (Scalise et al., 2018a), which correlated well with the 3D structure (Garaeva et al., 2018, 2019). Soon after, the modulation of the transport function by cholesterol was described by structure/function relationship

studies (Scalise et al., 2019). Again, this last finding correlated well with structural data obtained by CryoEM (Yu et al., 2019). In the frame of substrate specificity, previous results showed that some transporters of the SLC1 family, as well as their bacterial homologs, can be forced to switch the specificity from neutral amino acids to acidic ones (glutamate or aspartate) or vice versa, by mutating some specific residues (Scopelliti et al., 2013, 2018; Canul-Tec et al., 2017). Noteworthy, besides these artificial mutations, the very first report on mice ASCT2 showed Na⁺ and pH-dependent transport of glutamate with a Km in the millimolar range, indicating a lower affinity compared to that of neutral amino acids (Utsunomiya-Tate et al., 1996; Broer et al., 1999). Then, it was shown that glutamate triggered the glutamine efflux in rat astrocytes but without a definitive molecular explanation (Deitmer and Rose, 1996; Broer and Brookes, 2001). The rat ASCT2 reconstituted in liposomes catalyzed a glutamine/glutamate antiport even though at a lower efficiency in comparison to that of neutral amino acids (Oppedisano et al., 2007) correlating with the data collected in intact cells. No data on direct glutamate transport by the human isoform of ASCT2 was available so far, then, we have further dealt with the issue of substrate “adaptation” by investigating the capacity of the hASCT2 to transport glutamate and aspartate. Indeed, we here demonstrated that the wild type hASCT2 can mediate a Na⁺ dependent aspartate_{ex}-glutamate_{ex}/glutamine_{in} antiport without any artificial modification of its primary structure. This novel aspect represents a step forward in the understanding of the actual physiological role of hASCT2 with potential outcomes also in pharmaceutical applications.

MATERIALS AND METHODS

Materials

The *P. pastoris* wild type strain (X-33), the pPICZB vector, zeocin, Ni-NTA agarose resin were from Invitrogen; PD-10 columns were from GE Healthcare; L-[³H]Glutamine and L-[³H]glutamic acid were from Perkin Elmer; C₁₂E₈ was from TCI Europe; Cholesterol, Amberlite XAD-4, egg yolk phospholipids (3-sn-phosphatidylcholine from egg yolk), Sephadex G-75, L-glutamine, L-glutamic acid monosodium salt, DEPC, valinomycin, nigericin, pyranine (8-Hydroxypyrene-1,3,6-trisulfonic acid trisodium salt) and all the other reagents were from Sigma-Aldrich.

Recombinant Production of hASCT2-6His

To produce the recombinant hASCT2-6His protein a previously pointed out approach was employed (Pingitore et al., 2013). In brief: 10 μg of pPICZB-ASCT2-6His WT construct was linearized with *PmeI*. The linearized plasmid was used to transform *P. pastoris* wild type strain X-33 by electroporation (Oberberg et al., 2011). Prior large scale protein production, transformed *P. pastoris* cells were selected using YPDS plates containing 2,000 μg/ml zeocin; then, cells were inoculated in BMGY medium (Buffered glycerol-complex medium) and grown at 30°C under rotatory stirring (Scalise et al., 2018b). Then, the

BMGY medium was removed by centrifuging *P. pastoris* cells which were resuspended at final OD of 1 in 250 ml BMMY medium (Buffered complex methanol medium) containing 0.5% methanol. The cells were placed in a 2 L conical flask and grown in the same medium at 30°C under rotatory stirring, for 3 days. Fresh methanol was added every 24 h. The *P. pastoris* membrane fraction was prepared using, as starting material, 30–40 g of cells resuspended in 300 ml of a buffer composed by 50 mM Tris-HCl pH 7.4, 150 mM NaCl, 2 mM β -mercaptoethanol and 0.5 mM PMSF. The cell suspension was loaded in the chamber of a bead beater (BioSpec Product) for disruption using glass beads (0.5 mm) for 5 min cycle reaching 90% of cell disruption. Then, the broken cell suspension was centrifuged in a JA10 rotor at 10,000 g for 30 min at 4°C. The collected supernatant, containing membrane and cytosolic fractions, was subjected to centrifugation in a JA30.50 rotor at 45,000 g for 90 min at 4°C. The resulting pellet containing membrane fraction was washed with a buffer composed by 5 mM Tris-HCl pH 7.4, 2 mM EDTA, 2 mM EGTA and 4 M urea, followed by another centrifugation cycle as above described. The washed membrane fraction was resuspended in a buffer composed by 25 mM Tris-HCl pH 7.4, 250 mM NaCl, 2 mM β -mercaptoethanol and 10% glycerol to reach a concentration of about 400 mg/ml. The membranes were homogenized with a potter and 3 mL aliquots were stored at -80°C before solubilization.

Solubilization and Purification of hASCT2-6His

The purification of hASCT2-6His was performed starting from about 1.2 g of washed membranes (400 mg/ml) that were solubilized in a buffer composed by 25 mM Tris-HCl pH 7.4, 250 mM NaCl, 6 mM β -mercaptoethanol, 1 mM L-glutamine, 10% glycerol and 2% C₁₂E₈ (w/w). The solubilization was performed under rotatory stirring for 3 h at 4°C followed by centrifugation at 18,000 \times g for 45 min. The supernatant was applied to 2 ml Ni-nitrilotriacetic acid (NTA) agarose resin pre-equilibrated with a buffer containing 20 mM Tris-HCl pH 7.4, 300 mM NaCl, 10% glycerol, 6 mM β -mercaptoethanol, 0.03% C₁₂E₈, 1 mM L-glutamine and 50 mM imidazole and incubated over-night, with gentle agitation, at 4°C. Then, the Ni-NTA resin was packed by gravity into a glass-column and washed with 30 ml of the same buffer above described. Elution of protein was, then, performed using 10 ml of a buffer containing 20 mM Tris-HCl pH 7.4, 300 mM NaCl, 10% glycerol, 6 mM β -mercaptoethanol, 0.03% C₁₂E₈, 1 mM L-glutamine and 500 mM imidazole. 2.5 ml of purified protein were pooled and desalted on a PD-10 column from which 3.5 ml were collected. The column was pre-equilibrated and eluted with a buffer composed by 20 mM Tris-HCl pH 7.4, 100 mM NaCl, 10% glycerol, 6 mM β -mercaptoethanol, 0.03% C₁₂E₈ and 1 mM L-glutamine.

Inclusion of Cholesterol in Liposome Preparation

7.5 mg of cholesterol were added to 100 mg of egg yolk phospholipids and solubilized with 1 mL of chloroform obtaining

a completely clear solution. After short incubation under rotatory stirring (30°C 5 min 1200 rpm) open tube is dried O.N. at room temperature. The dried lipid film was resuspended in 1 mL water (10% final concentration) and unilamellar liposomes were formed by two sonication cycles of 1 min (1 pulse ON and 1 pulse OFF, 40 W) with a Vibracell VCX-130 sonifier as previously suggested (Hanson et al., 2008).

Reconstitution of the hASCT2-6His Into Liposomes

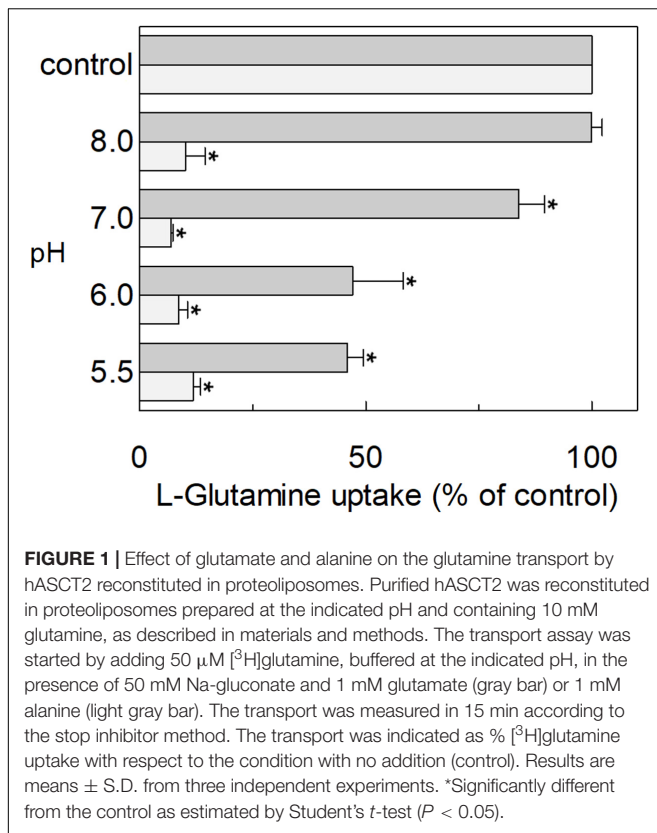
The purified hASCT2 was reconstituted by detergent removal in a batch-wise procedure. Mixed micelles of detergent, protein and phospholipids were incubated with 0.5 g Amberlite XAD-4 resin under rotatory stirring (1,200 rpm) at 23°C for 40 min as previously described (Scalise et al., 2019). The composition of the reconstitution was: 50 μl of the purified hASCT2 (5 μg protein), 2 mM EDTA, 220 μl of a mixture composed by 100 μl of 10% (w/v) egg yolk phospholipids (with or without included cholesterol as described in section 2.4) in the form of sonicated liposomes and 120 μl of 10% C₁₂E₈, 10 mM L-glutamine (or other amino acids as specified in the figure legend), 20 mM Hepes Tris pH 6.0 (or different pH as specified in the figure legend) and 10 mM NaCl (deriving from the purified protein and EDTA) in a final volume of 700 μl . All the operations were performed at room temperature.

Transport Measurements

To remove the external compounds, 600 μL of proteoliposomes was passed through a sephadex G-75 column (0.7 cm diameter \times 15 cm height) pre-equilibrated with a buffer composed by 20 mM Hepes Tris pH 6.0 and sucrose to balance the internal osmolarity. Uptake experiments were started in a 100 μl proteoliposomes sample by adding 50 μM [³H]glutamine or 500 μM [³H]glutamic acid (or other radiolabeled substrates as indicated in the figure legends) together with 50 mM Na-gluconate to, at 25°C. The transport reaction was stopped at the indicated times using 100 μM HgCl₂. The control sample, blank, was prepared by adding the same inhibitor at time zero according to the inhibitor stop method (Palmieri and Klingenberg, 1979). At the end of the transport, 100 μL of proteoliposomes was passed through a sephadex G-75 column (0.6 cm diameter \times 8 cm height) buffered with 50 mM NaCl to separate the external from the internal radioactivity. Then, proteoliposomes were eluted with 1 ml 50 mM NaCl and added with 3 ml of scintillation mixture, vortexed and counted. The experimental values were analyzed by subtracting to each sample the respective blank; the initial rate of transport was measured by stopping the reaction after 15 min, i.e., within the initial linear range of radiolabeled substrate uptake into the proteoliposomes.

Spectrofluorometric Assays

The intraliposomal pH changes were monitored by measuring the fluorescence emission of pyranine included inside the proteoliposomes. Reconstitution mixture was performed as described in section 2.4 with some modifications: 25 μg purified



protein was used for the reconstitution mixture and 0.1 mM pyranine at pH 7.0 was included in proteoliposomes. After reconstitution, 600 μ L of proteoliposomes was passed through a sephadex G-75 column, pre-equilibrated with 20 mM Hepes Tris pH 7.0 and 10 mM sucrose, except where differently indicated. Then, 150 μ L proteoliposomes were diluted in 3 ml of the same buffer containing 100 mM Na-gluconate, except where differently indicated. In the blank sample, 10 μ M HgCl₂ was added according to the stop inhibitor method above described. To start the transport assay, 5 mM glutamate buffered at pH 7.0, except where differently indicated, was added to induce glutamine_{in}/glutamate_{ex} antiport; the uptake of protons was measured as a reduction of pyranine fluorescence included in proteoliposomes. The measurement was performed in the fluorescence spectrometer (LS55) from Perkin Elmer under rotatory stirring. The fluorescence was measured following time drive acquisition protocol with λ excitation = 450 nm and λ emission = 520 nm (slit 5/5) according to manufacturer instructions of pyranine. Calibration of the internal fluorescence changes vs. pH inside the proteoliposomes has been performed by reconstituting proteoliposomes with different pH buffers (from pH 6.0 to pH 7.5). Then, the fluorescence of internal pyranine was measured as function of the internal pH finding a linear correlation. The calibration was used to report the data of **Figure 9B** as nmol of protons transported inside proteoliposomes with glutamate and to calculate the stoichiometry of proton uptake vs. glutamate uptake.

Sequence Alignment and Molecular Docking Approach

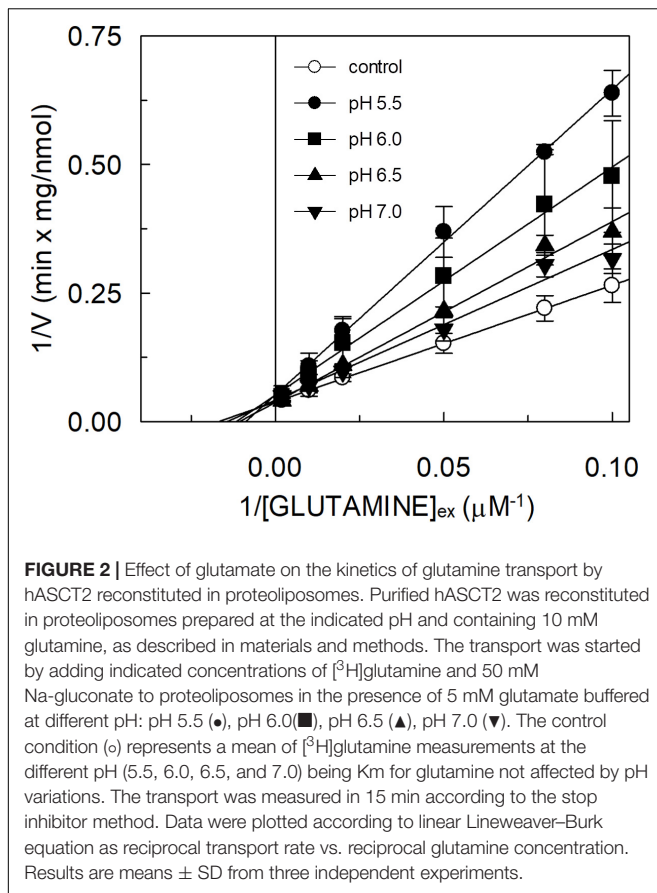
Multiple sequence alignment of SLC1 members was performed using Clustal Omega, after downloading amino acid sequences from UniProt. Docking analysis was performed using AutoDock Vina v.1.1.2 (Trott and Olson, 2010). The grid box was generated on the binding site, on the basis of glutamine coordination, and its size was set to 40 \times 40 \times 40 \AA (x, y, and z) with spacing 0.375. Glutamate was downloaded from PubChem in sdf format. The ligand was prepared using LigPrep (Schrödinger, 2020a) within Schrödinger-Maestro v.12.4 (Schrödinger, 2020b). Default parameters were applied, except for the pH range since the ligand was prepared at two pH, 2.0 \pm 0.5 and 7.0 \pm 0.5, to have two different protonation states. Glutamate, with two different protonation states, was docked into refined ASCT2 (PDB ID: 6GCT, chain A). Lamarckian Genetic Algorithm was employed to search for the best conformation space of the ligand. Default parameters were used and 20 different conformations of glutamic acid were generated. The pose with the lowest binding energy conformation was chosen. Molecular visualization was performed with the UCSF Chimera v.1.14 software (Pettersen et al., 2004) (Resource for Biocomputing, Visualization, and Informatics, University of California, San Francisco, CA, United States).

Cell Culture and Transport Assay in Intact Cells

HeLa cells were maintained in Dulbecco's Modified Eagle Medium (DMEM) supplemented with 10% (v/v) fetal bovine serum (FBS), 1 mM sodium pyruvate and 4 mM glutamine. The cells were grown in a humidified incubator in a 5% CO₂ atmosphere at 37°C. Cells for the transport assay were seeded into a 12 well dish up to 80% confluence. After 24 h, the medium was removed and the cells were washed twice with warm transport medium containing 20 mM Tris-HCl pH 7.4, 130 mM NaCl, 10 mM BCH, 10 mM MeAIB and 100 μ M nimesulide. For efflux experiments, cells were allowed to take in 10 μ M [3 H]glutamine up to 10 min. Thus, uptake buffer was removed and cells were rinsed two times with 0.5 mL per well of ice-cold transport buffer containing 20 mM Tris-HCl pH 7.4; [3 H]glutamine efflux was measured in 0.5 mL of transport buffer containing 130 mM NaCl and 20 mM Tris-HCl pH 7.0 or pH 6.0 as indicated in the figure legends in the presence of 10 mM different substrates. The efflux was measured within 1 min and cells from each well were solubilized in 500 μ l of 1% TX-100 solution. Intracellular radioactivity was measured by adding 3 mL of Scintillation Cocktail to 400 μ l of cell extract.

Other Methods

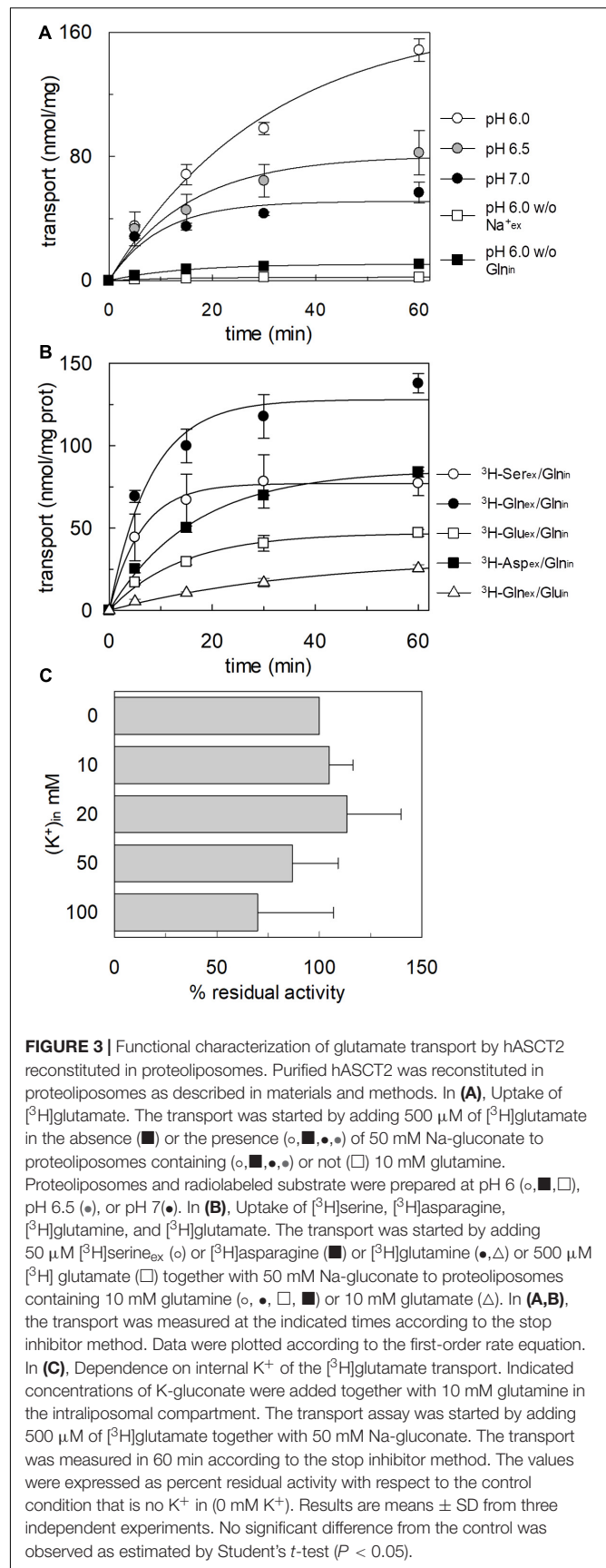
To generate imposed membrane potential, valinomycin (0.75 μ g/mg of phospholipid) was added to proteoliposomes prepared with intraliposomal 50 mM K-gluconate. Proteoliposomes were passed through sephadex-G75 and, then, treated with valinomycin for 30 sec before transport



measurement to allow potassium diffusion downhill its concentration gradient. To generate an artificial pH gradient (ΔpH), nigericin (0.15 $\mu\text{g}/\text{mg}$ phospholipid) was added to proteoliposomes in the presence of an inwardly directed K^+ gradient. Proteoliposomes were passed through sephadex-G75 and, then, treated with nigericin for 30 sec before transport measurement to allow potassium/proton exchange. For DEPC treatment, proteoliposomes were incubated after passage through sephadex G-75 column with 5 mM DEPC solution for 5 min under rotatory stirring (1,200 rpm) at 23°C prior transport measurement. Stock solutions of valinomycin, nigericin and DEPC in ethanol were prepared daily, and intermediate dilutions of this reagent into buffer were prepared immediately before use. The amount of purified recombinant hASCT2 WT was estimated from Coomassie blue-stained 12% SDS-PAGE gels by using the ChemiDoc imaging system equipped with Quantity One software (Bio-Rad) as previously described (Giancaspero et al., 2015).

Data Analysis

Results are expressed as means ± SD. GraFit 5.0.13 software was used to calculate kinetic parameters, to derive per cent of residual activity values in inhibition assays and to measure transport rate by first-order rate equation. The statistical significance of experimental data was assessed by Student's test for $p < 0.05$ as specified in the figure legends.



RESULTS

Effect of Glutamate on the Glutamine Transport by hASCT2 Reconstituted in Proteoliposomes

The hASCT2 was reconstituted in proteoliposomes and the transport was assayed as Na^+ - ^3H glutamate_{ex}/glutamine_{in} antiport. The effect of glutamate added to the proteoliposomes was tested on the transport function. As shown in **Figure 1**, glutamate inhibits the glutamine antiport in a pH-dependent fashion; the extent of inhibition varied substantially being maximal, around 50%, at acidic pH and very low or null at pH 7.0 and pH 8.0, respectively. The pH-dependent effect was specific for glutamate: indeed, when alanine was added to the proteoliposomes at the same concentration of glutamate, the inhibition ranged from 80 to 90%, being nearly pH-independent. As expected, the extent of inhibition by alanine was stronger than that by glutamate, given the higher affinity of ASCT2 toward alanine (Zander et al., 2013; Scalise et al., 2014). To characterize the inhibition, kinetic experiments were conducted (**Figure 2**). The dependence of the transport rate on glutamine concentration was measured in the presence of 5 mM glutamate at different pH values from pH 5.5 to pH 7.0. The pattern depicted in **Figure 2** is typical of competitive inhibition, suggesting that glutamate binds to the glutamine binding site and, hence, it could be a potential substrate of the transporter.

Transport of Glutamate by hASCT2 Reconstituted in Proteoliposomes

To confirm that hASCT2 could mediate the glutamate transport, the ^3H glutamate uptake in proteoliposomes containing internal glutamine, in the presence of external sodium, was measured. As shown by the figure, the reconstituted transporter is indeed able to mediate the uptake of ^3H glutamate as a function of time (**Figure 3A**). In line with the results from **Figure 2**, the uptake of ^3H glutamate is dependent on pH with an optimum at pH 6.0. According to the peculiar three-substrate reaction of hASCT2, the transport of ^3H glutamate requires both internal glutamine and external sodium. Indeed, the uptake was not measurable in the absence of the internal substrate or external sodium. To compare the efficiency of the Na^+ ^3H glutamate_{ex}/glutamine_{in} antiport with that of other neutral amino acids, the antiport of ^3H serine or ^3H asparagine in exchange for internal glutamine was measured (**Figure 3B**). The transport rate of ^3H glutamate_{ex}/glutamine_{in} antiport is only four or two times lower than that of ^3H serine_{ex}/glutamine_{in} or ^3H asparagine_{ex}/glutamine_{in}, respectively. Interestingly, the reverse reaction, i.e., ^3H glutamine_{ex}/glutamate_{in} was the least stimulated suggesting that glutamate is preferentially transported from the external to the internal side of cells, in line with the feature of the glutamine/glutamate cycle (Leke and Schousboe, 2016). The activity of glutamate transporters belonging to the SLC1 family is dependent on intracellular potassium; then, increasing concentrations of intraliposomal (intracellular) potassium were tested on the ^3H glutamate uptake via hASCT2 (**Figure 3C**). None or negligible effect was

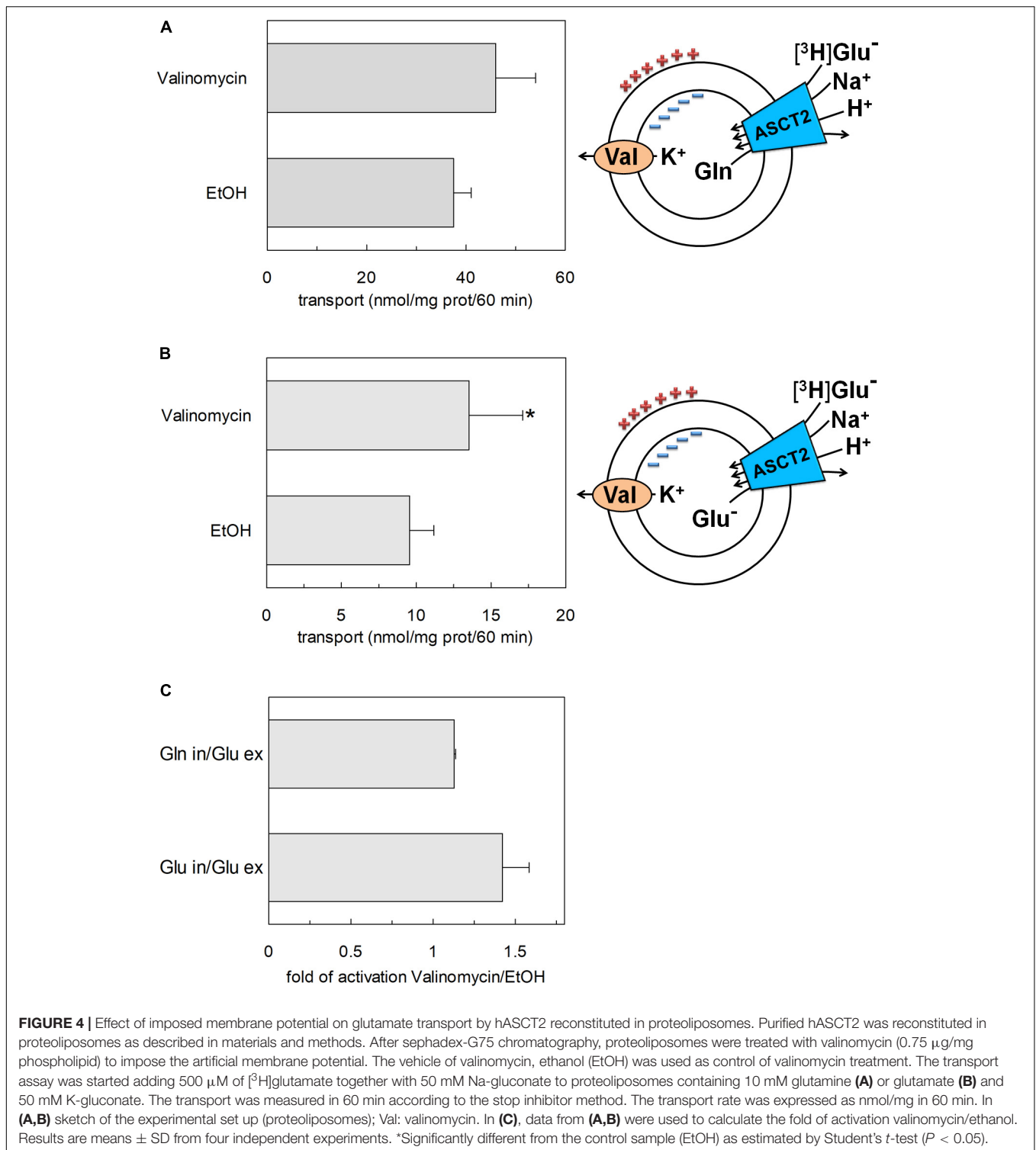
measured on hASCT2 transport activity. Moreover, the electric nature of the Na^+ ^3H glutamate_{ex}/glutamine_{in} antiport was investigated imposing a K^+ diffusion membrane potential in the presence of valinomycin, as previously described for the Na^+ ^3H glutamine_{ex}/glutamine_{in} antiport (Pingitore et al., 2013; Scalise et al., 2014). This triggered a slight stimulation of the Na^+ ^3H glutamate_{ex}/glutamine_{in} transport (**Figure 4A**). In line with the electrical nature of the vectorial reaction, the homoexchange Na^+ ^3H glutamate_{ex}/glutamate_{in} (**Figure 4B**) is more stimulated than the heteroexchange Na^+ ^3H glutamate_{ex}/glutamine_{in} (**Figure 4C**). However, the homoexchange ($\text{Glu}_{\text{ex}}/\text{Glu}_{\text{in}}$) is less efficient than the heteroexchange ($\text{Glu}_{\text{ex}}/\text{Gln}_{\text{in}}$) in line with the results obtained from the experiments reported in **Figure 3B**.

Kinetics of Glutamate Transport by hASCT2 Reconstituted in Proteoliposomes

The kinetic analysis of the ^3H glutamate_{ex}/glutamine_{in} antiport was performed as the dependence of the transport rate on glutamate concentration at different pH conditions (**Figure 5A**). The collected data showed that the K_m was virtually not affected by the pH, while the V_{max} doubled at pH 6.0 with respect to pH 7.0. K_m values in the millimolar range were obtained at the different pH values: 4.8 ± 1.9 mM, 5.3 ± 1.4 mM and 3.9 ± 1.5 mM at pH 6.0, pH 6.5, and pH 7.0, respectively. The data reported in **Figure 5A** were re-plotted against proton concentration to evaluate the affinity of the hASCT2 toward proton at different glutamate concentrations, reported in **Figure 5B**. Interestingly, the K_m toward proton was only slightly affected by the glutamate concentrations in a range from 0.5 to 5 mM, being around a proton concentration corresponding to pH 7.0. On the contrary, V_{max} increased by increasing glutamate concentration. It is worthy of note that the range of pH used in these experiments is above the pK_a of the side chain carboxylic group of glutamate; in these conditions, the majority (from 98.3% at pH 6.0 to 99.8% at pH 7.0) of glutamate is in a dissociated form, suggesting that the proton should not be bound to glutamate during the transport process.

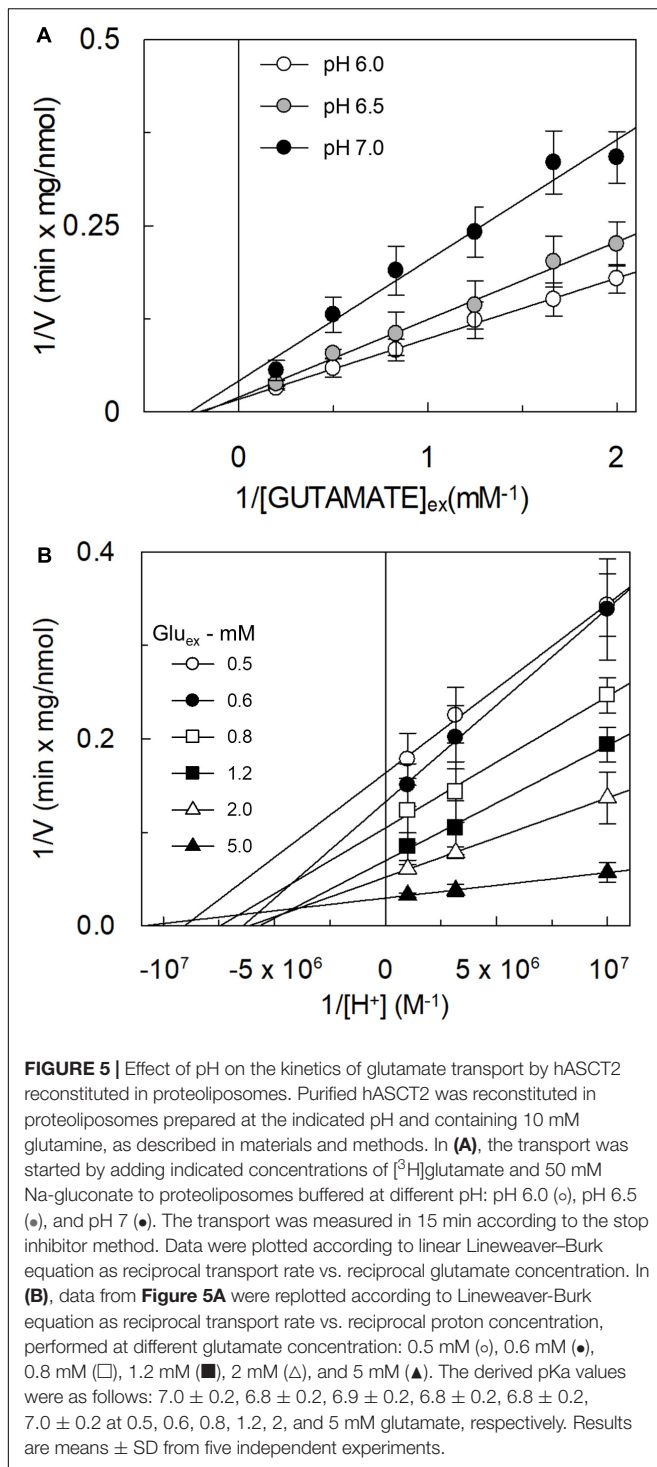
Involvement of Proton in the Transport of Glutamate by hASCT2 in Proteoliposomes

The transport of glutamate via the high-affinity glutamate transporters of the SLC1 family occurs together with the movement of a proton across the plasma membrane (Zerangue and Kavanaugh, 1996). Therefore, the possible involvement of proton in the transport of glutamate via hASCT2 was investigated. According to the results described in **Figure 5**, two hypotheses could explain the collected data: (i) the proton is transported along a different pathway than that of glutamate; (ii) the proton binds to a transporter site, facilitating the glutamate transport, but is not transported itself. To discriminate between the two possibilities, we employed different approaches. At first, the ^3H glutamate_{ex}/glutamine_{in} antiport was measured in the presence of a ΔpH (**Figure 6**). In particular, the

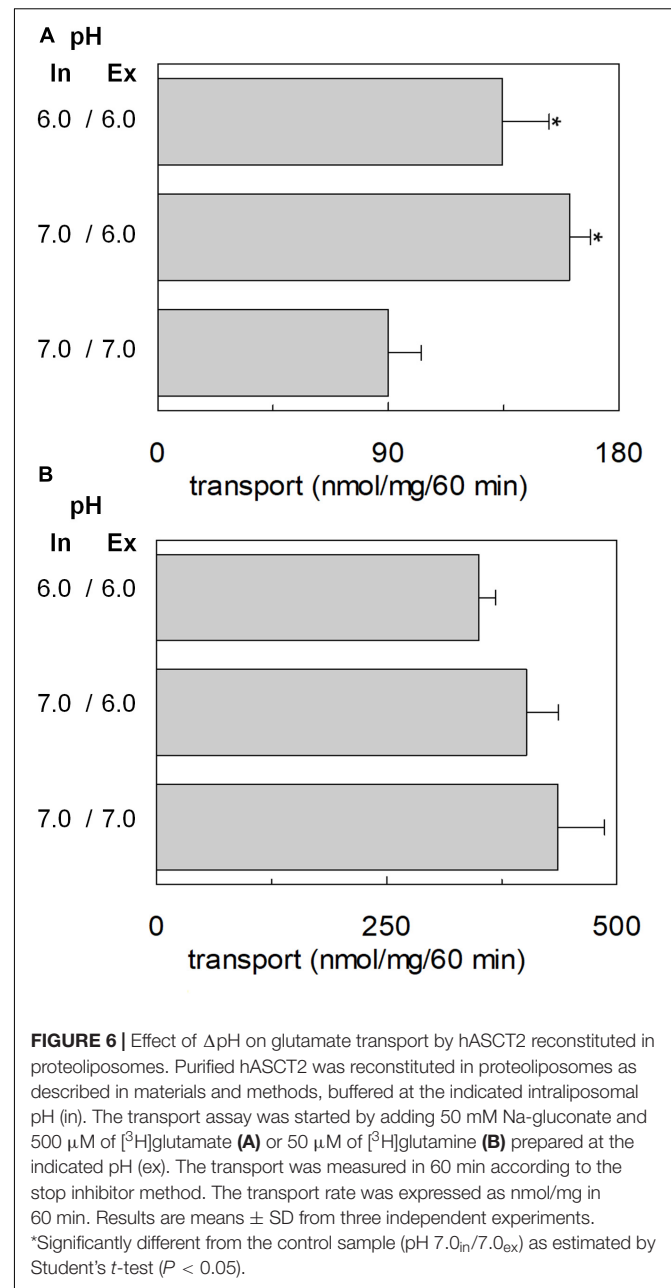


transport of [3 H]glutamate in proteoliposomes was stimulated by a pH gradient pH 6.0_{ex}/pH 7.0_{in} if compared to the conditions with no gradient, i.e., pH 7.0_{ex}/pH 7.0_{in} or pH 6.0_{ex}/pH 6.0_{in} (**Figure 6A**). This feature was specific for the glutamate transport; indeed, when the same experiment was

conducted using [3 H]glutamine, the transport in the presence of the pH gradient was less active than the control condition at pH 7.0_{ex}/pH 7.0_{in}, i.e., the optimal transport condition for the glutamine antiport (**Figure 6B**). To confirm the observed effect on the Na⁺[3 H]glutamate_{ex}/glutamine_{in}, a pH gradient was



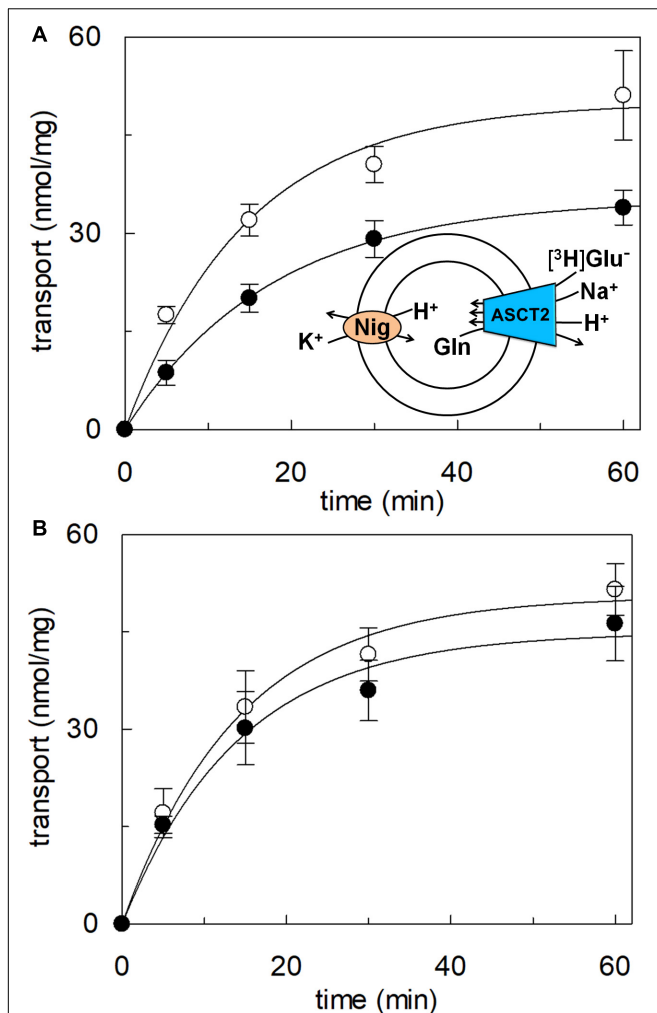
generated by using nigericin, an ionophore able to mediate the exchange of K^+ with H^+ (sketch in **Figure 7A**). In this condition, an inwardly directed pH gradient was generated and an increased [^3H]glutamate uptake was observed in comparison to the control, i.e., no nigericin (**Figure 7A**). The extent of activation is about 75% at the initial transport rate, as derived from the time-course analysis. In good agreement with this data, when the same



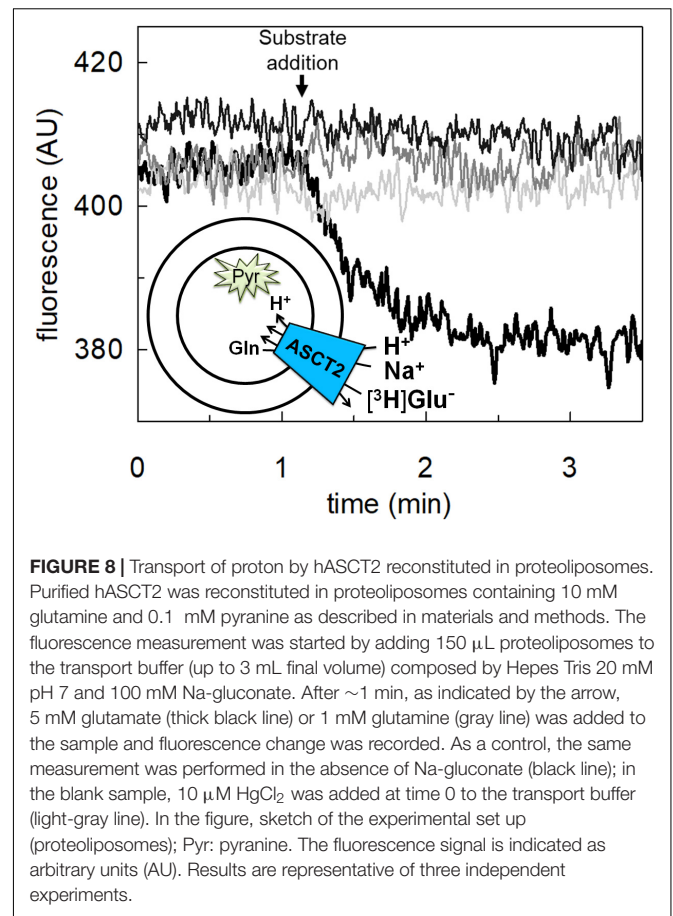
experiment was conducted without K^+ in the extraliposomal compartment, no stimulation was observed (**Figure 7B**).

Transport of Proton by hASCT2 in Proteoliposomes

To achieve the final proof of proton movement across the membrane, an alternative strategy was employed based on spectrofluorometric measurement using the pH-sensitive dye pyranine whose fluorescence emission increases with the pH (Giuliano and Gillies, 1987; Indiveri et al., 1994). Therefore, pyranine was included in the intraliposomal compartment (see Materials and methods) and the uptake of protons was measured



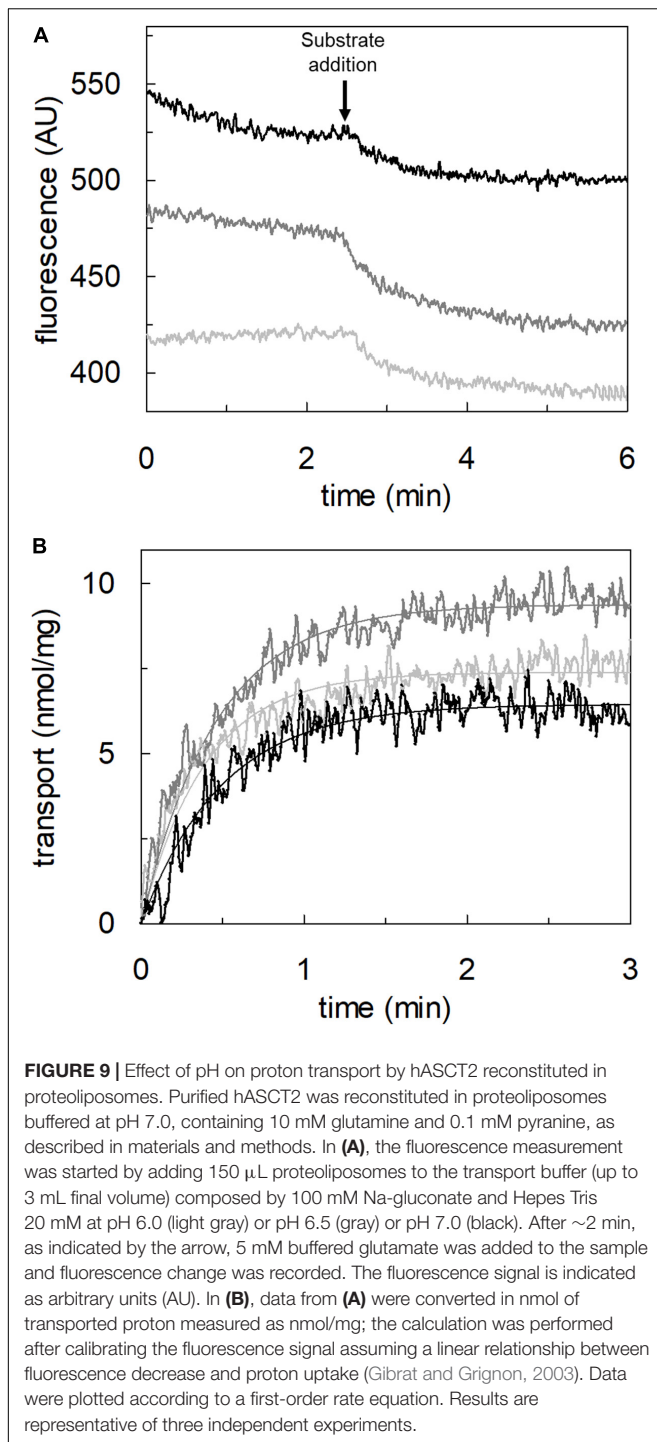
in the presence of glutamate or glutamine externally added (Figure 8). As shown in the figure, the addition of glutamate caused a time-dependent decrease of the fluorescence, in line with the uptake of protons coupled to that of glutamate. As a control, the addition of glutamine did not induce any fluorescence changes, i.e., protons were not taken up during the glutamine/glutamine antiport reaction. According to the sodium dependence of glutamate transport, proton movement was not detected when sodium was not included in the transport



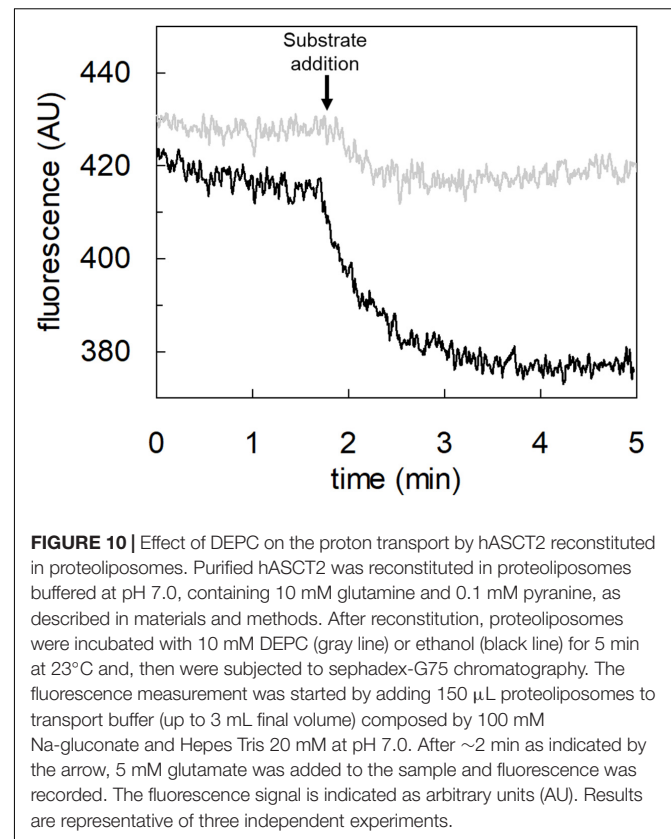
buffer. Finally, the proton uptake, i.e., fluorescence decrease, was abolished by the addition of the inhibitor, HgCl_2 (Figure 8). The dependence on pH was also evaluated in the spectrofluorometric assay (Figure 9); the decrease of fluorescence, i.e., the increase of proton concentration in the intraliposomal compartment, is indeed pH-dependent (Figure 9A). The maximal fluorescence decrease is observed at pH 6.5. To quantify the extent of proton transport, the data from Figure 9A was used to calculate the nmol of proton taken up in proteoliposomes at different pH values (Figure 9B). The uptake of protons in terms of specific transport, i.e., nmol/mg protein taken up, was in the same order of magnitude of that measured for glutamate under similar experimental conditions (Figure 5A), being in favor of a 1:1 stoichiometry for $\text{H}^+:\text{Glu}^-$ transport. The hASCT2 harbors in its primary structure four histidine residues; therefore, we argued that at least one of them could be involved in the proton transport. Then, DEPC was employed for spectrofluorometric measurements performed at pH 6.5 (Figure 10). Interestingly, the decrease of fluorescence, i.e., the proton flux toward the intraliposomal compartment, was reduced in the presence of 10 mM DEPC.

Docking of Glutamate to hASCT2

The binding site for neutral amino acids on hASCT2 was previously identified by a site-directed mutagenesis approach



(Scalise et al., 2018a) and then confirmed by the recently obtained 3D structure (Garaeva et al., 2018, 2019; Yu et al., 2019). The competitive inhibition data reported in **Figure 2**, suggested that also glutamate binds to the substrate-binding site of hASCT2. To further support this biochemical finding, we performed docking analysis on the available 3D structure of hASCT2 in the inward open conformation (PDB 6GCT) (**Figures 11A,B**). Glutamate, both in the protonated (**Figure 11A**) and



deprotonated (**Figure 11B**) state, positioned similarly to glutamine (**Figure 11C**), docked as a control (**Figure 11C**). Interestingly, docked glutamate did not directly interact with Cys467 but with the residues of the hASCT2 substrate-binding site conserved among the SLC1 family members (**Figure 11D**).

Transport of Aspartate by hASCT2 Reconstituted in Proteoliposomes

The high-affinity glutamate transporters of the SLC1 family can mediate the flux of aspartate as well. Therefore, the inhibition of the [3 H]glutamate transport by aspartate added to the extraliposomal compartment was evaluated; indeed, aspartate inhibited the hASCT2 mediated glutamate transport (**Figure 12A**). Then, we evaluated the direct transport of [3 H]aspartate via hASCT2 reconstituted in proteoliposomes; interestingly, as it is shown in **Figure 12B**, the transport of aspartate was lower than that of glutamate in line with the lack of complete inhibition of glutamate transport (**Figure 12A**).

Glutamine Efflux Induced by Glutamate via hASCT2 in Intact Cells and Proteoliposomes

The ability of glutamate to induce efflux of glutamine was investigated in both proteoliposomes and intact cells (**Figure 13**). In line with the data from **Figure 3**, glutamate was able to induce the efflux of [3 H]glutamine from preloaded proteoliposomes (**Figure 13A**). As shown by the figure, externally added glutamate

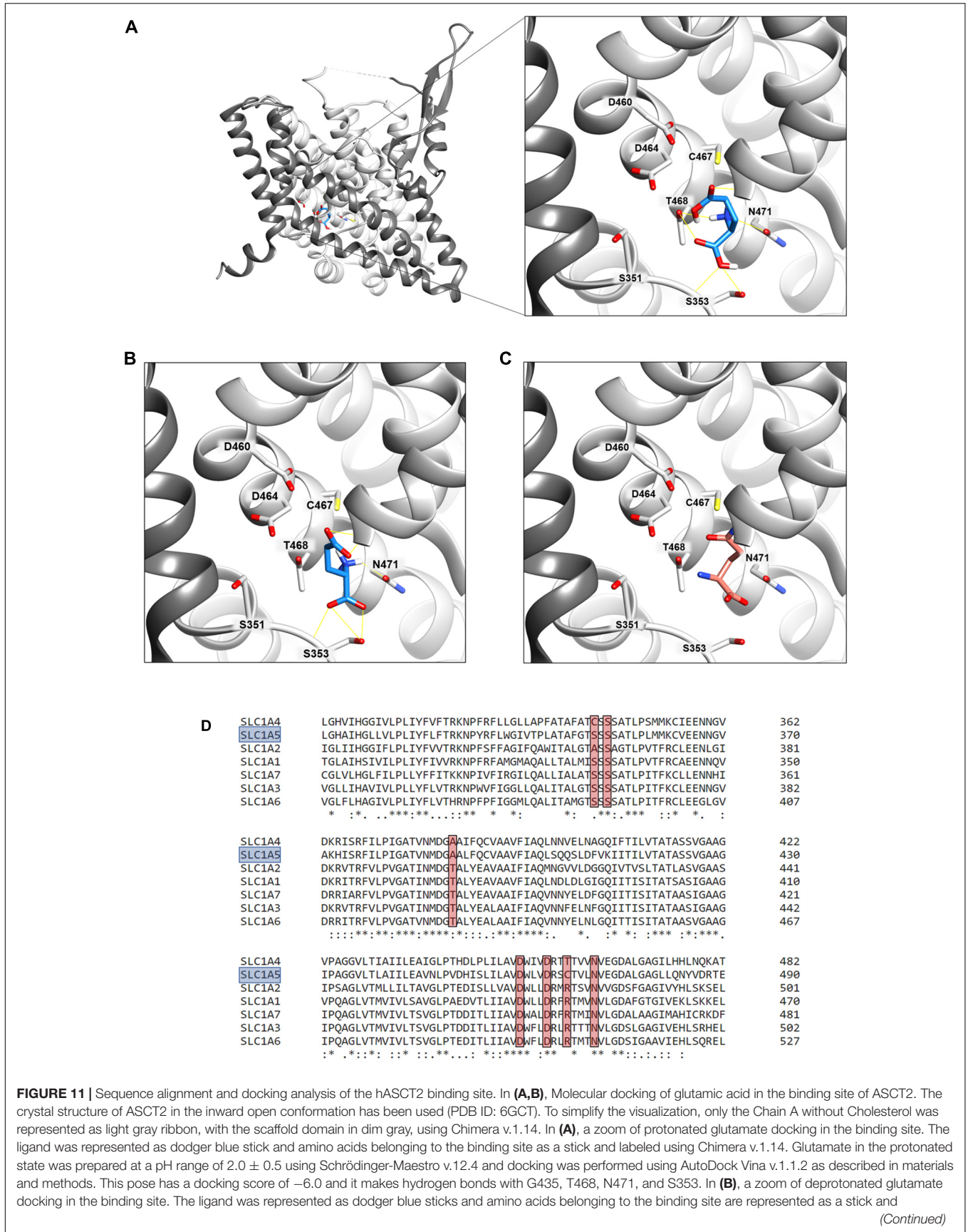


FIGURE 11 | labeled using Chimera v.1.14. Glutamate in the deprotonated state was prepared at a pH range of 7.0 ± 0.5 using Schrödinger-Maestro v.12.4 and docking was performed using AutoDock Vina v.1.1.2 as described in Methods. The best pose has a docking score of -6.1 and it makes interaction with G430, G434, G435, N471, and S353. In **(C)** visualization of the glutamine binding site. Glutamine is represented as salmon sticks and the amino acids belonging to the binding site are represented as a stick and labeled using Chimera v.1.14. In **(D)**, Multiple sequence alignment of SLC1 members. To simplify, the multiple alignment is represented from L311 to E490 referring to SLC1A5 (boxed in light blue). Residues belonging to the binding site (A390, S351, S353, D460, D464, C467, N471 in SLC1A5) are highlighted with a red box.

caused a reduction of intraliposomal radioactivity of about 65% at pH 6.0. As controls, glutamine or buffer alone was externally added: 85% or 0% efflux was detected, respectively. The data confirmed that hASCT2 could mediate the antiport of glutamate_{ex}/ [³H]glutamine_{in}, even though at a lower extent with respect to glutamine_{ex}/ [³H]glutamine_{in}. In line with the ability of hASCT2 to mediate also aspartate transport, a similar extent of efflux was observed adding aspartate in the place of glutamate. In good agreement with the uptake of radiolabeled glutamate, the described phenomenon is also pH-dependent; indeed, the addition of glutamate or aspartate buffered at pH 7.0, caused a lower efflux compared to that measured at pH 6.0. As a control, in the case of glutamine, nearly no difference was observed at the different pH values. A similar experiment was performed in intact HeLa cells, which are known to express ASCT2 and have been previously used for studying ASCT2 transport (Torres-Zamorano et al., 1998; Scalise et al., 2014, 2019). Also in this case, glutamate and aspartate evoked a glutamine efflux of about 50% and 25%, respectively, in comparison to the control. Glutamine, as expected, induced a greater efflux, reaching about 60%. Collectively, the data from intact cells and proteoliposomes confirmed the ability of glutamate to induce glutamine efflux in line with the glutamine/glutamate cycle (Leke and Schousboe, 2016).

DISCUSSION

Transport of Glutamate via hASCT2

In this work, different assays have been employed to shed light on the substrate specificity of hASCT2; this represents a vintage but very relevant issue in the understanding of hASCT2 biology in both physiological and pathological conditions with potential outcomes in pharmacology. In line with very early but disregarded observations on mice and rat ASCT2 (Utsunomiya-Tate et al., 1996; Broer et al., 1999; Oppedisano et al., 2007), the capacity of the hASCT2 to mediate a Na⁺ and H⁺ dependent glutamate_{ex}/glutamine_{in} antiport emerged. The rate of this reaction is comparable to the well-assessed antiport of neutral amino acids (Figure 3B). As a matter of fact, the substrate-binding site of wild type hASCT2 can accept glutamate and, at a lower extent, aspartate (Figure 12). The critical variation, with respect to the conventional hASCT2 transport mode, is the requirement for acidic pH that suggests the involvement of protons in the transport mechanism, reminiscent of the other glutamate transporters belonging to the SLC1 family, i.e., the EAAT members. Based on the kinetic data on WT hASCT2, it can be assumed that the transported form of glutamate is the anionic one (Figure 5); this is in line

with the observation that the Km values toward glutamate do not change when varying the pH of the transport assay, reflecting the concentration of glutamate in the anionic form. It is then expected that the proton flux occurs through an independent transport path, even though at this stage, we cannot completely exclude that the proton might be transported together with glutamate.

Transport of Proton via hASCT2

The availability of recombinant hASCT2 reconstituted in proteoliposomes allowed to directly measure the proton movement by fluorescence changes induced by the glutamate transport. This approach represents a methodological novelty in the study of the transporter; the advancement was made feasible thanks to the improvement of the functional protein fraction following the discovery that cholesterol facilitates the formation of the trimeric functional assembly of the protein (Garaeva et al., 2018, 2019; Scalise et al., 2019). These achievements resulted in a substantial increase in the active space of proteoliposomes and, hence, of the volume available for the fluorescence detection by pyranine (Indiveri et al., 1994). The results collected by the spectrofluorometric assays correlated well with the transport assay of glutamate by radioactivity. The stoichiometry of transport is in favor of an overall Na⁺ dependent transport reaction of 1H⁺:1Glu⁻ in exchange for internal glutamine. From the kinetic data reported in Figure 5, a further biochemical conclusion can be drawn: the pH dependence of glutamate transport, that is maximal at pH 6.0, is in line with the Km toward proton calculated as a proton concentration corresponding to pH 7.0 (Figure 5B). Indeed, when measuring glutamate transport at pH 6.0, the proton concentration is 10 times above the Km, i.e., close to saturation, correlating well with the doubling of the Vmax of glutamate transport from pH 7.0 to pH 6.0. In line with the proposed charge movement, valinomycin imposed membrane potential positively affects the glutamate transport via hASCT2. In good agreement with the hypothesis that glutamate is transported in the anionic form, the stimulation by the imposed membrane potential is amplified when the glutamate⁻_{ex}/glutamate⁻_{in} antiport is measured: the homologous glutamate/glutamate antiport, *per se*, is indeed electroneutral with consequent net inward movement of two positive charges deriving from sodium and proton. In the case of glutamate⁻_{ex}/glutamine_{in} exchange, the negative charge of glutamate compensates one of the co-transported positive charges. It has to be stressed that the charge movement accounts only partially in the overall driving force of transport, that mainly derives by the antiport component and the sodium gradient (Scalise et al., 2014) similarly to

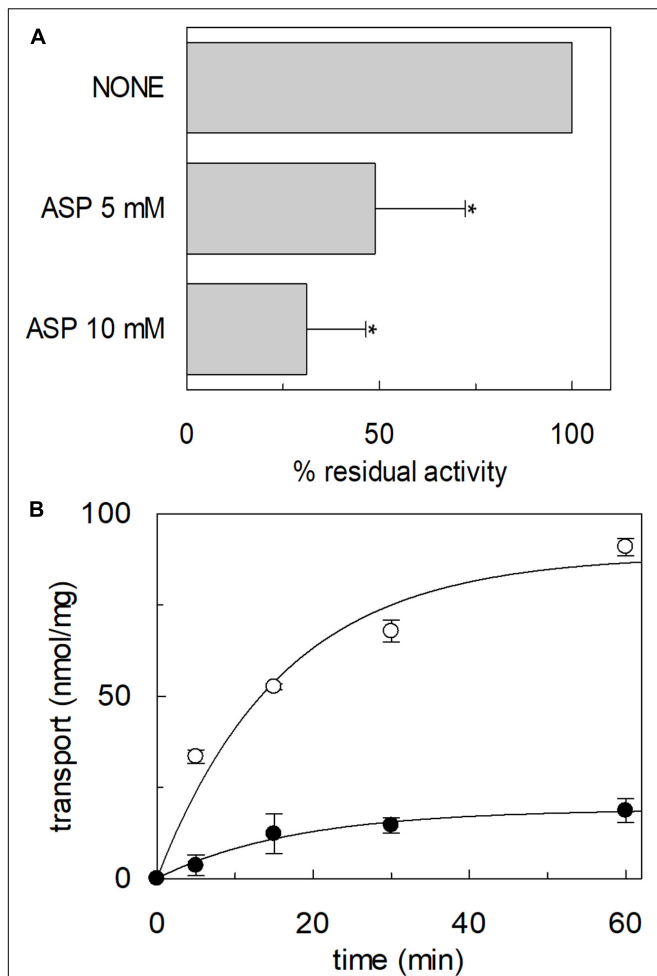


FIGURE 12 | Interaction of hASCT2 reconstituted in proteoliposomes with aspartate. Purified hASCT2 was reconstituted in proteoliposomes containing 10 mM glutamine as described in materials and methods. In **(A)**, inhibition by aspartate of the glutamate transport by ASCT2 reconstituted in proteoliposomes. The transport assay was started by adding 500 μ M [3 H]glutamate together with 50 mM Na-gluconate to proteoliposomes in the presence of indicated concentrations of aspartate. The transport was measured in 60 min according to the stop inhibitor method. The transport was indicated as % residual activity with respect to the condition with no external addition (none). Results are means \pm SD from four independent experiments. *Significantly different from the control sample (none) as estimated by Student's *t*-test ($P < 0.05$). In **(B)**, uptake of glutamate and aspartate by ASCT2 in proteoliposomes. The transport assay was started by adding 500 μ M [3 H]glutamate (\circ) or 500 μ M [3 H]aspartate (\bullet) together with 50 mM Na-gluconate to proteoliposomes. The transport was stopped at the indicated times according to the stop inhibitor method. Data were plotted with the first-order rate equation. Results are means \pm SD from three independent experiments.

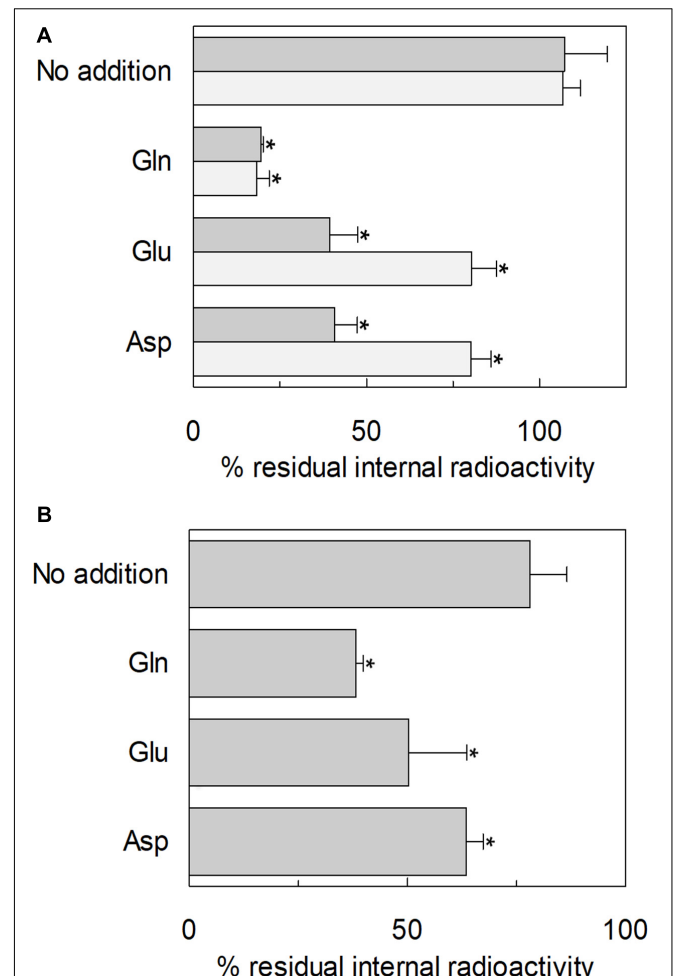


FIGURE 13 | Efflux of glutamine through hASCT2. In **(A)** [3 H]glutamine efflux from proteoliposomes. Purified hASCT2 was reconstituted in proteoliposomes containing 10 mM glutamine as described in materials and methods. The accumulation of radiolabeled glutamine was started by adding 50 μ M [3 H]glutamine in the presence of 50 mM Na-gluconate. After 60 min uptake, the [3 H]glutamine efflux was started in different conditions: no addition (control), the addition of 10 mM of glutamate or aspartate or 1 mM glutamine to the transport buffer in the presence of 50 mM Na-gluconate. The efflux was measured in 60 min using substrates buffered at pH 7.0 (light gray) or pH 6.0 (dark gray). In **(B)**, Efflux of [3 H]glutamine from HeLa intact cells. Cells were cultured as described in materials and methods; uptake was performed in 10 min adding 10 μ M [3 H]glutamine in the presence of 20 mM Tris-HCl pH 7.0 and 130 mM NaCl as described in materials and methods. The efflux was measured in 1 min in the presence of different conditions: no addition (control), the addition of 10 mM of glutamate or aspartate or 1 mM glutamine to the transport buffer constituted by 20 mM Tris-HCl pH 6.0 and 130 mM NaCl. Results are means \pm SD from four independent experiments. *Significantly different from the control sample (no addition) as estimated by Student's *t*-test ($P < 0.05$).

what previously observed for the rat ASCT2 (Zander et al., 2013). The electrogenic nature of the glutamate_{ex}/glutamine_{in} antiport is in agreement with the role of allosteric regulation by internal Na⁺, similar to that described in the case of the neutral amino acid antiport (Scalise et al., 2014). Noteworthy, when measuring the glutamine_{ex}/glutamate_{in} antiport, the transport activity was lower if compared to the *vice versa* reaction

(Figure 3B); besides the affinity issue, this can be explained by the electrogenicity of the hASCT2 mediated transport. Indeed, the exit of a net negative charge due to glutamate⁻ movement, would create a charge unbalance positive inside which counteracts the movement of Na⁺ and H⁺, from the external environment.

Transport of Acidic Amino Acids Within the SLC1 Family

Interestingly and differently from the high-affinity glutamate transporters of the SLC1 family, the glutamate transport via hASCT2 does not require internal potassium. This is in good agreement with data collected in the pre-3D structure era, in which a residue of glutamate of EAAT2 (previously known as GLT-1), namely E404, was identified as responsible for the EAAT-specific potassium stimulation; indeed, ASCTs does not harbor a glutamate residue in the corresponding position but a neutral glutamine residue (Kavanaugh et al., 1997; Grewer et al., 2003). Still in agreement with our data, the EAAT2-E404Q mutant is not sensitive to intracellular potassium (Grewer et al., 2003). The layout of hASCT2 binding site able to coordinate both neutral and negatively charged amino acids is a distinctive trait of hASCT2 with respect to the other members of SLC1 family (Figure 11). Over the years, several mutations have been generated on ASCT1 and EAATs to switch substrate specificity of these proteins. In the case of hASCT2, the presence of C467 seems to increase the range of acceptable substrates depending on the pH. This may find a possible explanation in the size of the cysteine side chain. Indeed, in old papers, it was already highlighted that cysteine, smaller than arginine of EAATs and smaller than threonine of ASCT1, creates a larger niche to accommodate substrates (Bendahhan et al., 2000). Later on, the 3D structure of hASCT2 showed the presence of a narrow space, between scaffold and transport domain, that forms a larger space directed to the intracellular side; this feature is peculiar of hASCT2 (Freidman et al., 2020). Furthermore, recent work showed that, even if lysine is not recognized as a substrate of hASCT2, small amino acids, modified to have basic side chains, can be translocated by hASCT2 and rASCT2 (Ndaru et al., 2020). Also in this case, the basic amino acid substrates do not interact with C467. The interaction of protons with the high-affinity glutamate transporters has been investigated in the very early studies conducted on EAAT2. The key residues H326, and a stretch constituted by D398, E404 and D470, were identified by site-directed mutagenesis. Interestingly, these amino acids are conserved in all the EAATs (Pines et al., 1995) and a similar mechanism was described for the proton dependent lac permease (Sahin-Toth and Kaback, 2001). Interestingly, in hASCT2, three out of the four mentioned residues are conserved, suggesting that they could be part of the proton path in the protein. Investigations are in the course for identifying the transport path of protons and glutamate in hASCT2.

Glutamate and Aspartate Transport in Physiological and Pathological Conditions

Besides the mere biochemical feasibility of the exchange of external glutamate or aspartate with internal glutamine, this vectorial reaction is plausible to take place also in the actual physiological context, as suggested by the experiments conducted on intact cells (Figure 13B). Indeed, the presence of ASCT2

in the placenta may account for the glutamate/glutamine cycle between placenta and fetus to sustain the metabolic requirement (Vaughn et al., 1995; Torres-Zamorano et al., 1998; Day et al., 2013). A similar role may be suggested for ASCT2 in the glutamate/glutamine cycle between neurons and astrocytes to sustain the activity of EAATs, i.e., the major players in the glutamate reuptake from the synaptic cleft to avoid glutamate excitotoxicity (Leke and Schousboe, 2016). It has to be noted that in synaptic cleft the transient concentration of glutamate may reach 100-200 mM (Meldrum, 2000; Gras et al., 2006), that is much higher than the K_m of ASCT2 for glutamate. However, given the major role played by EAATs and the relatively low expression of ASCT2 in the adult brain, it can be speculated that the role of ASCT2 in the reuptake of glutamate in the brain may become relevant in pathological conditions characterized by transient pH changes, such as in hypoxia (Deitmer and Rose, 1996). Besides the transport of glutamate, a physiological explanation of recognizing negatively charged amino acids by hASCT2, relies on the transport of aspartate across the BBB, as previously suggested in mice to maintain the homeostasis of excitatory amino acids in the brain (Tetsuka et al., 2003). A glutamate/glutamine cycle has been proposed also in activated macrophages in CNS following HIV infection, as a neuroprotective mechanism (Gras et al., 2006). Recently, a glutamate/glutamine cycle has been suggested to occur between cancer and stromal cells to sustain the metabolic changes (Lyssiotis and Kimmelman, 2017; Bott et al., 2019). Interestingly, a pH-dependent glutamate uptake was described in the intestine, where luminal pH is acidic. This glutamate transport was attributed to the ASC transporter by competitive inhibition studies (Munck and Munck, 1999; Munck et al., 2000). From the described scenario, it can be speculated that the substrate specificity of ASCT2 may change according to the tissues in which the protein is expressed following also developmental stage and/or post-translational modifications that may refine the preference toward one or more amino acids. Furthermore, the possibility of mediating the uptake of glutamate and aspartate further enlarges the significance of ASCT2 overexpression in the context of cancer metabolic rewiring; as an example, aspartate is required for nucleotide biosynthesis and glutamate is required for redox balance in cancer initiation and progression (Lieu et al., 2020). Taken together, the novelties on substrate specificity here presented further points out that ASCT2 is one of the key players for the metabolism of highly proliferative cells. Furthermore, the identification of other substrates, rather than neutral amino acids, may have also a relevance in providing new clues for pharmacological research. Indeed, ASCT2 is considered an eminent druggable target and the design of drugs able to specifically interact with this protein is subjected to its improved biochemical characterization.

DATA AVAILABILITY STATEMENT

The raw data supporting the conclusions of this article will be made available by the authors, without undue reservation, to any qualified researcher.

AUTHOR CONTRIBUTIONS

MS and CI conceived, designed the experiments, and analyzed the data. MS and TM performed the proteoliposome functional assays. JC and FR performed the docking analysis. LP and TM prepared the yeast constructs and optimized yeast cell growth. GP performed the yeast cell growth for protein over-expression and purification. MS, TM, and CI wrote the manuscript. CI supervised the entire work.

REFERENCES

- Bendahan, A., Armon, A., Madani, N., Kavanaugh, M. P., and Kanner, B. I. (2000). Arginine 447 plays a pivotal role in substrate interactions in a neuronal glutamate transporter. *J. Biol. Chem.* 275, 37436–37442. doi: 10.1074/jbc.m006536200
- Bhutia, Y. D., Babu, E., Ramachandran, S., and Ganapathy, V. (2015). Amino Acid transporters in cancer and their relevance to “glutamine addiction”: novel targets for the design of a new class of anticancer drugs. *Cancer Res.* 75, 1782–1788. doi: 10.1158/0008-5472.can-14-3745
- Bott, A. J., Maimouni, S., and Zong, W. X. (2019). The pleiotropic effects of glutamine metabolism in Cancer. *Cancers (Basel)* 11:770. doi: 10.3390/cancers11060770
- Broer, A., Brookes, N., Ganapathy, V., Dimmer, K. S., Wagner, C. A., Lang, F., et al. (1999). The astroglial ASCT2 amino acid transporter as a mediator of glutamine efflux. *J. Neurochem.* 73, 2184–2194. doi: 10.1046/j.1471-4159.1999.02184.x
- Broer, S., and Brookes, N. (2001). Transfer of glutamine between astrocytes and neurons. *J. Neurochem.* 77, 705–719. doi: 10.1046/j.1471-4159.2001.00322.x
- Canul-Tec, J. C., Assal, R., Cirri, E., Legrand, P., Brier, S., Chamot-Rooke, J., et al. (2017). Structure and allosteric inhibition of excitatory amino acid transporter 1. *Nature* 544, 446–451. doi: 10.1038/nature22064
- Day, P. E., Cleal, J. K., Lofthouse, E. M., Goss, V., Koster, G., Postle, A., et al. (2013). Partitioning of glutamine synthesised by the isolated perfused human placenta between the maternal and fetal circulations. *Placenta* 34, 1223–1231. doi: 10.1016/j.placenta.2013.10.003
- Deitmer, J. W., and Rose, C. R. (1996). pH regulation and proton signalling by glial cells. *Prog. Neurobiol.* 48, 73–103. doi: 10.1016/0301-0082(95)00039-9
- Freidman, N., Chen, L., Wu, Q., Briot, C., Holst, J., Font, J., et al. (2020). amino acid transporters and exchangers from the SLC1A family: structure, mechanism and roles in physiology and Cancer. *Neurochem. Res.* 45, 1268–1286. doi: 10.1007/s11064-019-02934-x
- Garaeva, A. A., Guskov, A., Slotboom, D. J., and Paulino, C. (2019). A one-gate elevator mechanism for the human neutral amino acid transporter ASCT2. *Nat. Commun.* 10:3427.
- Garaeva, A. A., Oostergetel, G. T., Gati, C., Guskov, A., Paulino, C., and Slotboom, D. J. (2018). Cryo-EM structure of the human neutral amino acid transporter ASCT2. *Nat. Struct. Mol. Biol.* 25, 515–521. doi: 10.1038/s41594-018-0076-y
- Giancaspero, T. A., Colella, M., Brizio, C., Difonzo, G., Fiorino, G. M., Leone, P., et al. (2015). Remaining challenges in cellular flavin cofactor homeostasis and flavoprotein biogenesis. *Front. Chem.* 3:30. doi: 10.3389/fchem.2015.00030
- Gibrat, R., and Grignon, C. (2003). Liposomes with multiple fluorophores for measurement of ionic fluxes, selectivity, and membrane potential. *Methods Enzymol.* 372, 166–186. doi: 10.1016/s0076-6879(03)72010-2
- Giuliano, K. A., and Gillies, R. J. (1987). Determination of intracellular pH of BALB/c-3T3 cells using the fluorescence of pyranine. *Anal. Biochem.* 167, 362–371. doi: 10.1016/0003-2697(87)90178-3
- Gras, G., Porcheray, F., Samah, B., and Leone, C. (2006). The glutamate-glutamine cycle as an inducible, protective face of macrophage activation. *J. Leukoc Biol.* 80, 1067–1075. doi: 10.1189/jlb.0306153
- Grewer, C., Watzke, N., Rauen, T., and Bicho, A. (2003). Is the glutamate residue Glu-373 the proton acceptor of the excitatory amino acid carrier 1? *J. Biol. Chem.* 278, 2585–2592. doi: 10.1074/jbc.m207956200
- Hanson, M. A., Cherezov, V., Griffith, M. T., Roth, C. B., Jaakola, V. P., Chien, E. Y., et al. (2008). A specific cholesterol binding site is established by the 2.8

All authors contributed to the article and approved the submitted version.

FUNDING

This work was supported by PRIN (Progetti di Ricerca di Interesse Nazionale) project no. 2017PAB8EM to CI granted by MIUR (Ministry of Education, University and Research) – Italy.

- A structure of the human beta2-adrenergic receptor. *Structure* 16, 897–905. doi: 10.1016/j.str.2008.05.001
- Indiveri, C., Palmieri, L., and Palmieri, F. (1994). Kinetic characterization of the reconstituted ornithine carrier from rat liver mitochondria. *Biochim. Biophys. Acta* 1188, 293–301. doi: 10.1016/0005-2728(94)90048-5
- Kavanaugh, M. P., Bendahan, A., Zerangue, N., Zhang, Y., and Kanner, B. I. (1997). Mutation of an amino acid residue influencing potassium coupling in the glutamate transporter GLT-1 induces obligate exchange. *J. Biol. Chem.* 272, 1703–1708. doi: 10.1074/jbc.272.3.1703
- Leke, R., and Schousboe, A. (2016). The glutamine transporters and their role in the glutamate/GABA-glutamine cycle. *Adv. Neurobiol.* 13, 223–257. doi: 10.1007/978-3-319-45096-4_8
- Lieu, E. L., Nguyen, T., Rhyne, S., and Kim, J. (2020). Amino acids in cancer. *Exp. Mol. Med.* 52, 15–30.
- Lyssiotis, C. A., and Kimmelman, A. C. (2017). Metabolic interactions in the tumor microenvironment. *Trends Cell Biol.* 27, 863–875. doi: 10.1016/j.tcb.2017.06.003
- Meldrum, B. S. (2000). Glutamate as a neurotransmitter in the brain: review of physiology and pathology. *J. Nutr.* 130, 1007S–1015S. doi: 10.1093/jn/130.4.1007s
- Munck, B. G., and Munck, L. K. (1999). Effects of pH changes on systems ASC and B in rabbit ileum. *Am. J. Physiol.* 276, G173–G184.
- Munck, L. K., Grondahl, M. L., Thorboll, J. E., Skadhauge, E., and Munck, B. G. (2000). Transport of neutral, cationic and anionic amino acids by systems B, b(o,+), X(AG), and ASC in swine small intestine. *Comp. Biochem. Physiol. A Mol. Integr. Physiol.* 126, 527–537. doi: 10.1016/s1095-6433(00)00227-0
- Ndaru, E., Garibhsingh, R. A., Zielewicz, L., Schlessinger, A., and Grewer, C. (2020). Interaction of the neutral amino acid transporter ASCT2 with basic amino acids. *Biochem. J.* 477, 1443–1457. doi: 10.1042/bcj20190859
- Oberg, F., Sjöhamn, J., Conner, M. T., Bill, R. M., and Hedfalk, K. (2011). Improving recombinant eukaryotic membrane protein yields in *Pichia pastoris*: the importance of codon optimization and clone selection. *Mol. Membr. Biol.* 28, 398–411. doi: 10.3109/09687688.2011.602219
- Oppedisano, F., Pochini, L., Galluccio, M., and Indiveri, C. (2007). The glutamine/amino acid transporter (ASCT2) reconstituted in liposomes: electrical nature of the glutamine/glutamate antiport. *Ital. J. Biochem.* 56, 275–278.
- Palmieri, F., and Klingenberg, M. (1979). Direct methods for measuring metabolite transport and distribution in mitochondria. *Methods Enzymol.* 56, 279–301. doi: 10.1016/0076-6879(79)56029-7
- Petersen, E. F., Goddard, T. D., Huang, C. C., Couch, G. S., Greenblatt, D. M., Meng, E. C., et al. (2004). UCSF Chimera—a visualization system for exploratory research and analysis. *J. Comput. Chem.* 25, 1605–1612. doi: 10.1002/jcc.20084
- Pines, G., Zhang, Y., and Kanner, B. I. (1995). Glutamate 404 is involved in the substrate discrimination of GLT-1, a (Na⁺ + K⁺)-coupled glutamate transporter from rat brain. *J. Biol. Chem.* 270, 17093–17097. doi: 10.1074/jbc.270.29.17093
- Pingitore, P., Pochini, L., Scalise, M., Galluccio, M., Hedfalk, K., and Indiveri, C. (2013). Large scale production of the active human ASCT2 (SLC1A5) transporter in *Pichia pastoris*—functional and kinetic asymmetry revealed in proteoliposomes. *Biochim. Biophys. Acta* 1828, 2238–2246. doi: 10.1016/j.bbame.2013.05.034
- Sahin-Toth, M., and Kaback, H. R. (2001). Arg-302 facilitates deprotonation of Glu-325 in the transport mechanism of the lactose permease from *Escherichiacoli*. *Proc. Natl. Acad. Sci. U.S.A.* 98, 6068–6073. doi: 10.1073/pnas.111139698

- Scalise, M., Pochini, L., Console, L., Losso, M. A., and Indiveri, C. (2018a). The human SLC1A5 (ASCT2) amino acid transporter: from function to structure and role in cell biology. *Front. Cell Dev. Biol.* 6:96. doi: 10.3389/fcell.2018.00096
- Scalise, M., Pochini, L., Console, L., Pappacoda, G., Pingitore, P., Hedfalk, K., et al. (2018b). Cys Site-directed mutagenesis of the human SLC1A5 (ASCT2) transporter: structure/function relationships and crucial role of Cys467 for redox sensing and glutamine transport. *Int. J. Mol. Sci.* 19:648. doi: 10.3390/ijms19030648
- Scalise, M., Pochini, L., Cosco, J., Aloe, E., Mazza, T., Console, L., et al. (2019). Interaction of cholesterol with the human SLC1A5 (ASCT2): insights into structure/function relationships. *Front. Mol. Biosci.* 6:110. doi: 10.3389/fmolb.2019.00110
- Scalise, M., Pochini, L., Panni, S., Pingitore, P., Hedfalk, K., and Indiveri, C. (2014). Transport mechanism and regulatory properties of the human amino acid transporter ASCT2 (SLC1A5). *Amino Acids* 46, 2463–2475. doi: 10.1007/s00726-014-1808-x
- Scalise, M., Pochini, L., Pingitore, P., Hedfalk, K., and Indiveri, C. (2015). Cysteine is not a substrate but a specific modulator of human ASCT2 (SLC1A5) transporter. *FEBS Lett.* 589, 3617–3623. doi: 10.1016/j.febslet.2015.10.011
- Schrödinger, R. (2020a). *LigPrep*, Schrödinger. New York, NY: LLC.
- Schrödinger, R. (2020b). *Maestro*, Schrödinger. New York, NY: LLC.
- Scopelliti, A. J., Font, J., Vandenberg, R. J., Boudker, O., and Ryan, R. M. (2018). Structural characterisation reveals insights into substrate recognition by the glutamine transporter ASCT2/SLC1A5. *Nat. Commun.* 9:38.
- Scopelliti, A. J., Ryan, R. M., and Vandenberg, R. J. (2013). Molecular determinants for functional differences between alanine-serine-cysteine transporter 1 and other glutamate transporter family members. *J. Biol. Chem.* 288, 8250–8257. doi: 10.1074/jbc.M112.441022
- Tetsuka, K., Takanaga, H., Ohtsuki, S., Hosoya, K., and Terasaki, T. (2003). The L-isomer-selective transport of aspartic acid is mediated by ASCT2 at the blood-brain barrier. *J. Neurochem.* 87, 891–901. doi: 10.1046/j.1471-4159.2003.02063.x
- Torres-Zamorano, V., Leibach, F. H., and Ganapathy, V. (1998). Sodium-dependent homo- and hetero-exchange of neutral amino acids mediated by the amino acid transporter ATB degree. *Biochem. Biophys. Res. Commun.* 245, 824–829. doi: 10.1006/bbrc.1998.8434
- Trott, O., and Olson, A. J. (2010). AutoDock vina: improving the speed and accuracy of docking with a new scoring function, efficient optimization, and multithreading. *J. Comput. Chem.* 31, 455–461.
- Utsunomiya-Tate, N., Endou, H., and Kanai, Y. (1996). Cloning and functional characterization of a system ASC-like Na⁺-dependent neutral amino acid transporter. *J. Biol. Chem.* 271, 14883–14890. doi: 10.1074/jbc.271.25.14883
- Vaughn, P. R., Lobo, C., Battaglia, F. C., Fennessey, P. V., Wilkening, R. B., and Meschia, G. (1995). Glutamine-glutamate exchange between placenta and fetal liver. *Am. J. Physiol.* 268, E705–E711.
- Yu, X., Plotnikova, O., Bonin, P. D., Subashi, T. A., McLellan, T. J., Dumlaio, D., et al. (2019). Cryo-EM structures of the human glutamine transporter SLC1A5 (ASCT2) in the outward-facing conformation. *Elife* 8:e48120.
- Zander, C. B., Albers, T., and Grewer, C. (2013). Voltage-dependent processes in the electroneutral amino acid exchanger ASCT2. *J. Gen. Physiol.* 141, 659–672. doi: 10.1085/jgp.201210948
- Zerangue, N., and Kavanaugh, M. P. (1996). Flux coupling in a neuronal glutamate transporter. *Nature* 383, 634–637. doi: 10.1038/383634a0
- Conflict of Interest:** The authors declare that the research was conducted in the absence of any commercial or financial relationships that could be construed as a potential conflict of interest.
- Copyright © 2020 Scalise, Mazza, Pappacoda, Pochini, Cosco, Rovella and Indiveri. This is an open-access article distributed under the terms of the Creative Commons Attribution License (CC BY). The use, distribution or reproduction in other forums is permitted, provided the original author(s) and the copyright owner(s) are credited and that the original publication in this journal is cited, in accordance with accepted academic practice. No use, distribution or reproduction is permitted which does not comply with these terms.



CG4928 Is Vital for Renal Function in Fruit Flies and Membrane Potential in Cells: A First In-Depth Characterization of the Putative Solute Carrier UNC93A

Mikaela M. Ceder^{1*}, Tanya Aggarwal^{1†}, Kimia Hosseini^{1†}, Varun Maturi², Sourabh Patil¹, Emelie Perland¹, Michael J. Williams³ and Robert Fredriksson¹

OPEN ACCESS

Edited by:

Mariafrancesca Scalise,
University of Calabria, Italy

Reviewed by:

Geoff Abbott,
University of California, Irvine,
United States
Vadivel Ganapathy,
Texas Tech University Health
Sciences Center, United States

*Correspondence:

Mikaela M. Ceder
Mikaela.Ceder@farmbio.uu.se
orcid.org/0000-0002-9681-5129

[†] These authors have contributed
equally to this work

Specialty section:

This article was submitted to
Cellular Biochemistry,
a section of the journal
Frontiers in Cell and Developmental
Biology

Received: 05 July 2020

Accepted: 16 September 2020

Published: 14 October 2020

Citation:

Ceder MM, Aggarwal T,
Hosseini K, Maturi V, Patil S,
Perland E, Williams MJ and
Fredriksson R (2020) CG4928 Is Vital
for Renal Function in Fruit Flies
and Membrane Potential in Cells:
A First In-Depth Characterization
of the Putative Solute Carrier
UNC93A.
Front. Cell Dev. Biol. 8:580291.
doi: 10.3389/fcell.2020.580291

¹ Department of Pharmaceutical Biosciences, Molecular Neuropharmacology, Uppsala University, Uppsala, Sweden,

² Department of Pharmacy, Drug Delivery, Uppsala University, Uppsala, Sweden, ³ Department of Neuroscience, Functional Pharmacology, Uppsala University, Uppsala, Sweden

The number of transporter proteins that are not fully characterized is immense. Here, we used *Drosophila melanogaster* and human cell lines to perform a first in-depth characterization of CG4928, an ortholog to the human UNC93A, of which little is known. Solute carriers regulate and maintain biochemical pathways important for the body, and malfunctioning transport is associated with multiple diseases. Based on phylogenetic analysis, CG4928 is closely related to human UNC93A and has a secondary and a tertiary protein structure and folding similar to major facilitator superfamily transporters. Ubiquitous knockdown of CG4928 causes flies to have a reduced secretion rate from the Malpighian tubules; altering potassium content in the body and in the Malpighian tubules, homologous to the renal system; and results in the development of edema. The edema could be rescued by using amiloride, a common diuretic, and by maintaining the flies on ion-free diets. CG4928-overexpressing cells did not facilitate the transport of sugars and amino acids; however, proximity ligation assay revealed that CG4928 co-localized with TASK¹ channels. Overexpression of CG4928 resulted in induced apoptosis and cytotoxicity, which could be restored when cells were kept in high-sodium media. Furthermore, the basal membrane potential was observed to be disrupted. Taken together, the results indicate that CG4928 is of importance for generating the cellular membrane potential by an unknown manner. However, we speculate that it most likely acts as a regulator or transporter of potassium flows over the membrane.

Keywords: solute carrier, putative solute carrier, major facilitator superfamily, *D. melanogaster*, CG4928, UNC93A

INTRODUCTION

Transporters, especially solute carriers (SLCs), have been underrepresented in research (Cesar-Razquin et al., 2015). In fact, many transporters remain orphans, and details about their expression and function are still unknown (Perland and Fredriksson, 2017). Today there are around 2,000 genes in humans that encode for proteins that mediate, sense, and/or regulate the transport of

different solutes across membranes (Urban et al., 2006). Transporters are vital for biochemical pathways to maintain the cellular concentrations of solutes, to excrete waste products, and to generate electrochemical gradients (Saier, 2000). Malfunctioning transport systems are associated with a disturbance of cellular processes, which cause several diseases and disorders (Zhang et al., 2018), e.g., metabolic disorders (Dupuis et al., 2010) and kidney dysfunction (Kottgen et al., 2010). One of these orphan transporters is UNC93A, which was revealed by protein sequence analysis (Hellsten et al., 2017; Perland and Fredriksson, 2017; Perland et al., 2017a) and genome annotation (Fredriksson et al., 2008) to be a putative SLC of major facilitator superfamily (MFS) type. Members of the MFS are facilitators and secondary active transporters with various expressions, functions, and substrate profiles (Pao et al., 1998; Reddy et al., 2012). Like many SLCs of MFS type, UNC93A is evolutionary conserved (Ceder et al., 2017).

Studies on UNC93A have been performed using *Caenorhabditis elegans* (Levin and Horvitz, 1992; de la Cruz et al., 2003), *Aedes aegypti* (Campbell et al., 2011), *Drosophila melanogaster* (Wang et al., 2004; Stofanko et al., 2008; Mohr et al., 2018; Ceder et al., 2020), *Anguilla anguilla* (Kalujnaia et al., 2007), *Mus musculus* (Ceder et al., 2017, 2020; Perland and Fredriksson, 2017; Perland et al., 2017a), and humans (Liu et al., 2002; Son et al., 2015; Schlosser et al., 2020), but a majority of these studies are not focusing on the localization and/or the function of UNC93A. The ortholog found in *C. elegans* is suggested to be a regulatory protein of a potassium channel (de la Cruz et al., 2003). Interestingly, there is also evidence that UNC93A is a membrane-bound protein (Levin and Horvitz, 1992; Liu et al., 2002; Ceder et al., 2017) with a 2D topology resembling an authentic transporter according to predictions (Ceder et al., 2017; Perland et al., 2017a). In *D. melanogaster*, the ortholog CG4928 was found to be highly expressed in the Malpighian tubules, equivalent to the human kidneys (Wang et al., 2004), to be important for hemocyte development (Stofanko et al., 2008), and to be one of several genes that confer manganese toxicity resistance (Mohr et al., 2018). Furthermore, the human UNC93A was recently identified as a metabolite-associated locus in chronic kidney disease patients (Schlosser et al., 2020).

Recently, we confirmed that UNC93A is evolutionary conserved in mammals and found that it is expressed in metabolic active organs such as the brain and the kidneys. Furthermore, *Unc93a* and *CG4928* are affected by dietary restrictions and starvation in mice and fruit flies (Ceder et al., 2017, 2020). The role of UNC93A and its implications in processes, such as homeostasis and pathology, are not completely known, and to explore its role in humans would be difficult and time consuming. To address these issues and to perform in-depth characterization, we first used the well-studied and simpler organism *D. melanogaster* and cell lines. In this paper, we aimed to characterize the ortholog protein of UNC93A. RNA interference (RNAi) was used to knock down *CG4928* expression and to monitor phenotypic data. We found that *CG4928* is crucial for renal function in the fly. Second, we performed proximity ligation assay (PLA) and confirmed that UNC93A co-localized with TASK¹ channels. Next, *CG4928* was overexpressed

in human HEK293T cells to study the substrate profile. We found that *CG4928* does not facilitate the transport of sugars and amino acids but induces apoptosis and cytotoxicity as well as disrupts the basal membrane potential. Taken together, the results indicate that *CG4928*, and possibly also UNC93A, has an impact on ion homeostasis *via* interactions with TASK¹ channels and/or by facilitating the movement of ions over the membrane.

MATERIALS AND METHODS

Fly Work

Fly Stocks and Maintenance

CG4928 expression was visualized by crossing *CG4928-Gal4* (stock no: 104449, Kyoto Stock Center) and *Pin/Pin-UAS-GFP* (derived from *yw;Pin/CyO, UAS-mCG8-GFP* stock no: 5130, Bloomington). For functional characterization, two *CG4928 RNAi* lines (*CG4928-RNAi-UAS* stock nos: 103750 and 6143, VDRC) were used and crossed to the ubiquitous *da-Gal4* (kindly donated by Prof. D. Nässel, Stockholm University), *c601-Gal4* (stock no: 30844, Bloomington), *Uro-Gal4*, *c42-Gal4*, *c324-Gal4*, and *c724-Gal4* (all kindly donated by Prof. J.A. Dow, Glasgow University). *CG4928 RNAi* lines have one reported off-target gene encoding tryptophan hydroxylase (*CG9122*) that was accounted for. *W¹¹¹⁸* (stock no: 5905, Bloomington) was used for control crosses.

Stocks and crosses were maintained at 25°C with 60% humidity on a 12:12-h light/dark cycle; the exceptions for crosses from *CG4928 RNAi GD* and *da-Gal4* were kept at 18°C. Offspring were raised at 28°C for 5 days before the experiments. All flies, unless otherwise stated, had free access to enriched Jazz mix standard fly food (Fisher Scientific).

Gene Expression Analysis With GFP

Adult flies were dissected to study the gene expression pattern in Malpighian tubules. To induce *CG4928* cells to express green fluorescent protein (GFP), the *Pin/Pin-UAS-GFP* and the enhancer trap *CG4928-GAL4* lines were crossed. Flies were fixed in 4% formaldehyde for 1 h, followed by washing five times in 1 × phosphate-buffered saline with Tween-20 (PBST; 137 mM NaCl, 2.7 mM KCl, 10 mM Na₂HPO₄, 1.8 mM KH₂PO₄, and 0.1% Tween-20, Sigma Aldrich). Dissection was performed in 1 × PBST on silicon-coated petri dishes. Tissues were mounted on Superfrost Plus slides in 50% glycerol solution. Images were acquired with an Olympus microscope BX55 with an Olympus DP73 camera and the cellSens Dimension v1.14 (Olympus). Images were then handled using ImageJ, Fiji edition (Schindelin et al., 2012).

Fly and Malpighian Tubules Imaging

Flies were quickly frozen in −80°C and imaged using a Leica M125 microscope with a ProgRes C14 plus camera (Jenoptik) and the ProgRes CapturePro 2.8 Jenoptik Optical system. The Malpighian tubules from female and male adult flies were dissected and mounted in 50% glycerol before imaging. Images were handled using ImageJ, Fiji edition (Schindelin et al., 2012).

Secretion Assay (Ramsay Assay)

Female flies ($n = 50$) were collected, anesthetized, and dissected. The procedure was performed as described in Schellinger and Rodan (2015). Briefly, the mounted tubules were set up to leak for 2 h before the droplets were measured using an ocular micrometer where one pitch = 0.07 mm. The secretion rate was calculated according to $V = \Pi d^3/6$. The average secretion rate (\pm SD) was plotted, and differences were calculated using one-way ANOVA with Bonferroni's corrections ($*p < 0.05$, $**p < 0.01$, $***p < 0.001$) using GraphPad Prism, version 5.

Body and Hemolymph Measurements

Adult flies ($n = 30$ per replicate) were collected in pre-weighted 1.5-ml Eppendorf tubes, and body weight was measured using a precision balance (VWR). Flies were then transferred to 0.5-ml Eppendorf tubes, with a hole at the bottom of each tube and placed in 1.5-ml Eppendorf tubes. Hemolymph was collected by centrifugation for 25 min at room temperature at $6,000 \times g$ before the hemolymph weight was measured using a precision balance (VWR). The procedure was repeated six to 10 times for each genotype, and the weight was corrected against the number of flies. Graphs represent mean (\pm SD), and differences were calculated with Kruskal–Wallis and Dunn's correction ($*p < 0.05$, $**p > 0.01$, $***p > 0.001$) using GraphPad Prism, version 5.

Sodium, Potassium, and Osmolality Measurements

Hemolymph samples, 20 μ l in total (*da-Gal4* > CG4928 RNAi, $n = 500$; *da-Gal4* > w^{1118} , $n = 800$, w^{1118} > CG4928 RNAi, $n = 800$), were collected to measure osmolality and sodium and potassium concentrations. Osmolality was measured using an osmometer (Fiske 210 micro-sample Osmometer Norwood). Concentrations were determined using flame spectrophotometry (model IL543, Instrumentation Lab). The percentages for each genotype were calculated and presented in graphs generated using GraphPad Prism, version 5.

Element Analysis

Malpighian tubules from 3-day-old females (*da-Gal4* > CG4928 RNAi, *da-Gal4* > w^{1118} , and w^{1118} > CG4928 RNAi) were dissected, pooled, and frozen in -80°C until analysis. A total of three replicates per genotype were collected, each replicate containing 60 Malpighian tubules. Analysis was performed using inductive coupled plasma sector field mass spectrometry (ICP-SFMS) to analyze a total of 69 elements (ions) in each sample. A control sample was used to measure background in the collecting media. The data were within group, normalized using geometric mean before means (\pm SD) were calculated and outliers were removed. GraphPad Prism, version 5, was used to perform one-way ANOVA using unpaired *t*-test with Bonferroni's multiple correction (adjusted *p*-values: $*p < 0.0492$, $**p < 0.0099$, $***p < 0.0001$). The observed data points for boron, cadmium, cobalt, and potassium, which were the only elements found to be altered, are plotted using scatter plot, where the line displays the mean value. The remaining elements are summarized in **Supplementary Table S1** with abbreviation, full name of the element, and mean (\pm SD).

RNA Extraction and cDNA Synthesis

Total RNA and cDNA were acquired as described in Chomczynski and Sacchi (1987) and Williams et al. (2016b).

RNA extraction

Briefly, flies ($n = 10$ flies per replicate) were homogenized in 60 μ l Trizol (Invitrogen). Additional 650 μ l Trizol was added followed by incubation for 5 min at room temperature. Then, 160 μ l of chloroform (Sigma Aldrich) was added, and the samples were shaken and incubated for 4 min, followed by centrifugation at 14,000 rpm (microcentrifuge from Thermo Fisher Scientific, $24 \times 1.5/2.0$ ml rotor) at 4°C for 12 min. The upper phase was transferred to a new Eppendorf tube and precipitated with 400 μ l isopropanol (Sigma Aldrich) before storing at -20°C for 30 min before centrifugation. The supernatant was discarded, and the RNA pellet was washed three times in 75% ethanol (Sigma Aldrich) and spun for 5 min. During the second wash, DNase treatment (Thermo Scientific, DNase I, RNase Free, 1 U/ μ l) was added. The pellet was air-dried for 15 min before dissolving in 20 μ l of RNase-free water. The concentration was measured using a ND-1000 spectrophotometer (NanoDrop Technologies).

cDNA synthesis

Two micrograms of RNA template was used, and cDNA was synthesized with High Capacity RNA-to-cDNA kit (Applied Biosystems) according to the manufacturer's instructions. The samples were diluted to approximately 10 ng/ μ l.

Primer Design and Quantitative Real-Time PCR

The primers were designed, and qPCR was performed as described in Ceder et al. (2017). The following housekeeping genes were used: *rp49* forward 5'-cacacaaatcttcaaaaatgtgtga-3' and reverse 5'-aatccggccttgacatg-3', *rpl11* forward 5'-ccatcggtatctatggtctgga-3' and reverse 5'-catcgtatttctgctggaacc-3', and *Actin42a* forward 5'-caacacttccgctcctt-3' and reverse 5'-gaacacaatatggtttgctt-3', CG4928 forward 5'-cggattcgattgccta-3' and reverse 5'-agtacagccagcagaatg-3', CG9122 forward 5'-gtggctctacaggagtg-3' and reverse 5'-cgcatgtgtggaatcctttta-3', *Pxt* forward 5'-atgcagggtggtgtagtg-3' and reverse 5'-tcggagttggtcacacaggag-3', *Rpt4R* forward 5'-ctgaaatcggtggacttggt-3' and reverse 5'-aagaatgtggcgtccatctg-3', and *OATP58Db* forward 5'-ctcactgtgcatgaaaa-3' and reverse 5'-gcgtagaagaggaacac-3'. Ct values were obtained using the MyIQ5 software, and primer efficiency was calculated using LinRegPCR software. Normalization was performed against three housekeeping genes (*Actin42a*, *Rpl11*, and *Rp49*). The relative mRNA expression (\pm SEM) was plotted, gene expression was compared with both controls, and Driver control was set to 100%. Expression differences were calculated using one-way ANOVA and Bonferroni's correction ($*p < 0.05$, $**p < 0.01$, $***p < 0.001$) using GraphPad Prism, version 5.

Activity and Starvation Resistance Assay

Activity and starvation assay was performed as described in Artero et al. (1998) and Williams et al. (2016a). In short, adult male flies ($n = 30$) were transferred to 5-mm glass tubes, prepared with 1% agarose, and contained in *Drosophila* activity monitoring systems (DAMS) until the last laser-beam break. Trikinetics

software was used to collect bin data; last laser-beam crossing per fly was defined as the timepoint of death. GraphPad Prism, version 5, was used to generate a box plot that represents median ($\pm q1$ and $q3$), and one-way ANOVA with Bonferroni's correction was performed as statistical analysis ($*p < 0.05$, $**p < 0.01$, $***p < 0.001$).

Capillary Feeding Assay

The method was conducted as described in Hua et al. (2010) and Williams et al. (2014). Briefly, male adult flies ($n = 5$, per replicate) were transferred to vials supplied with 1% agarose (Conda) and sealed with parafilm. A capillary glass tube (5 μ l, VWR International) filled with liquid food (5% sucrose, 5% yeast extract, and 0.5% food-coloring dye) was added to the vial. Initial and final food levels were marked to define the daily food intake. The experiments were carried out at room temperature for 24 h. Food intake per genotype ($n = 8$ –10, with five flies in each) was monitored, and the average food intake in nanoliters (\pm SEM) is presented in the graph. Differences were calculated using one-way ANOVA with Bonferroni's corrections ($*p < 0.05$, $**p < 0.01$, $***p < 0.001$) using GraphPad Prism, version 5.

Nutrient Quantification

Triacylglyceride (TAG) assay

Male flies were kept on 0, 12, and 24 h of starvation before they were euthanized. Six replicates were made, with five flies in each. The samples were homogenized in 1 \times PBST on ice, and 10 μ l was collected and stored at -80°C to be used later for protein content measurement. The samples were heat-inactivated at 70°C for 10 min before incubation at 37°C for 45 min with either triglyceride reagent (Sigma Aldrich) or 1 \times PBST. The samples were transferred to a 96-well plate, and free glycerol reagent (Sigma Aldrich) was added for 5 min at 37°C . Absorbance was recorded using a multiscan microplate spectrophotometer (Multiskan GO; Thermo Scientific) at 540 nm. TAG was determined by subtracting the amount of free glycerol in the PBST-treated sample from the total glycerol present in the sample treated with triglyceride reagent. Glycerol standard solution (Sigma Aldrich) was used to make equivalent standards.

Protein quantification

Total protein was quantified with a protein quantification kit—rapid (Sigma Aldrich) according to the manufacturer's protocol. Briefly, the homogenates were plated in a 96-well plate in replicates of three, as well as the bovine serum albumin (BSA) standards, and incubated with Coomassie brilliant blue G. Absorbance was measured at 595 nm. Protein concentration was obtained by plotting the calibration curve between the BSA concentration and the value of absorbance.

Sugar assay

Male flies were starved for 0, 12, and 24 h before they were euthanized. Ten replicates per genotype, with 10 flies in each, were collected. Hemolymph was collected after decapitation. The flies were weighed, placed in 1 \times phosphate-buffered saline (PBS; pH 7.4) and centrifuged. Hemolymph was used to measure the circulating sugars: glucose and trehalose (Sigma Aldrich). To measure the stored sugars (glycogen and trehalose),

the bodies were homogenized in 1 \times PBS and centrifuged at $12,000 \times g$ at 4°C for 15 min, resulting in a body supernatant. For final analysis, the extracted substrates were converted to glucose. Trehalose was converted by porcine kidney trehalase (Sigma Aldrich) incubation overnight at 37°C and glycogen by amyloglycosidase from *Aspergillus niger* (Sigma Aldrich) overnight at 25°C . The glucose levels were quantified using the glucose assay kit with glucose oxidase and peroxidase (Liquick Cor-Glucose diagnostic kit; Cormay), according to the manufacturer's protocol. Absorbance was measured at 500 nm on a multiscan microplate spectrophotometer (Multiskan GO; Thermo Scientific) and converted to a millimolar concentration of glucose using linear regression obtained by a calibration curve of known glucose concentrations. The glucose measurements are presented in their original unit after conversion.

GraphPad Prism, version 5, was used to generate graphs that represent mean (\pm SD) and to calculate differences using one-way ANOVA with Bonferroni's corrections ($*p < 0.05$, $**p > 0.01$, $***p > 0.001$).

Diuretics, Sugar Diets, and High-Ion Diets—Attempts to Rescue the Phenotype

Male flies ($n = 30$ per replicate, 6 to 10 replicates per genotype) were kept on diuretics, different sugar diets, and high-ion diets for 5 days before they were collected and euthanized. The following diuretics and control diets were used: furosemide (25 mg/ml, Sigma Aldrich) dissolved in acetone (Sigma Aldrich), amiloride (25 mg/ml, Sigma Aldrich) dissolved in water, mannitol (25 mg/ml, Sigma Aldrich) dissolved in water, and acetone-supplemented food. The sugar diets were made with either 40 and 10 g sucrose or glucose (Sigma Aldrich). All sugar diets contained 10 g yeast (protein, Merck Millipore) and were made on deionized water. Diets enriched in NaCl (0.1 mg/ml, Sigma Aldrich) and KCl (0.1 mg/ml, Sigma Aldrich) were made by adding the ion solution to the standard Jazz mix food. Flies raised on untreated standard Jazz mix food were used as control. Body and hemolymph weights were measured as described previously, and photos were taken with a Leica M125 microscope with a ProgRes C14 plus camera (Jenoptik) and the ProgRes CapturePro 2.8 Jenoptik Optical system. The images were handled using ImageJ, Fiji edition (Schindelin et al., 2012). Graphs represent mean (\pm SD), and differences were calculated with Kruskal–Wallis and Dunn's correction ($*p < 0.05$, $**p > 0.01$, $***p > 0.001$) using GraphPad Prism, version 5.

RNA Sequencing

mRNA was separated from total RNA using Dynabeads mRNA Purification kit (Thermo Scientific) according to the manufacturer's protocol. Poly-A selected RNA was treated with RNaseIII according to the Ion Total RNA-Seq protocol (Thermo Fisher) and purified with Magnetic Bead Cleanup Module (Thermo Fisher). The size and the quantity of the RNA fragments were assessed on Agilent 2100 Bioanalyzer system (RNA 6000 Pico kit, Agilent Technologies) before proceeding to library preparation, using the Ion Total RNA-Seq kit for the AB Library Builder System (Thermo Fisher). The libraries were amplified according to the protocol and purified with Magnetic Bead

Cleanup Module (Life Technologies). The samples were then quantified using the Agilent 2100 Bioanalyzer system (High Sensitivity DNA Kit, Agilent Technologies) and pooled, followed by emulsion PCR on the Ion OneTouch 2 system using the Ion PI Hi-Q OT2 200 chemistry (Thermo Fisher). Enriching was conducted using the Ion OneTouch ES (Thermo Fisher). The samples were loaded on an Ion PI v3 Chip (3 samples per chip) and sequenced on the Ion Proton System using Ion PI Hi-Q Sequencing chemistry (200-bp read length, Thermo Fisher).

The reads can be found at the SRA with following PRJNA663443, were mapped against the *D. melanogaster* genome assembly 6.09 using STAR mapper (Dobin et al., 2013). Mapping was done against a genome index generated with the FlyBase GTF annotating file for the 6.09 genome assembly to direct mapping toward annotated genes. A total of 232,620,764 transcripts (**Supplementary Dataset S1**) were mapped uniquely and used in subsequent analysis. The assembled transcripts were used in CuffLinks and Cuffmerge to obtain a final transcriptome assembly. Subsequently, Cuffquant and Cuffdiff were used to calculate the differential expression, and finally the packaged CummrBound was used in R¹ to plot the results. The version for all CuffLinks (Trapnell et al., 2010, 2013; Roberts et al., 2011) tools was 2.2.1. Genes were considered to be differentially expressed if they were significantly different (\log_2 fold change > 1.5 or < -1.5) in CG4928 knockdown flies compared with both controls in the CuffDiff analysis; the genes are summarized in **Supplementary Table S2**. DAVID bioinformatics resources were used to investigate clustering and pathway mapping (Huang et al., 2007).

Proteomics

Identification of Proteins Related to UNC93A and Sup-9

A hidden Markov model (Eddy, 2011) for human UNC93A (data version: GRCh38.pep.all) was built and used as described in Ceder et al. (2017) to search the protein data sets listed in **Supplementary Table S3**. Briefly, the data sets were obtained from Ensembl, version 86 (Cunningham et al., 2015); sequences originating from the same locus and pseudogenes were removed. The longest transcripts were combined in a multiple PSI/TM tcoffee sequence alignment (Notredame et al., 2000), and relationships were concluded with Bayesian approach (Huelsenbeck et al., 2001). The analysis was run *via* the Beagle library (Ayres et al., 2012), five heated and one cold chains, with two runs in parallel (n runs = 2). To analyze protein identification, pairwise global sequence alignments were performed using the Needle approach (Li et al., 2015).

The phylogenetic relationship between *C. elegans* Sup-9 and its ortholog protein sequences in *Homo sapiens* and *D. melanogaster* were investigated (**Supplementary Dataset S2**). Protein sequences were downloaded from Uniprot (UniProt Consortium, 2019). The sequences were aligned using MAFFT (Katoh et al., 2002), and mrBayes 3.2.2 (Huelsenbeck et al., 2001) software was used to generate the tree. The procedure was run on a non-heated chain with two runs in parallel (n runs = 2) under

the mixed amino acid model with eight gamma categories and invgamma as gamma rates, for a total of 2,000,000 generations.

Secondary and Tertiary Structure

Predictions of the CG4928 structure were modeled using the FBpp0074118 sequence obtained from flybase.org. The secondary structure was modeled using Protter (Omasits et al., 2014), and the tertiary structure was predicted as described in Kelley et al. (2015) and Ceder et al. (2017). The CG4928 tertiary structure was modeled against glycerol-3-phosphate transporter from *E. coli* (PDB id d1pw4a), with 99.9% confidence and 89% amino acid sequence coverage.

Cell Work

Cell Cultures and Transfection

HEK293T cells, cultured in Dulbecco's modified Eagle's medium (DMEM; Thermo Scientific) with 10% fetal bovine serum (FBS) and 1% penicillin and streptomycin, and SH-SY5Y cells, cultured in DMEM: F12 (Thermo Scientific) with 15% FBS and 1% penicillin and streptomycin, were used. The cell lines were transfected with 0.5 $\mu\text{g}/\mu\text{l}$ pcDNA3.1-CG4928-Flag (Invitrogen, 17AD6RSP), pcDNA3.1-CG4928-eGFP (Invitrogen, 17ADONXP) (for sequences, see **Supplementary Dataset S3**), or pcDNA3.1-empty (Invitrogen) plasmids using Lipofectamine 3000 (Thermo Scientific) and Fugene HD transfection reagent [Promega, membrane preparation and solid-supported membrane (SSM)-based electrophysiology].

Immunocytochemistry

Immunocytochemistry (ICC) was performed as described in Perland et al. (2016) on transfected SH-SY5Y cells and wild-type HEK293T cells (only anti-UNC93A) with antibodies all diluted in anti-UNC93A [rabbit, 1:100ab69443, Abcam, (Ceder et al., 2017)], anti-KCNK3 [mouse, 1:100, ab186352 Abcam, (Schmidt et al., 2015)], anti-KCNK9 (mouse, 1:100, Sigma, K0514), and anti-Flag [mouse, 1:200, F3165, Sigma, (Sriramachandran et al., 2019)]. Images were acquired using Olympus microscope BX55 with an Olympus DP73 camera and the cellSens Dimension v1.14 (Olympus) and were then handled using ImageJ, Fiji edition (Schindelin et al., 2012). The epitope against UNC93A was pair-wise aligned against the three isoforms of CG4928 (FBpp0074118, FBpp0074119, and FBpp0309738) using EMBOSS Needle (global alignment) and EMBOSS Water (local alignment) to investigate protein identity and similarity (Li et al., 2015) (**Supplementary Dataset S4**).

Proximity Ligation Assay

Transfected and non-transfected SH-SY5Y cells were washed in 1 \times PBS and fixed using 4% formaldehyde (Sigma Aldrich) for 30 min, followed by permeabilization with 0.1% Triton-100 (Sigma Aldrich) for 10 min. PLA was performed using the DuolinkTM *in situ* detection reagent orange kit (Sigma Aldrich) according to the manufacturer's instructions. Briefly, the cells were washed twice in 1 \times Tris-buffered saline with Tween-20 (TBST) before these were blocked in DuolinkTM blocking buffer for 1 h at room temperature, followed by incubation with primary

¹<https://www.r-project.org/other-docs.html>

antibodies anti-UNC93A, anti-KCNK3, anti-KCNK9, and anti-Flag overnight at 4°C. The cells were washed twice in 1 × TBST and incubated for 1 h at room temperature with PLA probes diluted 1:5. The cells were once again washed before incubation in hybridization solution (diluted 1:5) for 15 min at 37°C. Ligation (ligation solution diluted 1:5, ligase diluted 1:40) was performed at 37°C for 15 min before amplification (amplification stock diluted 1:5, polymerase diluted 1:80) at 37°C for 90 min. The cells were washed twice for 10 min in 1 × Wash Buffer B at room temperature before washing twice for 2 min in TBST and detection solution. The detection solution (diluted 1:5) was added to the cells, followed by incubation for 30 min at 37°C. The cells were mounted with ProLong Gold antifade reagent with DAPI (Thermo Fisher), followed by imaging. Images were acquired with an Olympus microscope BX55 with an Olympus DP73 camera and the cellSens Dimension v1.14 (Olympus). The images were then handled using ImageJ, Fiji edition (Schindelin et al., 2012), and Duolink™ Image tool (Olink Bioscience) was used to perform the analysis. GraphPad Prism, version 5, was used to retrieve graphs with mean (±SD) and perform the statistics. Kruskal–Wallis test, with Mann–Whitney as *post hoc* test, was used to detect differences in PLA signal (adjusted *p*-values: **p* < 0.0491, ***p* < 0.00995, ****p* < 0.00099).

Membrane Preparation

The transfected HEK293T cells were collected in 1 × PBS using a cell scraper. The cells were lysed in lysis buffer containing 250 mM sucrose in 10 mM Tris, pH 7.5, and protease inhibitor cocktail using a freeze/thaw method. The lysates were centrifuged at 6,000 × *g* at 4°C for 10 min to isolate the nuclear pellet. Later, the supernatant was centrifuged at 100,000 × *g* at 4°C for 30 min to isolate the membrane pellet. This membrane pellet was dissolved in storing buffer containing 140 mM NaCl and 2 mM MgCl₂ in 30 mM Tris, pH 7.5. The isolated membrane samples were then used for western blot and further analyzed by Nanion Technologies (Munich, Germany) through SSM-based electrophysiology to identify possible substrates.

Western Blot

Western blot was performed as described in Perland et al. (2016). The protein concentration of membrane samples from HEK293T cell cultures were analyzed using tryptophan measurement on a Tecan plate reader. Lysis buffer (25 mM Tris pH 7.8, 150 mM NaCl, 1 mM EDTA, 5% glycerol, 1% Triton X-100, and protease inhibitor cocktail) was added to the membrane samples before denaturation using dithiothreitol and sodium dodecyl sulfate containing Laemmli sample buffer at 95°C for 5 min. Then, 5 μg was added, and as reference, a molecular weight marker was used (prestained dual color, Bio-Rad). Anti-UNC93A (1:100) was used for protein visualization. The membrane was developed using Clarity Western ECL Substrate (Bio-Rad), and the staining was visualized using a CCD camera (Bio-Rad). The staining was compared with the molecular weight marker using Image Lab software v5.2.1 build 11 (Bio-Rad). Western blot was quantified using ImageJ, Fiji edition (Schindelin et al., 2012), and protein expression was normalized against β-actin. GraphPad Prism, version 5, was used to compile graphs.

SSM-Based Electrophysiology

Solid-supported membrane-based electrophysiology using SURFE²RN1 was performed as described in Bazzone et al. (2017) on membrane samples obtained from transfected HEK293T cells. The membrane was run on three sensors per replicate: duplicates (control: empty vector-transfected cells) and triplicates (for remaining runs). In short, 200 mM fructose, galactose, glucose, lactose, saccharose, or xylose was added to the membranes after 1 s and removed after approximately 2 s. SGLT1 was used as a positive control, and 250, 100, 20, 4, and 1 mM glucose was added. For amino acids, 20 mM of glycine, glycyglycine, alanine, glutamate, arginine, lysine, leucine, proline, cysteine, glutamine, aspartate, and allantoin was added after 1 s and removed after 2 s. PepT1 was used as a positive control and 100, 33, 11, 3.7, 1.2, and 0.4 mM glycyglycine were added. Graphs were generated using GraphPad Prism, version 5.1, and current (nA) was plotted against time (s) for each compound.

Apoptosis, Cell Cytotoxicity, and Viability Measurement

Apoptosis, cell cytotoxicity, and viability measurements were performed on (I) transfected HEK293T cells 24 h post-transfection and on (II) 24-h post-transfected HEK293T cells kept on different media [control: DMEM (Thermo Scientific); no glucose: DMEM, no glucose, no glutamine, no phenol red (A1443001, Thermo Scientific); high glucose; no glucose, DMEM supplemented with 50 mM Glucose (Sigma Aldrich); high-NaCl DMEM: DMEM media supplemented with 10 g/L extra NaCl; high KCl: DMEM media supplemented with 0.4 g/L extra KCl; low-NaCl media: MEM vitamin solution (100×) (11120037, Thermo Scientific), MEM amino acids solution (50×) (11130051, Thermo Scientific), 0.4 g/L KCl, 0.264 g/L CaCl₂, 0.2 MgSO₄, and 25 mM glucose (Sigma Aldrich); low-KCL media: MEM vitamin solution (100×) (11120037, Thermo Scientific), MEM amino acid solution (50×) (11130051, Thermo Scientific), 3.7 g/L NaHCO₃, 0.14 g/L NaH₂PO₄, 0.2 g/L KCl, 0.264 g/L CaCl₂, 0.2 MgSO₄, and 25 mM glucose (Sigma Aldrich)] using the ApoTox-Glo™ Triplex kit (Promega) according to the manufacturer's protocol. Fluorescence and luminescence were measured using a BMG Labtech Omega plate reader. The (I) mean fluorescence and luminescence signal (±SEM) (*n* = 2, with 12 measurement points in each) and the (II) mean fluorescence and luminescence signal (±standard error of the difference) (*n* = 6) were plotted using GraphPad Prism 5, and differences were studied using (I) unpaired *t*-test (**p* < 0.05, ***p* < 0.01, ****p* < 0.001) and (II) appropriate ANOVA [one-way ANOVA (differences in apoptosis) or Kruskal–Wallis (differences in cytotoxicity)] with unpaired *t*-test or Mann–Whitney as *post hoc* test (adjusted *p*-values: * < 0.0489, ** < 0.0099, *** < 0.0001).

Membrane Potential Measurement

The membrane potential on transfected cells was measured using the FluoVolt™ Membrane Potential kit (Ceriani and Mammano, 2013; Bedut et al., 2016) (Thermo Scientific) according to the manufacturer's instructions. Briefly, cells were washed twice in Live Cell Imaging Solution (LCIS; Thermo), before 2 ml FluoVolt™ loading solution was added, and incubated for

15 min at room temperature. The FluoVolt™ loading solution was removed, and the cells were washed twice in LCIS. Then, 2 ml of 20 mM glucose stock in LCIS was added, followed by imaging using fluorescence signal which was recorded using an ImageXpress Micro XLS (Molecular Devices) microscope with ×20 objective. Images were taken at an interval of 10 s, for 10 timepoints, with FITC filter (excitation: 482 nm; emission: 536 nm). Each well was imaged for two sites in FITC channel with four replicates. All experiments were performed at a controlled temperature of 37°C. The basal membrane potential was measured as well as after treatment with valinomycin (V1644, Thermo Scientific). The images were handled, and the fluorescent intensity was measured using ImageJ, Fiji edition (Schindelin et al., 2012). The average fluorescent intensity per area was calculated from each frame at each timepoint per well. Graphs with 95% confidence interval were generated, and statistical analysis was performed using GraphPad Prism 5. Unpaired *t*-tests were performed (**p* < 0.05, ***p* < 0.01, ****p* < 0.001).

RESULTS

CG4928 Is Evolutionary Conserved and Orthologs to UNC93A

Previously, hsUNC93A has been presented to be conserved in mammals and *C. elegans*, but the proteome from *D. melanogaster* has not been included. Here a Hidden Markov model for UNC93A was built and used to search for related sequences. Nine proteomes were included in the search: *A. aegypti*, *Anolis carolinensis*, *C. elegans*, *Ciona intestinalis*, *Danio rerio*, *D. melanogaster*, *Gasterosteus aculeatus*, *Gallus gallus*, and *M. musculus*. Orthologs to UNC93A were found in all included proteomes representing several branches of organisms (Table 1), and its closest relatives MFSD11 and UNC93B1 were also identified, consistent with earlier findings (Ceder et al., 2017). UNC93A had one ortholog in all species except *D. melanogaster* (CG4928, 34.8%; CG2121, 26.8%) and *A. aegypti* (aaUNC93A1, 30.2%; aaUNC93A2, 37.1%), where two orthologs were found. MFSD11 was found in all proteomes except in *A. carolinensis*, and UNC93B1 was not found in *D. melanogaster*, *A. aegypti*, and *A. carolinensis* (Figure 1A). Furthermore, global protein alignments between human proteins and orthologs in *D. melanogaster* were studied using EMBOSS Needle (Li et al., 2015). CG4928 was found to be most identical to hsUNC93A, indicating that CG4928 is the ortholog to UNC93A. However, of the two copies identified in *D. melanogaster*, CG4928 also had the highest resemblance to hsUNC93B1, but the protein identity was lower between these two orthologs compared with the protein identity of CG4928 and hsUNC93A. CG18549 is the orthologous protein to hsMFSD11 (Table 2).

CG4928 Is Expressed in Malpighian Tubules

The gene expression of CG4928 in Malpighian tubules and in the intestine was investigated using the GAL4-UAS system coupled to GFP. The expression was visualized by crossing the enhancer trap

TABLE 1 | Amino acid identity comparison (Li et al., 2015; Madeira et al., 2019) of human protein sequences of UNC93A, UNC93B1, and MFSD11 and their identified orthologs.

Species	Protein name and amino acid identity		
<i>H. sapiens</i>	UNC93A	UNC93B1	MFSD11
<i>A. aegypti</i>	aaUNC93A1 30.2%		aaMFSD11 44.9%
	aaUNC93A2 37.1%		
<i>A. carolinensis</i>	acUNC93A 57.3%	acUNC93B1 66.2%	
<i>C. elegans</i>	ceUNC-93 20.6%		ceMFSD11g 32.5%
<i>C. intestinalis</i>	ciUNC93A 39.6%		ciMFSD11 50.4%
<i>D. melanogaster</i>	CG4928 34.8%		CG18549 41.5%
	CG2121 26.8%		
<i>D. rerio</i>	drUNC93A 55.2%	drUNC93B1 56%	drMFSD11 66.7%
<i>G. aculeatus</i>	gaUNC93A 55.9%	gaUNC93B1 61%	gaMFSD11 64.6%
<i>G. gallus</i>	ggUNC93A 64.1%	ggUNC93B1 57.4%	ggMFSD11 81.8%
<i>M. musculus</i>	mmUNC93A 71.9%	mmUNC93B1 87.4%	mmMFSD11 93.1%

TABLE 2 | Comparing the amino acid identity of UNC93 protein sequences identified in human, *D. melanogaster*, and *C. elegans*.

	hsUNC93A (%)	hsUNC93B1 (%)	ceUNC-93 (%)
CG4928	34.8	20.9	22
CG2121	26.8	16.8	21.3

hs, *H. sapiens*; ce, *C. elegans*.

line, CG4928-Gal4, to the UAS line coupled to GFP, and the organ was dissected and imaged. Expression was found in Malpighian tubules, located to round cells, compared with controls (CG4928-Gal4 and UAS-GFP lines) (see Supplementary Figure S1A). Meanwhile, the expression in the intestine was difficult to image since food caused autofluorescence. However, a few cells were found to display GFP expression, but whether the cells are located within the wall of the intestine or are surrounding hemocytes remains uncertain (Supplementary Figure S1B).

Ubiquitous Knockdown of CG4928 Induce Renal Dysfunction

To study the function of CG4928, gene expression was reduced with the ubiquitous daughterless-Gal4 (*da-Gal4*) and CG4928-UAS-RNAi lines. Crosses were placed in 25°C, and offspring were raised in 28°C. Knockdown of CG4928, using the CG4928-UAS-RNAi KK line (CG4928 knockdown), caused edema, where accumulation of fluid appeared both in the body (abdominal cavity) and the Malpighian tubules in males and females raised at 28°C (Figure 1B), while offspring did not survive pupation at 29°C. The CG4928-UAS-RNAi GD line did not produce viable offspring. It was possible to get female offspring to enclose at

18°C and few of them developed edema (data not shown), but the number of offspring was limited, and knockdown was not sufficient (data not shown); hence, the line was not used further. To verify the knockdown of *CG4928*, qRT-PCR was performed. *CG4928* expression was reduced compared with the controls *da-Gal4 > w1118* (Driver control) and *w1118 > CG4928-UAS-RNAi KK* (RNAi control) (**Supplementary Figure S1C**). Due to the phenotype, *CG4928* knockdown was performed using several Malpighian tubule-specific Gal4 lines, but these crosses did not reproduce edema and were, hence, not used further. It could be that these are weaker compared to *da-Gal4* or that the expression needs to be reduced in all tissues that express *CG4928* for the phenotype to develop. There is one reported off-target gene *CG9122* that encodes a tryptophan hydroxylase, which was accounted for. When performing knockdown of the off-target gene, no edema was observed (data not shown).

Malpighian tubules were dissected to compare the morphology between the Driver control, RNAi control, and *CG4928* knockdown flies. The tubules collected from *CG4928* knockdown females had a prominent yellow-colored substrate and fluid accumulation (**Figure 1C**), observed within the cells, compared with both controls. To investigate the renal function in *CG4928* knockdown flies, Ramsay assay was performed. Briefly, the Malpighian tubules from females were dissected, and the secretion capacity was measured after 2 h of secretion. *CG4928* knockdown was found to result in a marked reduction of fluid secretion with a secretion rate five times lower than both controls (**Figure 1D**). To further investigate how the edema affected the osmotic balance, the hemolymph osmolality was measured. The Driver control had an osmolality of around 1,000 mOsm/kg, RNAi control had 800 mOsm/kg, and *CG4928* knockdown had 500 mOsm/kg (**Figure 1E**), indicating that the *CG4928* knockdown has a lower concentration of substances dissolved in the hemolymph. It is important to note that the osmolality for the control flies is higher than normal, probably due to desiccation when raised at high temperatures (Albers and Bradley, 2004).

Edema was quantified through body and hemolymph weighing, where both *CG4928* knockdown males and females were found to be heavier than controls (**Figure 1F**). The extracted hemolymph from both *CG4928* knockdown males and females weighed more compared with those of the controls (**Figure 1G**). Furthermore, the sodium and the potassium levels in the extracted hemolymph were measured. The sodium level in the 20- μ l hemolymph extracted from *CG4928* knockdown was 38.7% higher, while the potassium level was 8.6% lower, compared with those of the controls (**Figure 1H**). However, the sample for the *CG4928* knockdown flies was collected from 500 flies and for both controls from 800 flies. This skewness in sample size would indicate that the masses of sodium and potassium were approximately 121 and 46% higher, respectively, in the *CG4928* knockdown flies compared with the controls.

CG4928 Knockdown Affect Ion Levels in Malpighian Tubules

Within the Malpighian tubules, there is a continuous flow of ions to drive the transport of various molecules. The accumulation

observed in the abdominal cavity and the Malpighian tubules, the low secretion rate, and the altered status of the hemolymph indicate that there is a disturbance in cellular processes affecting the concentrations of molecules over the membranes of the cells in Malpighian tubules, but plausible also with other excretory organs such as the hindgut. However, this organ was not further examined.

To get a more detailed view, Malpighian tubules were dissected and an elemental (ion) analysis was performed. In total, 69 elements were measured using ICP-SFMS. *CG4928* knockdown flies had altered amounts of boron, cadmium, cobalt, and potassium (**Figures II–L**), where boron and cobalt were higher and cadmium and potassium were lower compared with those of the controls. For the remaining element, no alterations were observed or the detected levels were too low (**Supplementary Table S1**).

CG4928 Has 12 Transmembrane Helices Predicted to Fold Like MFS Transporters

Homology modeling using PROTTER (Omasits et al., 2014) predicted a 2D topology of *CG4928* (**Figure 2A**) similar to the common structure of MFS proteins with 12 transmembrane helices (Madej et al., 2013). The homology model for *CG4928* has long N- and C-termini that are present on the same side of the membrane compared to the predicted model for hsUNC93A that has shorter termini (Ceder et al., 2017). The tertiary model predicted using Phyre2 (Kelley et al., 2015) revealed a globular protein that folds like MFS proteins (Yan, 2015) (**Figure 2B**). Furthermore, 89% of the amino acids were modeled with 99.9% confidence, and 12% of the amino acids matched the template structure. The high confidence of the overall assimilation suggests that *CG4928* has the overall structure illustrated.

RNA Sequencing Reveals CG4928 Knockdown to Affect Membrane-Bound Biosynthesis and Signaling Genes

RNA sequencing was performed on *CG4928* knockdown flies and controls to investigate if *CG4928* knockdown caused alterations in the mRNA expression profile of the flies. The sequencing was performed using Ion Total RNA sequencing, and the results were analyzed using STAR mapper (Dobin et al., 2013) and Cufflink (Trapnell et al., 2010, 2013) software. Genes were considered differentially expressed if they were significantly different (\log_2 fold change > 1.5 or < -1.5) in *CG4928* knockdown flies compared with both controls. This approach generated 160 differentially expressed genes, and of those, approximately 53.1% (62 genes) could be categorized into 13 gene clusters: (i) integral membrane components, (ii) membrane transporters, (iii) ATP and nucleotide transport, (iv) enzyme and proteolysis, (v) secondary metabolites biosynthesis, (vi) carbohydrate metabolism, (vii) reduction and oxidation reactions, (viii) signaling, (ix) transcription, (x) cell growth and differentiation, (xi) life cycle and circadian rhythm, (xii) circulation, and (xiii) immunity (**Figure 2C**). It is noteworthy that one gene can cluster into more than one gene cluster. In total, 50 genes were upregulated and 12 were downregulated

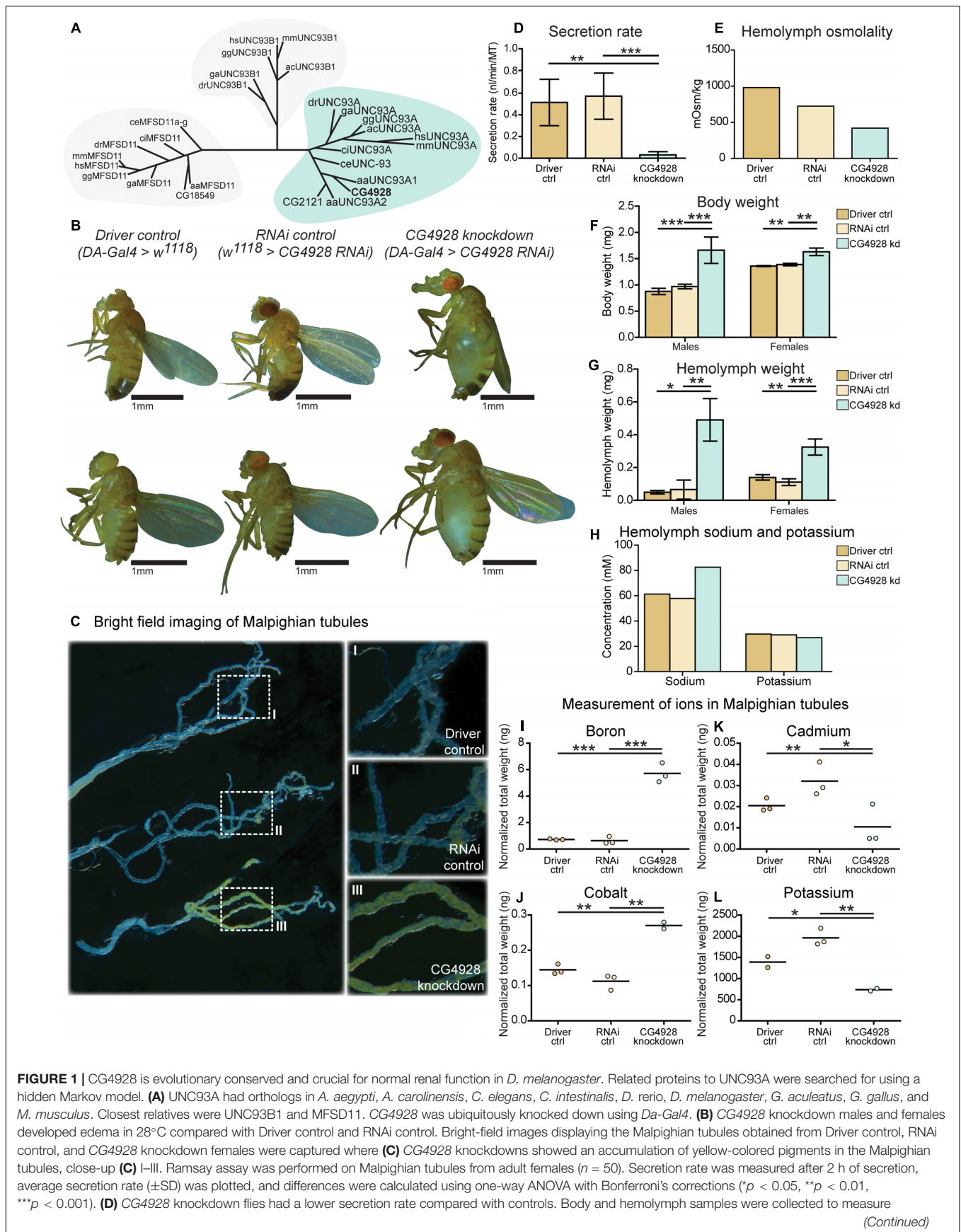


FIGURE 1 | Continued

osmolality, differences in body and hemolymph weight, and concentrations of sodium and potassium. Then, 20 μ l of hemolymph sample from adult flies (*CG4928* knockdown $n = 500$, Driver control $n = 800$, RNAi control $n = 800$) was collected to measure osmolality and sodium and potassium concentrations. **(E)** *CG4928* knockdowns had lower osmolality. Body and hemolymph weight were measured in males and females ($n = 30$); weight was calculated against the number of flies. Graphs represent mean (\pm SD); differences were calculated with Kruskal–Wallis and Dunn's correction ($*p < 0.05$, $**p > 0.01$, $***p > 0.001$). *CG4928* knockdown flies were heavier, **(F)** body and **(G)** hemolymph weight, than controls and were found to have **(H)** 38.7% higher concentration of sodium and 8.6% lower concentration of potassium. Ion levels in Malpighian tubules from adult females were measured using ICP-SFMS ($n = 2–3$ per genotype, with Malpighian tubules from 60 flies in each). Data are plotted with a scatter plot; differences were calculated using unpaired *t*-test with Bonferroni's correction (adjusted *p*-values: $*p < 0.0492$, $**p < 0.0099$, $***p < 0.0001$). *CG4928* knockdown flies had altered levels of **(I)** boron, **(J)** cadmium, **(K)** cobalt, and **(L)** potassium.

(**Figure 2D** and **Supplementary Table S2**), where one third of the regulated proteins, mostly orphan genes without a known function, were categorized as non-clustering genes. The emerging pattern did not point to a clear pathway that *CG4928* could be involved in; however, it appears important for normal cellular status since genes responsible for transcription, membrane permeability, transport, and synthesis were affected. Some regulated and non-regulated genes were *Yp1*, *Yp2*, and *Pxt* that were upregulated, *Oatp58Db* and *Hsp70Aa* that were downregulated, and *CG9122* (off-target to *CG4928*) and *Rpt4R* that were not altered (**Figure 2E**). To verify RNA sequencing, qPCR was performed on matched samples for four of the genes: *Pxt*, *CG9122*, *Rpt4R*, and *Oatp58Db* (**Supplementary Figures S1D–G**). Gene expression was similar compared with the findings from RNA sequencing, except *Oatp58Db* that was upregulated when performing qPCR.

CG4928 Knockdown Flies Are Sensitive to Starvation

Since *CG4928* knockdown implies to affect the ion homeostasis and genes involved in metabolism, the metabolic condition of the *CG4928* knockdown flies was studied further. We explored several aspects of metabolism, starvation tolerance, and locomotor by monitoring their activity in DAMS and food intake as well as measuring the stored and circulating macronutrient levels. The *CG4928* knockdowns had lower starvation tolerance, but no difference in activity and food intake were observed (**Supplementary Figures S1H–J**). However, differences in stored and circulating sugars, fats, and proteins could give an indication why they starve faster. The *CG4928* knockdowns had higher levels of stored and circulating sugars before starvation (0 h) (**Supplementary Figures S1K–N**). No difference was observed after 12 and 24 h of starvation. The levels of sugars gradually decreased over the time of starvation, suggesting that *CG4928* knockdown flies can recruit sugars and do not deplete the storage too quickly. A similar result was observed for circulating lipids (**Supplementary Figure S1O**). No difference was seen for the protein levels in the hemolymph (**Supplementary Figure S1P**). Hence, the sensitivity to starvation could not be explained by altered activity, food intake, and macronutrient deficiencies; hence, what exactly provokes this phenotype is still unknown.

The Edema Is Minimized With Amiloride and Rescued With Ion-Free Diets

Five-day-old *CG4928* knockdown male flies and controls were transferred and fed diuretics commonly used for treating edema

in humans and ion-free (containing sugar and yeast) diets to treat the edema. In addition, diets enriched with NaCl or KCl were used. Photos of the flies were captured, and body and hemolymph weight was measured, respectively.

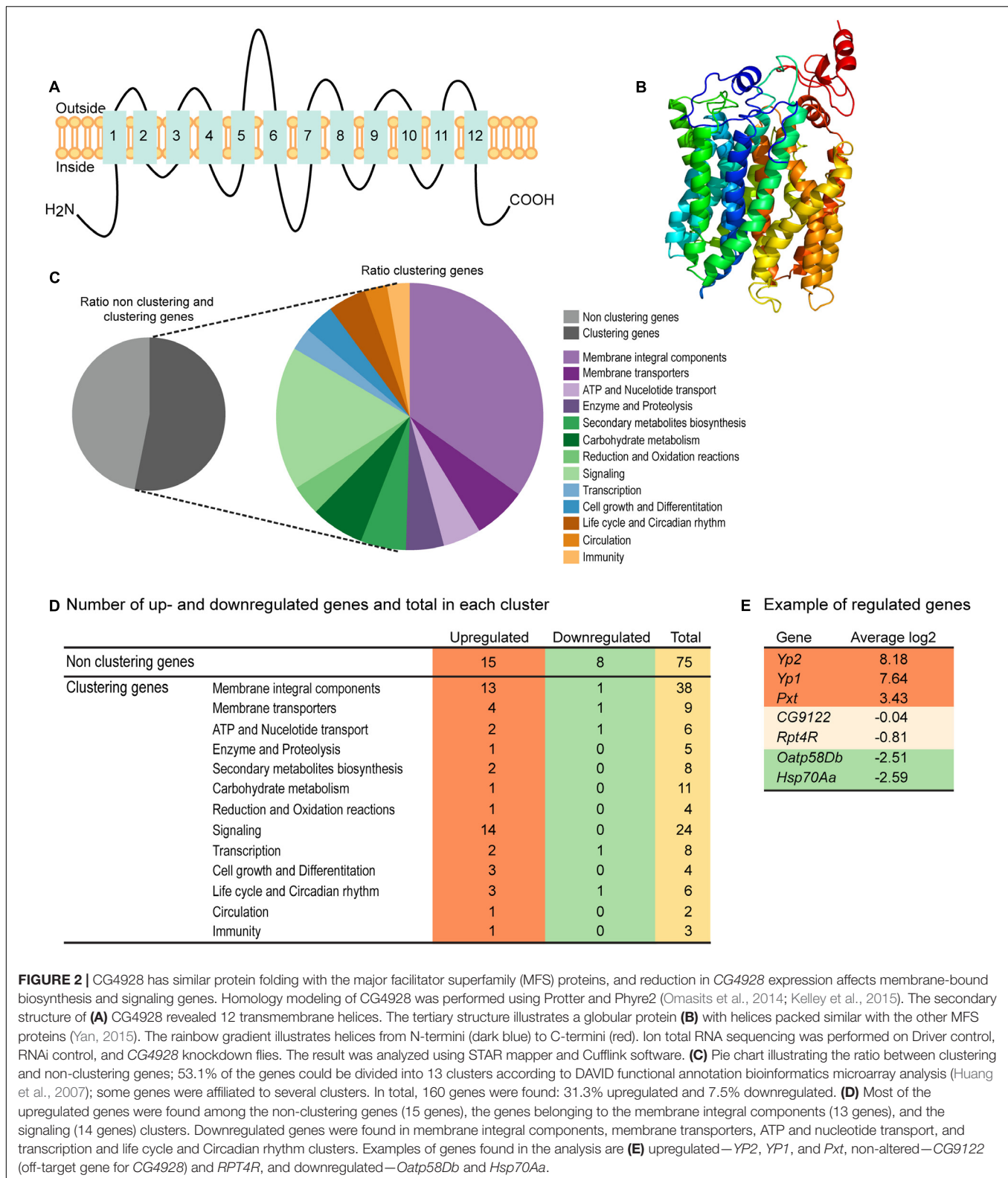
Amiloride—a blocker for epithelial sodium channels (ENaCs), mannitol—a sugar alcohol, and furosemide—an inhibitor of the Na-K-Cl cotransporter (NKCC) were used. Diuretics were dissolved in water and added to the standard food, except furosemide that was dissolved in acetone before its addition to food. On standard food, the *CG4928* knockdowns (used as control) developed edema as observed before (**Figure 3A**). Amiloride reduced both body and hemolymph weight compared with *CG4928* knockdown flies on standard food (**Figures 3B,L,M**), while mannitol only decreased the body weight (**Figures 3C,L,M**). Since furosemide was solved in acetone, the flies maintained on standard food with acetone (acetone control) were used as controls. The flies kept on food supplemented with acetone had a similar phenotype as the *CG4928* knockdown on standard food (**Figures 3D,L,M**), and furosemide did not rescue the phenotype (**Figures 3E,L,M**). When comparing the body and hemolymph weight against the Driver control and the RNAi control, only mannitol restored the body weight of *CG4928* knockdown flies compared with both controls, while the hemolymph weight was not affected by any of the diuretics (**Supplementary Figures 1Q,T**).

The ion-free diets were made with 0.1 mg/ml yeast and either sucrose or glucose in two concentrations, 0.1 and 0.4 mg/ml. Sugar and yeast were dissolved in deionized water. All diets restored the body and hemolymph weight and rescued the phenotype, both compared with the *CG4928* knockdown flies fed standard food (**Figures 3F–I,N,O**) and compared with the Driver and RNAi controls (**Supplementary Figures S1R,U**).

When feeding flies with sodium- and potassium-enriched food, the phenotype was not affected (**Figures 3J,K,P,Q** and **Supplementary Figures S1S,V**).

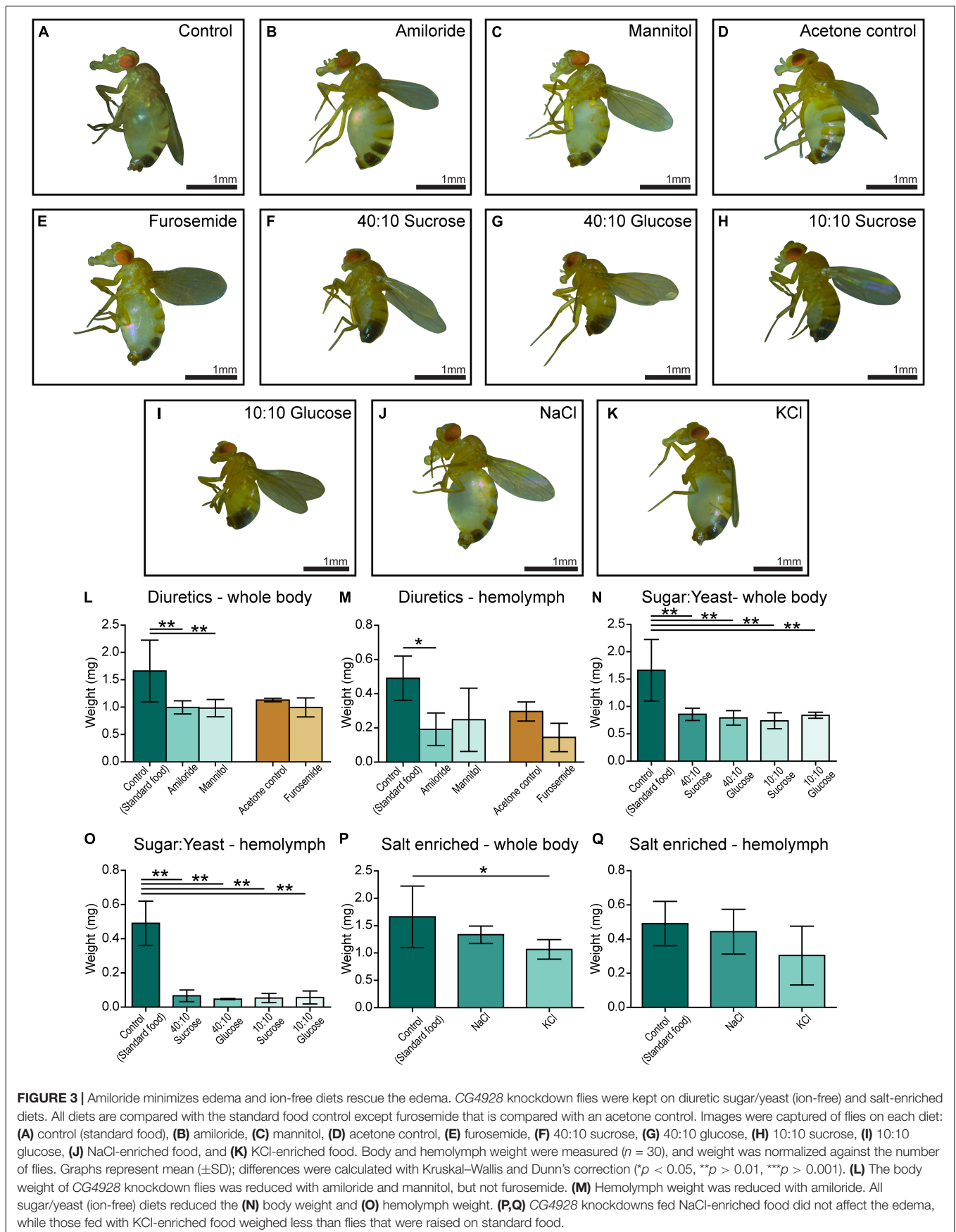
UNC93A as a Regulatory Subunit of TASK¹ Channels

In *C. elegans*, Unc-93 is suggested to act as a regulatory subunit of Sup-9, an ortholog to the human KCNK family of potassium transports important for resting membrane potentials (Goldstein et al., 2001; Talley et al., 2001). The phylogenetic relationship between human, fly, and *C. elegans* was analyzed, and Sup-9 was found to be most similar to KCNK3, KCNK9, and KCNK15 in humans and TASK6 and TASK7 in flies (**Figure 4A**), which is consistent with earlier findings



(de la Cruz et al., 2003). To investigate if KCNK3, KCNK9, and UNC93A co-localize, ICC and PLA were performed on wild-type and CG4928:Flag-transfected SH-SY5Y cells. KCNK15

was not included in the study since the antibodies that are commercially available were not suitable to use with the anti-UNC93A antibody. The immunoreactivity revealed



similar staining patterns for UNC93A, KCNK3, and KCNK9 in wild-type SH-SY5Y cells (Figures 4B,C), and no signal was detected in the negative control (Supplementary Figure S2A). The immunoreactivity for anti-Flag on CG4928:Flag-transfected SH-SY5Y cells also displayed an overlap with KCNK3 and KCNK9, while the negative control was blank (Supplementary Figures S2B–D). The ICC suggests that they are located in the same cell, and therefore PLA was conducted: the total, cytoplasmic, and nucleic PLA signal per cell was calculated using Duolink™ Image tool. UNC93A and KCNK3 were found to co-localize (Figures 4D,E), and a comparable result was observed for UNC93A and KCNK9 (Figures 4E,G). In CG4928:Flag-transfected cells, anti-Flag, anti-UNC93A, and anti-KCNK3 were found to co-localize (Supplementary Figures S2E,F,M,N), while no or weak co-localization could be detected with KCNK9 (Supplementary Figures S2G,O). No PLA signal was detected in the negative controls for Flag, UNC93A, and KCNK3 antibodies, while weak signals were detected for KCNK9 (Supplementary Figures S2H–K).

CG4928 as a Transporter

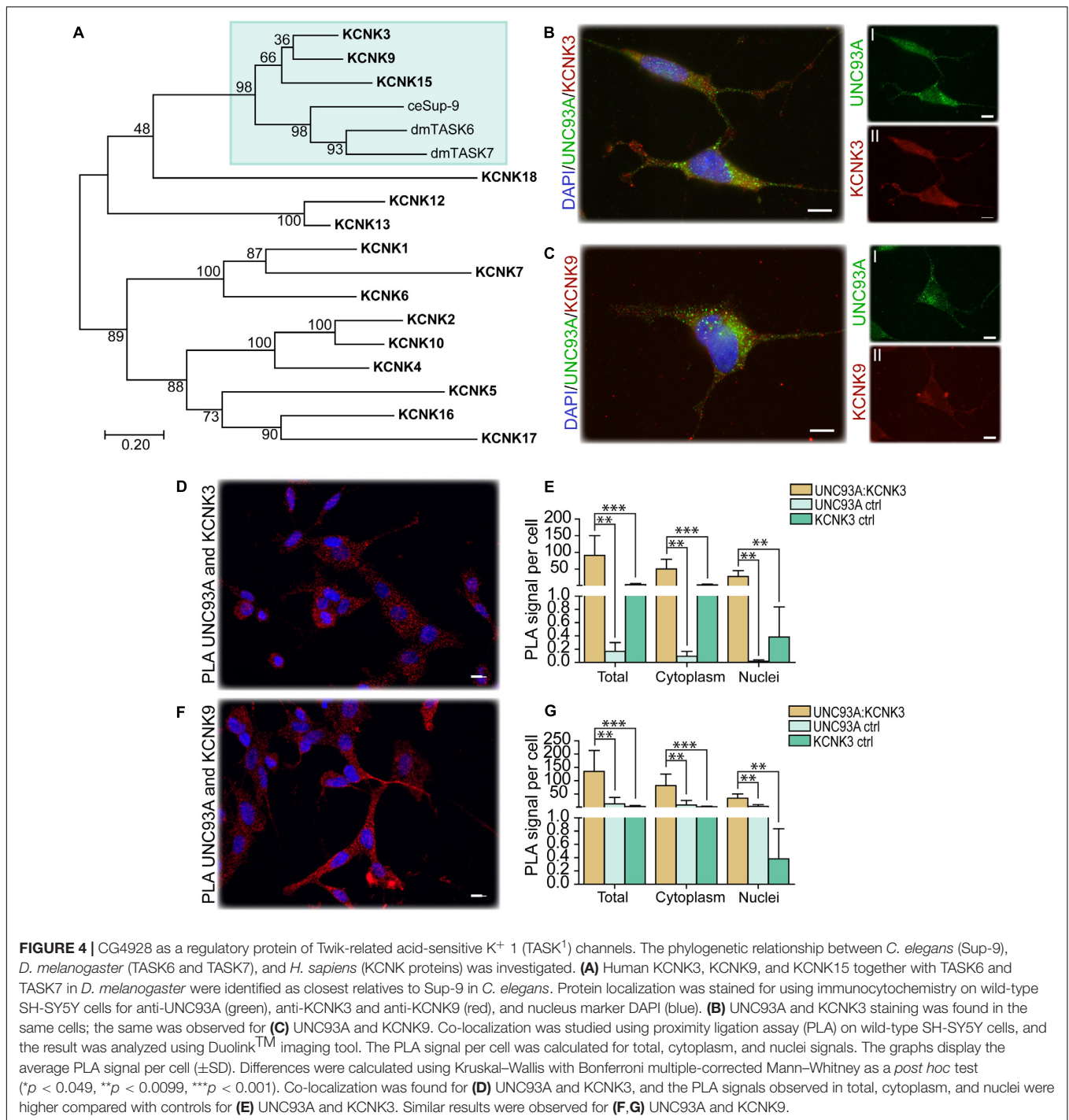
Human UNC93A has the characteristics and 2D topology to be an authentic transporter (Ceder et al., 2017), and it has been predicted to be a putative SLC (Perland and Fredriksson, 2017; Perland et al., 2017a). Hence, one can assume that CG4928 possesses similar characteristics, and the substrate profile of CG4928 was investigated. Before performing transport assays, we investigated the endogenous UNC93A expression in HEK293T cells using ICC to determine the baseline expression of UNC93A. Immunoreactivity for UNC93A was detected in the cells (Supplementary Figure S2L).

Thereafter, HEK293T cells were transfected with CG4928:eGFP, CG4928:Flag, or control (empty) vectors, the membranes were isolated, and western blot was used to verify the transfection. There is no antibody available for CG4928, and therefore the human anti-UNC93A antibody was used during western blot. To determine the binding probability and specificity to CG4928 using the human anti-UNC93A, antibody protein alignments were performed. However, the epitope for anti-UNC93A is not specified by the company, except that it is an 18-amino-acid-long sequence located at the C-terminus of the human UNC93A. Therefore, protein alignments, both global and local, were performed between the three isoforms of CG4928 and human UNC93A (Supplementary Dataset S4). The alignment suggests that the antibody could bind to the fly ortholog, but probably not as specific as to the human protein. Anti- β -actin was used for normalization, and anti-UNC93A was used to stain for vector insertion. One band was detected for β -actin at 43 kDa, and one band for UNC93A was detected at 46 kDa (Supplementary Figures S2P,Q), which is consistent with previous findings (Ceder et al., 2017). Similar bands were detected for CG4928:Flag-transfected cells (data not shown). After normalization with anti- β -actin, the protein expression of UNC93A was higher in both CG4928:eGFP- and CG4928:Flag-transfected cells compared with the control (Supplementary Figures S2R,S). Hence, we proceeded with the transfected cells and performed SSM-based electrophysiology

(Bazzone et al., 2017). In total, six sugars (fructose, galactose, glucose, lactose, saccharose, and xylose; 200 mM) and 12 amino acids and peptides (alanine, allantoin, arginine, aspartate, cysteine, glutamate, glutamine, glycine, glycyglycine, leucine, lysine, and proline; 20 mM) were tested. No changes in current were observed when adding the different sugars at pH 7 and 5 (Figures 5A,B and Supplementary Figures S2T–W). For amino acids, alterations in current for aspartate and lysine were observed (Figures 5C,D). However, a change was also observed for the control vector (Supplementary Figure S2X), and when the currents between all three vectors were compared, no difference was detected (Figures 5E,F).

Overexpression of CG4928 Induces Apoptosis and Alters the Membrane Potential

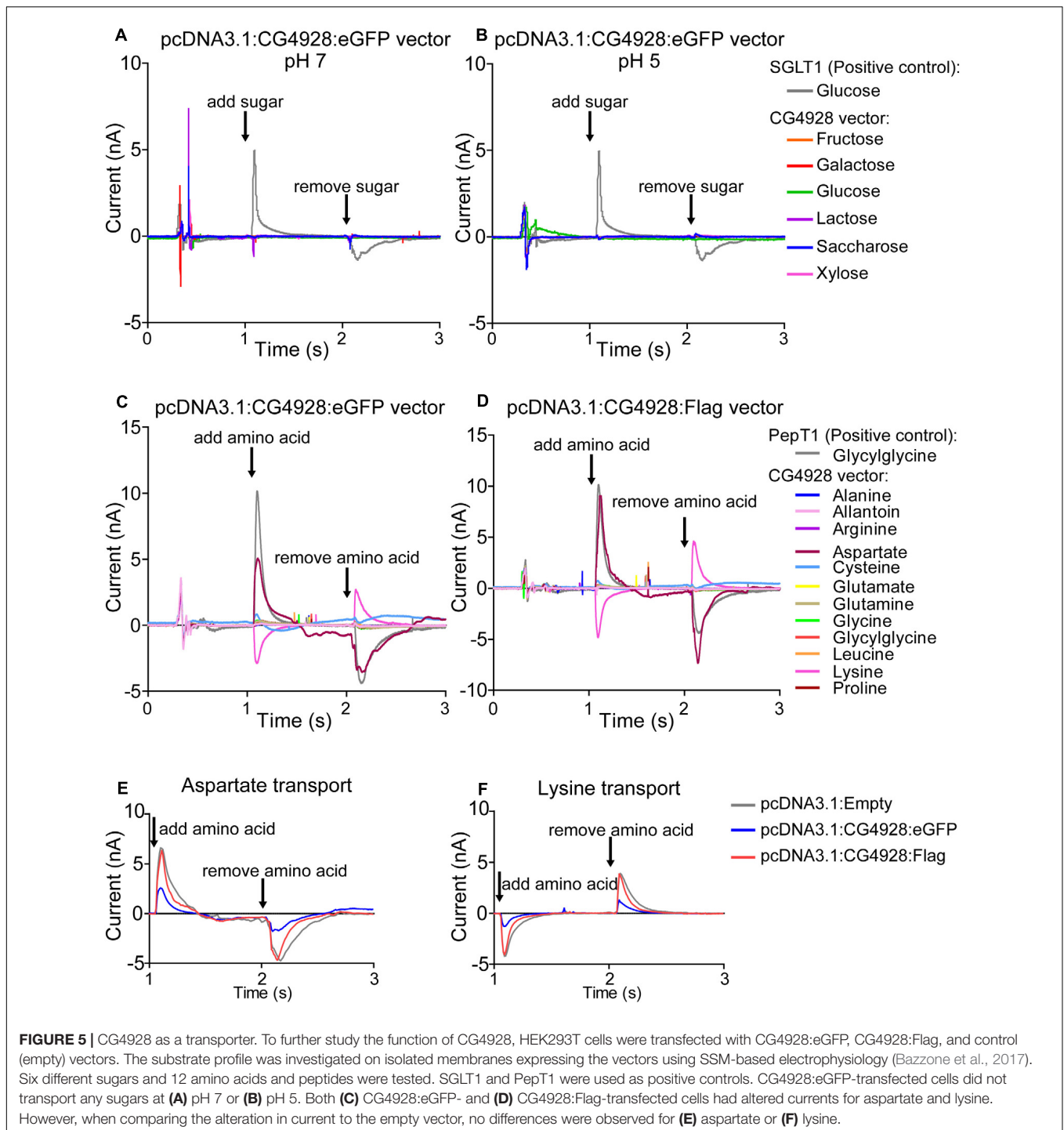
An observation at 24 h post-transfection of CG4928 vectors was the increased cell death. Therefore, apoptosis, cytotoxicity, and viability were measured using the ApoTox-Glo™ Triplex kit, where protease activity and caspase-3/7 cleavage are measured (Niles et al., 2007). The CG4928:eGFP-transfected cells had a higher degree of apoptosis and cytotoxicity and reduced viability compared with the control (Figures 6A–C). Similar results were obtained for HEK293T cells transfected with CG4928:Flag (data not shown). To further investigate if cell death could be prevented, CG4928:eGFP cells and control cells were maintained on different media: DMEM (control), high sodium, high potassium, low sodium, and low potassium. The average luminescence or fluorescence differences between CG4928:eGFP cells and control cells were investigated (Figure 6), and the comparisons between CG4928:eGFP cells and control cells for each media are plotted in Supplementary Figures S2Y,Z, where also no glucose and high glucose media were included. The degree of apoptosis and cytotoxicity decreased when cells were kept on high-sodium media, while the conditions were unchanged or worsened on high-potassium, low-sodium, and low-potassium media (Figures 6D,E). Compared with the control, only high sodium hindered apoptosis, while the increased cytotoxicity was only reproduced in cells maintained on DMEM and high-potassium and low-potassium media (Supplementary Figures S2Y,Z). The results show that overexpression of CG4928 induces cell death when maintained on media containing 150 mM sodium, but 300 mM of extracellular sodium helps the cell to survive. This could be due to a change in the net charge over the membrane if CG4928 forms a complex with TASK¹ channels as suggested. If this is true, the CG4928-overexpressing cells should display a disturbance of the resting (basal) membrane potential. To test this, the potential was measured using FluoVolt™ membrane potential kit, which detects changes in membrane potential (Ceriani and Mammano, 2013; Bedut et al., 2016). Briefly, CG4928:eGFP- and control-transfected cells were stained with FluoVolt™, images were taken with FITC at an interval of 10 s for 10 timepoints in four wells per vector, and the average fluorescence intensity per area was calculated for each well. As a positive control, valinomycin was added to the transfected cells, which depolarized the cell and increased the fluorescence



signal. Valinomycin, as predicted, increased the membrane potential (**Supplementary Figure S2AA**). The basal membrane potential was found to be lower in CG4928:eGFP-transfected cells compared with the control (**Figures 6F,G**), supporting the hypothesis that CG4928 alters membrane potential, probably by dysregulating KCNK3 and/or KCNK9 (Gabriel et al., 2012; Sun et al., 2016), leading to hyperpolarization of the cells (as illustrated in **Figure 6H**).

DISCUSSION

Lately, several orphan transporters suggested to be putative SLCs (Perland and Fredriksson, 2017; Perland et al., 2017a) have begun to be characterized with focus on evolutionary relationship, protein structure prediction, and expression profile (Perland et al., 2016, 2017b,c; Ceder et al., 2017; Lekholm et al., 2017). Previous phylogenetic analyses predicted UNC93A

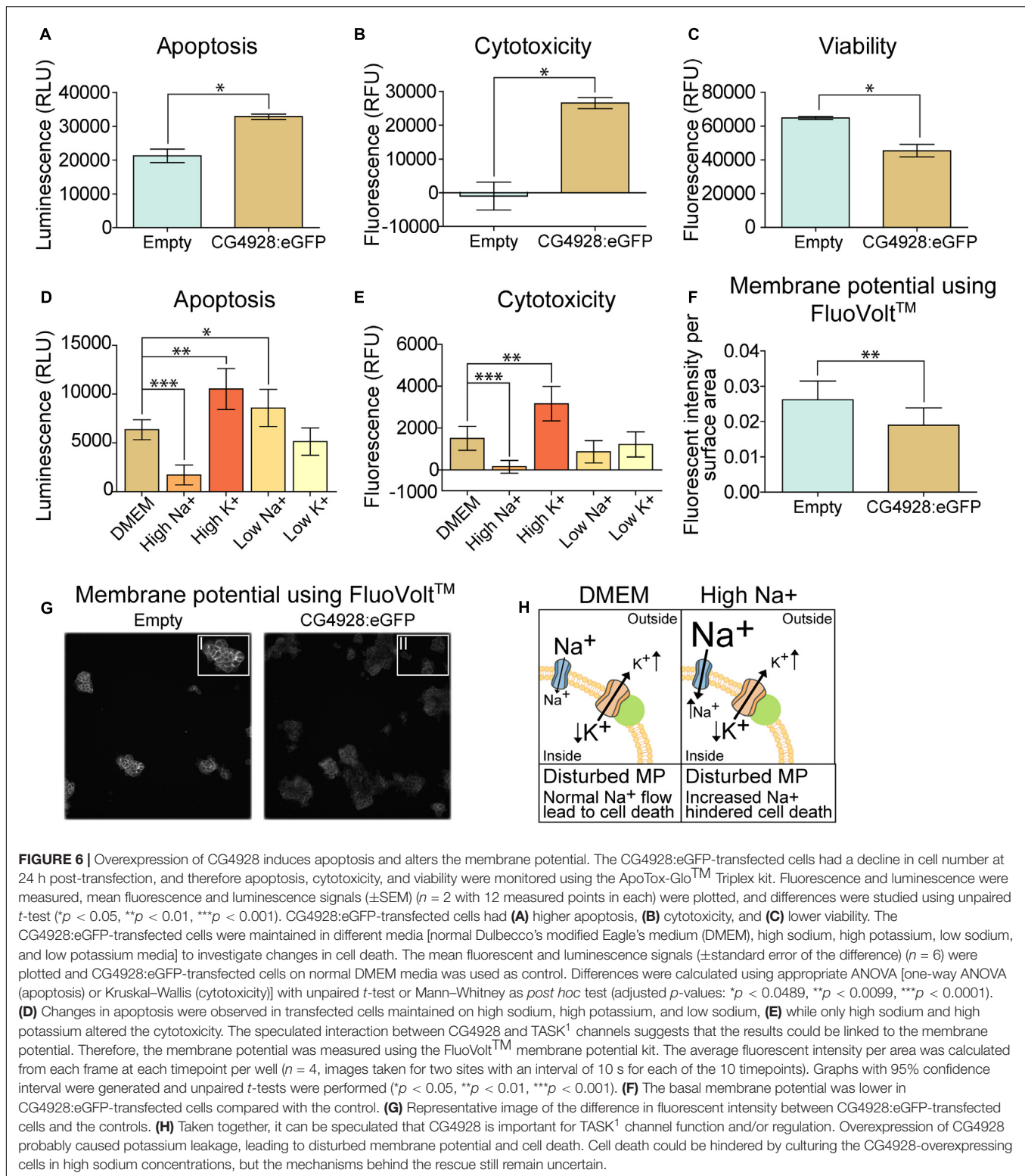


to be evolutionary preserved (Ceder et al., 2017; Perland and Fredriksson, 2017; Perland et al., 2017a), which we also confirmed. In comparison to mammals, two copies of UNC93A, CG4928, and CG2121 were identified. CG4928 was found to be most similar to hsUNC93A but also resembled human UNC93B1, indicating that this orthologous protein in *D. melanogaster* might possess features from both proteins in human. The tissue expression of the two UNC93 proteins varies in humans.

According to NCBI² and the human protein atlas³, UNC93B1 is abundantly expressed in the body, whereas UNC93A is mainly expressed in the digestive tract and the kidney (Fagerberg et al., 2014; Uhlen et al., 2015). However, *Unc93a* has been found to have an abundant gene expression in mice, but also here

²www.ncbi.nlm.nih.gov/gene

³www.proteinatlas.org



the expression was higher in peripheral organs, with a high expression reported in the intestine, liver, spleen, and fat tissues (Ceder et al., 2017). In *D. melanogaster*, little is known about the orthologs' expression, and verifications have not been performed

for all tissues. However, CG4928 is reported to be expressed in several, but not all, organs of the fly, with highest expression in the salivary gland, hindgut, and Malpighian tubules. Meanwhile, in larvae, the expression is much more restricted to the gut and

Malpighian tubules⁴ (Robinson et al., 2013). *CG2121*, on the other hand, is lowly to moderately expressed in almost all organs in the adult fly (Robinson et al., 2013). According to the tissue expression profiles in these three species, *UNC93A* and *CG4928* seem to be more alike compared to *UNC93B1* and *CG4928*.

CG4928 is, according to transcriptome analyses, highly expressed in the digestive system and Malpighian tubules in both larvae and adult fly (Chintapalli et al., 2007). A study has found that *CG4928* is 13 times more highly expressed in Malpighian tubules compared to whole-body expression (Wang et al., 2004), which corresponds well to our findings. *CG4928* was found in large cells in the lower and the main segment of Malpighian tubules, which are simplified versions of the human kidneys in terms of their cellular structure and function (Gautam et al., 2017). Within the Malpighian tubules, there are two major cell types carrying out most actions, the principal cells and the stellate cells (Sozen et al., 1997). *CG4928* is possibly expressed in the principal cells based on the morphological similarities to these cells (Sozen et al., 1997; Soderberg et al., 2011; Roy et al., 2015), which are important for maintaining ion and fluid balance. GFP expression was also detected in cells surrounding, or possibly located within, the membrane of the midgut and the hindgut, but the number of cells expressing GFP, hence being *CG4928*-expressing cells, were few and did not correspond well to the microarray data. *CG4928* has also been reported in hemocytes (Stofanko et al., 2008), the “white blood cells” of flies (Holz et al., 2003). When puncturing and mounting whole larvae from *Gal4-CG4928 > UAS-GFP* offspring to visualize the tissue expression, we detected GFP in “free-floating” cells, probably hemocytes, but we were not able to verify the results (data not shown). It is important to note that further research is needed to establish the role of *CG4928* in hemocytes, the midgut, and the hindgut. However, it is possible that the observed phenotype is linked to one or more of these tissues.

Interestingly, in comparison to the protein structure of *UNC93A*, *CG4928* is predicted to have longer N- and C-termini, which is more similar to the predicted structure of *hsUNC93B1*, once more suggesting that *CG4928* might possess features from both variants in humans. Despite structural evidence of both *UNC93A* (Ceder et al., 2017) and *CG4928* to be authentic transporters, we were not able to identify a substrate of transport. The setup of the SSM-based electrophysiology has its limitations and, for example, we cannot detect ion-ion cotransport nor uniport activity. Therefore, there is still the possibility that *CG4928* is an authentic transporter. However, there are SLC families that lack the ability to act as transporters themselves and that have lost the ability to facilitate transport (Fotiadis et al., 2013; Abbott, 2017); however, this is less likely for *CG4928*. So far, our results support the current suggested theory that it is a regulatory unit of potassium channels (Levin and Horvitz, 1992; de la Cruz et al., 2003). Both the immunostaining and PLA confirm the co-localization of *UNC93A* and *CG4928* with *KCNK3* and *KCNK9*, respectively, which supports the theory. It is noteworthy that *UNC93B1* also features a 2D topology of an authentic transporter, but it transfers Toll-like receptor

(TLR) from the endoplasmic reticulum to the plasma membrane (Lee et al., 2013; Huh et al., 2014) and maintain TLR protein expression by acting as a trafficking chaperone (Pelka et al., 2018) and not by acting as a typical SLC. These suggest that *UNC93A* could be involved in the trafficking and/or the retention of the *TASK¹* channels to the plasma membrane. Several other potassium channels also need regulatory subunits that both regulate their function and location (Capera et al., 2019), and there are several other protein families, e.g., anchoring proteins and scaffolding proteins, needed for the correct membrane insertion of potassium channels (Capera et al., 2019). Recently, new interesting functions have been added to the SLCs, and there are evidences that they form complexes and interact with other membrane proteins to form “transceptors” (Jung et al., 2015; Rebsamen et al., 2015; Wang et al., 2015) and “chansporters” (Neverisky and Abbott, 2015; Abbott, 2017, 2020). These findings give rise to a new hypothesis regarding *CG4928* that, in contrast of only being a subunit, it might form a chansporter complex with *TASK¹* channels. In fact, the type of interaction and the crosstalk between channels and transporters have been detailed and elegantly described for other potassium channels, e.g., the *KCNQs* (Abbott, 2020). However, the exact mechanisms and the functional interaction between *CG4928* and *TASK¹* channels are still not clear, and further studies are needed to establish if they act as a chansporter complex. However, despite not knowing the exact mechanism of action, the results presented here establish that *CG4928* is vital for the normal physiology of the body and cell. Potassium, most commonly found in intracellular compartments, is important for several processes occurring in the body, e.g., motility (de la Cruz et al., 2003), vesicle release, blood glucose regulation, renal function, but most importantly, it sets and maintains the membrane potential (Adler and Fraley, 1977; Palmer and Clegg, 2016). *TASK¹* channels are so-called leak channels which are important for resting potential (Talley and Bayliss, 2002; Plant et al., 2012) and are regulated by factors such as pH. *KCNK3* is an outwardly rectifying channel (Duprat et al., 1997; Plant et al., 2012), while *KCNK9* is a pH-dependent, voltage-insensitive background channel (Chapman et al., 2000; Vega-Saenz, de Miera et al., 2001; Plant et al., 2012), where both channels allow the movement of potassium depending on the electrochemical gradient.

The correct plasma level of potassium is essential for tuning the resting potential of cells. We found that the overexpression of *CG4928* in HEK293T cells leads to a reduction in basal membrane potential. The result indicates that the cell is less depolarized; hence, the cell will need greater-than-“normal” stimuli to depolarize itself. The loss of function in membrane potential halts several essential properties of the cell (Abdul Kadir et al., 2018), which most likely cause an induction in apoptosis and cytotoxicity. Except for potassium, sodium influx is a main event of depolarization (Seyama and Irisawa, 1967). Interestingly, apoptosis and cytotoxicity were hindered when the cells were maintained on high-sodium media, implying that the *CG4928*-overexpressing cells are less depolarized. The normal extracellular sodium concentration cannot initiate a change in membrane potential, while maintaining the cells in a

⁴flybase.org

high extracellular concentration of sodium can enable them to prevent apoptosis.

When analyzing the hemolymph content, we established that *CG4928* knockdown flies had higher sodium and potassium levels in the hemolymph and a lower level of potassium within the Malpighian tubules. Potassium is of great significance for the function of Malpighian tubules and, in contrast to mammals, the primary urine production in flies is potassium dependent (Dow et al., 1998). Furthermore, the secretion rate was found to be five times lower in the *CG4928* knockdown flies' Malpighian tubules compared with that of the controls. Similar observations have been made for other potassium channels, e.g., *Irk1* and *Irk2*, two channels responsible for transepithelial potassium fluxes in the principal cells (Wu et al., 2015). Taken together, these two findings are most likely the causes of edema. However, *CG4928* is, according to microarray analysis, also expressed in the hindgut, an organ that is equally important for systemic water homeostasis (Luan et al., 2015). The hindgut has also been suggested to be sensitive to elevated intracellular concentrations of sodium and potassium during external hypertonic states (Huang et al., 2002). Hence, the organ is proposed to possess an osmoprotective role, where sodium and potassium, by an unknown function, are transported out of the cell, returning the cell volume and the intracellular ion concentration back to normal (Huang et al., 2002; Luan et al., 2015). This corroborates our findings about the increased levels of sodium and potassium in the extracellular fluid collected from adult flies suffering from edema. Moreover, knockdown of the sodium- and chloride-dependent neurotransmitter transporter family ortholog *Ine*, which is expressed in the basolateral epithelium of the hindgut, results in findings similar to those seen in *CG4928* knockdown flies, e.g., sensitivity to desiccation, altered hemolymph volume and total body water mass (Luan et al., 2015). However, in comparison to the Malpighian tubule for which sophisticated tools have been developed to study its function, the mechanisms of water conservation, absorption, and secretion of the hindgut are less elucidated in the adult fly (Luan et al., 2015). This, together with the low GFP expression (which would indicate the *CG4928* expression) visualized in the hindgut, made it cumbersome to evaluate the function of *CG4928* in this particular organ, and the focus remained on the Malpighian tubules. Also, hindgut-specific Gal4 lines were not able to reproduce the edema, suggesting that this organ is not the main factor causing the edema, but it can neither be ruled out and further research is needed to establish if *CG4928* can be a potential gene in the regulation of water homeostasis through the hindgut.

The edema was minimized by amiloride, but not mannitol and furosemide. The differences in the mechanism of action are the most likely explanation to this finding. Amiloride binds and blocks ENaCs and thereby inhibits sodium reabsorption, leading to excretion of sodium and water from the body, while reducing potassium excretion (Wishart et al., 2018), similar effects have been observed in *D. melanogaster* by acting *via* the Na⁺/H⁺ exchangers (Giannakou and Dow, 2001; Zelle et al., 2013). It is therefore possible that the phenotype is minimized by inhibiting transepithelial sodium secretion and thereby increasing fluid secretion, but it is not enough to treat the edema. In humans,

mannitol is metabolically inert; however, it can be metabolized in flies. When feeding higher concentrations of mannitol, it is likely that not all is metabolized and therefore it acts as a weak osmotic molecule within the digestive tract, increasing water excretion *via* feces. Meanwhile, furosemide causes sodium, potassium, and chloride loss in the urine, leading to lowered water reabsorption by inhibiting the NKCC (Wishart et al., 2018). However, in flies, the NKCC is located on the apical membrane, which means that inhibition of NKCC will lead to less potassium uptake into the Malpighian tubules (Rodan et al., 2012). Since the primary urine production of flies is potassium dependent, fluid secretion will decrease, and the flies will retain the edema. Ion-free diets, regardless of sugar type and concentration, rescued the edema. This suggests that *CG4928* knockdown flies can handle endogenous ion levels, indicating that there are other biochemical pathways that have the capability to use, store, and handle the faulty potassium fluxes (Seifter and Chang, 2017).

If the potassium transport is not working, as suggested, other ion levels will be affected, which could be a reason to the altered boron, cadmium, cobalt, and sodium levels observed in *CG4928* knockdown flies. TASK¹ channels are not known to facilitate the movement of these four ions. However, the transport of, e.g., boron and sodium is dependent on both passive and active coupled transport, and the transport is sometimes linked directly to the level of potassium (Arroyo et al., 2013; Schnetkamp, 2013) or through other molecules such as hydrogen (Yoshinari and Takano, 2017). Hydrogen is commonly coupled to potassium and sodium transport by different ATPases and other SLCs⁵; hence, this could be a possible explanation to the increased boron in the hemolymph. The link between ion concentration and the cells' ability to regulate electrochemical balance could also possibly be the explanation to the decrease in cadmium and the increase in cobalt. Generally, an increase in osmotic molecules and disturbed water homeostasis worsen the condition of the flies; water will be transported to the extracellular compartments, the electrolyte balance will be altered, and ion-coupled transporters and pumps would be affected (Castillo et al., 2015). This is observed among the RNA sequencing results, where both sodium/neurotransmitter symporter (Gat, SLC6A1 in humans) and sodium/substrate co-transporter (CG9657) were found to be upregulated.

The phenomena of accumulation of pigments and fluid in the Malpighian tubules have been observed earlier for the knockdown of genes important for transport and trafficking, e.g., *w*, *cho*, *ma*, *mah*, and *red*. Many of them are involved directly in the biosynthesis or the transport of components within the biosynthesis of eye pigments in flies (Lloyd et al., 1998; Grant et al., 2016). For example, knockdown of *Vps16A* (vacuolar protein sorting 16A, also known as *ma*), a gene that is a part of the HOPS complex that together with Syntaxin 17 mediates autophagosome-lysosome fusion (Pulipparacharuvil et al., 2005; Jiang et al., 2014), leads to the accumulation of yellow pigments in Malpighian tubules (Bridges, 1918). Similar pigment accumulation was observed for our knockdown flies, but the fluid accumulation was rather located to the abdominal

⁵slc.bioparadigms.org

cavity and not in the Malpighian tubules. Together with the findings that UNC93A affects viral budding due to errors in the endosomal trafficking process (Campbell et al., 2011), it is suggested that *CG4928* could be involved in organelle trafficking. How this is linked to the theory of being a regulator of potassium channels is unclear, but potassium is also of significance for vesicle release, and therefore it is possible that the accumulation is due to dysfunctional vesicle release from, e.g., the autophagosome and/or the lysosome. Further experiments are needed to establish that mechanism. Importantly, the Malpighian tubules are vital for detoxification (Chahine and O'Donnell, 2011), and a recent study presented that *CG4928* is linked to manganese toxicity and might be involved in the process of detoxification (Mohr et al., 2018), and the human UNC93A was recently identified as a metabolite-associated locus in chronic kidney disease patients (Schlosser et al., 2020). Both findings suggest a role in the renal system, and it is clear that *CG4928* affects the function of the renal system in flies.

The orthologs to the human TASK¹ channels, *Task6* and *Task7*, are lowly expressed in the body, while *CG4928* is expressed throughout the body of both larvae and adult flies. Neither of the two potassium channels was found to have altered mRNA expression as a response to *CG4928* knockdown in RNA sequencing, suggesting that *CG4928* does not regulate them by transcriptional regulation. Other potassium channels, e.g., *Irk3*, have a higher specific expression in the Malpighian tubules (Wang et al., 2004) and have been suggested to have a more unique role in the Malpighian tubules compared to *Task6* and *Task7*. However, other potassium channels with low expression have been documented in the tubule and been shown to accomplish important functions there (Dow et al., 1994; Wang et al., 2004; Gautam et al., 2017). Furthermore, *Irk3* is an inward-rectifying potassium channel, which means that it passes current into the cell rather than out of the cell, implying that potassium channels such as the TASK¹ channels could also be needed. It is also possible that *CG4928* interacts with different potassium channels, not only the TASK¹ channels, since the expression distribution of these proteins differs from each other in murine brain tissues (Karschin et al., 2001; Medhurst et al., 2001; Marinc et al., 2014; Ceder et al., 2017).

The disturbances in ion levels and the accumulation of substrates could explain why *CG4928* knockdowns starve faster even if they have high glycogen and glucose levels. Insulin and potassium are tightly connected, where the level of insulin regulates cellular potassium intake, as well as glucose intake (Palmer and Clegg, 2016). Hence, the high levels of glycogen and glucose could be a secondary effect of the altered plasma level of potassium. In addition, dehydration makes the flies more vulnerable to starvation (Albers and Bradley, 2004), and it is possible that the diuretic hormones are altered (Cannell et al., 2016), which are linked to desiccation and starvation resistance. Recently, *CG4928* and UNC93A were shown to be altered by fluctuating glucose levels in flies and primary cortex cell lines from mice (Ceder et al., 2020). In addition, depletion of Kir channels in salivary glands has been shown to alter the performance of the gland and affect sugar feeding in flies (Swale et al., 2017). However, further

experiments are needed to reveal the connection between *CG4928* and carbohydrate metabolism and if it is linked to altered potassium levels.

The findings in *D. melanogaster* support the theory that *CG4928* is important for ion and osmotic balance. When reducing *CG4928* expression in flies, it is likely that it disturbs the membrane potential, as observed when overexpressing protein in cells, and/or the ion balance, suggesting that *CG4928* is important for transmembrane ion flows. This finding could also explain why both the *Da-Gal4 > CG4928RNAi GD* line and the *Da-Gal4 > CG4928RNAi KK* line, at temperatures above 29°C, did not produce viable offspring. Both TASK¹ channels and *CG4928* are expressed during the development, and potassium has been found to be of importance for normal development (Haug-Collet et al., 1999; Dahal et al., 2017), indicating that *CG4928* most likely is connected to potassium. Furthermore, the salivary gland has an important role for proper pupation and metamorphosis (Shirk et al., 1988; Farkas and Mechler, 2000; Takemoto et al., 2007; Wang et al., 2008), and the high expression of *CG4928* in that particular tissue could possibly also point out a reason why the offspring died before or during pupation.

In conclusion, *CG4928* is an evolutionary conserved protein consisting of 12 transmembrane helices. It co-localizes with TASK¹ channels, and both overexpression as well as reduction of *CG4928* dysregulate cellular processes that involve potassium, e.g., membrane potential in cells and urine production in fruit flies. The findings in this paper suggest that *CG4928* could be connected to KCNK3, possibly also KCNK9 and KCNK15. However, structural evidence also points to the possibility that it can perform ion transport over lipid membranes, i.e., being an authentic transporter, where *CG4928* expression is linked to proper membrane potential and ion concentrations in the cellular compartments. However, the key mechanisms about the interaction with potassium channels, if *CG4928* is an authentic transporter with a substrate that was not identified in this screen or if it has lost its transport function, still remain uncertain. This first in-depth characterization of *CG4928* provides a clear example on why orphan transporters are important to study and why gathering of information about them can aid in the understanding about and to establish their role in health and disease.

DATA AVAILABILITY STATEMENT

The datasets presented in this study can be found in online repositories. The names of the repository/repositories and accession number(s) can be found in the article/**Supplementary Material**.

AUTHOR CONTRIBUTIONS

MC designed the project and experiments, compiled the figures and tables, drafted the manuscript, prepared the

material, performed the dissections, RNA and mRNA extraction, cDNA synthesis, qPCR, Ramsay assay, weighing, spectrometry, sodium/potassium measurements, element analysis, starvation assay, locomotory, food intake, and phenotype rescue, captured photos, and modeled the protein structures, RNA sequencing analysis, analysis, cell imaging, analyzing of western blot, analyzed PLA, transport assay, and membrane potential. TA prepared the material, performed dissections, weighing measurements, sugar, tag and protein assays, and membrane potential measurements, assisted in compiling graphs, figures, and **Supplementary Figures**, and drafted parts of methods. KH performed SH-SY5Y and HEK293T cell cultures and ApoToxTM-GLO measurements, assisted in membrane preparation, performed ICC and PLA, assisted in imaging and compiling of graphs for figures and **Supplementary Figures**, and drafted parts of methods. VM performed HEK293T cell cultures, membrane preparation, and western blot, and drafted parts of methods. SP prepared material and performed dissections, RNA extractions, cDNA synthesis, and qPCR. EP performed the phylogenetic analysis, compiled the phylogenetic tree and data for **Table 1**, and drafted parts of methods. MW designed the project and aided in data analysis, experimental setup, and interpretation of results, RF performed RNA sequencing analysis, designed vectors, aided in data analysis, experimental setup, and interpretation of results and drafted the manuscript. All the authors have read and approved the manuscript.

REFERENCES

- Abbott, G. W. (2017). Chansporter complexes in cell signaling. *FEBS Lett.* 591, 2556–2576. doi: 10.1002/1873-3468.12755
- Abbott, G. W. (2020). KCNQs: ligand- and voltage-gated potassium channels. *Front. Physiol.* 11:583. doi: 10.3389/fphys.2020.00583
- Abdul Kadir, L., Stacey, M., and Barrett-Jolley, R. (2018). Emerging roles of the membrane potential: action beyond the action potential. *Front. Physiol.* 9:1661. doi: 10.3389/fphys.2018.01661
- Adler, S., and Fraley, D. S. (1977). Potassium and intracellular pH. *Kidney Int.* 11, 433–442. doi: 10.1038/ki.1977.61
- Albers, M. A., and Bradley, T. J. (2004). Osmotic regulation in adult *Drosophila melanogaster* during dehydration and rehydration. *J. Exp. Biol.* 207(Pt 13), 2313–2321. doi: 10.1242/jeb.01024
- Arroyo, J. P., Kahle, K. T., and Gamba, G. (2013). The SLC12 family of electroneutral cation-coupled chloride cotransporters. *Mol. Aspects Med.* 34, 288–298. doi: 10.1016/j.mam.2012.05.002
- Artero, R. D., Terol-Alcayde, J., Paricio, N., Ring, J., Bagues, M., Torres, A., et al. (1998). saliva, a new *Drosophila* gene expressed in the embryonic salivary glands with homologues in plants and vertebrates. *Mech. Dev.* 75, 159–162. doi: 10.1016/s0925-4773(98)00087-2
- Ayres, D. L., Darling, A., Zwickl, D. J., Beerli, P., Holder, M. T., Lewis, P. O., et al. (2012). BEAGLE: an application programming interface and high-performance computing library for statistical phylogenetics. *Syst. Biol.* 61, 170–173. doi: 10.1093/sysbio/syr100
- Bazzone, A., Barthmes, M., and Fendler, K. (2017). SSM-based electrophysiology for transporter research. *Methods Enzymol.* 594, 31–83. doi: 10.1016/bs.mie.2017.05.008
- Bedut, S., Seminatore-Nole, C., Lamamy, V., Caignard, S., Boutin, J. A., Nosjean, O., et al. (2016). High-throughput drug profiling with voltage- and calcium-sensitive fluorescent probes in human iPSC-derived cardiomyocytes. *Am. J. Physiol. Heart Circ. Physiol.* 311, H44–H53.

FUNDING

This study was supported by the Swedish Research Council (2016-01972), the Swedish Brain Foundation (FO2018-0130), the Swedish Society for Medical Research (201507), the Novo Nordisk Foundation (34224), Åhlens Foundation (193027), Engkvists Foundation (20160614), and Magnus Bergvalls Foundation (201601754).

ACKNOWLEDGMENTS

We would like to express our greatest gratitude toward Prof. Julian A. Dow, Prof. Fredrik Palm, and research engineer Angelica Fasching, to the unit of NGS at SciLifeLab facility in Uppsala, to ALS Scandinavia facility in Luleå, and to Nanion Technologies GmbH in München. Thanks to Andre Bazzone for all your expertise and help with the SSM-based electrophysiology and to MC for the preparation of material for and assistance with the Ramsay assay.

SUPPLEMENTARY MATERIAL

The Supplementary Material for this article can be found online at: <https://www.frontiersin.org/articles/10.3389/fcell.2020.580291/full#supplementary-material>

- Bridges, C. B. (1918). Maroon: a recurrent mutation in *Drosophila*. *Proc. Natl. Acad. Sci. U.S.A.* 4, 316–318. doi: 10.1073/pnas.4.10.316
- Campbell, C. L., Lehmann, C. J., Gill, S. S., Dunn, W. A., James, A. A., and Foy, B. D. (2011). A role for endosomal proteins in alphavirus dissemination in mosquitoes. *Insect Mol. Biol.* 20, 429–436. doi: 10.1111/j.1365-2583.2011.01078.x
- Cannell, E., Dornan, A. J., Halberg, K. A., Terhzaz, S., Dow, J. A. T., and Davies, S. A. (2016). The corticotropin-releasing factor-like diuretic hormone 44 (DH44) and kinin neuropeptides modulate desiccation and starvation tolerance in *Drosophila melanogaster*. *Peptides* 80, 96–107. doi: 10.1016/j.peptides.2016.02.004
- Capera, J., Navarro-Perez, M., Cassinelli, S., and Felipe, A. (2019). The potassium channel odyssey: mechanisms of traffic and membrane arrangement. *Int. J. Mol. Sci.* 20:734. doi: 10.3390/ijms20030734
- Castillo, J. P., Rui, H., Basilio, D., Das, A., Roux, B., Latorre, R., et al. (2015). Mechanism of potassium ion uptake by the Na(+)/K(+)-ATPase. *Nat. Commun.* 6:7622.
- Ceder, M. M., Lekholm, E., Hellsten, S. V., Perland, E., and Fredriksson, R. (2017). The neuronal and peripheral expressed membrane-bound UNC93A respond to nutrient availability in mice. *Front. Mol. Neurosci.* 10:351. doi: 10.3389/fnmol.2017.00351
- Ceder, M. M., Lekholm, E., Klaesson, A., Tripathi, R., Schweizer, N., Weldai, L., et al. (2020). Glucose availability alters gene and protein expression of several newly classified and putative solute carriers in mice cortex cell culture and *D. melanogaster*. *Front. Cell Dev. Biol.* 8:579. doi: 10.3389/fcell.2020.00579
- Ceriani, F., and Mammano, F. (2013). A rapid and sensitive assay of intercellular coupling by voltage imaging of gap junction networks. *Cell Commun. Signal.* 11, 78. doi: 10.1186/1478-811x-11-78
- Cesar-Razquin, A., Snijder, B., Frappier-Brinton, T., Isserlin, R., Gyimesi, G., Bai, X., et al. (2015). A call for systematic research on solute carriers. *Cell* 162, 478–487. doi: 10.1016/j.cell.2015.07.022

- Chahine, S., and O'Donnell, M. J. (2011). Interactions between detoxification mechanisms and excretion in *Malpighian tubules* of *Drosophila melanogaster*. *J. Exp. Biol.* 214(Pt 3), 462–468. doi: 10.1242/jeb.048884
- Chapman, C. G., Meadows, H. J., Godden, R. J., Campbell, D. A., Duckworth, M., Kelsell, R. E., et al. (2000). Cloning, localisation and functional expression of a novel human, cerebellum specific, two pore domain potassium channel. *Brain Res. Mol. Brain Res.* 82, 74–83. doi: 10.1016/s0169-328x(00)00183-2
- Chintapalli, V. R., Wang, J., and Dow, J. A. (2007). Using flyatlas to identify better *Drosophila melanogaster* models of human disease. *Nat. Genet.* 39, 715–720. doi: 10.1038/ng2049
- Chomczynski, P., and Sacchi, N. (1987). Single-step method of RNA isolation by acid guanidinium thiocyanate-phenol-chloroform extraction. *Anal. Biochem.* 162, 156–159. doi: 10.1006/abio.1987.9999
- Cunningham, F., Amode, M. R., Barrrell, D., Beal, K., Billis, K., Brent, S., et al. (2015). Ensembl 2015. *Nucleic Acids Res.* 43, D662–D669.
- Dahal, G. R., Pradhan, S. J., and Bates, E. A. (2017). Inwardly rectifying potassium channels influence *Drosophila* wing morphogenesis by regulating Dpp release. *Development* 144, 2771–2783. doi: 10.1242/dev.146647
- de la Cruz, I. P., Levin, J. Z., Cummins, C., Anderson, P., and Horvitz, H. R. (2003). sup-9, sup-10, and unc-93 may encode components of a two-pore K⁺ channel that coordinates muscle contraction in *Caenorhabditis elegans*. *J. Neurosci.* 23, 9133–9145. doi: 10.1523/jneurosci.23-27-09133.2003
- Dobin, A., Davis, C. A., Schlesinger, F., Drenkow, J., Zaleski, C., Jha, S., et al. (2013). STAR: ultrafast universal RNA-seq aligner. *Bioinformatics* 29, 15–21. doi: 10.1093/bioinformatics/bts635
- Dow, J. A., Maddrell, S. H., Gortz, A., Skaer, N. J., Brogan, S., and Kaiser, K. (1994). The malpighian tubules of *Drosophila melanogaster*: a novel phenotype for studies of fluid secretion and its control. *J. Exp. Biol.* 197, 421–428.
- Dow, J. A. T., Davies, S. A., and Sozen, M. A. (1998). Fluid secretion by the *Drosophila* Malpighian tubule. *Am. Zool.* 38, 450–460.
- Duprat, F., Lesage, F., Fink, M., Reyes, R., Heurteaux, C., and Lazdunski, M. (1997). TASK, a human background K⁺ channel to sense external pH variations near physiological pH. *Embo J.* 16, 5464–5471. doi: 10.1093/emboj/16.17.5464
- Dupuis, J., Langenberg, C., Prokopenko, I., Saxena, R., Soranzo, N., Jackson, A. U., et al. (2010). New genetic loci implicated in fasting glucose homeostasis and their impact on type 2 diabetes risk. *Nat. Genet.* 42, 105–116.
- Eddy, S. R. (2011). Accelerated profile HMM searches. *PLoS Comput. Biol.* 7:e1002195. doi: 10.1371/journal.pcbi.1002195
- Fagerberg, L., Hallstrom, B. M., Oksvold, P., Kampf, C., Djureinovic, D., Odeberg, J., et al. (2014). Analysis of the human tissue-specific expression by genome-wide integration of transcriptomics and antibody-based proteomics. *Mol. Cell. Proteomics* 13, 397–406. doi: 10.1074/mcp.m113.035600
- Farkas, R., and Mechler, B. M. (2000). The timing of drosophila salivary gland apoptosis displays an I(2)gl-dose response. *Cell Death Differ.* 7, 89–101. doi: 10.1038/sj.cdd.4400621
- Fotiadis, D., Kanai, Y., and Palacin, M. (2013). The SLC3 and SLC7 families of amino acid transporters. *Mol. Aspects Med.* 34, 139–158. doi: 10.1016/j.mam.2012.10.007
- Fredriksson, R., Nordstrom, K. J., Stephansson, O., Hagglund, M. G., and Schiöth, H. B. (2008). The solute carrier (SLC) complement of the human genome: phylogenetic classification reveals four major families. *FEBS Lett.* 582, 3811–3816. doi: 10.1016/j.febslet.2008.10.016
- Gabriel, L., Lvov, A., Orthodoxou, D., Rittenhouse, A. R., Kobertz, W. R., and Melikian, H. E. (2012). The acid-sensitive, anesthetic-activated potassium leak channel, KCNK3, is regulated by 14-3-3beta-dependent, protein kinase C (PKC)-mediated endocytic trafficking. *J. Biol. Chem.* 287, 32354–32366. doi: 10.1074/jbc.m112.391458
- Gautam, N. K., Verma, P., and Tapadia, M. G. (2017). *Drosophila* malpighian tubules: a model for understanding kidney development, function, and disease. *Results Probl. Cell Differ.* 60, 3–25. doi: 10.1007/978-3-319-51436-9_1
- Giannakou, M. E., and Dow, J. A. (2001). Characterization of the *Drosophila melanogaster* alkali-metal/proton exchanger (NHE) gene family. *J. Exp. Biol.* 204(Pt 21), 3703–3716.
- Goldstein, S. A., Bockenbauer, D., O'Kelly, I., and Zilberberg, N. (2001). Potassium leak channels and the KCNK family of two-P-domain subunits. *Nat. Rev. Neurosci.* 2, 175–184. doi: 10.1038/35058574
- Grant, P., Maga, T., Loshakov, A., Singhal, R., Wali, A., Nwankwo, J., et al. (2016). An eye on trafficking genes: identification of four eye color mutations in *Drosophila*. *G3* 6, 3185–3196. doi: 10.1534/g3.116.032508
- Haug-Collet, K., Pearson, B., Webel, R., Szerencsei, R. T., Winkfein, R. J., Schnetkamp, P. P., et al. (1999). Cloning and characterization of a potassium-dependent sodium/calcium exchanger in *Drosophila*. *J. Cell Biol.* 147, 659–670. doi: 10.1083/jcb.147.3.659
- Hellsten, S. V., Lekholm, E., Ahmad, T., and Fredriksson, R. (2017). The gene expression of numerous SLC transporters is altered in the immortalized hypothalamic cell line N25/2 following amino acid starvation. *FEBS Open Biol.* 7, 249–264. doi: 10.1002/2211-5463.12181
- Holz, A., Bossinger, B., Strasser, T., Janning, W., and Klapper, R. (2003). The two origins of hemocytes in *Drosophila*. *Development* 130, 4955–4962. doi: 10.1242/dev.00702
- Hua, H., Georgiev, O., Schaffner, W., and Steiger, D. (2010). Human copper transporter Ctrl1 is functional in *Drosophila*, revealing a high degree of conservation between mammals and insects. *J. Biol. Inorg. Chem.* 15, 107–113. doi: 10.1007/s00775-009-0599-0
- Huang, D. W., Sherman, B. T., Tan, Q., Collins, J. R., Alvord, W. G., Roayaei, J., et al. (2007). The DAVID gene functional classification tool: a novel biological module-centric algorithm to functionally analyze large gene lists. *Genome Biol.* 8:R183.
- Huang, X., Huang, Y., Chinnappan, R., Bocchini, C., Gustin, M. C., and Stern, M. (2002). The *Drosophila* inebriated-encoded neurotransmitter/osmolyte transporter: dual roles in the control of neuronal excitability and the osmotic stress response. *Genetics* 160, 561–569.
- Huelsensbeck, J. P., Ronquist, F., Nielsen, R., and Bollback, J. P. (2001). Bayesian inference of phylogeny and its impact on evolutionary biology. *Science* 294, 2310–2314. doi: 10.1126/science.1065889
- Huh, J. W., Shibata, T., Hwang, M., Kwon, E. H., Jang, M. S., Fukui, R., et al. (2014). UNC93B1 is essential for the plasma membrane localization and signaling of toll-like receptor 5. *Proc. Natl. Acad. Sci. U.S.A.* 111, 7072–7077. doi: 10.1073/pnas.1322838111
- Jiang, P., Nishimura, T., Sakamaki, Y., Itakura, E., Hatta, T., Natsume, T., et al. (2014). The HOPS complex mediates autophagosome-lysosome fusion through interaction with syntaxin 17. *Mol. Biol. Cell* 25, 1327–1337. doi: 10.1091/mbc.e13-08-0447
- Jung, J., Genau, H. M., and Behrends, C. (2015). Amino acid-dependent mTORC1 regulation by the lysosomal membrane protein SLC38A9. *Mol. Cell. Biol.* 35, 2479–2494. doi: 10.1128/mcb.00125-15
- Kalujnaia, S., McWilliam, I. S., Zaguinaiko, V. A., Feilen, A. L., Nicholson, J., Hazou, N., et al. (2007). Transcriptomic approach to the study of osmoregulation in the European eel *Anguilla anguilla*. *Physiol. Genomics* 31, 385–401.
- Karschin, C., Wischmeyer, E., Preisig-Muller, R., Rajan, S., Derst, C., Grzeschik, K. H., et al. (2001). Expression pattern in brain of TASK-1, TASK-3, and a tandem pore domain K(+) channel subunit, TASK-5, associated with the central auditory nervous system. *Mol. Cell. Neurosci.* 18, 632–648. doi: 10.1006/mcne.2001.1045
- Katoh, K., Misawa, K., Kuma, K., and Miyata, T. (2002). MAFFT: a novel method for rapid multiple sequence alignment based on fast Fourier transform. *Nucleic Acids Res.* 30, 3059–3066. doi: 10.1093/nar/gkf436
- Kelley, L. A., Mezulis, S., Yates, C. M., Wass, M. N., and Sternberg, M. J. (2015). The Phyre2 web portal for protein modeling, prediction and analysis. *Nat. Protoc.* 10, 845–858. doi: 10.1038/nprot.2015.053
- Kottgen, A., Pattaro, C., Boger, C. A., Fuchsberger, C., Olden, M., Glazer, N. L., et al. (2010). New loci associated with kidney function and chronic kidney disease. *Nat. Genet.* 42, 376–384.
- Lee, B. L., Moon, J. E., Shu, J. H., Yuan, L., Newman, Z. R., Schekman, R., et al. (2013). UNC93B1 mediates differential trafficking of endosomal TLRs. *eLife* 2:e00291.
- Lekholm, E., Perland, E., Eriksson, M. M., Hellsten, S. V., Lindberg, F. A., Rostami, J., et al. (2017). Putative membrane-bound transporters MFSD14A and MFSD14B are neuronal and affected by nutrient availability. *Front. Mol. Neurosci.* 10:11. doi: 10.3389/fnmol.2017.00011

- Levin, J. Z., and Horvitz, H. R. (1992). The *Caenorhabditis elegans* unc-93 gene encodes a putative transmembrane protein that regulates muscle contraction. *J. Cell Biol.* 117, 143–155. doi: 10.1083/jcb.117.1.143
- Li, W., Cowley, A., Uludag, M., Gur, T., McWilliam, H., Squizzato, S., et al. (2015). The EMBL-EBI bioinformatics web and programmatic tools framework. *Nucleic Acids Res.* 43, W580–W584.
- Liu, Y., Dodds, P., Emilion, G., Mungall, A. J., Dunham, I., Beck, S., et al. (2002). The human homologue of unc-93 maps to chromosome 6q27 - characterisation and analysis in sporadic epithelial ovarian cancer. *BMC Genet.* 3:20. doi: 10.1186/1471-2156-3-20
- Lloyd, V., Ramaswami, M., and Kramer, H. (1998). Not just pretty eyes: *Drosophila* eye-colour mutations and lysosomal delivery. *Trends Cell Biol.* 8, 257–259. doi: 10.1016/s0962-8924(98)01270-7
- Luan, Z., Quigley, C., and Li, H.-S. (2015). The putative Na⁺/Cl⁻-dependent neurotransmitter/osmolyte transporter inebriated in the *Drosophila* hindgut is essential for the maintenance of systemic water homeostasis. *Sci. Rep.* 5, 7993.
- Madeira, F., Park, Y. M., Lee, J., Buso, N., Gur, T., Madhusoodanan, N., et al. (2019). The EMBL-EBI search and sequence analysis tools APIs in 2019. *Nucleic Acids Res.* 47, W636–W641.
- Madej, M. G., Dang, S., Yan, N., and Kaback, H. R. (2013). Evolutionary mix-and-match with MFS transporters. *Proc. Natl. Acad. Sci. U.S.A.* 110, 5870–5874. doi: 10.1073/pnas.1303538110
- Marinc, C., Derst, C., Pruss, H., and Veh, R. W. (2014). Immunocytochemical localization of TASK-3 protein (K2P9.1) in the rat brain. *Cell Mol. Neurobiol.* 34, 61–70. doi: 10.1007/s10571-013-9987-7
- Medhurst, A. D., Rennie, G., Chapman, C. G., Meadows, H., Duckworth, M. D., Kelsell, R. E., et al. (2001). Distribution analysis of human two pore domain potassium channels in tissues of the central nervous system and periphery. *Brain Res. Mol. Brain Res.* 86, 101–114. doi: 10.1016/s0169-328x(00)00263-1
- Mohr, S. E., Rudd, K., Hu, Y., Song, W. R., Gilly, Q., Buckner, M., et al. (2018). Zinc detoxification: a functional genomics and transcriptomics analysis in *Drosophila melanogaster* cultured cells. *G3* 8, 631–641. doi: 10.1534/g3.117.300447
- Neverisky, D. L., and Abbott, G. W. (2015). Ion channel-transporter interactions. *Crit. Rev. Biochem. Mol. Biol.* 51, 257–267. doi: 10.3109/10409238.2016.1172553
- Niles, A. L., Moravec, R. A., Eric, P., Scurria, M. A., Daily, W. J., Riss, T. L., et al. (2007). A homogeneous assay to measure live and dead cells in the same sample by detecting different protease markers. *Anal. Biochem.* 366, 197–206. doi: 10.1016/j.ab.2007.04.007
- Notredame, C., Higgins, D. G., and Heringa, J. (2000). T-Coffee: a novel method for fast and accurate multiple sequence alignment. *J. Mol. Biol.* 302, 205–217. doi: 10.1006/jmbi.2000.4042
- Omasits, U., Ahrens, C. H., Muller, S., and Wollscheid, B. (2014). Protter: interactive protein feature visualization and integration with experimental proteomic data. *Bioinformatics* 30, 884–886. doi: 10.1093/bioinformatics/btt607
- Palmer, B. F., and Clegg, D. J. (2016). Physiology and pathophysiology of potassium homeostasis. *Adv. Physiol. Educ.* 40, 480–490. doi: 10.1152/advan.00121.2016
- Pao, S. S., Paulsen, I. T., and Saier, M. H. Jr. (1998). Major facilitator superfamily. *Microbiol. Mol. Biol. Rev.* 62, 1–34.
- Pelka, K., Bertheloot, D., Reimer, E., Phulphagar, K., Schmidt, S. V., Christ, A., et al. (2018). The chaperone UNC93B1 regulates toll-like receptor stability independently of endosomal TLR transport. *Immunity* 48, 911.e17–922.e17.
- Perland, E., Bagchi, S., Klaesson, A., and Fredriksson, R. (2017a). Characteristics of 29 novel atypical solute carriers of major facilitator superfamily type: evolutionary conservation, predicted structure and neuronal co-expression. *Open Biol.* 7, 170142. doi: 10.1098/rsob.170142
- Perland, E., Hellsten, S. V., Lekholm, E., Eriksson, M. M., Arapi, V., and Fredriksson, R. (2017b). The novel membrane-bound proteins MFSD1 and MFSD3 are putative SLC transporters affected by altered nutrient intake. *J. Mol. Neurosci.* 61, 199–214. doi: 10.1007/s12031-016-0867-8
- Perland, E., Hellsten, S. V., Schweizer, N., Arapi, V., Rezayee, F., Bushra, M., et al. (2017c). Structural prediction of two novel human atypical SLC transporters, MFSD4 and MFSD9, and their neuroanatomical distribution in mice. *PLoS One* 12:e0186325. doi: 10.1371/journal.pone.0186325
- Perland, E., and Fredriksson, R. (2017). Classification systems of secondary active transporters. *Trends Pharmacol. Sci.* 38, 305–315. doi: 10.1016/j.tips.2016.11.008
- Perland, E., Lekholm, E., Eriksson, M. M., Bagchi, S., Arapi, V., and Fredriksson, R. (2016). The putative SLC transporters Mfsd5 and Mfsd11 are abundantly expressed in the mouse brain and have a potential role in energy homeostasis. *PLoS One* 11:e0156912. doi: 10.1371/journal.pone.0156912
- Plant, L. D., Zuniga, L., Araki, D., Marks, J. D., and Goldstein, S. A. (2012). SUMOylation silences heterodimeric TASK potassium channels containing K2P1 subunits in cerebellar granule neurons. *Sci. Signal.* 5:ra84. doi: 10.1126/scisignal.2003431
- Pulipparacharuvil, S., Akbar, M. A., Ray, S., Sevrioukov, E. A., Haberman, A. S., Rohrer, J., et al. (2005). *Drosophila* Vps16A is required for trafficking to lysosomes and biogenesis of pigment granules. *J. Cell Sci.* 118(Pt 16), 3663–3673. doi: 10.1242/jcs.02502
- Rebsamen, M., Pochini, L., Stasyk, T., de Araujo, M. E., Galluccio, M., Kandasamy, R. K., et al. (2015). SLC38A9 is a component of the lysosomal amino acid sensing machinery that controls mTORC1. *Nature* 519, 477–481. doi: 10.1038/nature14107
- Reddy, V. S., Shlykov, M. A., Castillo, R., Sun, E. I., and Saier, M. H. Jr. (2012). The major facilitator superfamily (MFS) revisited. *FEBS J.* 279, 2022–2035. doi: 10.1111/j.1742-4658.2012.08588.x
- Roberts, A., Trapnell, C., Donaghey, J., Rinn, J. L., and Pachter, L. (2011). Improving RNA-Seq expression estimates by correcting for fragment bias. *Genome Biol.* 12:R22.
- Robinson, S. W., Herzyk, P., Dow, J. A., and Leader, D. P. (2013). FlyAtlas: database of gene expression in the tissues of *Drosophila melanogaster*. *Nucleic Acids Res.* 41, D744–D750.
- Rodan, A. R., Baum, M., and Huang, C. L. (2012). The *Drosophila* NKCC Ncc69 is required for normal renal tubule function. *Am. J. Physiol. Cell Physiol.* 303, C883–C894.
- Roy, A., Al-bataineh, M. M., and Pastor-Soler, N. M. (2015). Collecting duct intercalated cell function and regulation. *Clin. J. Am. Soc. Nephrol.* 10, 305–324. doi: 10.2215/cjn.08880914
- Saier, M. H. Jr. (2000). A functional-phylogenetic classification system for transmembrane solute transporters. *Microbiol. Mol. Biol. Rev.* 64, 354–411. doi: 10.1128/mmbr.64.2.354-411.2000
- Schellinger, J. N., and Rodan, A. R. (2015). Use of the ramsay assay to measure fluid secretion and ion flux rates in the *Drosophila melanogaster* malpighian tubule. *J. Vis. Exp.* 105:53144.
- Schindelin, J., Arganda-Carreras, I., Frise, E., Kaynig, V., Longair, M., Pietzsch, T., et al. (2012). Fiji: an open-source platform for biological-image analysis. *Nat. Methods* 9, 676–682. doi: 10.1038/nmeth.2019
- Schlosser, P., Li, Y., Sekula, P., Raffler, J., Grundner-Culemann, F., Pietzner, M., et al. (2020). Genetic studies of urinary metabolites illuminate mechanisms of detoxification and excretion in humans. *Nat. Genet.* 52, 167–176. doi: 10.1038/s41588-019-0567-8
- Schmidt, C., Wiedmann, F., Voigt, N., Zhou, X. B., Heijman, J., Lang, S., et al. (2015). Upregulation of K(2P)3.1K+ current causes action potential shortening in patients with chronic atrial fibrillation. *Circulation* 132, 82–92. doi: 10.1161/circulationaha.114.012657
- Schnetkamp, P. P. (2013). The SLC24 gene family of Na⁺/Ca²⁺-K⁺ exchangers: from sight and smell to memory consolidation and skin pigmentation. *Mol. Aspects Med.* 34, 455–464. doi: 10.1016/j.mam.2012.07.008
- Seifter, J. L., and Chang, H. Y. (2017). Extracellular acid-base balance and ion transport between body fluid compartments. *Physiology* 32, 367–379. doi: 10.1152/physiol.00007.2017
- Seyama, I., and Irisawa, H. (1967). The effect of high sodium concentration on the action potential of the skate heart. *J. Gen. Physiol.* 50, 505–517. doi: 10.1085/jgp.50.3.505
- Shirk, P. D., Roberts, P. A., and Harn, C. H. (1988). Synthesis and secretion of salivary gland proteins in *Drosophila gibberosa* during larval and prepupal development. *Roux Arch. Dev. Biol.* 197, 66–74. doi: 10.1007/bf00375929
- Soderberg, J. A., Birse, R. T., and Nassel, D. R. (2011). Insulin production and signaling in renal tubules of *Drosophila* is under control of tachykinin-related peptide and regulates stress resistance. *PLoS One* 6:e19866. doi: 10.1371/journal.pone.0019866

- Son, H. Y., Sohn, S. W., Im, S. H., Kim, H. J., Lee, M. K., Gombojav, B., et al. (2015). Family-based association study of pulmonary function in a population in Northeast Asia. *PLoS One* 10:e0139716. doi: 10.1371/journal.pone.0139716
- Sozen, M. A., Armstrong, J. D., Yang, M., Kaiser, K., and Dow, J. A. (1997). Functional domains are specified to single-cell resolution in a *Drosophila epithelium*. *Proc. Natl. Acad. Sci. U.S.A.* 94, 5207–5212. doi: 10.1073/pnas.94.10.5207
- Sriramachandran, A. M., Meyer-Teschendorf, K., Pabst, S., Ulrich, H. D., Gehring, N. H., Hofmann, K., et al. (2019). Arkadia/RNF111 is a SUMO-targeted ubiquitin ligase with preference for substrates marked with SUMO1-capped SUMO2/3 chain. *Nat. Commun.* 10:3678.
- Stofanko, M., Kwon, S. Y., and Badenhorst, P. (2008). A misexpression screen to identify regulators of *Drosophila* larval hemocyte development. *Genetics* 180, 253–267. doi: 10.1534/genetics.108.089094
- Sun, H., Luo, L., Lal, B., Ma, X., Chen, L., Hann, C. L., et al. (2016). A monoclonal antibody against KCNK9 K(+) channel extracellular domain inhibits tumour growth and metastasis. *Nat. Commun.* 7:10339.
- Swale, D. R., Li, Z., Guerrero, F., Pérez, De León, A. A., and Foil, L. D. (2017). Role of inward rectifier potassium channels in salivary gland function and sugar feeding of the fruit fly, *Drosophila melanogaster*. *Pestic. Biochem. Physiol.* 141, 41–49. doi: 10.1016/j.pestbp.2016.11.005
- Takemoto, K., Kuranaga, E., Tonoki, A., Nagai, T., Miyawaki, A., and Miura, M. (2007). Local initiation of caspase activation in *Drosophila* salivary gland programmed cell death in vivo. *Proc. Natl. Acad. Sci. U.S.A.* 104, 13367–13372. doi: 10.1073/pnas.0702733104
- Talley, E. M., and Bayliss, D. A. (2002). Modulation of TASK-1 (Kcnk3) and TASK-3 (Kcnk9) potassium channels: volatile anesthetics and neurotransmitters share a molecular site of action. *J. Biol. Chem.* 277, 17733–17742. doi: 10.1074/jbc.m200502200
- Talley, E. M., Solorzano, G., Lei, Q., Kim, D., and Bayliss, D. A. (2001). Cns distribution of members of the two-pore-domain (KCNK) potassium channel family. *J. Neurosci.* 21, 7491–7505. doi: 10.1523/jneurosci.21-19-07491.2001
- Trapnell, C., Hendrickson, D. G., Sauvageau, M., Goff, L., Rinn, J. L., and Pachter, L. (2013). Differential analysis of gene regulation at transcript resolution with RNA-seq. *Nat. Biotechnol.* 31, 46–53. doi: 10.1038/nbt.2450
- Trapnell, C., Williams, B. A., Pertea, G., Mortazavi, A., Kwan, G., van Baren, M. J., et al. (2010). Transcript assembly and quantification by RNA-Seq reveals unannotated transcripts and isoform switching during cell differentiation. *Nat. Biotechnol.* 28, 511–515. doi: 10.1038/nbt.1621
- Uhlen, M., Fagerberg, L., Hallstrom, B. M., Lindskog, C., Oksvold, P., Mardinoglu, A., et al. (2015). Proteomics. Tissue-based map of the human proteome. *Science* 347:1260419.
- UniProt Consortium (2019). UniProt: a worldwide hub of protein knowledge. *Nucleic Acids Res.* 47, D506–D515.
- Urban, T. J., Sebro, R., Hurowitz, E. H., Leabman, M. K., Badagnani, I., Lagpacan, L. L., et al. (2006). Functional genomics of membrane transporters in human populations. *Genome Res.* 16, 223–230. doi: 10.1101/gr.4356206
- Vega-Saenz, de Miera, E., Lau, D. H., Zhadina, M., Pountney, D., Coetzee, W. A., et al. (2001). KT3.2 and KT3.3, two novel human two-pore K(+) channels closely related to TASK-1. *J. Neurophysiol.* 86, 130–142. doi: 10.1152/jn.2001.86.1.130
- Wang, J., Kean, L., Yang, J., Allan, A. K., Davies, S. A., Herzyk, P., et al. (2004). Function-informed transcriptome analysis of *Drosophila* renal tubule. *Genome Biol.* 5:R69. doi: 10.1097/00004424-196803000-00014
- Wang, L., Evans, J., Andrews, H. K., Beckstead, R. B., Thummel, C. S., and Bashirullah, A. (2008). A genetic screen identifies new regulators of steroid-triggered programmed cell death in *Drosophila*. *Genetics* 180, 269–281. doi: 10.1534/genetics.108.092478
- Wang, S., Tsun, Z. Y., Wolfson, R. L., Shen, K., Wyant, G. A., Plovnich, M. E., et al. (2015). Metabolism. Lysosomal amino acid transporter SLC38A9 signals arginine sufficiency to mTORC1. *Science* 347, 188–194. doi: 10.1126/science.1257132
- Williams, M. J., Goergen, P., Rajendran, J., Zheleznyakova, G., Hagglund, M. G., Perland, E., et al. (2014). Obesity-linked homologues Tfp2 and Twz establish meal frequency in *Drosophila melanogaster*. *PLoS Genet.* 10:e1004499. doi: 10.1371/journal.pgen.1004499
- Williams, M. J., Klockars, A., Eriksson, A., Voisin, S., Dnyansagar, R., Wiemerslage, L., et al. (2016a). The *Drosophila* ETV5 homologue Ets96B: molecular link between obesity and bipolar disorder. *PLoS Genet.* 12:e1006104. doi: 10.1371/journal.pgen.1006104
- Williams, M. J., Perland, E., Eriksson, M. M., Carlsson, J., Erlandsson, D., Laan, L., et al. (2016b). Recurrent sleep fragmentation induces insulin and neuroprotective mechanisms in middle-aged flies. *Front. Aging Neurosci.* 8:180. doi: 10.3389/fnagi.2016.00180
- Wishart, D. S., Feunang, Y. D., Guo, A. C., Lo, E. J., Marcu, A., Grant, J. R., et al. (2018). DrugBank 5.0: a major update to the DrugBank database for 2018. *Nucleic Acids Res.* 46, D1074–D1082.
- Wu, Y., Baum, M., Huang, C. L., and Rodan, A. R. (2015). Two inwardly rectifying potassium channels, Irk1 and Irk2, play redundant roles in *Drosophila* renal tubule function. *Am. J. Physiol. Regul. Integr. Comp. Physiol.* 309, R747–R756.
- Yan, N. (2015). Structural biology of the major facilitator superfamily transporters. *Annu. Rev. Biophys.* 44, 257–283. doi: 10.1146/annurev-biophys-060414-033901
- Yoshinari, A., and Takano, J. (2017). Insights into the mechanisms underlying boron homeostasis in plants. *Front. Plant Sci.* 8:1951. doi: 10.3389/fpls.2017.01951
- Zelle, K. M., Lu, B., Pyfrom, S. C., and Ben-Shahar, Y. (2013). The genetic architecture of degenerin/epithelial sodium channels in *Drosophila*. *G3* 3, 441–450. doi: 10.1534/g3.112.005272
- Zhang, Y., Zhang, Y., Sun, K., Meng, Z., and Chen, L. (2018). The SLC transporter in nutrient and metabolic sensing, regulation, and drug development. *J. Mol. Cell Biol.* 11, 1–13. doi: 10.1093/jmcb/mjy052

Conflict of Interest: The authors declare that the research was conducted in the absence of any commercial or financial relationships that could be construed as a potential conflict of interest.

Copyright © 2020 Ceder, Aggarwal, Hosseini, Maturi, Patil, Perland, Williams and Fredriksson. This is an open-access article distributed under the terms of the Creative Commons Attribution License (CC BY). The use, distribution or reproduction in other forums is permitted, provided the original author(s) and the copyright owner(s) are credited and that the original publication in this journal is cited, in accordance with accepted academic practice. No use, distribution or reproduction is permitted which does not comply with these terms.



Transferrin Receptor Functionally Marks Thermogenic Adipocytes

Jin Qiu^{1†}, Zhiyin Zhang^{2†}, Sainan Wang^{1†}, Yanru Chen^{2†}, Caizhi Liu¹, Sainan Xu¹, Dongmei Wang¹, Junlei Su², Mengshan Ni², Jian Yu¹, Xiangdi Cui¹, Lu Ma¹, Tianhui Hu¹, Yepeng Hu³, Xuejiang Gu^{3*}, Xinran Ma^{1,3*}, Jiqiu Wang^{2*} and Lingyan Xu^{1*}

¹ Shanghai Key Laboratory of Regulatory Biology, Institute of Biomedical Sciences, School of Life Sciences, East China Normal University, Shanghai, China, ² Department of Endocrinology and Metabolism, China National Research Center for Metabolic Diseases, Ruijin Hospital, Shanghai Jiao Tong University School of Medicine, Shanghai, China, ³ Department of Endocrine and Metabolic Diseases, the First Affiliated Hospital of Wenzhou Medical University, Wenzhou, China

OPEN ACCESS

Edited by:

Cesare Indiveri,
University of Calabria, Italy

Reviewed by:

Prashant Rajbhandari,
Icahn School of Medicine at Mount
Sinai, United States

Liwei Xie,

Guangdong Academy of Sciences,
China

Xingxing Kong,

UCLA Department of Pediatrics,
United States

*Correspondence:

Xuejiang Gu
guxuejiang@wmu.edu.cn

Xinran Ma

xrma@bio.ecnu.edu.cn

Jiqiu Wang

wangjq@shsmu.edu.cn

Lingyan Xu

lyxu@bio.ecnu.edu.cn

[†] These authors have contributed
equally to this work

Specialty section:

This article was submitted to
Cellular Biochemistry,
a section of the journal
Frontiers in Cell and Developmental
Biology

Received: 14 June 2020

Accepted: 12 October 2020

Published: 05 November 2020

Citation:

Qiu J, Zhang Z, Wang S, Chen Y,
Liu C, Xu S, Wang D, Su J, Ni M,
Yu J, Cui X, Ma L, Hu T, Hu Y, Gu X,
Ma X, Wang J and Xu L (2020)
Transferrin Receptor Functionally
Marks Thermogenic Adipocytes.
Front. Cell Dev. Biol. 8:572459.
doi: 10.3389/fcell.2020.572459

Background: Thermogenic adipocytes, including beige and brown adipocytes, are critical for thermogenesis and energy homeostasis. Identification of functional cell surface markers of thermogenic adipocytes is of significance for potential application in biological and clinical practices.

Methods: With a combination of RNA-sequencing of *in vivo* and *in vitro* models, we identified transferrin receptor (Tfr1), a receptor specialized for cellular iron uptake, as a previously unappreciated cell surface molecule for thermogenic adipocytes compared to white adipocytes. The alternation of Tfr1 levels under physiological and pathological stimuli was assessed, and the mitochondria functionality, browning capacity, and iron metabolism of mature adipocytes were examined with *Tfr1* knockdown.

Results: Tfr1 was expressed predominantly in thermogenic adipocytes versus white adipocyte, and its expression levels were tightly correlated with the activation or inhibition status of thermogenic adipocytes under external stimuli. Besides, *Tfr1* gene deficiency in thermogenic adipocytes led to reduced thermogenic gene programs and mitochondrial integrity.

Conclusion: Tfr1 functionally marks thermogenic adipocytes and could serve as a potential thermogenic adipocyte surface marker.

Keywords: Tfr1, iron homeostasis, thermogenic adipocytes, brown gene program, mitochondrial integrity

INTRODUCTION

The obesity pandemic in modern society predisposes a large population to metabolic diseases, including Type 2 diabetes, hepatic steatosis, and cardiovascular diseases, thus greatly burdening the healthcare system (Jung and Choi, 2014; Chung et al., 2016). Obesity is manifested as excess accumulation of fat in adipose tissues. Three classes of adipose tissues were identified, featuring distinct location, morphology, and function (Hildebrand et al., 2018). White adipose tissue is

Abbreviations: Tfr1, transferrin receptor; Ucp1, uncoupling protein 1; IR β , insulin receptor β ; HFD, high-fat diet; DFO, deferoxamine; PFA, paraformaldehyde; BMI, body mass index; SVFs, stromal vascular fractions; iWAT, inguinal adipose tissue; eWAT, epididymal adipose tissue; BAT, brown adipose tissue; GWAS, genome-wide association studies; GO, gene ontology; MFs, molecular functions; CC, cellular component; KEGG, Kyoto Encyclopedia of Genes and Genomes.

a major site for energy storage in the form of triglyceride, while brown adipose tissue (BAT) is thermogenically poised to consume fuel for thermogenesis and energy expenditure. Beige adipocytes, a newly discovered type of adipose tissue, reside heterogeneously with white adipocytes in certain white fat depots. It resembles white adipocyte in resting state, while becoming highly inducible upon cold or β -adrenergic signaling activation and retains thermogenic capacity similar to brown adipocyte through a process referred to as “browning of white fat.” The functions of these three kinds of adipose tissues balance energy depository and expenditure, thus determining overall body weight and energy homeostasis (Scheja and Heeren, 2016; Brandão et al., 2017).

Recently, research interests have been piqued toward the thermogenic adipocytes including brown and beige adipocytes for their potent capability in dissipating excessive calories upon activation. In addition, brown and beige adipocytes consume large amounts of lipid and glucose as fuels for thermogenesis, thus serving as a metabolic sink crucial for maintaining blood lipid/glucose levels (Sidossis and Kajimura, 2015). Evidences from genetic animal models attest to the crucial protective roles of thermogenic adipocytes against obesity and metabolic homeostasis. For example, genetic ablation of critical thermogenic genes *Prdm16* and *Pgc1 α* led to obesity and metabolic dysfunctions in mice (Gastaldi et al., 2007; Hasegawa et al., 2018). Importantly, in adult humans, functional brown and beige fat exist as a heterogeneous mixture located in deeper cervical, supraclavicular, and paraspinal areas, the exact constituents of which are dependent on their depth under the skin (Scheele et al., 2014). Moreover, white depots in humans also possess browning ability upon stimulation. For example, pheochromocytoma patients usually feature a pathologically lean status because of the strong white fat browning in various white depots caused by the sustained elevation of β 3-adrenergic signaling (Wang et al., 2011; Frontini et al., 2013). Importantly, the ability of brown and beige fat activation significantly declined in obese or elderly subjects (Diaz et al., 2014), indicative of the potential of targeting thermogenic adipocytes to prevent and treat obesity or metabolic dysfunctions in humans. To date, cold and β 3-androgenic agonists, i.e., Mirabegron, have been shown to activate thermogenic adipocytes in humans, but their wide applications have been hindered by side effects on cardiovascular systems (Ng et al., 2017; Baskin et al., 2018), warranting continued search for targeting strategies on thermogenic adipocytes.

It would be critical to take a few caveats into consideration when designing novel strategies to activate thermogenic adipocytes. For example, since white and brown/beige adipocytes share many common protein expressions, molecules specific to brown/beige adipocytes need to be identified to ensure target specificity and avoid undesired effects on white adipocytes. Hitherto, a number of genes have been identified that featured distinct expressions in thermogenic adipocytes compared to white adipocyte, including *Tbx1* and *Tmem26* for beige fat; uncoupling protein 1 (*Ucp1*), *Cidea*, and *Prdm16* for brown fat; and *Pat2* and *P2rx5* for brown/beige fat (Ussar et al., 2014;

De Jong et al., 2015; Rockstroh et al., 2015). However, these markers either have intracellular expressions that limited their implications in intact tissues or *in vivo* studies, or are surface markers without functionality evaluations. In this sense, it would be vital to identify novel cell surface molecules of thermogenic adipocytes that could impact thermogenic functions.

In the present study, we sought to identify cell surface molecules for thermogenic adipocytes versus white adipocytes using a combination of RNA-sequencing analysis, *in vitro* assays, and *in vivo* approaches. We unveiled that the surface molecule transferrin receptor (Tfr1) features high expressions in thermogenic adipocytes versus white adipocytes in cells and rodents. Tfr1, as a membrane protein, plays critical roles in iron homeostasis and is involved in various physiological and pathological processes by formation of the Tfr1–Transferrin (Tfr)–iron complex, internalization into endosomes, and disassociation from iron in acidification to eventually release iron into the cytosol via Divalent metal transporter 1 (Dmt1) on the endosomal membrane (Touret et al., 2003). In this work, we found that Tfr1 expression level is tightly correlated with metabolic status, and it is indispensable for intact thermogenic and mitochondrial programs in brown/beige adipocytes. Thus, we proposed Tfr1 as a promising therapeutic cell surface target for obesity and metabolic diseases.

MATERIALS AND METHODS

Preadipocyte Isolation and Differentiation

Adipocytes and stromal vascular fraction (SVF) from mice epididymal, subcutaneous, and brown fat were separated as described previously (Lavery et al., 2016). Briefly, tissue was fractionated by collagenase for 30 min at 37°C immediately after excision. The released cells were sieved through a 200- μ m polypropylene filter. Floating cells (adipocytes) were transferred to a 2-ml tube, washed in 1 ml of Hanks' Balanced Salt Solution (HBSS, 14025092, Gibco, Germany) with 5% bovine serum albumin (BSA, SRE0096, Sigma-Aldrich, United States), and collected after floating. The non-floating cells (SVF) were centrifuged at 3000 rpm for 5 min, and the supernatant was removed. The SVFs were cultured and differentiated following a standard protocol. Briefly, after reaching confluence (day 0), differentiation was initiated by adding differentiation medium containing 5 μ g/ml insulin (HI0240, Eli Lilly, United States), 0.5 mM isobutylmethylxanthine (I7018, Sigma, United States), 1 μ M dexamethasone (D4902, Sigma, United States), 1 nM T3 (T2877, Sigma, United States), and 1 μ M rosiglitazone (R2408, Sigma, United States). After 2 days, the medium was replaced with insulin and T3. Medium was changed every 2 days until day 8. The adipocytes and SVF were kept for further usage. The immortalized beige and brown preadipocytes were kind gifts from the Chinese Academy of Sciences (Prof. Qiurong Ding) and Fudan University Shanghai Medical College (Prof. Dongning Pan).

RNA-seq and Bioinformatic Analysis

Total RNA was extracted with Trizol (9109, Takara, Japan) and purified by RNeasy Micro kit (74004, QIAGEN, Germany). The quality of purified RNA was examined by NanoDrop ND-1000 and Agilent Bioanalyzer 2100 (Agilent Technologies, Santa Clara, CA, United States). RNA libraries were prepared using the TruSeq RNA Library Preparation Kit (Illumina, San Diego, CA, United States) and were performed on an Illumina HiSeq 2500 sequencing instrument (Illumina, San Diego, CA, United States). The high-quality reads were aligned to the mouse genome (GRCm38/mm10) assembled against mouse mRNA annotation using HTSeq. Differential gene expression was determined using cufflink (version:2.1.1). The fold change was calculated using the ratio of inguinal adipose tissue (iWAT)/epididymal adipose tissue (eWAT) using DESeq2 package. The differentially expressed genes with a *P* less than 0.05 and fold change greater than 2 were considered for further evaluation.

The heatmap was generated by R software (version 3.6.3) and the Venn diagram was performed with the web tool¹. Selected gene sets were annotated by Gene ontology (GO) analysis (Ashburner et al., 2000), divided into molecular function (MF), biological process (BP), and cellular component (CC), as well as Kyoto Encyclopedia of Genes and Genomes (KEGG) database (Altermann and Klaenhammer, 2005). GO and KEGG enrichment analysis were conducted by DAVID database (DAVID 6.8)² (Huang et al., 2009a,b).

Mice Experiments

C57BL/6J and *129/Sv* mice were maintained on a 12-h light/dark cycle and had free access to food and water. For establishment of animal models, *C57BL/6J* male mice were used in the study. To induce browning of adipose tissues, 8-week-old male mice were housed at either 22°C normal or 5°C cold environment in a thermo-controlled incubator for 1 week. Besides, 4-month-old mice were injected intraperitoneally with either saline or CL316243 (1 µg/g body weight) daily for 14 days, as described previously (Labbe et al., 2016) or intraperitoneally with either saline or Rosiglitazone (10 µg/g body weight) daily for 10 days. To study the effects of obesity and aging on gene expression, 2-month-old male mice with *C57BL/6J* background were fed either chow diet or high-fat diet (HFD) containing 60% fat (Research diet) for 8 weeks. Meanwhile, 5-month-old *db/db*, 18-month-old mice, and their individual controls were also used. All animal experiments were approved by the Animal Care and the Animal Ethics Committee of East China Normal University.

Real-Time PCR

RNAs from adipocytes and mouse tissues were extracted using Trizol (9109, Takara, Japan). Total RNA (1 µg) was reversely transcribed with PrimeScript RT reagent Kit with gDNA Eraser kit (PR047Q, Takara, Japan) and qPCR was performed using SYBR green (11143ES50, Yeasen, China) on the LightCycler480

system (Roche, Switzerland). mRNA levels were calculated by the $\Delta\Delta$ CT method with the level of 36B4 as the internal control. The primers used for qPCR are in **Supplementary Table S1**.

Western Blot and Membrane Fractionation Isolation

For Western blot, the protein concentrations were quantified using a BCA Protein Assay kit (P0010, Beyotime Biotechnology, China), and equal amounts of protein were subjected to 8% sodium dodecyl sulfate polyacrylamide gel electrophoresis (SDS-PAGE) and then transferred to a NC membrane (66485, PALL, United States). After blocking with 5% skimmed milk, the membrane was incubated overnight at 4°C with indicated primary antibodies and subsequently incubated with secondary antibody at room temperature for 1 h. The images of the blots were detected using the Odyssey imaging system (LI-COR Biotechnology, United States) (Yue et al., 2019). Proteins from the membrane and cytoplasm fractions of adipocytes were separated using the Membrane and Cytosol Protein Extraction Kit (P0033, Beyotime Biotechnology, China), according to the manufacturer's instruction. Briefly, 100 mg of iWAT or BAT were homogenized on ice in Membrane Protein Extraction Reagent A containing proteasome inhibitor cocktail (Sigma). The homogenate was placed on ice for 15 min and centrifuged at 700 × *g* for 10 min, followed by further centrifuge at 14,000 × *g* for 30 min, and supernatant (cytosol protein) was carefully collected and the pellet was then resuspended in Membrane Protein Extraction Reagent B and centrifuged at 14,000 × *g* for 5 min. The supernatant containing cell membrane protein was eventually collected. Antibodies used for Western blot are as follows: anti-Tfr1 (ab84036, Abcam, United Kingdom), anti-Gapdh (sc-32233, Santa Cruz, United States), anti-Tubulin (AF5012, Beyotime, China), anti-Insulin Receptor β (IRβ) (ab69508, Abcam, United Kingdom), IRDye 800CW Goat anti-Rabbit IgG (P/N 926-32211, LI-COR Biotechnology, United States), and IRDye 800CW Goat anti-Mouse IgG (P/N 926-32210, LI-COR Biotechnology, United States).

Knockdown of *Tfr1* and Modulation of Iron Levels in Adipocyte and Adipose Tissue

Immortalized beige and brown adipocytes were transfected with siRNA targeting *Tfr1* (*siTfr1*) and a negative control siRNA (NC) with TransExcellent™-siRNA (Cenji Biotechnology, Shanghai, China) at day 4 after differentiation. For iron level modulation, mature adipocytes were treated with 300 mM iron chelator deferoxamine (DFO) (D9533, Sigma, United States) or 160 µg/ml FeSO₄ (F8633, Sigma, United States) for 48 h.

To silence *Tfr1* expression *in vivo*, *siTfr1* or NC was transferred unilaterally into iWAT of *C57BL/6J* mice by a commercialized kit (Entranster-*in vivo*; Engreen Biosystem, Beijing, China) as previously reported (Zhou et al., 2015). The iWAT was taken 2 days later for further analysis. The experiment was approved by the Animal Care and the Animal Ethics Committee of East China Normal University.

¹<http://bioinformatics.psb.ugent.be/webtools/Venn/>

²<https://david.ncifcrf.gov/>

Immunostaining of Adipocytes and Adipose Tissues

For immunofluorescent staining, mature immortalized beige and brown adipocytes were fixed with 4% paraformaldehyde (PFA), blocked with 10% normal goat serum in 0.1% Tween-20/PBS, and incubated for 2 h with primary antibody Tfr1 (Abcam, ab84036) followed by AlexaFluor-488 goat anti-mouse IgG (B40941, Thermo Fisher, United States) as a secondary antibody. Slides were mounted with Vectashield (Vector Labs, United States) containing DAPI (P36931, Invitrogen, United States).

For immunohistochemistry staining, adipose tissues were placed in Bouin fixative, embedded in paraffin, and subsequently cut into 5- μ m sections. Sections were deparaffinized, hydrated in xylene and graded ethanol, and rinsed in PBS for 5 min before incubated with pepsin (Sigma, United States). The sections were incubated for 10 min in 0.3% H₂O₂ to quench endogenous peroxidase activity. Sections were blocked and incubated at 4°C overnight with diluted polyclonal antibodies against Ucp1 (ab10983, Abcam, United Kingdom) and Tfr1 (ab84036, Abcam, United Kingdom) and with HRP-conjugated goat anti-rabbit IgG for 1 h. DAB chromogen (DAB Substrate Kit, H-2200, Vector Labs, United States) was used for peroxidase detection of immunoreactivity. Images were taken with a Zeiss 710 confocal microscope.

MitoTracker Analysis

Mitochondria quality and membrane integrity were assessed by staining with MitoTracker[®] Red CMXRos (Thermo Fisher, United States). Immortalized brown and beige adipocytes were differentiated to day 4 and transfected with si*Tfr1*. After 48 h, mature adipocytes were incubated with 100 nM MitoTracker for 20 min and then washed three times with PBS. Cells were fixed with 4% PFA for 10 min and fluorescent images were obtained using the Nikon inverted microscope ECLIPSE Ts2.

Bioenergetic Analysis

Oxygen consumption rate (OCR) and extracellular acidification rate (ECAR) were measured using the XF24 Analyzers (Seahorse Bioscience). All compounds and media were prepared according to the manufacturers' instructions. C3H10T1/2 cells were differentiated for 4 days and transfected with NC or si*Tfr1*; OCR and ECAR were measured 2 days later. OCR was measured under basal conditions, following the addition of ATP synthase inhibitor oligomycin, the mitochondrial uncoupler FCCP, and the complex III inhibitor antimycin A. ECAR was measured following the addition of glucose or 2-deoxyglucose (2-DG) at the indicated time.

Determination of Lipid Peroxidation

Lipid peroxidation was assessed using lipid peroxidation kit (ab243377, Abcam, United Kingdom) according to the manufacturer's instructions. Briefly, lipid peroxidation sensor was added to adipocytes and incubated for 30 min. After washing

with HBSS, fluorescence was detected at Ex/Em = 490 nm (FITC)/530 nm (FITC) and 545 nm (TRITC)/600 nm (TRITC) with a fluorescence microscope. Adipocytes were photographed and the lipid peroxidation was quantified as the FITC/TRITC signal ratio (Molecular Devices). H₂O₂ treatment was used as a positive control.

Detection of Intracellular ROS

Intracellular ROS levels were measured by the fluorescent 2',7'-dichlorodihydrofluorescein (DCF) assay. Briefly, mature adipocytes were seeded in 96-well plates. After siRNA transfection for 48 h, culture medium was removed and adipocytes were incubated with 10 μ mol/L DCFH-DA reagent (Reactive Oxygen Species Assay Kit, S0033S, Beyotime, China) for 20 min. After washing with serum-free cell culture medium to completely remove DCFH-DA, adipocytes were photographed and mean DCF fluorescent intensities were detected using a SpectraMax M2 microplate fluorometer (Molecular Devices).

Determination of Iron Concentration

Intracellular iron level was determined using the iron assay kit (ab83366, Abcam, United Kingdom) according to the manufacturer's instructions. Briefly, immortal brown and beige preadipocytes were differentiated following standard protocol to day 0, 2, 4, and 6. Cells were collected and washed in ice-cold PBS and homogenized in iron assay buffer on ice, followed by centrifugation (16,000 \times g, 10 min) at 4°C to remove insoluble material. Supernatant was collected and incubated with iron reducer for 30 min at 25°C. Next, 100 μ l of iron probe was added and mixed well with a horizontal shaker for 60 min at 25°C. The absorbance was then measured at 593 nm using SpectraMax 190 Microplate Reader (Molecular Devices).

Cell Viability Assay

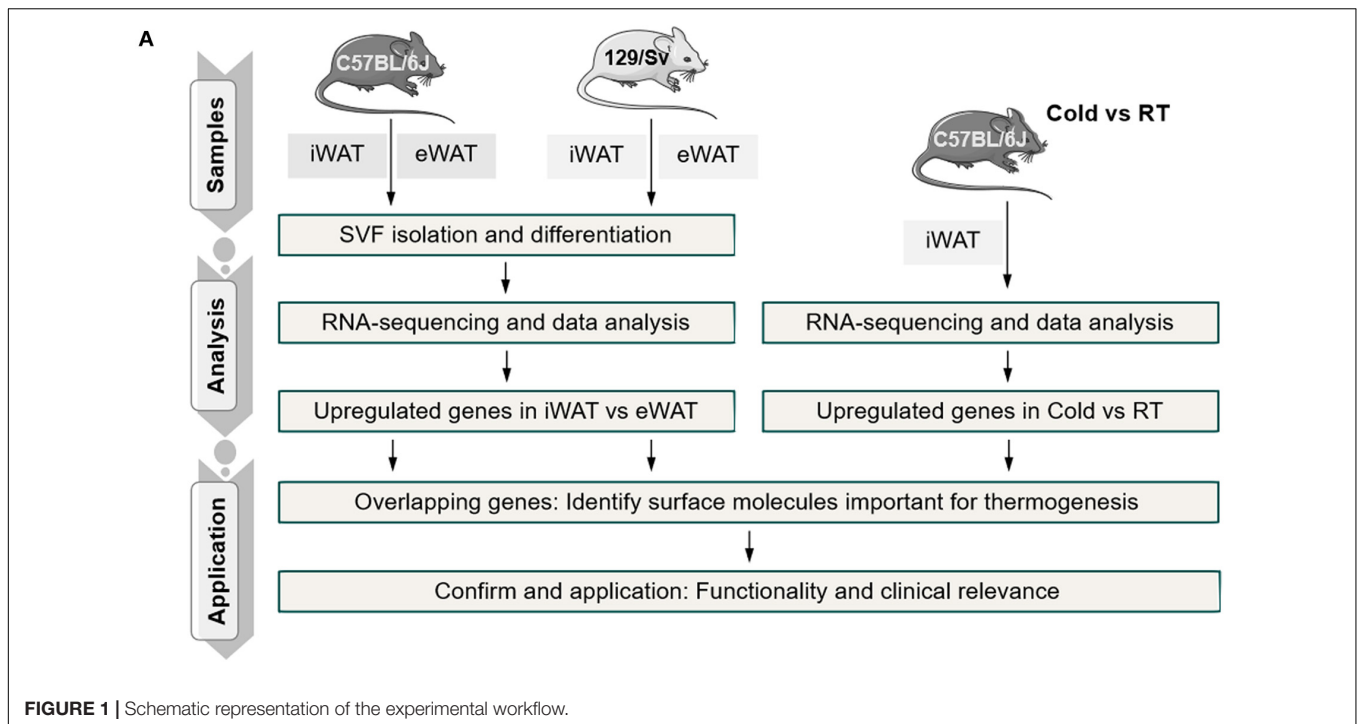
Cell viability was evaluated using the cell counting kit-8 (C0042, Beyotime, China). Briefly, 10 μ l of CCK8 solution was added to each well and incubated for 2 h at 37°C. The optical density (OD) value of each well at 450 nm was measured and recorded using SpectraMax 190 Microplate Reader (Molecular Devices).

Cellular TG and NEFA Measurement

After removing the cell culture medium, adipocytes were lysed with RIPA buffer and centrifuged to remove cell debris. Supernatant was collected from cellular TG (triglyceride) and NEFA (non-esterified free fatty acids) examination with Triglyceride Assay and NEFA Kit (A110-2-1, A042-2-1, Jincheng, Nanjing, China) and normalization to total protein concentration.

Lentiviral Constructions and Infection

Transferrin receptor lentiviral particles were constructed and concentrated by GeneChem company (Shanghai). Immortalized beige preadipocytes were infected with 2 \times 10⁹ PFU lentiviral particles carrying Tfr1 or Gfp with 4 mg/ml sequalone (S2667, Sigma, United States) for 24 h and switched to fresh medium for another 2 days. Samples were collected for real-time PCR and Western blot analysis.



Statistical Analysis

Data are presented as means \pm SEM. Student's *t* test analysis was performed with GraphPad Prism software and $P < 0.05$ was considered as significant.

RESULTS

In silico Analysis of Cell Surface Molecules of Beige Versus White Adipocytes

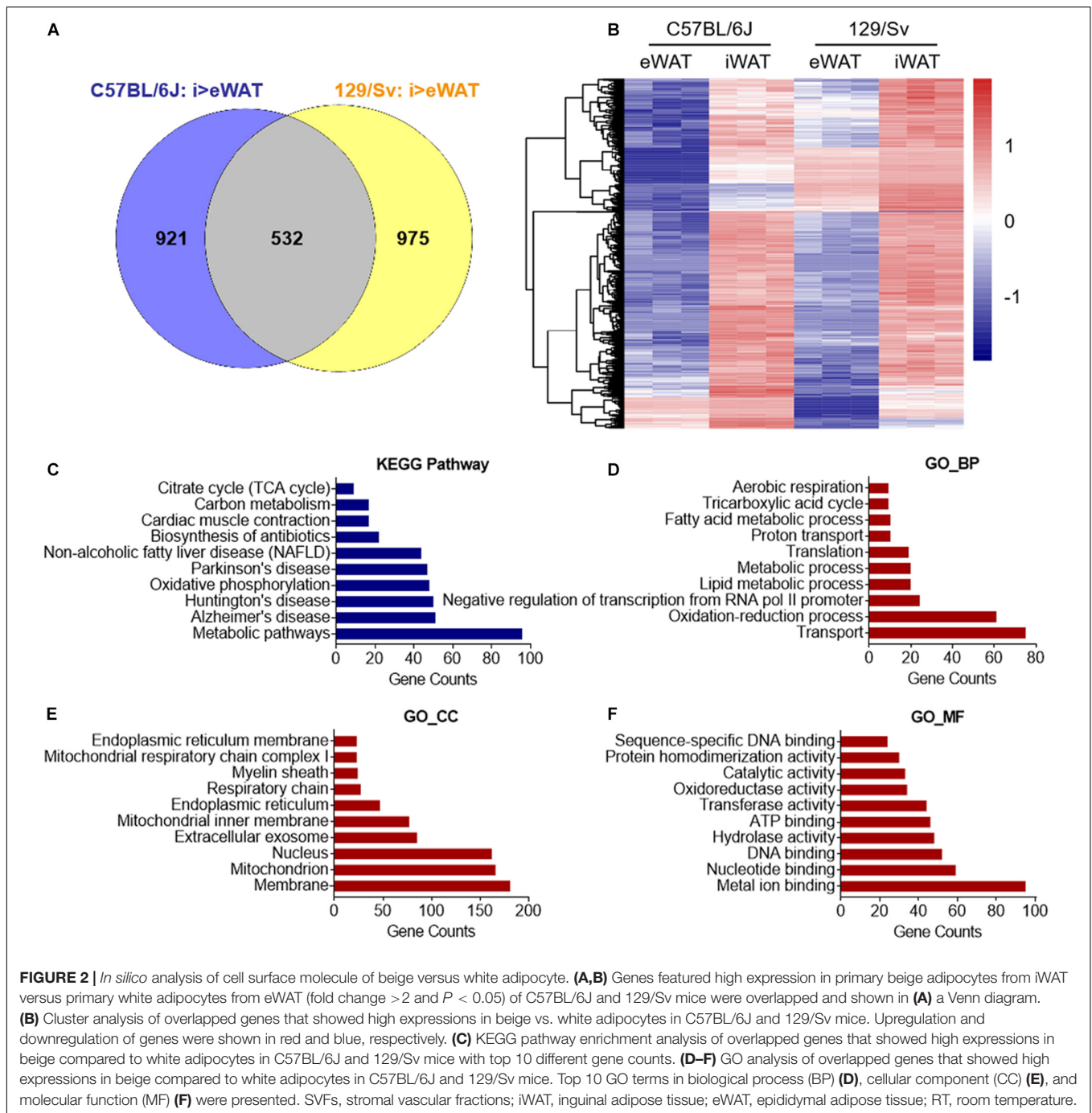
Primary SVFs were isolated from iWAT, which undergoes the most profound induction of beige adipocytes, and from eWAT, which are particularly resistant to beigeing and are considered white adipocytes from 2-month-old *C57BL/6J* and *129/Sv* male mice, the two most commonly used inbred mice in scientific studies. These SVFs were cultured and induced for differentiation with brown gene program-inducing cocktails (Tseng et al., 2008). After 8 days, fully differentiated mature adipocytes of iWAT and eWAT origin were subjected to RNA-sequencing analysis (Figure 1). To identify thermogenic-specific genes, we focused on oscillating genes that feature significant changes (>2 -fold change and $P < 0.05$) in iWAT versus eWAT in both *C57BL/6J* and *129/Sv* mice, which rendered 532 genes after overlapping (Figures 2A,B). KEGG pathway enrichment analysis revealed that these genes were enriched for metabolic pathways (Figure 2C). Notably, top terms in GO analysis of BP, CC, and MF are enriched for transport, membrane, and metal ion binding, respectively (Figures 2D–F). Furthermore, since cold stimuli strongly induce browning of beige adipocytes, we thus performed RNA-sequencing using iWATs from *C57BL/6J*

mice maintained under room temperature or under 1-week cold stimuli. KEGG as well as GO analysis on oscillating genes of iWAT under cold or room temperature with significant changes (>2 -fold change and $P < 0.05$) also enriched similar results, particularly in metal ion binding/transport signaling (Supplementary Figures S1A–D). These results suggested a potential critical role of metal ion binding/transporting membrane proteins in beige fat function.

Tfr1 Marks Thermogenic Adipocyte Both *in vivo* and *in vitro*

To identify surface molecules important for thermogenesis, we overlapped enriched gene sets from *in vitro* induced beige adipocytes versus white adipocytes derived from *C57BL/6J* mice and *129/Sv* mice, as well as *in vivo* beige adipocytes under cold stimuli versus room temperature (Figure 3A). Interestingly, this overlap generated 46 genes that characterize both specific expression in beige adipocytes versus white adipocytes and strong induction upon cold stimuli, indicative of their potential function in the browning process (Figure 3B and Supplementary Table S2). Of note, among the list, Tfr1 (also named as Tfrc), a receptor specialized for cellular iron uptake, is the only gene encoding a membrane protein. Thus, we next focused our following studies on Tfr1.

We first validated Tfr1 expression levels in different adipose depots. Consistent with RNA-seq results, we found that *Tfr1* mRNA is highly expressed in mice iWAT and BAT, far eclipsed that in eWAT, suggesting the specific expression of *Tfr1* in thermogenic adipose tissues (Figure 3C). Immunohistological analysis showed that Tfr1 protein also featured dominant



expressions in iWAT and BAT as compared to eWAT in a pattern that resembled *Ucp1* expression (Figure 3D). Furthermore, profound *Tfr1* mRNA and proteins also existed in primary or immortalized mature beige and brown adipocytes versus white adipocytes (Figures 3E–G). We found that *Tfr1* characterizes cell membrane localization in beige and brown adipocytes as shown by immunostaining and Western blot using a classic cell surface receptor $IR\beta$ and a cytosolic protein Tubulin as positive controls (Figures 3H,I and Supplementary Figure S2A). Of note, high-resolution confocal

images suggested that a small fraction of *Tfr1* also underwent internalization (Supplementary Figure S2A), as previously reported (Jabara et al., 2016).

Meanwhile, it has to be noted that, by generating a cDNA tissue library containing brain, heart, liver, spleen, lung, kidney, pancreas, gastrocnemius, and soleus muscle from 2-month-old *C57BL/6J* male mice, we found that *Tfr1* also expressed in other tissues, overall suggesting that *Tfr1* may be critical for iron homeostasis in various tissues (Supplementary Figure S2B). Though it may not serve as a unique marker for brown/beige

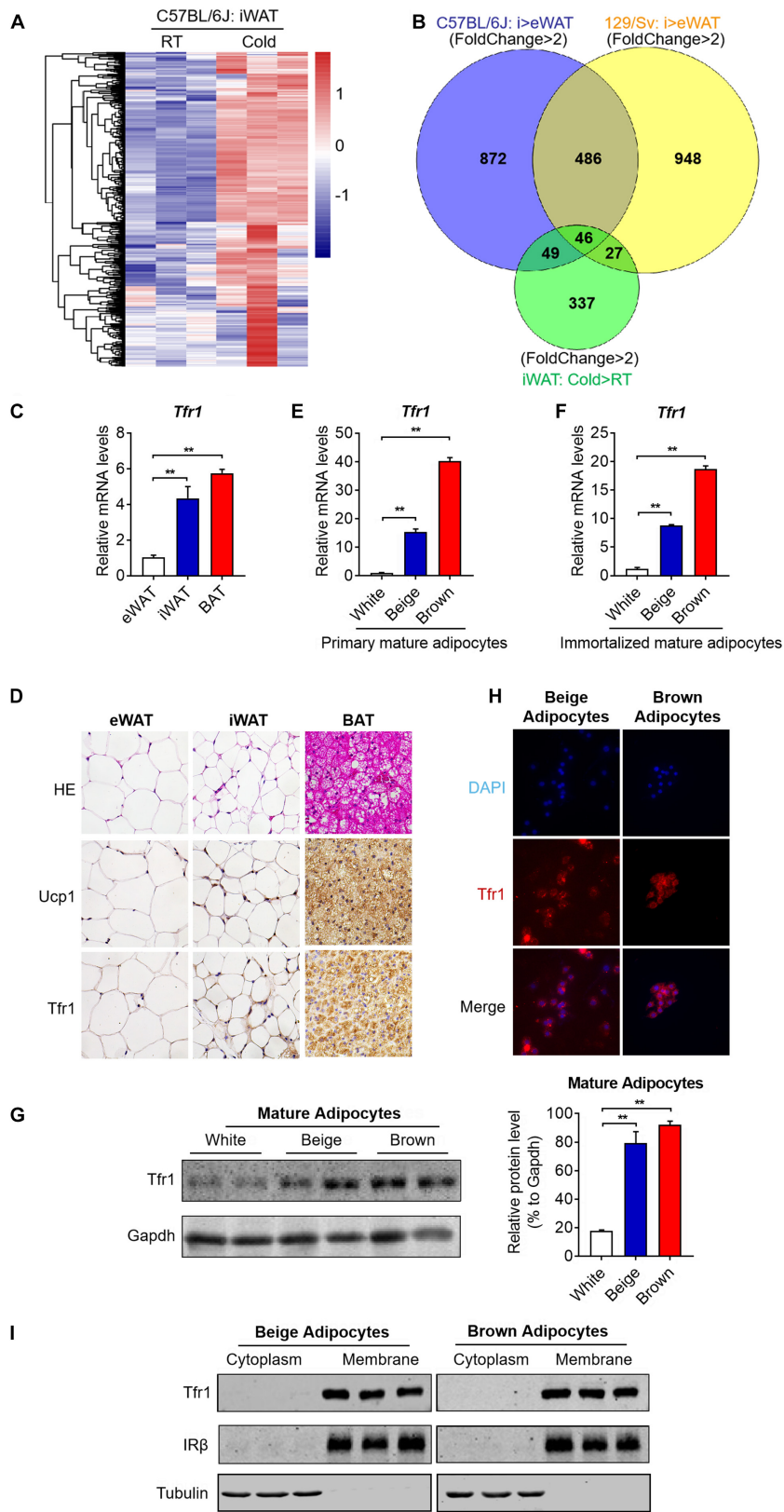


FIGURE 3 | Continued

FIGURE 3 | Screening by *silico* analysis and validation of the thermogenic adipocyte surface marker. **(A)** Cluster analysis of overlapped genes that showed high expressions in iWAT from C57BL/6J mice under cold stimuli vs. RT (fold change >2 and $P < 0.05$). Upregulation and downregulation of genes were shown in red and blue, respectively. **(B)** Genes that featured high expressions in beige compared to white adipocytes in C57BL/6J and 129/Sv mice as well as genes that showed high expressions in iWAT from C57BL/6J mice under cold stimuli vs. RT (fold change >2 and $P < 0.05$) were overlapped and shown in a Venn diagram. **(C)** Gene expression analysis of *Tfr1* in eWAT, iWAT, and BAT. **(D)** Representative H&E staining and immunostaining of Ucp1 and Tfr1 of eWAT, iWAT, and BAT. **(E,F)** Gene expression analysis of *Tfr1* in primary **(E)** and immortalized **(F)** mature adipocytes. **(G)** Western blot analysis (left) and quantification (right) of Tfr1 in thermogenic and white adipocytes. **(H)** Representative pictures of immunofluorescent staining of Tfr1 in thermogenic adipocytes. Tfr1 and nucleus were indicated in red and blue, respectively. **(I)** Western blot analysis of Tfr1 in cytoplasm and membrane fractions of immortalized thermogenic adipocytes using the membrane protein IR β and cytosolic protein Tubulin as positive controls. Data are presented as mean \pm SEM. iWAT, inguinal adipose tissue; eWAT, epididymal adipose tissue; BAT, brown adipose tissue. ** $P < 0.01$. The results are representative of at least three independent experiments.

adipocytes, Tfr1 may be valuable to distinguish between thermogenic versus white adipocytes.

Tfr1 Predominantly Expressed in Mature Thermogenic Adipocytes

Beige and brown preadipocytes differentiate into mature adipocytes to become fully functional metabolically and thermogenically. The expression levels of an array of genes important for thermogenic adipocyte functions are induced gradually during the differentiation process and peaked in mature adipocytes, i.e., Ppar γ , aP2, and Ucp1. We found that *Tfr1* expressed predominantly in mature adipocytes compared to preadipocytes in SVFs from mouse iWAT and BAT and immortalized beige and brown adipocytes (Figures 4A,B). Moreover, Tfr1 expressions increased during the differentiation process in a pattern similar to Ppar γ , aP2, and Ucp1 (Figures 4C–F and Supplementary Figure S3), accompanied by increased cellular iron levels (Figures 4G,H). Of note, *Tfr1* knockdown in adipocytes during differentiation affected gene programs related to adipogenesis, lipid synthesis, oxidative phosphorylation, fatty acid oxidation, as well as cellular TG and NEFA levels (Supplementary Figure S4). These results suggested that Tfr1 may play biological roles mainly in mature thermogenic adipocytes.

Tfr1 Levels in Thermogenic Adipocytes Responds to Metabolic Status

To further understand the role of Tfr1 in thermogenic adipocytes, we examined Tfr1 levels in fat tissues under various physiological or pathological scenarios that are known to induce or suppress beige/brown fat thermogenic capacity. Importantly, compared to mice housed at room temperature, *Tfr1* levels were highly induced along with Ucp1, a marker for thermogenic activation, in beige and brown fat from mice maintained in cold environment for 1 week (Figure 5A and Supplementary Figure S5A). β 3-adrenergic receptor agonist CL316243 and Ppar γ full agonist Rosiglitazone treatment have been shown to promote white fat browning in mice (Ohno et al., 2012; De Jong et al., 2015). Consistently, daily CL316243 injection for 2 weeks and Rosiglitazone injection for 10 days in mice both significantly elevated *Tfr1* and Ucp1 expressions in iWAT and BAT (Figures 5B,C and Supplementary Figures S5B,C). On the other hand, we tested *Tfr1* levels in beige and brown fat from multiple mice models with impaired thermogenesis and increased whitening phenotype, including diet-induced obese

mice (HFD mice), genetic obese mice (*db/db* mice), as well as aging mice. We found significantly decreased *Tfr1* levels along with declined Ucp1 expressions compared to control mice (Figures 5D–F and Supplementary Figures S5D–F). Moreover, protein levels of Tfr1 in iWAT and BAT changed consistently with its mRNA levels (Figures 5G–J). Importantly, *Tfr1* levels were positively correlated with the expressions of Ucp1 in iWAT and BAT (Figures 6A,B). In addition, Tfr1 and Ucp1 proteins also showed similar high induction in iWAT under cold treatment (Figure 6C), suggesting a tight correlation of Tfr1 levels with the metabolic status of thermogenic adipocytes. Furthermore, the correlation of *Tfr1* expression with Ucp1 was recapitulated in immortalized brown/beige adipocytes treated with Forskolin or H89, the classic *in vitro* cellular models of thermogenic activation and suppression (Supplementary Figures S5G–J). Meanwhile, in addition to *Tfr1* and Ucp1, iron metabolic regulator *Irf1* and *Irf2* levels were also increased in iWAT upon cold stimulation compared to thermoneutral environment, suggesting a systematic mobilization of iron regulatory genes (Supplementary Figures S5K,L). Overall, these results indicated that Tfr1 levels fluctuated in response to physiological and pathological changes impacting thermogenic adipocyte functions both *in vivo* and *in vitro*.

Tfr1 Is Indispensable for Functional Thermogenic Adipocytes

Since we have demonstrated that Tfr1 is highly expressed in thermogenic adipocytes and responds to metabolic changes, we next examined whether Tfr1 plays active roles in mature thermogenic adipocyte functionality. Indeed, *Tfr1* suppression in mature brown and beige adipocytes resulted in impaired mitochondrial quality and membrane integrity as revealed by MitoTracker staining (Figure 7A and Supplementary Figure S6A). Moreover, *Tfr1* knockdown suppressed cellular oxygen consumption and glycolysis as revealed by Seahorse analysis (Figures 7B,C), which was consistent with reduced expressions of brown gene programs, including thermogenic genes (*Ucp1*, *Pgc1a*, *Cidea*, *Elovl3*, and *Prdm16*), mitochondrial genes (*CytC*, *Cox4 β* , *Mfn1*, *Mfn2*, *Cpt1a*, and *ATPsyn β*), mitochondrial respiratory complex genes (I–V), and glycolytic genes (*Pfk1*, *Pkm2*, and *Hk2*) both *in vitro* and *in vivo* (Figures 7D–G and Supplementary Figures S6B–D). These data suggested that Tfr1 might be indispensable for energy expenditure and mitochondrial function in thermogenic adipocytes.

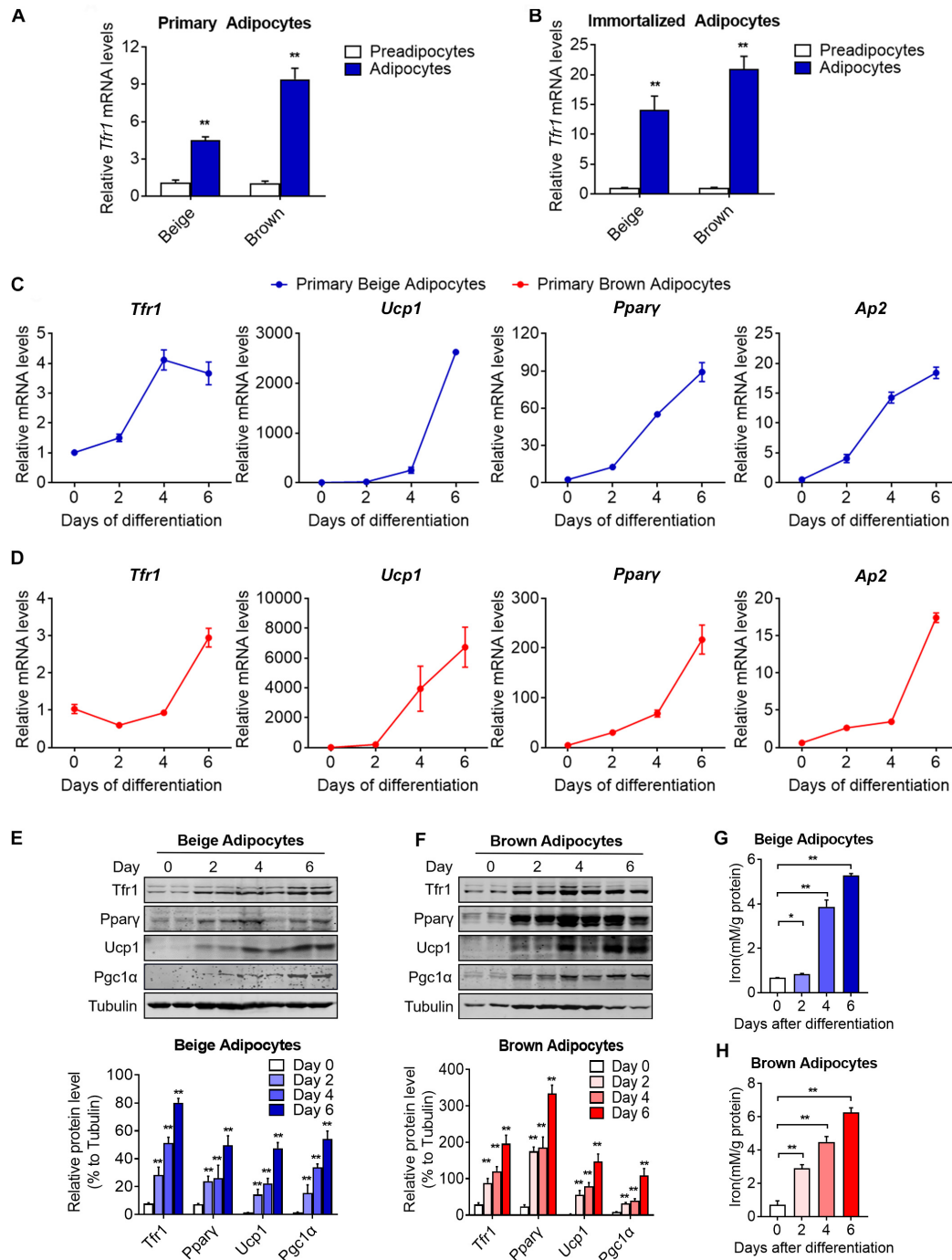


FIGURE 4 | Tfr1 expression levels and iron concentrations during thermogenic adipocytes differentiation. **(A,B)** Gene expression analysis of *Tfr1* in mature primary **(A)** and immortalized **(B)** thermogenic adipocytes compared to preadipocytes. **(C,D)** Gene expression analysis of *Tfr1*, *Ucp1*, *Pparγ*, and *Ap2* at indicated time points during differentiation in primary beige **(C)** and brown **(D)** adipocytes. **(E,F)** Western blot analysis (up) and quantification (down) of *Tfr1*, *Pparγ*, *Ucp1*, and *Pgc1α* at indicated time points during differentiation in immortalized beige **(E)** and brown **(F)** adipocytes. **(G,H)** Intracellular iron level at indicated time points during differentiation in beige **(G)** and brown **(H)** adipocytes. Data are presented as mean ± SEM. **P* < 0.05; ***P* < 0.01. The results are representative of at least three independent experiments.

Transferrin receptor exerts its function mainly through binding to transferrin for extracellular iron uptake. Iron has been shown to be vital in a plethora of cellular processes. For

example, iron plays a critical role in oxidative phosphorylation by functioning as a metal core of iron-sulfur (Fe-S) complex and promoting electron transfer by shifting from Fe²⁺ to

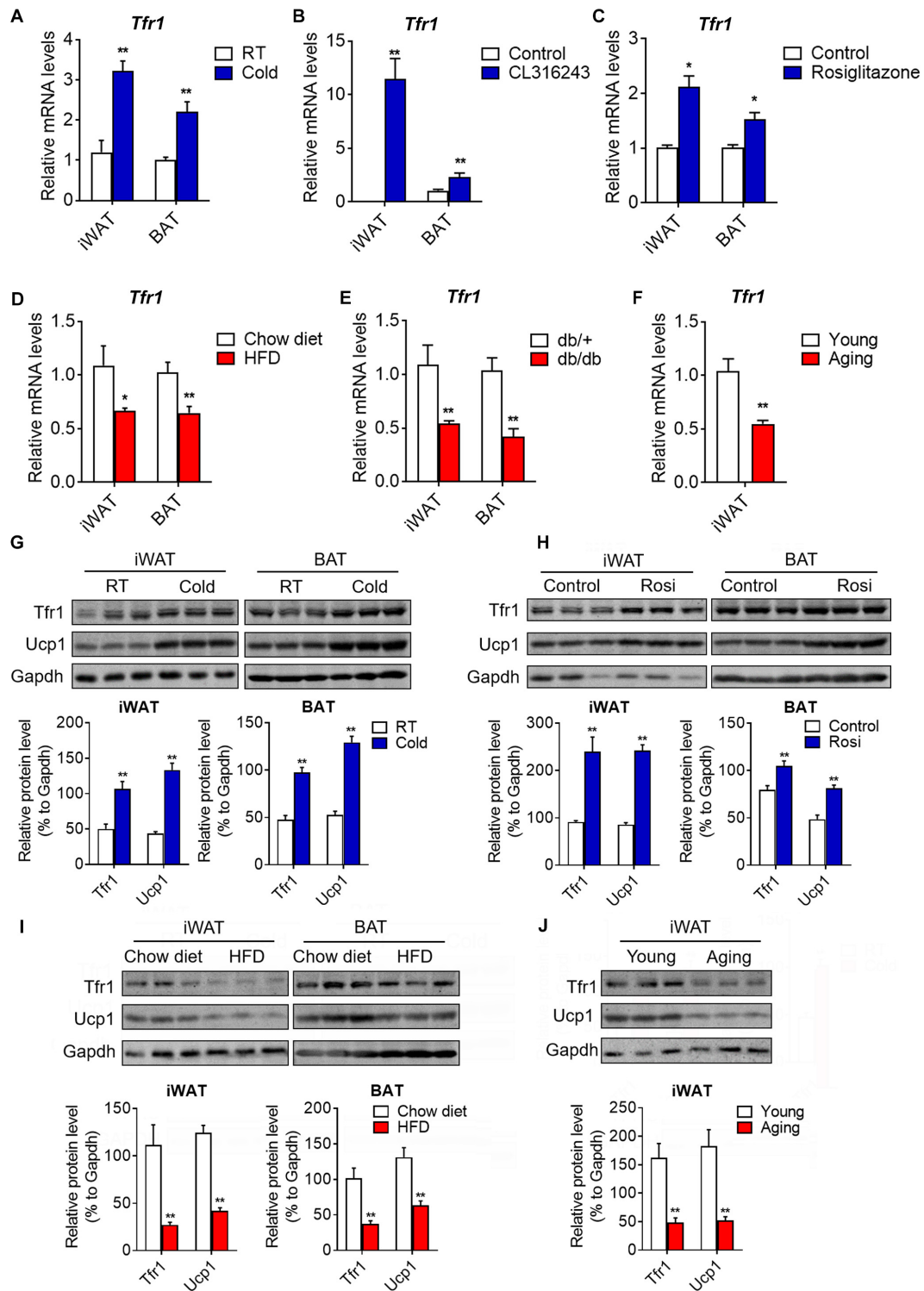
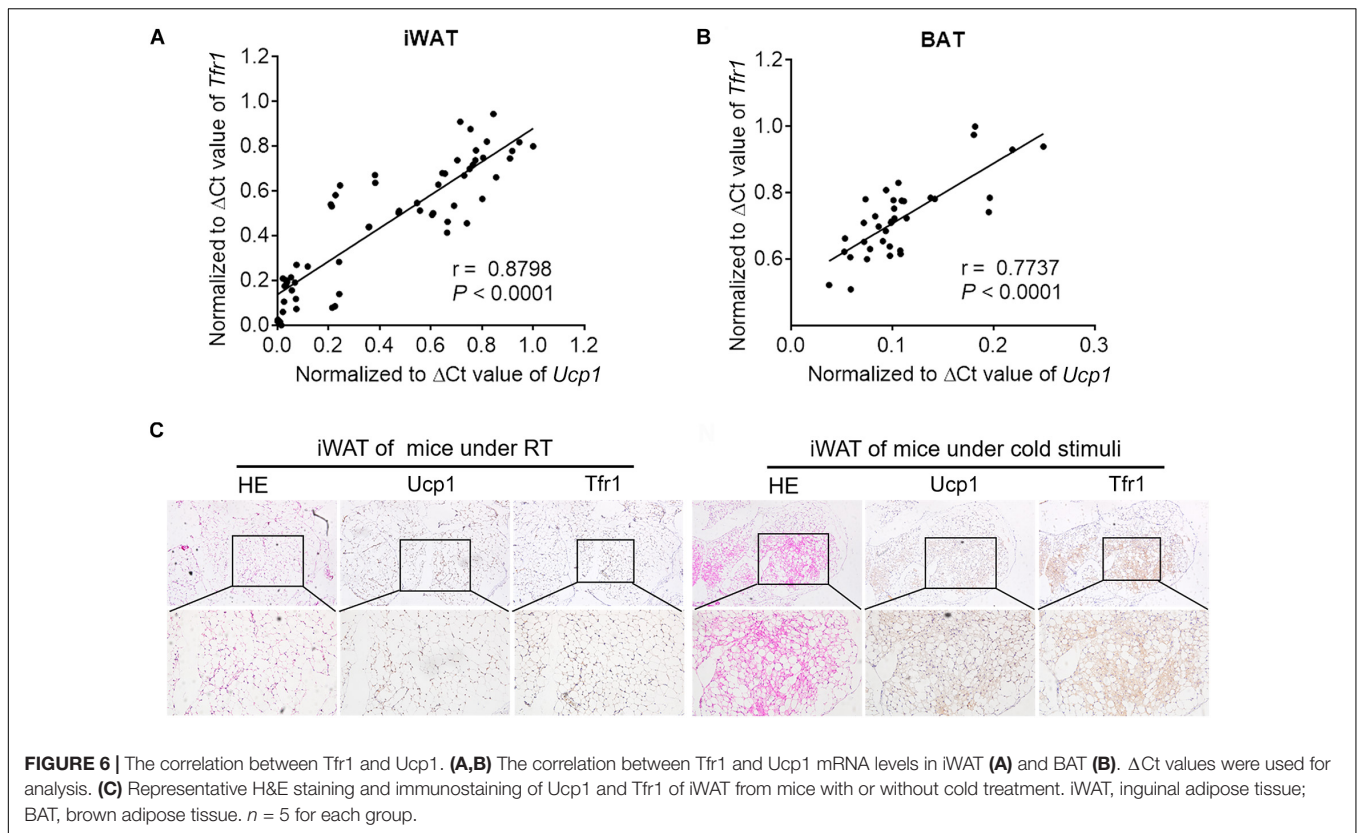


FIGURE 5 | Tfr1 expression upon physiological and pathological stimulation *in vivo* and *in vitro*. **(A–C)** Gene expression analysis of *Tfr1* in BAT and iWAT from mice under chronic cold condition **(A)**, CL316243 injection **(B)**, or Rosiglitazone treatment **(C)**, compared to their individual control mice. **(D–F)** Gene expression analysis of *Tfr1* in BAT and iWAT from HFD-fed **(D)**, *db/db* **(E)**, or aging **(F)** mice, compared to their individual control mice (Chow diet, *db/+* or young mice). **(G,H)** Western blot analysis (up) and quantification (down) of Tfr1 and Ucp1 in BAT and iWAT from mice under chronic cold condition **(G)** or Rosiglitazone treatment **(H)**, compared to their control mice. **(I,J)** Western blot analysis (up) and quantification (down) of Tfr1 and Ucp1 in BAT and iWAT from HFD-fed **(I)** or aging **(J)** mice, compared to their control mice. Data are presented as mean ± SEM. iWAT, inguinal adipose tissue; BAT, brown adipose tissue; Rosi: Rosiglitazone. **P* < 0.05; ***P* < 0.01. *n* = 5 for each group.



Fe^{3+} states in respiratory chain complexes I, II, and III located in the inner mitochondrial membrane (Rouault and Tong, 2005). We thus examined whether iron homeostasis is critical for thermogenic functions of mature beige adipocytes. Intriguingly, clearance of cellular iron concentration through treatment of the iron chelator DFO decreased expressions of brown gene programs, while forced elevation of iron levels by addition of FeSO_4 -induced brown gene programs in thermogenic adipocytes (Figure 7H). Importantly, *Tfr1* knockdown largely blunted the induction of *Ucp1* by FeSO_4 , indicating that iron may enhance thermogenesis through *Tfr1* (Figure 7I). On the other hand, overexpression *Tfr1* in beige adipocytes increased mRNA and protein levels of thermogenic marker *Ucp1* (Figures 7J,K). Thus, these results suggested that iron metabolism may be important for energy homeostasis in thermogenic fat, possibly through its membrane transporter, *Tfr1*.

We have shown that *Tfr1* knockdown disrupted mitochondrial integrity and functionality, and we further assessed whether it is caused by possible cell death. In fact, we showed that *Tfr1* knockdown reduced cellular lipid peroxidation and cellular ROS levels in brown and beige adipocytes (Figures 8A,B and Supplementary Figures S7A,B). Besides, although iron metabolic gene levels were suppressed upon *Tfr1* knockdown, ferroptotic gene levels were unaltered (Figure 8C and Supplementary Figure S7C). Furthermore, the cell viability assay suggested that *Tfr1* knockdown did not lead to ferroptosis-induced cell death (Figure 8D and Supplementary Figure S7D).

DISCUSSION

In the present study, we identified *Tfr1*, previously named CD71, as a surface molecule that features specific expression in thermogenic adipocytes, including brown and beige adipocytes, versus white adipocytes. These data showed that *Tfr1* deficiency reduced gene programs of iron uptake and storage, thermogenesis, and mitochondrial functionality. Furthermore, we showed that the absence of *Tfr1* impaired cellular energetics and glycolysis as evaluated by cellular oxygen consumption (OCR) and ECAR analysis using Seahorse instruments, indicative of a vital role of *Tfr1*/iron metabolism on cellular energy homeostasis. On the other hand, we found that deteriorating events such as lipid peroxidation and cellular ROS stress were suppressed after *Tfr1* knockdown, without obvious effects on ferroptosis or cell viability, suggesting a multifaceted impact of *Tfr1* in thermogenic adipocytes.

A number of studies have provided potential molecules that specifically expressed in brown and beige adipocytes versus white adipocytes for better target efficiency. For example, by characterizing single cell clones from isolated preadipocyte of white, brown, and beige fat, it has been shown that compared to white adipocytes, brown adipocytes express high levels of *Ucp1*, *Zic1*, and *Lhx8*, and beige adipocytes express *Tbx1*, *Tmem26*, and *Tnsfrsf9*, in addition to *Ucp1* (De Jong et al., 2015). However, utilization of these molecules as therapeutic targets encountered difficulties since they are either intracellular markers that are not suitable for direct targeting *in vivo*, or

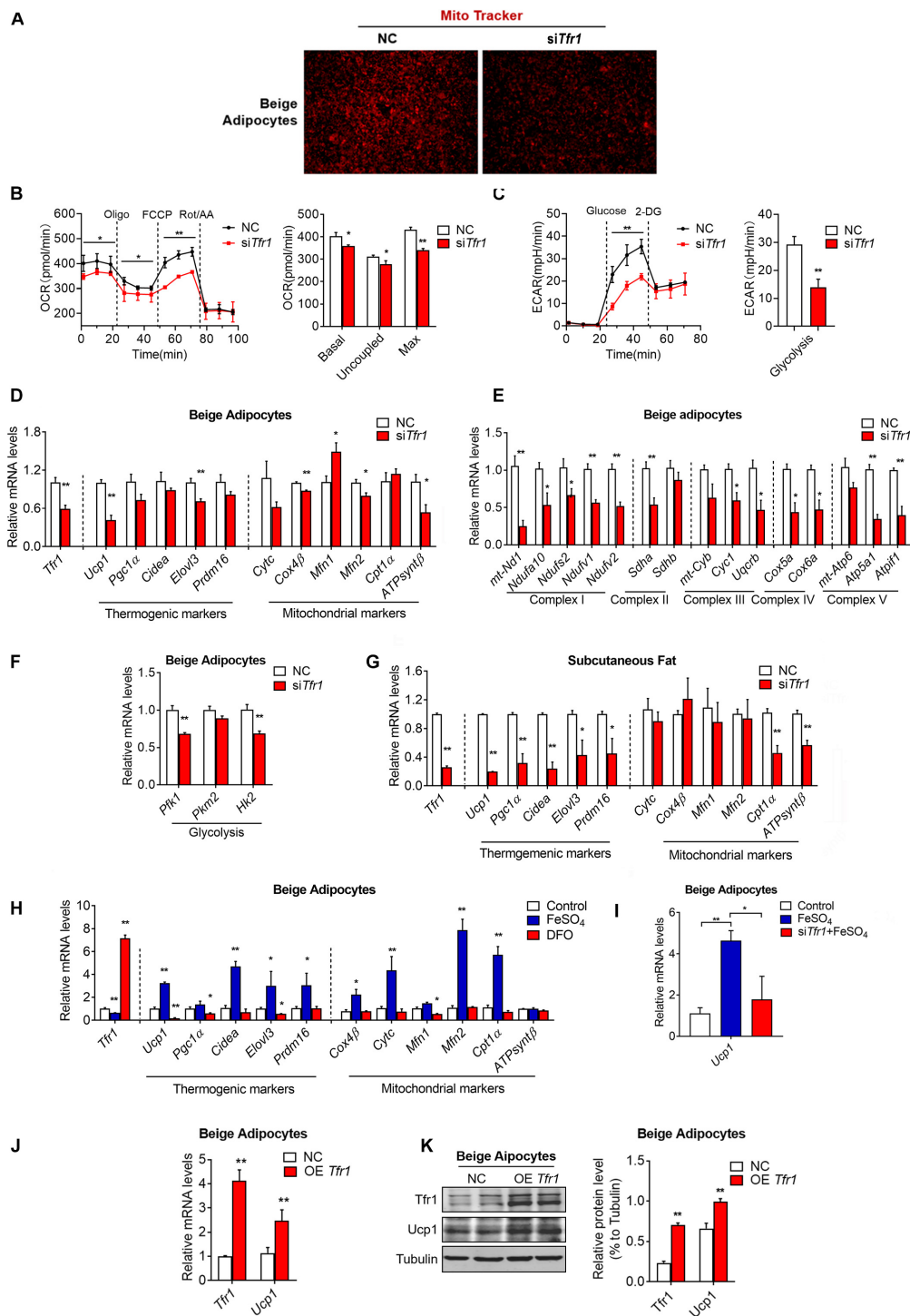


FIGURE 7 | The effect of *Tfr1* knockdown (si*Tfr1*) on thermogenic adipocyte function *in vivo* and *in vitro*. **(A)** Mito Tracker staining of mature beige adipocytes with or without *Tfr1* knockdown (si*Tfr1*). **(B,C)** Measurement of cellular oxygen consumption rate (OCR) and ECAR of mature C3H10T1/2 adipocytes with or without *Tfr1* knockdown (si*Tfr1*). **(D–F)** Gene expression analysis of *Tfr1*, thermogenic markers, mitochondrial markers (E), and glycolytic markers (F) from beige adipocytes with or without *Tfr1* knockdown (si*Tfr1*). **(G)** Gene expression analysis of *Tfr1*, thermogenic markers, and mitochondrial markers from subcutaneous fat with or without *Tfr1* knockdown (si*Tfr1*). **(H)** Gene expression analysis of *Tfr1*, thermogenic markers, and mitochondrial markers from DFO-treated or FeSO₄-treated beige adipocytes. **(I)** *Ucp1* mRNA levels in beige adipocytes treated with FeSO₄ with or without *Tfr1* knockdown (si*Tfr1*). **(J)** Gene expression analysis of *Tfr1* and *Ucp1* from beige adipocytes after *Tfr1* overexpression (OE *Tfr1*). **(K)** Western blot analysis (left) and quantification (right) of *Tfr1* and *Ucp1* from beige adipocytes after *Tfr1* overexpression (OE *Tfr1*). Data are presented as mean ± SEM. **P* < 0.05; ***P* < 0.01. The results are representative of at least three independent experiments. OCR, oxygen consumption rate; ECAR, extracellular acidification rate; NC, negative control; DFO, deferoxamine.

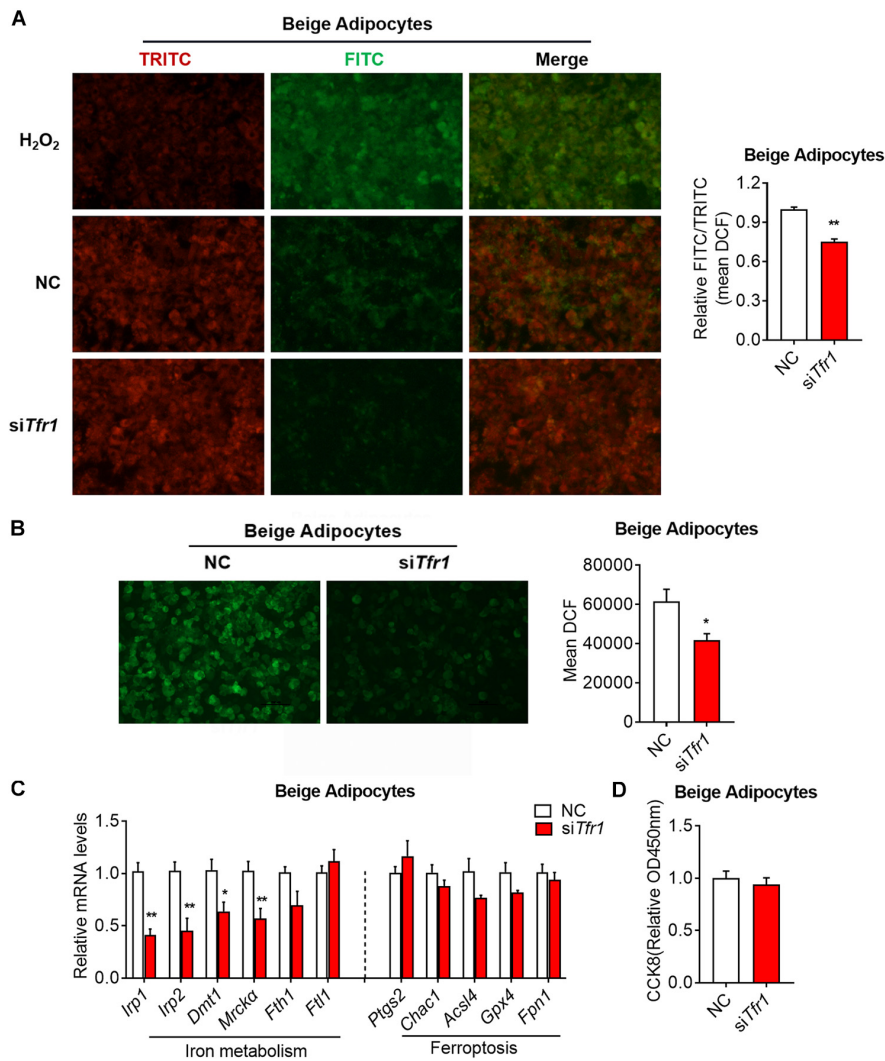


FIGURE 8 | The effect of *Tfr1* knockdown (si*Tfr1*) on cellular stress and iron metabolism in beige adipocytes. **(A)** Lipid peroxidation analysis with pre-lipid peroxidation (red, TRITC) and post-lipid peroxidation (green, FITC) from beige adipocytes after *Tfr1* knockdown (si*Tfr1*). Left: representative images of lipid peroxidation staining; right: lipid peroxidation fluorescence intensity presented as FITC/TRITC signal ratio. **(B)** ROS activity analysis with DCF (green) from beige adipocytes after *Tfr1* knockdown (si*Tfr1*). Left: representative images of ROS staining; right: ROS fluorescence intensity. **(C)** Gene expression analysis of iron metabolic and ferroptotic markers from beige adipocytes with or without *Tfr1* knockdown (si*Tfr1*). **(D)** Relative cellular viability analysis from beige adipocytes with or without *Tfr1* knockdown (si*Tfr1*). Data are presented as mean \pm SEM. * $P < 0.05$; ** $P < 0.01$. The results are representative of at least three independent experiments. ROS, reactive oxygen species; NC, negative control.

under debate for expression specificity (Xue et al., 2015). On the other hand, by data mining gene expression database, Ussar et al. (2014) searched surface markers that feature high expression association with *Ucp1*, the critical thermogenic marker gene. They identified surface proteins Pat2 and P2rx5 that show high specificity to brown/beige adipocytes, though whether Pat2 and P2rx5 affect thermogenic adipocyte functions remained unexamined. In the present study, we proposed *Tfr1* as a previously unidentified cell surface molecule for thermogenic adipocytes with functional assessment. *Tfr1* is highly responsive to environmental cues, and its levels were induced upon classical browning stimuli, including cold, β_3 adrenergic signaling, and Ppar γ agonist treatment, while its levels negatively responded

to whitening stimuli, including HFD and aging, suggesting that *Tfr1* levels may be a suitable indicator that dynamically reflects the amount and function of thermogenic adipocytes under various physiological status. Moreover, *Tfr1* knockdown in mature beige adipocytes led to reduced mitochondrial integrity and reduced brown gene programs, indicative of an active role of *Tfr1* in beige adipocyte function. Interestingly, comparing *Tfr1* with previously reported markers revealed a difference in their responses to browning stimuli. For example, *Tmem26* levels did not change under cold exposure or β_3 adrenergic stimulation with CL316243. Pat2 levels were induced by CL316243 induction but not cold stimulation, while *Tfr1* and P2rx5 sensed both stimulations. Thus, it would be informative to study the

detailed functions of these intracellular or surface markers of thermogenic adipocytes.

Of note, we did not identify cell surface markers that show differential expression pattern between brown and beige adipocytes. Similarly, Ussar et al. (2014) demonstrated that Pat2 and P2rx5 were specific surface markers for both brown/beige adipocyte. It is possible that though beige and brown adipocytes have distinct developmental origins, they share high similarity in functions after activation and thus may have similar spectrum of surface markers. Besides, we found that, although Tfr1 is predominantly expressed in mature thermogenic adipocytes, it is also detectable in other tissues, not unlike that of Pat2/P2rx5. Given the specificity and membrane location feature, Tfr1 would be an ideal surface marker with local applications for identifying and sorting thermogenic adipocytes in isolated mice white fat or in human fat tissues.

Transferrin receptor plays an important role for cellular iron uptake and homeostasis (Gammella et al., 2017). Recently, via analyzing Tfr1 fat-conditional knockout mice, Tfr1 was found to be vital for fat biology since Tfr1 deficiency promoted the transdifferentiation of brown adipocytes into muscle-like cells, blunted cold-induced browning of white fat and thermogenesis, but led to HFD-induced hyperlipidemia, insulin resistance, and local inflammation (Li et al., 2020). The present study and the study of Li et al. (2020) share a few similar conclusions, but the present study also provided novel insights into and mechanistic details about Tfr1 and iron metabolism in thermogenic adipocytes. Firstly, beige adipocytes share many similarities with white adipocytes and are hard to distinguish and target, which limited their implications. Moreover, it has been shown that physiological stimuli like cold induced different responses in beige adipocytes compared to pharmacologic stimuli. Thus, the fundamental goals of the present study are to identify a specific surface marker that plays important roles under a physiological setting while, at the same time, distinguishing beige and white adipocytes. To achieve this, we performed unbiased RNA-seq in beige and white fat depots from two mouse strains of different genetic backgrounds, as well as beige fat from mice with or without cold acclimation, and overlapped differential expressions of surface molecules from these datasets to find candidates that have tight physiological association with thermogenic ability and distinct expression in beige versus white fat. In comparison, Li et al. used beige fats from control mice and mice with pharmacologic stimulation for β -adrenergic activation for RNA-seq analysis. Secondly, we provided additional mechanistic insights including cellular oxygen consumption and glycolysis measured by Seahorse instrument, lipid peroxidation and cellular ROS levels, and Tfr1 gain-of-function analysis, further suggesting the importance of iron homeostasis in fat biology. Lastly, Li et al. (2020) studied Tfr1 functionality through adipocyte developmental/differentiation stages, including differentiation of primary SVF isolated from wild-type and Tfr1 fat-conditional knockout mice, as well as C3H10T1/2 cells stably transfected with or without Tfr1 shRNA. On the other hand, we focused on the role of Tfr1 in mature beige adipocytes by utilizing a siRNA system to manipulate Tfr1 levels directly in differentiated

adipocytes. Thus, our study together with Li's study provided a comprehensive picture of Tfr1 function in various stages of thermogenic adipocytes.

In addition to iron, other metals, such as copper (Cu), calcium, and zinc, also play fundamental roles in mitochondrial functionality and are involved in fat biology. Specifically, complexes I–IV of the electron transport chain in mitochondria require Fe–S clusters and Cu centers for normal functionality (Maio et al., 2017; Boulet et al., 2018). Besides, calcium is one of the most well-studied ions in mitochondria. An increase in mitochondrial calcium levels can activate ATP production, brown fat thermogenesis, and browning of white fat by altering the activity of calcium-sensitive proteins such as NCLX and SERCA2b (Williams et al., 2015; Ding et al., 2018; Pathak and Trebak, 2020). Zinc may also play important roles in mitochondrial functionality by serving as ion center for zinc finger proteins. Zinc finger protein family is one of the largest protein family. Various critical zinc finger proteins, including Prdm16, Znf638, Zfp423, etc., have been shown to play critical roles in mitochondrial and fat biology (Shao et al., 2016a,b; Kissig et al., 2017; Perie et al., 2019). Thus, further studies are warranted to understand the finely tuned functions of ion signaling in mitochondrial functionality and thermogenesis.

In addition to the vital function of Tfr1 on mature thermogenic adipocytes, we also assessed possible involvement of Tfr1 in beige progenitor cells. Interestingly, based on a recent study (Nicole et al., 2020, Nature), we analyzed Tfr1 levels from SVF of beige adipocytes during aging using data from Mouse Aging Cell Atlas. Interestingly, the numbers of Tfr1-positive SVFs declined during the aging process (**Supplementary Figure S8**), suggesting the involvement of iron metabolism in functionality of progenitor cells and cellular senescence.

In summary, we identified that Tfr1 is expressed predominantly in thermogenic adipocytes versus white adipocyte, and its expression levels are tightly correlated with browning status. Importantly, Tfr1 is a functional cell surface marker as its deficiency led to impaired mitochondrial quality and membrane integrity in thermogenic adipocytes, overall suggesting that Tfr1 gene may serve as a functional surface molecule of thermogenic adipocytes for future application purposes.

DATA AVAILABILITY STATEMENT

The authors acknowledge that the data presented in this study must be deposited and made publicly available in an acceptable repository, prior to publication. Frontiers cannot accept a manuscript that does not adhere to our open data policies.

ETHICS STATEMENT

The animal study was reviewed and approved by Shanghai Jiao Tong University (Shanghai, China), East China Normal University (Shanghai, China).

AUTHOR CONTRIBUTIONS

LX, JW, XM, and XG conceived the project and designed the experiments. JQ, SW, ZZ, and YC carried out most of the experiments. CL, DW, JS, XC, LM, and MN assisted in some experiments and data analysis. SX, JY, TH, and YH provided rodent biological samples for association analysis. XM, JW, and LX wrote the manuscript. XG contributed valuable comments and advice on the manuscript. All authors contributed to the article and approved the submitted version.

FUNDING

This project is supported by funds from the National Key Research and Development Program of China (2018YFC1313803 and 2019YFA0904500), the National Natural Science Foundation of China (31770840, 31800989, and 91957124), the Program for Professor of Special Appointment (Eastern Scholar) at Shanghai Institutions of Higher Learning (TP2017042), the Animal Program of Shanghai Municipal Science and Technology Commission (KW-201978403), the Natural Science Foundation of Zhejiang Province (LY20H070003), and the Shanghai Young Top Notch Talents and ECNU public platform for Innovation.

ACKNOWLEDGMENTS

We acknowledge Prof. Qiurong Ding at the Chinese Academy of Sciences and Prof. Dongning Pan at Fudan University Shanghai Medical College for providing us immortalized beige and brown adipocytes.

SUPPLEMENTARY MATERIAL

The Supplementary Material for this article can be found online at: <https://www.frontiersin.org/articles/10.3389/fcell.2020.572459/full#supplementary-material>

Supplementary Figure 1 | *In silico* analysis of significantly altered genes in iWAT of mice with or without cold exposure. (A–D) KEGG pathway enrichment analysis (A) and GO analysis (B–D) of significantly altered genes in iWAT from mice under cold exposure or room temperature with top 10 different gene counts.

Supplementary Figure 2 | Tfr1 expression pattern in multiple tissues. (A) Confocal images of immunofluorescence staining of Tfr1 (Phalloidin-Alexa488, green) and DAPI (blue). (B) Gene expression analysis of Tfr1 in heart, liver, spleen, lung, kidney, brain, pancreas, gastrocnemius, and soleus muscle of 2-month-old C57BL/6J mice.

Supplementary Figure 3 | Tfr1 expression levels during immortalized adipocyte differentiation. (A–C) Gene expression analysis of Tfr1, Ucp1, Pparg, and Ap2 at

indicated time point during differentiation in immortalized beige adipocytes (A), C3H10T1/2 adipocytes (B), and immortalized brown adipocytes (C). Data are presented as mean ± SEM. **P* < 0.05; ***P* < 0.01. The results are representative of at least three independent experiments.

Supplementary Figure 4 | The effect of Tfr1 knockdown (siTfr1) on lipid metabolism in thermogenic adipocytes. (A,B) Gene expression analysis of Tfr1, adipogenesis markers, lipid synthesis markers, oxidative phosphorylation markers and fatty acid oxidation markers from beige (A) and brown (B) adipocytes after 2 days of Tfr1 knockdown (siTfr1) on day 2 of differentiation. (C) Gene expression analysis of Tfr1, adipogenesis markers, lipid synthesis markers, oxidative phosphorylation markers, and fatty acid oxidation markers from beige adipocytes after 2 days of Tfr1 knockdown (siTfr1) on day 4 of differentiation. (D) TG and NEFA contents from beige adipocytes after 2 days of Tfr1 knockdown (siTfr1) on day 4 of differentiation. (E) Gene expression analysis of Tfr1, adipogenesis markers, lipid synthesis markers, oxidative phosphorylation markers, and fatty acid oxidation markers from brown adipocytes after 2 days of Tfr1 knockdown (siTfr1) on day 4 of differentiation. (F) TG and NEFA contents from brown adipocytes after 2 days of Tfr1 knockdown (siTfr1) on day 4 of differentiation. Data are presented as mean ± SEM. **P* < 0.05; ***P* < 0.01. The results are representative of at least three independent experiments. NC, negative control.

Supplementary Figure 5 | Tfr1 expression level in iWAT and BAT under physiological and pathological stimuli. (A–C) Ucp1 mRNA levels in iWAT and BAT from mice under chronic cold condition (A), CL316243 injection (B) or Rosiglitazone treatment (C), compared to their individual control mice. (D–F) Ucp1 mRNA levels in iWAT and BAT from HFD diet fed (D), db/db (E) or aging (F) mice, compared to their individual control mice (Chow diet, db/+ or young mice). (G–J) Ucp1 (G,H) and Tfr1 (I,J) mRNA levels in immortalized adipocytes treated with or without Forskolin (FSK) and H89. (K–L) Irf1, Irf2 (K), Tfr1 and Ucp1 (L) mRNA levels in iWAT from mice under chronic cold condition, compared to thermalneutral condition. Data are presented as mean ± SEM. iWAT, inguinal adipose tissue; BAT, brown adipose tissue; RT, room temperature. **P* < 0.05; ***P* < 0.01. The results are representative of at least three independent experiments.

Supplementary Figure 6 | The effect of Tfr1 knockdown (siTfr1) on mitochondrial function in brown adipocytes. (A) Mito Tracker staining of mature brown adipocytes with or without Tfr1 knockdown (siTfr1). (B) Gene expression analysis of Tfr1, thermogenic markers and mitochondrial markers from brown adipocytes with or without Tfr1 knockdown (siTfr1). (C) Gene expression analysis of five mitochondrial respiratory chain complex markers from brown adipocytes with or without Tfr1 knockdown (siTfr1). (D) Gene expression analysis of glycolysis markers from brown adipocytes with or without Tfr1 knockdown (siTfr1). Data are presented as mean ± SEM. **P* < 0.05; ***P* < 0.01. The results are representative of at least three independent experiments. NC, negative control.

Supplementary Figure 7 | The effect of Tfr1 knockdown (siTfr1) on cellular stress and iron metabolism in brown adipocytes. (A) Lipid peroxidation analysis with pre-lipid peroxidation (red, TRITC) and post-lipid peroxidation (green, FITC) from brown adipocytes after Tfr1 knockdown (siTfr1). Left: representative images of lipid peroxidation staining; right: lipid peroxidation fluorescence intensity presented as FITC/TRITC signal ratio. (B) ROS activity analysis with DCF (green) from brown adipocytes after Tfr1 knockdown (siTfr1). Left: representative images of ROS staining; right: ROS fluorescence intensity. (C) Gene expression analysis of iron metabolic and ferroptotic markers from brown adipocytes with or without Tfr1 knockdown (siTfr1). (D) Relative cellular viability analysis from brown adipocytes with or without Tfr1 knockdown (siTfr1). Data are presented as mean ± SEM. **P* < 0.05; ***P* < 0.01. The results are representative of at least three independent experiments. NC, negative control.

Supplementary Figure 8 | Single-cell sequencing data showing Tfr1-positive cell numbers from iWAT SVF of mice at different ages. **P* < 0.05; ***P* < 0.01.

REFERENCES

- Altermann, E., and Klaenhammer, T. R. (2005). PathwayVoyager: pathway mapping using the kyoto encyclopedia of genes and genomes (KEGG) database. *BMC Genomics* 6:60. doi: 10.1186/1471-2164-6-60
- Ashburner, M., Ball, C. A., Blake, J. A., Botstein, D., Butler, H., Cherry, J. M., et al. (2000). Gene ontology: tool for the unification of biology. *Nat. Genet.* 25, 25–29. doi: 10.1038/75556
- Baskin, A. S., Linderman, J. D., Brychta, R. J., McGehee, S., Anflück-Chames, E., and Cero, C. (2018). Regulation of human adipose tissue activation, gallbladder

- size, and bile acid metabolism by a beta3-Adrenergic receptor agonist. *Diabetes* 67, 2113–2125. doi: 10.2337/db18-0462
- Boulet, A., Vest, K. E., Maynard, M. K., Gammon, M. G., Russell, A. C., and Mathews, A. T. (2018). The mammalian phosphate carrier SLC25A3 is a mitochondrial copper transporter required for cytochrome c oxidase biogenesis. *J. Biol. Chem.* 293, 1887–1896. doi: 10.1074/jbc.RA117.000265
- Brandão, B. B., Guerra, B. A., and Mori, M. A. (2017). Shortcuts to a functional adipose tissue: the role of small non-coding RNAs. *Redox Biol.* 12, 82–102. doi: 10.1016/j.redox.2017.01.020
- Chung, H., Chou, W., Sears, D. D., Patterson, R. E., Webster, N. J. G., and Ellies, L. G. (2016). Time-restricted feeding improves insulin resistance and hepatic steatosis in a mouse model of postmenopausal obesity. *Metabolism* 65, 1743–1754. doi: 10.1016/j.metabol.2016.09.006
- De Jong, J. M. A., Larsson, O., Cannon, B., and Nedergaard, J. (2015). A stringent validation of mouse adipose tissue identity markers. *Am. J. Physiol. Endoc. Metab.* 308, E1085–E1105. doi: 10.1152/ajpendo.00023.2015
- Diaz, M. B., Herzig, S., and Vegiopoulos, A. (2014). Thermogenic adipocytes: from cells to physiology and medicine. *Metabolism* 63, 1238–1249. doi: 10.1016/j.metabol.2014.07.002
- Ding, L., Yang, X., Tian, H., Liang, J., Zhang, F., and Mathews, A. T. (2018). Seipin regulates lipid homeostasis by ensuring calcium-dependent mitochondrial metabolism. *EMBO J.* 37:e97572. doi: 10.15252/embj.201797572
- Frontini, A., Vitali, A., Perugini, J., Murano, I., Romiti, C., and Ricquier, D. (2013). White-to-brown transdifferentiation of omental adipocytes in patients affected by pheochromocytoma. *Biochim. Biophys. Acta* 1831, 950–959. doi: 10.1016/j.bbali.2013.02.005
- Gammella, E., Buratti, P., Cairo, G., and Recalcati, S. (2017). The transferrin receptor: the cellular iron gate. *Metallomics* 9, 1367–1375. doi: 10.1039/c7mt00143f
- Gastaldi, G., Russell, A., Golay, A., Giacobino, J. P., Habicht, F., and Barthassat, V. (2007). Upregulation of peroxisome proliferator-activated receptor gamma coactivator gene (PGC1A) during weight loss is related to insulin sensitivity but not to energy expenditure. *Diabetologia* 50, 2348–2355. doi: 10.1007/s00125-007-0782-1
- Hasegawa, Y., Ikeda, K., Chen, Y., Alba, D. L., Stifler, D., Shinoda, K., et al. (2018). Repression of adipose tissue fibrosis through a PRDM16-GTF2IRD1 complex improves systemic glucose homeostasis. *Cell Metab.* 27, 180–194. doi: 10.1016/j.cmet.2017.12.005
- Hildebrand, S., Stumer, J., and Pfeifer, A. (2018). PVAT and its relation to brown, beige, and white adipose tissue in development and function. *Front. Physiol.* 9:70. doi: 10.3389/fphys.2018.00070
- Huang, D. W., Sherman, B. T., and Lempicki, R. A. (2009a). Bioinformatics enrichment tools: paths toward the comprehensive functional analysis of large gene lists. *Nucleic Acids Res.* 37, 1–13. doi: 10.1093/nar/gkn923
- Huang, D. W., Sherman, B. T., and Lempicki, R. A. (2009b). Systematic and integrative analysis of large gene lists using DAVID bioinformatics resources. *Nat. Protoc.* 4, 44–57. doi: 10.1038/nprot.2008.211
- Jabara, H. H., Boyden, S. E., Chou, J., Ramesh, N., Massaad, M. J., and Benson, H. (2016). A missense mutation in TFRC, encoding transferrin receptor 1, causes combined immunodeficiency. *Nat. Genet.* 48, 74–78. doi: 10.1038/ng.3465
- Jung, U. J., and Choi, M. S. (2014). Obesity and its metabolic complications: the role of adipokines and the relationship between obesity, inflammation, insulin resistance, dyslipidemia and nonalcoholic fatty liver disease. *Int. J. Mol. Sci.* 15, 6184–6223. doi: 10.3390/ijms15046184
- Kissig, M., Ishibashi, J., Harms, M. J., Lim, H. W., Stine, R. R., and Won, K. J. (2017). PRDM16 represses the type I interferon response in adipocytes to promote mitochondrial and thermogenic programming. *EMBO J.* 36, 1528–1542. doi: 10.15252/embj.201695588
- Labbe, S. M., Caron, A., Chechi, K., Laplante, M., Lecomte, R., and Richard, D. (2016). Metabolic activity of brown, “beige,” and white adipose tissues in response to chronic adrenergic stimulation in male mice. *Am. J. Physiol. Endocrinol. Metab.* 311, E260–E268. doi: 10.1152/ajpendo.00545.2015
- Lavery, C. A., Kurowska-Stolarska, M., Holmes, W. M., Donnelly, I., Caslake, M., and Collier, A. (2016). miR-34a(-/-) mice are susceptible to diet-induced obesity. *Obesity* 24, 1741–1751. doi: 10.1002/oby.21561
- Li, J., Pan, X., Pan, G., Song, Z., He, Y., and Zhang, S. (2020). Transferrin receptor 1 regulates thermogenic capacity and cell fate in Brown/Beige adipocytes. *Adv. Sci.* 7:1903366. doi: 10.1002/adv.201903366
- Maio, N., Kim, K. S., Singh, A., and Rouault, T. A. (2017). A single adaptable cochaperone-scaffold complex delivers nascent iron-sulfur clusters to mammalian respiratory chain complexes I-III. *Cell Metab.* 25, 945.e6–953.e6. doi: 10.1016/j.cmet.2017.03.010
- Ng, R., Hussain, N. A., Zhang, Q., Chang, C., Li, H., and Fu, Y. (2017). miRNA-32 drives brown fat thermogenesis and trans-activates subcutaneous white fat browning in mice. *Cell Rep.* 19, 1229–1246. doi: 10.1016/j.celrep.2017.04.035
- Nicole, A., Jane, A., Ankit, S. B., Isaac, B., Ishita, B., and Ben, A. B. (2020). Tabula muris consortium. a single-cell transcriptomic atlas characterizes ageing tissues in the mouse. *Nature* 583, 590–595. doi: 10.1038/s41586-020-2496-1
- Ohno, H., Shinoda, K., Spiegelman, B. M., and Kajimura, S. (2012). PPARgamma agonists induce a white-to-brown fat conversion through stabilization of PRDM16 protein. *Cell Metab.* 15, 395–404. doi: 10.1016/j.cmet.2012.01.019
- Pathak, T., and Trebak, M. (2020). NCLX pumps up the heat. *Cell Calcium* 92:102280. doi: 10.1016/j.ceca.2020.102280
- Perie, L., Verma, N., Xu, L., Ma, X., and Mueller, E. (2019). Transcriptional regulation of ZNF638 in thermogenic cells by the cAMP response element binding protein in male mice. *J. Endocr. Soc.* 3, 2326–2340. doi: 10.1210/js.2019-00238
- Rockstroh, D., Landgraf, K., Wagner, I. V., Gesing, J., Tauscher, R., and Lakowa, N. (2015). Direct evidence of brown adipocytes in different fat depots in children. *PLoS One* 10:e117841. doi: 10.1371/journal.pone.0117841
- Rouault, T. A., and Tong, W. H. (2005). Iron-sulphur cluster biogenesis and mitochondrial iron homeostasis. *Nat. Rev. Mol. Cell Biol.* 6, 345–351. doi: 10.1038/nrm1620
- Scheele, C., Larsen, T. J., and Nielsen, S. (2014). Novel nuances of human brown fat. *Adipocyte* 3, 54–57. doi: 10.4161/adip.26520
- Scheja, L., and Heeren, J. (2016). Metabolic interplay between white, beige, brown adipocytes and the liver. *J. Hepatol.* 64, 1176–1186. doi: 10.1016/j.jhep.2016.01.025
- Shao, M., Hepler, C., Vishvanath, L., MacPherson, K. A., Busbuso, N. C., and Gupta, R. K. (2016a). Fetal development of subcutaneous white adipose tissue is dependent on Zfp423. *Mol. Metab.* 6, 111–124. doi: 10.1016/j.molmet.2016.11.009
- Shao, M., Ishibashi, J., Kusminski, C. M., Wang, Q. A., Hepler, C., and Vishvanath, L. (2016b). Zfp423 maintains white adipocyte identity through suppression of the beige cell thermogenic gene program. *Cell Metab.* 23, 1167–1184. doi: 10.1016/j.cmet.2016.04.023
- Sidossis, L., and Kajimura, S. (2015). Brown and beige fat in humans: thermogenic adipocytes that control energy and glucose homeostasis. *J. Clin. Invest.* 125, 478–486. doi: 10.1172/JCI78362
- Touret, N., Furuya, W., Forbes, J., Gros, P., and Grinstein, S. (2003). Dynamic traffic through the recycling compartment couples the metal transporter Nramp2 (DMT1) with the transferrin receptor. *J. Bio Chem.* 278, 25548–25557. doi: 10.1074/jbc.M212374200
- Tseng, Y. H., Kokkotou, E., Schulz, T. J., Huang, T. L., Winnay, J. N., and Taniguchi, C. M. (2008). New role of bone morphogenetic protein 7 in brown adipogenesis and energy expenditure. *Nature* 454, 1000–1004. doi: 10.1038/nature07221
- Ussar, S., Lee, K. Y., Dankel, S. N., Boucher, J., Haering, M. F., Kleinridders, A., et al. (2014). ASC-1, PAT2, and P2RX5 are cell surface markers for white, beige, and brown adipocytes. *Sci. Transl. Med.* 6, 103r–247r.
- Wang, Q., Zhang, M., Ning, G., Gu, W., Su, T., and Xu, M. (2011). Brown adipose tissue in humans is activated by elevated plasma catecholamines levels and is inversely related to central obesity. *PLoS One* 6:e21006. doi: 10.1371/journal.pone.0021006
- Williams, G. S., Boyman, L., and Lederer, W. J. (2015). Mitochondrial calcium and the regulation of metabolism in the heart. *J. Mol. Cell Cardio* 78, 35–45. doi: 10.1016/j.yjmcc.2014.10.019
- Xue, R., Lynes, M. D., Dreyfuss, J. M., Shamsi, F., Schulz, T. J., and Zhang, H. (2015). Clonal analyses and gene profiling identify genetic biomarkers of the

- thermogenic potential of human brown and white preadipocytes. *Nat. Med.* 21, 760–768. doi: 10.1038/nm.3881
- Yue, L., Zhao, W., Wang, D., Meng, M., Zheng, Y., and Li, Y. (2019). Silver nanoparticles inhibit beige fat function and promote adiposity. *Mol. Metab.* 22, 1–11. doi: 10.1016/j.molmet.2019.01.005
- Zhou, J. N., Zeng, Q., Wang, H. Y., Zhang, B., Li, S. T., and Nan, X. (2015). MicroRNA-125b attenuates epithelial-mesenchymal transitions and targets stem-like liver cancer cells through small mothers against decapentaplegic 2 and 4. *Hepatology* 62, 801–815. doi: 10.1002/hep.27887
- Conflict of Interest:** The authors declare that the research was conducted in the absence of any commercial or financial relationships that could be construed as a potential conflict of interest.

Copyright © 2020 Qiu, Zhang, Wang, Chen, Liu, Xu, Wang, Su, Ni, Yu, Cui, Ma, Hu, Hu, Gu, Ma, Wang and Xu. This is an open-access article distributed under the terms of the Creative Commons Attribution License (CC BY). The use, distribution or reproduction in other forums is permitted, provided the original author(s) and the copyright owner(s) are credited and that the original publication in this journal is cited, in accordance with accepted academic practice. No use, distribution or reproduction is permitted which does not comply with these terms.



Extracellular Citrate Is a Trojan Horse for Cancer Cells

Agata Petillo, Vittorio Abruzzese, Prashant Koshal, Angela Ostuni* and Faustino Bisaccia*

Laboratory of Cell Biochemistry, Department of Sciences, University of Basilicata, Potenza, Italy

OPEN ACCESS

Edited by:

Cesare Indiveri,
University of Calabria, Italy

Reviewed by:

Tibor Kristian,
University of Maryland, Baltimore,
United States
Vito De Pinto,
University of Catania, Italy

*Correspondence:

Angela Ostuni
angela.ostuni@unibas.it
Faustino Bisaccia
faustino.bisaccia@unibas.it

Specialty section:

This article was submitted to
Cellular Biochemistry,
a section of the journal
Frontiers in Molecular Biosciences

Received: 11 August 2020

Accepted: 16 October 2020

Published: 12 November 2020

Citation:

Petillo A, Abruzzese V, Koshal P,
Ostuni A and Bisaccia F (2020)
Extracellular Citrate Is a Trojan Horse
for Cancer Cells.
Front. Mol. Biosci. 7:593866.
doi: 10.3389/fmolb.2020.593866

The first intermediate in the mitochondrial tricarboxylic acid (TCA) cycle is citrate, which is essential and acts as a metabolic regulator for glycolysis, TCA cycle, gluconeogenesis, and fatty acid synthesis. Within the cytosol, citrate is cleaved by ATP citrate lyase (ACLY) into oxaloacetate (OAA) and acetyl-CoA; OAA can be used for neoglucogenesis or in the TCA cycle, while acetyl-CoA is the precursor of some biosynthetic processes, including the synthesis of fatty acids. Accumulating evidence suggests that citrate is involved in numerous physiological and pathophysiological processes such as inflammation, insulin secretion, neurological disorders, and cancer. Considering the crucial role of citrate to supply the acetyl-CoA pool for fatty acid synthesis and histone acetylation in tumors, in this study we evaluated the effect of citrate added to the growth medium on lipid deposition and histone H4 acetylation in hepatoma cells (HepG2). At low concentration, citrate increased both histone H4 acetylation and lipid deposition; at high concentration, citrate inhibited both, thus suggesting a crucial role of acetyl-CoA availability, which prompted us to investigate the effect of citrate on ACLY. In HepG2 cells, the expression of ACLY is correlated with histone acetylation, which, in turn, depends on citrate concentration. A decrease in H4 acetylation was also observed when citrate was added at a high concentration to immortalized human hepatic cells, whereas ACLY expression was unaffected, indicating a lack of control by histone acetylation. Considering the strong demand for acetyl-CoA but not for OAA in tumor cells, the exogenous citrate would behave like a trojan horse that carries OAA inside the cells and reduces ACLY expression and cellular metabolism. In addition, this study confirmed the already reported dual role of citrate both as a promoter of cell proliferation (at lower concentrations) and as an anticancer agent (at higher concentrations), providing useful tips on the use of citrate for the treatment of tumors.

Keywords: citrate, HepG2, IHH, ATP citrate lyase, histone acetylation, cancer, epigenetics

INTRODUCTION

Metabolism is a fundamental biological process in all living organisms for various cellular activities, such as maintaining homeostasis and producing functional energy, building blocks, enzymatic cofactors, and signaling molecules. However, these metabolic processes are also associated with the generation of several metabolites and in the activation of many enzymes, which are involved in the regulation of gene expression, immunoreactions, cellular apoptosis, and cancer progression

(van der Knaap and Verrijzer, 2016; He et al., 2017). It is widely accepted that cancer cells alter their metabolic pathways to generate more fatty acids from lipogenesis to meet the increasing energy demand for rapid cell division and propagation (De Berardinis and Chandel, 2016). The reprogramming of metabolic pathways in cancer cells alters the expression of certain genes and directly controls glycolysis, lipogenesis, and nucleotide synthesis, which have the potential to be considered as prognostic markers and therapeutic targets in the development of new anti-cancerous agents (Fritz and Fajas, 2010; Furuta et al., 2010; Liao, 2017; Liu et al., 2019).

One classical example of a reprogrammed metabolic pathway in cancer is the Warburg effect or aerobic glycolysis, which is characterized by an increased rate of glycolysis, resulting in a high production of lactic acid despite having sufficient oxygen (Liberti and Locasale, 2016; Burns and Manda, 2017). However, some cancer cells are also able to switch their metabolism between glycolysis and mitochondrial oxidative phosphorylation (Roth et al., 2020). Reprogramming of glucose metabolism and targeting altered metabolic pathways related with glucose metabolism may contribute to designing novel treatment strategies for improving the efficacy of cancer therapy (Luengo et al., 2017; Lin et al., 2020).

Citrate is an essential intermediate in the tricarboxylic acid (TCA) cycle which comes from the metabolism of glucose and glutamine (Icard et al., 2012). It is released into the cytoplasm through the mitochondrial citrate transporter SLC25A1, a member of the solute carrier transporter family that operates as a citrate/malate exchanger (Bisaccia et al., 1989) and, if added to the culture medium (exogenous citrate), enters the cells through the sodium-dependent transporter SLC13A5 (Costello and Franklin, 2016). Both exogenously added and mitochondrially produced (endogenous) citrate are cleaved into acetyl-CoA and oxaloacetate (OAA) in the cytosol by ATP citrate lyase (ACLY). In normal cells, when citrate is produced by TCA cycle and ATP levels are high, citrate exerts a negative feedback on glycolysis and TCA cycle itself. In the cytosol, ACLY provides acetyl-CoA, which sustains some biosynthetic processes, including lipid synthesis and acetylation of both histone and non-histone proteins. In cancer cells, to prevent the suppression of glycolysis, citrate is rapidly converted into OAA and acetyl-CoA by ACLY, which is overexpressed (Zaidi et al., 2012; Khwairakpam et al., 2015; Khwairakpam et al., 2020). The conversion of OAA into malate by malate dehydrogenase produces NAD^+ to sustain glycolysis (Gatenby and Gillies, 2004). Besides being a source of acetyl-CoA to sustain lipid biosynthesis, citrate is a key substrate for the activity of histone transacetylases, which, together with histone deacetylases, are responsible for some epigenetic modifications (Wellen et al., 2009).

Citrate acts as a regulator of multiple physiological and pathophysiological processes such as insulin secretion (Mohammad et al., 2007), inflammation (Williams and O'Neill, 2018), neurological disorders (Abdel-Salam et al., 2014), and cancer. There is growing evidence suggesting that the anti-tumor effect of exogenous citrate may be due to the regulation of some key enzymes of glycolysis, TCA cycle, gluconeogenesis, and fatty acid synthesis (Pastorino and Hoek, 2008; Ren et al.,

2017). *In vitro* and *in vivo* studies showed that citrate at a high concentration inhibited the proliferation of several cancer cell types by inducing mitochondria-mediated apoptosis (Wang et al., 2018; Caiazza et al., 2019). Nevertheless, some citrate-resistant cells are able to adapt to high citrate concentrations. Interestingly, it has been observed that, at physiological concentrations (200 $\mu\text{mol/L}$), some tumor cell lines take up larger amounts of citrate than the normal cells and that gluconate, by inhibiting the citrate plasma membrane carrier, reduced the growth of human pancreatic tumors implanted subcutaneously in mice (Mycielska et al., 2018).

Considering the crucial role of citrate to supply the acetyl-CoA pool for fatty acid synthesis and histone acetylation in tumors (Wellen et al., 2009; Lee et al., 2014; Khwairakpam et al., 2020), in the present study, we assessed the effect of exogenous citrate supplementation on both ACLY expression and histone H4 acetylation in hepatoma cells (HepG2). All the experiments were performed at high and low glucose concentrations in order to verify that the observed effects are attributable to the involvement of citrate into glucose metabolism as well as to make a quantitative assessment. Moreover, this approach allowed to exclude possible non-specific effects due to the chelating activity of citrate (Sul et al., 2016). We sought to determine the effect of citrate on human immortalized cells (IHH) to understand the specificity of action of exogenous citrate on tumor vs normal cell types.

Interestingly, all the results also allowed to analyze the contrasting and dose-dependent effects of externally administered citrate to cancer cells and to suggest a molecular mechanism underlying the antitumor effect of citrate when used at a high concentration.

MATERIALS AND METHODS

Cell Culture and Treatments

Human hepatocellular carcinoma cell line (HepG2) was maintained in Dulbecco's modified Eagle's medium (DMEM) containing 25 or 5 mM glucose, supplemented with 10% fetal bovine serum (FBS), 2 mM L-glutamine, penicillin (100 U/ml), and streptomycin (100 mg/ml), and immortalized human hepatocyte (IHH) cells were maintained in DMEM F-12 supplemented with 10% FBS, 1% of 100 IU/ml penicillin, 100 $\mu\text{g/ml}$ streptomycin, 1 μM dexamethasone, and 10^{-12} M insulin. All the cell lines were cultured at 37°C and 5% CO_2 in a humidified incubator. The HepG2 and IHH cells were seeded on culture plates and treated for 24 h with sodium citrate and Trichostatin A (TSA), which is an inhibitor of histone deacetylase (HDAC) that prevents the removal of acetyl groups from lysine residues on histone tails. Sodium citrate was dissolved in distilled water at 770 mg/ml; TSA was dissolved in dimethyl sulfoxide (DMSO) at 2 mg/ml as stock solution, which was then diluted with cultured medium to the desired concentrations (Salvia et al., 2017). The final concentration of DMSO did not exceed 0.25% v/v. The control cells were treated at the same final percentage of DMSO. All compounds were purchased from Sigma-Aldrich (unless otherwise indicated).

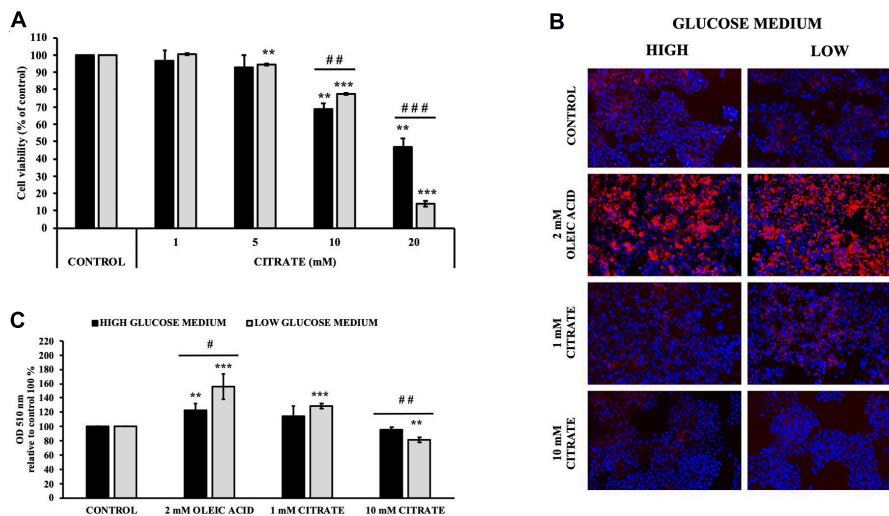


FIGURE 1 | Effect of citrate on HepG2 cell viability and lipid droplet accumulation. **(A)** Viability of Cells grown at 25 mM (black bars) or 5 mM (gray bars) glucose were treated with different concentrations of citrate (1, 5, 10, and 20 mM) for 24 h. Data were expressed as percentage of the control group and presented as means \pm SD of three replicates from three independent experiments. $**p < 0.01$, $***p < 0.001$ cells treated with citrate vs untreated control; $\#p < 0.01$, $###p < 0.001$ cells grown in low-glucose medium vs cells grown in high-glucose medium. **(B)** Microscope images of HepG2 cells grown at 25 mM (high) or 5 mM (low) glucose, treated with citrate 1 and 10 mM for 24 h and stained with Oil Red O to detect hepatic lipid droplets (red). The nuclei were stained with 4',6-diamidino-2-phenylindole (blue). Cells without citrate are considered as control. Oleic acid treatment (2 mM) was used as positive control of intracellular neutral lipids accumulation. **(C)** Lipid droplets were quantified at 510 nm. Data were expressed as percentage of the control group and presented as means \pm SD of three replicates from three independent experiments $**p < 0.01$, $***p < 0.001$ treated cells vs control cells; $\#p < 0.05$, $\#p < 0.01$, cells grown in low-glucose medium (gray bars) vs cells grown in high-glucose medium (black bars).

Viability Assay

Cells were seeded at a density of 1.5×10^3 /well in 96-well plates and incubated with various concentrations of sodium citrate (1, 5, 10, and 20 mM) for 24 h (except the untreated control). The cells were treated with 0.75 mg/ml of [3-(4,5-dimethyl thiazol-2yl)-2,5-diphenyl tetrazolium bromide] (MTT) solution in DMEM for 4 h at 37°C. The solution was subsequently removed, and the cells were lysed using a solubilization solution (1:1 DMSO/isopropanol with 1% of Triton X-100). The solubilized formazan product was spectrophotometrically quantified at 570 nm using a microplate reader (Multiskan™ GO Microplate Spectrophotometer, Thermo Fisher Scientific). The results were presented as percentage of the control, defined as 100% of cell viability. Each test was repeated three times in triplicate.

Western Blot Analysis

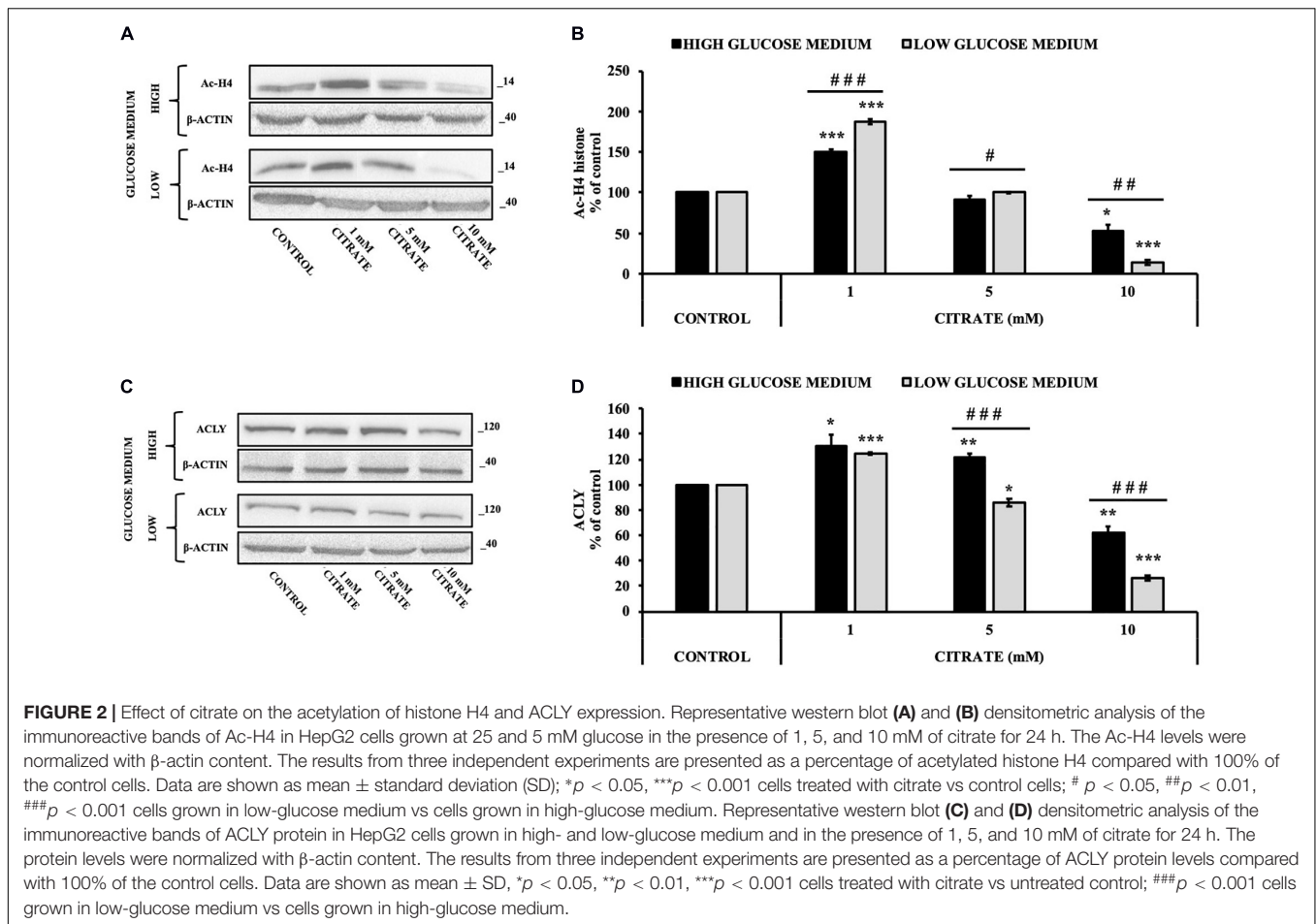
Western blot analysis was performed as previously reported (Miglionico et al., 2017), with some modification. Cells were lysed in Laemmli sample buffer (4% SDS, 20% glycerol, 200 mM DTT, 0.01% bromophenol blue, and 0.1 M Tris-HCl, pH 6.8) by sonication with Bandelin Sonopuls Ultrasonic Homogenizers. Finally, the proteins were resolved on 12% SDS-PAGE gels. After electroblotting on nitrocellulose membrane (AmershamProtran, GE Healthcare Life Sciences), membranes were blocked for 1 h with 5% non-fat milk in PBS-T, pH 7.4, and incubated overnight at 4°C with specific primary antibodies: 1:10,000 anti- β -actin, 1:400 anti-ACLY (Invitrogen), and 1:400 anti-Ac-H4 histone (Santa Cruz Biotechnology), diluted in PBST

with 2.5% non-fat milk. The membranes were washed with PBS-T and incubated with appropriate horseradish peroxidase-conjugated secondary antibody at room temperature for 1 h; the signals were visualized by Chemiluminescent Peroxidase Substrate-1 or Super Signal West Femto Maximum Sensitivity Substrate (Thermo Fisher Scientific), using a Chemidoc™ XRS detection system equipped with Image Lab Software (Bio-Rad). Densitometric analysis was performed by using ImageJ software (National Institute of Health, Bethesda, MD, United States). Protein expression level in the control sample was taken as 100%. Each result was expressed as a percentage of the value of the control sample. Each test was repeated three times.

Lipid Accumulation Assay

Staining of intracellular neutral lipids was performed using Oil Red O. Stock solution was prepared by dissolving 0.14 g in 40 ml 2-propanol 100% (0.35% w/v). This stock solution was stored at room temperature for 2 h. The working solution was obtained by diluting three parts of stock solution with two parts of distilled water. Working solution was prepared freshly for each experiment and filtered immediately before use.

For qualitative analysis, HepG2 cells were seeded on coverslips (1.5×10^5 cells/well) in a 24-well tissue culture plate and then treated with 10 mM sodium citrate for 24 h (except the untreated control); as a positive control of intracellular neutral lipid production, 2 mM oleic acid was used. The cells were washed twice with phosphate-buffered saline (PBS) and fixed with 4% paraformaldehyde in PBS for 30 min. Formalin was removed,



and 2-propanol 60% was added for 5 min. 2-Propanol 60% was removed, and the cells were stained with Oil Red O working solution for 20 min at room temperature. After extensive washing with distilled water, the coverslips were removed from the wells and blotted to remove any excess water. Oil droplets were observed using fluorescence microscopy FLoid CellTM Imaging Station (Thermo Fisher Scientific) in cells with 4',6-diamidino-2-phenylindole-stained nuclei (FluoroshieldTM with DAPI, Sigma).

For quantitative analysis, HepG2 cells were seeded (1.5×10^5 cells/well) in a clear 24-well microtiter plate and then incubated with 10 mM sodium citrate for 24 h (except the untreated control). After addition of Oil Red O working solution for 20 min at room temperature, the cells were treated with 2-propanol, and lipid accumulation was measured using a microplate reader (MultiskanTM GO, Thermo Fisher Scientific) and absorbance was recorded at 510 nm. The results were presented as percentage of the control (cells untreated), defined as 100% of neutral lipid production. Each test was repeated three times in triplicate.

Statistical Analysis

The data are presented as mean \pm SD. Student's *t*-test was performed pairwise to compare the control and the treated samples. Differences were considered significant whenever

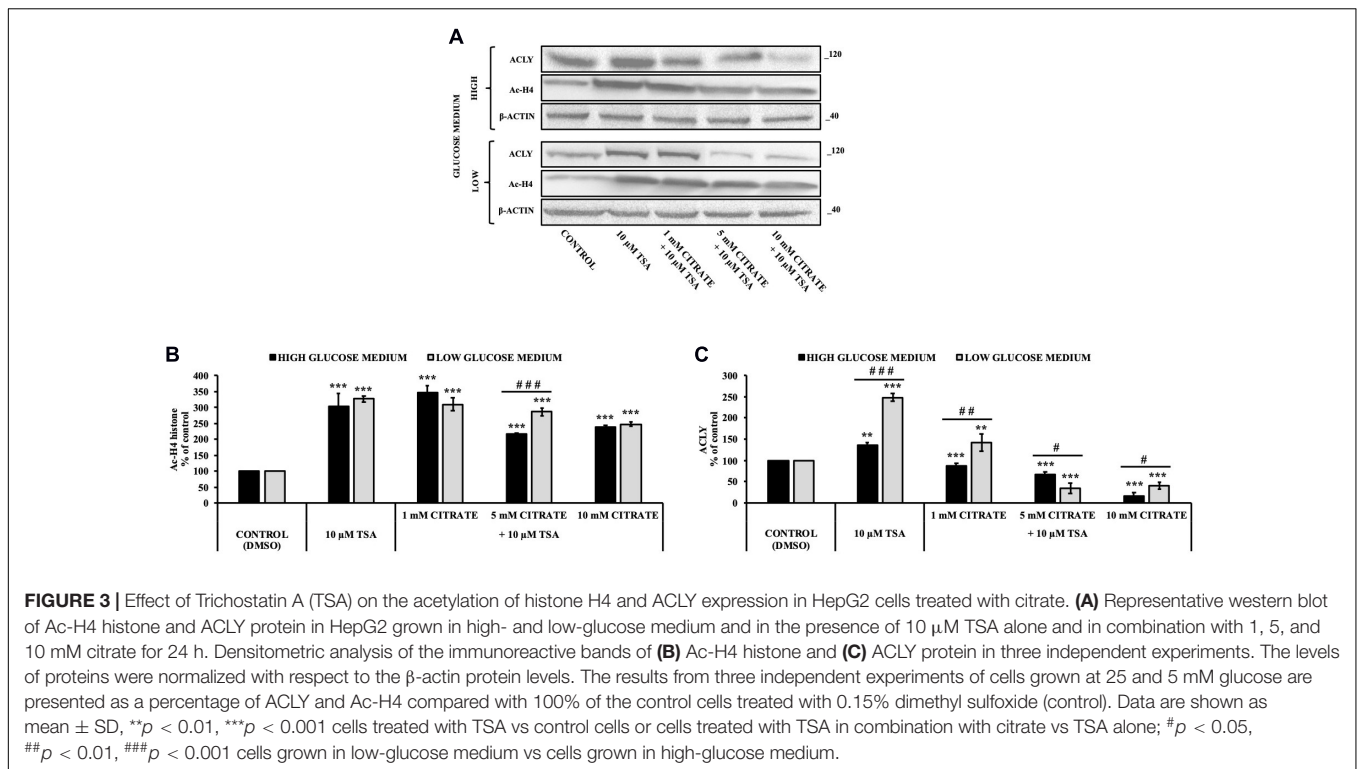
p -value < 0.05. Statistical analysis was performed using statistical GraphPad software.

RESULTS

Effect of Citrate on Acetyl Group Availability in HepG2 Cells

The cell viability of HepG2 cells grown in 5 mM (low) and 25 mM (high) glucose medium and citrate was evaluated using the MTT assay. Incubation with sodium citrate for 24 h at concentrations ranging from 1 to 20 mM decreased the viability of HepG2 cells in a dose-dependent manner (Figure 1A). Citrate did not have a significant effect on cell viability at concentrations ≤ 5 mM. The IC₅₀ values were approximately 17 and 13 mM for the cells grown in high- and low-glucose medium, respectively. At 20 mM concentration, the viability of cells was about 50 and 15% in high- and low-glucose media, respectively. In the cytosol, citrate is cleaved into acetyl-CoA and OAA by ACLY. Since citrate is a source of acetyl groups, its effect on lipid deposition and histone H4 acetylation has been evaluated.

Cells treated with 1 mM citrate showed a slight increase in lipid deposition as demonstrated by Oil Red O staining. Contrary to what was expected, no increase in lipid accumulation was



observed with increasing citrate concentration, thus suggesting a lower availability of acetyl-CoA (Figures 1B,C).

The cells were treated with various concentrations of citrate for 24 h, and the acetylation of histone H4 (Ac-H4 histone) was evaluated. In the presence of sodium citrate at 1 and 5 mM, an increase of Ac-H4 histone has been observed; however, at 10 mM citrate, the acetylated histone decreased both at high and low glucose concentrations (Figures 2A,B). These results prompted us to investigate the effect of citrate on ACLY expression (Figures 2C,D). The addition of citrate at 1 mM increased the ACLY expression when the cells were grown in both high- and low-glucose medium. However, the expression of ACLY was reduced at 5 mM citrate and decreased significantly at 10 mM citrate with a trend similar to that observed for the acetylation of H4 histone (Figure 2B), thus suggesting that the expression of ACLY is epigenetically controlled by acetylation of histone H4.

Since histone acetylation involves a balance between the activities of enzymes that catalyze histone acetylation (HAT) and deacetylation (HDAC), we evaluated the effect of citrate on the expression of ACLY and the acetylation of histone H4 in the presence of TSA, a deacetylation inhibitor. HepG2 cells were grown in high- and low-glucose medium and treated with 10 μ M TSA alone and in combination with different concentrations of citrate (Figure 3A) for 24 h. The acetylated histone and the expression of ACLY increased after treatment with TSA, as compared to the control. With 1 mM citrate and TSA, the acetylation of histone H4 did not change significantly as compared to TSA alone (Figure 3B), whereas the expression of ACLY was considerably lowered (Figure 3C). Moreover, with TSA and citrate at a higher concentration, both acetylation

of H4 and ACLY expression decreased in a dose-dependent manner. These results confirmed that citrate epigenetically modulates ACLY also in the presence of TSA, reducing the acetylation of histone H4.

Effect of Citrate on the Viability, Acetylation of Histone H4, and ACLY Expression in Immortalized Human Hepatocytes

With the aim to verify the effect of citrate on normal cells, we performed some experiments on IHH cells. The administration of citrate at different concentrations, from 5 to 20 mM, significantly decreased the viability of IHH cells in a dose-dependent manner (Figure 4A). At 20 mM concentration of sodium citrate, the viability of IHH cells was reduced to about 40%.

We investigated the level of Ac-H4 histone and ACLY expression in cells grown with sodium citrate for 24 h at concentrations that ranged from 1 to 10 mM (Figure 4B). A significant decrease of Ac-H4 histone in up to 10 mM concentration of citrate has been observed (Figure 4C). On the contrary, the expression of ACLY did not change at 5 and 10 mM citrate; at 1 mM, it even increased as compared to the control (Figure 4D), thus suggesting that, in non-tumor cells, changes of acetylated histone level do not correspond to a change of ACLY expression, as instead shown by HepG2 cells.

In addition, we evaluated Ac-H4 histone and the expression of ACLY in IHH grown at different concentrations of citrate in combination with 10 μ M TSA (Figure 4E). When cells are treated with the deacetylase inhibitor, citrate decreased the acetylation

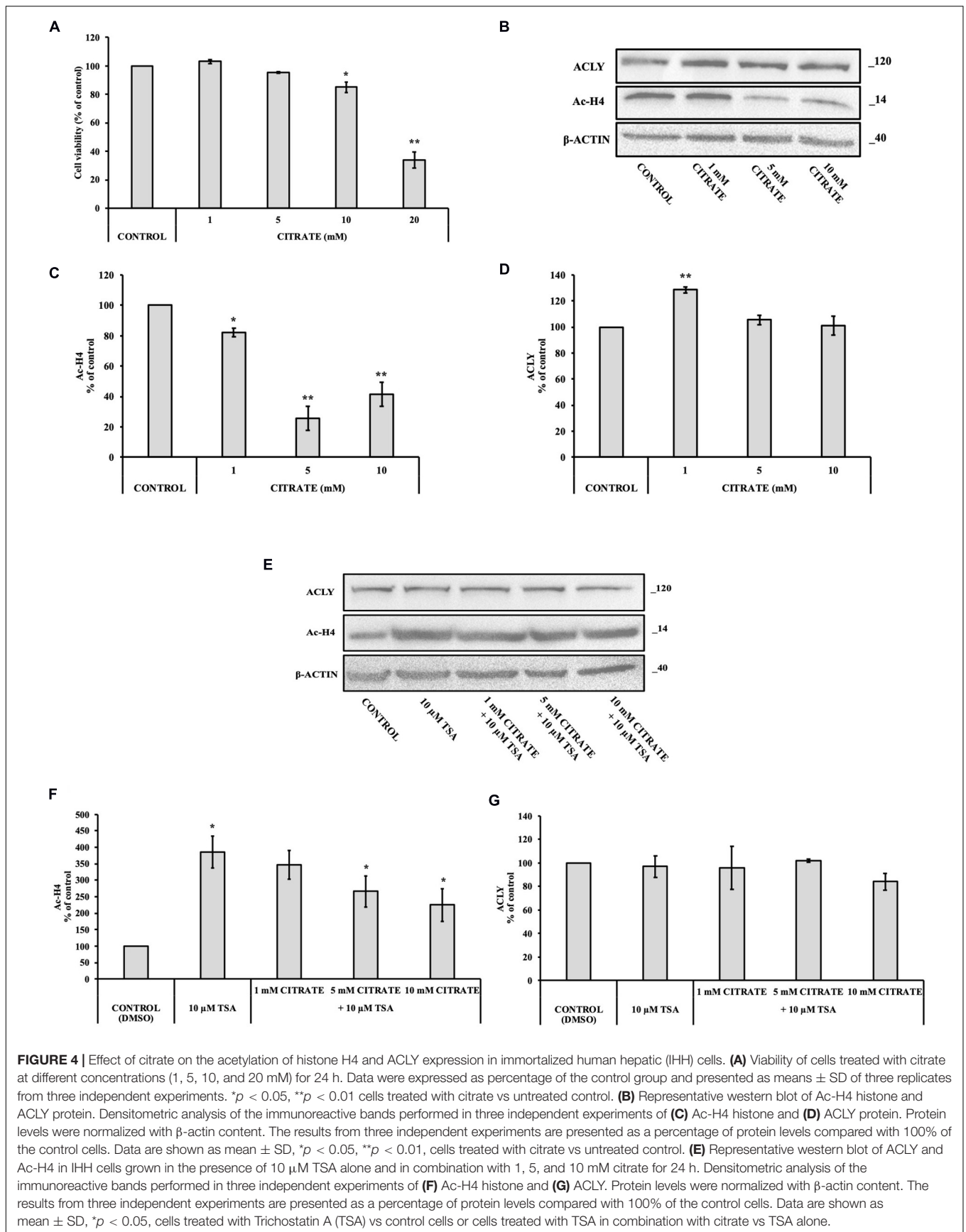


FIGURE 4 | Effect of citrate on the acetylation of histone H4 and ACLY expression in immortalized human hepatic (IHH) cells. **(A)** Viability of cells treated with citrate at different concentrations (1, 5, 10, and 20 mM) for 24 h. Data were expressed as percentage of the control group and presented as means ± SD of three replicates from three independent experiments. **p* < 0.05, ***p* < 0.01 cells treated with citrate vs untreated control. **(B)** Representative western blot of Ac-H4 histone and ACLY protein. Densitometric analysis of the immunoreactive bands performed in three independent experiments of **(C)** Ac-H4 histone and **(D)** ACLY protein. Protein levels were normalized with β-actin content. The results from three independent experiments are presented as a percentage of protein levels compared with 100% of the control cells. Data are shown as mean ± SD, **p* < 0.05, ***p* < 0.01, cells treated with citrate vs untreated control. **(E)** Representative western blot of ACLY and Ac-H4 in IHH cells grown in the presence of 10 μM TSA alone and in combination with 1, 5, and 10 mM citrate for 24 h. Densitometric analysis of the immunoreactive bands performed in three independent experiments of **(F)** Ac-H4 histone and **(G)** ACLY. Protein levels were normalized with β-actin content. The results from three independent experiments are presented as a percentage of protein levels compared with 100% of the control cells. Data are shown as mean ± SD, **p* < 0.05, cells treated with Trichostatin A (TSA) vs control cells or cells treated with TSA in combination with citrate vs TSA alone.

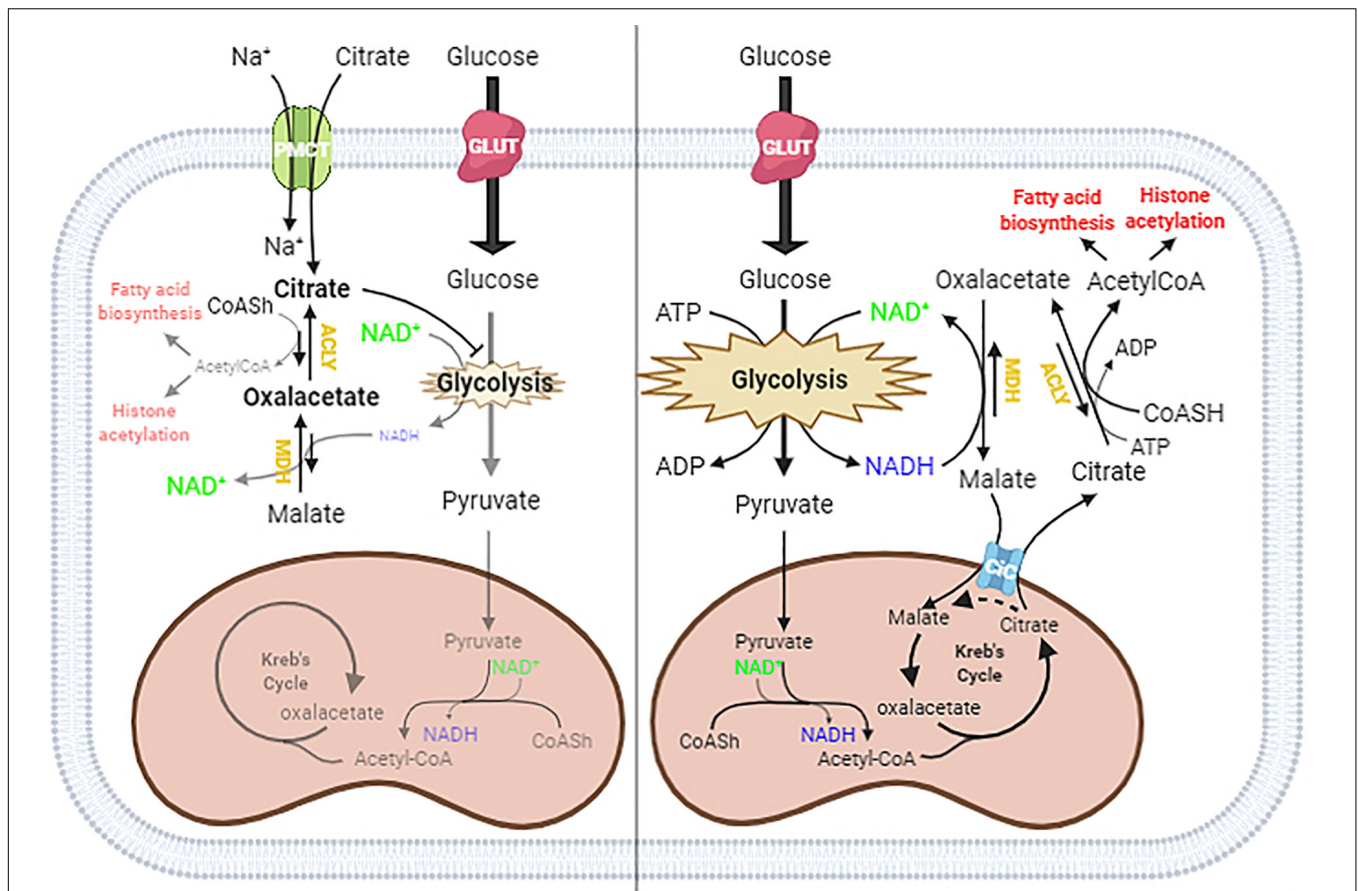


FIGURE 5 | Proposed mechanism of citrate effect at a higher concentration. In the absence of exogenous citrate or with low citrate concentration (right panel), citrate formed in the TCA cycle moves to the cytoplasm through the citrate/malate exchanger and supplies acetyl groups for histone acetylation and lipid biosynthesis. Since citrate is converted by ATP citrate lyase (ACLY) in acetyl-CoA and oxaloacetate, which in turn goes back in the mitochondria after reduction to malate in exchange with citrate, the full process results in an outflow of acetyl groups. When citrate is administered at a high concentration (left panel), the oxaloacetate accumulates in the cytosol because of the lack of reducing equivalents needed to convert to malate, due to citrate itself acting as an inhibitor of glycolysis. The equilibrium balance of the reaction catalyzed by ACLY is shifted toward the reagents, lowering the availability of acetyl groups for lipid biosynthesis and histone acetylation.

of histone H4 in a dose-dependent manner (Figure 4F). Once again, the expression of ACLY did not change (Figure 4G), thus confirming that, in IHH cells, citrate did not control ACLY expression by changing the acetylation of histone H4.

DISCUSSION

Citrate is an important metabolite in cellular energy metabolism, and it has multiple physiological and pathological functions. It acts as a regulator of glucose and lipid metabolism and controls the acetyl group availability. The anticancer properties of citrate were reported on different tumor cell lines; however, the effects of citrate to support cell proliferation have been also described (Zhang et al., 2009; Icard et al., 2012; Lincet et al., 2013; Xia et al., 2018).

In this study, we investigated the effects of different concentrations of extracellularly administered citrate, focusing on its main intracellular functions, i.e., to provide acetyl-CoA for

the biosynthesis of fatty acids and histone acetylation. These two important processes are required by cancer cells to synthesize large quantities of lipids to build cell membranes and regulate gene expression, respectively.

Lipid deposition as well as acetylated histone H4 in HepG2 cells was increased when grown with 1 mM citrate and decreased with 10 mM citrate (Figures 1, 2). Since citrate is converted to acetyl-CoA and OAA by ACLY and acetyl-CoA is a substrate for both lipid synthesis and histone acetylation, one would expect an increase of both processes upon citrate supplementation. The unexpected inhibition of the ACLY activity in cells grown with high citrate concentration suggested us to further investigate the effects of citrate on ACLY expression. HepG2 cells grown in the presence of different citrate concentrations showed a clear correlation between acetylated H4 histone and ACLY protein expression. The same correlation was confirmed even in the presence of TSA, an inhibitor of histone deacetylases, thus suggesting that ACLY expression is partly controlled by histone H4 acetylation (Figure 3).

In order to verify if the unexpected result that we found after treatment with citrate 10 mM is due to a specific behavior of cancer cells, experiments were performed on IHH cells, which have a metabolism very similar to normal hepatocytes. The addition of 10 mM citrate decreased the acetylation of histone H4, which is similar to what was observed in HepG2 cells, suggesting that the regulation of histone acetylation occurs the same way in both tumor and non-tumor cells. In contrast, ACLY expression in IHH cells was not modified after citrate exposure, suggesting that, in this case, ACLY expression was not regulated by histone H4 acetylation (Figure 4). These results therefore suggest that the epigenetic regulation of ACLY in cancer cells is one way to adapt the metabolism for specific cellular requirements.

In the schematic diagram shown in Figure 5, we propose a possible explanation of what might happen in cells under normal conditions and when citrate is given at a high concentration. In the cytoplasm, ACLY catalyzes the cleavage of citrate into acetyl-CoA and OAA. In normal conditions, citrate produced by mitochondria effluxes into the cytoplasm through the mitochondrial citrate carrier that exchanges the citrate with malate produced by the reduction of OAA: in this way, the acetylation process is strictly linked to the reduction of OAA to malate by the NADH produced by glycolysis.

The exogenous citrate enters the cells through the sodium-dependent transporter SLC13A5 (Costello and Franklin, 2016) and is cleaved in acetyl-CoA and OAA. In the presence of high exogenous citrate, we found decreased lipid deposition and histone acetylation, indicative of a decreased availability of acetyl-CoA, which suggested an inhibition of ACLY activity. The inhibition of ACLY may be due to several causes that we can consider individually or in combination, such as the strong inhibition of glycolysis, which leads to a decrease in NADH necessary for OAA reduction, OAA directly inhibiting ACLY, or simply a shift in the balance of the reaction catalyzed by ACLY due to the accumulation of OAA, which prevents the further synthesis of acetyl-CoA and OAA.

Considering the strong demand for acetyl-CoA in tumor cells but not for OAA, the administration of citrate at a high concentration to HepG2 cells determines an accumulation of OAA, which reduces the further synthesis of OAA and acetyl-CoA and therefore ACLY expression. For this reason, we suggest that the exogenous citrate would behave like a trojan horse that releases OAA in the cells, where it could exert its therapeutic effect also on hepatoma cells. Our hypothesis is also supported by what has already been reported on the antitumor potential of OAA due to its ability to inhibit glycolysis through the enhancement of oxidative phosphorylation (Kuang et al., 2018). Although further experiments are needed to define the molecular

mechanism by which high concentrations of citrate inhibit ACLY, the results reported in this work shed light on some data in the literature regarding the use of citrate in the treatment of cancer. The most important discovery is undoubtedly the demonstration that high concentrations of citrate decrease the availability of acetyl-CoA, a key molecule both in the metabolism of sugars and lipids and in the control of gene transcription that lays the basis for the understanding of all the pathophysiological activities sensitive to citrate. Another important aspect that emerges from this work is that, although citrate is a metabolic intermediate, the exogenous citrate behaves differently from the endogenous citrate because the latter, due to the exchange mechanism with which the mitochondrial citrate transport operates, when it is cleaved by the ACLY, releases acetyl-CoA in the cytoplasm and reduced oxaloacetate to malate in the mitochondria which, in addition to feeding the mitochondrial activity, prevents the accumulation of oxaloacetate.

As citrate metabolism provides a connection between carbohydrate metabolism, fatty acid metabolism, and epigenetic reprogramming, its administration to higher concentrations compared to the physiological ones may be useful as anticancer drug for liver cancer.

DATA AVAILABILITY STATEMENT

The original contributions presented in the study are included in the article/supplementary material, further inquiries can be directed to the corresponding authors.

AUTHOR CONTRIBUTIONS

FB and AO conceived this work, designed the experiments, analyzed the data, and wrote the manuscript. AP performed the experiments. VA performed statistical analysis. PK critically read the manuscript. FB supervised the work. All authors contributed to the article and approved the submitted version.

FUNDING

This work was in part supported by PRIN (Progetti di Ricerca di Interesse Nazionale), project no. 2017PAB8EM, “Membrane transporters, the doors of cellular metabolism. Investigation of biochemical features structure/function relationships, metabolic regulation, and physio-pathological aspects by *in vitro* and *in vivo* experimental models” granted by MIUR (Ministry of Education, University and Research)—Italy.

REFERENCES

- Abdel-Salam, O. M. E., Youness, E. R., Mohammed, N. A., Morsy, S. M. Y., Omara, E. A., and Sleem, A. A. (2014). Citric acid effects on brain and liver oxidative stress in lipopolysaccharide-treated mice. *J. Med. Food* 17, 588–598. doi: 10.1089/jmf.2013.0065
- Bisaccia, F., De Palma, A., and Palmieri, F. (1989). Identification and purification of the tricarboxylate carrier from rat liver mitochondria. *Biochim. Biophys. Acta* 977, 171–176.
- Burns, J. S., and Manda, G. (2017). Metabolic pathways of the warburg effect in health and disease: perspectives of choice, chain or chance. *Int. J. Mol. Sci.* 18, 1–28. doi: 10.3390/ijms18122755

- Caiazza, C., D'Agostino, M., Passaro, F., Faicchia, D., Mallardo, M., Paladino, S., et al. (2019). Effects of long-term citrate treatment in the PC3 prostate cancer cell line. *Int. J. Mol. Sci.* 20, 1–18. doi: 10.3390/ijms20112613
- Costello, L. C., and Franklin, R. B. (2016). Plasma citrate homeostasis: how it is regulated; and its physiological and clinical implications. an important, but neglected, relationship in medicine. *Hum. Endocrinol.* 1:5. doi: 10.24966/he-9640/100005
- De Berardinis, R. J., and Chandel, N. S. (2016). Fundamentals of cancer metabolism. *Sci. Adv.* 2:e1600200. doi: 10.1126/sciadv.1600200
- Fritz, V., and Fajas, L. (2010). Metabolism and proliferation share common regulatory pathways in cancer cells. *Oncogene* 29, 4369–4377. doi: 10.1038/onc.2010.182
- Furuta, E., Okuda, H., Kobayashi, A., and Watabe, K. (2010). Metabolic genes in cancer: their roles in tumor progression and clinical implications. *Biochim. Biophys. Acta Rev. Cancer* 180, 141–152. doi: 10.1016/j.bbcan.2010.01.005
- Gatenby, R. A., and Gillies, R. J. (2004). Why do cancers have high aerobic glycolysis? *Nat. Rev. Cancer* 4, 891–899. doi: 10.1038/nrc1478
- He, Y., Gao, M., Cao, Y., Tang, H., Liu, S., and Tao, Y. (2017). Nuclear localization of metabolic enzymes in immunity and metastasis. *Biochim. Biophys. Acta Rev. Cancer* 1868, 359–371.
- Icard, P., Poulain, L., and Lincet, H. (2012). Understanding the central role of citrate in the metabolism of cancer cells. *Biochim. Biophys. Acta Rev. Cancer* 1825, 111–116. doi: 10.1016/j.bbcan.2011.10.007
- Khwairakpam, A., Mayengbam, S., Bethsebie, S., Sivakumar, R., and Ganesan, P. (2015). ATP citrate lyase (ACLY): a promising target for cancer prevention and treatment. *Curr. Drug Targets* 16, 156–163. doi: 10.2174/1389450115666141224125117
- Khwairakpam, A. D., Banik, K., Girisa, S., Shabnam, B., Shakibaei, M., Fan, L., et al. (2020). The vital role of ATP citrate lyase in chronic diseases. *J. Mol. Med.* 98, 71–95. doi: 10.1007/s00109-019-01863-0
- Kuang, Y., Han, X., Xu, M., and Yang, Q. (2018). Oxaloacetate induces apoptosis in HepG2 cells via inhibition of glycolysis. *Cancer Med.* 7, 1416–1429. doi: 10.1002/cam4.1410
- Lee, J. V., Carrer, A., Shah, S., Snyder, N. W., Wei, S., Venneti, S., et al. (2014). Akt-dependent metabolic reprogramming regulates tumor cell histone acetylation. *Cell Metab.* 20, 306–319. doi: 10.1016/j.cmet.2014.06.004
- Liao, Y. (2017). Cancer metabolism as we know it today: a prologue to a special issue of cancer metabolism. *Genes Dis.* 4, 4–6. doi: 10.1016/j.gendis.2017.02.001
- Liberti, M. V., and Locasale, J. W. (2016). The warburg effect: how does it benefit cancer cells? *Trends Biochem. Sci.* 41, 211–218. doi: 10.1016/j.tibs.2015.12.001
- Lin, X., Xiao, Z., Chen, T., Liang, S. H., and Guo, H. (2020). Glucose metabolism on tumor plasticity, diagnosis, and treatment. *Front. Oncol.* 10:317. doi: 10.3389/fonc.2020.00317
- Lincet, H., Kafara, P., Giffard, F., Abeillard-Lemoisson, E., Duval, M., Louis, M. H., et al. (2013). Inhibition of Mcl-1 expression by citrate enhances the effect of bcl-x l inhibitors on human ovarian carcinoma cells. *J. Ovarian Res.* 6, 1–10. doi: 10.1186/1757-2215-6-72
- Liu, Y., Zhang, Z., Wang, J., Chen, C., Tang, X., Zhu, J., et al. (2019). Metabolic reprogramming results in abnormal glycolysis in gastric cancer: a review. *OncoTargets Ther.* 12, 1195–1204. doi: 10.2147/OTT.S189687
- Luengo, A., Gui, D. Y., and Vander Heiden, M. G. (2017). Targeting metabolism for cancer therapy. *Cell Chem. Biol.* 24, 1161–1180. doi: 10.1016/j.chembiol.2017.08.028
- Miglionico, R., Ostuni, A., Armentano, M. F., Milella, L., Crescenzi, E., Carosino, M., et al. (2017). ABCC6 Knockdown in HepG2 cells induces a senescent-like cell phenotype. *Cell. Mol. Biol. Lett.* 22:7. doi: 10.1186/s11658-017-0036-2
- Mohammad, A., Monjok, E., Kouamou, G., Ohia, S. E., Bagchi, D., and Lokhandwala, M. F. (2007). Super CitriMax (HCA-SX) attenuates increases in oxidative stress, inflammation, insulin resistance, and body weight in developing obese zucker rats. *Mol. Cell. Biochem.* 304, 93–99. doi: 10.1007/s11010-007-9489-3
- Mycielska, M. E., Dettmer, K., Rummele, P., Schmidt, K., Prehn, C., Milenkovic, V. M., et al. (2018). Extracellular citrate affects critical elements of cancer cell metabolism and supports cancer development in vivo. *Cancer Res.* 78, 2513–2523. doi: 10.1158/0008-5472.CAN-17-2959
- Pastorino, J. G., and Hoek, J. B. (2008). Regulation of hexokinase binding to VDAC. *J. Bioenerg. Biomembr.* 40, 171–182.
- Ren, J. G., Seth, P., Ye, H., Guo, K., Hanai, J. I., Husain, Z., et al. (2017). Citrate suppresses tumor growth in multiple models through inhibition of glycolysis, the tricarboxylic acid cycle and the IGF-1R pathway. *Sci. Rep.* 7, 1–13. doi: 10.1038/s41598-017-04626-4
- Roth, K. G., Mambetsariev, I., Kulkarni, P., and Salgia, R. (2020). The mitochondrion as an emerging therapeutic target in cancer. *Trends Mol. Med.* 26, 119–134. doi: 10.1016/j.molmed.2019.06.009
- Salvia, A. M., Cuvillo, F., Coluzzi, S., Nuccorini, R., Attolico, I., Pascale, S. P., et al. (2017). Expression of some ATP-binding cassette transporters in acute myeloid leukemia. *Hematol. Rep.* 9, 137–141. doi: 10.4081/hr.2017.7406
- Sul, J. W., Kim, T. Y., Yoo, H. J., Kim, J., Suh, Y. A., Hwang, J. J., et al. (2016). A novel mechanism for the pyruvate protection against zinc-induced cytotoxicity: mediation by the chelating effect of citrate and isocitrate. *Arch. Pharm. Res.* 39, 1151–1159. doi: 10.1007/s12272-016-0814-9
- van der Knaap, J. A., and Verrijzer, C. P. (2016). Undercover: gene control by metabolites and metabolic enzymes. *Genes Dev.* 30, 2345–2369. doi: 10.1101/gad.289140.116
- Wang, T. A., Xian, S. L., Guo, X. Y., Zhang, X. D., and Lu, Y. F. (2018). Combined 18F-FDG PET/CT imaging and a gastric orthotopic xenograft model in nude mice are used to evaluate the efficacy of glycolysis-targeted therapy. *Oncol. Rep.* 39, 271–279. doi: 10.3892/or.2017.6060
- Wellen, K. E., Hatzivassiliou, G., Sachdeva, U. M., Bui, T. V., Cross, J. R., and Thompson, C. B. (2009). ATP-citrate lyase links cellular metabolism to histone acetylation. *Science* 324, 1076–1080. doi: 10.1126/science.1164097
- Williams, N. C., and O'Neill, L. (2018). A role for the krebs cycle intermediate citrate in metabolic reprogramming in innate immunity and inflammation. *Front. Immunol.* 9:141. doi: 10.3389/fimmu.2018.00141
- Xia, Y., Zhang, X., Bo, A., Sun, J., and Li, M. (2018). Sodium citrate inhibits the proliferation of human gastric adenocarcinoma epithelia cells. *Oncol. Lett.* 15, 6622–6628. doi: 10.3892/ol.2018.8111
- Zaidi, N., Swinnen, J. V., and Smans, K. (2012). ATP-citrate lyase: a key player in cancer metabolism. *Cancer Res.* 72, 3709–3714. doi: 10.1158/0008-5472.CAN-11-4112
- Zhang, X., Varin, E., Allouche, S., Yunfei, L., Poulain, L., and Icard, P. (2009). Effect of citrate on malignant pleural mesothelioma cells: a synergistic effect with cisplatin. *Anticancer Res.* 29, 1249–1254.

Conflict of Interest: The authors declare that the research was conducted in the absence of any commercial or financial relationships that could be construed as a potential conflict of interest.

Copyright © 2020 Petillo, Abruzzese, Koshal, Ostuni and Bisaccia. This is an open-access article distributed under the terms of the Creative Commons Attribution License (CC BY). The use, distribution or reproduction in other forums is permitted, provided the original author(s) and the copyright owner(s) are credited and that the original publication in this journal is cited, in accordance with accepted academic practice. No use, distribution or reproduction is permitted which does not comply with these terms.



CFTR Deficiency Affects Glucose Homeostasis via Regulating GLUT4 Plasma Membrane Transportation

Junzhong Gu^{1†}, Weiwei Zhang^{2†}, Lida Wu^{1*} and Yuchun Gu^{1,3*}

¹ Molecular Pharmacology Laboratory, Institute of Molecular Medicine, Peking University, Beijing, China, ² Peking-Tsinghua Center for Life Sciences, Peking University, Beijing, China, ³ Translational and Regenerative Medicine Centre, Aston Medical School, Aston University, Birmingham, United Kingdom

OPEN ACCESS

Edited by:

Cesare Indiveri,
University of Calabria, Italy

Reviewed by:

Valeria Rachela Vilella,
European Institute for Research in
Cystic Fibrosis (IERFC), Italy
Paul Hruz,
Washington University in St. Louis,
United States

*Correspondence:

Lida Wu
wldpaper@pku.edu.cn;
wldpaper@gmail.com
Yuchun Gu
ycgu@pku.edu.cn

[†] These authors have contributed
equally to this work and share first
authorship

Specialty section:

This article was submitted to
Cellular Biochemistry,
a section of the journal
Frontiers in Cell and Developmental
Biology

Received: 19 November 2020

Accepted: 27 January 2021

Published: 15 February 2021

Citation:

Gu J, Zhang W, Wu L and Gu Y
(2021) CFTR Deficiency Affects
Glucose Homeostasis via Regulating
GLUT4 Plasma Membrane
Transportation.
Front. Cell Dev. Biol. 9:630654.
doi: 10.3389/fcell.2021.630654

Cystic Fibrosis (CF) is an autosomal recessive disorder caused by mutations in the Cystic Fibrosis Transmembrane Conductance Regulator (CFTR) gene. CF-related diabetes (CFRD) is one of the most prevalent comorbidities of CF. Altered glucose homeostasis has been reported in CF patients. The mechanism has not been fully elucidated. Besides the consequence of pancreatic endocrine dysfunction, we focus on insulin-responsive tissues and glucose transportation to explain glucose homeostasis alteration in CFRD. Herein, we found that CFTR knockout mice exhibited insulin resistance and glucose tolerance. Furthermore, we demonstrated insulin-induced glucose transporter 4 (GLUT4) translocation to the cell membrane was abnormal in the CFTR knockout mice muscle fibers, suggesting that defective intracellular GLUT4 transportation may be the cause of impaired insulin responses and glucose homeostasis. We further demonstrated that PI(4,5)P₂ could rescue CFTR related defective intracellular GLUT4 transportation, and CFTR could regulate PI(4,5)P₂ cellular level through PIP5KA, suggesting PI(4,5)P₂ is a down-stream signal of CFTR. Our results revealed a new signal mechanism of CFTR in GLUT4 translocation regulation, which helps explain glucose homeostasis alteration in CF patients.

Keywords: cystic fibrosis, CFTR, CF-related diabetes, glucose homeostasis disorder, GLUT4

INTRODUCTION

Cystic fibrosis (CF) is one of the most common autosomal recessive disorders in the Caucasian population. It is caused by mutations in the CFTR gene. CF-related diabetes (CFRD) affects 19% of adolescents with CF (Moran et al., 2010), 50% adults CF patients (Moran et al., 2009, 2010), indicating that CFRD is a progressive complication of CF. Despite advances in therapies designed to address the disease's symptoms, the death rate is still high. As a result, it is crucial to study the mechanism of CFRD thoroughly.

One of the prevailing mechanistic beliefs is that CFRD results from defective insulin secretion of pancreatic β -cell, which is due to the combination of chronic pancreatitis and eventual loss of the islet cells (Cucinotta et al., 1994; Marshall et al., 2005; Costa et al., 2007; Mohan et al., 2009; Guo et al., 2014). Autopsy data confirmed the eventual loss of islet tissue and decreased β -cell

Abbreviations: CF, Cystic Fibrosis; CFTR, Cystic Fibrosis Transmembrane Conductance Regulator; CFRD, Cystic Fibrosis related diabetes; GLUT4, Glucose Transporter 4.

numbers in aged CF patients (Iannucci et al., 1984; Lohr et al., 1989). However, most CF patients demonstrate abnormalities in glycaemic control regardless of the class and severity of the CFTR mutation (Wooldridge et al., 2015). Of the thousand CFTR mutations that have been identified, approximately 20 are understood to be disease-causing and are categorized into five classes of mutations of increasing disease severity (Manderson Koivula et al., 2017). CFTR in the regulation of insulin secretion and β cell function has also been reported as the mechanism of CFRD by several recent studies (Stalvey et al., 2006; Edlund et al., 2014; Guo et al., 2014; Fontes et al., 2015), which cannot fully explain the impaired insulin responses and glucose homeostasis reported in CF patients. In addition to the traditional view that CFRD is the consequence of pancreatic endocrine dysfunction, we speculated that CFRD might also affect insulin-responsive tissues' function.

Several studies found that CF patients with overt diabetes exhibited peripheral and hepatic insulin resistance (Moran et al., 1994; Holl et al., 1995; Hardin et al., 2001; Fontes et al., 2015; Boudreau et al., 2016). However, little is known regarding the mechanism of CFTR loss-of-function in insulin resistance. Insulin facilitates the entry of glucose into muscle, adipose, and several other tissues. The typical mechanism by which cells can take up glucose is by facilitated diffusion through a family of hexose transporters. Skeletal muscle provides the most substantial contribution (~70%) of insulin-dependent glucose disposal, and this process is mediated by the insulin-responsive glucose transporter 4 (GLUT4) (Bouche et al., 2004; Leto and Saltiel, 2012). As a result, we speculated that CFTR deficiency might result in impaired insulin action and GLUT4 dysfunction in skeletal muscle. In this study, we found that CFTR knockout mice exhibited altered glucose homeostasis, and the reason was defective intracellular GLUT4 transportation.

MATERIALS AND METHODS

Cell Culture and Transfection

Flexor Digitorum Brevis (FDB) muscle fibers isolation from mice skeletal muscle was previously described (Park et al., 2014). Mouse skeletal muscle cell lines, C2C12 myoblasts, were cultured in DMEM (GIBCO #11965) supplemented with 10% FBS (HyClone #30071.03). C2C12 myotubes differentiation was then induced by switching the medium to DMEM supplemented with 2% HS (GIBCO #26050070). The medium was changed every 24 h. The plasmid of myc-GLUT4-EGFP, bearing the c-Myc epitope tag in the first extracellular loop and GFP at the carboxyl terminus, was purchased from addgene (#52872). According to the manufacturer's instructions, the plasmid was transfected into HEPG2 and Hela cells using Lipofectamine 2000 (Invitrogen). C2C12 myoblasts and myotubes were transfected with adenovirus (Vigenebio, China) to express myc-GLUT4-EGFP protein.

Immunofluorescent Analysis

Cells that express myc-GLUT4-EGFP were cultured with media supplemented with 1% FBS overnight and then were treated

with insulin (100 nM) for 30 min. Cells were then fixed with 4% paraformaldehyde, followed by immunocytochemistry using the anti-Myc antibody (Beijing TDY Biotech LTD, #TDY002) and Cy3-conjugated anti-mouse IgG antibody (Beijing CWBIO, #CW0145S). The cells were imaged with a spin disk confocal system (Revolution XD; ColdSpring Science Corporation) with a CSU-X1 confocal head (Yokogawa) mounted on an inverted microscope (IX81ZDC2; Nikon) with Perfect Focus, using an EMCCD camera (iXon3 DU-897D-C00-#BV; Andor). MetaMorph controlled image acquisition and all other peripherals.

Animal Experiments

All methods were carried out following relevant guidelines and regulations. All experimental protocols were approved by the University Ethics Committee, Institute of Molecular Medicine, Peking University. All animals received humane care in compliance Guide for the Institutional Animal Care and Use Committee (IACUC). CFTR knockout (KO) and heterozygote (HET) mice were purchased from Jackson Lab (CFTR S489X-) and bred to generate homozygous mutants (KO), heterozygote (HET), and wild-type (WT) mice. CFTR KO mice were genotyped by standard PCR according to the genotyping protocol. Mice were housed under controlled temperature (21°C) on a 12 h light-dark cycle with unrestricted access to food and water.

FABP-hCFTR-CFTR transgenic mice harbor the FABP-hCFTR transgene and a targeted knock-out mutation of the CFTR. This model may be used to assess the effects of the null mutation and may be useful as a mouse model of severe phenotype cystic fibrosis.

Glucose Tolerance Test, Insulin Tolerance Tests, and Determination of Insulin Levels *in vivo*

For glucose tolerance tests (GTTs), the mice were starved overnight and were given 2.5 g/kg body weight of glucose by IP injection. Blood was then taken from the tail vein before and 15, 30, 60, and 120 min after injection to determine blood glucose by using an Accu-Chek blood glucose monitor (Roche). To determine insulin plasma levels, blood was collected, and the plasma was obtained, and analysis was performed with an insulin ELISA (Millipore). For ITT, 5 h fasted mice were given human insulin (0.75 U/kg, Novolin) by IP injection. The blood glucose concentration was monitored before and after 15, 30, 60, and 120 min after injection. During GTT and ITT, mice were caged with blinded identity and random orders.

Immunoblotting

The expression and phosphorylation of each protein were analyzed by Western blot analysis. The membrane protein was extracted by using a membrane protein extraction kit (Merck Millipore). The protein was quantified using the Bradford reagent (BioRad). Before loading into the 10% SDS-PAGE, the samples were mixed with a 5x loading buffer and boiled at 98°C for 5 min. After gel electrophoresis, the proteins

were then transferred to a PVDF membrane (0.45 μm , Merck Millipore) under 250 mA for 90 min. The membranes were incubated with a blocking buffer (5% non-fat milk in Tris-buffered saline containing 0.5% Tween-20) for 1 h at room temperature and then incubated with the indicated primary antibodies at 4°C overnight. The membrane was incubated with horseradish peroxidase-conjugated secondary antibody for 1 h at room temperature. The target protein bands were visualized using Amersham Imager 600 (GE healthcare).

Rabbit polyclonal to GLUT4(ab654,1:2,000), Rabbit polyclonal to PIP5K1A(ab654,1:1,000), and Mouse monoclonal to alpha 1 Sodium Potassium ATPase(ab7671, 5 $\mu\text{g}/\text{ml}$) were purchased from Abcam (United Kingdom); Mouse Monoclonal Antibody to β -tubulin(TDY041, 1:1,000), Mouse Monoclonal Antibody to β -actin(TDY045, 1:1,000), Goat Polyclonal Antibody to Mouse IgG (H + L), HRP Conjugated(S001, 1:1,000), and Goat Polyclonal Antibody to Rabbit IgG (H + L), HRP Conjugated(S004, 1:1,000) were from TDY(Beijing, China).

Dot-Blot Analysis

PI(4,5) P_2 were measured by dot-blot analysis. C2C12 myotubes were treated with CFTR (inh)-172(Chemegen) for 24 h. FDB muscle fibers isolated from CFTR KO, HET, WT mice. The whole-cell lysates were then extracted from C2C12 myotubes, and FDB muscle fibers were blotted onto nitrocellulose membranes (Bio-Rad Laboratories). These were probed with PI(4,5) P_2 antibody (Abcam, # ab11039) at a 1:500 dilution and detected using a horseradish peroxidase-conjugated secondary antibody (Beijing TDY Biotech LTD, #E009) and were visualized using Amersham Imager 600 (GE healthcare). Experiments were repeated at least three times.

[³H]2-Deoxy-D-Glucose Uptake Assay

Uptake of [³H]2-deoxyglucose (Sigma, 73698-45-0) was measured in C2C12 myocytes differentiated in 24-well plates. After differentiation, cells were washed twice with DMEM (GIBCO #11965) and incubated in the DMEM for 2 h at 37°C. Cells were then washed twice in PBS and then incubated in KRBB (G-clone, RS1800) in the presence or absence of insulin for 30 min at 37°C. CFTR (inh)-172 was added 30 min before insulin. After insulin treatment, uptake of 10 μM [³H]2-deoxyglucose was measured for 15 min at 37°C. Reactions were terminated by rapidly washing the cells twice with cold KRBB. Cells were then lysed in 0.1 N NaOH with SDS 0.1%, and radioactivity was determined by liquid scintillation counting and normalized according to the total protein content. Non-specific uptake was determined in the presence of 20 μM cytochalasin B.

The mice's skeletal muscle was quickly dissected after killing the mice. Before the experiment, mice have fasted for 12 h. Do not disturb the mice and keep them in a resting state. The muscles were incubated in KRBB in the presence or absence of insulin for 30 min at 37°C, uptake of 10 μM [³H]2-deoxyglucose was measured for 15 min at 37°C, as described above.

Statistical Analysis

All statistical calculations were carried out using Graphpad Prism 6. Data are expressed as average \pm SEM of at least

three independent experiments. The statistical significance was determined using a *t*-test when comparing two groups and ANOVA when comparing multiple groups. A value of $P < 0.05$ was considered statistically significant.

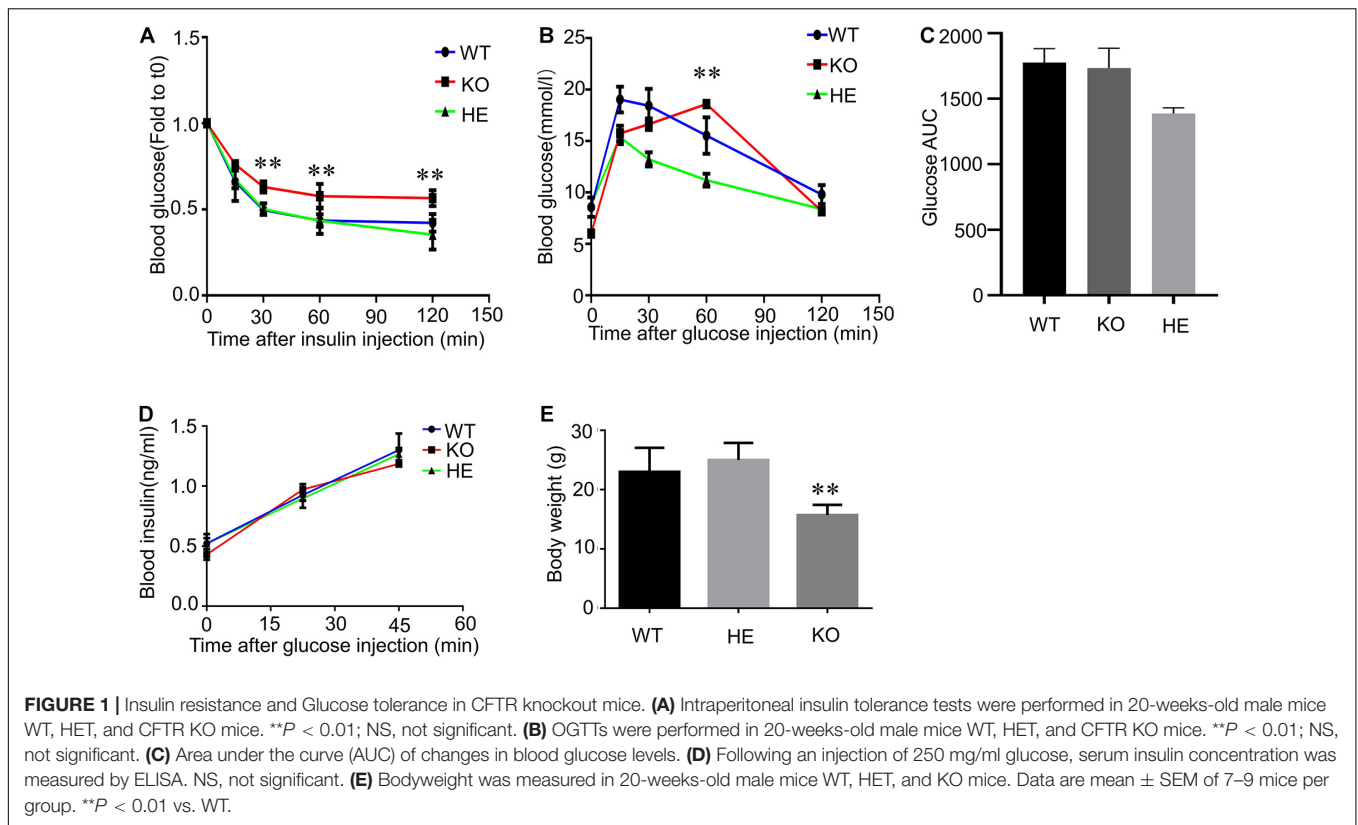
RESULTS

CFTR Dysfunction Affects Mice's Glucose Homeostasis and Body Weight

To investigate the connection between CFTR and glucose homeostasis, we performed insulin tolerance tests and glucose tolerance tests in 20-weeks-old male WT, heterozygous(HET), and CFTR KO mice (Figures 1A,B). During intraperitoneal insulin tolerance tests, the decrease in blood glucose was less marked in CFTR^{-/-} mice than that of WT and HET mice following 10 mg/ml insulin injection (Figure 1A), suggesting insulin resistance. Moreover, the blood glucose level in CFTR^{-/-} mice was also much higher than that of WT and HET mice 2 h after insulin injection (Figure 1A). It took CFTR^{-/-} mice 60 min to reach the blood glucose summit in response to glucose tolerance tests, while it only took 15 min in WT and HET mice(Figure 1B). However, the glucose AUC was similar among WT and KO groups but slightly lower in the HE group (Figure 1C), indicating that the delay in attaining peak glucose levels during the OGTT suggests delayed glucose absorption. Reduced first, second, and amplifying phase secretion in CF islets have been reported by numerous researchers (Sun et al., 2017; Kelly et al., 2019); however, it was found that serum insulin level of CFTR^{-/-} mice showed no significant difference than WT and HET mice by ELISA (Figure 1D), indicating that the amount of insulin secretion by CFTR^{-/-} mice was normal before CFRD. Notably, maintained in a stable environment with standard chow and water, CFTR^{-/-} mice's average body weight was much lower than WT and HET mice (Figure 1E). We suspected that the lower body weight of CFTR^{-/-} mice resulted from inadequate glucose intake, but other possibilities include CFTR-related glucosuria or increased metabolic rate, requiring further confirmation. In conclusion, CFTR dysfunction affects mice's glucose homeostasis and body weight.

CFTR Is Essential to Insulin-Induced GLUT4 Cell Membrane Translocation and Glucose Uptake

When GLUT4 glucose transporters are present in cytoplasmic vesicles, they are useless for transporting glucose. The binding of insulin to receptors on such cells leads rapidly to the fusion of those vesicles with the plasma membrane and the insertion of the glucose transporters, thereby giving the cell the ability to take up glucose efficiently. As a result, glucose uptake depends on insulin-stimulated membrane translocation of the GLUT4. To investigate the relation between CFTR and GLUT4, GLUT4 cell membrane expression was measured by western blot in mice skeletal muscle fibers and C2C12 myotubes. The Flexor Digitorum Brevis (FDB) muscle fibers



total membrane protein were immediately isolated from WT, HET, and CFTR KO mice 30 min after insulin injection stimulation. Evident membrane translocation of GLUT4 was found in WT and HET mice muscle fibers with insulin stimulation (Figure 2A). However, there was no membrane expression of GLUT4 in CFTR^{-/-} mice with or without insulin stimulation (Figure 2A). Consistent with this, the insulin-stimulated GLUT4 cell surface translocation was also blocked by a specific CFTR inhibitor [CFTR (inh)-172] in differentiated C2C12 myotubes (Figure 2B). To directly show the translocation of GLUT4, C2C12 myoblasts and myotubes were transiently transfected with myc-GLUT4-EGFP fusion plasmids. Myc epitope was inserted in the first exofacial loop of GLUT4 N terminus and presented outside of the cell membrane, which could be detected by the antibody without perforation. C2C12 Cells were then fixed (without perforation) and labeled with an anti-Myc antibody followed by Texas Red secondary to track the membrane translocation of GLUT4 (red). We found that GLUT4 was expressed in the cytoplasm (Figures 2C,D, Control), and insulin could induce translocation of GLUT4 to cell membranes both in C2C12 myoblasts and myotubes (Figures 2C,D). However, this process could be blocked by CFTR (inh)-172 (Figures 2C,D). The effects of CFTR (inh)-172 on insulin-stimulated glucose uptake activity were also tested in differentiated C2C12 myotubes and freshly isolated Flexor Digitorum Brevis (FDB) muscle fibers cells. We found that CFTR (inh)-172 significantly decreased 2-DG uptake in insulin-stimulated C2C12 myotubes (Figure 2E) and

freshly isolated Flexor Digitorum Brevis (FDB) muscle fibers cells (Figure 2F).

Some tissues, such as the liver, do not require insulin for efficient uptake of glucose; this is because these cells do not use GLUT4 to import glucose, but rather, GLUT1 and GLUT2 are not insulin-dependent. We wondered if similar results could be observed in liver cells. HEPG2 cells were transiently transfected with myc-GLUT4-EGFP fusion plasmids. HEPG2 Cells were then fixed (without perforation) and labeled with an anti-Myc antibody followed by Texas Red secondary to track the membrane translocation of GLUT4 (red). It was found that CFTR (inh)-172 could also block insulin-induced GLUT4 membrane translocation in HEPG2 (Supplementary Figure S1A) and Hela cells (Supplementary Figure S1B). To further confirm CFTR's role on GLUT4 translocation, as Hela cells endogenously express CFTR (Billet et al., 2017), we knocked out CFTR in Hela cells by CRISPR/Case9 (Supplementary Figure S1C). It was found that insulin could no longer induce GLUT4 translocation to the cell membrane in CFTR^{-/-} cells (Supplementary Figure S1D). Taken together, these results suggested that CFTR was required in insulin-induced membrane translocation of GLUT4.

PI(4,5)P₂ Rescues CFTR Related Defective GLUT4 Translocation

Several studies indicated that Rab8A and Rab13 could also contribute to the translocation of GLUT4 (Sano et al., 2007;

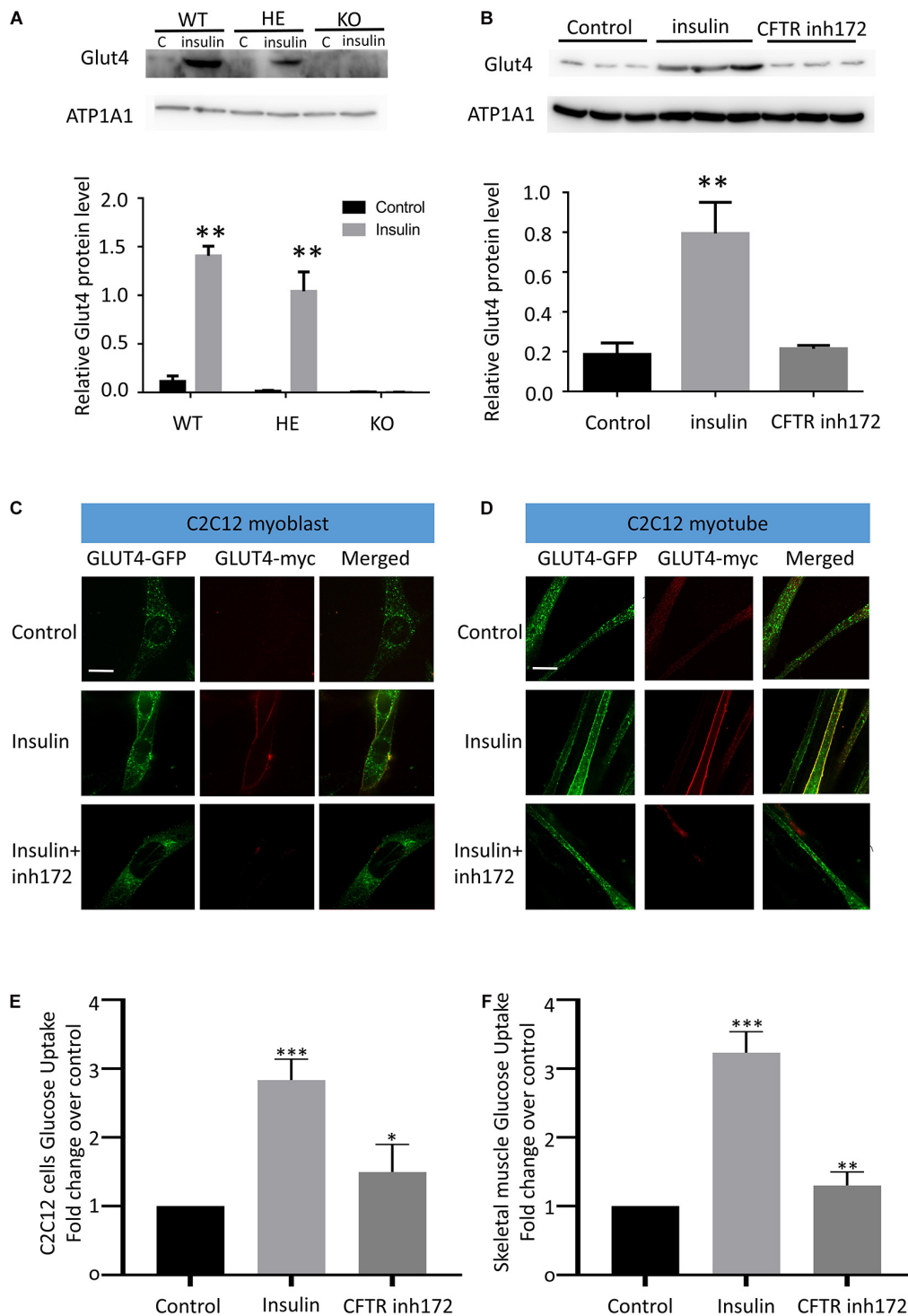


FIGURE 2 | CFTR regulates GLUT4 membrane translocation and glucose homeostasis. **(A)** The membrane localization of GLUT4 in CFTR KO mice FDB muscle after injection of 10 mg/ml insulin was measured by Western blot. Images are representative of triplicate experiments with similar results. $**P < 0.01$ compared with control ($n = 3$). **(B)** The membrane expression of GLUT4 in C2C12 myotubes was measured by Western blot. $**P < 0.01$ compared with control ($n = 3$). **(C)** myc-GLUT4- GFP was transfected into C2C12 myoblasts by adenoviruses. The cells were stimulated with insulin (100 nM) for 30 min. GLUT4 translocation to the plasma membrane was detected by confocal microscopy. Glut4-GFP(green), Glut4-myc(red). Scale bar, 10 μ m. **(D)** GLUT4 translocation to the plasma membrane of differentiated C2C12 myotubes was detected by confocal microscopy. Glut4-GFP(green), Glut4-myc(red). Scale bar, 10 μ m. **(E)** The glucose uptake assay of C2C12 cells. Data are mean \pm SD values for two independent assays performed in triplicate. $***P < 0.001$, $*P < 0.05$. **(F)** The glucose uptake assay of Flexor Digitorum Brevis muscle fibers cells. Data are mean \pm SD values for two independent assays performed in triplicate. $***P < 0.001$, $**P < 0.01$.

Randhawa et al., 2008; Sun et al., 2010). Rab8A or Rab13 was co-transfected with myc-GLUT4-EGFP in HeLa cells; we found that Rab8A or Rab13 could not rescue GLUT4 membrane translocation under CFTR (inh)-172 treatment (**Figure 3A**), suggesting Rab8A or Rab13 is not involved in this process. PI(4,5)P₂ mediated insulin-induced actin remodeling is another crucial component in GLUT4 translocation (Kanzaki and Pessin, 2001; Kanzaki et al., 2004; Leto and Saltiel, 2012; Lim et al., 2015). To identify the role of PI(4,5)P₂ in the process of GLUT4 translocation, C2C12 myotubes were transiently transfected with myc-GLUT4-EGFP fusion plasmids. Insulin-induced GLUT4 translocation in C2C12 myotubes was blocked after endogenous PI(4,5)P₂ was depleted by application of both PI₃K inhibitor (wortmanin) and PLC agonist (**Figure 3B**). The defective GLUT4 membrane translocation induced by CFTR (inh)-172 could also be rescued by exogenous PI(4,5)P₂ (**Figure 3B**). As CFTR is a chloride channel, we suspected whether the chloride channel property of CFTR was also involved with GLUT4 translocation. By replacing the chloride with arginine in bath solution, we found that the translocation of GLUT4 was still blocked by CFTR (inh)-172 (**Supplementary Figure S2A**). In conclusion, these results indicated that CFTR regulated GLUT4 membrane translocation by PI(4,5)P₂.

CFTR Affects PI(4,5)P₂ Concentration via PIP5K1A

To confirm the speculation that inhibition of CFTR might affect cellular PI(4,5)P₂ concentration. PI(4,5)P₂ concentration was detected by dot-blot analysis. C2C12 myotubes were treated with CFTR (inh)-172 for 24 h, and we found that CFTR (inh)-172 could significantly down-regulate PI(4,5)P₂ concentration (**Figure 4A**). We also measured the concentration of PI(4,5)P₂ in FDB muscle fibers isolated from CFTR WT, HET, and KO mice. The concentration of PI(4,5)P₂ in CFTR^{-/-} mice FDB muscle fibers was significantly lower than WT and HET mice (**Figure 4B**). PIP5K1A induces the phosphorylation of phosphatidylinositol 4-phosphate (PtdIns4P) to generation PI(4,5)P₂. Studies indicated that that PI(4,5)P₂ generation by PIP5K1A was associated with GLUT4 vesicle recycling (Kanzaki et al., 2004) and autophagic lysosome reformation (Rong et al., 2012). To understand how CFTR regulates PI(4,5)P₂ expression, the PIP5K1A expression level was measured. We found that CFTR (inh)-172 induced a reduction of PIP5K1A expression in C2C12 myotubes (**Figure 4C**). The expression of PIP5K1A was also significantly decreased in CFTR^{-/-} FDB muscle fibers (**Figure 4D**). These results suggest that the effect of CFTR on PI(4,5)P₂ concentration is via the regulation of PIP5K1A expression.

DISCUSSION

In this study, we discovered a previously unrecognized regulation effect of CFTR to the GLUT4 cellular translocation, which provides a new perspective on the mechanism of CFRD. It was found that CFTR^{-/-} mice exhibited normal insulin secretion

but reduced insulin sensitivity and glucose tolerance. Insulin facilitates the entry of glucose into muscle through GLUT4. Meanwhile, Insulin-induced GLUT4 translocation to the cell membrane was also blocked in CFTR^{-/-} mice, suggesting glucose homeostasis alteration from defective intracellular GLUT4 transportation. Unexpectedly, PI(4,5)P₂ could rescue the effect of CFTR deficiency. Furthermore, it was found that CFTR deficiency leads to a significantly decreased expression of PIP5K1A, which reflected on PI(4,5)P₂ concentration. Taken together, we discovered a new signal pathway of CFTR/GLUT4, which helps explain the glucose homeostasis disorder in CF patients.

To explain CFRD, several studies have shown that CFTR played a vital role in the regulation of insulin secretion and β cell function (Tofe et al., 2005; Noronha et al., 2011; Konrad et al., 2013; Edlund et al., 2014; Guo et al., 2014). Some studies suggested that insulin resistance was not an essential determinant in CFRD compared with insulin secretion (Cucinotta et al., 1994; Yung et al., 2002). Other studies proved that insulin resistance was highly involved in CFRD, and impaired insulin responses were also reported in CF patients (Hardin et al., 1997; Hardin et al., 2001; Fontes et al., 2015). Our data show that insulin secretion is normal in CFTR^{-/-} mice (**Figure 1C**); the problem is insulin sensitivity (**Figure 1A**) and glucose absorption (**Figure 1B**). Consistent with previous studies (Paroni et al., 2013; Fontes et al., 2015), we also found that the body weight was lower in CFTR^{-/-} mice than WT and HET controls (**Figure 1D**). Gradual pancreatic destruction in cystic fibrosis causes progressive insulin deficiency. Our results show that in the early stage of CFRD, insulin secretion is expected, so insulin deficiency may not be due to the destruction of pancreatic islets, leading to insufficient insulin secretion, but because CFTR dysfunction affects the insulin-responsive tissues, which manifests as insulin deficiency. In summary, we believe that CFTR affects the pancreas functionality and the insulin-responsive tissues; both contribute to cystic fibrosis-related diabetes (CFRD).

How does CFTR knock out affected insulin sensitivity and glucose tolerance? By binding and activating its cell-surface receptor, insulin triggers signaling cascades that regulate many cellular processes, including stimulating the muscle to dispose of dietary glucose (Richter and Hargreaves, 2013). Insulin stimulation of glucose uptake into muscle depends on the mobilization of GLUT4 to the plasma membrane (Lauritzen et al., 2010; Klip et al., 2014). As Akt2 is an essential kinase in insulin resistance (Cho et al., 2001; McCurdy and Cartee, 2005), we investigate the phosphorylation of Akt2 in CFTR^{-/-} mice. Surprisingly, CFTR deficiency showed no connection with phosphorylation of Akt2 and its downstream protein AS160 (data not shown). Furthermore, other regulators, such as Rab8A and Rab13, also showed no significant impact on CFTR deficiency-induced GLUT4 translocation (**Figure 3A**). As a result, we focused on the "railway" of protein trafficking in the cell, and studies showed that actin remodeling also played an essential regulatory role in insulin-induced GLUT4 translocation (Kanzaki and Pessin, 2001; Tong et al., 2001). The role of actin dynamic

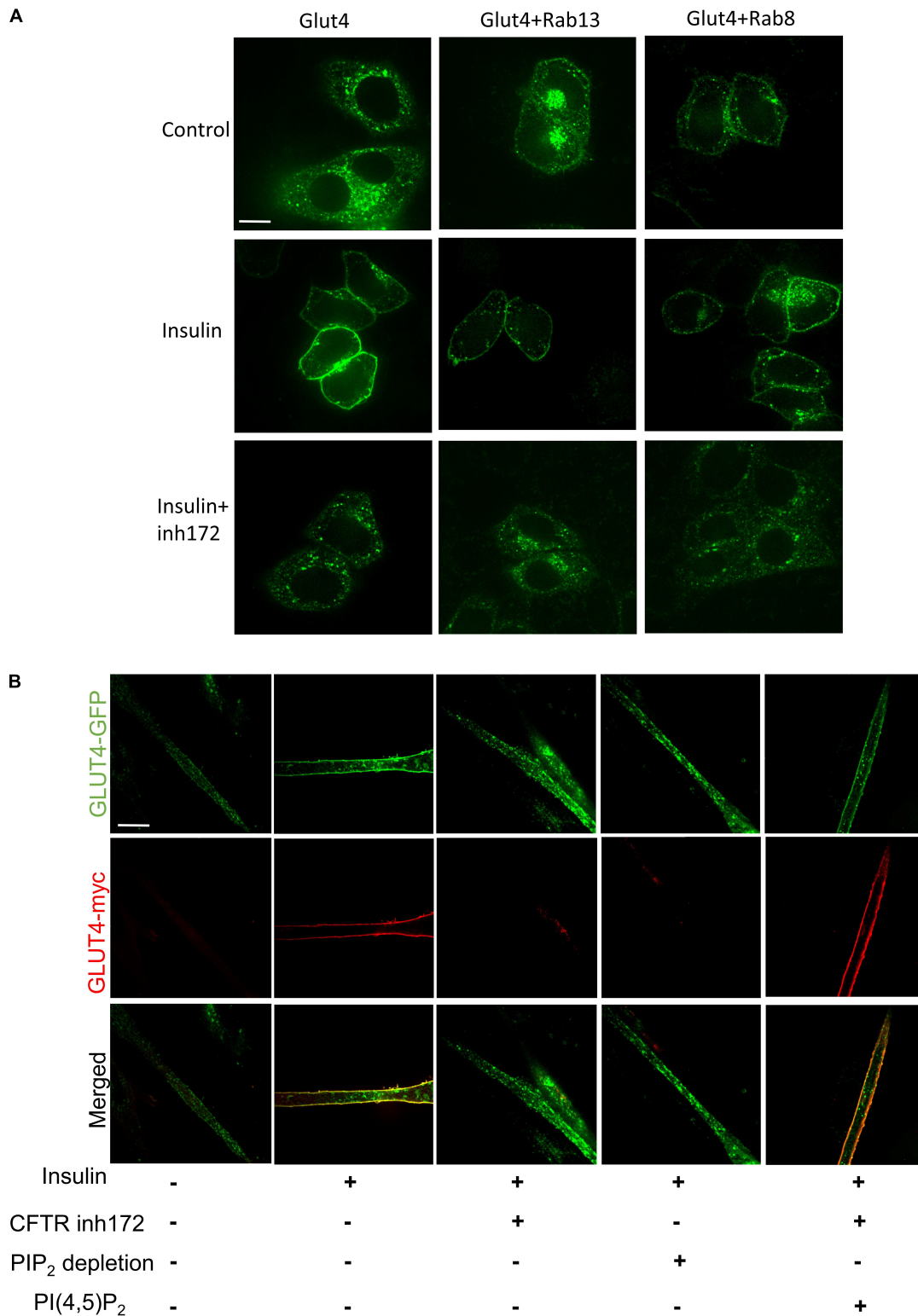


FIGURE 3 | PI(4,5)P₂ rescues CFTR related defective GLUT4 translocation. **(A)** The membrane localization of GLUT4 in HeLa cells after overexpression of Rab8 and Rab13 was detected by confocal microscopy. Glut4 (green), Scale bar, 10 μm. **(B)** C2C12 myotubes were treated with insulin, CFTR inh172, PIP₂ depletion agents, or PI(4,5)P₂. PIP₂ depletion agents are consist of P₁₃K inhibitor (1 μM wortmanin) and PLC agonist (50 μM m-3M3FBS). GLUT4 translocation to the plasma membrane was detected by confocal microscopy. Glut4-GFP (green), Glut4-myc (red). Scale bar, 10 μm.

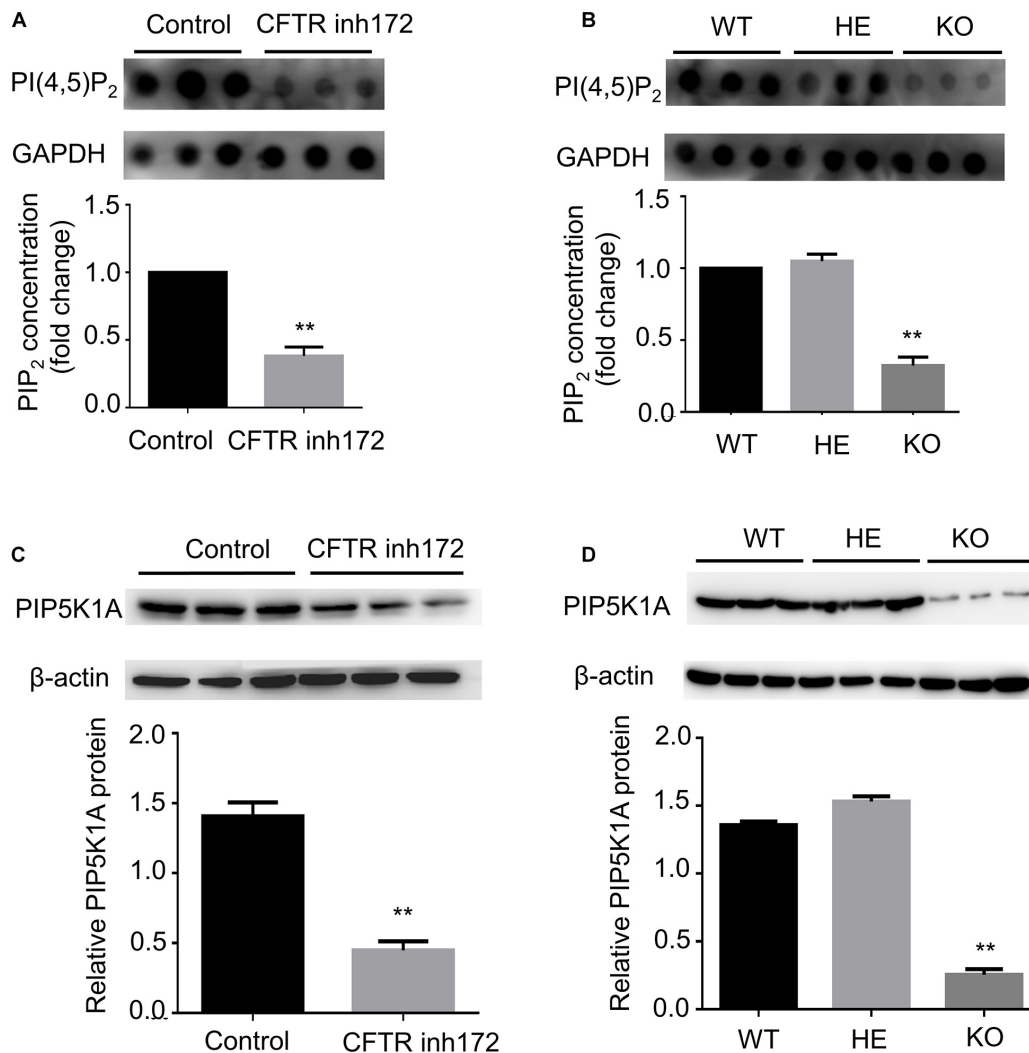


FIGURE 4 | CFTR regulates PIP5KA expression and PI(4,5)P₂ concentration. **(A)** C2C12 myotubes were treated with CFTR inh172, and the concentration of PI(4,5)P₂ was measured by dot blot. ***P* < 0.01 compared with control (*n* = 3). **(B)** The concentration of PI(4,5)P₂ in mice FDB muscle was measured by dot blot. ***P* < 0.01 compared with control (*n* = 3). **(C)** C2C12 myotubes were treated with CFTR inh172, and the protein level of PIP5KA was measured by western blot. ***P* < 0.01 compared with control (*n* = 3). **(D)** The protein level of PIP5KA in mice FDB muscle was measured by western blot. ***P* < 0.01 compared with control (*n* = 3).

regulated by PI(4,5)P₂ in GLUT4 translocation has been proved by recent studies (Kanzaki and Pessin, 2001; Kanzaki et al., 2004; Leto and Saltiel, 2012; Lim et al., 2015). Our data show that the depletion of PI(4,5)P₂ blocks GLUT4 trafficking to the cell membrane, and exogenous PI(4,5)P₂ can rescue the effect of CFTR deficiency. Thus, we conclude that CFTR in GLUT4 translocation regulation is mediated by PI(4,5)P₂. In addition to insulin-stimulation, the translocation of GLUT4 to the plasma membrane is also affected by skeletal muscle contraction. Whether CFTR has a role in skeletal muscle contraction needs further clarification.

As CFTR is an ion channel, which makes no sense in catalyzing PI(4,5)P₂ generation. We proved that the chloride channel property of CFTR was not involved with GLUT4 translocation; only the protein itself is involved in translocation. Therefore,

we speculated that CFTR allosteric affects some kinase proteins in the regulation of PI(4,5)P₂ generation. The differential gene expression induced by CFTR deficiency has been reported by several studies (Ichikawa et al., 2000; Ogilvie et al., 2011; Chen et al., 2012). We suspected that inhibition or knockdown of CFTR might lead to decreased PIP5K1A expression, which regulates PI(4,5)P₂ generation. We found that the expression of PIP5K1A in CFTR^{-/-} mice and CFTR (inh)-172 treated C2C12 was significantly reduced, causing lower PI(4,5)P₂ concentration. In conclusion, PIP5K1A is one of the regulators between CFTR and PI(4,5)P₂, but further investigation is needed to assess how CFTR deficiency regulates PIP5K1A expression.

In summary, our results suggest a new mechanism of glucose homeostasis disorder in CF patients. These findings identify the role of GLUT4 translocation in CFTR related glucose

homeostasis disorder in CF patients, which provides a new potential treatment strategy.

DATA AVAILABILITY STATEMENT

The original contributions presented in the study are included in the article/**Supplementary Material**, further inquiries can be directed to the corresponding author/s.

ETHICS STATEMENT

The animal study was reviewed and approved by the University Ethics Committee, Institute of Molecular Medicine, Peking University.

AUTHOR CONTRIBUTIONS

YG and LW conceived and coordinated the study. JG and LW conducted molecular experiments and wrote the manuscript. WZ and JG performed the imaging-related experiments. All authors

made critical contributions to data analysis, interpretation, discussion, and manuscript preparation and approved the final version.

FUNDING

This work was supported by the National Basic Research Program of China (973 Program) (2013CB531206 and 2012CB517803) and the National Natural Science Foundation of China (81170236 and 31127001).

SUPPLEMENTARY MATERIAL

The Supplementary Material for this article can be found online at: <https://www.frontiersin.org/articles/10.3389/fcell.2021.630654/full#supplementary-material>

Supplementary Figure 1 | Insulin-induced GLUT4 translocation in HEPG2 and HeLa cells.

Supplementary Figure 2 | Chloride channel property of CFTR and insulin-induced GLUT4 translocation.

REFERENCES

- Billet, A., Froux, L., Hanrahan, J. W., and Becq, F. (2017). Development of automated patch clamp technique to investigate cfr chloride channel function. *Front. Pharmacol.* 8:195. doi: 10.3389/fphar.2017.00195
- Bouche, C., Serdy, S., Kahn, C. R., and Goldfine, A. B. (2004). The cellular fate of glucose and its relevance in type 2 diabetes. *Endocr. Rev.* 25, 807–830. doi: 10.1210/er.2003-0026
- Boudreau, V., Coriati, A., Hammana, I., Ziai, S., Desjardins, K., Berthiaume, Y., et al. (2016). Variation of glucose tolerance in adult patients with cystic fibrosis: what is the potential contribution of insulin sensitivity? *J. Cystic Fibr.* 15, 839–845. doi: 10.1016/j.jcf.2016.04.004
- Chen, J., Fok, K. L., Chen, H., Zhang, X. H., Xu, W. M., and Chan, H. C. (2012). Cryptorchidism-induced CFTR down-regulation results in disruption of testicular tight junctions through up-regulation of NF-kappaB/COX-2/PGE2. *Hum. Reprod.* 27, 2585–2597. doi: 10.1093/humrep/des254
- Cho, H., Mu, J., Kim, J. K., Thorvaldsen, J. L., Chu, Q., Crenshaw, E. B. III, et al. (2001). Insulin resistance and a diabetes mellitus-like syndrome in mice lacking the protein kinase Akt2 (PKB beta). *Science* 292, 1728–1731. doi: 10.1126/science.292.5522.1728
- Costa, M., Potvin, S., Hammana, I., Malet, A., Berthiaume, Y., Jeanneret, A., et al. (2007). Increased glucose excursion in cystic fibrosis and its association with a worse clinical status. *J. Cystic Fibr.* 6, 376–383. doi: 10.1016/j.jcf.2007.02.005
- Cucinotta, D., De Luca, F., Gigante, A., Arrigo, T., Di Benedetto, A., Tedeschi, A., et al. (1994). No changes of insulin sensitivity in cystic fibrosis patients with different degrees of glucose tolerance: an epidemiological and longitudinal study. *Eur. J. Endocrinol.* 130, 253–258. doi: 10.1530/eje.0.1300253
- Edlund, A., Esguerra, J. L., Wendt, A., Flodstrom-Tullberg, M., and Eliasson, L. (2014). CFTR and Anoctamin 1 (ANO1) contribute to cAMP amplified exocytosis and insulin secretion in human and murine pancreatic beta-cells. *BMC Med.* 12:87. doi: 10.1186/1741-7015-12-87
- Fontes, G., Ghislain, J., Benterki, I., Zarrouki, B., Trudel, D., Berthiaume, Y., et al. (2015). The DeltaF508 mutation in the cystic fibrosis transmembrane conductance regulator is associated with progressive insulin resistance and decreased functional beta-cell mass in mice. *Diabetes* 64, 4112–4122. doi: 10.2337/db14-0810
- Guo, J. H., Chen, H., Ruan, Y. C., Zhang, X. L., Zhang, X. H., Fok, K. L., et al. (2014). Glucose-induced electrical activities and insulin secretion in pancreatic islet beta-cells are modulated by CFTR. *Nat. Commun.* 5:4420.
- Hardin, D. S., LeBlanc, A., Lukenbough, S., and Seilheimer, D. K. (1997). Insulin resistance is associated with decreased clinical status in cystic fibrosis. *J. Pediatr.* 130, 948–956. doi: 10.1016/s0022-3476(97)70282-8
- Hardin, D. S., Leblanc, A., Marshall, G., and Seilheimer, D. K. (2001). Mechanisms of insulin resistance in cystic fibrosis. *Am. J. Physiol. Endocrinol. Metab.* 281, E1022–E1028.
- Holl, R. W., Heinze, E., Wolf, A., Rank, M., and Teller, W. M. (1995). Reduced pancreatic insulin release and reduced peripheral insulin sensitivity contribute to hyperglycaemia in cystic fibrosis. *Eur. J. Pediatr.* 154, 356–361. doi: 10.1007/s004310050303
- Iannucci, A., Mukai, K., Johnson, D., and Burke, B. (1984). Endocrine pancreas in cystic fibrosis: an immunohistochemical study. *Hum. Pathol.* 15, 278–284. doi: 10.1016/s0046-8177(84)80191-4
- Ichikawa, J. K., Norris, A., Bangera, M. G., Geiss, G. K., van 't Wout, A. B., Bumgarner, R. E., et al. (2000). Interaction of *Pseudomonas aeruginosa* with epithelial cells: identification of differentially regulated genes by expression microarray analysis of human cDNAs. *Proc. Natl. Acad. Sci. U.S.A.* 97, 9659–9664. doi: 10.1073/pnas.160140297
- Kanzaki, M., Furukawa, M., Raab, W., and Pessin, J. E. (2004). Phosphatidylinositol 4,5-bisphosphate regulates adipocyte actin dynamics and GLUT4 vesicle recycling. *J. Biol. Chem.* 279, 30622–30633. doi: 10.1074/jbc.m401443200
- Kanzaki, M., and Pessin, J. E. (2001). Insulin-stimulated GLUT4 translocation in adipocytes is dependent upon cortical actin remodeling. *J. Biol. Chem.* 276, 42436–42444. doi: 10.1074/jbc.m108297200
- Kelly, A., De Leon, D. D., Sheikh, S., Camburn, D., Kubrak, C., Peleckis, A. J., et al. (2019). Islet hormone and incretin secretion in cystic fibrosis after four months of ivacaftor therapy. *Am. J. Respir. Crit. Care Med.* 199, 342–351. doi: 10.1164/rccm.201806-1018oc
- Klip, A., Sun, Y., Chiu, T. T., and Foley, K. P. (2014). Signal transduction meets vesicle traffic: the software and hardware of GLUT4 translocation. *Am. J. Physiol. Cell Physiol.* 306, C879–C886.
- Konrad, K., Scheuing, N., Badenhop, K., Borkenstein, M. H., Gohlke, B., Schoff, C., et al. (2013). Cystic fibrosis-related diabetes compared with type 1 and type 2 diabetes in adults. *Diabetes* 29, 568–575.
- Lauritzen, H. P., Galbo, H., Toyoda, T., and Goodyear, L. J. (2010). Kinetics of contraction-induced GLUT4 translocation in skeletal muscle fibers from living mice. *Diabetes* 59, 2134–2144. doi: 10.2337/db10-0233
- Leto, D., and Saltiel, A. R. (2012). Regulation of glucose transport by insulin: traffic control of GLUT4. *Nat. Rev. Mol. Cell Biol.* 13, 383–396. doi: 10.1038/nrm3351

- Lim, C. Y., Bi, X., Wu, D., Kim, J. B., Gunning, P. W., Hong, W., et al. (2015). Tropomodulin3 is a novel Akt2 effector regulating insulin-stimulated GLUT4 exocytosis through cortical actin remodeling. *Nat. Commun.* 6:5951. doi: 10.1038/ncom08595
- Lohr, M., Goertchen, P., Nizze, H., Gould, N. S., Gould, V. E., Oberholzer, M., et al. (1989). Cystic fibrosis associated islet changes may provide a basis for diabetes. An immunocytochemical and morphometrical study. *Virchows Arch. A Pathol. Anat. Histopathol.* 414, 179–185. doi: 10.1007/bf00718598
- Manderson Koivula, F. N., McClenaghan, N. H., Harper, A. G. S., and Kelly, C. (2017). Correction to: islet-intrinsic effects of CFTR mutation. *Diabetologia* 60, 2544. doi: 10.1007/s00125-017-4474-1
- Marshall, B. C., Butler, S. M., Stoddard, M., Moran, A. M., Liou, T. G., and Morgan, W. J. (2005). Epidemiology of cystic fibrosis-related diabetes. *J. Pediatr.* 146, 681–687. doi: 10.1016/j.peds.2005.05.011
- McCurdy, C. E., and Cartee, G. D. (2005). Akt2 is essential for the full effect of calorie restriction on insulin-stimulated glucose uptake in skeletal muscle. *Diabetes* 54, 1349–1356. doi: 10.2337/diabetes.54.5.1349
- Mohan, K., Miller, H., Dyce, P., Grainger, R., Hughes, R., Vora, J., et al. (2009). Mechanisms of glucose intolerance in cystic fibrosis. *Diabet. Med.* 26, 582–588. doi: 10.1111/j.1464-5491.2009.02738.x
- Moran, A., Becker, D., Casella, S. J., Gottlieb, P. A., Kirkman, M. S., Marshall, B. C., et al. (2010). Committee CFRD consensus conference committee. Epidemiology, pathophysiology, and prognostic implications of cystic fibrosis-related diabetes: a technical review. *Diabet. Care* 33, 2677–2683. doi: 10.2337/dc10-1279
- Moran, A., Dunitz, J., Nathan, B., Saeed, A., Holme, B., and Thomas, W. (2009). Cystic fibrosis-related diabetes: current trends in prevalence, incidence, and mortality. *Diabet. Care* 32, 1626–1631. doi: 10.2337/dc09-0586
- Moran, A., Pyzdrowski, K. L., Weinreb, J., Kahn, B. B., Smith, S. A., Adams, K. S., et al. (1994). Insulin sensitivity in cystic fibrosis. *Diabetes* 43, 1020–1026. doi: 10.2337/diabetes.43.7.1020
- Noronha, R. M., Calliari, L. E., Damaceno, N., Muramatu, L. H., and Monte, O. (2011). Update on diagnosis and monitoring of cystic fibrosis-related diabetes mellitus (CFRD). *Arq. Bras. Endocrinol. Metabol.* 55, 613–621. doi: 10.1590/s0004-27302011000800016
- Ogilvie, V., Passmore, M., Hyndman, L., Jones, L., Stevenson, B., Wilson, A., et al. (2011). Differential global gene expression in cystic fibrosis nasal and bronchial epithelium. *Genomics* 98, 327–336. doi: 10.1016/j.ygeno.2011.06.008
- Park, K. H., Weisleder, N., Zhou, J., Gumpfer, K., Zhou, X., Duann, P., et al. (2014). Assessment of calcium sparks in intact skeletal muscle fibers. *J. Vis. Exp.* 84:e50898. doi: 10.3791/51137
- Paroni, M., Moalli, F., Nebuloni, M., Pasqualini, F., Bonfield, T., Nonis, A., et al. (2013). Response of CFTR-deficient mice to long-term chronic *Pseudomonas aeruginosa* infection and PTX3 therapy. *J. Infect. Dis.* 208, 130–138. doi: 10.1093/infdis/jis636
- Randhawa, V. K., Ishikura, S., Talior-Volodarsky, I., Cheng, A. W., Patel, N., Hartwig, J. H., et al. (2008). GLUT4 vesicle recruitment and fusion are differentially regulated by Rac, AS160, and Rab8A in muscle cells. *J. Biol. Chem.* 283, 27208–27219. doi: 10.1074/jbc.m804282200
- Richter, E. A., and Hargreaves, M. (2013). Exercise, GLUT4, and skeletal muscle glucose uptake. *Physiol. Rev.* 93, 993–1017. doi: 10.1152/physrev.00038.2012
- Rong, Y., Liu, M., Ma, L., Du, W., Zhang, H., Tian, Y., et al. (2012). Clathrin and phosphatidylinositol-4,5-bisphosphate regulate autophagic lysosome reformation. *Nat. Cell Biol.* 14, 924–934. doi: 10.1038/ncb2557
- Sano, H., Eguez, L., Teruel, M. N., Fukuda, M., Chuang, T. D., Chavez, J. A., et al. (2007). Rab10, a target of the AS160 Rab GAP, is required for insulin-stimulated translocation of GLUT4 to the adipocyte plasma membrane. *Cell Metab.* 5, 293–303. doi: 10.1016/j.cmet.2007.03.001
- Stalvey, M. S., Muller, C., Schatz, D. A., Wasserfall, C. H., Campbell-Thompson, M. L., Theriaque, D. W., et al. (2006). Cystic fibrosis transmembrane conductance regulator deficiency exacerbates islet cell dysfunction after beta-cell injury. *Diabetes* 55, 1939–1945. doi: 10.2337/db05-1647
- Sun, X., Yi, Y., Xie, W., Liang, B., Winter, M. C., He, N., et al. (2017). CFTR influences beta cell function and insulin secretion through non-cell autonomous exocrine-derived factors. *Endocrinology* 158, 3325–3338. doi: 10.1210/en.2017-00187
- Sun, Y., Bilan, P. J., Liu, Z., and Klip, A. (2010). Rab8A and Rab13 are activated by insulin and regulate GLUT4 translocation in muscle cells. *Proc. Natl. Acad. Sci. U.S.A.* 107, 19909–19914. doi: 10.1073/pnas.1009523107
- Tofe, S., Moreno, J. C., Maiz, L., Alonso, M., Escobar, H., and Barrio, R. (2005). Insulin-secretion abnormalities and clinical deterioration related to impaired glucose tolerance in cystic fibrosis. *Eur. J. Endocrinol.* 152, 241–247. doi: 10.1530/eje.1.01836
- Tong, P., Khayat, Z. A., Huang, C., Patel, N., Ueyama, A., and Klip, A. (2001). Insulin-induced cortical actin remodeling promotes GLUT4 insertion at muscle cell membrane ruffles. *J. Clin. Invest.* 108, 371–381. doi: 10.1172/jci200112348
- Wooldridge, J. L., Szczesniak, R. D., Fenchel, M. C., and Elder, D. A. (2015). Insulin secretion abnormalities in exocrine pancreatic sufficient cystic fibrosis patients. *J. Cystic Fibr.* 14, 792–797. doi: 10.1016/j.jcf.2015.02.009
- Yung, B., Noormohamed, F. H., Kemp, M., Hooper, J., Lant, A. F., and Hodson, M. E. (2002). Cystic fibrosis-related diabetes: the role of peripheral insulin resistance and beta-cell dysfunction. *Diabet. Med.* 19, 221–226. doi: 10.1046/j.1464-5491.2002.00666.x

Conflict of Interest: The authors declare that the research was conducted in the absence of any commercial or financial relationships that could be construed as a potential conflict of interest.

Copyright © 2021 Gu, Zhang, Wu and Gu. This is an open-access article distributed under the terms of the Creative Commons Attribution License (CC BY). The use, distribution or reproduction in other forums is permitted, provided the original author(s) and the copyright owner(s) are credited and that the original publication in this journal is cited, in accordance with accepted academic practice. No use, distribution or reproduction is permitted which does not comply with these terms.



Functional Expression of the Human Glucose Transporters GLUT2 and GLUT3 in Yeast Offers Novel Screening Systems for GLUT-Targeting Drugs

Sina Schmidl¹, Sebastian A. Tamayo Rojas¹, Cristina V. Iancu², Jun-Yong Choe^{2,3*} and Mislav Oreb^{1*}

OPEN ACCESS

Edited by:

Cesare Indiveri,
University of Calabria, Italy

Reviewed by:

Sergi Puig,
Institute of Agrochemistry and Food
Technology (IATA), Spain
Mariafrancesca Scalise,
University of Calabria, Italy

*Correspondence:

Mislav Oreb
m.oreb@bio.uni-frankfurt.de
Jun-Yong Choe
Choej18@ecu.edu

Specialty section:

This article was submitted to
Cellular Biochemistry,
a section of the journal
Frontiers in Molecular Biosciences

Received: 24 August 2020

Accepted: 23 December 2020

Published: 18 February 2021

Citation:

Schmidl S, Tamayo Rojas SA,
Iancu CV, Choe J-Y and Oreb M (2021)
Functional Expression of the Human
Glucose Transporters GLUT2 and
GLUT3 in Yeast Offers Novel
Screening Systems for GLUT-
Targeting Drugs.
Front. Mol. Biosci. 7:598419.
doi: 10.3389/fmolb.2020.598419

¹Institute of Molecular Biosciences, Faculty of Biological Sciences, Goethe University Frankfurt, Frankfurt am Main, Germany, ²Department of Chemistry, East Carolina Diabetes and Obesity Institute, East Carolina University, Greenville, NC, United States, ³Department of Biochemistry and Molecular Biology, The Chicago Medical School, Rosalind Franklin University of Medicine and Science, North Chicago, IL, United States

Human GLUT2 and GLUT3, members of the GLUT/SLC2 gene family, facilitate glucose transport in specific tissues. Their malfunction or misregulation is associated with serious diseases, including diabetes, metabolic syndrome, and cancer. Despite being promising drug targets, GLUTs have only a few specific inhibitors. To identify and characterize potential GLUT2 and GLUT3 ligands, we developed a whole-cell system based on a yeast strain deficient in hexose uptake, whose growth defect on glucose can be rescued by the functional expression of human transporters. The simplicity of handling yeast cells makes this platform convenient for screening potential GLUT2 and GLUT3 inhibitors in a growth-based manner, amenable to high-throughput approaches. Moreover, our expression system is less laborious for detailed kinetic characterization of inhibitors than alternative methods such as the preparation of proteoliposomes or uptake assays in *Xenopus* oocytes. We show that functional expression of GLUT2 in yeast requires the deletion of the extended extracellular loop connecting transmembrane domains TM1 and TM2, which appears to negatively affect the trafficking of the transporter in the heterologous expression system. Furthermore, single amino acid substitutions at specific positions of the transporter sequence appear to positively affect the functionality of both GLUT2 and GLUT3 in yeast. We show that these variants are sensitive to known inhibitors phloretin and quercetin, demonstrating the potential of our expression systems to significantly accelerate the discovery of compounds that modulate the hexose transport activity of GLUT2 and GLUT3.

Keywords: GLUT2, GLUT3, Glucose transport inhibitor, drug screening system, hxt⁰ yeast strain

INTRODUCTION

Transport of hexoses across plasma membranes marks the first and rate-limiting step of energy metabolism in cells of all domains of life. In humans, 14 glucose transporter family members (GLUTs, SLC2 gene family), with differing tissue distributions, mediate the facilitative diffusion of sugar along a concentration gradient. Despite a high sequence similarity, GLUTs differ in substrate specificity and affinity (Mueckler and Thorens, 2013), matching the demands for complex, tissue-dependent hexose uptake. Abnormal expression, localization or function of GLUTs are related to the pathogenesis of several diseases including cancer (Barron et al., 2016), diabetes (Ohtsubo et al., 2005; Hajiaghaalipour et al., 2015), and other severe metabolic disorders (Santer et al., 1997; Brockmann, 2009), making these transporters important drug targets.

GLUT2 is the primary GLUT isoform found in the liver. It also mediates glucose transport in the kidney, intestine, pancreatic β -cells and the central nervous system (Fukumoto et al., 1988; Thorens, 2015). It exhibits a low affinity for glucose ($K_M = \sim 17$ mM (Uldry et al., 2002)) and even lower for fructose, galactose, and mannose ($K_M = \sim 76$, ~ 92 , and ~ 125 mM, respectively (Mueckler and Thorens, 2013)). For glucosamine, however, GLUT2 shows a very high substrate affinity ($K_M = \sim 0.8$ mM) (Uldry et al., 2002). Under normal physiological conditions, the glucose concentration in human blood is ~ 5.5 mM (Jung et al., 2013); the glucose uptake by GLUT2 would be inefficient, indicating that it is not the primary function of this transporter. More likely, glucose sensing (Ohtsubo et al., 2005) and/or signaling (Guillemain et al., 2000) are the main functions of GLUT2, consistent with its expression in tissues with high glucose fluxes. In murine pancreatic β -cells, GLUT2 mediates glucose stimulated insulin secretion, thereby regulating blood glucose levels. The absence of this function impairs glucose homeostasis leading to diabetes (Ohtsubo et al., 2005). Furthermore, GLUT2 may also be involved in mediating transcriptional glucose signaling (Guillemain et al., 2000). Loss of GLUT2 function causes the Fanconi Bickel Syndrome (Santer et al., 1997), a rare autosomal disease with various symptoms like hepatomegaly, tubular nephropathy, glucose and galactose intolerance, fasting hypoglycemia, rickets, and retarded growth (Santer et al., 2002).

In contrast to GLUT2, GLUT3 exhibits a high affinity for glucose ($K_M = 1.4$ mM (Colville et al., 1993)). Other substrates of GLUT3 are mannose, galactose, and xylose (Simpson et al., 2008). GLUT3 shares a high sequence identity (66%) with GLUT1 (Deng et al., 2015), and together they are predominantly responsible for glucose uptake in the brain - GLUT1 in the blood-brain barrier and GLUT3 in neurons (Simpson et al., 2007). Accordant with its high affinity for glucose, GLUT3 plays a pivotal role in the glucose uptake of cell types with a high demand for energy, such as sperm, circulating white blood cells, and preimplantation embryos (Simpson et al., 2007). Consistently, as tumor tissues have an increased need for carbon sources to sustain uncontrolled proliferation, GLUT3 is upregulated in many cancers, including gliomas, lung, laryngeal and bladder tumors (Ancey et al., 2018; Barron et al., 2016). In

general, high expression of GLUT3 (and GLUT1) is associated with severe pathogenesis and poor survival in most cancer tissues (Ancey et al., 2018). Recently, an association between diverse diseases and variations of copy numbers of the GLUT3 gene has been hypothesized (Ziegler et al., 2020). Hence, the discovery of activating or inhibiting drugs specific for GLUT2 or GLUT3 is highly desirable.

Both transporters GLUT2 and GLUT3 belong to the Class I GLUT family, therefore sharing certain structure similarities as, for example, the position of the glycosylation site in the extracellular loop between the transmembrane helices (TM) 1 and 2 (Joost and Thorens, 2009). For GLUT2, it has been proposed that its glycosylation is essential for proper anchoring of the transporter to the plasma membrane of β -cells and its stability in these cells (Ohtsubo et al., 2005). However, the loop itself differs in the two transporters, with GLUT2 exhibiting a significantly larger loop size than GLUT3. The role of the cytoplasmic and extracellular loops between transmembrane domains of GLUTs is still dramatically understudied and putatively underestimated. The C-terminal intracellular domain of GLUT2 has been implicated in the low glucose affinity of this transporter (Katagiri et al., 1992). Furthermore, it has been shown that conformational changes in facilitators like GLUTs, during the rocker switch mechanism, are the primary force for the translocation of sugar (Qureshi et al., 2020). Therefore, residues distant from the sugar-binding sites likely influence transport dynamics significantly, including the role of hydrophilic regions. Investigation of the extra-membrane domains will further elucidate the origins of the transporter's different properties.

The need for a convenient platform to investigate GLUTs has been recognized, and among different systems (Gould and Lienhard, 1989; Zamora-Leon et al., 1996; Kraft et al., 2015), the yeast cell-based investigation system has many benefits (Schmidl et al., 2018). The yeast *Saccharomyces cerevisiae* is a widely used GRAS organism and a model organism for diverse research applications. Cells are easily manipulated and maintained and exhibit a short generation time. By deleting all endogenous hexose transporter genes (*HXT1-17*, *GAL2*) and the genes of hexose transporting maltose transporters (*AGT1*, *MPH2*, *MPH3*) with the loxP-Cre recombinase system in a CEN.PK2-1C strain background (Entian and Kötter, 2007), a hexose transporter-deficient (*hxt*⁰) strain, incapable of growing on glucose or related monosaccharides, was constructed and named EBY.VW4000 (Wieczorke et al., 1999; Solis-Escalante et al., 2015). The strain is maintained on maltose, a disaccharide taken up by specialized maltose symporters (Chow et al., 1989), and cleaved inside the cell into two glucose molecules. The selective uptake of the respective monosaccharide by a heterologously expressed transporter can, therefore, be examined by simple growth tests or uptake assays with the radiolabeled sugar (Boles and Oreb, 2018; Schmidl et al., 2018). Moreover, a radiolabel-free assay to determine transport kinetics in the *hxt*⁰ yeast system has been recently developed (Schmidl et al., 2021).

However, the functional, heterologous expression of GLUTs in this strain is a challenging task. In previous studies, the

transformation of EBY.VW4000 cells with native rat GLUTs did not yield cell growth on glucose (for GLUT1 and GLUT4) (Kasahara and Kasahara, 1996; Kasahara and Kasahara, 1997) or fructose (for GLUT5) (Tripp et al., 2017). Nevertheless, single point mutations in the TM2 of GLUT1 and GLUT5 enabled their activity in EBY.VW4000 (Wieczorke et al., 2002; Tripp et al., 2017). Also, wild-type GLUT1 was functionally expressed in a *hxt*⁰ strain harboring the additional *fgy1* (“functional expression of GLUT1 in yeast”) mutation (Wieczorke et al., 2002) that affects the scaffold protein Efr3 (Wieczorke and Boles, personal communication). Efr3 is essential for recruiting the Stt4 phosphatidylinositol-4-kinase to the plasma membrane and, consequently, builds a prerequisite for normal membrane phosphatidylinositol-4-phosphate levels (Wu et al., 2014). The corresponding strain was named EBY.S7 (Wieczorke et al., 2002). Murine GLUT4 was only active in a strain named SDY.022 that, besides the *fgy1* mutation, had a mutation in the *ERG4* gene, coding for the terminal enzyme of the ergosterol biosynthesis pathway (Boles et al., 2004). The latter mutation putatively leads to a different sterol composition in the yeast plasma membrane, which seems beneficial for GLUT4 activity.

Here, we report the functional expression of human GLUT2 and GLUT3 in the *hxt*⁰ yeast system. Thereby, we complete the accessibility of the well-characterized Class I GLUTs (GLUTs1–4, categorized according to their sequence similarities (Joost and Thorens, 2009)) in a convenient system that enables detailed characterizations of these transporters and the screening for small molecules affecting their activity in a high-throughput manner. These new platforms facilitate the rapid discovery of drugs addressing severe diseases associated with these essential human transporters.

MATERIALS AND METHODS

Strains and Media

The construction of the strains CEN.PK2-1C (Entian and Kötter, 2007), EBY.VW4000 (Wieczorke et al., 1999), EBY.S7 (Wieczorke et al., 2002) and SDY.022 (Boles et al., 2004) used in this study was reported previously and their genotypes are listed in **Supplementary Table S1**. For maintenance and preparation of competent cells, plasmid-free cells were grown in standard YEP-media (1% (w/v) yeast extract, 2% (w/v) peptone) supplemented with 1% (w/v) maltose. Frozen competent cells were prepared and transformed according to Gietz and Schiestl (Gietz and Schiestl, 2007). The transformants were plated on solid, selective synthetic complete (SC) medium with 1% (w/v) maltose (M) in which uracil was omitted (-URA) to maintain the selection pressure. For experiments with *envyGFP* constructs at the microscope, EBY.S7 or CEN.PK2-1C cells were grown in filter-sterilized, low fluorescent, synthetic complete medium (If-SC) containing 6.9 g/l YNB with ammonium sulfate, without amino acids, without folic acid and without riboflavin (MP Biomedicals), containing 1% (w/v) maltose (for EBY.S7) or 2% (w/v) glucose (for CEN.PK2-1C) and amino acids as stated in Bruder et al. (Bruder et al., 2016), in which uracil was

omitted. For subcloning of plasmids, *E. coli* strain DH10B (Gibco BRL, Gaithersburg, MD) was used.

PCR and Plasmid Construction

DNA Sequences of GLUT2 and GLUT3 are listed in **Supplementary Table S2**. PCRs were performed with Phusion polymerase (New England Biolabs GmbH) and the respective primers, according to the intended modifications, which are listed in **Supplementary Table S3**. The resulting fragments were transformed together with the EcoR1/BamH1 linearized p426H7 vector into EBY.VW4000, EBY.S7 or SDY.022 frozen competent cells, respectively, to allow for plasmid assembly via homologous recombination (Oldenburg et al., 1997). Cells were plated on SCM (1% (w/v)) -URA agar plates and incubated for 3 days at 30°C. The grown colonies were then replica plated onto solid SC -URA medium with 0.2% (w/v) glucose (SCD (0.2% (w/v))). If growth occurred on glucose medium, single colonies from these plates were picked, sub-cultivated and plasmids were recovered by the standard alkaline lysis protocol. If no growth on glucose was observed, colonies from the maltose plates were picked and treated accordingly. For propagation and amplification, plasmids were transformed via electroporation in *E. coli*. Plasmid isolation from overnight *E. coli* cultures was carried out using a GeneJET Plasmid Miniprep Kit (Thermo Scientific) according to the manufacturer's instructions and sequenced at GATC Biotech (Konstanz, Germany). For subcloning into a vector with a dominant marker, the respective transporter sequences were amplified from the p426H7 plasmids as described, with primers exhibiting overhangs to the *HXT7* promoter or *CYC1* terminator, respectively, and PCR products were transformed together with the linearized pRS62K plasmid, which contains the same promoter and terminator regions, into EBY.VW4000 cells to allow for homologous recombination. To check the *in vivo* localization, *envyGFP* (Slubowski et al., 2015) was fused to the C-terminus of transporter constructs via homologous recombination of PCR fragments presenting the specific overhangs, and the whole construct which was flanked by the *HXT7* promoter and the *CYC1* terminator was inserted into the low-copy CEN6/ARS4 vector pUCPY1. All plasmids used in this study are listed in **Supplementary Table S4**.

Growth Tests

For growth tests on solid medium, drop tests were performed on minimal SC -URA medium, containing the respective sugar, with cells expressing transporter constructs in the p426H7 vector backbone. Pre-cultures were grown overnight in 10 ml SCM (1% (w/v)) -URA medium at 30°C and 180 rpm, centrifuged (3,000 g, 3 min, 20°C) and washed twice in double-distilled, sterile water (ddH₂O). Cells were resuspended in ddH₂O and OD_{600nm} was adjusted to 1. Dilutions of OD_{600nm} 0.1, 0.01 and 0.001 were prepared and 4 µl of each dilution was dropped onto the agar plate. Plates were incubated at 30°C for 5 days.

Cell growth in liquid YEP medium was measured with the Cell Growth Quantifier (Aquila Biolabs) (Bruder et al., 2016). Pre-cultures of cells expressing the transporter constructs in the pRS62K vector backbone were grown overnight in 10 ml

YEPM (1% (w/v)) medium with 200 µg/ml G418 for plasmid selection, harvested by centrifugation (3,000 g, 3 min, 20°C) and washed twice with ddH₂O. Washed cells were used to inoculate 30 ml YEP G418 (200 µg/ml) medium with the indicated sugar to an OD_{600nm} of 0.2 in 300 ml Erlenmeyer flasks, which were mounted onto the sensor plate. Quantification of cell growth and calculation of apparent maximal growth rates were performed with the CGQuant software (Aquila Biolabs) as previously described (Bruder et al., 2016).

Fluorescence Microscopy

To investigate the *in vivo* localization of the (modified) transporters, CEN.PK2-1C and EBY.S7 cells expressing the envyGFP-tagged constructs on the low-copy CEN.ARS plasmid pUCPY1 were grown overnight in filter-sterilized, low fluorescent SC medium in which uracil was omitted (If-SC -URA) and 1% (w/v) maltose (for EBY.S7 cells) or 2% (w/v) glucose (for CEN.PK2-1C) was added. 500 µl cell suspension of an OD_{600nm} between 1.5 and 3 was mixed with 500 µl If-SC -URA medium with the respective sugar containing 1.2% (w/v) low melting agarose (Roth) to reach a suspension with 0.6% (w/v) low melting agarose for immobilization. Six microliters were applied to an object plate, sealed with a cover slip and GFP fluorescence was located with the Confocal Laser Scanning Microscope (Zeiss LSM 780, Jena, Germany).

To confirm the activity of envyGFP-tagged transporter constructs, EBY.S7 cells expressing the respective construct were streaked out on solid SC -URA medium with 0.2% (w/v) glucose and growth was recorded after 5 days of incubation at 30°C.

Structural Modeling of GLUT2 and GLUT3

The crystal structure of GLUT2 is unknown and only the outward-facing GLUT3 structures are available. The homology models of the inward-facing GLUT2 and GLUT3 were generated with the 'Homology Model' function of the program package Molecular Operating Environment (MOE; Chemical Computing Group, <https://www.chemcomp.com>), using as a template the crystal structure of GLUT1 (PDB ID 4PYP). The homology models for the outward-facing GLUT2 were generated with MOE from the crystal structure of GLUT3 (PDB ID 5C65 or 4ZWC). The amino acid sequence identity and similarity between GLUT2 and GLUT3 are 50% and 68%, between GLUT1 and GLUT2 are 52% and 68%, and between GLUT1 and GLUT3 are 63% and 78%, respectively, as determined with the alignment function from MOE. The homology models generated were scored with GB/VI. The mutations were performed in MOE Protein Designing function and subject to energy minimization with the Forcefield Amber10.

Transport Assay for Inhibition Studies

The culturing of yeast cells was done at 30°C with shaking (180 rpm). EBY.S7 yeast cells expressing GLUT2_{ΔloopS_Q455R} were grown for a day in YEPM (1% (w/v)) media containing 200 µg/ml G418. Cells were washed once in YEP media containing 0.2% (w/v) glucose (YEPG) and 200 µg/ml G418 and transferred in the same media so that OD_{600nm} ~ 0.5 and

grown further for 1 to 2 days. GLUT3_{S66Y} expressed in EBY.S7 were grown for two days in SC-URA with 1% (w/v) maltose, then washed and transferred in SC-URA with 0.2% (w/v) glucose, followed by further growth for 1-2 days. For transport activity assay, cells were centrifuged (1000 g, 5 min), washed once with PBS solution (10 mM Na₂HPO₄, 1.8 mM KH₂PO₄, 2.7 mM KCl, 137 mM NaCl, pH 7.4), and resuspended in PBS buffer at an OD_{600nm} ~ 10; each assay determination contained 100 µl of this cell solution. Transport activity assay was started by adding C¹⁴-glucose (10 mM for GLUT2_{ΔloopS_Q455R} or 1 mM for GLUT3_{S66Y}). Transport activity assay was halted after 10 min by adding 3 ml ice-chilled Quench buffer (0.1 M KPi, 0.1 M LiCl, pH 5.5), followed by filtration through a glass fiber channel (GC50; Advantec, Tokyo, Japan) under vacuum, and another two washes with 3 ml Quench buffer and filtration. The filtration membranes were transferred into scintillation vials with 10 ml of Scintillation Solution (BioSafeII; Research Products International, Mount Prospect, IL, United States), and vortexed briefly. The radioactivity was determined with a scintillation counter (Tri-carb 2900TR, Perkin Elmer, Waltham, MA, USA). Phloretin and quercetin were dissolved in DMSO at 20 mM stock concentration, and inhibitor concentrations used for IC₅₀ determination were 100x stocks so that the final concentration of DMSO in the assay was 1%. Controls for determining the relative transport activity included 1% (v/v) DMSO to account for DMSO presence due to inhibitor, and the cells transformed with the empty vector. We found that the background activity with the empty vector was comparable to the transport activity of the transporters at 200 µM phloretin. Data were analyzed with the nonlinear fit analysis of GraphPad Prism (San Diego, CA, United States).

RESULTS

Generation of GLUT Constructs that Mediate Glucose Uptake into the hxt⁰ Yeast Strain

A GLUT3 Mutant Shows Enhanced Activity in the hxt⁰ Yeast System

A plasmid for the expression of GLUT3 in yeast was generated using either the native human coding sequence or a codon-optimized sequence for the expression in insect cells. Amplification of the open reading frame (ORF) with oligonucleotides having 30-40 base pair overhangs to the applied promoter (*HXT7*¹⁻³²⁹) or terminator (*CYC1*) region, respectively, and co-transformation with the linearized host plasmid (p426H7) in EBY.VW4000, EBY.S7, and SDY.022 cells allowed for the plasmid assembly via homologous recombination (Oldenburg et al., 1997; Boles and Oreb, 2018). The strong, truncated *HXT7* promoter region and the *CYC1* terminator were chosen to achieve high expression levels. Transformants were plated on selective SC -URA medium, containing 1% (w/v) maltose, and incubated for three days at 30°C, resulting in the growth of approximately 1000 colonies per plate. Subsequently, cells were replica plated on SC -URA

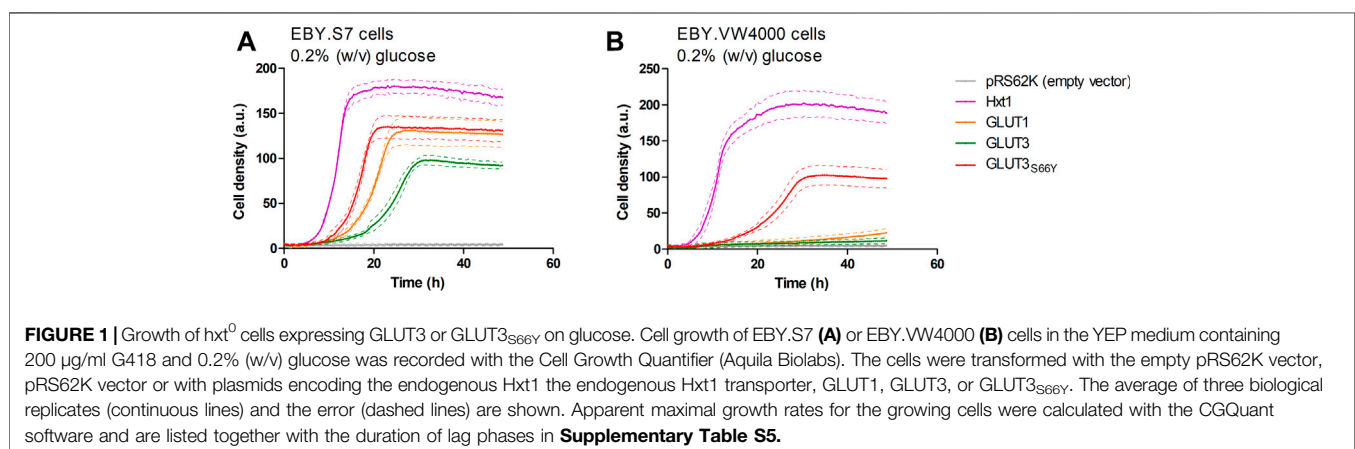
medium, containing 0.2% (w/v) glucose, to screen for cells that regained the ability to use glucose as a carbon source. EBY.VW4000 transformants did not show any growth on the solid glucose medium, even after a prolonged incubation of seven days. Most of the EBY.S7 and SDY.022 transformants grew after five days of incubation on glucose. To investigate if wild-type GLUT3 is active in these strain backgrounds, we isolated and sequenced plasmids of several colonies with various sizes. In bigger colonies, one single mutation (S66Y) was found, located in TM2. However, also unmodified GLUT3 mediated the growth of EBY.S7 and SDY.022 transformants on glucose. Re-transformation of the native GLUT3 and the modified GLUT3_{S66Y} construct in EBY.S7 cells resulted in growth on glucose medium, proving that no further mutations, except for the *fgy1* mutation, in the yeast strain were essential for this phenotype. However, while wild-type GLUT3 was incapable of mediating growth of EBY.VW4000 cells on solid glucose medium, slight growth was observed for GLUT3_{S66Y}-expressing EBY.VW4000 cells (**Supplementary Figure S7A**). Furthermore, the drop test of the EBY.S7 and SDY.022 cells expressing the different constructs (GLUT3 and GLUT3_{S66Y}) on a plasmid, revealed larger colonies for those expressing the mutated version (**Supplementary Figures S7B,C**), indicating that the S66Y mutation is beneficial for the functionality of the transporter in the heterologous system. Growth tests with *hxt*⁰ cells expressing GLUT3 or GLUT3_{S66Y} were performed in liquid YEP medium with 0.2% (w/v) glucose, for which the GLUT3 ORFs were transferred to pRS62K plasmid backbones. Consistent with the results observed in the drop tests, both constructs enabled the growth of EBY.S7 cells, but GLUT3-expressing cells showed a significantly longer lag phase and a 1.8 times lower apparent maximal growth rate than those expressing GLUT3_{S66Y} (**Figure 1A**; **Supplementary Table S5**). For EBY.VW4000 cells, only GLUT3_{S66Y} mediated growth, while the unmodified GLUT3 did not (**Figure 1B**). Positive controls were GLUT1, as a representative of a heterologous transporter active in EBY.S7 cells (Wieczorke et al., 2002), and Hxt1, an endogenous low-affinity transporter for glucose and fructose (Leandro et al., 2009).

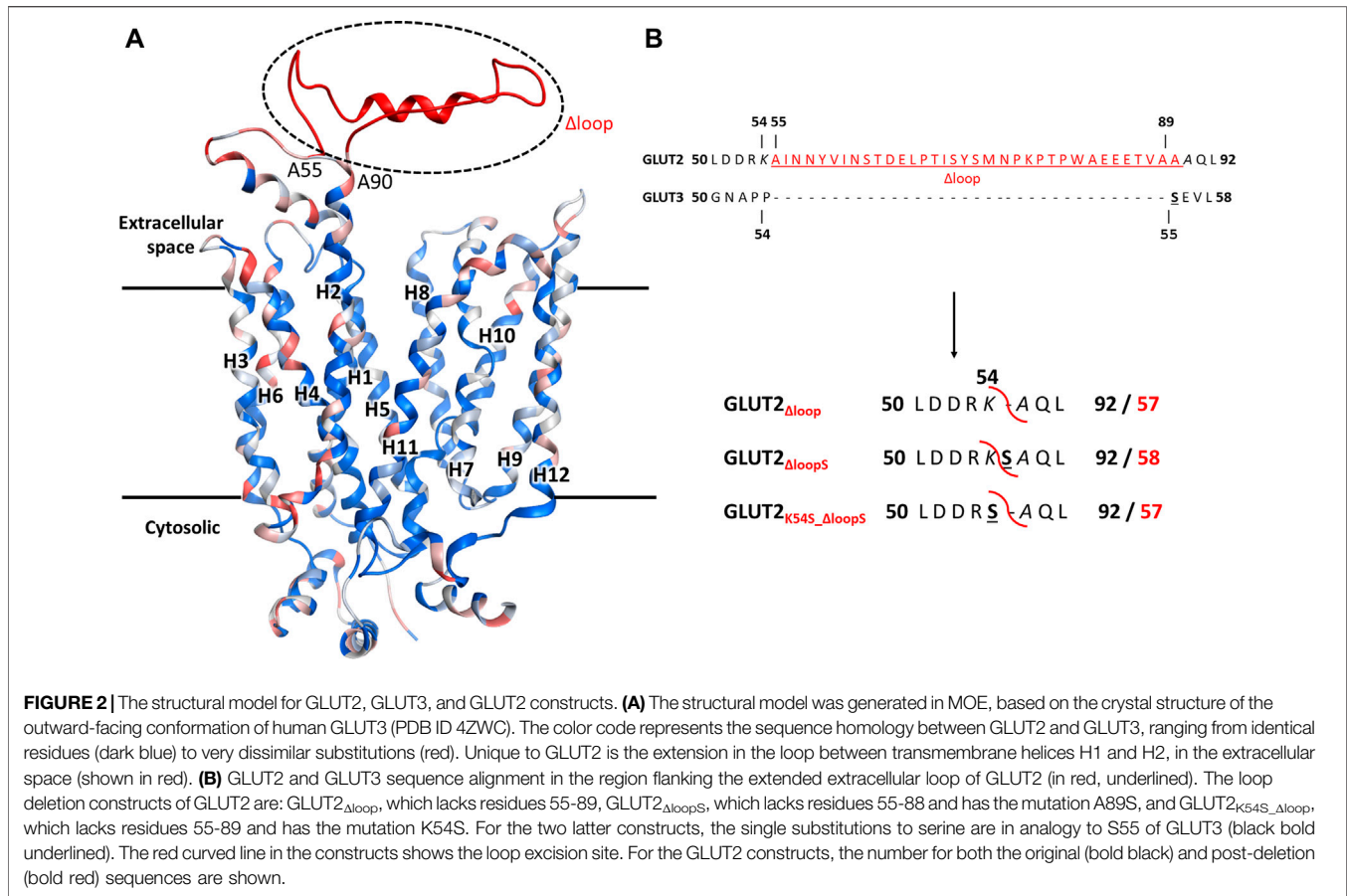
Site-Directed Mutagenesis Approaches to Enable GLUT2 Activity in Yeast

Expression plasmids carrying either the native or a codon-optimized (for insect cells) human GLUT2 sequence were generated as described above for GLUT3. However, after replica plating, EBY.VW4000, EBY.S7, or SDY.022 transformants, of which more than 1000 colonies grew on solid maltose medium, showed no growth on glucose-containing agar plates, even after prolonged incubation at 30°C for one week.

Like the S66Y mutation in GLUT3, previous studies found single point mutations in the second transmembrane region of GLUT1 (e.g., V69M) (Wieczorke et al., 2002) and GLUT5 (e.g., S72Y and S76I) (Tripp et al., 2017) that enabled or improved the functional expression of these GLUTs in yeast. Therefore, we focused on this critical region in GLUT2 as well. Comparison of the amino acids 96 – 104 in GLUT2 with the corresponding area in GLUT1, GLUT3, and GLUT5 (**Supplementary Figure S2**) revealed that GLUT2 primary sequence has two consecutive serines at positions 102-103 vs. hydrophobic amino acids in the other GLUTs successfully expressed in yeast (**Supplementary Figure S2**).

Interestingly, in GLUT3 and GLUT5, a single serine mutation to a more hydrophobic amino acid enabled or improved the functional expression of these two transporters in yeast (as shown in this study and by Tripp et al. (Tripp et al., 2017)). This observation prompted us to direct mutagenesis to the amino acids 101-103, including the valine at position 101, considering the effect of the V69M mutation in GLUT1 (Wieczorke et al., 2002). By using degenerate primers that allow for the introduction of different nucleotides at a particular position (Kwok et al., 1994) (see **Supplementary Table S3**), different codons were inserted to mutate the chosen amino acids. The following degenerate codons were used to insert the desired range of substitutions: at position 101, RTK (encoding Ile, Met and Val); at position 102, RYT (encoding Ala, Ile, Thr and Val); at position 103, ATK (encoding Ile and Met). Considering all permutations, a library encoding 24 different protein sequence variants of the critical region resulted from this approach. The sequencing of the isolated plasmids from random clones confirmed the successful introduction of the expected range of substitutions. Still, screening of more than 1000 colonies for growth on glucose-

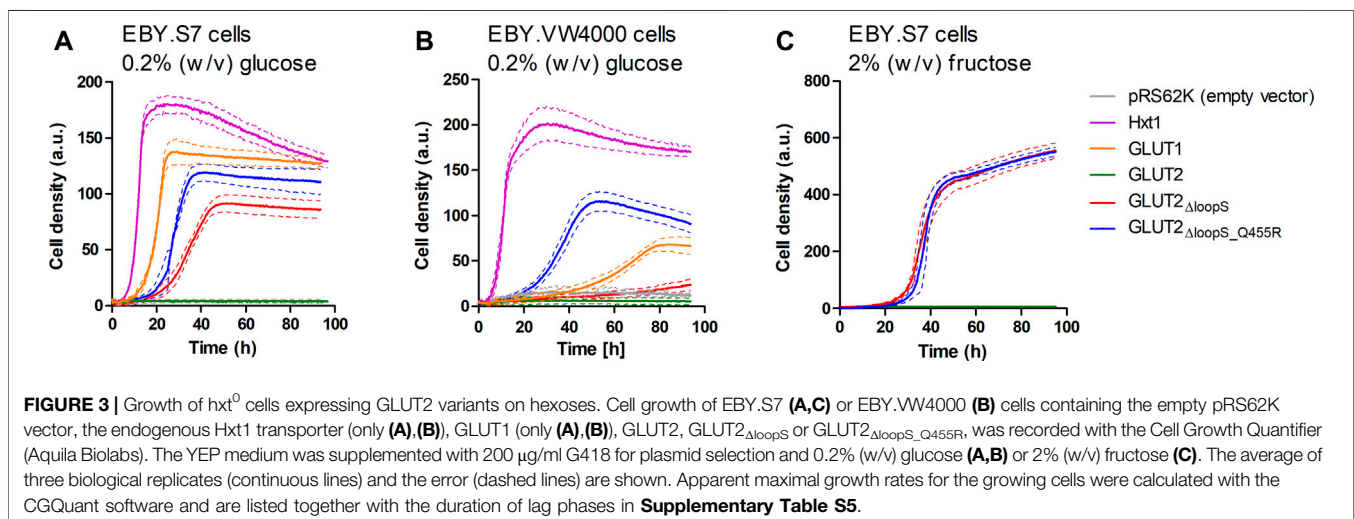




containing agar plates yielded no positive clones. In addition to these mutations in TM2, we mutated the N glycosylation site at position 62 (GLUT2_{N62Q}) within the first extracellular loop, just in case the glycosylation disturbed the activity of the transporter in yeast cells. This modification also failed to restore *hxt*⁰ yeast cell growth on glucose.

Modification of the Extended Extracellular Loop of GLUT2

A conspicuous structural difference between GLUT2 and the other Class I GLUTs, which are active in yeast, is the extension of the extracellular loop connecting the TM helices H1 and H2 (Figure 2).

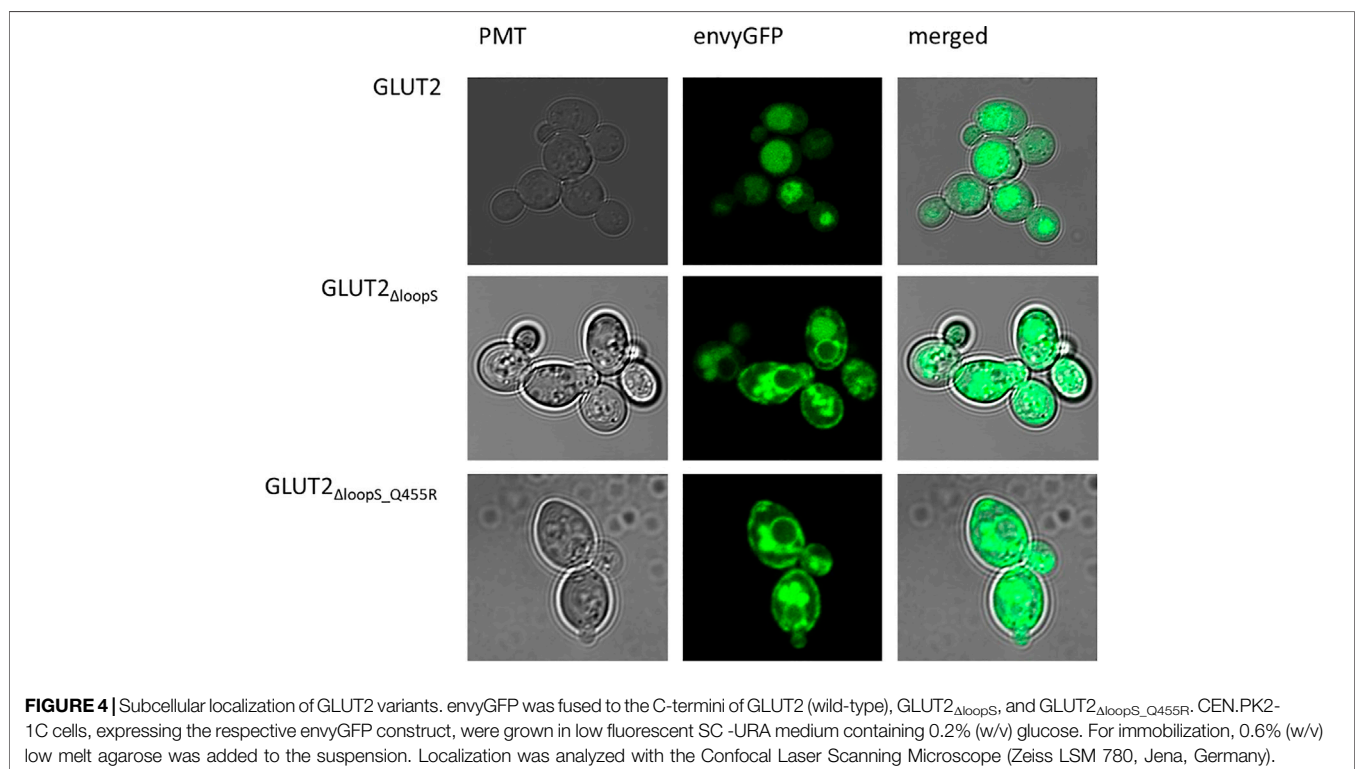


Since minor sequence modifications have not led to an active expression of GLUT2 in hxt⁰ yeast strains, we reasoned that shortening the extension, thereby introducing a GLUT3-like-loop, could promote GLUT2 activity in the heterologous system.

In addition to just deleting the amino acids 55-89 (GLUT2_{Δloop}), we also constructed one chimera in which those amino acids were replaced by one serine (GLUT2_{ΔloopS}) and one in which the lysine preceding the deleted region was mutated to serine (GLUT2_{K54S_Δloop}) (**Figure 2B**). Compared to GLUT3, the loop of GLUT2_{Δloop} is one residue shorter, lacking the residue corresponding to S55 of GLUT3, while that of GLUT2_{ΔloopS} is the same length and includes a residue in analogy to S55 of GLUT3. GLUT2_{K54S_Δloop} contains the mutation corresponding to S55 of GLUT3 but at the beginning instead of the end of the deleted loop. The modifications were introduced into the ORFs via PCR (primers are listed in **Supplementary Table S3**), and the individual fragments were transformed together with a linearized p426H7 vector in EB.Y.VW4000, EB.Y.S7, or SDY.022 cells. Transformants that grew on solid maltose medium (more than 1000 colonies per plate) were then replica plated onto glucose containing plates. A substantial number (approximately 60%) of colonies expressing one of the three loop-modified constructs, respectively, grew on glucose. Multiple plasmids from each strain background and loop-construct combination were isolated and sequenced. Most of these plasmids did not show mutations other than those intentionally introduced. Strikingly, in 2 out of 3 sequenced plasmids harboring the GLUT2_{ΔloopS} construct that were isolated from EB.Y.VW4000 cells, a point mutation led to the substitution of the amino acid glutamine at position 455 with

either lysine (Q455K) or arginine (Q455R). Also, Q455R mutation was found in one out of three GLUT2_{ΔloopS} constructs isolated from SDY.022 cells, indicating an additional beneficial effect of this mutation on the glucose uptake via GLUT2. The isolated loop constructs GLUT2_{Δloop}, GLUT2_{K55S_Δloop}, GLUT2_{ΔloopS}, and GLUT2_{ΔloopS_Q455R} were re-transformed in all three hxt⁰ strains, and their growth was analyzed by a drop test on solid glucose medium (**Supplementary Figure S9**). The ability to grow on glucose was regained by EB.Y.S7 and SDY.022 cells with all loop constructs, whereas cells expressing GLUT2_{ΔloopS} and especially GLUT2_{ΔloopS_Q455R}, respectively, showed bigger colonies in comparison to GLUT2_{Δloop} or GLUT2_{K55S_Δloop} expressing cells (**Supplementary Figures S9B,C**). EB.Y.VW4000 cells grew significantly only when expressing GLUT2_{ΔloopS_Q455R} (**Supplementary Figure S9**), providing further evidence for a crucial effect of this additional point mutation, when combined with the ΔloopS modification, on GLUT2 activity.

As with GLUT3, the ORFs of different GLUT2 variants were transferred into the pRS62K vector and tested for growth in liquid YEP media, using the Cell Growth Quantifier (Aquila Biolabs) (Bruder et al., 2016). In agreement with the results from the drop test, only GLUT2_{ΔloopS} and GLUT2_{ΔloopS_Q455R}, but not wild-type GLUT2, conferred growth of EB.Y.S7 cells on 0.2% (w/v) glucose (**Figure 3A**). For EB.Y.VW4000 cells, the additional point mutation in GLUT2_{ΔloopS_Q455R} was essential for growth in this medium (**Figure 3B**). Interestingly, no growth of EB.Y.S7 cells expressing either of the loop constructs was observed on 0.2% (w/v) fructose medium, while the positive controls expressing Hxt1 showed normal growth (data not shown).



This is likely due to the very low affinity of GLUT2 for fructose ($K_M = \sim 76$ mM) (Mueckler and Thorens, 2013). However, on 2% (w/v) fructose, both loop constructs conferred robust growth (Figure 3C). Analysis of the apparent maximal growth rates with the CGQuant Software (Bruder et al., 2016) showed a significantly faster doubling rate for EB.Y.S7 cells expressing GLUT2 $_{\Delta loopS_Q455R}$ compared to GLUT2 $_{\Delta loopS}$ -expressing cells on 0.2% (w/v) glucose medium (1.7 times) as well as on 2% (w/v) fructose medium (1.5 times) (Supplementary Table S5).

Subcellular Localization of Different GLUT2 Variants

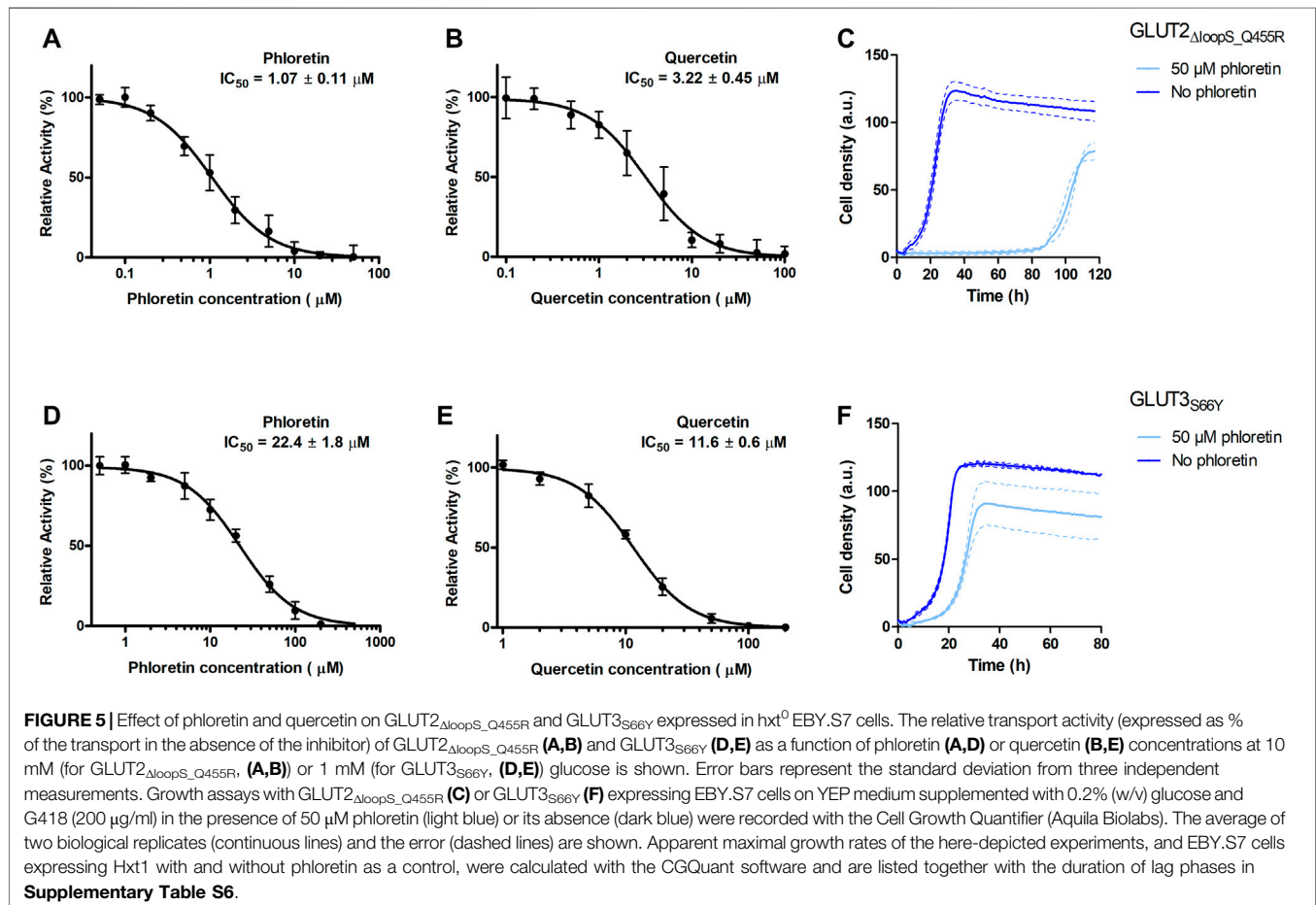
One hypothesis to explain the adverse effect of the extended loop on GLUT2 activity in yeast is possible interference with the transporter's targeting to the plasma membrane. To test if our loop modifications influence the transporter trafficking, we fused the strong GFP variant envyGFP (Slubowski et al., 2015) to the C-terminal ends of the two most active constructs GLUT2 $_{\Delta loopS}$ and GLUT2 $_{\Delta loopS_Q455R}$, and of the inactive wild-type GLUT2. The activity of these envyGFP-tagged transporters was confirmed by the growth of GLUT2 $_{\Delta loopS_Q455R}$ -envyGFP and GLUT2 $_{\Delta loopS}$ -envyGFP-expressing EB.Y.S7 cells on solid SC -URA 0.2% (w/v)

glucose medium (Supplementary Figure S11). Fluorescence microscopy of CEN.PK2-1C cells indeed revealed significant differences between the localization of the wild-type GLUT2 and the two truncated constructs. While cells expressing the latter showed a patchy distribution at the plasma membrane and partial retention in the endomembrane system, unmodified GLUT2 does not reach the plasma membrane and is located in vacuoles (Figure 4), thereby being destined for degradation.

The same pattern was observed in EB.Y.S7 cells (Supplementary Figure S10), demonstrating that the effect of the loop is not dependent on the strain background. Therefore, we conclude that the implemented loop modifications rescue the trafficking defect of GLUT2 in yeast cells. The additional point mutation appears not to influence the subcellular localization of the transporter and putatively improves the transporter's substrate-gating activity by other effects (see below).

The Yeast Platform is Suitable for Screening and Characterizing GLUT Inhibitors

Since the best activities of GLUT2 and GLUT3 constructs were observed in the EB.Y.S7 cells, this strain background was chosen to establish a yeast-based platform for screening and



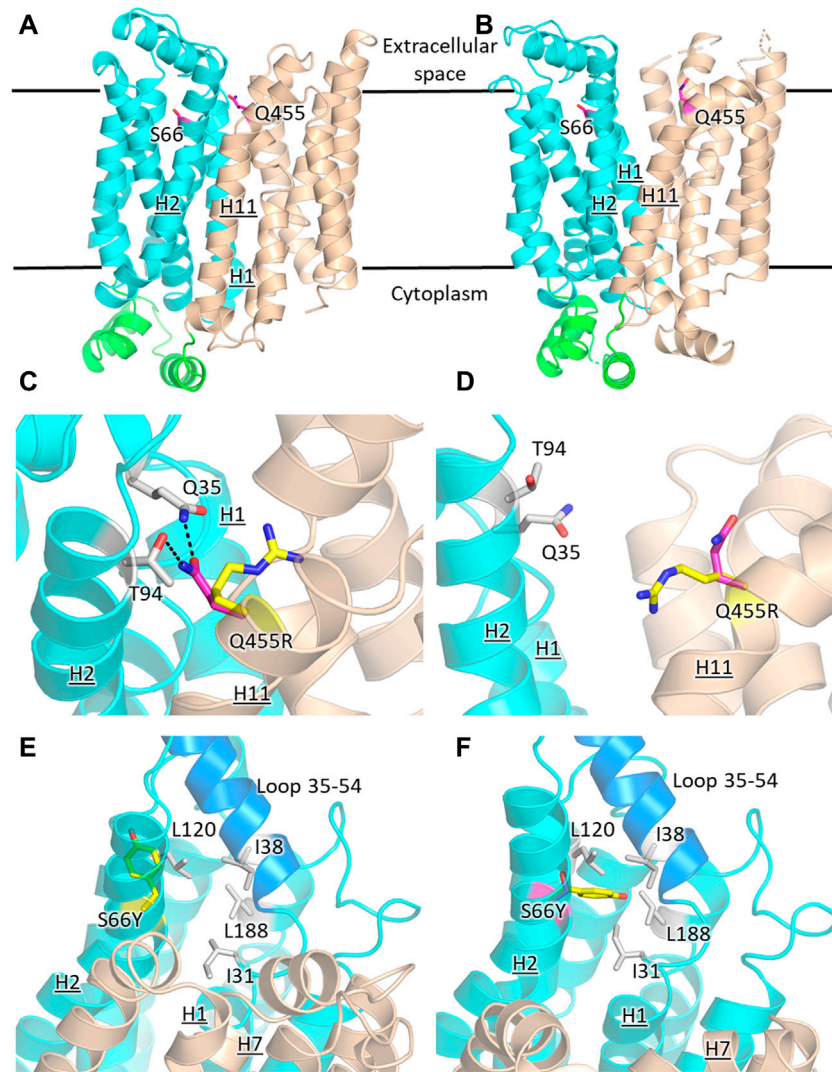


FIGURE 6 | Structural models of GLUT2 and GLUT3 variants with functional transporter expression in *hxt⁰* cells. Inward-facing (**A,C,E**) and outward-facing (**B,D,F**) conformations of GLUT2 and GLUT3 based on the crystal structures for the corresponding conformations of GLUT1 (PDB ID 4PYP, inward-facing) or GLUT3 (PDB ID 5C65, outward-facing), showing the locations of the single-site mutations that increased the transport activity of GLUT2_{loop} and GLUT3 expressed in *hxt⁰* yeast cells: S66 in H2 of GLUT3 and Q455 in H11 of GLUT2_{loop}. The transporter N- and C-halves are in magenta and gold, respectively, and the transmembrane helices are labeled as H1-H12. (**C,D**) Close-up views of (**A,B**), respectively, focused on Q455R in GLUT2_{loop}, showing the original side-chain (magenta), and the mutant (yellow). (**E,F**) Close-up views of (**A,B**), respectively, focused on S66Y in GLUT3. The mutant side chain is shown in yellow. The extracellular loop between helices H1 and H2 (residues 35-54, shown in blue) is close to the mutated side chain Y66 in the outward-facing conformation (**F**). Compared with the inward-facing conformation, in the outward-facing conformation, the loop spanning residues 35-54 moves at least 1 Å in the direction indicated by the red arrow. Figures were drawn using Open-Source PyMol Version 2.3.0 (The PyMOL Molecular Graphics System, Version 2.3.0 Schrödinger, LLC).

characterizing GLUT inhibitors. Phloretin (Kwon et al., 2007) and quercetin (Lee et al., 2015) are well-known inhibitors of GLUT2 and GLUT3 (Kwon et al., 2007; Augustin, 2010; Lee et al., 2015), and, therefore, we determined their half maximal inhibitory concentration (IC_{50} values) for GLUT2_{ΔloopS_Q455R} expressed in EB.Y.S7 (**Figures 5A,B**).

The values obtained for GLUT2_{ΔloopS_Q455R} (IC_{50} of 1.07 ± 0.11 and $3.22 \pm 0.45 \mu\text{M}$ for phloretin and quercetin, respectively) indicate a strong inhibition and confirm that yeast-expressed GLUT2 can be reliably used to identify and

characterize transport inhibitors despite the deletion of the extended extracellular loop. This is supported by growth tests in the presence of phloretin. We found that $50 \mu\text{M}$ phloretin inhibited the growth of EB.Y.S7 cells expressing GLUT2_{ΔloopS_Q455R} significantly, leading to an extensive long lag phase of 87.4 hours, a diminished apparent maximal growth rate (**Supplementary Table S6**) and a lower maximal cell density (**Figure 5C**).

Inhibition of GLUT3_{S66Y} with phloretin and quercetin is less potent than for GLUT2_{ΔloopS_Q455R} but still effective, as

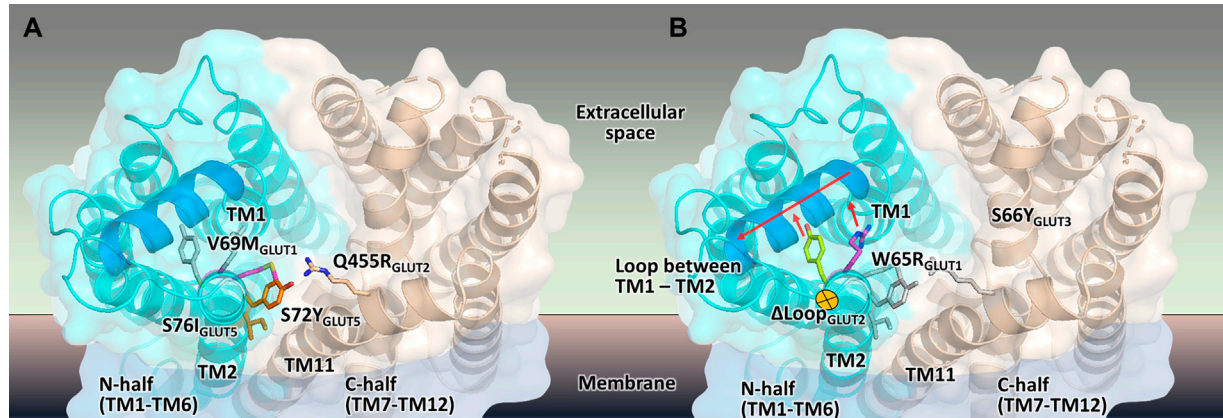


FIGURE 7 | Mapping the mutations that render different GLUTs active in *hxt⁰* yeast cells. **(A,B)** The structural model of the outward-facing conformation for GLUT1-3 and GLUT5 showing the single-site mutations that provide or increase transport activity of the respective human GLUT upon expression in *hxt⁰* yeast cells, viewed from the extracellular side. The mutants are generally substitutions to bulkier side chains and fall into two categories. **(A)** Mutants that disrupt the packing between the N- and C-domains (colored as cyan and wheat, respectively), such as S72I and S76Y of GLUT5, Q455R of GLUT2, and V69M of GLUT1. **(B)** Mutants that dislocate the loop between TM helices TM1 and TM2 (the part of the loop that needs to move to accommodate the mutations is shown in blue), causing it to move away from the central cavity, such as S66Y of GLUT3 and W65R of GLUT1.

demonstrated by the IC_{50} values ($22.4 \pm 1.8 \mu\text{M}$ for phloretin and $11.6 \pm 0.6 \mu\text{M}$ for quercetin) (**Figures 5D,E**). Moreover, the phloretin IC_{50} values are in the same range as those reported for the related GLUT1 and GLUT4 (Kasahara and Kasahara, 1997). Reflecting the higher IC_{50} values of phloretin compared to those measured with GLUT2 $_{\Delta\text{loopS_Q455R}}$, the growth delay of GLUT3 $_{\text{S66Y}}$ expressing EBYS7 cells in glucose containing medium in the presence of 50 μM phloretin is less pronounced but still significant (**Figure 5F**; **Supplementary Table S6**). In contrast, the apparent maximal growth rates of Hxt1-expressing EBYS7 cells do not show significant differences when grown in the absence or presence of 50 μM phloretin (**Supplementary Table S6**). As all tested transporters were expressed under the control of the truncated Hxt7 promoter, the Hxt1 control shows that the diminished growth phenotypes of GLUT2 $_{\Delta\text{loopS_Q455R}}$ and GLUT3 $_{\text{S66Y}}$ -expressing EBYS7 cells upon phloretin addition do not arise from lowered expression levels. Together, these data demonstrate that the yeast system can be conveniently used to screen large compound libraries for potential inhibitors of GLUT2 and GLUT3 in a simple, growth-based manner, amenable to high throughput screening.

Structural Analysis of GLUT2 and GLUT3 Constructs

The prevailing transport mechanism for the Major Facilitator Superfamily (MFS) proteins, including GLUTs, postulates that the substrate cavity of the transporter is alternately open to either side of the membrane with the transporter cycling between the so-called outward- and inward-facing conformations, through a relative rocking of the transporter N- and C- halves (domains) around the active site (Abramson et al., 2003; Yan, 2015). The structural models for GLUT2 $_{\Delta\text{loopS}}$, GLUT2 $_{\Delta\text{loopS_Q455R}}$, GLUT3, and GLUT3 $_{\text{S66Y}}$ were based on the crystal structures of the inward-

facing conformation for GLUT1 (PDB ID 4PYP) and the outward-facing conformation of GLUT3 (PDB ID 5C65 or 4ZWC) (**Figure 6**).

GLUT2 and GLUT3 share 50% and 68% amino acid sequence identity and homology, respectively (determined with MOE, Chemical Computing Group). Cell growth of GLUT-expressing EBYS7 cells showed that additional single mutations in GLUT2 $_{\Delta\text{loopS}}$ and GLUT3 improved the transport activities (**Figures 1, 3**): Q455R in GLUT2 $_{\Delta\text{loopS}}$ and S66Y in GLUT3. Q455 of GLUT2 is in the outward edge of the TM helix H11, close to the interface between the N- and C-domains (**Figure 6A**). Its substitution with arginine is inconsequential for the outward-facing conformation (**Figures 6B,D**), but disruptive for the inward-facing conformation of the transporter; the bulkier guanidinium moiety can no longer participate in the hydrogen bond interactions with Q35 of H1 and T94 of H2 (**Figure 6C**), sterically crowding its vicinity. In GLUT3, S66 is in the outer periphery of H2, part of a hydrophobic pocket composed of N-domain residues including, I31, I38, L120, and L188, close to the soluble loop linking H1 and H2 (**Figures 6A,E,F**). In the outward-facing conformation of GLUT3, S66 substitution with the larger side-chain of a tyrosine integrates well, as there is ample space around the loop connecting H1 and H2 (loop 35-54) (**Figure 6F**). Conversely, in the inward-facing

TABLE 1 | Mutations that enable the transport activity of human GLUTs expressed in *hxt⁰* cells.

Protein	Mutation	Reference
GLUT1	W65R V69M	Wieczorke et al. (2002)
GLUT2 $_{\Delta\text{loopS}}$	Q455R	This study
GLUT3	S66Y	This study
GLUT	S72Y S76I	Tripp et al. (2017)

conformation, loop 35-54 packs near H7, and the tyrosine side-chain is pushed away from the hydrophobic pocket (**Figure 6E**).

DISCUSSION

The work here completes the generation of GLUT-specific assay systems for class I GLUTs in the versatile and simple platform provided by the engineered yeast cells, *hxt*⁰. These systems enable high-throughput ligand screening for a particular GLUT and determination of the potency and selectivity of the ligand candidates relative to closely related GLUTs within class I, and also class II member, GLUT5. The co-existence of several GLUT isoforms within one tissue or cancer cell line complicates efforts to understand the role of a particular GLUT in the cell pathology or physiology. Thus, besides their medical importance as potential drugs, GLUT-selective inhibitors can also serve as investigative tools to unravel how healthy and abnormal cells adjust their energetic needs through GLUT expression, regulation or function (Carreño et al., 2019). Additionally, GLUT-specific substrate analogs can be optimized as diagnostic tools, especially in cancer detection (Barron et al., 2016; George Thompson et al., 2016; Wuest et al., 2018). Finally, discovery of GLUT-selective activators would be of particular interest in the case of GLUT4 or GLUT2, as strategies to ameliorate diabetes.

Having a GLUT2 assay system is particularly useful. The low affinity for glucose and fructose of this transporter makes it difficult to study its activity when other GLUT isoforms are present, even when GLUT2 is overexpressed. Deleting the loop extension between TM1 and TM2 helices was necessary for the functional expression of GLUT2, and the two transporters showed differences in their inhibition by phloretin and quercetin, with GLUT2 being significantly more sensitive than GLUT3 (**Figure 5**).

Besides their value for GLUT-specific ligand discovery and characterization, the GLUT expressing yeast systems point to intriguing clues regarding the regions important for transporters activity. As shown here for GLUT2 and GLUT3 and previously reported for GLUT1 (Wieczorke et al., 2002) and GLUT5 (Tripp et al., 2017), the functional expression of these transporters is facilitated or improved by single amino acid substitutions in the transporter sequence (summarized in **Table 1**, **Figure 7**). Although the elucidation of the underlying mechanism is complex and not in the scope of this study, structural modeling can help derive hypotheses to explain the observations.

Wild-type transporters and GLUT2_{ΔloopS}, although localized at the membrane, could not compensate for the absence of the endogenous hexose transporters when *EBY.VW4000* cells were grown in media with glucose or fructose as the carbon source. W65R and V69M of GLUT1 (Wieczorke et al., 2002), S66Y of GLUT3 (this study), S72Y and S76I of GLUT5 (Tripp et al., 2017) are all residues in the TM2, near the loop connecting TM helices 1 and 2, which in turn either packs closely to TM helices 7 and 11 (in the inward-facing conformation) or relaxes by moving at least 1 Å away from these helices (in the outward-facing conformation). Intriguingly, Q455R of GLUT2_{ΔloopS} is at the end of TM11, which also approaches the same region: TM1, TM2, and their connecting loop (residues 35-54) (**Figures 6, 7**). The convergence in the location of the mutations that functionalize the transporters (**Figure 7**), whether they are part of the Class I GLUTs (like GLUT1-3)

or Class II (like GLUT5), suggests that this region is critical for transport activity of human GLUTs in the yeast system. Consistent with the proposed role of the mutations in GLUT5 (Tripp et al., 2017), the ones described here for GLUT3 and GLUT2_{ΔloopS} (S66Y and Q455R, respectively) also seem to destabilize the inward-facing conformation while leaving the outward-facing one unaffected. More generally, the substitutions that functionalize GLUTs in yeast cells favor an open substrate cavity towards the extracellular space (i.e., outward-facing conformation), either by destabilizing the N- and C-domain interface of the inward-facing conformation (**Figure 7A**) or by pushing the TM1-TM2 extracellular loop away, leading to a more accessible substrate cavity from the extracellular side (**Figure 7B**).

Evidently, the lipid composition of the yeast's plasma membrane also impacts the heterologous expression of some human GLUTs (Wieczorke et al., 2002; Schmidl et al., 2018).

In *EBY.S7*, a strain in which the phosphatidylinositol-4-phosphate composition is putatively altered due to the *fyg1* mutation (Schmidl et al., 2018), wild-type GLUT1 and GLUT3, and GLUT2_{ΔloopS}, are actively expressed without any further point mutations. Conceivably, the cycling between the transporter conformations depends on the lipid environment; the relative stabilization of the outward-facing conformation vs. the inward-facing one may be a feature of functional expression of human GLUTs in yeast cells. Activating transport by stabilizing the outward-facing conformation has been documented for another classic MFS protein, LacY, for which interaction of the transporter periplasmic loops with a nanobody against the outward-facing conformation increased the substrate affinity 50-fold (Smirnova et al., 2014). Strikingly, the critical role of lipids in yeast for the functionality of transporters that undergo conformational changes during the transport cycle has been recently demonstrated, supporting our hypothesis (van't Klooster et al., 2020a; van't Klooster et al., 2020b).

For GLUT2, introducing point mutations or screening a combinatorial mini-library of 24 possible aminoacid combinations in the critical TM2 region was not sufficient for activating the transporter, even in strain backgrounds *EBY.S7* and *SDY.022* exhibiting an altered lipid composition. We demonstrated that truncating the large extension of the second extracellular loop, which is a distinctive property of GLUT2 compared to other GLUTs functionally expressed in yeast, was a successful strategy based on a rational approach. As shown by fluorescence microscopy, this modification promotes the trafficking of the transporter to the plasma membrane, whereas the full-length protein is largely retained in the vacuole. In general, the role of the soluble loops in MFS transporters is not well understood, but it is believed that they might affect the gating and conformational dynamics of the transporters (Qureshi et al., 2020). Our results suggest that the GLUT2-specific extension of the second loop is not essential for glucose transport per se. It might rather have a regulatory function, which is probably relevant only within its native environment in the human cells. Similar to our observations, the soluble loops were dispensable for the function of the human nucleoside transporters (belonging to the MFS superfamily) expressed in *Xenopus* oocytes (Aseervatham et al., 2015).

In summary, despite the necessary modifications of their sequence, our transporter variants retain their native function in facilitating glucose (GLUT2, GLUT3) and fructose (GLUT2) uptake. Importantly, they are sensitive to the known inhibitors phloretin and quercetin, which validates our system as a platform for screening and characterizing potential transport inhibitors.

DATA AVAILABILITY STATEMENT

The raw data supporting the conclusions of this article will be made available by the authors, without undue reservation.

AUTHOR CONTRIBUTIONS

Experimental work was performed by SS, SR, and CI. All authors contributed to experimental design and manuscript preparation. J-YC and MO guided the project.

REFERENCES

- Abramson, J., Smirnova, I., Kasho, V., Verner, G., Iwata, S., and Kaback, H.R. (2003). The lactose permease of *Escherichia coli*: overall structure, the sugar-binding site and the alternating access model for transport. *FEBS Lett.* 555, 96–101. doi:10.1016/S0014-5793(03)01087-1
- Ancey, P.-B., Contat, C., and Meylan, E. (2018). Glucose transporters in cancer-tumor cells to the tumor microenvironment. *FEBS J.* 285, 2926–2943. doi:10.1111/febs.14577
- Aseervatham, J., Tran, L., Machaca, K., and Boudker, O. (2015). The role of flexible loops in folding, trafficking and activity of equilibrative nucleoside transporters. *PLoS One* 10, e0136779. doi:10.1371/journal.pone.0136779
- Augustin, R. (2010). The protein family of glucose transport facilitators: It's not only about glucose after all. *IUBMB life* 62, 315–333. doi:10.1002/iub.315
- Barron, C. C., Bilan, P. J., Tsakiridis, T., and Tsiani, E. (2016). Facilitative glucose transporters: Implications for cancer detection, prognosis and treatment. *Metabolism* 65, 124–139. doi:10.1016/j.metabol.2015.10.007
- Boles, E., Dlugai, S., Mueller, G., and Voss, D. (2004). Use of *Saccharomyces cerevisiae* ERG4 mutants for the expression of glucose transporters from mammals. Geneva, Switzerland: World Intellectual Property Organization. WO002004026907A3.
- Boles, E., and Oreb, M. (2018). A growth-based screening system for hexose transporters in yeast. *Methods Mol. Biol.* 1713, 123–135. doi:10.1007/978-1-4939-7507-5_10
- Brockmann, K. (2009). The expanding phenotype of GLUT1-deficiency syndrome. *Brain Dev.* 31, 545–552. doi:10.1016/j.braindev.2009.02.008
- Bruder, S., Reifenrath, M., Thomik, T., Boles, E., and Herzog, K. (2016). Parallelised online biomass monitoring in shake flasks enables efficient strain and carbon source dependent growth characterisation of *Saccharomyces cerevisiae*. *Microb. Cell Fact.* 15, 127. doi:10.1186/s12934-016-0526-3
- Carreño, D., Corro, N., Torres-Estay, V., Véliz, L. P., Jaimovich, R., Cisternas, P., et al. (2019). Fructose and prostate cancer: toward an integrated view of cancer cell metabolism. *Prostate Cancer Prostatic Dis.* 22, 49–58. doi:10.1038/s41391-018-0072-7
- Chow, T. H. C., Sollitti, P., and Marmor, J. (1989). Structure of the multigene family of MAL loci in *Saccharomyces*. *Mol. Gen. Genet.* 217, 60–69. doi:10.1007/BF00330943
- Colville, C. A., Seatter, M. J., Jess, T. J., Gould, G. W., and Thomas, H. M. (1993). Kinetic analysis of the liver-type (GLUT2) and brain-type (GLUT3) glucose transporters in *Xenopus* oocytes: substrate specificities and effects of transport inhibitors. *Biochem. J.* 290, 701–706. doi:10.1042/bj2900701
- Deng, D., Sun, P., Yan, C., Ke, M., Jiang, X., Xiong, L., et al. (2015). Molecular basis of ligand recognition and transport by glucose transporters. *Nature* 526, 391–396. doi:10.1038/nature14655

FUNDING

Financial support by NIH, grant number R01-GM123103 (to J-YC and MO) and the Boehringer Ingelheim Fonds (travel grant to SS) is gratefully acknowledged.

ACKNOWLEDGMENTS

We thank Christine Essl for assistance and Eckhard Boles for stimulating discussions.

SUPPLEMENTARY MATERIAL

The Supplementary Material for this article can be found online at: <https://www.frontiersin.org/articles/10.3389/fmolb.2020.598419/full#supplementary-material>.

- Entian, K.-D., and Kötter, P. (2007). 25 yeast genetic strain and plasmid collections. *Methods Microbiol.* 36, 629–666. doi:10.1016/S0580-9517(06)36025-4
- Fukumoto, H., Seino, S., Imura, H., Seino, Y., Eddy, R. L., Fukushima, Y., et al. (1988). Sequence, tissue distribution, and chromosomal localization of mRNA encoding a human glucose transporter-like protein. *Proc. Natl. Acad. Sci. U.S.A.* 85, 5434–5438. doi:10.1073/pnas.85.15.5434
- George Thompson, A. M., Ursu, O., Babkin, P., Iancu, C. V., Whang, A., Oprea, T. I., et al. (2016). Discovery of a specific inhibitor of human GLUT5 by virtual screening and *in vitro* transport evaluation. *Sci. Rep.* 6, 24240. doi:10.1038/srep24240
- Gietz, R. D., and Schiestl, R. H. (2007). Frozen competent yeast cells that can be transformed with high efficiency using the LiAc/SS carrier DNA/PEG method. *Nat. protoc.* 2, 1–4. doi:10.1038/nprot.2007.17
- Gould, G. W., and Lienhard, G. E. (1989). Expression of a functional glucose transporter in *Xenopus* oocytes. *Biochemistry* 28, 9447–9452. doi:10.1021/bi00450a030
- Guillemain, G., Loizeau, M., Pinnçon-Raymond, M., Girard, J., and Leturque, A. (2000). The large intracytoplasmic loop of the glucose transporter GLUT2 is involved in glucose signaling in hepatic cells. *J. Cell Sci.* 113, 841–847.
- Hajiaghaalipour, F., Khalilpourfarshbafi, M., and Arya, A. (2015). Modulation of glucose transporter protein by dietary flavonoids in type 2 diabetes mellitus. *Int. J. Biol. Sci.* 11, 508–524. doi:10.7150/ijbs.11241
- Joost, H.-G., and Thorens, B. (2009). The extended GLUT-family of sugar/polyol transport facilitators: Nomenclature, sequence characteristics, and potential function of its novel members. *Mol. Membr. Biol.* 18, 247–256. doi:10.1080/09687680110090456
- Jung, J. H., Wang, X. D., and Loeken, M. R. (2013). Mouse embryonic stem cells established in physiological-glucose media express the high Km Glut2 glucose transporter expressed by normal embryos. *Stem Cell Transl. Med.* 2, 929–934. doi:10.5966/sctm.2013-0093
- Kasahara, T., and Kasahara, M. (1996). Expression of the rat GLUT1 glucose transporter in the yeast *Saccharomyces cerevisiae*. *Biochem. J.* 315, 177–182. doi:10.1042/bj3150177
- Kasahara, T., and Kasahara, M. (1997). Characterization of rat Glut4 glucose transporter expressed in the yeast *Saccharomyces cerevisiae*: comparison with Glut1 glucose transporter. *Biochim. Biophys. Acta* 1324, 111–119. doi:10.1016/S0005-2736(96)00217-9
- Katagiri, H., Asano, T., Ishihara, H., Tsukuda, K., Lin, J.-L., Inukai, K., et al. (1992). Replacement of intracellular C-terminal domain of GLUT1 glucose transporter with that of GLUT2 increases Vmax and Km of transport activity. *J. Biol. Chem.* 267, 22550–22555.
- Kraft, T. E., Hresko, R. C., and Hruz, P. W. (2015). Expression, purification, and functional characterization of the insulin-responsive facilitative glucose transporter GLUT4. *Protein Sci.* 24, 2008. doi:10.1002/pro.2812

- Kwok, S., Chang, S.-Y., Sninsky, J. J., and Wang, A. (1994). A guide to the design and use of mismatched and degenerate primers. *PCR Meth. Appl.* 3, 39–47. doi:10.1101/gr.3.4.s39
- Kwon, O., Eck, P., Chen, S., Corpe, C. P., Lee, J.-H., Kruhlak, M., et al. (2007). Inhibition of the intestinal glucose transporter GLUT2 by flavonoids. *FASEB J.* 21, 366–377. doi:10.1096/fj.06-6620com
- Leandro, M. J., Fonseca, C., and Gonçalves, P. (2009). Hexose and pentose transport in ascomycetous yeasts: An overview. *FEMS Yeast Res.* 9, 511–525. doi:10.1111/j.1567-1364.2009.00509.x
- Lee, Y., Lim, Y., and Kwon, O. (2015). Selected phytochemicals and culinary plant extracts inhibit fructose uptake in Caco-2 cells. *Molecules* 20, 17393–17404. doi:10.3390/molecules200917393
- Mueckler, M., and Thorens, B. (2013). The SLC2 (GLUT) family of membrane transporters. *Mol. Aspects Med.* 34, 121–138. doi:10.1016/j.mam.2012.07.001
- Ohtsubo, K., Takamatsu, S., Minowa, M. T., Yoshida, A., Takeuchi, M., and Marth, J. D. (2005). Dietary and genetic control of glucose transporter 2 glycosylation promotes insulin secretion in suppressing diabetes. *Cell* 123, 1307–1321. doi:10.1016/j.cell.2005.09.041
- Oldenburg, K., Vo, K. T., Michaelis, S., and Paddon, C. (1997). Recombination-mediated PCR-directed plasmid construction *in vivo* in yeast. *Nucleic Acids Res.* 25, 451–452. doi:10.1093/nar/25.2.451
- Qureshi, A. A., Suades, A., Matsuoka, R., Brock, J., McComas, S. E., Nji, E., et al. (2020). The molecular basis for sugar import in malaria parasites. *Nature* 578, 321–325. doi:10.1038/s41586-020-1963-z
- Santer, R., Groth, S., Kinner, M., Dombrowski, A., Berry, G. T., Brodehl, J., et al. (2020). The mutation spectrum of the facilitative glucose transporter gene SLC2A2 (GLUT2) in patients with Fanconi-Bickel syndrome. *Hum. Genet.* 110, 21–29. doi:10.1007/s00439-001-0638-6
- Santer, R., Schneppenheim, R., Dombrowski, A., Götze, H., Steinmann, B., and Schaub, J. (1997). Mutations in GLUT2, the gene for the liver-type glucose transporter, in patients with Fanconi-Bickel syndrome. *Nat. Genet.* 17, 324–326. doi:10.1038/ng1197-324
- Schmidl, S., Iancu, C. V., Choe, J.-Y., and Oreb, M. (2018). Ligand screening systems for human glucose transporters as tools in drug discovery. *Front. Chem.* 6, 183. doi:10.3389/fchem.2018.00183
- Schmidl, S., Iancu, C. V., Reifsnrath, M., Choe, J.-Y., and Oreb, M. (2021). A label-free real-time method for measuring glucose uptake kinetics in yeast. *FEMS Yeast Res.* 21, foaa069. doi:10.1093/femsyr/foaa069
- Simpson, I. A., Carruthers, A., and Vannucci, S. J. (2007). Supply and demand in cerebral energy metabolism: The role of nutrient transporters. *J. Cereb. Blood. Flow. Metab.* 27, 1766–1791. doi:10.1038/sj.jcbfm.9600521
- Simpson, I. A., Dwyer, D., Malide, D., Moley, K. H., Travis, A., and Vannucci, S. J. (2008). The facilitative glucose transporter GLUT3: 20 years of distinction. *Am. J. Physiol. Endocrinol. Metab.* 295, E242–E253. doi:10.1152/ajpendo.90388.2008
- Slubowski, C. J., Funk, A. D., Roesner, J. M., Paulissen, S. M., and Huang, L. S. (2015). Plasmids for C-terminal tagging in *Saccharomyces cerevisiae* that contain improved GFP proteins. *Envy and Ivy. Yeast* 32, 379–387. doi:10.1002/yea.3065
- Smirnova, I., Kasho, V., Jiang, X., Pardon, E., Steyaert, J., and Kaback, H. R. (2014). Outward-facing conformers of LacY stabilized by nanobodies. *Proc. Natl. Acad. Sci. U.S.A.* 111, 18548–18553. doi:10.1073/pnas.1422265112
- Solis-Escalante, D., van den Broek, M., Kuijpers, N. G. A., Pronk, J. T., Boles, E., Daran, J.-M., et al. (2015). The genome sequence of the popular hexose-transport-deficient *Saccharomyces cerevisiae* strain EBY.VW4000 reveals LoxP/Cre-induced translocations and gene loss. *FEMS Yeast Res.* 15, fou004. doi:10.1093/femsyr/fou004
- Thorens, B. (2015). GLUT2, glucose sensing and glucose homeostasis. *Diabetologia* 58, 221–232. doi:10.1007/s00125-014-3451-1
- Tripp, J., Essl, C., Iancu, C. V., Boles, E., Choe, J.-Y., and Oreb, M. (2017). Establishing a yeast-based screening system for discovery of human GLUT5 inhibitors and activators. *Sci. Rep.* 7, 124. doi:10.1038/s41598-017-06262-4
- Uldry, M., Ibberson, M., Hosokawa, M., and Thorens, B. (2002). GLUT2 is a high affinity glucosamine transporter. *FEBS Lett.* 524, 199–203. doi:10.1016/s0014-5793(02)03058-2
- van't Klooster, J. S., Cheng, T.-Y., Sikkema, H. R., Jeucken, A., Moody, B., and Poolman, B. (2020a). Periprotein lipidomes of *Saccharomyces cerevisiae* provide a flexible environment for conformational changes of membrane proteins. *eLife* 9, e57003. doi:10.7554/eLife.57003
- van't Klooster, J. S., Cheng, T.-Y., Sikkema, H. R., Jeucken, A., Moody, D. B., and Poolman, B. (2020b). Membrane lipid requirements of the lysine transporter Lyp1 from *Saccharomyces cerevisiae*. *J. Mol. Biol.* 432, 4023–4031. doi:10.1016/j.jmb.2020.04.029
- Wieczorke, R., Krampe, S., Weierstall, T., Freidel, K., Hollenberg, C. P., and Boles, E. (1999). Concurrent knock-out of at least 20 transporter genes is required to block uptake of hexoses in *Saccharomyces cerevisiae*. *FEBS Lett.* 464, 123–128. doi:10.1016/S0014-5793(99)01698-1
- Wu, X., Chi, R. J., Baskin, J. M., Lucast, L., Burd, C. G., De Camilli, P., et al. (2014). Structural insights into assembly and regulation of the plasma membrane phosphatidylinositol 4-kinase complex. *Dev. Cell* 28, 19–29. doi:10.1016/j.devcel.2013.11.012
- Wuest, M., Hamann, I., Bouvet, V., Glubrecht, D., Marshall, A., Trayner, B., et al. (2018). Molecular imaging of GLUT1 and GLUT5 in breast cancer: a multitracer positron emission tomography imaging study in mice. *Mol. Pharmacol.* 93, 79–89. doi:10.1124/mol.117.110007
- Yan, N. (2015). Structural biology of the major facilitator superfamily transporters. *Annu. Rev. Biophys.* 44, 257–283. doi:10.1146/annurev-biophys-060414-033901
- Zamora-Leon, S. P., Golde, D. W., Concha, I. I., Rivas, C. I., Delgado-Lopez, F., Baselga, J., et al. (1996). Expression of the fructose transporter GLUT5 in human breast cancer. *Proc. Natl. Acad. Sci. U.S.A.* 93, 1847–1852. doi:10.1073/pnas.93.5.1847
- Ziegler, G. C., Almos, P., McNeill, R. V., Jansch, C., and Lesch, K.-P. (2020). Cellular effects and clinical implications of SLC2A3 copy number variation. *J. Cell. Physiol.* 2020, 1–16. doi:10.1002/jcp.29753

Conflict of Interest: The authors declare that the research was conducted in the absence of any commercial or financial relationships that could be construed as a potential conflict of interest.

Copyright © 2021 Schmidl, Tamayo Rojas, Iancu, Choe and Oreb. This is an open-access article distributed under the terms of the Creative Commons Attribution License (CC BY). The use, distribution or reproduction in other forums is permitted, provided the original author(s) and the copyright owner(s) are credited and that the original publication in this journal is cited, in accordance with accepted academic practice. No use, distribution or reproduction is permitted which does not comply with these terms.



A GC-MS/Single-Cell Method to Evaluate Membrane Transporter Substrate Specificity and Signaling

Stephen J. Fairweather^{1,2*}, Shoko Okada³, Gregory Gauthier-Coles¹, Kiran Javed¹, Angelika Bröer¹ and Stefan Bröer¹

¹Research School of Biology, Australian National University, Canberra, ACT, Australia, ²Research School of Chemistry, Australian National University, Canberra, ACT, Australia, ³Commonwealth Scientific and Industrial Research Institute (CSIRO) Land and Water, Canberra, ACT, Australia

OPEN ACCESS

Edited by:

Piotr Koprowski,
Nencki Institute of Experimental
Biology (PAS), Poland

Reviewed by:

Elena Bossi,
University of Insubria, Italy
Ovidio Bussolati,
University of Parma, Italy
Christof Grewer,
Binghamton University, United States
Pattama Wiriyasermkul,
Jikei University School of Medicine,
Japan

*Correspondence:

Stephen J. Fairweather
Stephen.fairweather@anu.edu.au

Specialty section:

This article was submitted to
Cellular Biochemistry,
a section of the journal
Frontiers in Molecular Biosciences

Received: 27 December 2020

Accepted: 17 February 2021

Published: 13 April 2021

Citation:

Fairweather SJ, Okada S,
Gauthier-Coles G, Javed K, Bröer A
and Bröer S (2021) A GC-MS/Single-
Cell Method to Evaluate Membrane
Transporter Substrate Specificity
and Signaling.
Front. Mol. Biosci. 8:646574.
doi: 10.3389/fmolb.2021.646574

Amino acid transporters play a vital role in metabolism and nutrient signaling pathways. Typically, transport activity is investigated using single substrates and competing amounts of other amino acids. We used GC-MS and LC-MS for metabolic screening of *Xenopus laevis* oocytes expressing various human amino acid transporters incubated in complex media to establish their comprehensive substrate profiles. For most transporters, amino acid selectivity matched reported substrate profiles. However, we could not detect substantial accumulation of cationic amino acids by SNAT4 and ATB^{0,+} in contrast to previous reports. In addition, comparative substrate profiles of two related sodium neutral amino acid transporters known as SNAT1 and SNAT2, revealed the latter as a significant leucine accumulator. As a consequence, SNAT2, but not SNAT1, was shown to be an effective activator of the eukaryotic cellular growth regulator mTORC1. We propose, that metabolomic profiling of membrane transporters in *Xenopus laevis* oocytes can be used to test their substrate specificity and role in intracellular signaling pathways.

Keywords: mTORC1 signaling, SNAT2, slc38a2, GC-MS, metabolomics, *Xenopus laevis* oocytes, amino acid transporters, amino acid signaling

INTRODUCTION

Mass spectrometry (MS) is a sensitive, high-throughput and relatively inexpensive technology for the identification of small metabolites in complex chemical matrices. With the standardization of chemical libraries and chemical fragmentation conditions, gas chromatography-mass spectrometry (GC-MS) and liquid chromatography-mass spectrometry (LC-MS) have become ‘gold standards’ for metabolomics research (Fiehn, 2016), advancing our understanding of biological metabolism [reviewed in (Sarker and Nahar, 2012; Hübschmann, 2015; Lu et al., 2017)]. Despite widespread use, MS has rarely been utilized to study the dynamic flux of primary metabolites across plasma membranes, a process mediated by membrane transporters. Membrane transporters are proteins embedded in and/or spanning a membrane bilayer and are grouped by genetic sequence similarity within the Solute Carrier (SLC) superfamily (Kandasamy et al., 2018). Mechanistically, they can be classified as uniporters, symporters and exchangers (antiporters), utilizing electrochemical gradients to drive substrate transport and can consist of single or multiple protein subunits of the same or different genetic origin (Fairweather et al., 2020). Although GC-MS and LC-MS have been sporadically used to measure transporter substrate specificity and activity

(Grundemann et al., 2005; Abplanalp et al., 2013; Ebert et al., 2017) there has been little investigation of their potential utility in the study of the membrane flux of complex, physiologically relevant mixtures.

Single substrate techniques have been overwhelmingly used to understand transporter function [reviewed in (Broer, 2010; Grewer et al., 2013; Jani and Krajcsi, 2014; Fitzgerald et al., 2017; Broer and Fairweather, 2018)]. A large majority of known human transporters are capable of translocating multiple substrates across membranes and function in complex biological matrices. For instance, the amino acid exchanger LAT1-4F2hc (slc7a5-slc3a2) has over 50 known substrates to date (Uchino et al., 2002; Li and Whorton, 2005; Su et al., 2005; Wongthai et al., 2015; Zur et al., 2016; Ebert et al., 2017; Chien et al., 2018). Metabolomics utilizing GC- and/or LC-MS can expand our understanding of membrane transporters and related cellular phenotypes.

A widely used model for studying transport physiology are the oocytes of the female South-African clawed frog *Xenopus laevis* (Broer, 2010). This large single-cell system lends itself to measuring amino acid flux and metabolism as endogenous concentrations of most amino acids are low (Taylor and Smith, 1987; Meier et al., 2002). In addition, only two endogenous amino acid transport systems are detectable in oocytes, both expressed at much lower levels than heterologously expressed transporters (Taslimifar et al., 2017). Metabolic analysis using GC-MS has been performed once on *X. laevis* oocytes, however the aim was to conduct high sensitivity metabolomics from minimal sample volumes (Koek et al., 2010). *Xenopus* oocytes have also been utilized to reconstitute conserved multicellular signaling pathways by introducing a minimal number of exogenous membrane components (Vera and Rosen, 1990).

One potentially useful application of combining *X. laevis* transporter expression with metabolomic analyses would be to correlate intracellular amino acid levels with the status of intracellular signaling pathways such as mTOR and GCN2. The mTORC1 complex monitors cytosolic and lysosomal amino acid levels using indicative amino acids such as arginine, leucine (Hara et al., 1998; Christie et al., 2002; Beugnet et al., 2003; Nicklin et al., 2009; Jewell et al., 2015; Yoon et al., 2016; Zheng et al., 2016; Wyant et al., 2017; Lee et al., 2018), methionine (Gu et al., 2017), serine (Fan et al., 2016) and tryptophan (Christie et al., 2002). Both metabolic synthesis and plasma membrane uptake of glutamine have also been implicated in mTORC1 activation (Tan et al., 2017).

Multiple transporters have been advanced as direct or indirect activators of the mTORC1 pathway including SNAT2 (slc38a2) (Evans et al., 2007; Hyde et al., 2007; Evans et al., 2008), SNAT9 (slc38a9) (Rebsamen et al., 2015; Wang et al., 2015), LAT1-4F2hc (slc7a5-slc3a2) (Fuchs et al., 2007; Nicklin et al., 2009), ASCT2 (slc1a5) (Fuchs et al., 2007; Nicklin et al., 2009), PAT1 (slc36a1) (Heublein et al., 2010; Zoncu et al., 2011; Wu et al., 2016; Zhao et al., 2019) and PAT4 (slc36a4) (Heublein et al., 2010; Fan et al., 2016; Zheng et al., 2016). A number of studies have now firmly established that SNAT9 is a lysosomal arginine sensor for mTORC1 (Jung et al., 2015; Rebsamen et al., 2015; Wang

et al., 2015; Rebsamen and Superti-Furga, 2016; Wyant et al., 2017) by direct interaction of the transport N-terminal with the Rag GTPase-Ragulator-FLCN:FNIP2 complex upon arginine sensing (Fromm et al., 2020; Lei et al., 2020). Another widely proposed mechanism is glutamine accumulation by ASCT2, followed by its exchange for leucine import via LAT1-4F2hc (Fuchs et al., 2007; Nicklin et al., 2009). However, ASCT2 knock-out studies in several cell lines have failed to observe a reduction of mTORC1 activity (Broer et al., 2000; Bode et al., 2002; Broer et al., 2016). SNAT2 and Golgi localized PAT4 have been suggested as mTORC1 activators by acting as membrane ‘transceptors’, where extracellular binding of substrate and allosterically-mediated signal transduction causes activation of mTORC1 (Goberdhan et al., 2005; Pinilla et al., 2011; Fan et al., 2016). For leucine, however, the transceptor mechanism appears unlikely as leucine-mediated mTORC1 activation has been shown to require an intracellular leucine increase (Christie et al., 2002; Beugnet et al., 2003).

In this study we combine the advantages of *X. laevis* oocytes in studying membrane transporter physiology with metabolomics to study membrane transporters in complex biochemical matrices. We show that single cell/metabolomics can be used to identify the comprehensive substrate profile of numerous amino acid transporters of various mechanisms in a time-efficient, robust manner using minimal sample preparation. As a proof-of-concept we identify the small neutral amino acid transporter SNAT2 as a direct and specific activator of mTORC1.

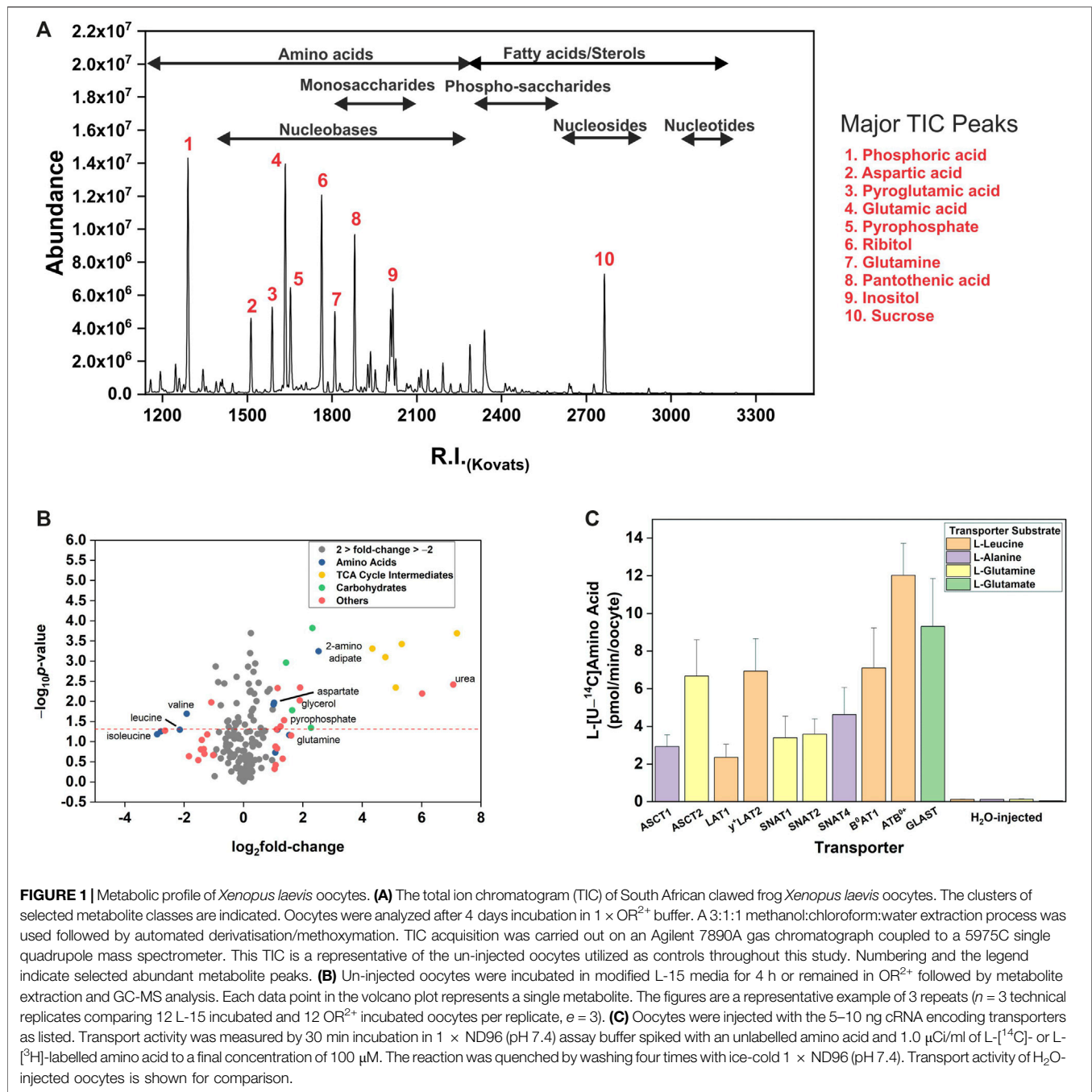
MATERIALS AND METHODS

Xenopus laevis Surgery and Oocyte Preparation

Female *Xenopus laevis* frogs were anaesthetised by submersion for 30 min in 3-Aminobenzoic acid ethyl ester (1.5 g/L) (Sigma-Aldrich, St Louis, MO, United States). Anesthetized frogs were placed on ice to slow blood flow and surgery was conducted as previously described (Broer, 2010; Parker et al., 2019). Pieces of ovary were transferred into OR²⁻ buffer (82.5 mM NaCl, 2.5 mM KCl, 1 mM MgCl₂, 1 mM Na₂HPO₄, 5 mM Hepes-NaOH, pH 7.8) in a fresh Petri dish and cut into small clumps of ~ 15 to 30 oocytes and were digested in 1.5 mg/ml collagenase D and 0.1 mg/ml collagenase A (Sigma-Aldrich) dissolved in OR²⁻ (pH 7.8) buffer for 2–4 h at 28°C. Following digestion, oocytes were washed and examined for the extent of defolliculation and individual separation. Defolliculated oocytes were maintained in OR²⁺ buffer (OR²⁻ supplemented with 1.5 mM CaCl₂ and 50 µg/ml gentamycin, pH 7.8) at 16–18°C. Maintenance of animals and preparation of oocytes was approved by the Australian National University animal ethics review board (ANU Protocol A2017/36).

Transporter Expression in Oocytes

Transporter and other gene constructs were all subcloned into the pGem-He-Juel (pGHJ) expression vector as previously described (Supplementary Table S1). Constructs were linearized using *Sall* or *NotI* restriction endonucleases (NEB, Ipswich, MA, United States) and mRNA was synthesized using *in vitro*



transcription with either T7 or SP6 mMessage mMachine kits (Ambion, Austin, TX, United States). After purification using phenol-chloroform extraction and precipitation, cRNA was quantified using a Nanodrop spectrophotometer and adjusted to 1 mg/ml (Thermo Fisher Scientific, Scoresby, VIC, Australia) ($\text{OD}_{260}/\text{OD}_{280}$) (Broer, 2003; Kowalczyk et al., 2008). Micro-injection of cRNA into oocytes was performed using a Micro4TM micro-syringe pump controller and A203XVY nanoliter injector (World Precision Instruments). The injection amount of all cRNAs was optimized previously or for this study (Broer et al., 2000; Broer et al., 2001; Bohmer et al., 2005; Kowalczyk

et al., 2008; Fairweather et al., 2012). Oocytes were used 2–4 days post-injection unless otherwise indicated and as previously optimized for specific transporters. Oocytes were maintained in OR^{2+} (pH 7.8) buffer.

Oocyte Flux Experiments

Flux experiments in oocytes have been detailed previously (Broer, 2010; Fairweather et al., 2015). Briefly, batches of 7–10 oocytes were incubated in $1 \times \text{ND96}$ oocyte assay buffer (96 mM NaCl, 2 mM KCl, 1 mM MgCl_2 , 1.8 mM CaCl_2 , 5 mM HEPES-NaOH pH 7.4) spiked with an unlabelled amino acid and $1.0 \mu\text{Ci/ml}$ of

L-[¹⁴C]- or L-[³H]-labelled amino acid at a final concentration of 100 µM in order to quantify the uni-directional flux. Oocytes were incubated with radiolabeled substrate for 20–30 min before the reaction was quenched by washing four times with ice-cold ND96 followed by transfer into a 96-well plate (PerkinElmer, Waltham, Massachusetts, United States). Oocytes were then lysed using 10% (w/v) SDS and mixed with 5 × volume of scintillation fluid for radioactive counting in a MicroBeta²® 2450 96-well Microplate counter (PerkinElmer).

A modified formulation of Leibovitz's L-15 cell culture medium was developed for oocyte incubation prior to GC-MS or LC-MS analysis. To this end, L-15 was supplemented with 20% (v/v) Fetal Calf Serum (FCS, Gibco), 20 mM HEPES and four amino acids absent from the standard formulation (see **Supplementary Table S2**). To adjust for osmolarity, the medium was diluted with 14% (v/v) MilliQ H₂O. For metabolomics experiments, 12 oocytes were washed three times and then incubated in 35 mm cell culture dishes with 2 ml of modified L-15 for the indicated period of times. The number of oocytes used was optimized by balancing the requirement to detect all possible substrates for each transporter, even low affinity ones, with the need to keep large metabolite peaks under GC-Q detection threshold and to minimize the increase in endogenous oocyte metabolites such as TCA cycle intermediates and anionic amino acids. For sample extraction, oocytes were transferred to 1.5 ml Eppendorf tubes and washed four times with 1 ml of ice-cold MilliQ H₂O before sample extraction for MS analysis (see below).

To analyze amino acid exchanger activity, oocytes were preloaded with either 10 mM of unlabelled substrate or unlabelled substrate supplemented with [¹⁴C]-labelled amino acid at 16°C for 24 h. All substrates were dissolved in ND96 oocyte assay buffer. Once pre-loading was complete oocytes were washed four times with 1 ml of ice-cold MilliQ H₂O, or washed three times in modified L-15 depending on the experimental condition. For experiments where mTORC1 substrates were detected, oocytes were incubated with various media as indicated in figure legends, specifically either the L-15 based media, Leu alone at 1 mM or a 20 canonical amino acid mix with each amino acid at 1 mM concentration.

Oocyte Metabolite Extraction and GC-MS Analysis

Preparation of all oocyte samples for GC-MS analysis was conducted following an established protocol for untargeted metabolomics (Carroll et al., 2010; Fiehn, 2016; Javed et al., 2018). Metabolites from oocyte samples were extracted using a 3:1:1 ratio of CH₃OH:CHCl₃:H₂O (v/v) mixture. Ribitol (100 ng/µl) was added to each mixture as an internal standard. Samples were vortexed vigorously to lyse and homogenize oocytes and then centrifuged at 16,000 × g for 5 min at 4°C. The supernatant was transferred to a new tube and ½ volume equivalent of MilliQ H₂O (0.2 µm-filtered) was added to extract hydrophilic metabolites. The samples were centrifuged again at 16,000 × g for 5 min at 4°C. The upper aqueous phase was transferred to a new tube and stored for up to 1 week at –80°C for later use. For

immediate GC-MS analysis, 200 µl of the extract was transferred into 12 × 32 mm amber crimp top vials with 300 µl capacity inserts (5188-6594, Agilent Technologies, Palo Alto, CA, United States). The samples were desiccated using a miVac DUO concentrator (SP Scientific, Ipswich, United Kingdom) for 4 h and then sealed using 11 mm PTFE/rubber septa crimp caps (Agilent Technologies).

A single quadrupole GC/MSD instrument was used in this study, with the GC (Agilent 7890A) coupled to a single quadrupole mass spectrometer (Agilent 5975C). The GC was equipped with a J&W VF-5 ms column (30 m × 0.25 mm; 0.25 µm), connected to a 10 m EZ-Guard column (Agilent Technologies, Palo Alto, CA, United States). Two derivatization steps (methoximation and trimethylsilylation) and sample injection were performed by a robotic Gerstel MPS2 multipurpose auto-sampler and injector (GERSTEL GmbH and Co. KG, Mülheim an der Ruhr, Germany). To this end the dried extracts were first incubated with 10 µl of anhydrous pyridine (Sigma-Aldrich) containing 20 mg/ml methoxyamine hydrochloride (Sigma-Aldrich) at 37°C for 90 min. Subsequently, 15 µl of N-methyl-N-(trimethylsilyl) trifluoroacetamide (MSTFA; Sigma-Aldrich) was added at 37°C for 30 min to ensure maximal derivatization. For Kovats non-isothermal retention index (RI) matching, n-alkanes (5 µl of 29 mg/L, C12, C15, C19, C22, C28, C33, C36, Sigma-Aldrich) were also added to the derivatized samples and incubated for 1 min at 37°C, followed by injection onto the column. All samples were run in splitless injection mode, with 1 µl injected at a rate of 50 µl/sec. The inlet temperature was 230°C and helium (He₂) was used as a carrier gas at a flowrate of 1 ml/min. The GC column oven was held at an initial temperature of 70°C for 1 min before increasing to 325°C at a ramp rate of 15°C/min. The solvent delay for the 15°C/min ramp was 6.2 min. Once the oven reached 325°C it was held for 3 min, making a total run time of 21 min/sample. The electron impact (EI) ion source and quadrupole were kept at 250 and 150°C, respectively. The filament current was set at 70 eV. The auxiliary transfer line was at 260°C and the quadrupole mass analyser was operated in full MS scan acquisition mode from 40 to 600 m/z using a scan rate of 3.6 Hz. Quality control (QC) samples were prepared by pooling aliquots from all sample extracts, dried down and derivatized as per oocyte extracts. Derivatized QC samples were injected at the start of the run and also after every 8 samples until the end of each run. Blank samples of 200 µl 1:1 CH₃OH:H₂O were run at the start and end of each batch to monitor column contaminants in addition to washing with 3 × injections of 1 µl methanol before and after the running of each batch. All batches included a standard mix containing 20 canonical amino acids plus L-ornithine that was dried down, derivatized and analyzed at the beginning, mid-run and at the end of each batch. Amino acids with good response factors were added at 1 µg/amino acid, those with poorer response factors (L-Arg, L-Ala, L-His, L-Trp, L-Cys) were added at 10 µg/amino acid.

For the quantification of endogenous *X. laevis* oocyte amino acids calibration curves from ultrapure amino acid standards (Sigma) were generated. The linear range of each amino acid was

TABLE 1 | Free endogenous amino acid pools in stage 5 and 6 *Xenopus laevis* oocytes.

Amino acid	EIC (m/z)	GC-MS ^a		HPLC
		Concentration (μ M)	pmol/oocyte (mean \pm S.E.M)	Range ^b (pmol/oocyte)
Valine	144	499 \pm 121	182 \pm 55	40–195
Leucine	158	77 \pm 25	28 \pm 9	20–44
Isoleucine	158	110 \pm 36	40 \pm 13	16–34
Proline	142	310 \pm 110	113 \pm 40	30–83
Glycine	174	64 \pm 9	23 \pm 3	22–92
Serine	204	290 \pm 38	106 \pm 14	112–263
Alanine	188	222 \pm 33	81 \pm 12	32–94
Threonine	218	96 \pm 33	35 \pm 12	16–106
Aspartic acid	232	2349 \pm 1050	857 \pm 383	409–2200 ^d
Methionine	176	124 \pm 52	45 \pm 19	6–27
Cysteine	220	58 \pm 16	21 \pm 6	9–21
Glutamic acid	246	1869 \pm 669	682 \pm 244	793–2000 ^e
Phenylalanine	216	93 \pm 38	34 \pm 14	10–33
Asparagine	231	650 \pm 214	237 \pm 78	–
Glutamine	156	1455 \pm 104	531 \pm 38	–
Arginine	157	288 \pm 105	105 \pm 38	51–188
Lysine	156	85 \pm 44	31 \pm 16	25–195
Histidine	154	121 \pm 47	44 \pm 17	28–236
Tyrosine	280	493 \pm 80	180 \pm 29	27–92
Tryptophan	202	33 \pm 11	12 \pm 4	–

^aConcentrations calculated for oocytes assuming an intracellular water-accessible volume of 365 nL as previously reported (Stegen et al., 2000).

^bConcentrations taken from (Taylor and Smith, 1987; Meier et al., 2002) for HPLC measurements take into account the full range of reported values included means \pm S.D.

^cIncludes values for both glutamate and glutamine combined.

^dIncludes values for both aspartate and asparagine combined.

determined first and as a result they were run as grouped standards based on their comparative response factors (R_f), either as high, medium, or low R_f amino acids. Standards were interspersed throughout runs and six data points used per amino acid to generate linear nmol vs peak height plots. Concentrations of endogenous amino acids were calculated and converted to pmol/oocyte based on a previously determined water-accessible volume of stage 5–6 oocytes (Stegen et al., 2000) and compared with previously determined values using HPLC (Table 1) (Taylor and Smith, 1987; Meier et al., 2002). We further confirmed that trimethylsilyl (TMS) derivatization of detected metabolites was consistent and produced a predominately single TMS-derivative of potential substrates (Supplementary Table S3). The proportional TMS-derivatization of all 20 proteinogenic amino acids and some of their GC-MS by-products demonstrated that, besides aspartic acid and serine, all were detected by a single TMS-variant at greater than 80% of the total signal. All raw GC-MS raw data sets are available on the MetaboLights repository (www.ebi.ac.uk/metabolights/MTBLS2476) (Haug et al., 2020).

GC-MS Sample Data Analysis

For GC-MS data acquisition the Agilent MSD Chemstation software (version E.02) was used. The acquired MS data was converted into CDF format by Agilent MSD Chemstation software (Agilent Technologies). Ribitol was used as the internal standard spiked into all GC-MS samples to ensure consistency of oocyte sample extraction by measuring m/z peak height and integrated area in every sample. If the ribitol signal deviated by more than 10%, then the samples were discarded. The peaks associated with the internal standard (ribitol) and n-alkanes standards for R.I. calculation

(n-alkanes) were removed from processed data sets unless otherwise shown. Any identified m/z peaks which increased over the time of a batch run independently of any other variable was removed. Any column contaminants as observed from sample blanks derivatized blank samples were also removed.

Peak extraction and quantification from total ion chromatograms (TICs) was conducted using the MetabolomeExpress online software (<https://www.metabolome-express.org/>) according to published protocols (Carroll et al., 2010; Javed et al., 2018). Briefly, for each GC-MS run the retention times of internal alkane standards were used to generate a R.I. calibration file for metabolite identification by MetabolomeExpress. Raw data files were loaded onto the MetabolomeExpress server and peaks detected using the following parameters (all units are arbitrary MS abundance units unless otherwise stated): slope threshold = 200, min. peak area = 1,000, min peak height = 500, min. peak purity factor = 2, min. scan threshold for peak width = 5. Peak detection was followed by peak identification using the following parameters: RI window = 4, MST centroid distance = \pm 1R.I., min peak area = 1,000, MS Qualifier Ion Ratio Error Tolerance = 30%, min number of correct ratio MS qualifier ions = 2, max. average MS ratio error = 70%, min similarity product = 60%. The two libraries used for metabolite identification were the Pooled Tea. MSRI (Public MetabolomeExpress Library) and Golm Metabolome database (GMD, <http://gmd.mpimp-golm.mpg.de/>).

Extracted peak tables (EIC) were exported as mzrtMATRIX files for further metabolite identification and analysis using additional software. Several criteria were used to unambiguously identify metabolites. Identification criterion 1 (Supplementary Table S4) utilized the GMD and automated

identification in the AMDIS program (Hummel et al., 2010). For this MetabolomeExpress was used for peak deconvolution prior to identification by AMDIS, to overcome a previously highlighted flaw in AMDIS, where m/z peaks were not reported if not present in all samples (Lu et al., 2008; Behrends et al., 2011). This approach also assisted in helping to remove any false positive metabolite identification by AMDIS. Extracted peaks were verified (a) by correct R.I. (± 3.0 R.I. units), and (b) the presence of four characteristic m/z peaks (with a score of ≥ 850 for overall metabolite similarity). For inclusion in the analysis, symmetry about the peak centroid, and a minimal abundance of ≥ 500 units of the AMDIS deconvoluted peak were required. Verification of the 20 canonical amino acids following criterion 1 combined with the use of standards represents identification criterion 2. EIC quantification was derived only from MetabolomeExpress as AMDIS does not use a common m/z ion fragments when quantifying the same metabolite across multiple samples (Aggio et al., 2011). If a metabolite could not be identified by criteria 1 or 2, we used automated and manual searches of the NIST library. Any metabolite identified with a reverse spectral (head to tail) match score of ≥ 700 and verified by the presence of the two most abundant m/z peaks was listed as identified by criterion 3 (Supplementary Table S4). Using these 3 criteria, all peaks were further verified manually using the GMD and the Human Metabolome database (HMDB, <http://www.hmdb.ca/>). Any manual identification or verification of EIC identity excluded the use of major TMS peaks at 73 and 147 m/z .

Oocyte Sample Extraction and LC-MS Analysis

To corroborate data from GC-MS and radiolabeled amino acid uptake experiments, we used LC-MS (Supplementary Table S5). Samples were prepared from oocytes using the same extraction protocol as for GC-MS with the exception that ribitol was substituted with 2.4 μl [^{13}C]labeled amino acids (MSK-A2-1.2 and CLM-1822-H-0.1; Cambridge Isotope Laboratories; pooled together at a concentration of 500 μM) as the internal standards. Dried extracts were dissolved in 10 mM ammonium acetate: acetonitrile (15:85 + 0.15% formic acid) for LC-MS analysis.

Amino acids for SNAT4 and ATB⁰⁺ flux assay (Figure 4A) were detected using an Orbitrap Q-Exactive Plus (Thermo Fisher) coupled to an UltiMate 3000 RS UHPLC system (Dionex) and separated by a 3 μm ZIC cHILIC 2.1 \times 150 mm column (EMD Millipore). The mobile phase was composed of A (10 mM ammonium acetate +0.15% formic acid) and B (acetonitrile + 0.15% formic acid) and was delivered at a flow rate of 0.4 ml/min with the following gradient elution: 15% A from 0 to 5 min, then a linear increase to 36% at 10 min, followed by an increase to 64% at 12.1 min where it was held until 17 min before returning to 15% at 17.1 min where it was maintained until the end of the run to re-equilibrate the column. The total run time for each sample was 21 min. Sample injection volume was 4 μl and the column oven temperature was kept at 35°C. Analytes were ionized in positive mode by heated electrospray ionization with an ion spray voltage of 3,500 V. Sheath gas flow was set to 50 units, auxiliary gas flow

to 13 units and sweep gas flow to 3 units. Capillary temperature was 263°C and auxiliary gas heater temperature was 300°C. Analysis was performed in full scan mode ($R = 35,000$) and quantification was achieved using Xcalibur (Thermo Fisher) by comparing the area under the peak of each amino acid and their respective isotope-labelled internal standard. Data for cRNA injected oocyte samples was represented by fold changes over the un-injected oocyte controls incubated in matched conditions. Blanks were included throughout each sequence run to monitor analyte carry-over and external standards were included at the beginning and end of each sequence for quality-control purposes.

For the detection of uninjected oocyte metabolites (Supplementary Table S5), slight modifications were made to the chromatographic method. The gradient started with 80% mobile phase B (Acetonitrile; 0.1% v/v Formic acid) and 20% mobile phase A (10 mM ammonium formate; 0.1% v/v formic acid) at a flow rate of 300 $\mu\text{l}/\text{min}$, followed by a linear gradient to 20% mobile phase B over 18 min. A re-equilibration phase of 12 min using 80% mobile phase B was done with the same flow rate, making a total run time of 30 min. The column temperature and injection volume remain unchanged to the above method. The settings for the mass detection were also changed slightly with resolution set to 70,000 m/z range 60–900, AGC target set to 3×10^6 , sheath gas set to 40 units, auxiliary gas set to 10 units, sweep gas flow set to 2 units, capillary temperature set to 250°C, and spray voltage set to +3.5 kV. The MS/MS data was collected through data dependent top 5 scan mode using High-energy C-trap Dissociation (HCD) with resolution 17,500 m/z , AGC target set to 1×10^5 and Normalized Collision Energy (NCE) 30%. A pooled sample of all extracts was used as a quality control (QC) sample to monitor signal reproducibility and stability of analytes. For LC-MS/MS data analysis of un-injected oocytes metabolites, the acquired raw metabolite data were converted into mzXML format and processed with the open-source software MS-DIAL (Tsugawa et al., 2015). The identification was done using publicly available MS/MS libraries by matching exact mass (MS tolerance 0.01 Da) and mass fragmentation pattern (MS tolerance 0.05 Da). Putative metabolite identifications were then confirmed by the use of standards. Raw peak height was used for the quantification of metabolites.

Phylogenetic Identification and Analysis of *X. laevis* mTORC1 Substrates

X. laevis homologues of human mTORC1 pathway proteins were identified by using the human protein sequence to create a profile Hidden Markov Model (HMM) using the phmmer algorithm at the HMMER project (Potter et al., 2018) (Dates 12-2-2020 to 16-4-2020). For each mTORC1 pathway protein the HMM profile was searched against all reference proteomes with the following options: sequence e-value = 0.01, e-value hit = 0.03, open gap penalties = 0.02, extend gap penalties = 0.4, substitution rate matrix = BLOSUM62. Taxonomic filters were set to limit results to human and amphibians. Multiple sequence alignments for each protein were constructed using PROMALS3D (Pei and Grishin, 2007) and analyzed for conservation using BioEdit 7.2 followed by selection of the highest ranked *X. laevis* homologue. The homology of

mTORC1 *X. laevis* and human proteins were verified using OrthoDB v10.1.

Western Blotting on Oocytes of mTORC1 Substrates

Electrophoresis was performed using 4–12% Bis-Tris polyacrylamide NuPAGE gels (Thermo Fisher Scientific) in an XCell SureLock Mini-Cell (Thermo Fisher Scientific) under reducing conditions according to standard procedures and using either MES or MOPS buffer. The SeeBlue Plus 2 pre-stained protein ladder (Thermo Fisher Scientific) was used to estimate the apparent molecular weight of proteins. Following SDS-PAGE, proteins were transferred onto nitrocellulose membranes (GE Healthcare) using the Mini Trans-Blot Electrophoretic Transfer Cell (Bio-Rad) according to standard protocols. Blots were blocked for 2 h at room temperature (or overnight at 4°C) in 50 ml of 10% (w/v) skim milk in PBS, pH 7.4, with 0.15% Tween 20 (PBS-T). After washing thrice in PBS-T for 10 min each, the blots were incubated with the primary antibody for 2 h or overnight in 5 ml of skim milk (2%, w/v) in PBS-T. The following primary antibodies and dilutions were used: anti-4E-BP1 (1:2,000) (catalogue #9644), anti-Phospho-4E-BP1 (Thr37/46) (1:2,000) (#2855), anti-S6 (1:2,000) (#2217), anti-Phospho-S6 (Ser240/244) (1:1,000) (#5364), anti-p70S6K (1:1,000) (#2708), anti-Phospho-p70S6K (Ser371) (1:1,000) (#9208) (all Cell Signaling Technology). All antibodies to human immunogens were raised in rabbit and were previously validated against mTORC1 targets (Broer et al., 2016). The HRP-conjugated anti-rabbit secondary IgG was used at 1:2,000 dilution for all primary antibodies (Cell Signaling Technology). Excess primary antibody was removed by washing thrice in PBS-T. Blots were incubated with 5 ml of diluted secondary antibody for 2 h. After washing thrice in PBS-T and a final rinse in PBS, immunoreactive bands were detected by enhanced chemiluminescence using Luminata Crescendo or Luminata Forte Western HRP Substrate (Millipore Merck). For reprobing, the same blots were incubated for 30 min at 70°C in 50 ml of stripping buffer (62.5 mM Tris-HCl, pH 6.8, 2% SDS, 100 mM 2-mercaptoethanol) and then alternate proteins detected by the same procedure as outlined. Western blots were quantified, where indicated, by densitometry analysis using the ImageJ 1.53e.

Statistical and Data Analysis

In addition to Metabolomic software outlined above for metabolite peak extraction, deconvolution, and identification, the software package OriginPro 2020b was used for data analysis and graphics suite CoralDraw v7 and v22 for figure generation. All experimental groups were checked for both normality of the distribution using the Shapiro-Wilks test and homogeneity of the variance using Levene's test. Metabolite levels of transporter-expressing oocytes were first normalized by subtracting un-injected oocytes signals for each metabolite incubated in the same media for the same time period. Paired *t*-tests were used to compare the significance of mean differences between the same metabolite across two experimental conditions. Calibration curves for quantification of endogenous amino acids were fitted to linear functions and adjusted R^2 values were computed. The adjusted R^2 values for all single amino acid linear regression were greater than or equal to 0.94.

RESULTS

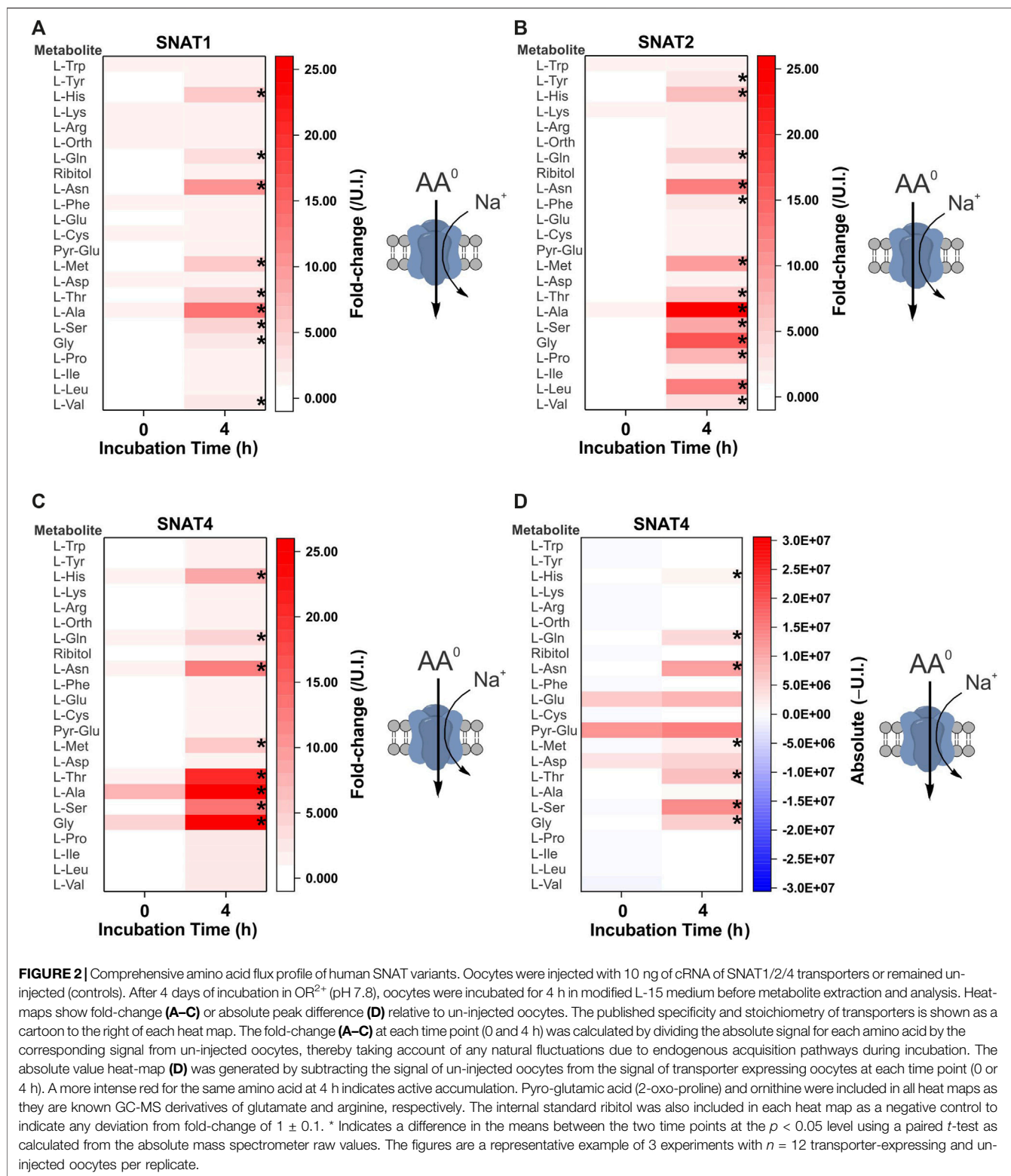
Validation of *X. laevis* Oocytes for Untargeted Metabolomics Profiling

Using two metabolomic analysis software packages and manual verification we identified 141 metabolites with GC-MS (Supplementary Table S4). The distribution density of major metabolite classes showed that amino acids ranged between values of 1180.0–2218.3, while monosaccharides were clustered from RI 1743.0 to 2078.1 (Figure 1A). In addition, we observed sugar phosphates, nucleotides, sterols and lipids clustered between RI 1992.0 and 3191.8. We were also able to detect all TCA cycle intermediates, numerous vitamins and other enzyme co-factors (Supplementary Table S4). Abundant metabolites characteristic for stage 5/6 *X. laevis* oocytes were pantothenic acid (vitamin B₅, RI 1984.3), sucrose (RI 2715.5), glutamic acid (RI 1616.1 and RI 1523.9 as pyroglutamic acid), and aspartic acid (RI 1421.1 for 2TMS derivative and 1508.0 for 3TMS derivative). After testing between six and 40 oocytes per experimental condition, the number required for robust and wide-ranging metabolite identification was established at twelve. Especially important was the ability to detect and identify all 20 proteinogenic amino acids and their main GC-MS by-products. As previously noted, substantial quantities of arginine are converted into ornithine, and of glutamate and glutamine into pyroglutamic acid (Leimer et al., 1977). However, all three amino acids were still detected chemically unaltered at lower abundance. We next established accurate endogenous concentrations for free AA in oocytes by generating calibration curves for all 20 proteinogenic AAs and quantifying them using LC-MS and GC-MS, with Table 1 showing GC-MS derived endogenous concentrations. As previously reported, all neutral and cationic AA were calculated to have endogenous intracellular oocyte concentrations below <500 μM with the exception of valine, asparagine and glutamine. Aspartate and glutamate were more abundant at ~2 mM. These data are in the range of previous results (Taylor and Smith, 1987; Meier et al., 2002), except that glutamate was lower in our oocyte preparation, while isoleucine, proline, methionine and tyrosine were higher, although none beyond the range of previous values if standard deviations are taken into account.

Our LC-MS metabolomics method was able to identify 38 metabolites, of which 31 had also been identified by GC-MS (Supplementary Table S5). Some water-soluble metabolites such as biotin, betaine, choline, citrulline, maltose and phosphocreatine were detected by LC-MS but not by GC-MS. Some of these are not present in the GOLM metabolite database (<http://gmd.mpimp-golm.mpg.de/>), indicating that GC-MS detection of these metabolites might be difficult and that our metabolomics analysis of *X. laevis* oocytes was not fully comprehensive.

Substrate Profiles of Membrane Transporters Measured by GC-MS

Oocytes from *X. laevis* have long been utilized for the comprehensive analysis of membrane transporters. To understand endogenous permeability, we wanted to observe if endogenous oocyte metabolites fluctuate during incubation in a complex substrate matrix (biomimetic L-15 medium). Due to the



large volume, un-injected oocytes required greater than 3 h incubation for detection of the lowest response factor amino acid alanine (R.I. 1360). Transporter-injected oocytes also required >2 h incubation in order to detect changes of all

substrate amino acids. As a result of this optimization, 4 h incubations were used for all subsequent transporter experiments. The majority of metabolites identified in un-injected oocytes showed a less than 2-fold ($\log_2 = 1$) increase

or decrease after 4 h incubation (**Figure 1B**). Several TCA cycle intermediates, numerous monosaccharides, urea, pyrophosphate and glycerol were increased > 2-fold. Amino acids showed a divergent response with aspartate, glutamine, and 2-aminoadipate increasing >2-fold, while branched-chain amino acids (BCAA) valine, leucine and isoleucine decreased >2-fold. This analysis suggests that endogenous oocyte metabolism needs to be considered during long-term incubation. Prior to the measurement of transporter-mediated membrane flux using GC-MS, functional expression of all transporters was confirmed using radiolabeled substrates (**Figure 1C**).

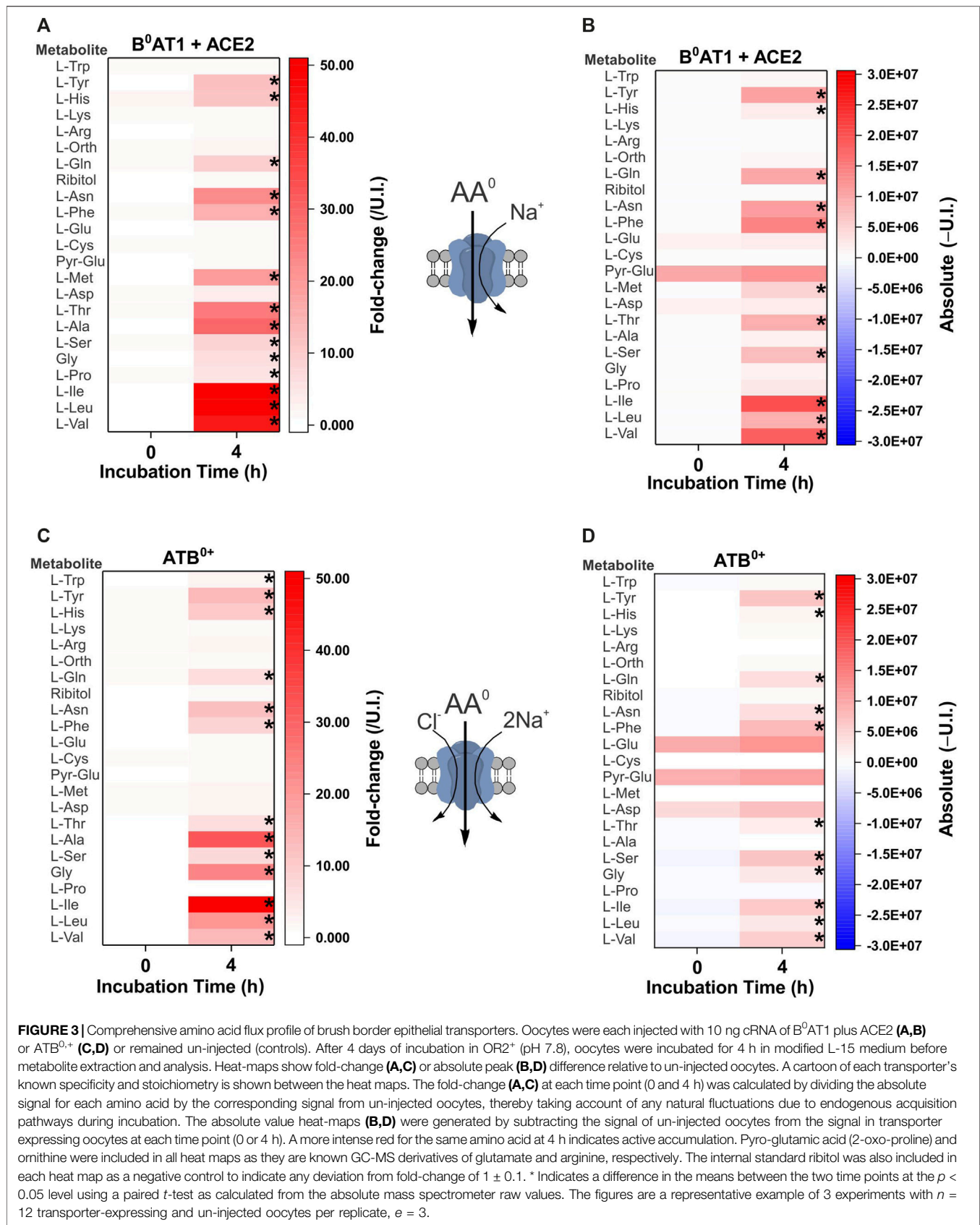
The first cohort of membrane transporters tested were the sodium-neutral-amino-acid symporters of the SNAT (slc38) family, which are ubiquitously expressed and represent the major acquisition pathway for neutral amino acids in many healthy and malignant human cells (Broer and Broer, 2017; Broer and Fairweather, 2018) (**Figure 2**). Symporters are well-suited to the study of metabolite fluxes following complex matrix incubation as they are able to accumulate intracellular substrates. The GC-MS analysis broadly replicated previously reported substrate specificity with some exceptions. Notably, SNAT2 was able to accumulate a broader range of neutral amino acids than SNAT1, including proline, leucine, and to a smaller extent phenylalanine and tyrosine (**Figures 2A,B**). Both had been previously characterized as having similar specificity for small and polar neutral amino acids with lower affinity for hydrophobic neutral amino acids (Hatanaka et al., 2000; Wang et al., 2000). SNAT4 had a similar substrate spectrum as SNAT1, with a preference for smaller amino acids, such as glycine, alanine, serine, asparagine and threonine. In contrast to previous reports (Sugawara et al., 2000; Hatanaka et al., 2001), we could not find evidence for accumulation of cationic amino acids from a complex substrate matrix—only the amphiprotic histidine was accumulated (**Figure 2C**). Fold-change analysis can miss accumulation by SNAT4 of solutes that are naturally abundant in oocytes. As a result, we also analyzed absolute signal differences, but were still unable to detect significant increases of arginine or lysine in SNAT4-expressing oocytes (**Figure 2D**).

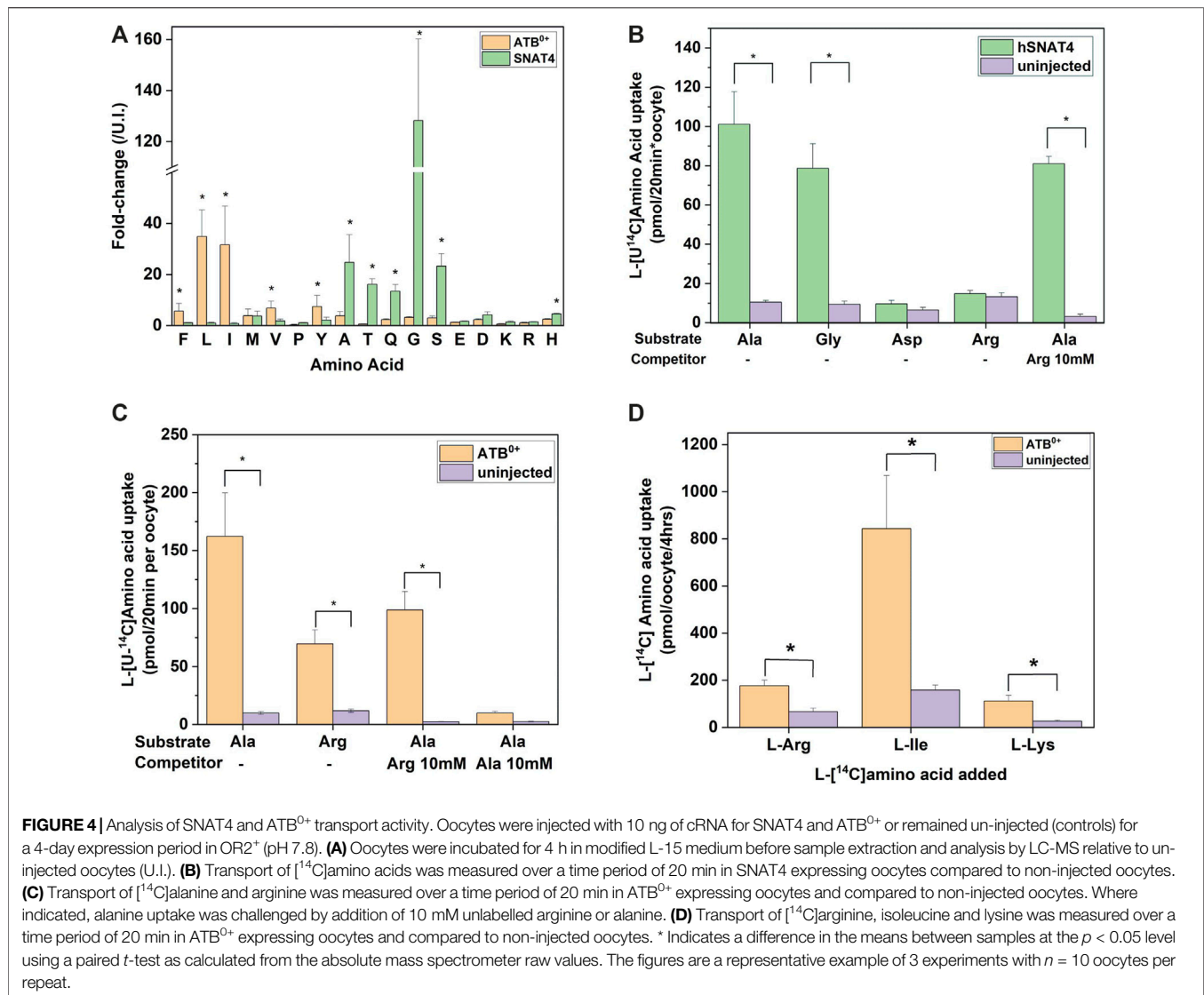
The second cohort of transporters we analyzed were the apical epithelial symporters B⁰AT1-ACE2 (slc6a19/ACE2) and ATB⁰⁺ (slc6a14) (**Figure 3**). The B⁰AT1-ACE2 transporter displayed a substrate profile that included all neutral amino acids (**Figure 3A**). This was consistent with well-established *in vitro* and *in vivo* profiles (Bohmer et al., 2005; Camargo et al., 2005; Kowalczyk et al., 2008; Singer et al., 2012; Javed and Broer, 2019) with the exception of Trp, a low affinity substrate of B⁰AT1. Due to the low tryptophan concentration in our biomimetic L-15 medium, its transport may have been outcompeted by other amino acids. Analyzing the absolute MS signal also did not reveal a significant increase of tryptophan in B⁰AT1-ACE2 expressing oocytes (**Figure 3B**). The substrate profile of ATB⁰⁺ also matched closely to the order of affinity for transporter substrates measured in isolation (Sloan and Mager, 1999), with the significant exception of cationic amino acids arginine, lysine and the neutral amino acid methionine, all of which remained unchanged (**Figure 3C**). Examining the change in absolute MS signal also did not reveal accumulation of cationic amino acids

(**Figure 3D**). Since arginine and lysine have both previously been reported as substrates of SNAT4 and ATB⁰⁺ (Sloan and Mager, 1999; Sugawara et al., 2000; Hatanaka et al., 2001), we utilized additional assays to evaluate substrate transport. We also could not rule out that the lack of arginine detection was due to its low R_f and incomplete derivatization (**Supplementary Table S3**), or chemical transformation to ornithine (Leimer et al., 1977; Halket et al., 2005). The lack of cationic AA accumulation by SNAT4- and ATB⁰⁺-expressing oocytes was nevertheless confirmed by quantitative LC-MS analysis (**Figure 4A**). LC-MS analysis confirmed glycine, alanine, serine, threonine and glutamine as SNAT4 substrates and revealed a preference of ATB⁰⁺ for branched-chain and aromatic amino acids. Using [¹⁴C]-arginine we were also unable to detect SNAT4-mediated uptake above levels seen with un-injected oocytes (**Figure 4B**), while [¹⁴C]-alanine and [¹⁴C]-glycine were confirmed as substrates of SNAT4. No aspartate uptake was observed, therefore confirming that small increases in GC-MS fold-change analysis most-likely represent *de novo* synthesis. Significant [¹⁴C]arginine uptake was observed in ATB⁰⁺-expressing oocytes compared to un-injected controls, however, net uptake was much slower than for the preferred ATB⁰⁺ substrate alanine (**Figure 4C**). Notably, when we attempted to out-compete ATB⁰⁺-mediated [¹⁴C]alanine uptake with a 100-fold greater concentration of unlabelled arginine, its uptake was only suppressed to the level of uninhibited [¹⁴C]arginine uptake (**Figure 4C**). Radiolabeled alanine uptake, by contrast, was totally abolished by a 100-fold excess of unlabelled alanine. We confirmed discrimination against cationic AA transport via ATB⁰⁺ by measuring uptake of [¹⁴C]arginine or [¹⁴C]lysine in a background of L-15 based incubation medium (**Figure 4D**). Over 4 h of incubation, accumulation of [¹⁴C]-cationic amino acids was much lower than that of the high affinity substrate isoleucine.

As the third cohort we examined glutamate transporters. Due to the high levels of endogenous anionic amino acids, glutamate accumulation was difficult to detect when analyzing fold-change. For instance, the rat brain glutamate/aspartate transporter EAAT1 (slc1a3) showed no significant changes in amino acid accumulation when analyzed by fold-change (**Figure 5A**), but its activity was revealed when absolute peak areas were compared (**Figure 5B**).

As the final transporter cohort, we analyzed amino acid exchangers. The equilibrium of exchanger-mediated flux is a normalization of all substrate levels on both sides of the membrane without changing the sum of all substrate concentrations. The antiport mechanism rendered our initial attempts to establish a substrate profile unsuccessful, because only very small non-significant variations in intracellular concentrations were observed. To increase the signal, we pre-incubated oocytes with 10 mM of a single substrate in ND96 buffer. During this 6 h preloading period, the chosen amino acid will be imported in exchange for preferred cytosolic amino acids. During the subsequent 4 h medium incubation, the previously preloaded AA will efflux in exchange for preferred extracellular substrates (**Figure 6**). Each panel has three samples: i) base line before preloading (column 0, -), ii) after 6 h preloading (column

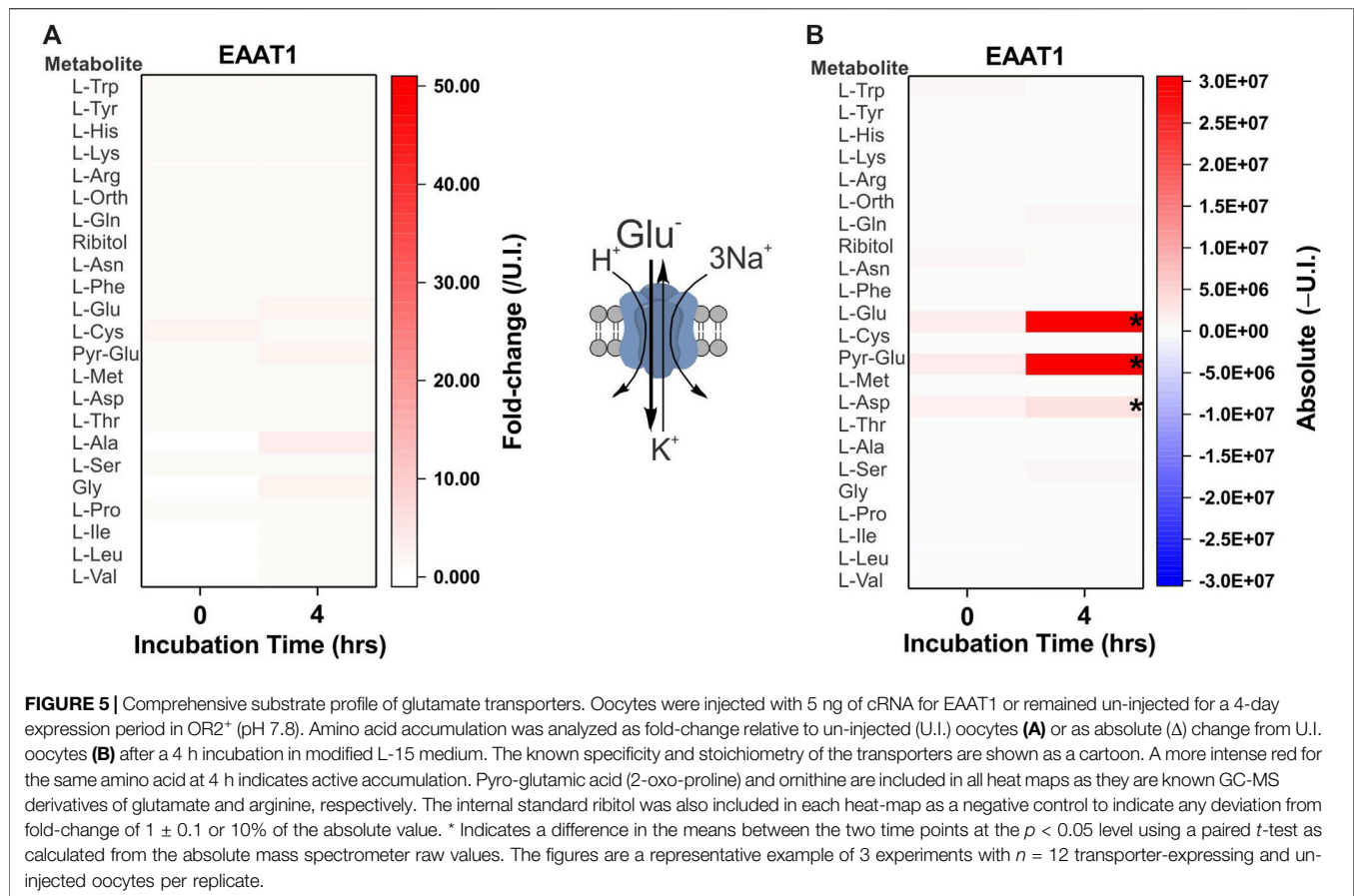




0,+) with 10 mM isoleucine or alanine and iii) after a 4 h incubation in medium (column “4”). Fold-change and absolute-change analysis were conducted after pre-loading and efflux phases to capture low abundance and high abundance amino acid changes. During the preloading phase for the ubiquitous human exchanger LAT1-4F2hc, tryptophan, tyrosine, histidine, phenylalanine and methionine were depleted, while isoleucine increased as expected (**Figures 6A,B**). The increase of a number of other amino acids during this phase is difficult to explain, particularly of essential amino acids. In the medium incubation phase leucine, valine, tryptophan, phenylalanine and tyrosine increased in abundance, while pre-loaded isoleucine and endogenous glutamine served as major efflux substrates. Histidine appeared to be a good efflux substrate, but its influx was not significant.

An analogous experiment was performed with ASCT2 using alanine as a preloading substrate. During the preloading phase alanine increased, while glutamine, asparagine, cysteine,

methionine, threonine and serine were found to be efflux substrates (**Figures 6C,D**). Due to its low R_f in GC-MS, alanine efflux was more easily detected in fold-change analysis than in absolute quantification. Aspartate and glutamate also increased in ASCT2 expressing oocytes during alanine preloading, suggesting transamination between alanine, α -ketoglutarate and oxaloacetate. During the medium incubation phase (comparing column 0,+ to column “4”) cysteine, glutamine, asparagine, methionine, threonine, alanine, serine and glycine entered the oocyte as indicated by a change from blue to white or blue to red, while alanine was released (red to blue). These changes could only be detected by fold-change analysis. Absolute quantification, however, suggested that glutamate was an additional efflux substrate. These results demonstrate the ability of our combined metabolomics method to determine the physiological profile and relative substrate specificity of mammalian amino acid transporters with a diverse range of transport mechanisms.

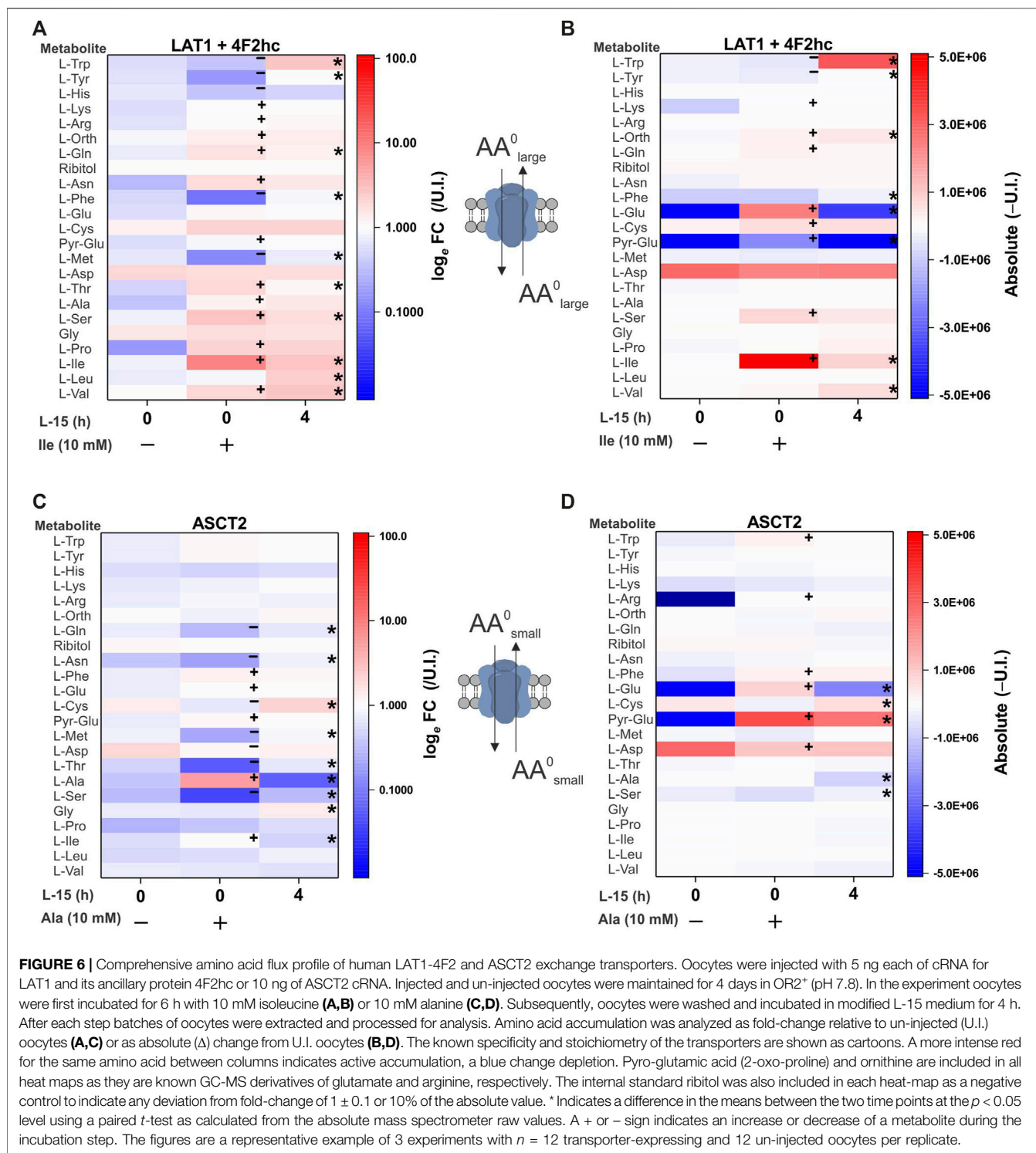


Identification of SNAT2 and as a Direct Rapid Activator of mTORC1

The role of plasma membrane amino acid transporters in the activation of mTORC1 is unresolved (Condon and Sabatini, 2019; Kim and Guan, 2019). The activation of several downstream mTORC1 signaling components 4E-BP1 and S6K1 has been established in *X. laevis* (Christie et al., 2002). However, many pathway components associated with upstream amino acid sensing and the central mTORC1 complexes remain unreported (**Figure 7A**). We identified *X. laevis* homologs of all major components of the mTORC1 complex, upstream amino acid sensors and downstream mTORC1 effectors with the exception of the LAMTOR4 protein of the Raptor complex (**Supplementary Table S6**). In addition, only three Ras-related GTPase (Rag) genes were identified instead of the usual four found in humans and other higher eukaryotes. The average sequence conservation of *X. laevis* mTORC1 amino acid sensing components to those in human homologues was 81.2% (**Figure 7B**), which was much higher than the global sequence conservation average for all ORFs (Session et al., 2016). Phosphorylation sites in the downstream mTORC1 effectors p70S6K1, S6 and 4E-BP1, were conserved as was, crucially for protein detection, the epitope recognition region of anti-human antibodies (**Figure 7C**). The conservation of antibody recognition epitopes in *X. laevis* mTORC1

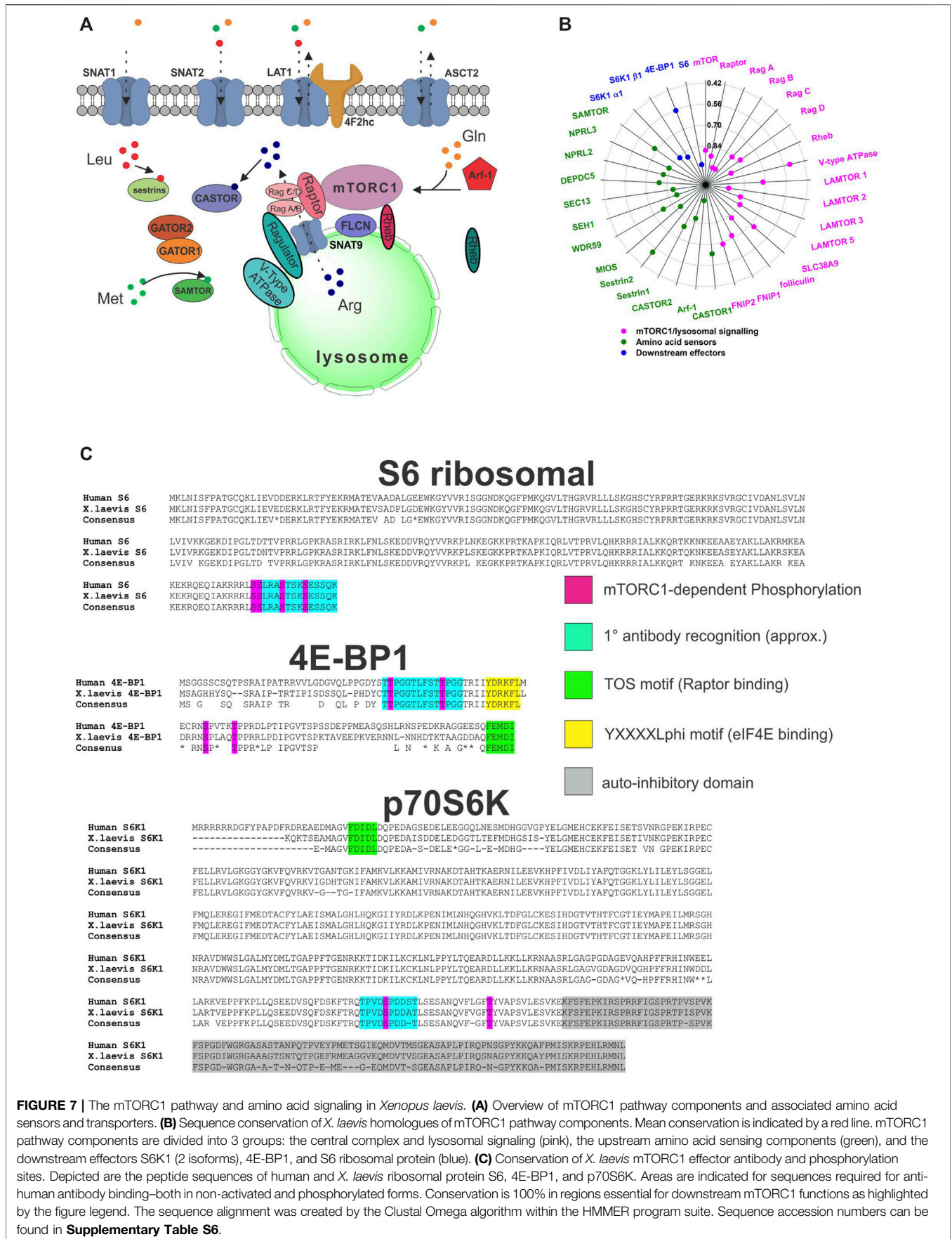
components allows for their detection by western blotting. Using these combined results we hypothesized that mTORC1 is functional in *X. laevis* cells and that phosphorylation of downstream substrates ribosomal S6 and 4E-BP1 will occur in a similar manner as in mammalian cells. This is in agreement with sequence comparisons made by other groups (Wolfson and Sabatini, 2017) (Tatebe and Shiozaki, 2017) and the response of mTORC1 in *Drosophila* S2 cells to amino acids (Zoncu et al., 2011).

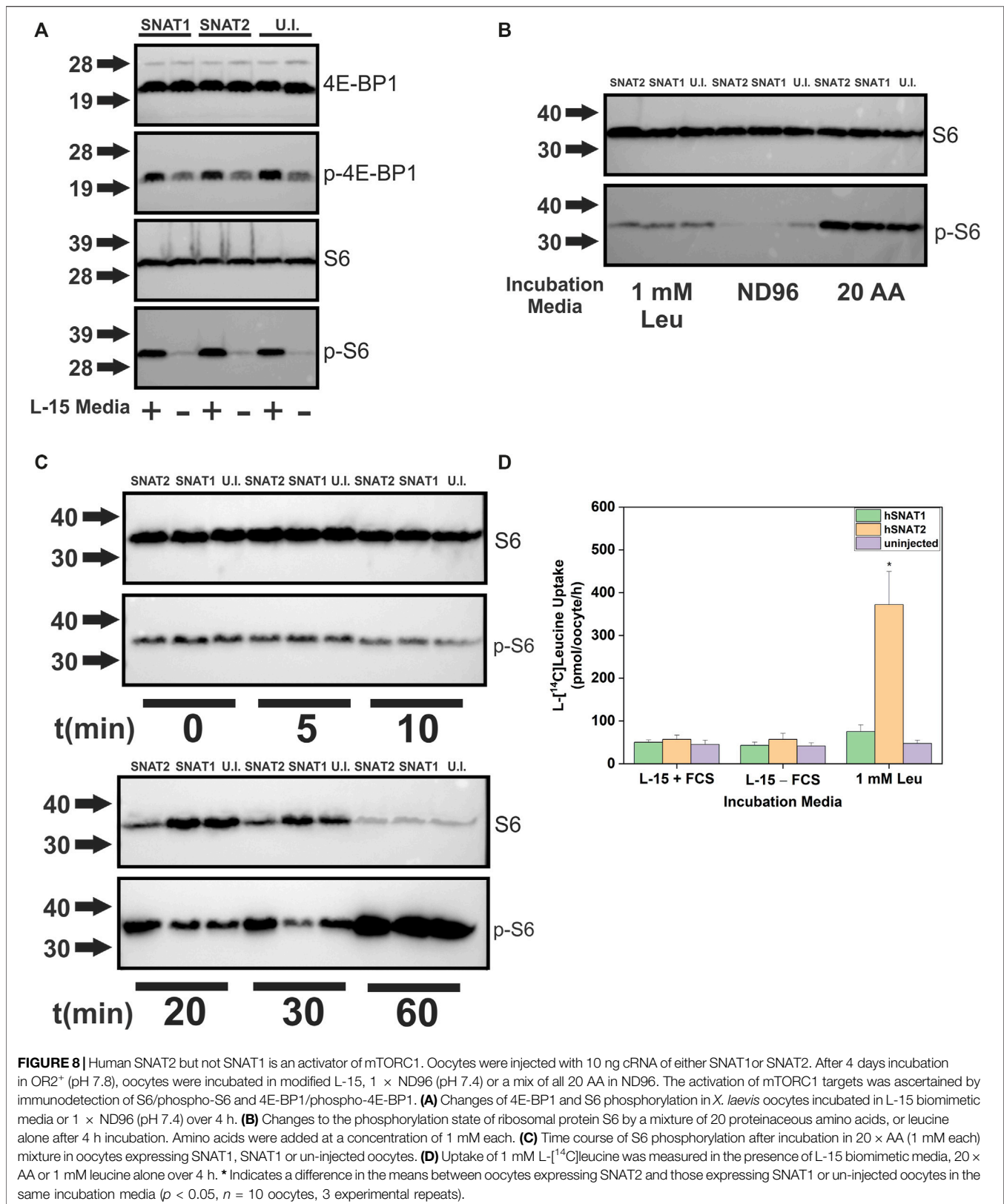
The transporter substrate profiles and conservation of amino acid sensing components in *X. laevis* allowed us to analyze transporters as potential mTORC1 activators (**Figure 8A**). SNAT2 was particularly interesting as our profile demonstrated its ability to accumulate a significant amount of cytosolic leucine, a known activator of mTORC1, in contrast to its close paralog SNAT1 (**Figures 2A,B**). Anti-human antibodies for 4E-BP1, phospho-4E-BP1, ribosomal protein S6 and phospho-S6 were able to detect *Xenopus* orthologues and their phosphorylation states upon incubation in modified L-15 (**Figure 8A**). Using a 4 h incubation period, heterologous expression of SNAT1 and SNAT2 did not affect mTORC1 signaling. In all subsequent immunoblot experiments we used phospho-S6 as the most reliable read-out of mTORC1 activation. To identify the minimal nutrient requirements needed for mTORC1 activation we replaced L-15 biomimetic medium

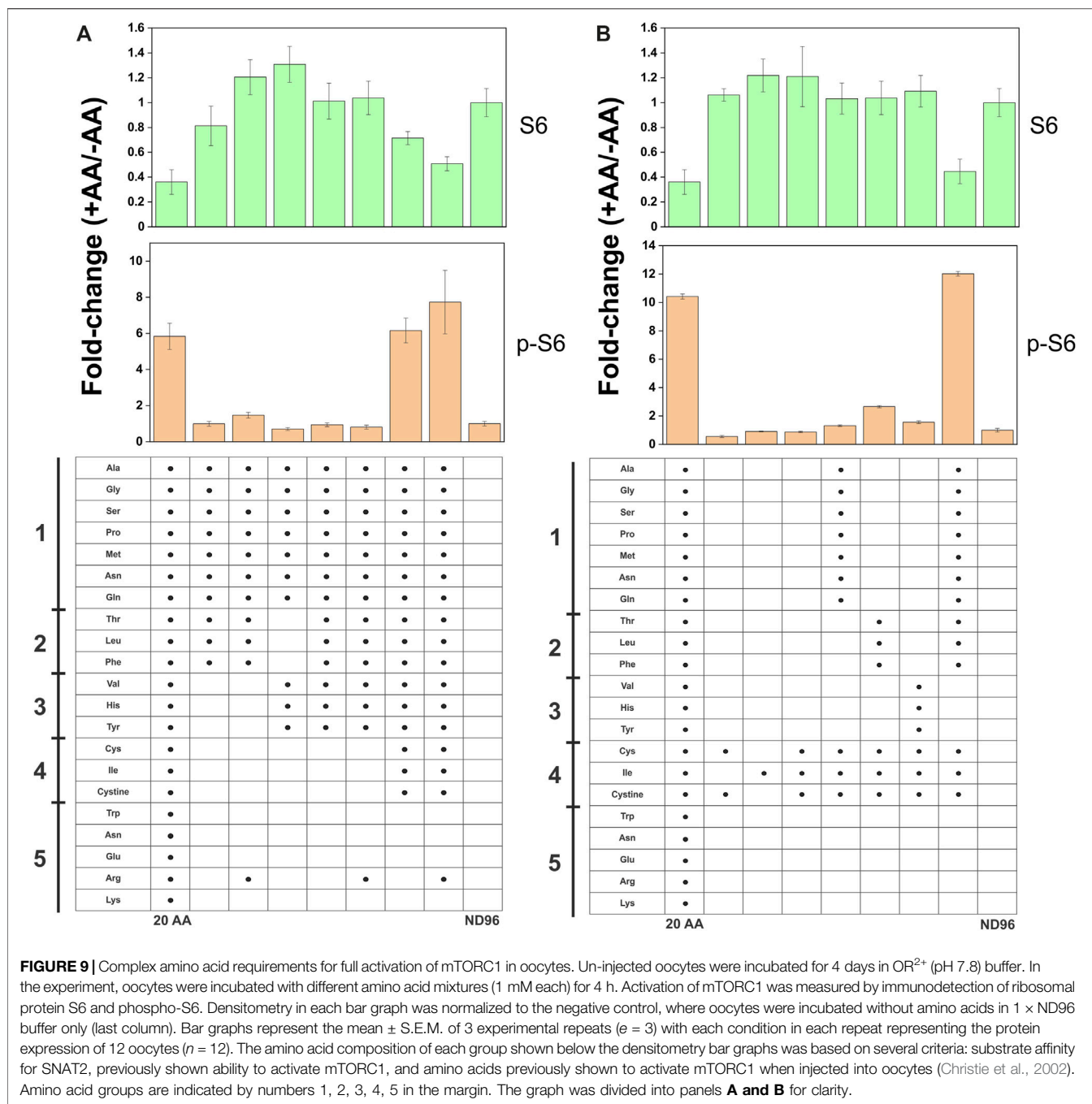


with ND96 buffer, which abolished mTORC1 activation (Figure 8B). Re-introducing leucine alone only partially activated mTORC1 after 4 h incubation, confirming previous reports that leucine or leucine plus arginine alone cannot fully activate the pathway in the absence of other amino acids (Hara

et al., 1998). This reflects the endogenous expression of oocyte AA transporters and the subsequent ability of oocytes to acquire amino acids sufficient to activate endogenous mTORC1 signaling. Accordingly, we reasoned that transporter-expressing oocytes with the capacity to achieve activation of







mTORC1 would do so more rapidly than un-injected oocytes, whether through accumulation of amino acids or transporter activity. Over a 60 min time-course (Figure 8C), SNAT2 demonstrated an advanced capacity to activate mTORC1, as evidenced by a significant increase in phospho-S6 between 10 and 30 min with a concurrent decrease in S6. By contrast, SNAT1-expressing oocytes activated mTORC1 only as well as un-injected oocytes. This result was notable as SNAT1 displays little difference in its substrate profile from SNAT2 apart from the latter's significantly greater capacity to accumulate leucine and

proline (compare Figures 2A,B). Given that leucine alone cannot fully activate mTORC1 in oocytes (Figure 8B) the result suggests that a combination of small neutral amino acids plus leucine may rapidly activate mTORC1 in oocytes. Activation of mTORC1 occurred at time-points where accumulation of leucine was marginal (Figure 8D). Given that heterologously expressed transporters were not essential to activate mTORC1 in oocytes, we divided amino acids into five groups to determine the optimal mixture required for mTORC1 activation (Figure 9). It was apparent that numerous amino acids were necessary for

full mTORC1 activation. The results confirmed that a mix of mainly SNAT2 substrates (alanine, serine, glycine, proline, methionine, asparagine, glutamine, threonine, leucine, phenylalanine, valine, histidine, tyrosine, cysteine, isoleucine, cystine) optimally activated mTORC1 (Figures 9A,B). Notably extracellular arginine was not required for full activation in *X. laevis* oocytes.

DISCUSSION

We have successfully developed a combined single-cell GC-MS/LC-MS method for elucidating the substrate profiles of multiple membrane transporters. The potential of this technique is shown by the substrate profiles we have established for several amino acid transporters in a physiologically relevant environment. The method readily demonstrates the capability of Na⁺-dependent symporters to load amino acids into a cell. The results largely confirm findings from numerous previous studies in which a mix of active transport and competition was used to determine substrate preference of amino acid transporters. More prominently than previously shown (Yao et al., 2000), we were able to detect that SNAT2 is very capable of accumulating leucine and proline compared to SNAT1 (Yao et al., 2000; Albers et al., 2001; Chaudhry et al., 2002; Mackenzie and Erickson, 2004). We could also confirm that SNAT4 has a narrower substrate specificity than SNAT1 and SNAT2, excluding larger polar neutral amino acids. However, we could not detect the accumulation of cationic amino acids by SNAT4, as reported earlier (Hatanaka et al., 2000). While we could detect the uptake of labeled cationic amino acids originally reported for human ATB⁰⁺ (Sloan and Mager, 1999), these were not accumulated in oocytes incubated in a complex matrix with the mouse homologue used in this study. Arginine-dependent effects in colon organoids were abolished in ATB⁰⁺ ko organoids (Ahmadi et al., 2018), but the amino acid content of the colon lumen is unknown. Accumulation of neutral amino acids is most readily detected as evidenced by the substrate specificity of B⁰AT1. The only exception for this transporter was tryptophan, the transport of which has been verified *in vivo* (Singer et al., 2012; Javed and Broer, 2019), but was hardly detectable in oocytes. Tryptophan is present in low concentration in L-15 medium, and thus it may have been out-competed by other amino acids. For ATB⁰⁺ this explains the lack of observed methionine accumulation at its relatively low concentration in L-15. Antiporters or exchangers can also be profiled using this method. However, we had to modify the method because the sum of their substrate concentrations remains the same on both sides of the membrane and neutral amino acid concentrations are fairly balanced. To detect antiport activity, an imbalance was introduced by incubating the oocytes with one dominant amino acid substrate in order to trans-stimulate movement of intracellular antiporter substrates. Using isoleucine we could detect tryptophan, tyrosine, histidine, phenylalanine, methionine, leucine, valine as LAT1 substrates, which is in agreement with previous studies (Yanagida et al., 2001; Morimoto et al., 2008). Glutamine was

also detected as an efflux substrate. For ASCT2, we used alanine as the pre-loading substrate. Glutamine, asparagine, cysteine, methionine, threonine and serine were found to be efflux substrates at neutral pH, while alanine was accumulated. During medium incubation cysteine, glutamine, asparagine, methionine, threonine, serine and glycine entered the oocyte, while alanine was the main efflux substrate. The transport of cysteine refutes some of the data using reconstituted ASCT2 in proteoliposomes, which suggested that cysteine is an allosteric modulator of the transporter (Scalise et al., 2015). We could confirm low-affinity transport of glutamate by ASCT2 (Scalise et al., 2020), which is only visible in the efflux direction, because intracellular glutamate is ~2 mM. A common feature of incubation in L-15 media over extended time periods is the increase in intracellular anionic amino acids, particularly aspartate. These increases occur in oocytes that are not expressing transporters but also occur more rapidly in those that do. The most likely explanation is the transamination of preloaded amino acids generating aspartate and glutamate. When using GC-MS to accurately identify the full biologically relevant substrate specificity, both fold-change and absolute values should be used during the analysis of initial experiments. Traditional GC-MS and LC-MS based metabolomics analysis rely on relative fold-changes to identify underlying important metabolic changes—an approach that can lead to potential false negatives if not accompanied by additional absolute signal analysis. Our quantification of endogenous amino acid concentrations in oocytes using GC-MS largely agreed with the value range previously established using HPLC in stage 5 or 6 oocytes (Taylor and Smith, 1987; Meier et al., 2002). The exception of glutamate can be explained by the inability to distinguish glutamate and glutamine in these previous studies, which, adding the two together, may over-estimate the glutamate concentration values provided. The moderately higher concentrations of isoleucine, proline, methionine and tyrosine we measured are more difficult to explain. However, large variations of amino acid concentrations have been noted (Taylor and Smith, 1987; Meier et al., 2002) between oocyte stages, time post-surgery, and ionic incubation conditions.

The method developed here can also be used to investigate amino acid signaling, the components of which are highly conserved in multicellular eukaryotes (Panchaud et al., 2013; Saxton and Sabatini, 2017; Tatebe and Shiozaki, 2017; Javed and Fairweather, 2019). Our results support the concept of SNAT2 as a transceptor (Pinilla et al., 2011), because mTORC1 activation was observed at time points where cytosolic leucine was barely increased. Another SNAT2 substrate glutamine has also been shown to activate mTORC1 in HepG2 and HeLa cells independent of the cytosolic Leu concentration, also suggesting SNAT2 can activate mTORC1 as a transceptor using glutamine (Chiu et al., 2012). Using groups of amino acids to activate mTORC1 in un-injected oocytes, we found an intriguing coincidence between the substrates of SNAT2 and their ability to activate mTORC1. The extended N-terminus of slc38 member SNAT9 has recently been shown to bind to the Raga/C heterodimer (Rebsamen et al., 2015; Wang et al., 2015; Fromm et al., 2020) and occupy the arginine binding site during

mTORC1 inactivation (Lei et al., 2018; Lei et al., 2020). A similar mechanism could be envisioned for the N-terminus of SNAT2 (Gaccioli et al., 2006; Hundal and Taylor, 2009; Poncet and Taylor, 2013), although the N-terminal is predicted to be 50 residues shorter than that of SNAT9. We cannot discount, however, the activation of mTORC1 through the accumulation of cytosolic amino acids, particularly but not exclusively leucine, mediated by SNAT2 (Wolfson et al., 2016). Alternatively, SNAT2 could mediate accumulation of amino acids via tertiary active transport involving endogenously expressed transporters which then could activate mTORC1. Our results support the notion that SNAT2 represents a likely candidate as an important mTORC1 activator/accelerator as has been previously proposed (Hyde et al., 2007; Baird et al., 2009; Pinilla et al., 2011; Poncet and Taylor, 2013; Broer and Broer, 2017; Broer, 2018; Hoffmann et al., 2018). The activation of mTORC1 by SNAT2 represents an alternative mechanism to the long-suggested combined action of the amino acid transporters LAT1 and ASCT2 (Nicklin et al., 2009). ASCT2, in particular, has recently been shown to be dispensable for mTORC1 activation due to compensation by SNAT2 (Broer et al., 2016). Key to the ability of SNAT2 to activate mTORC1 in our experiments is the capacity for leucine accumulation, which has been suggested but never directly shown to be a significant SNAT2 substrate previously (Hatanaka et al., 2000; Gazzola et al., 2001; Tang et al., 2018). The method outlined here can be applied to test the ability of other mammalian amino acid transporters, or combination of transporters, to activate mTORC1, including the frequently cited combination of LAT1 and ASCT2. Our method can also be applied to mammalian cells but would require genetic or pharmacological tools to inhibit endogenous transporters. Mammalian cell lines may express between 8 and 25 amino acid transporters at the plasma membrane—a significant proportion of which would have to be disrupted in order to isolate a specific transporter (Gauthier-Coles et al., 2021). In oocytes, proteomic and transcriptomic data demonstrate the presence of amino acid transporter paralogues of SLC1A5 (ASCT2), SLC3A2, SLC6A7 (PROT), SLC6A14 (B⁰⁺AT), SLC7A9 (b⁰⁺AT), SLC7A4 (CAT4, lysosomal), SLC36A1 (PAT1, lysosomal), SLC36A4 (PAT4), SLC38A9 (lysosomal) and SLC38A10 (ER) (Smits et al., 2014; Wühr et al., 2014). Despite many-fold higher expression of heterologous mRNA, silencing of endogenous oocyte transporters may increase the signal by slowing the endogenous activation of mTORC1. In this study we have not systematically investigated the minimal concentration of amino acids required to activate mTORC1 in *X. laevis* oocytes. Further investigation will be required to determine these minimal activating concentrations.

This study also represents the first comprehensive metabolic profiling of *X. laevis* oocytes, a widely used experimental system for membrane protein physiology and as a model in developmental biology. Moreover, we demonstrated, as suspected previously (Taylor and Smith, 1987; Broer, 2010; Sobczak et al., 2010) that oocytes are not metabolically silent. All oocyte incubations for 4 h in our L-15 media matrix led to increases in TCA cycle intermediates and anionic amino acids independent of the transporter expressed, suggesting the use of

neutral amino acids as anaplerotic substrates. We also suggest that decreases in multiple intracellular amino acids observed following transporter cRNA injection into oocytes (e.g., **Figure 6**) probably represent their use for protein synthesis.

In summary we show that single-oocyte metabolomics is a useful tool to explore the nexus between amino acid transport, amino acid homeostasis and signaling. The method can be applied to other types of transporters and may also be useful to explore the activity of organellar transporters and additional transporter-regulated intracellular signaling pathways.

DATA AVAILABILITY STATEMENT

The data presented in the study are deposited in the MetaboLights repository (<https://www.ebi.ac.uk/metabolights>), accession number MTBLS2476.

ETHICS STATEMENT

The animal study was reviewed and approved by the Animal Experimentation Ethics Committee, Australian National University.

AUTHOR CONTRIBUTIONS

SF and SB designed the study and wrote the manuscript. SF, GG-C, and AB performed experiments. SF, SO, GG-C, and KJ performed sample and data analysis.

FUNDING

This study was funded by the Australian Research Council, Grant DP180101702.

ACKNOWLEDGMENTS

We thank the staff of ANU Joint Mass Spectrometry Facility, Research School of Chemistry, especially Adam Carroll and Thy Truong for the maintenance and troubleshooting of the GC-MS equipment. We thank the staff of the Australian National University Research School of Biology Animal Services team for their assistance in maintaining the *X. laevis* frogs. In particular we thank Mr Benjamin Durant for assistance with surgeries to extract *X. laevis* oocytes. Lastly, we would like to thank Aditya Yadav for assistance in the synthesis of cRNA for oocyte microinjection.

SUPPLEMENTARY MATERIAL

The Supplementary Material for this article can be found online at: <https://www.frontiersin.org/articles/10.3389/fmolb.2021.646574/full#supplementary-material>.

REFERENCES

- Abplanalp, J., Laczko, E., Philp, N. J., Neidhardt, J., Zuercher, J., Braun, P., et al. (2013). The cataract and glucosuria associated monocarboxylate transporter MCT12 is a new creatine transporter. *Hum. Mol. Genet.* 22 (16), 3218–3226. doi:10.1093/hmg/ddt175
- Aggio, R., Villas-Bôas, S. G., and Ruggiero, K. (2011). Metab: an R package for high-throughput analysis of metabolomics data generated by GC-MS. *Bioinformatics* 27 (16), 2316–2318. doi:10.1093/bioinformatics/btr379
- Ahmadi, S., Xia, S., Wu, Y. S., Di Paola, M., Kisson, R., Luk, C., et al. (2018). SLC6A14, an amino acid transporter, modifies the primary CF defect in fluid secretion. *Elife* 7. doi:10.7554/eLife.37963
- Albers, A., Bröer, A., Wagner, C. A., Setiawan, I., Lang, P. A., Kranz, E. U., et al. (2001). Na⁺ transport by the neural glutamine transporter ATA1. *Pflugers Arch.* 443 (1), 92–101. doi:10.1007/s004240100663
- Baird, F., Bett, K., Maclean, C., Tee, A. R., Hundal, H. S., and Taylor, P. M. (2009). Tertiary active transport of amino acids reconstituted by coexpression of System A and L transporters in *Xenopus* oocytes. *Am. J. Physiol. Endocrinol. Metab.* 297, E822. doi:10.1152/ajpendo.00330.2009
- Behrends, V., Tredwell, G. D., and Bundy, J. G. (2011). A software complement to AMDIS for processing GC-MS metabolomic data. *Anal. Biochem.* 415 (2), 206–208. doi:10.1016/j.ab.2011.04.009
- Beugnet, A., Tee, A. R., Taylor, P. M., and Proud, C. G. (2003). Regulation of targets of mTOR (mammalian target of rapamycin) signalling by intracellular amino acid availability. *Biochem. J.* 372 (Pt 2), 555–566. doi:10.1042/bj20021266
- Bode, B. P., Fuchs, B. C., Hurley, B. P., Conroy, J. L., Suetterlin, J. E., Tanabe, K. K., et al. (2002). Molecular and functional analysis of glutamine uptake in human hepatoma and liver-derived cells. *Am. J. Physiol. Gastrointest. Liver Physiol.* 283 (5), G1062–G1073. doi:10.1152/ajpgi.00031.2002
- Böhmer, C., Bröer, A., Munzinger, M., Kowalczyk, S., Rasko, J. E., Lang, F., et al. (2005). Characterization of mouse amino acid transporter B0AT1 (slc6a19). *Biochem. J.* 389 (Pt 3), 745–751. doi:10.1042/bj20050083
- Bröer, A., Friedrich, B., Wagner, C. A., Fillon, S., Ganapathy, V., Lang, F., et al. (2001). Association of 4F2hc with light chains LAT1, LAT2 or γ -LAT2 requires different domains. *Biochem. J.* 355 (Pt 3), 725–731. doi:10.1042/bj3550725
- Bröer, A., Rahimi, F., and Bröer, S. (2016). Deletion of amino acid transporter ASCT2 (SLC1A5) reveals an essential role for transporters SNAT1 (SLC38A1) and SNAT2 (SLC38A2) to sustain glutaminolysis in cancer cells. *J. Biol. Chem.* 291 (25), 13194–13205. doi:10.1074/jbc.M115.700534
- Bröer, A., Wagner, C., Lang, F., and Bröer, S. (2000). Neutral amino acid transporter ASCT2 displays substrate-induced Na⁺ exchange and a substrate-gated anion conductance. *Biochem. J.* 346 Pt 3, 705–710. doi:10.1042/bj3460705
- Bröer, S. (2018). Amino acid transporters as disease modifiers and drug targets. *SLAS Discov.* 23 (4), 303–320. doi:10.1177/2472555218755629
- Bröer, S., and Bröer, A. (2017). Amino acid homeostasis and signalling in mammalian cells and organisms. *Biochem. J.* 474 (12), 1935–1963. doi:10.1042/bcj20160822
- Bröer, S., and Fairweather, S. J. (2018). Amino acid transport across the mammalian intestine. *Compr. Physiol.* 9 (1), 343–373. doi:10.1002/cphy.c170041
- Bröer, S. (2003). “*Xenopus laevis* oocytes, *Methods Mol. Biol.*,” in *Membrane transporters: methods and protocols*. Editor Q. Yan (Totowa, New Jersey: Humana Press), 227, 245–258. doi:10.1385/1-59259-387-9:245
- Broer, S. (2010). *Xenopus laevis* oocytes. *Methods Mol. Biol.* 637, 295–310. doi:10.1007/978-1-60761-700-6_16
- Camargo, S. M., Makrides, V., Virkki, L. V., Forster, I. C., and Verrey, F. (2005). Steady-state kinetic characterization of the mouse B(0)AT1 sodium-dependent neutral amino acid transporter. *Pflugers Arch.* 451 (2), 338–348. doi:10.1007/s00424-005-1455-x
- Carroll, A. J., Badger, M. R., and Harvey Millar, A. (2010). The MetabolomeExpress Project: enabling web-based processing, analysis and transparent dissemination of GC/MS metabolomics datasets. *BMC Bioinformatics* 11, 376. doi:10.1186/1471-2105-11-376
- Chaudhry, F. A., Schmitz, D., Reimer, R. J., Larsson, P., Gray, A. T., Nicoll, R., et al. (2002). Glutamine uptake by neurons: interaction of protons with system a transporters. *J. Neurosci.* 22 (1), 62–72. doi:10.1523/jneurosci.22-01-00062.2002
- Chien, H. C., Colas, C., Finke, K., Springer, S., Stoner, L., Zur, A. A., et al. (2018). Reevaluating the substrate specificity of the L-type Amino acid transporter (LAT1). *J. Med. Chem.* 61 (16), 7358–7373. doi:10.1021/acs.jmedchem.8b01007
- Chiu, M., Tardito, S., Barilli, A., Bianchi, M. G., Dall’Asta, V., and Bussolati, O. (2012). Glutamine stimulates mTORC1 independent of the cell content of essential amino acids. *Amino Acids* 43 (6), 2561–2567. doi:10.1007/s00726-012-1312-0
- Christie, G. R., Hajdich, E., Hundal, H. S., Proud, C. G., and Taylor, P. M. (2002). Intracellular sensing of amino acids in *Xenopus laevis* oocytes stimulates p70 S6 kinase in a target of rapamycin-dependent manner. *J. Biol. Chem.* 277 (12), 9952–9957. doi:10.1074/jbc.M107694200
- Condon, K. J., and Sabatini, D. M. (2019). Nutrient regulation of mTORC1 at a glance. *J. Cell Sci.* 132 (21). doi:10.1242/jcs.222570
- Ebert, K., Ludwig, M., Geillinger, K. E., Schoberth, G. C., Essenwanger, J., Stolz, J., et al. (2017). Reassessment of GLUT7 and GLUT9 as putative fructose and glucose transporters. *J. Membr. Biol.* 250 (2), 171–182. doi:10.1007/s00232-016-9945-7
- Evans, K., Nasim, Z., Brown, J., Butler, H., Kauser, S., Varoqui, H., et al. (2007). Acidosis-sensing glutamine pump SNAT2 determines amino acid levels and mammalian target of rapamycin signalling to protein synthesis in L6 muscle cells. *J. Am. Soc. Nephrol.* 18 (5), 1426–1436. doi:10.1681/asn.2006091014
- Evans, K., Nasim, Z., Brown, J., Clapp, E., Amin, A., Yang, B., et al. (2008). Inhibition of SNAT2 by metabolic acidosis enhances proteolysis in skeletal muscle. *J. Am. Soc. Nephrol.* 19 (11), 2119–2129. doi:10.1681/asn.2007101108
- Fairweather, S. J., Bröer, A., O’Mara, M. L., and Bröer, S. (2012). Intestinal peptidases form functional complexes with the neutral amino acid transporter B(0)AT1. *Biochem. J.* 446 (1), 135–148. doi:10.1042/bj20120307
- Fairweather, S. J., Bröer, A., Subramanian, N., Tumer, E., Cheng, Q., Schmol, D., et al. (2015). Molecular basis for the interaction of the mammalian amino acid transporters B0AT1 and B0AT3 with their ancillary protein collectrin. *J. Biol. Chem.* 290 (40), 24308–24325. doi:10.1074/jbc.M115.648519
- Fairweather, S. J., Shah, N., and Bröer, S. (2020). Heteromeric solute carriers: function, structure, pathology and pharmacology. *Adv. Exp. Med. Biol.* doi:10.1007/5584_2020_584
- Fan, S. J., Snell, C., Turley, H., Li, J. L., McCormick, R., Perera, S. M., et al. (2016). PAT4 levels control amino-acid sensitivity of rapamycin-resistant mTORC1 from the Golgi and affect clinical outcome in colorectal cancer. *Oncogene* 35 (23), 3004–3015. doi:10.1038/onc.2015.363
- Fiehn, O. (2016). Metabolomics by gas chromatography-mass spectrometry: combined targeted and untargeted profiling. *Curr. Protoc. Mol. Biol.* 114 (30), 30–32. doi:10.1002/0471142727.1002/0471142727.mb3004s1144
- Fitzgerald, G. A., Mulligan, C., and Mindell, J. A. (2017). A general method for determining secondary active transporter substrate stoichiometry. *Elife* 6. doi:10.7554/eLife.21016
- Fromm, S. A., Lawrence, R. E., and Hurley, J. H. (2020). Structural mechanism for amino acid-dependent Rag GTPase nucleotide state switching by SLC38A9. *Nat. Struct. Mol. Biol.* 27 (11), 1017–1023. doi:10.1038/s41594-020-0490-9
- Fuchs, B. C., Finger, R. E., Onan, M. C., and Bode, B. P. (2007). ASCT2 silencing regulates mammalian target-of-rapamycin growth and survival signaling in human hepatoma cells. *Am. J. Physiol. Cell Physiol.* 293 (1), C55–C63. doi:10.1152/ajpcell.00330.2006
- Gaccioli, F., Huang, C. C., Wang, C., Bevilacqua, E., Franchi-Gazzola, R., Gazzola, G. C., et al. (2006). Amino acid starvation induces the SNAT2 neutral amino acid transporter by a mechanism that involves eukaryotic initiation factor 2 α phosphorylation and cap-independent translation. *J. Biol. Chem.* 281 (26), 17929–17940. doi:10.1074/jbc.M600341200
- Gauthier-Coles, G., Vennitti, J., Zhang, Z., Comb, W. C., Javed, K., Broer, A., et al. (2021). A unified model of amino acid homeostasis in mammalian cells. *bioRxiv*, 430327. doi:10.1101/2021.02.08.430327
- Gazzola, R. F., Sala, R., Bussolati, O., Visigalli, R., Dall’Asta, V., Ganapathy, V., et al. (2001). The adaptive regulation of amino acid transport system A is associated to changes in ATA2 expression. *FEBS Lett.* 490 (1–2), 11–14. doi:10.1016/s0014-5793(01)02126-3
- Goberdhan, D. C., Meredith, D., Boyd, C. A., and Wilson, C. (2005). PAT-related amino acid transporters regulate growth via a novel mechanism that does not

- require bulk transport of amino acids. *Development* 132 (10), 2365–2375. doi:10.1242/dev.01821
- Grewer, C., Gameiro, A., Mager, T., and Fendler, K. (2013). Electrophysiological characterization of membrane transport proteins. *Annu. Rev. Biophys.* 42, 95–120. doi:10.1146/annurev-biophys-083012-130312
- Gründemann, D., Harlfinger, S., Golz, S., Geerts, A., Lazar, A., Berkels, R., et al. (2005). Discovery of the ergothioneine transporter. *Proc. Natl. Acad. Sci. U.S.A.* 102 (14), 5256–5261. doi:10.1073/pnas.0408624102
- Gu, Y., Albuquerque, C. P., Braas, D., Zhang, W., Villa, G. R., Bi, J., et al. (2017). mTORC2 regulates amino acid metabolism in cancer by phosphorylation of the cystine-glutamate antiporter xCT. *Mol. Cell* 67 (1), 128–e7. doi:10.1016/j.molcel.2017.05.030
- Halket, J. M., Waterman, D., Przyborowska, A. M., Patel, R. K., Fraser, P. D., and Bramley, P. M. (2005). Chemical derivatization and mass spectral libraries in metabolic profiling by GC/MS and LC/MS/MS. *J. Exp. Bot.* 56 (410), 219–243. doi:10.1093/jxb/eri069
- Hara, K., Yonezawa, K., Weng, Q. P., Kozłowski, M. T., Belham, C., and Avruch, J. (1998). Amino acid sufficiency and mTOR regulate p70 S6 kinase and eIF-4E BP1 through a common effector mechanism. *J. Biol. Chem.* 273 (23), 14484–14494. doi:10.1074/jbc.273.23.14484
- Hatanaka, T., Huang, W., Ling, R., Prasad, P. D., Sugawara, M., Leibach, F. H., et al. (2001). Evidence for the transport of neutral as well as cationic amino acids by ATA3, a novel and liver-specific subtype of amino acid transport system A. *Biochim. Biophys. Acta* 1510 (1–2), 10–17. doi:10.1016/s0005-2736(00)00390-4
- Hatanaka, T., Huang, W., Wang, H., Sugawara, M., Prasad, P. D., Leibach, F. H., et al. (2000). Primary structure, functional characteristics and tissue expression pattern of human ATA2, a subtype of amino acid transport system A. *Biochim. Biophys. Acta* 1467 (1), 1–6. doi:10.1016/s0005-2736(00)00252-2
- Haug, K., Cochrane, K., Nainala, V. C., Williams, M., Chang, J., Jayaseelan, K. V., et al. (2020). MetaboLights: a resource evolving in response to the needs of its scientific community. *Nucleic Acids Res.* 48 (D1), D440–d444. doi:10.1093/nar/gkz1019
- Heublein, S., Kazi, S., Ogmundsdóttir, M. H., Attwood, E. V., Kala, S., Boyd, C. A., et al. (2010). Proton-assisted amino-acid transporters are conserved regulators of proliferation and amino-acid-dependent mTORC1 activation. *Oncogene* 29 (28), 4068–4079. doi:10.1038/onc.2010.177
- Hoffmann, T. M., Cwiklinski, E., Shah, D. S., Stretton, C., Hyde, R., Taylor, P. M., et al. (2018). Effects of sodium and amino acid substrate availability upon the expression and stability of the SNAT2 (SLC38A2) amino acid transporter. *Front. Pharmacol.* 9, 63. doi:10.3389/fphar.2018.00063
- Hübschmann, H.-J. (2015). “Introduction,” in *Handbook of GC-MS: fundamentals and applications*. Editor H.-J. Hübschmann. 3rd ed (Weinheim, Germany: John Wiley & Sons), 6
- Hummel, J., Strehmel, N., Selbig, J., Walther, D., and Kopka, J. (2010). Decision tree supported substructure prediction of metabolites from GC-MS profiles. *Metabolomics* 6 (2), 322–333. doi:10.1007/s11306-010-0198-7
- Hundal, H. S., and Taylor, P. M. (2009). Amino acid transporters: gate keepers of nutrient exchange and regulators of nutrient signaling. *Am. J. Physiol. Endocrinol. Metab.* 296 (4), E603–E613. doi:10.1152/ajpendo.91002.2008
- Hyde, R., Cwiklinski, E. L., MacAulay, K., Taylor, P. M., and Hundal, H. S. (2007). Distinct sensor pathways in the hierarchical control of SNAT2, a putative amino acid transporter, by amino acid availability. *J. Biol. Chem.* 282 (27), 19788–19798. doi:10.1074/jbc.M611520200
- Jani, M., and Krajcsi, P. (2014). *In vitro* methods in drug transporter interaction assessment. *Drug Discov. Today Technol.* 12, e105–12. doi:10.1016/j.ddtec.2014.03.011
- Javed, K., and Bröer, S. (2019). Mice lacking the intestinal and renal neutral amino acid transporter SLC6A19 demonstrate the relationship between dietary protein intake and amino acid malabsorption. *Nutrients* 11 (9). doi:10.3390/nu11092024
- Javed, K., and Fairweather, S. J. (2019). Amino acid transporters in the regulation of insulin secretion and signalling. *Biochem. Soc. Trans.* 47 (2), 571–590. doi:10.1042/bst20180250
- Javed, K., Cheng, Q., Carroll, A., Truong, T., and Bröer, S. (2018). Development of biomarkers for inhibition of SLC6A19 (B0at1)-A potential target to treat metabolic disorders. *Ijms* 19 (11), 3597. doi:10.3390/ijms19113597
- Jewell, J. L., Kim, Y. C., Russell, R. C., Yu, F. X., Park, H. W., Plouffe, S. W., et al. (2015). Metabolism. Differential regulation of mTORC1 by leucine and glutamine. *Science* 347 (6218), 194–198. doi:10.1126/science.1259472
- Jung, J., Genau, H. M., and Behrends, C. (2015). Amino acid-dependent mTORC1 regulation by the lysosomal membrane protein SLC38A9. *Mol. Cell Biol.* 35 (14), 2479–2494. doi:10.1128/mcb.00125-15
- Kandasamy, P., Gyimesi, G., Kanai, Y., and Hediger, M. A. (2018). Amino acid transporters revisited: new views in health and disease. *Trends Biochem. Sci.* 43 (10), 752–789. doi:10.1016/j.tibs.2018.05.003
- Kim, J., and Guan, K. L. (2019). mTOR as a central hub of nutrient signalling and cell growth. *Nat. Cell Biol.* 21 (1), 63–71. doi:10.1038/s41556-018-0205-1
- Koek, M. M., Bakels, F., Engel, W., van den Maagdenberg, A., Ferrari, M. D., Coulier, L., et al. (2010). Metabolic profiling of ultrasmall sample volumes with GC/MS: from microliter to nanoliter samples. *Anal. Chem.* 82 (1), 156–162. doi:10.1021/ac9015787
- Kowalczyk, S., Bröer, A., Tietze, N., Vanslambrocker, J. M., Rasko, J. E., and Bröer, S. (2008). A protein complex in the brush-border membrane explains a Hartnup disorder allele. *FASEB J.* 22 (8), 2880–2887. doi:10.1096/fj.08-107300
- Lee, M., Kim, J. H., Yoon, I., Lee, C., Fallahi Sichani, M., Kang, J. S., et al. (2018). Coordination of the leucine-sensing Rag GTPase cycle by leucyl-tRNA synthetase in the mTORC1 signaling pathway. *Proc. Natl. Acad. Sci. U.S.A.* 115 (23), E5279–e5288. doi:10.1073/pnas.1801287115
- Lei, H.-T., Mu, X., Hattne, J., and Gonen, T. (2020). A conformational change in the N terminus of SLC38A9 signals mTORC1 activation. *Structure*. doi:10.1016/j.str.2020.11.014
- Lei, H. T., Ma, J., Sanchez Martinez, S., and Gonen, T. (2018). Crystal structure of arginine-bound lysosomal transporter SLC38A9 in the cytosol-open state. *Nat. Struct. Mol. Biol.* 25 (6), 522–527. doi:10.1038/s41594-018-0072-2
- Leimer, K. R., Rice, R. H., and Gehrke, C. W. (1977). Complete mass spectra of N-trifluoroacetyl-n-butyl esters of amino acids. *J. Chromatogr.* 141 (2), 121–144. doi:10.1016/s0021-9673(00)99131-3
- Li, S., and Whorton, A. R. (2005). Identification of stereoselective transporters for S-nitroso-L-cysteine: role of LAT1 and LAT2 in biological activity of S-nitrosothiols. *J. Biol. Chem.* 280 (20), 20102–20110. doi:10.1074/jbc.M413164200
- Lu, H., Liang, Y., Dunn, W. B., Shen, H., and Kell, D. B. (2008). Comparative evaluation of software for deconvolution of metabolomics data based on GC-TOF-MS. *Trac Trends Anal. Chem.* 27 (3), 215–227. doi:10.1016/j.trac.2007.11.004
- Lu, W., Su, X., Klein, M. S., Lewis, I. A., Fiehn, O., and Rabinowitz, J. D. (2017). Metabolite measurement: pitfalls to avoid and practices to follow. *Annu. Rev. Biochem.* 86, 277–304. doi:10.1146/annurev-biochem-061516-044952
- Mackenzie, B., and Erickson, J. D. (2004). Sodium-coupled neutral amino acid (System N/A) transporters of the SLC38 gene family. *Pflugers Arch.* 447 (5), 784–795. doi:10.1007/s00424-003-1117-9
- Meier, C., Ristic, Z., Klausner, S., and Verrey, F. (2002). Activation of system L heterodimeric amino acid exchangers by intracellular substrates. *Embo j* 21 (4), 580–589. doi:10.1093/emboj/21.4.580
- Morimoto, E., Kanai, Y., Kim, D. K., Chairoungdua, A., Choi, H. W., Wempe, M. F., et al. (2008). Establishment and characterization of mammalian cell lines stably expressing human L-type amino acid transporters. *J. Pharmacol. Sci.* 108 (4), 505–516. doi:10.1254/jphs.08232fp
- Nicklin, P., Bergman, P., Zhang, B., Triantafellow, E., Wang, H., Nyfeler, B., et al. (2009). Bidirectional transport of amino acids regulates mTOR and autophagy. *Cell* 136 (3), 521–534. doi:10.1016/j.cell.2008.11.044
- Panchaud, N., Péli-Gulli, M. P., and De Virgilio, C. (2013). SEACing the GAP that reGOCiates TORC1 activation: evolutionary conservation of Rag GTPase regulation. *Cell Cycle* 12 (18), 2948–2952. doi:10.4161/cc.26000
- Parker, K. E. R., Fairweather, S. J., Rajendran, E., Blume, M., McConville, M. J., Bröer, S., et al. (2019). The tyrosine transporter of *Toxoplasma gondii* is a member of the newly defined apicomplexan amino acid transporter (ApiAT) family. *PLoS Pathog.* 15 (2), e1007577. doi:10.1371/journal.ppat.1007577
- Pei, J., and Grishin, N. V. (2007). PROMALS: towards accurate multiple sequence alignments of distantly related proteins. *Bioinformatics* 23 (7), 802–808. doi:10.1093/bioinformatics/btm017
- Pinilla, J., Aledo, J. C., Cwiklinski, E., Hyde, R., Taylor, P. M., and Hundal, H. S. (2011). SNAT2 transporter signalling via mTOR: a role in cell growth and proliferation?. *Front. Biosci. (Elite Ed.)* 3, 1289–1299. doi:10.2741/e332
- Poncet, N., and Taylor, P. M. (2013). The role of amino acid transporters in nutrition. *Curr. Opin. Clin. Nutr. Metab. Care* 16 (1), 57–65. doi:10.1097/MCO.0b013e32835a885c
- Potter, S. C., Luciani, A., Eddy, S. R., Park, Y., Lopez, R., and Finn, R. D. (2018). HMMER web server: 2018 update. *Nucleic Acids Res.* 46 (W1), W200–w204. doi:10.1093/nar/gky448

- Rebsamen, M., Pochini, L., Stasyk, T., de Araújo, M. E., Galluccio, M., Kandasamy, R. K., et al. (2015). SLC38A9 is a component of the lysosomal amino acid sensing machinery that controls mTORC1. *Nature* 519 (7544), 477–481. doi:10.1038/nature14107
- Rebsamen, M., and Superti-Furga, G. (2016). SLC38A9: a lysosomal amino acid transporter at the core of the amino acid-sensing machinery that controls mTORC1. *Autophagy* 12 (6), 1061–1062. doi:10.1080/15548627.2015.1091143
- Sarker, S. D., and Nahar, L. (2012). An introduction to natural products isolation. *Methods Mol. Biol.* 864, 1–25. doi:10.1007/978-1-61779-624-1_1
- Saxton, R. A., and Sabatini, D. M. (2017). mTOR signaling in growth, metabolism, and disease. *Cell* 169 (2), 361–371. doi:10.1016/j.cell.2017.03.035
- Scalise, M., Mazza, T., Pappacoda, G., Pochini, L., Cosco, J., Rovella, F., et al. (2020). The human SLC1A5 neutral amino acid transporter catalyzes a pH-dependent glutamate/glutamine antiport, as well. *Front Cel Dev Biol.* 8, 603. doi:10.3389/fcell.2020.00603
- Scalise, M., Pochini, L., Pingitore, P., Hedfalk, K., and Indiveri, C. (2015). Cysteine is not a substrate but a specific modulator of human ASCT2 (SLC1A5) transporter. *FEBS Lett.* 589 (23), 3617–3623. doi:10.1016/j.febslet.2015.10.011
- Session, A. M., Uno, Y., Kwon, T., Chapman, J. A., Toyoda, A., Takahashi, S., et al. (2016). Genome evolution in the allotetraploid frog *Xenopus laevis*. *Nature* 538 (7625), 336–343. doi:10.1038/nature19840
- Singer, D., Camargo, S. M., Ramadan, T., Schäfer, M., Mariotta, L., Herzog, B., et al. (2012). Defective intestinal amino acid absorption in Ace2 null mice. *Am. J. Physiol. Gastrointest. Liver Physiol.* 303 (6), G686–G695. doi:10.1152/ajpgi.00140.2012
- Sloan, J. L., and Mager, S. (1999). Cloning and functional expression of a human Na⁺ and Cl⁻-dependent neutral and cationic amino acid transporter B(0+). *J. Biol. Chem.* 274 (34), 23740–23745. doi:10.1074/jbc.274.34.23740
- Smits, A. H., Lindeboom, R. G., Perino, M., van Heeringen, S. J., Veenstra, G. J., and Vermeulen, M. (2014). Global absolute quantification reveals tight regulation of protein expression in single *Xenopus* eggs. *Nucleic Acids Res.* 42 (15), 9880–9891. doi:10.1093/nar/gku661
- Sobczak, K., Bangel-Ruland, N., Leier, G., and Weber, W. M. (2010). Endogenous transport systems in the *Xenopus laevis* oocyte plasma membrane. *Methods* 51 (1), 183–189. doi:10.1016/j.jymeth.2009.12.001
- Stegen, C., Matskevich, L., Wagner, C. A., Paulmichl, M., Lang, F., and Bröer, S. (2000). Swelling-induced taurine release without chloride channel activity in *Xenopus laevis* oocytes expressing anion channels and transporters. *Biochim. Biophys. Acta* 1467 (1), 91–100. doi:10.1016/s0005-2736(00)00209-1
- Su, T. Z., Feng, M. R., and Weber, M. L. (2005). Mediation of highly concentrative uptake of pregabalin by L-type amino acid transport in Chinese hamster ovary and Caco-2 cells. *J. Pharmacol. Exp. Ther.* 313 (3), 1406–1415. doi:10.1124/jpet.104.082255
- Sugawara, M., Nakanishi, T., Fei, Y. J., Martindale, R. G., Ganapathy, M. E., Leibach, F. H., et al. (2000). Structure and function of ATA3, a new subtype of amino acid transport system A, primarily expressed in the liver and skeletal muscle. *Biochim. Biophys. Acta* 1509 (1–2), 7–13. doi:10.1016/s0005-2736(00)00349-7
- Tan, H. W. S., Sim, A. Y. L., and Long, Y. C. (2017). Glutamine metabolism regulates autophagy-dependent mTORC1 reactivation during amino acid starvation. *Nat. Commun.* 8 (1), 338. doi:10.1038/s41467-017-00369-y
- Tang, Y., Tan, B., Li, G., Li, J., Ji, P., and Yin, Y. (2018). The regulatory role of MeAIB in protein metabolism and the mTOR signaling pathway in porcine enterocytes. *Ijms* 19 (3), 714. doi:10.3390/ijms19030714
- Taslimifar, M., Oparija, L., Verrey, F., Kurtcuoglu, V., Olgac, U., and Makrides, V. (2017). Quantifying the relative contributions of different solute carriers to aggregate substrate transport. *Sci. Rep.* 7, 40628. doi:10.1038/srep40628
- Tatebe, H., and Shiozaki, K. (2017). Evolutionary conservation of the components in the TOR signaling pathways. *Biomolecules* 7 (4). doi:10.3390/biom7040077
- Taylor, M. A., and Smith, L. D. (1987). Accumulation of free amino acids in growing *Xenopus laevis* oocytes. *Dev. Biol.* 124 (1), 287–290. doi:10.1016/0012-1606(87)90480-5
- Tsugawa, H., Cajka, T., Kind, T., Ma, Y., Higgins, B., Ikeda, K., et al. (2015). MS-DIAL: data-independent MS/MS deconvolution for comprehensive metabolome analysis. *Nat. Methods* 12 (6), 523–526. doi:10.1038/nmeth.3393
- Uchino, H., Kanai, Y., Kim, D. K., Wempe, M. F., Chairoungdua, A., Morimoto, E., et al. (2002). Transport of amino acid-related compounds mediated by L-type amino acid transporter 1 (LAT1): insights into the mechanisms of substrate recognition. *Mol. Pharmacol.* 61 (4), 729–737. doi:10.1124/mol.61.4.729
- Vera, J. C., and Rosen, O. M. (1990). Reconstitution of an insulin signaling pathway in *Xenopus laevis* oocytes: coexpression of a mammalian insulin receptor and three different mammalian hexose transporters. *Mol. Cel Biol.* 10 (2), 743–751. doi:10.1128/mcb.10.2.743
- Wang, H., Huang, W., Sugawara, M., Devoe, L. D., Leibach, F. H., Prasad, P. D., et al. (2000). Cloning and functional expression of ATA1, a subtype of amino acid transporter A, from human placenta. *Biochem. Biophys. Res. Commun.* 273 (3), 1175–1179. doi:10.1006/bbrc.2000.3061
- Wang, S., Tsun, Z. Y., Wolfson, R. L., Shen, K., Wyant, G. A., Plovnich, M. E., et al. (2015). Metabolism. Lysosomal amino acid transporter SLC38A9 signals arginine sufficiency to mTORC1. *Science* 347 (6218), 188–194. doi:10.1126/science.1257132
- Wolfson, R. L., Chantranupong, L., Saxton, R. A., Shen, K., Scaria, S. M., Cantor, J. R., et al. (2016). Sestrin2 is a leucine sensor for the mTORC1 pathway. *Science* 351 (6268), 43–48. doi:10.1126/science.aab2674
- Wolfson, R. L., and Sabatini, D. M. (2017). The dawn of the age of amino acid sensors for the mTORC1 pathway. *Cell Metab* 26 (2), 301–309. doi:10.1016/j.cmet.2017.07.001
- Wongthai, P., Hagiwara, K., Miyoshi, Y., Wiriyasermkul, P., Wei, L., Ohgaki, R., et al. (2015). Boronophenylalanine, a boron delivery agent for boron neutron capture therapy, is transported by ATB0+, LAT1 and LAT2. *Cancer Sci.* 106 (3), 279–286. doi:10.1111/cas.12602
- Wu, X., Zhao, L., Chen, Z., Ji, X., Qiao, X., Jin, Y., et al. (2016). FLCN maintains the leucine level in lysosome to stimulate mTORC1. *PLoS One* 11 (6), e0157100. doi:10.1371/journal.pone.0157100
- Wühr, M., Freeman, R. M., Jr., Presler, M., Horb, M. E., Peshkin, L., Gygi, S., et al. (2014). Deep proteomics of the *Xenopus laevis* egg using an mRNA-derived reference database. *Curr. Biol.* 24 (13), 1467–1475. doi:10.1016/j.cub.2014.05.044
- Wyant, G. A., Abu-Remaileh, M., Wolfson, R. L., Chen, W. W., Freinkman, E., Danai, L. V., et al. (2017). mTORC1 activator SLC38A9 is required to efflux essential amino acids from lysosomes and use protein as a nutrient. *Cell* 171 (3), 642–e12. doi:10.1016/j.cell.2017.09.046
- Yanagida, O., Kanai, Y., Chairoungdua, A., Kim, D. K., Segawa, H., Nii, T., et al. (2001). Human L-type amino acid transporter 1 (LAT1): characterization of function and expression in tumor cell lines. *Biochim. Biophys. Acta* 1514 (2), 291–302. doi:10.1016/s0005-2736(01)00384-4
- Yao, D., Mackenzie, B., Ming, H., Varoqui, H., Zhu, H., Hediger, M. A., et al. (2000). A novel system A isoform mediating Na⁺/neutral amino acid cotransport. *J. Biol. Chem.* 275 (30), 22790–22797. doi:10.1074/jbc.M002965200
- Yoon, M. S., Son, K., Arauz, E., Han, J. M., Kim, S., and Chen, J. (2016). Leucyl-tRNA synthetase activates Vps34 in amino acid-sensing mTORC1 signaling. *Cell Rep* 16 (6), 1510–1517. doi:10.1016/j.celrep.2016.07.008
- Zhao, L., Zhang, X., Ji, X., Jin, Y., and Liu, W. (2019). The amino acid transporter PAT1 regulates mTORC1 in a nutrient-sensitive manner that requires its transport activity. *Cell Signal* 53, 59–67. doi:10.1016/j.cellsig.2018.09.017
- Zheng, L., Zhang, W., Zhou, Y., Li, F., Wei, H., and Peng, J. (2016). Recent advances in understanding amino acid sensing mechanisms that regulate mTORC1. *Int. J. Mol. Sci.* 17 (10). doi:10.3390/ijms17101636
- Zoncu, R., Bar-Peled, L., Efeyan, A., Wang, S., Sancak, Y., and Sabatini, D. M. (2011). mTORC1 senses lysosomal amino acids through an inside-out mechanism that requires the vacuolar H⁺-ATPase. *Science* 334 (6056), 678–683. doi:10.1126/science.1207056
- Zur, A. A., Chien, H. C., Augustyn, E., Flint, A., Heeren, N., Finke, K., et al. (2016). LAT1 activity of carboxylic acid bioisosteres: evaluation of hydroxamic acids as substrates. *Bioorg. Med. Chem. Lett.* 26 (20), 5000–5006. doi:10.1016/j.bmcl.2016.09.001

Conflict of Interest: The authors declare that the research was conducted in the absence of any commercial or financial relationships that could be construed as a potential conflict of interest.

Copyright © 2021 Fairweather, Okada, Gauthier-Coles, Javed, Bröer and Bröer. This is an open-access article distributed under the terms of the Creative Commons Attribution License (CC BY). The use, distribution or reproduction in other forums is permitted, provided the original author(s) and the copyright owner(s) are credited and that the original publication in this journal is cited, in accordance with accepted academic practice. No use, distribution or reproduction is permitted which does not comply with these terms.



SLC38A10 Transporter Plays a Role in Cell Survival Under Oxidative Stress and Glutamate Toxicity

Rekha Tripathi*, Tanya Aggarwal and Robert Fredriksson

Molecular Neuropharmacology, Department of Pharmaceutical Biosciences, Uppsala University, Uppsala, Sweden

OPEN ACCESS

Edited by:

Mariafrancesca Scalise,
University of Calabria, Italy

Reviewed by:

Tatiana Olivares,
Universidad Autónoma de Baja
California, Ensenada, Mexico
Arturo Ortega,
Centro de Investigación y de Estudios
Avanzados del Instituto Politécnico
Nacional, Mexico

*Correspondence:

Rekha Tripathi
rekha.tripathi@farmbio.uu.se

Specialty section:

This article was submitted to
Cellular Biochemistry,
a section of the journal
Frontiers in Molecular Biosciences

Received: 24 February 2021

Accepted: 09 April 2021

Published: 05 May 2021

Citation:

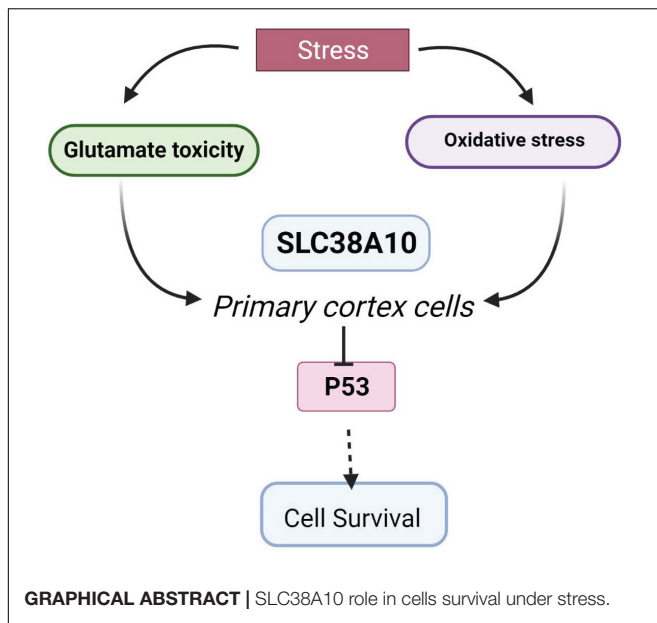
Tripathi R, Aggarwal T and
Fredriksson R (2021) SLC38A10
Transporter Plays a Role in Cell
Survival Under Oxidative Stress and
Glutamate Toxicity.
Front. Mol. Biosci. 8:671865.
doi: 10.3389/fmolb.2021.671865

Solute carrier (SLC) transporters regulate amino acids, glucose, ions, and metabolites that flow across cell membranes. In the brain, SLCs are the key regulators of neurotransmission, in particular, the glutamate/GABA-glutamine (GGG) cycle. Genetic mutations in SLCs are associated with various neurodevelopmental and neurodegenerative diseases. In this study, we have investigated the role of SLC38A10 under acute oxidative and glutamate stress in mouse primary cortical cells from SLC38A10 knockout (KO) mice. The ER/golgi localized transporter, SLC38A10, transports glutamate, glutamine, and alanine in brain cells, and the aim of this study was to determine the possible effects of removal of SLC38A10 in primary cortical cells under glutamate and oxidative challenges. Primary cortical neuronal cultures of wild-type (WT) cell and SLC38A10 KO mice were subjected to different concentrations of glutamate and hydrogen peroxide. There was no morphological change observed between KO and WT cortical neurons in culture. Interestingly, KO cells showed significantly lower cell viability and higher cell death compared to WT cells under both glutamate and hydrogen peroxide exposure. Further, we evaluated the possible role of p53 in neuronal cell apoptosis in KO cells. We found decreased intracellular p53 protein levels under glutamate and hydrogen peroxide treatment in KO cortical cells. In contrast, caspase 3/7 activity remains unaltered under all conditions. These results demonstrate an indirect relationship between the expression of SLC38A10 and p53 and a role in the cell defense mechanism against neurotoxicity.

Keywords: SLC38 family, SLC38A10, primary cortex cells, glutamate toxicity, oxidative stress, p53, cell survival

INTRODUCTION

Neuronal cells are the key players in the nervous system, with highly specialized roles in exchanging and transmitting signals. Cells maintain homeostasis with estimated cell growth and death rate. In the body, cells undergo a series of external and internal changes, an act of survival and adaptation forced by various internal and external stressors. Stress can result in either the activation of defense mechanisms to protect cells or the activation of signaling cascades leading to cell death (Fulda et al., 2010).



Oxidative stress in neuronal cells results from the presence of excess oxygen radicals that can disrupt the homeostasis of the cells, which can lead to cell death. In normal conditions, cells require a balance of antioxidants and oxygen that maintains the equilibrium between antioxidant defense mechanisms and pro-oxidant species (Fulda et al., 2010). Under stress, an increase in reactive oxygen species (ROS), such as hydrogen peroxide (H_2O_2), hydroxyl radical, and superoxide anion, can affect the critical processes of cell health, such as cellular respiration, metabolism, immunity, and cell death (Fulda et al., 2010; Wang and Michaelis, 2010; Salim, 2017). Another stress discussed in this study is glutamate excitotoxicity, which occurs due to increased amounts of glutamate. It is one of the leading causes of neuronal death and mitochondrial dysfunction, ultimately leading to neurodegenerative diseases (Lewerenz and Maher, 2015; Fricker et al., 2018).

Stress stimuli induce cellular stress that can support cell survival or lead to cell death (Fulda et al., 2010). The cells can initiate different death signaling pathways, depending on the type of cellular stress response. The cell death program can vary from programmed cell death (apoptosis and autophagy) to necrosis or other forms of unknown responses (Fricker and Tolkovsky, 2011). Apoptosis is characterized biochemically by events of DNA damage, chromatin condensation, nuclear fragmentation, phagocytosis of apoptotic bodies, and activation of different caspases leading to cell death (Kerr et al., 1972). Autophagy is an internally regulated mechanism to remove or clean the unnecessary or degenerated cell material. It is mostly initiated when cells undergo metabolic stress like starvation of nutrients and growth factors, leading to ROS accumulation ultimately, affecting mTOR signaling (Lum et al., 2005; Fricker et al., 2018). Necrosis is an unnatural cell death due to various factors such as glutamate toxicity, ROS, and calcium generation, leading to swelling and gain of cell volume and rupturing of the plasma membrane (Ankarcrona et al., 1995; Schulze-Osthoff et al., 1998).

In cells, amino acid transporters play vital roles of sensors and transporters of nutrients, neurotransmitters, drugs, and ions (Sundberg et al., 2008). Most amino acid transporters are members of the solute carrier (SLC) family that consists of 460 members, of which many are poorly characterized (Perland and Fredriksson, 2017). SLCs are membrane-bound transporters that are divided into 65 families with different biochemical properties and substrates of transport (Hediger et al., 2013; Kandasamy et al., 2018). In the brain, 287 SLCs have been shown to be expressed in the brain (Hu et al., 2020) and around 72 SLC genes correlated with human brain disorders such as epilepsy, neurodegenerative diseases, and autism. SLCs in the brain play important roles in regulating the homeostasis of neurotransmitters, such as GABA, glutamate, serotonin, dopamine, and noradrenaline, and in the regulation of their concentration in synaptic regions. Therefore, it is important to investigate the functions of SLCs expressed in the brain linked to neurotransmission. In this study, we have focused on one member of the SLC38 family, SLC38A10, and some other members of this family are involved in regulating the glutamate and glutamine cycle in the brain, for example, SLC38A3 and SLC38A5 (Şehirli and Aykaç, 2020). The SLC38 amino acid transporter family is known as the sodium-coupled neutral amino acid transporter (SNAT) family, and it consists of 11 members, SNAT1-11 (Sundberg et al., 2008). Most of the members are expressed in the brain in various cell types (Hägglund et al., 2011, 2015). SLC38A10 is found in endoplasmic reticulum (ER)/golgi of neurons and astrocytes in the mouse brain and transports glutamine, glutamate, and aspartate (Hellsten et al., 2017; Tripathi et al., 2019). The functional relevance remains unexplored in terms of the effect on the health of brain cells. This study presents the effect of SLC38A10 gene knockout (KO) on primary mouse cortical cells under normal and stressed conditions. We found that SLC38A10 KO cells showed differences in cell viability, proliferation, and cytotoxicity compared to wild-type(WT) cells.

MATERIALS AND METHODS

Animals

The study experiments using mice were approved by the Uppsala Animal Ethical Committee (3 5.8.18-09820/2018) and followed the Swedish welfare legislation. The animals were kept in an animal facility with a controlled environment, including humidity (45–65%), temperature (20–24°C), and a ventilation system with a 12-h light/dark cycle where they had access to food and water. C57BL/6 mice were used for both WT and as a background for a KO line. KO mice were bought from IMPC¹ with *Slc38a10*^{tm2a} (EUCOMM)Wtsi/H allele. For making the embryonic primary cultures, male and female mice were put together. A check for a vaginal plug was carried out in the morning after. The day when a vaginal plug was detected was defined as gestation day e0.5.

¹<https://www.mousephenotype.org>

Primary Mouse Cortical Cells and Treatments

Primary cortical cultures were performed as described previously (Hellsten et al., 2018), e15 embryos were removed and kept in cold Hank's Balanced Salt Solution (HBSS) (Gibco, United States). The mouse cortical tissue was dissected in 1X PBS with 10 mM glucose from WT and KO mice. The tissue dissociated using both chemical and mechanical procedures using an enzymatic mixture of DNase (Invitrogen, United States) (1 μ l) and papain (Sigma, United States) (10 μ l) in 1 ml diluted in PBS-10mM glucose for 20–30 minutes at 37°C, 5% CO₂. The tissue was replaced and mechanically dissociated in a plating media containing DMEM/F12 (Invitrogen, Thermo Fisher Scientific, United States), 10% FBS (Gibco, United States), 2 mM GlutaMax (Invitrogen, United States), 1 mM Na-pyruvate (Invitrogen, United States), and 1% Penicillin/streptomycin (Invitrogen, United States). The cell suspension was filtered through a 40- μ m cell strainer and counted with a hemocytometer. The plates/coverslips (12 mm, Menzel Glaser) to be used were coated with poly-L-lysine solution (P4707, Sigma-Aldrich, United States). Cells were plated at densities of 10,000 cells/well for 96-well-plates, 50,000 cells/well for 24-well-plates, and 100,000 cells/well for 6-well-plates. Cells were incubated for 3 h at 37°C in 5% CO₂. Once the cells were attached, the plating media (Gibco®, Life technologies, United States) was replaced with the media containing Neurobasal A media (Invitrogen, United States), 2% B27, 1% penicillin/streptomycin, 2 mM GlutaMax, and 1 mM Na-pyruvate. Two days after plating, half of the media was replaced with fresh media, followed by 7 days of culture.

For treatment, hydrogen peroxide (Sigma-Aldrich, United States, 386790-M, CAS Number 7722-84-1) was used to induce oxidative stress, and glutamate (Sigma-Aldrich, United States, G1251) was used to induce glutamate excitotoxicity. On day 7, the media was replaced with fresh media, and cells were treated with hydrogen peroxide (100 and 200 μ M) or glutamate (100 and 500 μ M) or without any treatment as controlled and incubated for 2 h at 37°C. After treatment, the cells were subjected to the experiments described below. All experiments were performed in triplicates.

Measurement of Cell Viability

Cell viability was measured with CellTiter 96 Aqueous One Solution Cell Proliferation Assay (Promega G3582, United States), which is composed of tetrazolium compound MTS [3-(4,5-dimethylthiazol-2-yl)-5-(3-carboxymethoxyphenyl)-2-(4-sulfophenyl)-2H-tetrazolium]. MTS is bio-reduced by cells to a colored formazan product that is soluble in the culture media. The quantity of formazan measured is directly proportional to the number of living cells in culture. Cells were cultured in 96-well-plates as described above, and after hydrogen peroxide and glutamate treatment, 20 μ l of CellTiter 96® Aqueous One Solution was added into each well containing 100 μ l of the culture medium, and absorbance was measured at 490 nm using a plate reader. Results were presented as a measure of the relative fluorescence unit.

Measurement of Cytotoxicity

Cytotoxicity was determined using CytoTox-Fluor Cytotoxicity (LDH) assay (Promega G9260, United States) according to the instructions of the manufacturer. The assay used the fluorogenic peptide substrate (bis-AAF-R110) to measure protease activity associated with cytotoxicity, which is proportional to amount of dead cells. Cells were grown in opaque-walled 96-well-plates for 7 days, followed by treatments. CytoTox-Fluor Cytotoxicity assay reagent (100 μ l) was added to the cells with 100 μ l of the media in each well. The plate was incubated for 30 min at 37°C, followed by fluorescence measurement using a fluorometer at 485 nmEx/520 nmEm, and the results were presented as a measure of relative fluorescence unit.

Assay for Caspase 3 and Caspase 7

Caspase 3 and 7 activities were measured using a luminescent Caspase-Glo 3/7 Assay System (Promega G8090, United States). It is based on cell lysis, followed by caspase cleavage of the luminogenic caspase-3/7 substrate and generation of the luminescence signal produced by luciferase. Luminescence produced is proportional to the amount of caspase activity. Cells were cultured in white-walled 96-well-plates followed by the treatments as described previously. Each well containing 100 μ l of the media was added with 100 μ l of the Caspase-Glo 3/7 reagent. Cells and plates were incubated at room temperature for 1 h. Then, luminescence was recorded with a plate reader.

Measurement of ATP Levels

ATP levels were measured using the Cell Titer-Glo Luminescent Cell Viability Assay (Promega G7570, United States) according to protocol of the manufacturer. The number of metabolically active cells in culture generates a luminescent signal directly proportional to the amount of ATP. Cortical cells were cultured in opaque-walled 96-well-plates. After treatment, 100 μ l of the Cell Titer-Glo reagent was added to wells containing 100 μ l of the media. The plate was incubated at room temperature for 10 min. Luminescence was recorded with the plate reader, and data were presented graphically compared to controls.

JC1 Assay

Cells were cultured and treated as described above but in 24-well-plates. On day 7, the cell culture medium (with or without treatment) was removed and washed once with a fresh medium. Then, the medium was replaced with a medium containing JC1-dye 2 μ M (Thermofisher, Cat No. 65-0851-38), and the cells were incubated for 20 min at 37°C. The medium was removed and replaced with PBS, and cells were imaged using ImageXpress Micro XLS microscope (Molecular Devices, United States) with FITC and TxRED filter. Cell profiler was used to analyze JC1 monomer (green) and JC1 aggregated (red) mean fluorescence intensity calculated per image. The ratio for red and green intensity was calculated and represented as mean with SD.

Western Blot

Protein samples were extracted from mouse cortical cells after 7 days of culture and treatment. Samples were made by cell

lysis in RIPA buffer, and protein concentration was measured using Bradford reagent (Sigma-Merck #B6916, United States) at 595 nm. SDS-PAGE was performed using 20 µg of protein sample diluted at 1:1 ratio in Laemmli buffer (Bio-Rad Lab) with β-mercaptoethanol (Sigma, United States) and heat-treated at 95°C for 5 min. Samples were loaded on 8–12% SDS PAGE gel (Biorad, United States), and after electrophoresis, they were transferred to Trans-Blot Turbo Mini 0.2 µm Nitrocellulose (Biorad #1704158, United States) membrane. As a molecular weight marker, the prestained protein ladder of 10–180 kDa (Thermo Fisher Scientific, United States) was used. The membrane was blocked in 5% milk TTBS blocking solution for 1 h followed by overnight incubation with primary antibodies, namely, LC3B antibody (Novus biologicals, United States, Cat No. NB100-2220), p70S6 (Cell signaling #9202), and b-Actin (Sigma, United States, Cat# A2228) at 4°C. The next day, the membrane was washed three times for 10 min with 1X TTBS and then incubated with a secondary antibody diluted to 1:10,000 (Invitrogen, United States) at room temperature for 1 h. The membrane was developed using Western ECL Substrate (Bio-Rad) and visualized using a CCD camera (ChemiDoc, Bio-Rad), and staining was compared to the molecular weight marker using Image Lab Software 5.2.1 build 11 (Bio-Rad). Blots were normalized against b-Actin blotted on the same membrane for hydrogen peroxide and on GAPDH for glutamate treatment. Western blots were analyzed using Image J as described in Hellsten et al. (2018).

In-Cell ELISA Assay

Measurement of intracellular p53 levels was monitored using Colorimetric Multispecies In-Cell ELISA Kit (Cat No. 62216) as per the protocol of the manufacturer.

Data Analysis

Mean and SD was calculated from all replicates of each experiment. All analyses were performed with Graph Pad Prism version 5. *t*-tests and two-way ANOVA analysis were performed with appropriate *post-hoc* tests for multiple comparisons for each experiment, as mentioned in figure legends.

RESULTS

Effects of Chemically Induced Oxidative Stress on KO Primary Cortex Cells

We found that KO cells are significantly less viable than WT cells measured with proliferation assay under controlled conditions and the results also showed that KO cells have significantly less viability than WT cells under oxidative stress (Figure 1A). On the other hand, KO cells are more resistant to stress treatment since the viable cell number is not affected to the same extent as the WT cells under stressed conditions (Figure 1A). When cell death was measured using cytotoxicity LDH assay (Figure 1B), the results showed similar levels of cell death for KO and WT cells in controlled conditions (Figure 1B).

On the other hand, KO cells showed an increase in death under hydrogen peroxide treatment (Figure 1B). ATP levels

were measured to assess mitochondrial activity and metabolically active cells under controlled and stressed conditions (Figure 1C). We found that the ATP levels were significantly lower in KO cells than WT cells under controlled conditions. However, ATP levels were not affected by H₂O₂ stress in KO cells, while it was reduced in WT cells, reaching the same low levels as the KO cells when exposed to the highest dose of H₂O₂.

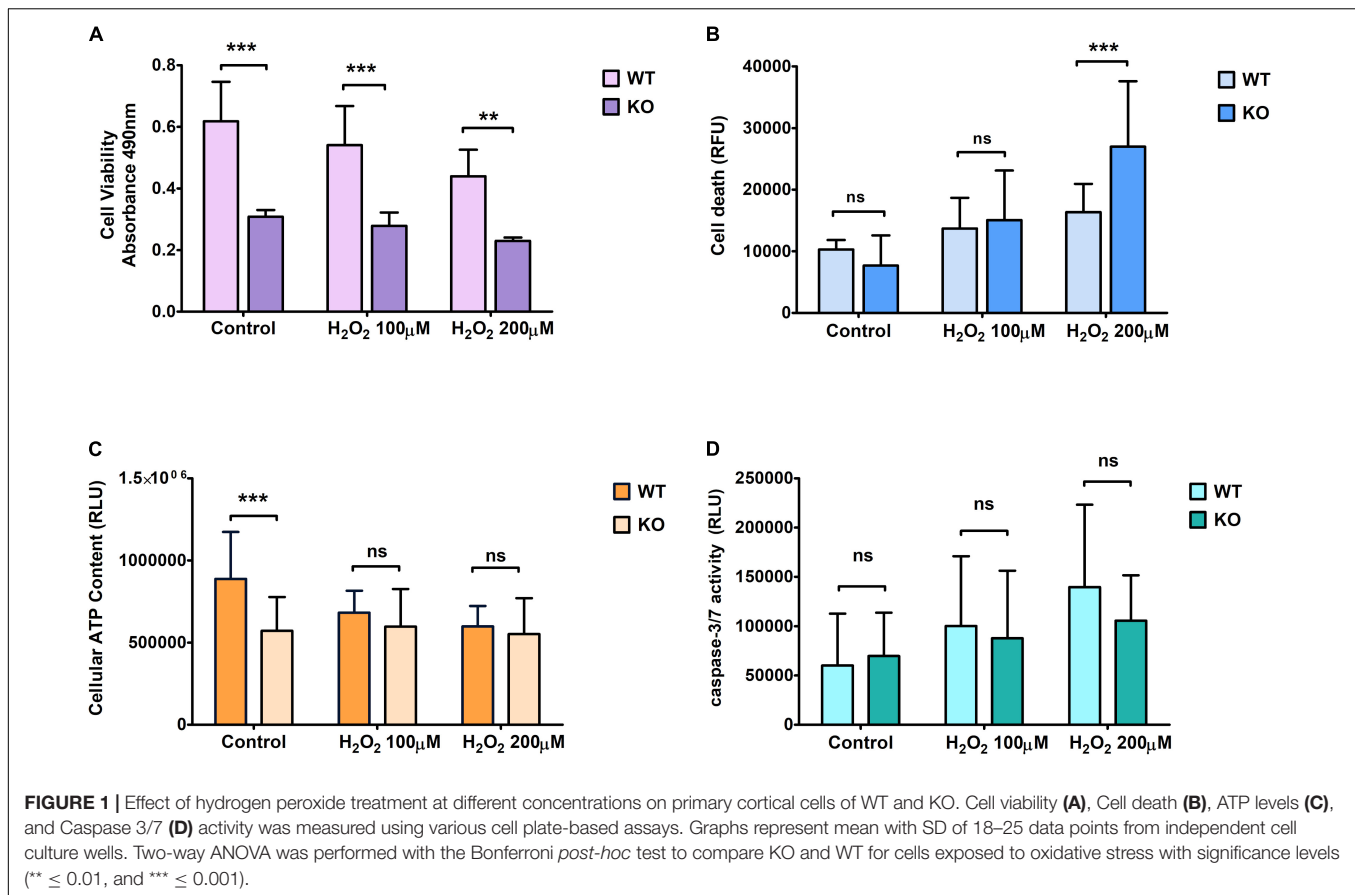
The relative luminescence was measured to check for Caspase 3/7 activity, which is based on the principle of cell lysis. We found no significant difference in caspase 3/7 activity between WT and KO cells under any conditions. The difference between controlled and stressed conditions showed a similar increment rate for both WT and KO cells (Figure 1D).

Effects of Chemically Induced Glutamate Excitotoxicity on KO Primary Cortical Cells

We found a trend similar to what we saw for hydrogen peroxide treatment regarding cell viability when cells were exposed to glutamate stress. KO cells showed more resistance under treated conditions compared to WT cells (Figure 2A). Cell death was measured using the LDH assay. KO cells showed an increased death rate under glutamate excitotoxicity (Figure 2B) compared to controlled conditions. The amount of cell death was significantly higher in KO cells than WT cells. ATP levels were reduced slightly more in WT cells than in KO cells when exposed to glutamate stress, reaching a level approximately similar to that of KO cells at the highest dose of exposure (Figure 2C). As for H₂O₂ stress, we found no significant difference in caspase 3/7 activity between WT and KO cells (Figure 2D). The bars in the graphs for control cells are the same, which are displayed in Figures 1, 2.

Unaltered Effect of KO Cells on Mitochondrial Membrane Potential Under Glutamate and Oxidative Stress Treatment

Mitochondrial dysfunction is a crucial feature of unhealthy cells and is a sign of apoptosis. Therefore, mitochondrial membrane potential (MMP) was measured using the fluorescent dye JC1. Monomer JC-1 showed green fluorescence and low MMP due to apoptotic cells, indicating mitochondrial dysfunction. Healthy cells showed higher MMP and formed JC-1 aggregates that are visible as red fluorescence. Thus, mitochondrial membrane depolarization can be measured by a ratio of red to green fluorescence. The fluorescent images showed mitochondrial activity in WT (Figure 3A) and KO (Figure 3D) cells under hydrogen peroxide and glutamate treatments. We found that KO cells showed lower MMP levels than WT cells under both stress treatment (hydrogen peroxide and glutamate) and control conditions (Figures 3B,C). This data shows that there is a possibility of mitochondrial dysfunction in KO cells.



Protein Expression of LC3B and p70S6 Under Hydrogen Peroxide Treatment

We monitored LC3 and p70S6 protein on KO primary cortex cells after hydrogen peroxide treatment (Figure 4A) and glutamate treatment (Figure 4B). There was no change in p70S6 protein in KO (Figure 4D) cells under hydrogen peroxide stress, but under glutamate treatment, p70S6 protein expression increased at 100 μM concentration and returned to the basal level at 500 μM glutamate concentration (Figure 4F). Interestingly, under 100 μM hydrogen peroxide treatment, LC3 expression was 20% lower compared with WT (Figure 4C). However, under glutamate stress at 100 μM of glutamate concentration, LC3 protein expression increased. However, under treatment with a higher concentration of glutamate, LC3 levels reached the same as basal levels of LC3 in KO primary (Figure 4E).

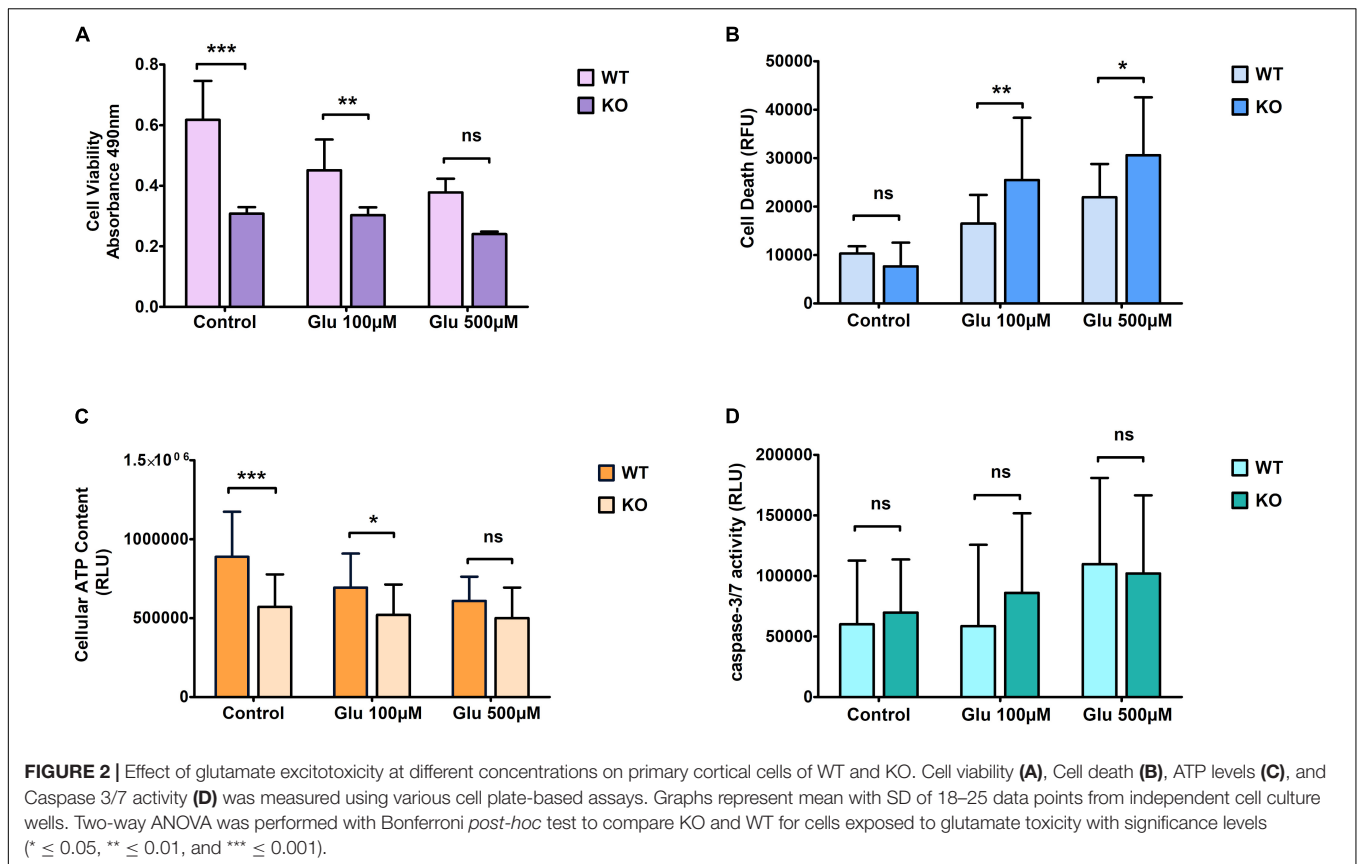
SLC38A10 KO Alters Intracellular p53 Level in KO and WT Primary Cortex Cells

Intracellular p53 levels were significantly lower in KO primary cortex cells compared with WT in controlled and glutamate exposed conditions. However, at a concentration of 100 μM , the effect is non-significant, although the trend remains the same (Figure 4H). Further, the same trend on p53 expression remains under H_2O_2 exposure (Figure 4G).

DISCUSSION

SLC38A10 is an amino acid transporter, mainly transporting glutamate, glutamine, and aspartic acid (Hellsten et al., 2017). SLC38A10 is localized in the ER and Golgi in neuronal and other cells (Tripathi et al., 2019). It was suggested that SLC38A10 plays a vital role in the regulation of neurotransmission (Hellsten et al., 2017), and polymorphisms in SLC38A10 are associated with autism spectrum disorders (Celestino-Soper et al., 2011), bipolar disorder, schizophrenia, and Alzheimer disorder in human (Guan et al., 2019). Many amino acid transporters are known to participate in redox homeostasis maintenance (Liu et al., 2020). However, there is no information available on the role of SLC38A10 on neuronal cell viability and its possible effect on acute oxidative and glutamate stress. In this study, we try to understand the role of SLC38A10 in cell survival and viability under acute stress.

Oxidative stress and glutamate toxicity are involved in the neuropathology of several neurodegenerative disorders. Glutamate, as a primary neurotransmitter in the brain, is used in around 40% of the synapses. Therefore, increased glutamate levels can result in excessive activation of glutamate receptor signaling, leading to excitotoxicity, and is connected with a wide range of acute and chronic neurodegenerative disorders (Coyle and Puttfarcken, 1993; Sheldon and Robinson, 2007). In



earlier studies of glutamate-induced cytotoxicity, various cell lines and primary cortical cells have been utilized (Kritis et al., 2015), and the glutamate transporter GLT1 and GLAST have been shown to link neurological disorders with oxidative and glutamate stress (Sheldon and Robinson; Olivares-Bañuelos et al., 2019). Abnormal glutamate levels and glutamate-glutamine cycle imbalances are one of the main causes of neurodegenerative diseases (Behrens et al., 2002), and it is therefore essential to understand the underlying function of glutamate transporters and their possible role as vital players in neurodegenerative disorders.

SLC38A10 is a known glutamate transporter, which could alter glutamate levels, which is known to affect the viability of neurons. It is known that abundant extracellular glutamate activates continuous depolarization in neurons to induce glutamate toxicity (Lewerenz and Maher, 2015; Mattson, 2019). Several neurodegenerative conditions such as Huntington's disease, Alzheimer's disease, lateral amyotrophic sclerosis, Parkinson's disease, stroke, and traumatic brain injury are associated with excitotoxicity (Hunt et al., 2010; Fendt and Verstreken, 2017).

We found that the cell viability of KO primary cortical cells is lower compared with WT, whereas under acute oxidative and glutamate stress, KO cells remain, in principle, unaffected. We found reduced levels of p53 in KO cells, which can be the underlying cause of their increased stress resistance. A lot of evidence supports that p53 can increase ROS and promote

cell elimination and death. p53 supports cell adaptation and survival in response to different stress, such as limited periods of nutrient starvation and hydrogen peroxide, glutamate, and ROS exposure to support survival (Coyle and Puttfarcken, 1993). In neurons, p53 is associated with acute and progressive neurological conditions (Xiang et al., 1996), and loss of p53 in the liver results in changed redox homeostasis and increased DNA damage (Tedeschi and Di Giovanni, 2009).

Previously, p53 has been shown to be involved in amino acid metabolism in cancer cells, specifically with a role in glutamine homeostasis (Tajan et al., 2018). There are several SLCs involved in amino acid homeostasis connected to neuronal disorders (Kandasamy et al., 2018). In cancer cells, the arginine transporter, SLC7A3, is regulated by p53 under glutamine starvation and participate in metabolic regulation of nutrient stress (Lowman et al., 2019). Recent studies have revealed that SLC7A11 promotes cystine uptake and glutathione biosynthesis, resulting in protection from oxidative stress and ferroptotic cell death, and plays critical roles in regulating the glucose and glutamine dependency of cancer cells (Koppula et al., 2018). Similarly, the transporters, SLC35A1 and SLC30A1, act as opposite regulators in cell survival. These transporters play a role in modulating cellular apoptotic response induced to oncolytic virus infections (Moskovskich et al., 2019). We observed similar results after removal of SLC38A10 primary cortex cells, where it does play a role in cell survival under stress. Also, similar to a previous study on primary cortical neurons in culture, homozygote p53 KO mice

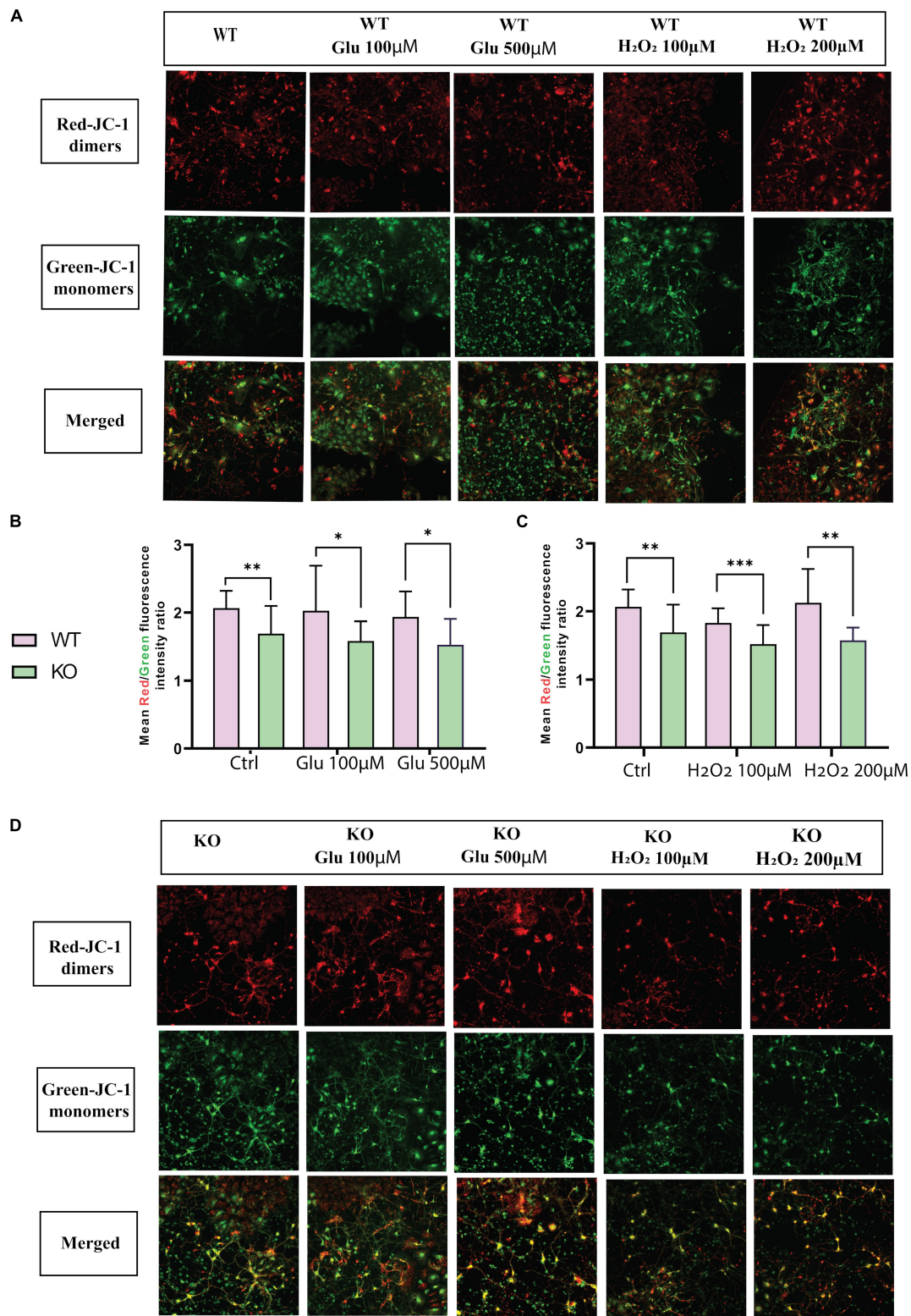


FIGURE 3 | MMP $\Delta\Psi_m$ was measured in primary cortex cells of WT (A) and KO (D) under different treatments of glutamate and hydrogen peroxide using the JC-1 dye. Images were captured using ImageXpress from a molecular device. The fluorescence intensity was measured for both JC-1 green for J-monomers or red for J-aggregates. The graph represents the means of the ratio of fluorescence intensity of red aggregates/green monomer per image for WT and KO primary cortex cells under glutamate toxicity (B) and hydrogen peroxide (C) treatments. Unpaired *t*-test was performed to compare KO and WT for cells exposed to glutamate excitotoxicity (B) and oxidative stress (C) with significance levels (* ≤ 0.05 , ** ≤ 0.01 , and *** ≤ 0.001).

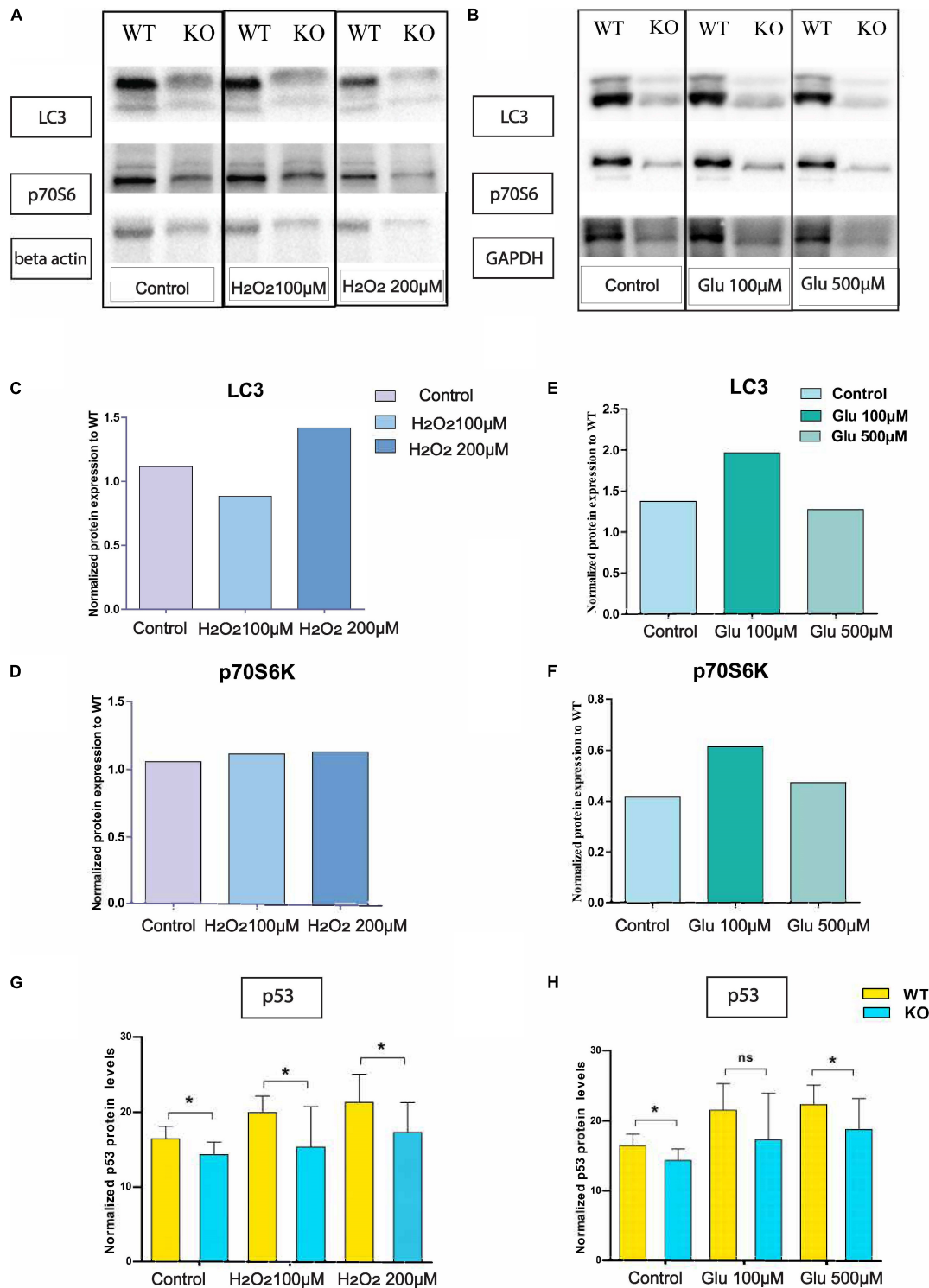


FIGURE 4 | Altered protein levels of protein expression in primary cortex cells of WT and KO under stress. Immunoblot data of antibody LC3 and p-70S6 on hydrogen peroxide (A) treated primary cortex cells from WT and KO. The graph represents the ratio of protein expression of LC3 (C) and p70S6 (D) in KO primary cortex cells compared to WT cells after normalization with respect to loading controls (beta-actin). Immunoblot data of antibody LC3 and p-70S6 under glutamate treated primary cortex cells from WT and KO (B). The graph represents the ratio of protein expression of LC3 (E) and p70S6 (F) in KO primary cortex cells compared to WT cells after normalization with respect to loading controls (GAPDH). Intracellular p53 protein expression was measured using an In-Cell ELISA p53 kit. The graph represents means with SD, and an unpaired *t*-test was performed to compare KO and WT for cells exposed to oxidative stress (G) and glutamate excitotoxicity (H) with significance levels (* ≤ 0.05).

exhibit little or no response or adverse effects to glutamate stress (Xiang et al., 1996). These results corroborate the findings that KO primary cortex cells remain unaffected in stress. Also, in the present study, we showed that SLC38A10 KO cells have lower p53 expression, which could in part be the cause of the increased resistance to excitotoxicity and H₂O₂ challenge.

CONCLUSION

SLC38A10 potentially has a role in the adaptation of primary cortex cells under acute stress. The absence of the SLC38A10 gene resulted in changed p53 levels and affected the mitochondrial function. Also, p53 helps to support cell adaptation and survival in response to stressors (Wang et al., 2014). This study establishes a possible correlation of SLC38A10 in cell survival, linked with p53, in primary cortex cells. Thus, there is a need to investigate in detail the role of SLC38A10 amino acid transporter in cellular health.

DATA AVAILABILITY STATEMENT

The original contributions presented in the study are included in the article/**Supplementary Material**, further inquiries can be directed to the corresponding author/s.

ETHICS STATEMENT

The animal study was reviewed and approved by (3 5.8.18-09820/2018).

REFERENCES

- Ankarcrona, M., Dypbukt, J. M., Bonfoco, E., Zhivotovsky, B., Orrenius, S., Lipton, S. A., et al. (1995). Glutamate-induced neuronal death: a succession of necrosis or apoptosis depending on mitochondrial function. *Neuron* 15, 961–973. doi: 10.1016/0896-6273(95)90186-8
- Behrens, P. F., Franz, P., Woodman, B., Lindenberg, K. S., Landwehrmeyer, G. B., and Behrens, P. F. (2002). Impaired glutamate transport and glutamate± glutamine cycling: downstream effects of the Huntington mutation. *Brain* 125, 1908–1922.
- Coyle, J. T., and Puttfarcken, P. (1993). Oxidative stress, glutamate, and neurodegenerative disorders. *Science* 262, 689–695. doi: 10.1126/science.7901908
- Fendt, S. M., and Verstreken, P. (2017). Neurons eat glutamate to stay alive. *J. Cell Biol.* 216, 863–865. doi: 10.1083/jcb.20170203
- Fricker, M., and Tolkovsky, A. M. (2011). “Necrosis, Apoptosis, and Autophagy: Mechanisms of Neuronal and Glial Cell Death,” in *Cell Culture Techniques*, eds M. Aschner, C. Suñol, and A. Bal-Price (Totowa: Humana Press), 305–330. doi: 10.1007/978-1-61779-077-5_15
- Fricker, M., Tolkovsky, A. M., Borutaite, V., Coleman, M., and Brown, G. C. (2018). Neuronal cell death. *Physiol. Rev.* 98, 813–880. doi: 10.1152/physrev.00011.2017
- Fulda, S., Gorman, A. M., Hori, O., and Samali, A. (2010). Cellular Stress Responses: cell Survival and Cell Death. *Int. J. Cell Biol.* 2010:214074. doi: 10.1155/2010/214074
- Guan, J., Cai, J. J., Ji, G., and Sham, P. C. (2019). Commonality in dysregulated expression of gene sets in cortical brains of individuals with autism, schizophrenia, and bipolar disorder. *Transl. Psychiatry* 9:152. doi: 10.1038/s41398-019-0488-4
- Häggglund, M. G. A., Hellsten, S. V., Bagchi, S., Philippot, G., Löfqvist, E., Nilsson, V. C. O., et al. (2015). Transport of L-glutamine, L-alanine, L-arginine and L-histidine by the neuron-specific *slc38a8* (SNAT8) in cns. *J. Mol. Biol.* 427, 1495–1512. doi: 10.1016/j.jmb.2014.10.016
- Häggglund, M. G. A., Sreedharan, S., Nilsson, V. C. O., Shaik, J. H. A., Almkvist, I. M., Bäcklin, S., et al. (2011). Identification of SLC38A7 (SNAT7) protein as a glutamine transporter expressed in neurons. *J. Biol. Chem.* 286, 20500–20511. doi: 10.1074/jbc.M110.162404
- Hediger, M. A., Cléménçon, B., Burrier, R. E., and Bruford, E. A. (2013). The ABCs of membrane transporters in health and disease (SLC series): introduction. *Mol. Aspect. Med.* 34, 95–107. doi: 10.1016/j.mam.2012.12.009
- Hellsten, S. V., Häggglund, M. G., Eriksson, M. M., and Fredriksson, R. (2017). The neuronal and astrocytic protein SLC38A10 transports glutamine, glutamate, and aspartate, suggesting a role in neurotransmission. *FEBS Open Bio.* 7, 730–746. doi: 10.1002/2211-5463.12219

AUTHOR CONTRIBUTIONS

RT wrote and drafted manuscript, planned and performed experiments, carried out analysis of data, prepared figures, performed interpretation of data and results, and wrote parts of the manuscript. TA planned and performed cell plate assay, western blot experiments, analysis part of data, and wrote parts of the manuscript. RF obtained funding for the project, supervised the project, performed data analysis and data interpreting, and wrote parts of the manuscript. All authors have read and approved the manuscript and helped with the interpretation of the results.

FUNDING

This study was supported by the Swedish Research Council, the Novo Nordisk Foundation, Åhlens foundation, Engkvist Foundation, Gunvor and Josef Anérs foundation, and the Swedish brain foundation.

ACKNOWLEDGMENTS

We thank Frida. A., Linderberg for knockout breeding and helping in primary cortex culture dissections. They also thank Anna Klem from BioImage Informatics Facility, SciLifeLab, for all her help with image analysis.

SUPPLEMENTARY MATERIAL

The Supplementary Material for this article can be found online at: <https://www.frontiersin.org/articles/10.3389/fmolb.2021.671865/full#supplementary-material>

- Hellsten, S. V., Tripathi, R., Ceder, M. M., and Fredriksson, R. (2018). Nutritional stress induced by amino acid starvation results in changes for Slc38 transporters in immortalised hypothalamic neuronal cells and primary cortex cells. *Front. Mol. Biosci.* 5:45. doi: 10.3389/fmolb.2018.00045
- Hu, C., Tao, L., Cao, X., and Chen, L. (2020). The solute carrier transporters and the brain: physiological and pharmacological implications. *Asian J. Pharmaceut. Sci.* 15, 131–144. doi: 10.1016/j.ajps.2019.09.002
- Hunt, W. T., Kamboj, A., Anderson, H. D., and Anderson, C. M. (2010). Protection of cortical neurons from excitotoxicity by conjugated linoleic acid. *J. Neurochem.* 115, 123–130. doi: 10.1111/j.1471-4159.2010.06908.x
- Kandasamy, P., Gyimesi, G., Kanai, Y., and Hediger, M. A. (2018). Feature Review Amino acid transporters revisited: new views in health and disease. *Trends Biochem. Sci.* 43, 752–789. doi: 10.1016/j.tibs.2018.05.003
- Kerr, J. F. R., Wyllie, A. H., and Currie, A. R. (1972). Apoptosis: a basic biological phenomenon with wide-ranging implications in tissue kinetics. *Br. J. Cancer* 26, 239–257. doi: 10.1038/bjc.1972.33
- Koppula, P., Zhang, Y., Zhuang, L., and Gan, B. (2018). Amino acid transporter SLC7A11/xCT at the crossroads of regulating redox homeostasis and nutrient dependency of cancer. *Cancer Commun.* 38:12. doi: 10.1186/s40880-018-0288-x
- Kritis, A. A., Stamoula, E. G., Paniskaki, K. A., and Vavilis, T. D. (2015). Researching glutamate – induced cytotoxicity in different cell lines: a comparative/collective analysis/study. *Front. Cell. Neurosci.* 9:91. doi: 10.3389/fncel.2015.00091
- Lewerenz, J., and Maher, P. (2015). Chronic glutamate toxicity in neurodegenerative diseases-What is the evidence? *Front. Neurosci.* 9:469. doi: 10.3389/fnins.2015.00469
- Celestino-Soper, P. B., Shaw, C. A., Sanders, S. J., Li, J., Murtha, M. T., Ercan-Sencicek, A. G., Davis, L., et al. (2011). *Use of array CGH to detect exonic copy number variants throughout the genome in autism families detects a novel deletion in TMLHE. *Hum. Mol. Genet.* 20, 4360–4370. doi: 10.1093/hmg/ddr363
- Liu, X., Fan, L., Lu, C., Yin, S., and Hu, H. (2020). Review Article Functional Role of p53 in the Regulation of Chemical-Induced Oxidative Stress. *Oxid. Med. Cell. Longev.* 2020:6039769. doi: 10.1155/2020/6039769
- Lowman, X. H., Hanse, E. A., Yang, Y., Ishak Gabra, M. B., Tran, T. Q., Li, H., et al. (2019). p53 Promotes Cancer Cell Adaptation to Glutamine Deprivation by Upregulating Slc7a3 to Increase Arginine Uptake. *Cell Rep.* 26, 3051–3060.e4. doi: 10.1016/j.celrep.2019.02.037
- Lum, J. J., Bauer, D. E., Kong, M., Harris, M. H., Li, C., Lindsten, T., et al. (2005). Growth factor regulation of autophagy and cell survival in the absence of apoptosis. *Cell* 120, 237–248. doi: 10.1016/j.cell.2004.11.046
- Mattson, M. P. (2019). "Excitotoxicity," in *Stress: Physiology, Biochemistry, and Pathology Handbook of Stress Series, Volume 3*. Amsterdam: Elsevier, 125–134. doi: 10.1016/B978-0-12-813146-6.00011-4
- Moskovskich, A., Goldmann, U., Kartnig, F., Lindinger, S., Konecka, J., Fiume, G., et al. (2019). The transporters SLC35A1 and SLC30A1 play opposite roles in cell survival upon VSV virus infection. *Sci. Rep.* 9, 1–11. doi: 10.1038/s41598-019-46952-9
- Olivares-Bañuelos, T. N., Chí-Castañeda, D., and Ortega, A. (2019). Glutamate transporters: gene expression regulation and signaling properties. *Neuropharmacology* 161:107550. doi: 10.1016/j.neuropharm.2019.02.032
- Perland, E., and Fredriksson, R. (2017). Classification systems of secondary active transporters. *Trend. Pharmacol. Sci.* 38, 305–315. doi: 10.1016/j.tips.2016.11.008
- Salim, S. (2017). Oxidative stress and the central nervous system. *J. Pharmacol. Exp. Ther.* 360, 201–205. doi: 10.1124/jpet.116.237503
- Schulze-Osthoff, K., Ferrari, D., Los, M., Wesselborg, S., and Peter, M. E. (1998). Apoptosis signaling by death receptors. *European J. Biochem.* 254, 439–459. doi: 10.1046/j.1432-1327.1998.2540439.x
- Şehirli, A. Ö, and Aykaç, A. (2020). The Role of the SLC Transporters Protein in the Neurodegenerative Disorders. *Clin. Psychopharmacol. Neurosci.* 18, 174–187. doi: 10.9758/cpn.2020.18.2.174
- Sheldon, A. L., and Robinson, M. B. (2007). The role of glutamate transporters in neurodegenerative diseases and potential opportunities for intervention. *Neurochem. Int.* 51, 333–355. doi: 10.1016/j.neuint.2007.03.012
- Sundberg, B. E., Wääg, E., Jacobsson, J. A., Stephansson, O., Rumaks, J., Svirskis, S., et al. (2008). The evolutionary history and tissue mapping of amino acid transporters belonging to solute carrier families SLC32, SLC36, and SLC38. *J. Mol. Neurosci.* 35, 179–193. doi: 10.1007/s12031-008-9046-x
- Tajan, M., Hock, A. K., Blagih, J., Robertson, N. A., Labuschagne, C. F., Kruiswijk, F., et al. (2018). A Role for p53 in the Adaptation to Glutamine Starvation through the Expression of SLC1A3. *Cell Metabol.* 28, 721–736.e6. doi: 10.1016/j.cmet.2018.07.005
- Tedeschi, A., and Di Giovanni, S. (2009). The non-apoptotic role of p53 in neuronal biology: enlightening the dark side of the moon. *EMBO Rep.* 10, 576–583. doi: 10.1038/embor.2009.89
- Tripathi, R., Hosseini, K., Arapi, V., Fredriksson, R., and Bagchi, S. (2019). SLC38A10 (SNAT10) is Located in ER and Golgi Compartments and Has a Role in Regulating Nascent Protein Synthesis. *Int. J. Mol. Sci.* 20:6265. doi: 10.3390/ijms20246265
- Wang, D. B., Kinoshita, C., Kinoshita, Y., and Morrison, R. S. (2014). P53 and mitochondrial function in neurons. *Biochim. Biophys. Acta* 1842, 1186–1197. doi: 10.1016/j.bbadis.2013.12.015
- Wang, X., and Michaelis, E. K. (2010). Selective neuronal vulnerability to oxidative stress in the brain. *Front. Aging Neurosci.* 2:12. doi: 10.3389/fnagi.2010.00012
- Xiang, H., Hochman, D. W., Saya, H., Fujiwara, T., Schwartzkroin, P. A., and Morrison, R. S. (1996). Evidence for p53-mediated modulation of neuronal viability. *J. Neurosci.* 16, 6753–6765. doi: 10.1523/jneurosci.16-21-06753.1996

Conflict of Interest: The authors declare that the research was conducted in the absence of any commercial or financial relationships that could be construed as a potential conflict of interest.

Copyright © 2021 Tripathi, Aggarwal and Fredriksson. This is an open-access article distributed under the terms of the Creative Commons Attribution License (CC BY). The use, distribution or reproduction in other forums is permitted, provided the original author(s) and the copyright owner(s) are credited and that the original publication in this journal is cited, in accordance with accepted academic practice. No use, distribution or reproduction is permitted which does not comply with these terms.



Substrate Specificities and Inhibition Pattern of the Solute Carrier Family 10 Members NTCP, ASBT and SOAT

Gary Grosser[†], Simon Franz Müller[†], Michael Kirstgen, Barbara Döring and Joachim Geyer^{*}

Institute of Pharmacology and Toxicology, Faculty of Veterinary Medicine, Justus Liebig University Giessen, Biomedical Research Center Seltersberg (BFS), Giessen, Germany

OPEN ACCESS

Edited by:

Cesare Indiveri,
University of Calabria, Italy

Reviewed by:

Giuliano Ciarimboli,
University of Münster, Germany
Miriam Zacchia,
University of Campania Luigi Vanvitelli,
Italy

*Correspondence:

Joachim Geyer
Joachim.M.Geyer@vetmed.uni-
giessen.de

[†]These authors have contributed
equally to this work and share first
authorship.

Specialty section:

This article was submitted to
Cellular Biochemistry,
a section of the journal
Frontiers in Molecular Biosciences

Received: 01 April 2021

Accepted: 04 May 2021

Published: 17 May 2021

Citation:

Grosser G, Müller SF, Kirstgen M,
Döring B and Geyer J (2021) Substrate
Specificities and Inhibition Pattern of
the Solute Carrier Family 10 Members
NTCP, ASBT and SOAT.
Front. Mol. Biosci. 8:689757.
doi: 10.3389/fmolb.2021.689757

Three carriers of the solute carrier family SLC10 have been functionally characterized so far. Na⁺/taurocholate cotransporting polypeptide NTCP is a hepatic bile acid transporter and the cellular entry receptor for the hepatitis B and D viruses. Its intestinal counterpart, apical sodium-dependent bile acid transporter ASBT, is responsible for the reabsorption of bile acids from the intestinal lumen. In addition, sodium-dependent organic anion transporter SOAT specifically transports sulfated steroid hormones, but not bile acids. All three carriers show high sequence homology, but significant differences in substrate recognition that makes a systematic structure-activity comparison attractive in order to define the protein domains involved in substrate binding and transport. By using stably transfected NTCP-, ASBT-, and SOAT-HEK293 cells, systematic comparative transport and inhibition experiments were performed with more than 20 bile acid and steroid substrates as well as different inhibitors. Tauroolithocholic acid (TLC) was identified as the first common substrate of NTCP, ASBT and SOAT with K_m values of 18.4, 5.9, and 19.3 μ M, respectively. In contrast, lithocholic acid was the only bile acid that was not transported by any of these carriers. Troglitazone, BSP and erythrosine B were identified as pan-SLC10 inhibitors, whereas cyclosporine A, irbesartan, ginkgolic acid 17:1, and betulinic acid only inhibited NTCP and SOAT, but not ASBT. The HBV/HDV-derived myr-preS1 peptide showed equipotent inhibition of the NTCP-mediated substrate transport of taurocholic acid (TC), dehydroepiandrosterone sulfate (DHEAS), and TLC with IC_{50} values of 182 nM, 167 nM, and 316 nM, respectively. In contrast, TLC was more potent to inhibit myr-preS1 peptide binding to NTCP with IC_{50} of 4.3 μ M compared to TC (IC_{50} = 70.4 μ M) and DHEAS (IC_{50} = 52.0 μ M). Based on the data of the present study, we propose several overlapping, but differently active binding sites for substrates and inhibitors in the carriers NTCP, ASBT, SOAT.

Keywords: SLC10A1, SLC10A2, substrate specificity, drug target, NTCP, transport inhibitor, cross-reactivity, SLC10A6

INTRODUCTION

The solute carrier family SLC10, also known as the “sodium bile acid cotransporter family” currently consists of seven members (SLC10A1-SLC10A7) (Geyer et al., 2006; Claro da Silva et al., 2013). Three of them (SLC10A1, SLC10A2, and SLC10A6) have been functionally characterized, while the members SLC10A3, SLC10A4, SLC10A5, and SLC10A7 are still orphan carriers (Fernandes

et al., 2007; Geyer et al., 2007; Godoy et al., 2007; Karakus et al., 2020). The founding members of the SLC10 carrier family were cloned in the early 1990s and were termed Na⁺/taurocholate cotransporting polypeptide (NTCP, gene symbol *SLC10A1*) (Hagenbuch and Meier, 1994) and apical sodium-dependent bile acid transporter (ASBT, gene symbol *SLC10A2*) (Wong et al., 1996), both sharing 39% amino acid sequence identity. NTCP is exclusively expressed at the basolateral (sinusoidal) membrane of hepatocytes (Ananthanarayanan et al., 1994; Stieger et al., 1994) and here mediates sodium-coupled uptake of taurocholic acid (TC) and other bile acids (BA) with a Na⁺:BA stoichiometry of 2:1 (Hagenbuch and Meier, 1996; Weinman, 1997). ASBT is typically expressed in the apical brush border membrane of enterocytes of the terminal ileum (Shneider et al., 1995), where it transports conjugated BAs with high affinity in a sodium-dependent manner (Craddock et al., 1998). Both carriers are essentially involved in the maintenance of the enterohepatic circulation of BAs (Döring et al., 2012). In 2007, we cloned an additional SLC10 carrier, named sodium-dependent organic anion transporter (SOAT, gene symbol *SLC10A6*) (Geyer et al., 2007). Although SOAT shows the highest sequence identity of 48% to ASBT, it does not represent a BA transporter (Geyer et al., 2007). In contrast, SOAT specifically transports 3' sulfated steroid hormones such as estrone-3-sulfate (E₁S), estradiol-3-sulfate, dehydroepiandrosterone sulfate (DHEAS), androstenediol-3-sulfate, androsterone-3-sulfate, and pregnenolone sulfate (PREGS) (Fietz et al., 2013) and, thereby, has a role for steroid supply to different organs (Geyer et al., 2017). In addition, SOAT transports 17' sulfated steroids such as testosterone-17β-sulfates, but not steroid disulfates such as 17β-estradiol-3,17-disulfate (Grosser et al., 2018).

Apart from their roles as physiological uptake carriers for BAs and sulfated steroid hormones, all three carriers were also established as drug targets. In 2012, NTCP was identified as the high-affinity hepatic entry receptor for the hepatitis B (HBV) and hepatitis D (HDV) viruses (Yan et al., 2012; Drexler et al., 2013). More precisely, both viruses bind to NTCP with their 2–48 N-terminal amino acids of the myristoylated preS1 domain (so-called myr-preS1 peptide) of the large envelope protein and this triggers the cellular entry of the virus/NTCP complex (Iwamoto et al., 2019). Interestingly, BA binding and myr-preS1 peptide binding to NTCP directly interfere with each other. BAs can block myr-preS1 peptide binding to NTCP and *in vitro* HBV/HDV infection, while myr-preS1 peptide binding to NTCP inhibits BA transport (König et al., 2014; Ni et al., 2014). Apart from the myr-preS1 peptide, several small molecules were detected that also block virus binding to NTCP *in vitro*, such as cyclosporine A, ezetimibe, irbesartan, ritonavir, troglitazone or betulinic acid (Fukano et al., 2019; Kirstgen et al., 2020; Li et al., 2020; Wettengel and Burwitz, 2020), but none of them is clinically approved for HBV/HDV entry inhibition yet. In contrast, pharmacological inhibitors of ASBT, such as odeixibat and maralixibat, are already in clinical use. These so-called bile acid reabsorption inhibitors (BARIs) are used to treat BA-related diseases such as intrahepatic cholestasis, primary biliary cholangitis, Alagille syndrome, or non-alcoholic

steatohepatitis (Karpen et al., 2020). In addition, BARIs are used to treat chronic constipation by increasing the intestinal BA content and to lower plasma LDL-cholesterol levels by increasing the *de novo* hepatic synthesis of BAs from the precursor cholesterol (Kramer and Glombik, 2006; Al-Dury and Marschall, 2018). SOAT is expressed in breast cancer and here mediates the uptake of pro-proliferative sulfated estrogen precursors. Inhibition of SOAT had anti-proliferative effects in breast cancer cells *in vitro*, and so was proposed as potential novel anti-cancer drug target (Karakus et al., 2018).

Since the cloning of SOAT it is still an open question why the close phylogenetic relationship of ASBT and SOAT is not reflected at the functional level, while the more distant carriers NTCP and ASBT are close functional homologs. Therefore, in the present study we aimed to compare systematically the substrate specificities of NTCP, ASBT and SOAT and their inhibition pattern. Based on the data of the present study, we propose several overlapping substrate and inhibitor binding sites at the three carriers that have to be considered as potential off-target sites when one of these carriers is addressed with pharmacological inhibitors. Furthermore, we identified tauroolithocholic acid (TLC) as the first common substrate of all three carriers.

MATERIALS AND METHODS

Radiochemicals and Chemicals

[³H]Dehydroepiandrosterone sulfate ([³H]DHEAS), [³H]estrone-3-sulfate ([³H]E₁S), [³H]cortisone, [³H]pregnenolone sulfate ([³H]PREGS), [³H]chenodeoxycholic acid, [³H]lithocholic acid and [³H]taurocholic acid ([³H]TC) were imported via BIOTREND Chemikalien GmbH (Cologne, Germany) from the manufacturer American Radiolabeled Chemicals, Inc. (St. Louis, United States). [³H]Cortisol was obtained from Perkin Elmer, Inc. (Boston, United States). [³H]Estrone-3β-D-glucuronide and [³H]estradiol-17β-D-glucuronide were generously provided by Dr. Bernhard Ugele (Munich, Germany). [³H]Cholic acid, [³H]deoxycholic acid, [³H]ursodeoxycholic acid, [³H]sarcosine cholic acid, [³H]glycodeoxycholic acid, [³H]glycochenodeoxycholic acid, [³H]glycoursodeoxycholic acid, [³H]taurodeoxycholic acid, [³H]taoursodeoxycholic acid and [³H]taurochenodeoxycholic acid were generously provided by Prof. Dr. Alan Hofmann, University of California (San Diego, United States). [³H]Tauroolithocholic acid ([³H]TLC) was synthesized as described before (Lowjaga et al., 2021).

Estrone-3-sulfate (E₁S), pregnenolone sulfate (PREGS), dehydroepiandrosterone sulfate (DHEAS), and taurocholic acid (TC) were obtained from Sigma-Aldrich (St. Louis, United States). Zeocin and hygromycin were purchased from Invitrogen (Groningen, Netherlands). A set of betulin derivatives (betulin, betulinic acid, lupenone, 3-O-caffeoyl betulin) was purchased from Adipogen AG (Liestal, Switzerland). Ezetimibe, bromosulfophthalein (BSP), irbesartan, losartan, erythrosine B, and ginkgolic acid C17:1, and all other chemicals if not stated otherwise were purchased from Sigma-Aldrich (St. Louis, United States). Cyclosporine A was purchased

from Tokyo Chemical Industry (Tokyo, Japan). Troglitazone was purchased from Cayman Chemical (Michigan, United States).

NTCP-HEK293, ASBT-HEK293, and SOAT-HEK293 Cells

The full-length open reading frames of NTCP, ASBT, and SOAT were cloned based on the cDNA sequences with GenBank accession numbers NM_003049 (NTCP), NM_000452 (ASBT) and NM_197965 (SOAT), respectively, as reported before (Geyer et al., 2007; Grosser et al., 2015). Sequence verified clones were used for stable transfection of FLP-In T-REX HEK293 cells (HEK293-FLPIn) according to the manufacturer's instructions (Invitrogen) as reported (Geyer et al., 2007). From the generated NTCP-HEK293, ASBT-HEK293, and SOAT-HEK293 cells transgene expression can be induced by tetracycline treatment. Cells were maintained under D-MEM/F12 medium supplemented with 10% fetal calf serum (Sigma-Aldrich), L-glutamine (4 mM), penicillin (100 U/ml), and streptomycin (100 µg/ml) (further referred to as standard medium) at 37°C, 5% CO₂, and 95% humidity. All cell culture materials and substances were purchased from Thermo Fisher Scientific (Waltham, United States) if not stated otherwise.

Cultivation and Induction of Stably Transfected HEK293 Cells for Uptake, Inhibition or Binding Studies

Stably SLC10 transporter transfected NTCP-HEK293, ASBT-HEK293, SOAT-HEK293 cells and the HEK293-FLPIn maternal cell line were seeded on 24-well plates (if not stated otherwise for individual assays). Well plates were coated with poly-D-lysine prior to seeding of 125,000 cells per well. Cells were grown with 1 ml of standard medium per well with or without tetracycline (1 mg/ml) for 72 h to induce carrier expression before respective assays were started. HEK293-FLPIn cells were cultivated with standard medium and served as control.

Substrate Screening in NTCP-HEK293, ASBT-HEK293, SOAT-HEK293, and HEK293-FLPIn Cells

Cells were washed three times with phosphate buffered saline (PBS) (137 mM NaCl, 2.7 mM KCl, 1.5 mM KH₂PO₄, 7.3 mM Na₂HPO₄, pH 7.4, 37°C). Afterward, cells were preincubated at 37°C with sodium transport buffer (containing 142.9 mM NaCl, 4.7 mM KCl, 1.2 mM MgSO₄, 1.2 mM KH₂PO₄, 1.8 mM CaCl₂, and 20 mM HEPES (all chemicals from Sigma-Aldrich), adjusted to pH 7.4), or with choline transport buffer (equimolar substitution of sodium chloride with choline chloride). Uptake experiments were initiated by replacing the preincubation buffer by 500 µL transport buffer containing the radiolabeled test compound and were performed at 37°C. Transport was terminated by removing the transport buffer and washing five-times with ice-cold PBS. Cell monolayers were lysed in 1 N NaOH with 0.1% SDS and the cell-associated radioactivity was determined by liquid scintillation counting. Protein content of

individual wells was determined by Lowry assay as reported before (Geyer et al., 2007).

Transport Inhibition in NTCP-HEK293, ASBT-HEK293, SOAT-HEK293, and HEK293-FLPIn Cells

Cells were washed three times with PBS and were preincubated with the respective inhibitor in sodium transport buffer for 5 min at 37°C. Uptake was initiated by adding the respective radiolabeled substrate to the well and incubating for a fixed time as indicated in the figures at 37°C. Transport was terminated by removing the transport buffer and washing five-times with ice-cold PBS. Cell monolayers were lysed in 1 N NaOH with 0.1% SDS and the cell-associated radioactivity and protein content was determined as described above. For uptake inhibition with the myr-preS1 peptide the sodium transport buffer contained additionally MEM-amino acid solution (ThermoFisher) at 1:50 dilution.

Binding Assays With the Myr-preS1 Peptide

NTCP-HEK293 cells were seeded into 24-well-dishes as described above. For every set of induced wells an equal number of not-induced wells were used as respective background controls. Cells were washed three times with PBS and then preincubated with sodium transport buffer supplemented with MEM-amino acid solution (ThermoFisher) at 1:50 dilution at 37°C for 5 min. The fluorescent myr-preS1-Al633 peptide was added with a final concentration of 10 nM and binding experiments were performed over 10 min at 37°C. Then, cells were washed twice with buffer at 37°C and transferred to the fluorescence reader Typhoon (GE Healthcare, Chicago, United States) to quantitatively determine bound fluorescence signals as established in our lab before (Müller et al., 2018). For calculation of the NTCP-specific binding signal, the mean background signal from the not-induced cells was subtracted. Net binding rates in the absence of any inhibitor were set to 100%.

Phylogenetic Analysis

Phylogenetic analysis of the SLC10 carriers was performed using the proteins with the following GenBank accession numbers. NP_003040.1 for NTCP/SLC10A1, NP_000443.2 for ASBT/SLC10A2, NP_689892.1 for SLC10A3, NP_689892.1 for SLC10A4, NP_001010893.1 for SLC10A5, NP_932069.1 for SOAT/SLC10A6, AAI50309.1 for SLC10A7, and O15245.2 for OCT1 as outroot. In addition, the bacterial proteins Asbt_{Nm} (PDB: 3ZUY.A) and Abst_{Yf} (PDB: 4N7X.A) were included. The phylogenetic tree was generated based on sequence alignment ClustalW (Lasergene DNASTAR) and was visualized with the FigTree tool (tree.bio.ed.ac.uk). Scale bar represents 0.1 changes per site on horizontal distance.

Quantitative Real Time PCR of Transporter Expression

The mRNA expression pattern of NTCP, ASBT and SOAT in the NTCP-HEK293, ASBT-HEK293, SOAT-HEK293, and HEK293-FLPIn

cells was analyzed by quantitative real-time PCR with cDNA from the indicated tetracycline induced stably transfected cell lines. RNA was isolated from the respective stably transfected cells or control cells grown in 6 well plates following 72 h of growth. The medium and any detached cells were removed from the well. Total RNA isolation was performed by using peqGOLD RNAPure reagent (PeqLab, Erlangen, Germany) according to the manufacturer's protocol. The RNA concentration was determined by measuring absorbance at 260 nm with a Beckmann spectrophotometer DU-640 (Beckmann, Munich, Germany). Complementary cDNA was synthesized from the RNA samples using SuperScript III First-Strand Synthesis System for RT-PCR according to the manufacturer's protocol (Invitrogen, Karlsruhe). Relative carrier expression was calculated by the $2^{-\Delta\Delta CT}$ method and represents carrier expression x-times higher compared with the calibrator (NTCP expression in SOAT-HEK293 cells). ACTB served as endogenous control. Values represent means of duplicate determinations. Relative gene expression analysis was performed by real-time PCR amplification on an ABI PRISM 7300 thermal cycler (Applied Biosystems, Darmstadt, Germany) using the TaqMan Gene Expression Assays Hs01399354_m1 for SOAT, Hs00166561_m1 for ASBT, Hs00161820_m1 for NTCP, and Hs99999903_m1 for ACTB (Applied Biosystems, Darmstadt, Germany). Real-time amplification was performed in 96-well optical plates using 5 μ L cDNA, 1.25 μ L TaqMan Gene Expression Assay, 12.5 μ L TaqMan universal PCR Master Mix and 6.25 μ L water in each 25 μ L reaction. The plates were heated for 10 min at 95°C, and 45 cycles of 15 s at 95°C and 60 s at 60°C were applied.

Data Analysis and Statistics

All transport or inhibition graphs were generated with GraphPad Prism 6.0 (GraphPad). Determination of IC₅₀ values was done by nonlinear regression analysis using the equation log (inhibitor) vs. response settings. If not stated otherwise in the legends all data represent means \pm SD of at least triplicate determinations of representative experiments.

In silico Docking

The crystal structures of two bacterial SLC10-homologous carriers have been published, namely Asbt from *Neisseria meningitidis* (Asbt_{Nm}) and Asbt from *Yersinia frederiksenii* (Asbt_{Yf}) (Hu et al., 2011; Zhou et al., 2014). Based on a more recent publication that verified the crystal structure of Abst_{Yf} (4n7x.1.a) as an outward facing model for BA transporters (Wang et al., 2021) we generated outward facing homology models of NTCP, ASBT and SOAT based on this structure via the SWISS-MODEL server (<https://swissmodel.expasy.org>). These models were used as input structures in SwissDock (<http://www.swissdock.ch/docking>) and were *in silico* docked with TLC with standard parameters. The obtained docked clusters and models were visualized with the UCSF CHIMERA software (<https://www.cgl.ucsf.edu/chimera/>). For visualization, docked clusters were reduced to TLC molecules in reasonable proximity to the putative outward facing binding pocket.

TABLE 1 | Substrate specificities and transport activity grading for NTCP, ASBT and SOAT. The primary transport data are indicated in **Figure 1**. The following grading was used. “—” represents no significant uptake compared to sodium-free control. Mean uptake “+” for values below 10, “++” for values between 10 and 100, and “+++” for values above 100 pmol/mg protein/10 min for sulfated steroid hormones. Mean uptake of bile acids “+” for values below 500, “++” for values between 500 and 1000, and “+++” for values above 1000 pmol/mg protein/30 min.

	NTCP	ASBT	SOAT
Cholic acid	++	+	—
Chenodeoxycholic acid	+	+	—
Deoxycholic acid	+	+	—
Ursodeoxycholic acid	+	—	—
Lithocholic acid	—	—	—
Sarcosine cholic acid	+	+	—
Glycocholic acid	+++	++	—
Glycochenodeoxycholic acid	+++	++	—
Glycodeoxycholic acid	+++	++	—
Glycoursodeoxycholic acid	+++	++	—
Taurocholic acid	+++	++	—
Taurochenodeoxycholic acid	+++	++	—
Taurodeoxycholic acid	+++	++	—
Tauroursodeoxycholic acid	+++	++	—
Taurolithocholic acid	+++	+++	++
DHEAS	+	—	++
E ₁ S	++	—	+
PREGS	+++	—	+++
Estrone-3 β -D-glucuronide	+	—	—
Estradiol-17 β -D-glucuronide	—	—	—
Cortisone	—	—	—
Cortisol	—	—	—

Pharmacophore Calculation

Generation of pharmacophore models was performed using PHASE (Dixon et al., 2006), integrated into the MAESTRO Molecular Modeling Interface (Version 12.2) of SCHRODINGER, Inc. (www.schrodinger.com, New York City, NY, United States). The following settings were used. Active/inactive (see **Table 1**), hypothesis should match at least 50% of actives, 4–5 features in the hypothesis, difference criterion 0.5, create excluded volume shell from actives and inactives, minimum number of inactives that must experience a clash = 1, minimum distance between active surface and excluded volumes 1 Å, excluded volume sphere radii 1 Å.

RESULTS

Comparative Substrate Screening for NTCP, ASBT, and SOAT

This study focused explicitly on comparative transport studies with NTCP, ASBT and SOAT. Therefore, stably transfected HEK293 cells were generated based on the identical HEK293-FlpIn cell line and following the identical protocol. The generated cell lines NTCP-HEK293, ASBT-HEK293, and SOAT-HEK293 showed significant overexpression of the respective carrier as shown by comparative quantitative expression analysis (see **Supplementary Figure S1**).

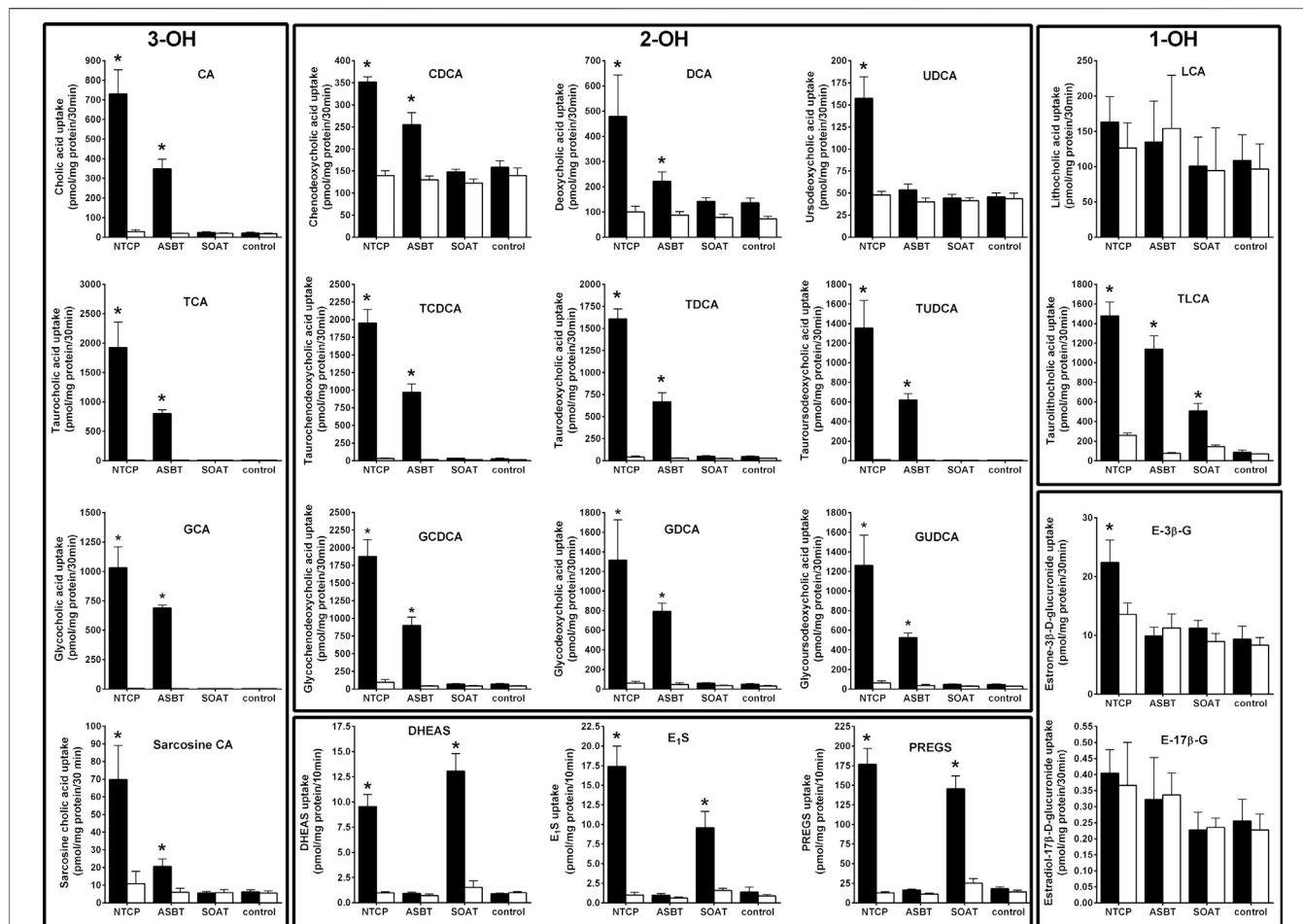


FIGURE 1 | Comparative substrate screening for bile acids and sulfated steroids in NTCP-, ASBT-, and SOAT-HEK293 cells. Transport assays were performed with the indicated substrates in NTCP-HEK293, ASBT-HEK293, SOAT-HEK293, and HEK293-FlpIn cells. Cells were washed and equilibrated with Na^+ -containing transport buffer (filled bars) or with Na^+ -free transport buffer (open bars) at 37°C . For uptake, cells were incubated with radiolabeled steroid compounds at a final concentration of 200 nM in Na^+ -containing or Na^+ -free transport buffer for 10 min. Radiolabeled bile acids were used at $1 \mu\text{M}$ concentrations and transport was analyzed over 30 min. HEK293-FlpIn cells served as additional controls. After the indicated time intervals, cells were washed with ice-cold PBS, lysed and subjected to liquid scintillation counting. Values represent means \pm SD of combined data of two independent experiments, each with quadruplicate determinations ($n = 8$). $^*p < 0.01$ (two-way ANOVA) indicating Na^+ -dependent uptake (Na^+ -containing vs. Na^+ -free transport buffer of the respective cell line). 3-OH, trihydroxylated BAs; 2-OH, dihydroxylated BAs; 1-OH, monohydroxylated BAs.

In a first approach, these cell lines were used to analyze the sodium-dependent uptake of different BAs and steroid derivatives (Figure 1). Therefore, all transport studies were performed in sodium-containing transport buffer (filled bars) as well as in sodium-free transport buffer (open bars). The non-transfected HEK293-FlpIn cell line served as additional control. In detail, this panel of test compounds included different unconjugated BAs as well as glycine-conjugated and taurine-conjugated BAs. All BAs derived from cholic acid can be classified as 3 α ,7 α ,12 α -trihydroxylated (3-OH) BAs. Together with the 3 α ,7 α -dihydroxylated (2-OH) chenodeoxycholic acid-derived BAs, these are primary BAs synthesized in the liver. Two other groups of dihydroxylated BAs, namely deoxycholic acid and ursodeoxycholic acid result from bacterial de-conjugation and isomerization, respectively. These are classified as secondary BAs. In

addition, the 3 α -monohydroxylated (1-OH) BA lithocholic acid results from bacterial de-conjugation in the gut. Secondary BAs are mostly reabsorbed in their unconjugated forms and then can be re-conjugated in the liver with glycine or taurine. As an additional BA derivative, sarcosine cholic acid was included. From the group of steroid conjugates, three sulfo-conjugated steroids, namely E₁S, DHEAS, and PREGS were analyzed, as well as the steroid glucuronides estrone-3 β -D-glucuronide and estradiol-17 β -D-glucuronide. Finally, the glucocorticoids cortisone and cortisol were used for transport experiments.

All primary transport data are presented in Figure 1. Additionally, the primary transport data were arranged in a graded manner in Table 1 for better overview and comparability. As expected, NTCP and ASBT showed significant and sodium-dependent transport activity for nearly

all BAs analyzed. The transport rates of taurine- and glycine-conjugated BAs by ASBT and NTCP are obviously higher compared to the unconjugated forms. Among the group of unconjugated BAs, ursodeoxycholic acid was only transported by NTCP, but not by ASBT, and lithocholic acid was the only BA that was transported neither by NTCP nor by ASBT. Of note, also the BA derivative sarcosine cholic acid was significantly transported by NTCP and ASBT in a sodium-dependent manner. Apart from the group of BAs, NTCP showed also significant transport activity for the steroid conjugates DHEAS, E₁S, PREGS, and estrone-3 β -D-glucuronide, but not for estradiol-17 β -D-glucuronide. The steroid sulfate carrier SOAT showed significant transport activity for DHEAS, E₁S, and PREGS as expected, but was transport negative for the steroid glucuronides and for nearly all BAs. Surprisingly, SOAT showed significant sodium-dependent uptake of TLC and, therefore, TLC is the only common substrate of all three carriers NTCP, ASBT and SOAT, identified so far.

Comparative Transport Kinetics for NTCP, ASBT, and SOAT

To closer analyze the TLC transport via NTCP, ASBT, and SOAT, transport kinetics were comparatively analyzed for all three carriers. In addition, the transport kinetics for TC, DHEAS, E₁S, and PREGS were determined. The primary transport data are presented in **Figure 2** and the Michaelis–Menten parameters K_m and V_{max} are listed in **Table 2**. The apparent K_m values for TLC were within the same range for all three carriers, being 18.4, 5.9, and 19.3 μM for NTCP, ASBT, and SOAT, respectively. The V_{max} values ranged in the order NTCP > ASBT > SOAT. The transport kinetics for TC were well comparable between NTCP and ASBT with K_m of 13.1 and 14.7 μM as well as V_{max} of 2395 and 1821 pmol/mg protein/min, respectively. Also, the transport kinetics for the sulfated steroid hormones were comparable between NTCP and SOAT with K_m of 56.1 and 28.7 μM for DHEAS, as well as 8.8 and 11.3 μM for PREGS, respectively. However, SOAT showed a much lower K_m of 12.0 μM and V_{max} of 585 pmol/mg protein/min compared to NTCP ($K_m = 57.6 \mu\text{M}$ and $V_{max} = 2367$ pmol/mg protein/min) for the substrate E₁S. Of note, the transport data of E₁S, DHEAS, and PREGS for SOAT were taken from a previous study, that used however exactly the same SOAT-HEK293 cell lines and measuring methodology (Geyer et al., 2007).

TLC, TC, and DHEAS as Inhibitors of NTCP, ASBT, and SOAT

As shown in **Figure 3**, TLC, TC, and DHEAS were used at increasing inhibitor concentrations to block the transport of the respective radiolabeled transport substrates [³H]TLC, [³H]TC, and [³H]DHEAS at all three carriers NTCP, ASBT, and SOAT. As expected, TLC inhibited the transport of [³H]TLC via NTCP, ASBT, and SOAT with comparable IC₅₀ values of 1.4 μM , 4.0 μM , and 2.6 μM , respectively (**Table 3**). Very similar was also the inhibition of the [³H]TC transport by increasing concentrations

of TC with IC₅₀ values of 5.4 μM and 5.7 μM for NTCP and ASBT, respectively. A large difference occurred, however, when DHEAS was used as inhibitor of the [³H]DHEAS transport via NTCP and SOAT. While an IC₅₀ value of 3.4 μM was measured for NTCP, this value was much higher (at 51.7 μM) for SOAT. This is most likely a result of the stimulatory effect of DHEAS on its own transport. This was observed at low micromolar concentrations several times before (data not shown). So, DHEAS can be classified as a mixed stimulator/inhibitor. When TLC was used as inhibitor of the [³H]TC or [³H]DHEAS transport via the respective carrier, the IC₅₀ values were all within the same range between 1.7 and 3.9 μM , indicating that TLC is an equipotent inhibitor of NTCP, ASBT, and SOAT, irrespective of the substrate used for transport measurements. In contrast, DHEAS showed a very different pattern, when it was used as transport inhibitor. With the transport substrate [³H]TLC, DHEAS was a potent inhibitor with an IC₅₀ of 15 μM for SOAT, but only a weak inhibitor (IC₅₀ = 431.7 μM) for NTCP, while ASBT was only inhibited by DHEAS at very high inhibitory concentrations above 1000 μM . In the same line, the IC₅₀ for DHEAS inhibition of the [³H]TC transport was much lower for NTCP (IC₅₀ = 21.5 μM) than for ASBT (IC₅₀ = 453.1 μM). This indicates that ASBT is not only transport negative for DHEAS, but seems to bind DHEAS as an inhibitor only at very high concentrations. In contrast, TC although not transported by SOAT, was a moderate inhibitor of SOAT when the transport of [³H]TLC (IC₅₀ = 143 μM) or [³H]DHEAS (IC₅₀ = 99.7 μM) was analyzed. Overall, this indicates that TLC, TC, and DHEAS are only good inhibitors at these carriers, which are also transport positive for the respective compound. Accordingly, TC is a weak inhibitor of SOAT, and DHEAS is a very weak inhibitor at ASBT. Another interesting observation was that the transport of [³H]TLC can only weakly be inhibited by TC and DHEAS, even if these compounds are transported by the respective carriers. This finding may point to the presence of separate or multiple binding sites for TLC and TC/DHEAS at the respective carriers.

Betulin-Based Inhibitors of NTCP, ASBT, and SOAT

As the next group of inhibitors, several betulin derivatives (structures see **Figure 8**) were analyzed at increasing concentrations as inhibitors of the [³H]TLC, [³H]TC, and [³H]DHEAS transport via the respective SLC10 carriers (**Table 4**). As shown in **Figure 4**, there is no common inhibition pattern and the half-maximal inhibitory concentrations showed a correlation neither for the individual carrier, nor for the betulin derivative used as inhibitor, nor for the substrate used for the transport measurements. While some of the betulin derivatives were quite potent inhibitors for NTCP and SOAT, this was not the case for ASBT. For this carrier, the only relevant inhibition was observed for 3-O-caffeoyl betulin when [³H]TLC was used as substrate with an IC₅₀ of 99.7 μM . In contrast, betulinic acid potently inhibited NTCP and SOAT, in particular when [³H]DHEAS was used as substrate (IC₅₀ = 0.3 and 1.2 μM , respectively). In a similar manner, lupenone and betulin

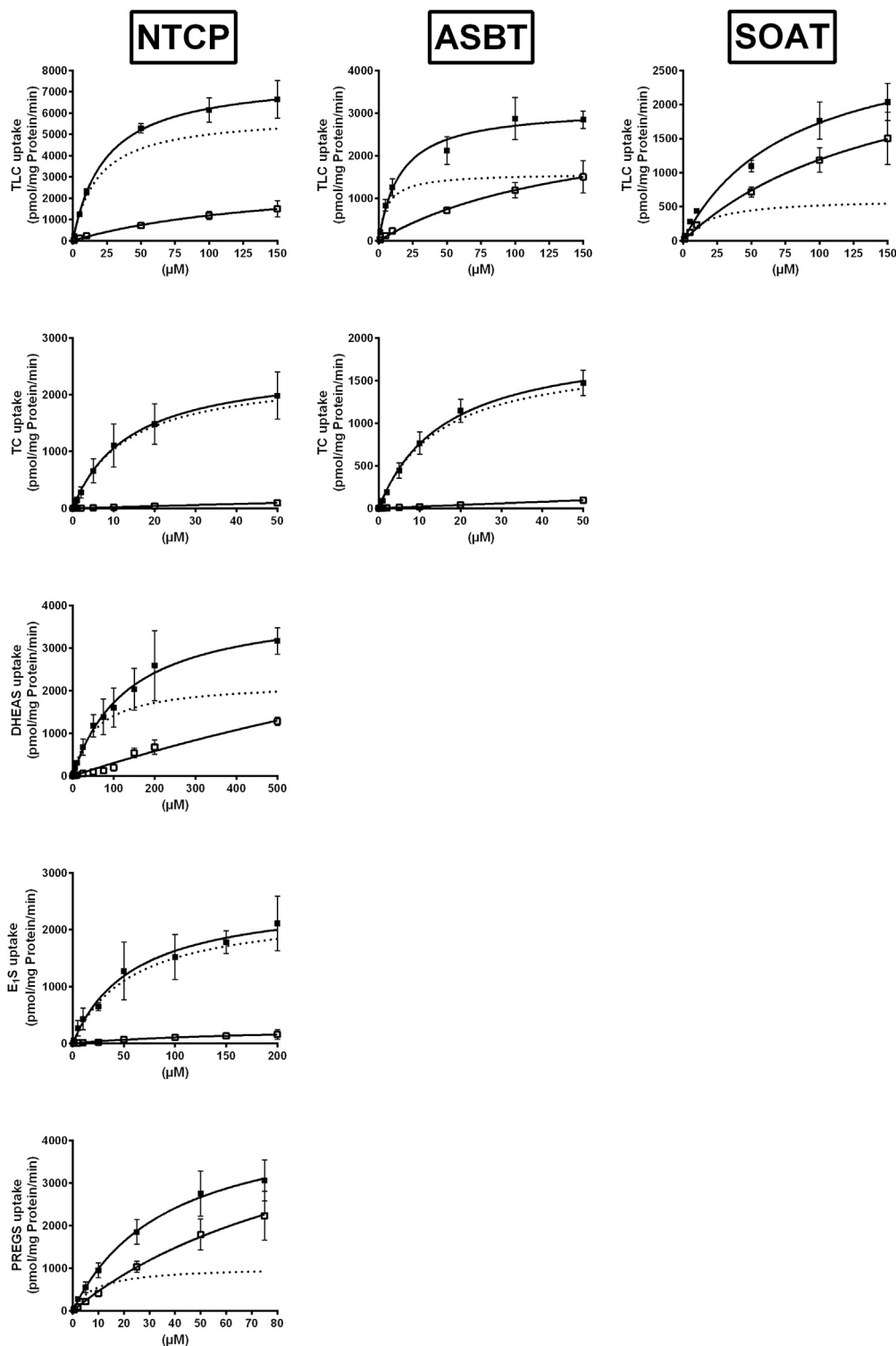


FIGURE 2 | NTCP, ASBT, and SOAT transport kinetics. Concentration-dependent uptake was analyzed in NTCP-HEK293, ASBT-HEK293, and SOAT-HEK293 cells for the indicated substrates at increasing substrate concentrations. Stably transfected HEK293 cells were pretreated with 1 $\mu\text{g/ml}$ tetracycline to induce carrier expression. HEK293-Flnp cells were used as control. Uptake was analyzed for 1 min at 37°C. Afterward, the medium was removed and each cell monolayer was washed and processed to determine the protein content and cell-associated radioactivity. Specific uptake was calculated by subtracting non-specific uptake of the HEK293-Flnp control cells (open squares) from uptake into carrier-overexpressing HEK293 cells (filled squares) and is shown by broken lines. The values represent means \pm SD of duplicate experiments, each with triplicate determinations ($n = 6$). Transport kinetic parameters are summarized in **Table 2**.

TABLE 2 | Transport kinetic parameters for TLC, TC, DHEAS, E₁S, and PREGS uptake via NTCP, ASBT, and SOAT. Michaelis-Menten kinetic parameters (K_m and V_{max}) were calculated by nonlinear regression analysis from the primary transport data shown in **Figure 2**. Values represent means \pm SD of combined data of two independent experiments, each with triplicate determinations ($n = 6$).

	Substrate	Apparent K_m (μ M)	V_{max} (pmol/mg protein/min)
NTCP	TLC	18.4 \pm 2.3	5915 \pm 189
	TC	13.1 \pm 0.8	2395 \pm 59
	DHEAS	56.1 \pm 8.0	2198 \pm 101.7
	E ₁ S	57.6 \pm 11.3	2367 \pm 170.8
	PREGS	8.8 \pm 2.1	1036 \pm 69.1
ASBT	TLC	5.9 \pm 1.8	1585 \pm 99.7
	TC	14.7 \pm 1.5	1821 \pm 75.1
SOAT	TLC	19.3 \pm 6.8	617 \pm 57
	<i>DHEAS^a</i>	<i>28.7 \pm 3.9</i>	<i>1899 \pm 81</i>
	<i>E₁S^a</i>	<i>12.0 \pm 2.3</i>	<i>585 \pm 34</i>
	<i>PREGS^a</i>	<i>11.3 \pm 3.0</i>	<i>2168 \pm 134</i>

^aValues in italic taken from Geyer et al. (2007).

are strong inhibitors at NTCP, when [³H]TLC was used as the substrate, while they lost their inhibitory potency, when [³H]DHEAS was used as substrate. This clearly indicates that the inhibitory potency of the individual betulins not only depends on the respective carrier, but also on the substrate that is used for the transport measurements. The fact that lupenone, 3-O-caffeoyl betulin and betulin had a generally higher inhibitory potency when [³H]TLC was used as the substrate additionally points to separated substrate binding sites for the substrates TLC and TC/DHEAS as already emphasized above. The only exception from this rule is betulinic acid that was much more potent as inhibitor at NTCP and SOAT when [³H]DHEAS was used as a substrate compared to [³H]TLC. However, it has to be noted that it cannot be completely excluded that betulinic acid is a transported substrate of these carrier as hypothesized before (Kirstgen et al., 2020). This could explain the differing inhibition pattern of this acidic derivative compared to the other non-acidic betulin derivatives.

Non-Steroidal Inhibitors of NTCP, ASBT, and SOAT

The inhibitor screening was also extended to compounds that previously were identified as non-steroidal inhibitors of NTCP or SOAT, including cyclosporine A, ezetimibe, bromosulphophthalein (BSP), irbesartan, losartan, troglitazone, erythrosine B, and ginkgolic acid 17:1 (Table 5, selected structures see Figure 8). All these compounds not only inhibited the transport function of NTCP, but also its role as HBV/HDV entry receptor in previous studies (Fukano et al., 2019). Therefore, these experiments also aimed to analyze the cross-reactivity of these antiviral drug candidates at the most NTCP-related proteins ASBT and SOAT. For these measurements, again all three potential transport substrates, [³H]TLC, [³H]TC, and [³H]DHEAS, were analyzed in the absence (positive control) and the presence of a fixed 100 μ M inhibitor concentration. All inhibitors then were graded as strong, medium or weak inhibitor based on the residual transport activity of 0–19% (+++), 20–49% (++) and 50–79% (+), respectively, in the presence of

inhibitor. Generally, these NTCP inhibitors showed significant cross-reactivity with SOAT and/or ASBT, at least with one of the investigated transport substrates. Therefore, compounds that were previously classified as specific NTCP inhibitors should rather be considered pan-SLC10 inhibitors. One exception was ezetimibe that only showed weak inhibitory potential at NTCP exclusively for TC as substrate. As previously shown for the betulin derivatives, the choice of the investigated SLC10 carrier substrate can affect the classification as inhibitor. As an example, losartan and ginkgolic acid 17:1 showed identical inhibitory classification for TLC and TC at NTCP, as well as for TLC and DHEAS at SOAT. However, their inhibitory potential for DHEAS as the transported substrate at NTCP revealed huge difference in classification. In contrast, irbesartan and cyclosporine A showed similar inhibition pattern at NTCP and SOAT, irrespective of the substrate used for transport measurements. However, irbesartan and cyclosporine A did not inhibit ASBT at all. This indicates that the transport of a particular substrate ([³H]TLC, [³H]TC, [³H]DHEAS) can be differentially addressed with a particular inhibitor, what would support the idea of different substrate binding sites in the SLC10 carriers.

Cross-Inhibition of the HBV/HDV-Derived Myr-preS1 Peptide with TLC, TC, and DHEAS

We used two different assays to analyze the myr-preS1 peptide binding behavior in dependence of the substrate used. First, [³H]TC, [³H]TLC, and [³H]DHEAS transport was analyzed at increasing concentrations of myr-preS1 serving as inhibitor of transport (Figure 5A). Interestingly, myr-preS1 was quasi equipotent for the inhibition of the [³H]TC and [³H]DHEAS transport with IC₅₀ values of 182 nM and 167 nM, respectively. In contrast, higher concentrations were needed for half-maximal inhibition of the [³H]TLC transport (IC₅₀ = 316 nM). In a second assay, the binding of the myr-preS1 peptide to NTCP was analyzed in the presence of increasing concentrations of TLC, TC, and DHEAS serving as peptide binding inhibitors (Figure 5B). Again, TC and DHEAS were quasi equipotent in this assay with IC₅₀ values of 70.4 μ M and 52.0 μ M, respectively, whereas an order of magnitude lower concentrations of TLC were needed to replace the myr-preS1 peptide from its binding sites at NTCP (IC₅₀ = 4.3 μ M). This again underlines the different behavior of TLC in its binding to NTCP compared with TC and DHEAS.

Comparative Analysis of NTCP, ASBT, and SOAT Homology Models

In order to visualize the 3-dimensional structures of NTCP, ASBT and SOAT, homology models were generated as shown in Figure 6. The backbone structures (Figure 6A) of the three carriers are very similar and are composed of nine transmembrane domains (TMDs). Structurally, the proteins can be subdivided into a core domain, composed of TMDs 2-4 and 7-9, and a panel domain, composed of TMDs 1, 5 and 6, according to the structures of the bacterial proteins Asbt_{Nm} (PDB: 3ZUY.A) and Abst_{Yr} (PDB: 4N7X.A) (Hu et al., 2011; Zhou et al., 2014). For homology modeling, the outward-

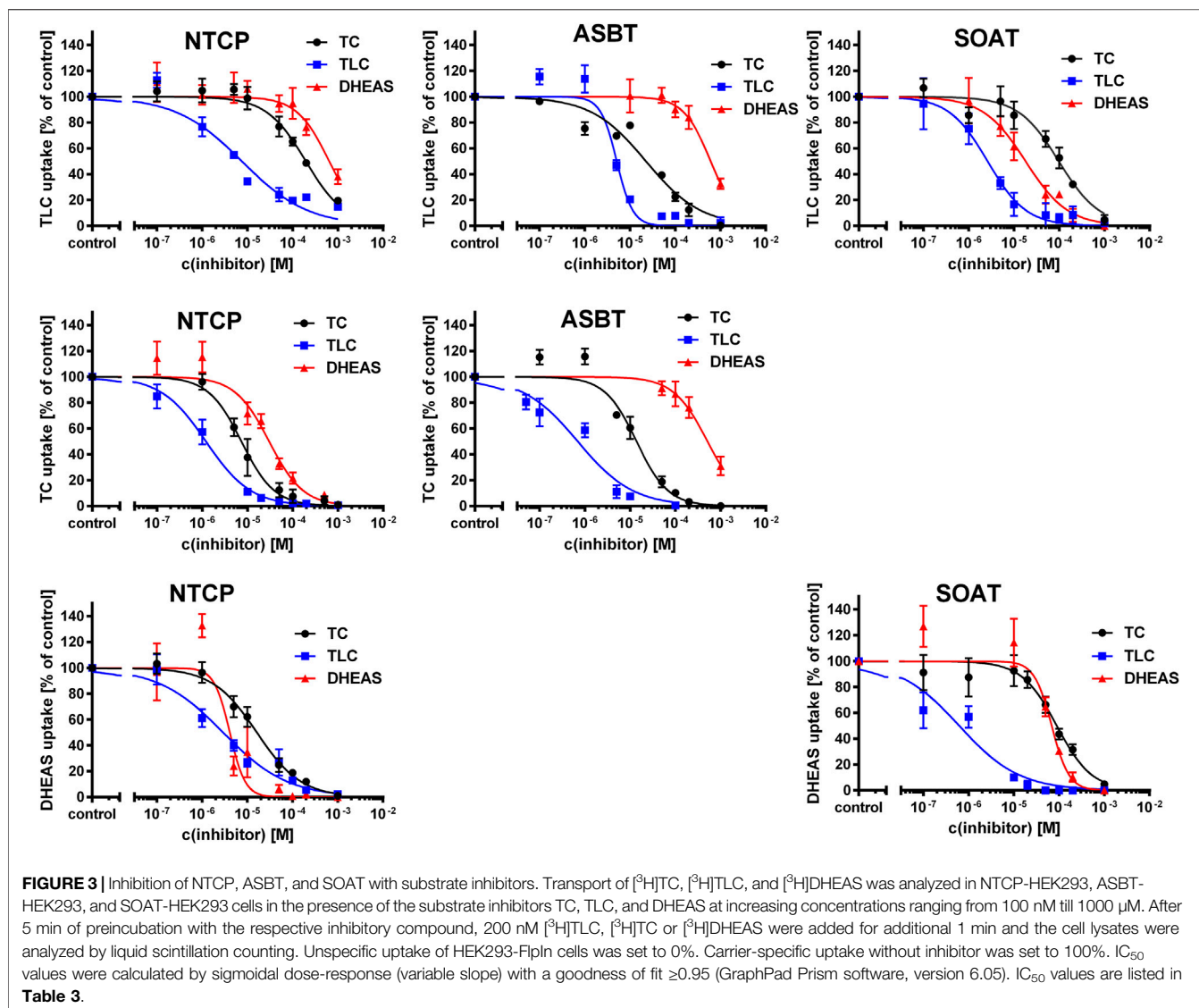


TABLE 3 | Half-maximal inhibitory concentrations (IC₅₀) for substrate inhibitors at NTCP, ASBT, and SOAT. [³H]TLC, [³H]TC, and [³H]DHEAS substrate uptake was analyzed in NTCP-HEK293, ASBT-HEK293, and SOAT-HEK293 cells in the presence of the indicated substrate inhibitors TC, TLC, and DHEAS at increasing concentrations. The primary transport data are presented in **Figure 3**.

Substrate	Inhibitor	NTCP (IC ₅₀ in μM)	ASBT (IC ₅₀ in μM)	SOAT (IC ₅₀ in μM)
[³ H]TLC	TC	140.8	45.9	143.0
	<u>TLC</u>	1.4	<u>4.0</u>	<u>2.6</u>
	DHEAS	431.7	>1000	15.0
[³ H]TC	<u>TC</u>	<u>5.4</u>	<u>5.7</u>	—
	TLC	1.7	1.9	—
	DHEAS	21.5	453.1	—
[³ H]DHEAS	TC	14.0	—	99.7
	<u>TLC</u>	<u>1.8</u>	—	<u>3.9</u>
	<u>DHEAS</u>	<u>3.4</u>	—	<u>51.7</u>

Bold face: inhibitor = not transported as substrate. Underlined: Inhibitor = transported substrate.

open Asbt_{Yf} model (PDB: 4N7X.1.A) was used that shows an outward-exposed substrate binding cavity between the panel and core domains as recently verified (Wang et al., 2021). The

molecular surface of the NTCP, ASBT and SOAT homology models was colored according to Coulomb potential (**Figure 6B**) or by amino acid residue hydrophobicity (**Figure 6C**) and revealed

TABLE 4 | Half-maximal inhibitory concentrations (IC_{50}) for non-substrate triterpenoid inhibitors at NTCP, ASBT, and SOAT. $[^3H]$ TLC, $[^3H]$ TC, and $[^3H]$ DHEAS substrate uptake was analyzed in NTCP-HEK293, ASBT-HEK293, and SOAT-HEK293 cells in the presence of the indicated non-substrate inhibitors at increasing concentrations. The primary transport data are presented in **Figure 4**.

Substrate	Inhibitor	NTCP (IC_{50} in μM)	ASBT (IC_{50} in μM)	SOAT (IC_{50} in μM)
$[^3H]$ TLC	Betulinic acid	5.7	193.3	9.5
	Lupenone	11.8	>1000	122.4
	3-O-Caffeoyl betulin	2.1	99.7	37.8
	Betulin	45.8	191.5	50.1
$[^3H]$ TC	Betulinic acid	0.8	>1000	—
	Lupenone	240.4	>1000	—
	3-O-Caffeoyl betulin	128.7	498.6	—
	Betulin	747.9	>1000	—
$[^3H]$ DHEAS	Betulinic acid	0.3	—	1.2
	Lupenone	>1000	—	664.5
	3-O-Caffeoyl betulin	49.1	—	301.1
	Betulin	>1000	—	912.2

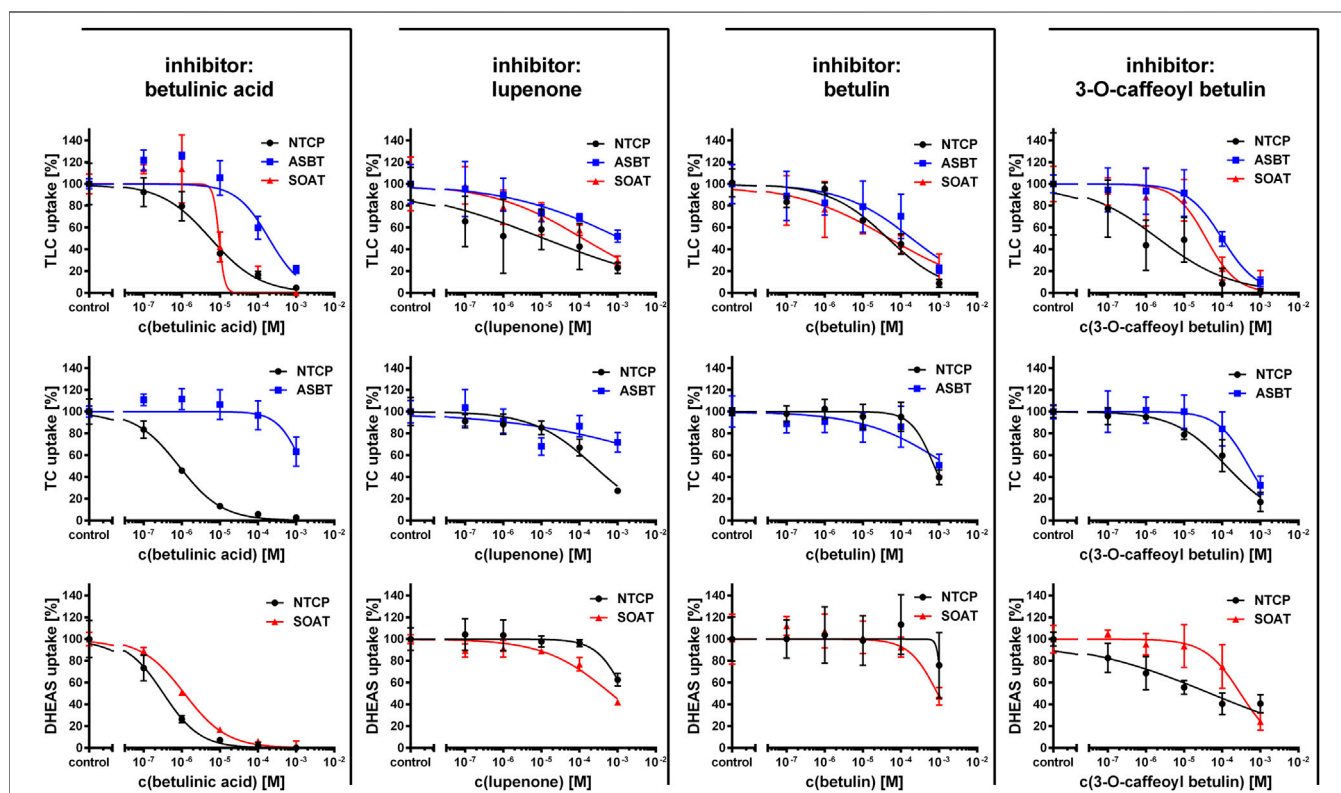


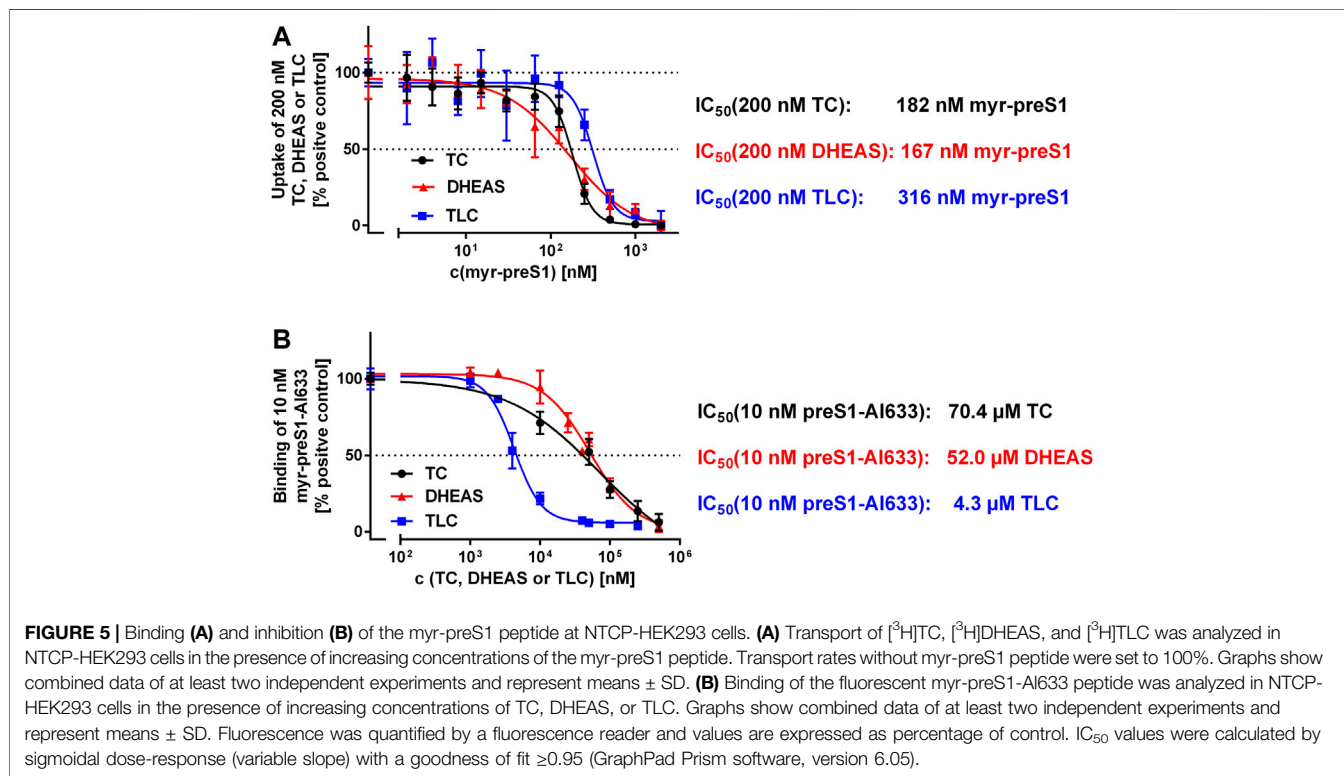
FIGURE 4 | Inhibition of NTCP, ASBT, and SOAT with non-substrate betulin-based inhibitors. Transport of $[^3H]$ TC, $[^3H]$ TLC, and $[^3H]$ DHEAS was analyzed in NTCP-HEK293, ASBT-HEK293, and SOAT-HEK293 cells in the presence of different supposed non-substrate triterpenoid inhibitors as indicated at increasing concentrations ranging from 100 nM till 1000 μM . After 5 min of preincubation with the respective inhibitory compound, 1 μM $[^3H]$ TLC, $[^3H]$ TC or $[^3H]$ DHEAS were added for additional 10 min at 37°C and the cell lysates were analyzed by liquid scintillation counting. Experiments performed without inhibitor were set to 100%. Means of negative controls were subtracted to calculate net transport rates (expressed as percentage of control). Data represent means \pm SD of quadruplicate determinations of representative experiments. IC_{50} values were calculated by sigmoidal dose-response (variable slope) with a goodness of fit ≥ 0.95 (GraphPad Prism software, version 6.05). IC_{50} values are listed in **Table 4**.

significant differences for both physical parameters. Therefore, no common pattern can be recognized in the substrate binding cavities of NTCP, ASBT, and SOAT. In addition, the models were used for *in silico* docking with TLC as the ligand, using the docking module of

SWISS-Dock. As shown in **Figure 6D**, TLC showed several potential docking/binding sites at the proposed substrate binding cavities and in this case showed partly overlapping orientation for the three carriers NTCP, ASBT, and SOAT (**Figure 6D**).

TABLE 5 | Inhibitor screening for NTCP, ASBT and SOAT. [^3H]TLC, [^3H]TC, and [^3H]DHEAS substrate uptake was analyzed in NTCP-HEK293, ASBT-HEK293, and SOAT-HEK293 cells in the presence of the indicated inhibitors at 100 μM inhibitory concentrations. Grading of the net uptake compared to the non-inhibited control was: “-” for 80–100% residual uptake of the respective substrate compared to positive control (w/o inhibitor), “+” for 50–79% residual uptake (weak inhibition), “++” for 20–49% residual uptake (medium inhibition) and “+++” for 0–19% residual uptake (strong inhibition). Experiments were performed in duplicate each with triplicate determinations ($n = 6$).

Inhibitor	NTCP substrate			ASBT substrate		SOAT substrate	
	TLC	TC	DHEAS	TLC	TC	TLC	DHEAS
Cyclosporine A	+	++	+++	-	-	+	+
Ezetimibe	-	+	-	-	-	-	-
BSP	+	++	++	+	++	+++	+++
Irbesartan	+	++	+++	-	-	+++	++
Troglitazone	+++	+++	++	+++	+++	+++	+++
Erythrosine B	+	+++	+	+	+	+	++
Ginkgolic acid 17:1	+	+	++	-	-	++	+++
Losartan	+	+	-	-	-	++	+++



Comparative Analysis of NTCP, ASBT, and SOAT Substrate Pharmacophore Models

Finally, the substrate recognition pattern of NTCP, ASBT, and SOAT was visualized by common substrate pharmacophore modeling based on the data shown in Table 1. The pharmacophores are presented for each transporter in the first line of Figure 7. In addition, the SLC10 substrates TLC, TC and DHEAS are fitted into all pharmacophore models. The NTCP and ASBT pharmacophores are quite similar and are characterized by one hydrogen bond donor, one hydrogen bond acceptor and three hydrophobic features that all are similarly oriented to each other. However, in comparison to NTCP, ASBT revealed much more excluding values. As

consequence, DHEAS does not fit into the ASBT pharmacophore model due to steric overlap of the 3' sulfate group with the excluded space. In contrast, TC and TLC fit quite well in both pharmacophores of NTCP and ASBT. The pharmacophore model of SOAT is significantly different from those of NTCP and ASBT and revealed two hydrogen bond acceptor groups and three hydrophobic features. In addition, the SOAT pharmacophore is significantly restricted by spacious excluding values. As consequence, TC does not fit into this pharmacophore model due to steric overlap of the 7' and 12' hydroxyl groups with the excluded space. In contrast, the flat DHEAS molecule fits perfectly into this pharmacophore. Interestingly, also TLC fits into the SOAT pharmacophore. While the terminal sulfate group of the taurine residue

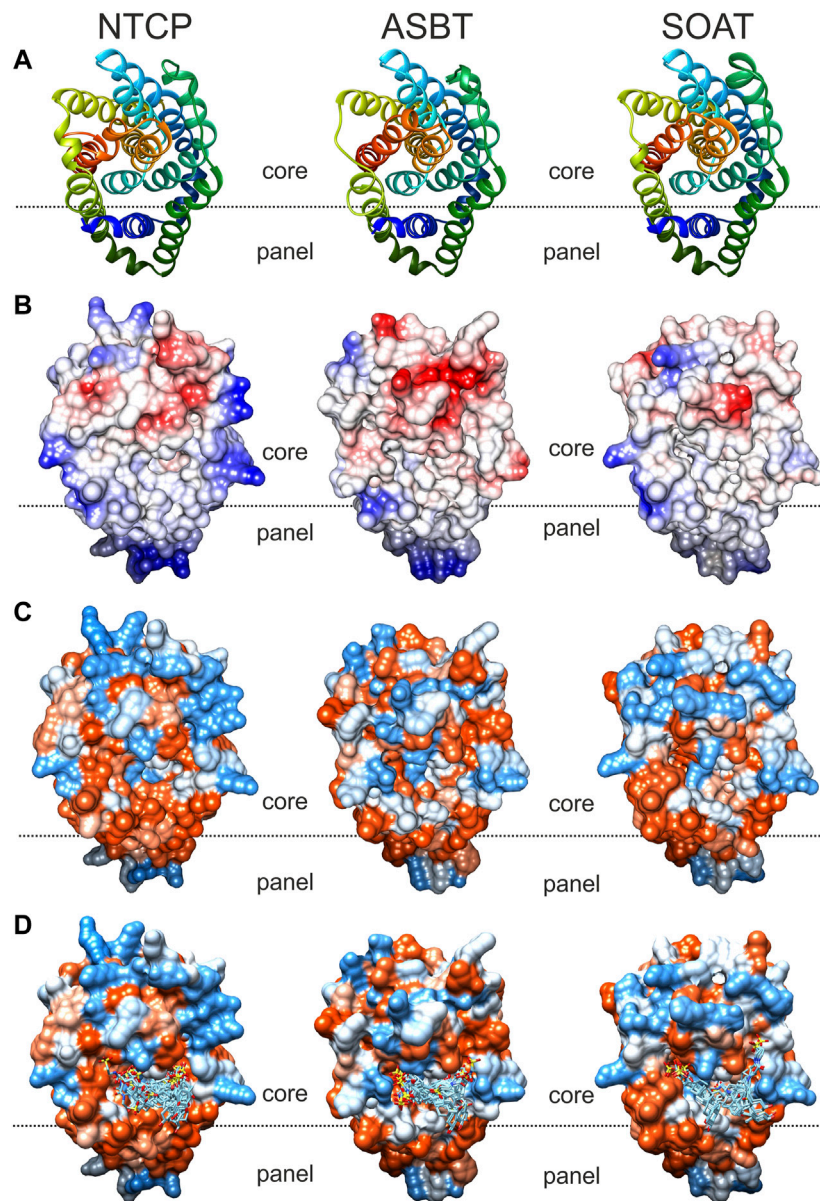


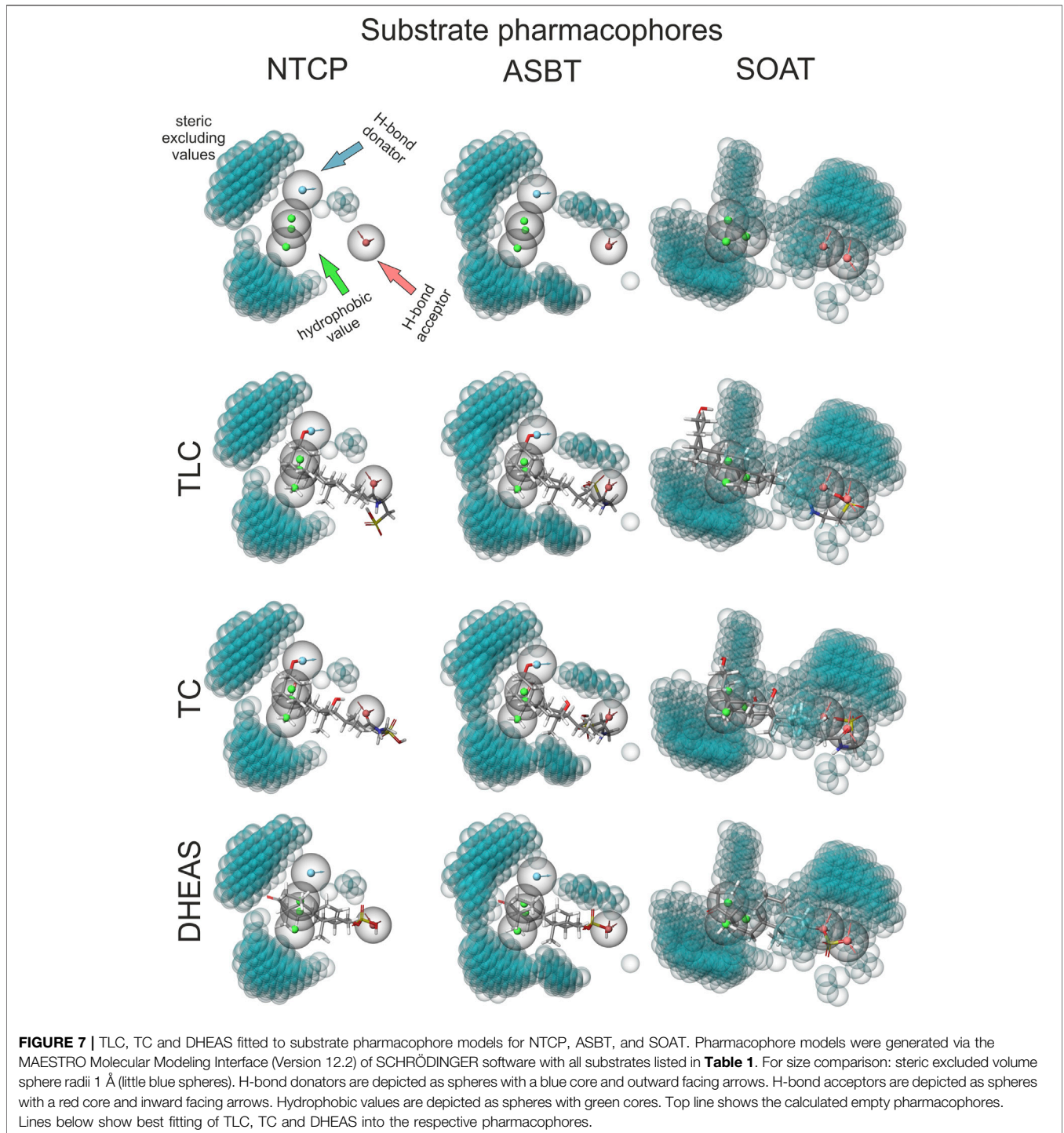
FIGURE 6 | Comparative substrate docking to homology models of NTCP, ASBT, and SOAT in outward-open conformation. Based on the crystal structure of bacterial Asbt_{Yr} (4n7x.1.a) outward open homology models of the SLC10 transporters NTCP, ASBT and SOAT were generated with SWISS-MODEL. All models are shown in identical orientation in top view. The dotted line gives an orientation for the localization of the proposed substrate-binding cavity between the panel and core domains of the respective carrier. **(A)** Backbone structure colored in rainbow-mode to depict similar transmembrane structure. **(B)** Molecular surface colored due to Coulomb force calculation (electrostatic forces); starting from -10 (red), over 0 (white), up to $+10$ (blue). **(C)** Hydrophobicity surface coloring due to amino acid residue sequence hydrophobicity ranging from hydrophilic (blue) over neutral (white) to lipophilic (red). **(D)** *In silico* docking of TLC by SwissDock. Docked clusters were reduced to TLC molecules in reasonable proximity to the putative outward facing binding pocket. All models were visualized with the UCSF CHIMERA software.

covers one of the hydrogen bond acceptor groups that is occupied by the 3' sulfate group in the case of DHEAS, the bent steroid rings A and B stretch out into the free space of the pharmacophore. This suggests substrate recognition of DHEAS and TLC in an antiparallel manner (see **Figure 8**). However, this is only possible when the BA molecule is not additionally hydroxylated, as it is the case for TC.

DISCUSSION

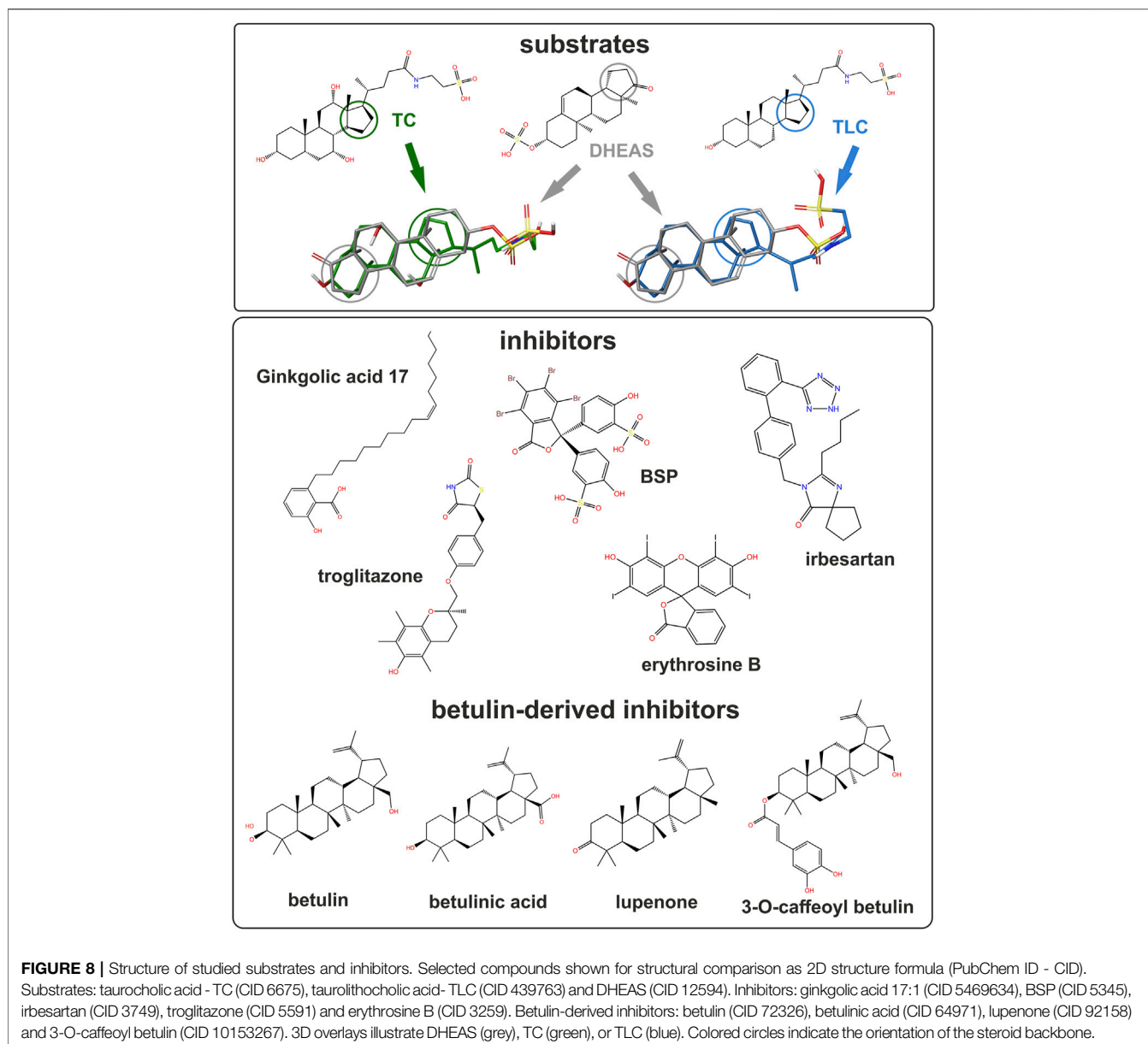
Physiological Relevance of NTCP, ASBT, and SOAT

The present study suggests overlapping substrate and inhibitor binding sites for the SLC10 carriers NTCP, ASBT, and SOAT. Nevertheless, each carrier has a unique substrate spectrum to fulfill



its tissue-specific role for the cellular uptake of BAs and/or sulfated steroid hormones. Based on the current knowledge, BA transport via NTCP in the liver and via ASBT in the ileum is essential for the maintenance of the enterohepatic circulation of BAs (Geyer et al., 2006) and so the physiological role of both carriers in BA transport is quite clear. In addition, NTCP could be important for the hepatic excretion of sulfated steroid hormones, such as DHEAS (Geyer et al., 2017). In contrast, a transport function for sulfated steroids

would not make sense physiologically for ASBT, because relevant levels of sulfated steroid hormones are not present in the lumen of the ileum. SOAT is more widespread in its expression and was detected in germ cells of the testis, skin, placenta, mammary gland and some other hormone-dependent tissues (Geyer et al., 2007; Fietz et al., 2013; Grosser et al., 2013; Karakus et al., 2018). By SOAT-mediated uptake of sulfated steroid hormones from the blood and subsequent cleavage by the steroid sulfatase (so-called



intracrine steroid synthesis) seems to contribute to the steroid regulation of many hormone-dependent tissues (Geyer et al., 2017). Apart from steroid hormones, BAs gained increasing attention as signaling molecules with broad metabolic effects acting via membrane bound (TGR5) and nuclear (FXR) receptors (Di Ciaula et al., 2017). Against this background, the transport of TLC via SOAT could also be of physiological relevance in the periphery. TLC is formed in the liver by taurine conjugation of lithocholic acid that is absorbed from the gut as secondary BA independent from carrier-/ASBT-mediated uptake. However, TLC excreted into the duodenum via bile can also be reabsorbed via ASBT in the terminal ileum before this compound undergoes bacterial deconjugation in more distal parts of the gut. TLC then can be taken up from the portal blood into hepatocytes by NTCP. In addition to this

intestinal and hepatic transport of TLC, SOAT might play a role for TLC transport in peripheral organs. Of note, TLC is getting increasing attention as signaling and regulatory molecule and SOAT could be involved in its distribution. As an example, TLC recently showed to induce relaxation of human and mouse peripheral airways that were pre-contracted by acetylcholine stimulation (Urso et al., 2020). As SOAT is also expressed in the lung (Fietz et al., 2013), SOAT-mediated uptake of TLC might be of relevance there.

Phylogenetic Relationship and Substrate Recognition of NTCP, ASBT, and SOAT

Based on Bayesian phylogenetic analysis we previously reported that the genes coding for ASBT (*SLC10A2*) and SOAT (*SLC10A6*)

emerged from a common ancestor by gene duplication (Geyer et al., 2006). This finding is supported by the very close homology of the gene structure of both genes with six coding exons and highly conserved sequences at the exon-intron boundaries. In the same way, the genes for NTCP (*SLC10A1*) and *SLC10A4* emerged from a common ancestor gene, but both genes are less homologous as indicated by the number of five (*SLC10A1*) and three (*SLC10A4*) coding exons. Even earlier, both subclades (*SLC10A2/SLC10A6* and *SLC10A1/SLC10A4*) have a common ancestor (see **Supplementary Figure S1**). Based on this, it is surprising that ASBT and SOAT show a contrary substrate spectrum. While ASBT is specific for BA transport, SOAT is a specific transporter for sulfate steroid hormones. NTCP, in contrast, has a much wider substrate spectrum and can transport both substrate groups and some additional compounds such as estradiol-3 β -D-glucuronide that are not transported by ASBT and SOAT (**Figure 1**). The most likely explanation for this functional divergence is that the common ancestor of NTCP, ASBT and SOAT already incorporated all functions. While these functions for BA and steroid sulfate transport then were split into ASBT and SOAT, respectively, NTCP maintained the full substrate spectrum of the common ancestor. This hypothesis is supported by the fact that SOAT can still bind BAs even if they are not transported and the binding sites for BAs and steroid sulfates even seem to overlap. Accordingly, the transport of [³H]DHEAS via SOAT can be potentially inhibited with TC (**Figure 3**) and several other BAs (Geyer et al., 2007). However, this does not fully apply for ASBT, which only can be inhibited with DHEAS at very high inhibitor concentrations. Therefore, ASBT seems to have lost the binding and transport function for sulfated steroids during emergence from the common SOAT/ASBT ancestor. For NTCP, an overlapping substrate-binding site for BAs (TC) and sulfated steroids (DHEAS) can be proposed. Both compounds are transported by NTCP and both are quite potent in inhibiting the transport of the respective other compound. The IC₅₀ for inhibition of the [³H]TC transport via NTCP by DHEAS was determined to 21.5 μ M, while inhibition of the [³H]DHEAS transport via NTCP by TC was at 14.0 μ M and so within the same range. However, it has to be mentioned that the human NTCP*2 polymorphism, characterized by the amino acid substitution S267F, showed reduced transport activity for TC, but not for E₁S, pointing to structural differences in the substrate recognition of these two substrates (Ruggiero et al., 2021).

NTCP, ASBT, and SOAT Share Different Overlapping Substrate/Inhibitor Binding Sites

Until now, it was considered that the substrate spectra of ASBT and SOAT have no overlap. Yet in the present study, we demonstrate that TLC can be transported by all three sodium-dependent SLC10 carriers, namely NTCP, ASBT and SOAT. Therefore, the present study established TLC as the first common substrate of these carriers. However, the question if TLC was also a substrate of the common NTCP/

ASBT/SOAT ancestor or if all three carriers later acquired the TLC transport function cannot be finally answered. However, it seems likely that TLC is not only a common, but also an ancient substrate of the SLC10 carriers. Anyhow, the highly conserved transport activity of all three carriers for TLC raises some questions about the exact mode of substrate recognition of this unique substrate.

Substrate recognition of TLC might occur by chance in the substrate-binding site of DHEAS, as TLC shows some structural overlap with DHEAS when oriented in an antiparallel manner, as illustrated in **Figure 8**. In this scenario, the terminal sulfate group of TLC would be recognized instead of the 3' sulfate group of DHEAS, while extensive overlapping hydrophobic interactions are possible via the unmodified steroid core structures of both molecules. Indeed, DHEAS and TLC showed an antiparallel fitting into the SOAT pharmacophore model as shown in **Figure 7**. This is, however, not possible when TLC is additionally hydroxylated at the 7' and/or 12' positions, as it is the case for the BAs TCA, TCDCA, or TDCA, which all are not transported by SOAT. According to this hypothesis, TLC would be recognized by the DHEAS substrate-binding site of SOAT, while it binds as a substrate to the BA binding site in NTCP and ASBT.

A second explanation could be a separate substrate-binding site for TLC that is conserved in all three carriers NTCP, ASBT and SOAT. Although this proposed TLC binding site seems to partly overlap with the binding sites for TC and DHEAS, it would allow TLC transport independent from the TC/DHEAS transport activity of the respective carrier. Several findings of the present study support this hypothesis: (I) TLC was found to be an equipotent inhibitor of all three carriers NTCP, ASBT, and SOAT irrespective of the substrate that was used to measure transport activity. This finding can be explained by common binding and transport of TLC for all three carriers and thereby unspecific inhibition of the transport of any other substrate. (II) As the transport of [³H]TLC can only weakly be inhibited by TC and DHEAS, even if these compounds are transported by the respective carriers, TLC transport seems to occur independent from TC/DHEAS binding and transport. (III) The non-substrate inhibitors lupenone, 3-O-caffeoyl betulin and betulin had much higher inhibitory potency when [³H]TLC was used as the transport substrate compared with [³H]TC and [³H]DHEAS, indicating that the inhibitor binding site of these betulin derivatives closer overlaps with the TLC binding site compared with the TC/DHEAS binding site.

A broader interpretation of this hypothesis would propose a larger substrate/inhibitor entry zone in the outward oriented space between the core and the panel domain that is characterized by multiple interaction domains for the different substrates (TLC, TC and DHEAS) and inhibitors. This would explain the large cross-inhibition pattern between the different substrate and inhibitor groups. From this entry zone, single or multiple pathways for substrate transport through the transporter protein might exist or only binding of a transport substrate might indeed induce conformational changes that open the substrate-binding zone to the intracellular compartment for substrate release. This scenario

would also explain the existence of pan-SLC10 substrates (TLC) and inhibitors (e.g. erythrosine B, troglitazone, or BSP), while other substrates (TC, DHEAS) and inhibitors (e.g. irbesartan, cyclosporine A, ginkgolic acid 17:1) are specific for a subgroup of SLC10 carriers.

Interestingly, the myr-preS1 lipopeptide showed equipotent inhibition of all substrates (TC, TLC, and DHEAS) of NTCP, suggesting that this peptide completely blocks the access of any substrate to its respective binding site. However, TLC was much more potent in blocking the binding of the myr-preS1 peptide from NTCP compared with TC and DHEAS. This could also be explained by the particular *trans*-inhibitory potential of this compound at NTCP (Lowjaga et al., 2021). TLC, after carrier-mediated uptake or passive diffusion, can bind to an intracellular TLC binding site of NTCP and thereby *trans*-inhibits myr-preS1 peptide and HDV binding from the outside of the cell. Interestingly, this *trans*-inhibitory effect of TLC also inhibited *in vitro* HDV infection of NTCP expressing HepG2 hepatoma cells (Lowjaga et al., 2021). In contrast, such a *trans*-inhibitory effect is not known for the substrates TC and DHEAS, what could explain their lower potential to inhibit myr-preS1 binding to NTCP.

The existence of overlapping multiple substrate binding sites as proposed in the present study for NTCP, ASBT, and SOAT, was described for several other carrier proteins before. As an example, mutagenesis studies of the rat Organic cation transporter 1 (rOCT1) revealed overlapping binding sites for different substrates and allosteric effectors (Koepsell, 2019). The multidrug efflux transporter MDR1 P-glycoprotein (syn. ABCB1) is another example of a carrier with multiple substrate binding sites. P-glycoprotein seems to have a large drug-binding pocket with different overlapping sites for binding of individual substrate groups. Thereby, P-glycoprotein can recognize and transport a vast variety of structurally unrelated drugs and toxins (Chufan et al., 2015).

Cross-Reactivity of Pharmacological Inhibitors of SLC10 Carriers and Clinical Implications

The discovery of NTCP as a high-affinity receptor for HBV and HDV opened the field for the development of HBV/HDV entry inhibitors, preferably based on small molecules with oral bioavailability (Yan et al., 2012; König et al., 2014). In a previous study, we could demonstrate that small molecules from the group of pentacyclic triterpenoids, including betulinic acid and lupenone, show anti-HDV activity *in vitro* making them attractive virus entry inhibitor candidates (Kirstgen et al., 2020). However, as demonstrated in the present study, both compounds show significant cross-reactivity with SOAT, while ASBT transport was not affected by these betulin derivatives. This exemplifies that inhibitors of NTCP, ASBT, and

SOAT should principally tested for cross-reactivity against the other SLC10 carriers. In conclusion, NTCP, ASBT, and SOAT are interesting drug targets and several pharmacological inhibitors have already been established against these carriers. In the present study, overlapping substrate and inhibitor binding sites are proposed that are differently active in NTCP, ASBT, and SOAT. TLC was identified as the first common substrate for all three carriers and it was clearly shown that most of the SLC10 inhibitors are not carrier-specific, but rather cross-react at least with one of the other related SLC10 carriers. This should be considered when pharmacological inhibitors are developed against NTCP, ASBT, or SOAT.

DATA AVAILABILITY STATEMENT

The original contributions presented in the study are included in the article/**Supplementary Material**, further inquiries can be directed to the corresponding author.

AUTHOR CONTRIBUTIONS

GG, SM, MK, and JG conceived the experiments; GG, SM, MK, and BD performed the experiments; GG, SM, MK, and JG analyzed and interpreted the results; GG, SM, MK, and JG wrote the manuscript. All authors reviewed the manuscript. All authors contributed to the article and approved the submitted version.

FUNDING

This study was supported in part by Flex Funds from the LOEWE-Center DRUID (Novel Drug Targets against Poverty-related and Neglected Tropical Infectious Diseases) and in part by the Deutsche Forschungsgemeinschaft (DFG, German Research Foundation)–Projektnummer 197785619 – SFB 1021.

ACKNOWLEDGMENTS

The authors thank Anita Neubauer, Klaus Schuh and Regina Leidolf for excellent technical assistance. The authors kindly thank Dr. Bernhard Ugele and Prof. Dr. Alan Hofmann for providing radiolabeled substances.

SUPPLEMENTARY MATERIAL

The Supplementary Material for this article can be found online at: <https://www.frontiersin.org/articles/10.3389/fmolb.2021.689757/full#supplementary-material>

REFERENCES

- Al-Dury, S., and Marshall, H.-U. (2018). Ileal Bile Acid Transporter Inhibition for the Treatment of Chronic Constipation, Cholestatic Pruritus, and NASH. *Front. Pharmacol.* 9, 931. doi:10.3389/fphar.2018.00931
- Ananthanarayanan, M., Ng, O. C., Boyer, J. L., and Suchy, F. J. (1994). Characterization of Cloned Rat Liver Na(+)-Bile Acid Cotransporter Using Peptide and Fusion Protein Antibodies. *Am. J. Physiol.-Gastrointestinal Liver Physiol.* 267 (4 Pt 1), G637–G643. doi:10.1152/ajpgi.1994.267.4.G637
- Chufan, E. E., Sim, H.-M., and Ambudkar, S. V. (2015). Molecular Basis of the Polyspecificity of P-Glycoprotein (ABCB1). *Adv. Cancer Res.* 125, 71–96. doi:10.1016/bs.acr.2014.10.003
- Claro da Silva, T., Polli, J. E., and Swaan, P. W. (2013). The Solute Carrier Family 10 (SLC10): beyond Bile Acid Transport. *Mol. Aspects Med.* 34 (2, 3), 252–269. doi:10.1016/j.mam.2012.07.004
- Craddock, A. L., Love, M. W., Daniel, R. W., Kirby, L. C., Walters, H. C., Wong, M. H., et al. (1998). Expression and Transport Properties of the Human Ileal and Renal Sodium-dependent Bile Acid Transporter. *Am. J. Physiol.-Gastrointestinal Liver Physiol.* 274 (1), G157–G169. doi:10.1152/ajpgi.1998.274.1.G157
- Di Ciaula, A., Garruti, G., Lunardi Baccetto, R., Molina-Molina, E., Bonfrate, L., Wang, D. Q.-H., et al. (2017). Bile Acid Physiology. *Ann. Hepatol.* 16, S4–S14. doi:10.5604/01.3001.0010.5493
- Dixon, S. L., Smondyrev, A. M., Knoll, E. H., Rao, S. N., Shaw, D. E., and Friesner, R. A. (2006). PHASE: a New Engine for Pharmacophore Perception, 3D QSAR Model Development, and 3D Database Screening: 1. Methodology and Preliminary Results. *J. Comput. Aided Mol. Des.* 20 (10-11), 647–671. doi:10.1007/s10822-006-9087-6
- Döring, B., Lütke, T., Geyer, J., and Petzinger, E. (2012). The SLC10 Carrier Family. *Curr. Top. Membr.* 70, 105–168. doi:10.1016/B978-0-12-394316-3.00004-1
- Drexler, J. F., Geipel, A., König, A., Corman, V. M., van Riel, D., Leijten, L. M., et al. (2013). Bats Carry Pathogenic Hepadnaviruses Antigenically Related to Hepatitis B Virus and Capable of Infecting Human Hepatocytes. *Proc. Natl. Acad. Sci.* 110 (40), 16151–16156. doi:10.1073/pnas.1308049110
- Fernandes, C. F., Godoy, J. R., Döring, B., Cavalcanti, M. C. O., Bergmann, M., Petzinger, E., et al. (2007). The Novel Putative Bile Acid Transporter SLC10A5 Is Highly Expressed in Liver and Kidney. *Biochem. Biophys. Res. Commun.* 361 (1), 26–32. doi:10.1016/j.bbrc.2007.06.160
- Fietz, D., Bakhaus, K., Wapelhorst, B., Grosser, G., Günther, S., Alber, J., et al. (2013). Membrane Transporters for Sulfated Steroids in the Human Testis - Cellular Localization, Expression Pattern and Functional Analysis. *PLoS One* 8 (5), e62638. doi:10.1371/journal.pone.0062638
- Fukano, K., Tsukuda, S., Watashi, K., and Wakita, T. (2019). Concept of Viral Inhibitors via NTCP. *Semin. Liver Dis.* 39 (1), 078–085. doi:10.1055/s-0038-1676804
- Geyer, J., Bakhaus, K., Bernhardt, R., Blaschka, C., Dezhkam, Y., Fietz, D., et al. (2017). The Role of Sulfated Steroid Hormones in Reproductive Processes. *J. Steroid Biochem. Mol. Biol.* 172, 207–221. doi:10.1016/j.jsbmb.2016.07.002
- Geyer, J., Döring, B., Meerkamp, K., Ugele, B., Bakhiya, N., Fernandes, C. F., et al. (2007). Cloning and Functional Characterization of Human Sodium-dependent Organic Anion Transporter (SLC10A6). *J. Biol. Chem.* 282 (27), 19728–19741. doi:10.1074/jbc.M702663200
- Geyer, J., Wilke, T., and Petzinger, E. (2006). The Solute Carrier Family SLC10: More Than a Family of Bile Acid Transporters Regarding Function and Phylogenetic Relationships. *Naunyn Schmied Arch. Pharmacol.* 372 (6), 413–431. doi:10.1007/s00210-006-0043-8
- Godoy, J. R., Fernandes, C., Döring, B., Beuerlein, K., Petzinger, E., and Geyer, J. (2007). Molecular and Phylogenetic Characterization of a Novel Putative Membrane Transporter (SLC10A7), Conserved in Vertebrates and Bacteria. *Eur. J. Cell Biol.* 86 (8), 445–460. doi:10.1016/j.ejcb.2007.06.001
- Grosser, G., Bennien, J., Sánchez-Guijo, A., Bakhaus, K., Döring, B., Hartmann, M., et al. (2018). Transport of Steroid 3-sulfates and Steroid 17-sulfates by the Sodium-dependent Organic Anion Transporter SOAT (SLC10A6). *J. Steroid Biochem. Mol. Biol.* 179, 20–25. doi:10.1016/j.jsbmb.2017.09.013
- Grosser, G., Döring, B., Ugele, B., Geyer, J., Kulling, S. E., and Soukup, S. T. (2015). Transport of the Soy Isoflavone Daidzein and its Conjugative Metabolites by the Carriers SOAT, NTCP, OAT4, and OATP2B1. *Arch. Toxicol.* 89 (12), 2253–2263. doi:10.1007/s00204-014-1379-3
- Grosser, G., Fietz, D., Günther, S., Bakhaus, K., Schweigmann, H., Ugele, B., et al. (2013). Cloning and Functional Characterization of the Mouse Sodium-dependent Organic Anion Transporter Soat (Slc10a6). *J. Steroid Biochem. Mol. Biol.* 138, 90–99. doi:10.1016/j.jsbmb.2013.03.009
- Hagenbuch, B., and Meier, P. J. (1994). Molecular Cloning, Chromosomal Localization, and Functional Characterization of a Human Liver Na+/bile Acid Cotransporter. *J. Clin. Invest.* 93 (3), 1326–1331. doi:10.1172/JCI117091
- Hagenbuch, B., and Meier, P. (1996). Sinusoidal (Basolateral) Bile Salt Uptake Systems of Hepatocytes. *Semin. Liver Dis.* 16 (2), 129–136. doi:10.1055/s-2007-1007226
- Hu, N.-J., Iwata, S., Cameron, A. D., and Drew, D. (2011). Crystal Structure of a Bacterial Homologue of the Bile Acid Sodium Symporter ASBT. *Nature* 478 (7369), 408–411. doi:10.1038/nature10450
- Iwamoto, M., Saso, W., Sugiyama, R., Ishii, K., Ohki, M., Nagamori, S., et al. (2019). Epidermal Growth Factor Receptor Is a Host-Entry Cofactor Triggering Hepatitis B Virus Internalization. *Proc. Natl. Acad. Sci. USA* 116, 8487–8492. doi:10.1073/pnas.1811064116
- Karakus, E., Wannowius, M., Müller, S. F., Leiting, S., Leidolf, R., Noppes, S., et al. (2020). The Orphan Solute Carrier SLC10A7 Is a Novel Negative Regulator of Intracellular Calcium Signaling. *Sci. Rep.* 10 (1), 7248. doi:10.1038/s41598-020-64006-3
- Karakus, E., Zahner, D., Grosser, G., Leidolf, R., Gundogdu, C., Sánchez-Guijo, A., et al. (2018). Estrone-3-Sulfate Stimulates the Proliferation of T47D Breast Cancer Cells Stably Transfected with the Sodium-Dependent Organic Anion Transporter SOAT (SLC10A6). *Front. Pharmacol.* 9, 941. doi:10.3389/fphar.2018.00941
- Karpen, S. J., Kelly, D., Mack, C., and Stein, P. (2020). Ileal Bile Acid Transporter Inhibition as an Anticholestatic Therapeutic Target in Biliary Atresia and Other Cholestatic Disorders. *Hepatol. Int.* 14 (5), 677–689. doi:10.1007/s12072-020-10070-w
- Kirstgen, M., Lowjaga, K. A. A. T., Müller, S. F., Goldmann, N., Lehmann, F., Alakurti, S., et al. (2020). Selective Hepatitis B and D Virus Entry Inhibitors from the Group of Pentacyclic Lupane-type Betulin-Derived Triterpenoids. *Sci. Rep.* 10 (1), 21772. doi:10.1038/s41598-020-78618-2
- Koepsell, H. (2019). Multiple Binding Sites in Organic Cation Transporters Require Sophisticated Procedures to Identify Interactions of Novel Drugs. *Biol. Chem.* 400 (2), 195–207. doi:10.1515/hsz-2018-0191
- König, A., Döring, B., Mohr, C., Geipel, A., Geyer, J., and Glebe, D. (2014). Kinetics of the Bile Acid Transporter and Hepatitis B Virus Receptor Na+/taurocholate Cotransporting Polypeptide (NTCP) in Hepatocytes. *J. Hepatol.* 61 (4), 867–875. doi:10.1016/j.jhep.2014.05.018
- Kramer, W., and Glombik, H. (2006). Bile Acid Reabsorption Inhibitors (BARI): Novel Hypolipidemic Drugs. *Curr. Med. Chem.* 13 (9), 997–1016. doi:10.2174/092986706776361003
- Li, X., Liu, H., Cheng, W., Wang, J., Zhang, H., Lu, F., et al. (2020). Junceollolide B, a Novel Inhibitor of Hepatitis B Virus. *Bioorg. Med. Chem.* 28 (16), 115603. doi:10.1016/j.bmc.2020.115603
- Lowjaga, K. A. A. T., Kirstgen, M., Müller, S. F., Goldmann, N., Lehmann, F., Glebe, D., et al. (2021). Long-term Trans-inhibition of the Hepatitis B and D Virus Receptor NTCP by Taurothiocholic Acid. *Am. J. Physiol.-Gastrointestinal Liver Physiol.* 320 (1), G66–G80. doi:10.1152/ajpgi.00263.2020
- Müller, S. F., König, A., Döring, B., Glebe, D., and Geyer, J. (2018). Characterisation of the Hepatitis B Virus Cross-Species Transmission Pattern via Na+/taurocholate Co-transporting Polypeptides from 11 New World and Old World Primate Species. *PLoS One* 13 (6), e0199200. doi:10.1371/journal.pone.0199200
- Ni, Y., Lempp, F. A., Mehrle, S., Nkongolo, S., Kaufman, C., Fälth, M., et al. (2014). Hepatitis B and D Viruses Exploit Sodium Taurocholate Co-transporting Polypeptide for Species-specific Entry into Hepatocytes. *Gastroenterology* 146 (4), 1070–1083. doi:10.1053/j.gastro.2013.12.024
- Ruggiero, M. J., Malhotra, S., Fenton, A. W., Swint-Kruse, L., Karanicolas, J., and Hagenbuch, B. (2021). A Clinically Relevant Polymorphism in the Na+/taurocholate Cotransporting Polypeptide (NTCP) Occurs at a Rheostat Position. *J. Biol. Chem.* 296, 100047. doi:10.1074/jbc.RA120.014889

- Shneider, B. L., Dawson, P. A., Christie, D. M., Hardikar, W., Wong, M. H., and Suchy, F. J. (1995). Cloning and Molecular Characterization of the Ontogeny of a Rat Ileal Sodium-dependent Bile Acid Transporter. *J. Clin. Invest.* 95 (2), 745–754. doi:10.1172/JCI117722
- Stieger, B., Hagenbuch, B., Landmann, L., Höchli, M., Schroeder, A., and Meier, P. J. (1994). *In situ* Localization of the Hepatocytic Na⁺/taurocholate Cotransporting Polypeptide in Rat Liver. *Gastroenterology* 107 (6), 1781–1787. doi:10.1016/0016-5085(94)90821-4
- Urso, A., D'Ovidio, F., Xu, D., Emala, C. W., Bunnett, N. W., and Perez-Zoghbi, J. F. (2020). Bile Acids Inhibit Cholinergic Constriction in Proximal and Peripheral Airways from Humans and Rodents. *Am. J. Physiol.-Lung Cell Mol. Physiol.* 318 (2), L264–L275. doi:10.1152/ajplung.00242.2019
- Wang, X., Lyu, Y., Ji, Y., Sun, Z., and Zhou, X. (2021). An Engineered Disulfide Bridge Traps and Validates an Outward-Facing Conformation in a Bile Acid Transporter. *Acta Cryst. Sect D Struct. Biol.* 77 (Pt 1), 108–116. doi:10.1107/S205979832001517X
- Weinman, S. A. (1997). Electrogenicity of Na⁽⁺⁾-Coupled Bile Acid Transporters. *Yale J. Biol. Med.* 70 (4), 331–340.
- Wettengel, J. M., and Burwitz, B. J. (2020). Innovative HBV Animal Models Based on the Entry Receptor NTCP. *Viruses* 12 (8), 828. doi:10.3390/v12080828
- Wong, M. H., Rao, P. N., Pettenati, M. J., and Dawson, P. A. (1996). Localization of the Ileal Sodium-Bile Acid Cotransporter Gene (SLC10A2) to Human Chromosome 13q33. *Genomics* 33 (3), 538–540. doi:10.1006/geno.1996.0233
- Yan, H., Zhong, G., Xu, G., He, W., Jing, Z., Gao, Z., et al. (2012). Sodium Taurocholate Cotransporting Polypeptide Is a Functional Receptor for Human Hepatitis B and D Virus. *eLife* 1, 1. doi:10.7554/eLife.00049
- Zhou, X., Levin, E. J., Pan, Y., McCoy, J. G., Sharma, R., Kloss, B., et al. (2014). Structural Basis of the Alternating-Access Mechanism in a Bile Acid Transporter. *Nature* 505 (7484), 569–573. doi:10.1038/nature12811

Conflict of Interest: The authors declare that the research was conducted in the absence of any commercial or financial relationships that could be construed as a potential conflict of interest.

Copyright © 2021 Grosser, Müller, Kirstgen, Döring and Geyer. This is an open-access article distributed under the terms of the Creative Commons Attribution License (CC BY). The use, distribution or reproduction in other forums is permitted, provided the original author(s) and the copyright owner(s) are credited and that the original publication in this journal is cited, in accordance with accepted academic practice. No use, distribution or reproduction is permitted which does not comply with these terms.

GLOSSARY

CA Cholic acid	TCDCA Taurochenodeoxycholic acid
CDCA Chenodeoxycholic acid	TUDCA Tauroursodeoxycholic acid
DCA Deoxycholic acid	TLCA/TLC Taurolithocholic acid
UDCA Ursodeoxycholic acid	DHEAS Dehydroepiandrosterone sulfate
LCA Lithocholic acid	PREGS Pregnenolone sulfate
Sarcosine CA Sarcosine cholic acid	E₁S Estrone-3-sulfate
GCA Glycocholic acid	E-3β-D-G Estrone-3 β -D-glucuronide
GDCA Glycodeoxycholic acid	E-17β-D-G Estradiol-17 β -D-glucuronide
GCDCA Glycochenodeoxycholic acid	HBV Human Hepatitis B Virus
GUDCA Glycoursodeoxycholic acid	HDV Human Hepatitis D Virus
TCA/TC Taurocholic acid	NTCP Na ⁺ /taurocholate cotransporting polypeptide (SLC10A1)
TDCA Taurodeoxycholic acid	ASBT Apical sodium-dependent bile acid transporter (SLC10A2)
	SOAT Sodium-dependent organic anion transporter (SLC10A6)



Vitamin K Vitamers Differently Affect Energy Metabolism in IPEC-J2 Cells

Chiara Bernardini¹, Cristina Algeri¹, Debora La Mantia¹, Fabiana Trombetti¹,
Alessandra Pagliarani^{1†‡}, Monica Forni^{1,2†‡} and Salvatore Nesci^{1*†}

¹ Department of Veterinary Medical Science, University of Bologna, Ozzano Emilia, Italy, ² Health Sciences and Technologies—Interdepartmental Center for Industrial Research (CIRI-SDV), Alma Mater Studiorum—University of Bologna, Bologna, Italy

OPEN ACCESS

Edited by:

Cesare Indiveri,
University of Calabria, Italy

Reviewed by:

Annamaria Tonazzi,
National Research Council (CNR), Italy
Stefan Kahlert,
Otto von Guericke University
Magdeburg, Germany

*Correspondence:

Salvatore Nesci
salvatore.nesci@unibo.it

†These authors share last authorship

‡These authors share senior
authorship

Specialty section:

This article was submitted to
Cellular Biochemistry,
a section of the journal
Frontiers in Molecular Biosciences

Received: 17 March 2021

Accepted: 16 April 2021

Published: 24 May 2021

Citation:

Bernardini C, Algeri C,
La Mantia D, Trombetti F, Pagliarani A,
Forni M and Nesci S (2021) Vitamin K
Vitamers Differently Affect Energy
Metabolism in IPEC-J2 Cells.
Front. Mol. Biosci. 8:682191.
doi: 10.3389/fmolb.2021.682191

The fat-soluble vitamin K (VK) has long been known as a requirement for blood coagulation, but like other vitamins, has been recently recognized to play further physiological roles, particularly in cell development and homeostasis. Vertebrates cannot *de novo* synthesize VK, which is essential, and it can only be obtained from the diet or by the activity of the gut microbiota. The IPEC-J2 cell line, obtained from porcine small intestine, which shows strong similarities to the human one, represents an excellent functional model to *in vitro* study the effect of compounds at the intestinal level. The acute VK treatments on the bioenergetic features of IPEC-J2 cells were evaluated by Seahorse XP Agilent technology. VK exists in different structurally related forms (vitamers), all featured by a naphthoquinone moiety, but with distinct effects on IPEC-J2 energy metabolism. The VK1, which has a long hydrocarbon chain, at both concentrations (5 and 10 μM), increases the cellular ATP production due to oxidative phosphorylation (OXPHOS) by 5% and by 30% through glycolysis. The VK2 at 5 μM only stimulates ATP production by OXPHOS. Conversely, 10 μM VK3, which lacks the long side chain, inhibits OXPHOS by 30% and glycolysis by 45%. However, even if IPEC-J2 cells mainly prefer OXPHOS to glycolysis to produce ATP, the OXPHOS/glycolysis ratio significantly decreases in VK1-treated cells, is unaffected by VK2, and only significantly increased by 10 μM VK3. VK1, at the two concentrations tested, does not affect the mitochondrial bioenergetic parameters, while 5 μM VK2 increases and 5 μM VK3 reduces the mitochondrial respiration (i.e., maximal respiration and spare respiratory capacity). Moreover, 10 μM VK3 impairs OXPHOS, as shown by the increase in the proton leak, namely the proton backward entry to the matrix space, thus pointing out mitochondrial toxicity. Furthermore, in the presence of both VK1 and VK2 concentrations, the glycolytic parameters, namely the glycolytic capacity and the glycolytic reserve, are unaltered. In contrast, the inhibition of glycoATP production by VK3 is linked to the 80% inhibition of glycolysis, resulting in a reduced glycolytic capacity and reserve. These data, which demonstrate the VK ability to differently modulate IPEC-J2 cell energy metabolism according to the different structural features of the vitamers, can mirror VK modulatory effects on the cell membrane features and, as a cascade, on the epithelial cell properties and gut functions: balance of salt and water, macromolecule cleavage, detoxification of harmful compounds, and nitrogen recycling.

Keywords: vitamin K, mitochondria, oxidative phosphorylation, glycolysis, IPEC-J2, ATP

INTRODUCTION

Vitamin K (VK) was originally recognized as a component in blood clotting, being a cofactor for vitamin K-dependent carboxylase, which facilitates the post-translational modification of glutamic acid to γ -carboxy-glutamic acid residues in selected proteins (Suttie, 1985). The relevant recognized VK role in coagulation, hence the symbol K, from the German term “Koagulation,” promptly enrolled VK among micronutrients.

Even if partially provided by gut microbiota, VK requires dietary uptake, even if the required amounts are still undefined. The intestinal absorption of VKs follows the dietary lipid pattern (Shearer et al., 2012).

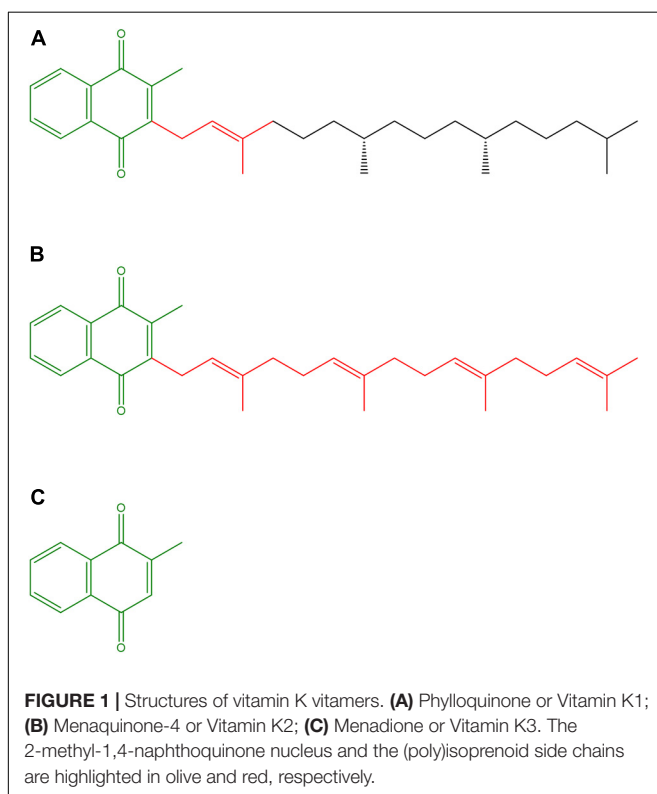
The VK family consists of structurally similar naphthoquinones (**Figure 1**), which, due to their lipophilicity, can easily cross cell membranes. VK naturally exists in two forms, namely, phyloquinone (VK1), which bears a phytyl side chain, mainly comes from vegetables and constitutes more than 90% of dietary VKs, and menaquinones (VK2), which exist in multiple structures, mainly come from bacterial synthesis in the gut, and occur in fermented foods (Schwalfenberg, 2017). The extent to which endogenous VK2 production contributes to the daily VK requirement is still unknown (Shearer et al., 2012). Accordingly, the VK2 form menaquinone-4 can be synthesized from VK1, which is absorbed in the small intestine, and represents the most abundant VK form in tissues (Okano et al., 2008). The VK homologs are characterized by a 2-methyl-1,4-naphthoquinone nucleus and a polyisoprenoid side chain at the 3-position (**Figure 1**). In VK2 vitamers the side chain varies

in both length and saturation degree (Tsugawa and Shiraki, 2020). The VK2 basic structure, which has a side chain with four double bonds, is similar to Coenzyme Q₁₀ (CoQ₁₀), involved as an electron carrier in mitochondrial respiration, but has a shorter hydrophobic side chain whose four prenyl units confer higher hydrophilicity. Finally, menadione, or VK3, lacks the hydrocarbon side chain and is considered as a metabolite or a provitamin (Schwalfenberg, 2017).

Over the last two decades, roles and action mechanisms of VKs other than the involvement in γ -carboxylation, a post-translational modification which modulates the function of various proteins, have been discovered. Recently, VKs were found to play a relevant role in extrahepatic metabolism, such as in bone and blood vessels, in energy metabolism (Tsugawa and Shiraki, 2020), and in counteracting inflammation, as VK deficiency has been associated with human diseases with inflammatory background. Until very recently, VKs were considered capable of playing a role against colorectal cancer and other cancer types (Schwalfenberg, 2017) by inhibiting the cell proliferation, including an active induction of the cell cycle arrest, and to induce apoptosis in different human gastrointestinal cancer cells (Orlando et al., 2015). VKs also improve cognitive function in elderly patients and decrease the risk of diabetes (Schwalfenberg, 2017). At least some of these emerging roles may also be related to the VK involvement in signaling as modulators of selected nuclear receptors. Accordingly, VK2 (menaquinone-4) binds to the transcription factor SXR/PXR, thus acting like a hormone like other lipophilic vitamins. Therefore, its effects are widely spread in body systems, and it is recognized to increase longevity (Gordeladze, 2017). VK2 can also bind the 17 β -Hydroxysteroid dehydrogenase type 4 (17 β -HSD4) and activate protein kinase A (PKA), but the mechanisms of binding and enzyme regulation remain unknown (Azuma and Inoue, 2019).

The CoQ₁₀-like structure of VK2 has raised hopes to exploit VK to treat some mitochondrial defects (Vos et al., 2012). However, the possible replacement of CoQ₁₀ by VK2 in the respiratory chain, as well as the putative role of vitamins K3 and C to improve ATP production by reducing cytochrome *c* through two coupled redox cycles (Ivanova et al., 2018), are still a matter of debate. Unexpectedly, VK2 was a poorly efficient respiratory substrate in human cells *in vitro* (Cerqua et al., 2019). VK3 is potentially toxic and able to counteract some cancer types (Schwalfenberg, 2017). Interestingly, VK3 affects the redox status of thiols, can induce oxidative stress in cancer cells, and seems the most efficient VK form in combination with vitamin C to restore oxidative phosphorylation (Ivanova et al., 2018).

Up to now, VK involvement in the bioenergetics of enterocytes, which are not only directly involved in VK absorption but also are in proximity with gut microbiota which provide VK2, has not been explored. The IPEC-J2 cell line (Vergauwen, 2015), initially established in 1989 and obtained from the small intestine of the pig, which shows anatomical and physiological similarities to humans, has been selected as *in vitro* model to investigate the action mechanisms at the biochemical and molecular level of a variety of compounds on mammalian intestine (Wu et al., 2019). Due to their features, IPEC-J2 cells provide an excellent *in vitro* model to



investigate the effects of VKs on cell bioenergetics. This cell line is neither transformed nor tumorigenic and reproduces the human physiology features more closely than any other cell line of non-human origin. Of note, this cell line guarantees the reproducibility of the results since it maintains the differentiated characteristics and exhibits strong similarities to primary cell cultures. As far as we are aware, only a few studies approached cell bioenergetics in this cell line under normal conditions (Tan et al., 2015; Bernardini et al., 2021), highlighting that these cells mirror the known behavior of intestinal cells, since they preferentially derive energy from glucose plus glutamine than from glucose alone. Enterocytes mainly use glycolysis to provide metabolic precursors to the liver, while mitochondrial respiration provides the main energy source (Nesci, 2017). IPEC-J2, as well as IPEC-J1, have the typical differentiation of an enterocyte, which is independent of the culture system. The aerobic environment can start the initial proliferation and sequential differentiation of intestinal epithelial cells and progeny loss (Nossol et al., 2011). Enterocyte mitochondrial function is important for gut permeability. Accordingly, mitochondrial uncoupling increases intestinal permeability, generating local and systemic inflammation, which is associated with the development of inflammatory bowel diseases (Bórquez et al., 2020).

This study, which focuses on VK effects on IPEC-J2 cells, aims at deepening the knowledge on the multiple VK roles and on the responses of the energy machinery to these quinone compounds. IPEC-J2 cells, which exhibit strong similarities to primary intestinal epithelial cells, may address studies on the most suitable VK form to modulate enterocyte bioenergetics. Accordingly, structural differences among VK vitamers may be relevant to produce different effects. Moreover, this study, by providing clues on the putative modulatory role of VKs on cell bioenergetics, may open further therapeutic perspectives of these fascinating micronutrients.

MATERIALS AND METHODS

Chemicals

α -Phylloquinone (Vitamin K1), Menaquinone-4 (Vitamin K2), and Menadiolone (Vitamin K3) were purchased from Cayman Chemical. Seahorse XF Assay Kits and Reagents were purchased from Agilent. All other chemicals were reagent grade and used without purification. Quartz double-distilled water was used for all reagent solutions, except when otherwise stated.

Cell Culture

The non-transformed cell line IPEC-J2 was purchased from the "Deutsche Sammlung von Mikroorganismen und Zellkulturen GmbH" (DSMZ). Cells were cultured in Dulbecco's Modified Eagle Medium (DMEM) (4.5 g/l glucose) added with 10% of fetal bovine serum (FBS, Life Technologies) and 1× antibiotic-antimycotic solution (Life Technologies) in a 5% CO₂ atmosphere at 37°C. Cultures were split weekly in T25 [0.5 × 10⁶ or T75 (1.5 × 10⁶) culture flasks (Corning-Becton Dickinson and Company Becton Drive, Franklin Lakes, NJ, United States). For cryopreservation, 1.5 × 10⁶ were resuspended in 1 ml of

freezing medium (DMEM added with 20% FBS, 1× antibiotic-antimycotic solution, and 10% DMSO). The cryovials were placed in a freezing box and stored at -80°C overnight. For long-term storage, the cryovials were transferred into a cryogenic biobank.

Cellular Bioenergetics

The Seahorse XFp analyzer (Agilent) was used to simultaneously measure oxygen consumption rate (OCR), an index of cell respiration (pmol/min), and extracellular acidification rate (ECAR), an index of glycolysis (mpH/min). IPEC-J2 cells (1 × 10⁴ / well) were grown in XFp cell culture miniplates (Agilent) for 24 h. On the experiment day, IPEC-J2 cells were switched to freshly made Seahorse XF DMEM medium pH 7.4 supplemented with 10 mM glucose, 1 mM sodium pyruvate, and 2 mM L-glutamine, in the absence (Control) and in the presence of 5 or 10 μM of each VK vitamer (VK1, VK2 or VK3) under study. The plates were incubated at 37°C in air for 45 min before measuring OCR and ECAR by the adequate programs (ATP Rate Assay, Cell Mito Stress Test and Cell Energy Phenotype Test). The injection ports of XFp sensor cartridges, which were hydrated overnight with XF calibrant at 37°C, were loaded with 10× concentration of inhibitors according to the instructions provided by Seahorse XFp ATP Rate Assay, Cell Mito Stress Test, and Cell Energy Phenotype Test. The final concentration used for ATP Rate Assay were 1.5 μM oligomycin (port A) and 0.5 μM rotenone (Rot) plus 0.5 μM antimycin A (AA) (port B). For Cell Mito Stress Test the final concentrations were 1.5 μM oligomycin (olig) (port A), 1.0 μM Carbonyl-cyanide-4-(trifluoromethoxy) phenylhydrazone (FCCP) (port B), and 0.5 μM rotenone plus antimycin A (port C), while for the Cell Energy Phenotype Test the final concentrations were 1.5 μM oligomycin plus 1.0 μM FCCP (port A). All the analysis were run at 37°C. All data were analyzed by WAVE software; OCR and ECAR values were normalized to the total number of cells per well. All parameter values were calculated per well, according to the manufacturer's instructions. Both ATP Rate Assay, Mito Stress Test, and Cell Energy Phenotype Test were carried out three times in independent experiments (Marcocchia et al., 2021).

The ATP Rate Assay provides the bioenergetic parameters currently used to characterize the cellular ATP production, namely ATP production rate, related to the conversion of glucose to lactate in the glycolytic pathway (glycoATP Production Rate) and to the mitochondrial OXPHOS (mitoATP Production Rate). Accordingly, the ratio between mitoATP Production Rate and glycoATP Production Rate (ATP Rate Index) is currently considered as a valuable parameter to detect changes and/or differences in the metabolic phenotype (a ratio > 1 means mainly OXPHOS pathway; a ratio < 1 means mainly glycolytic pathway).

The Mito Stress Test enables the characterization of cell respiration by the following parameters: basal respiration, detected as baseline OCR before oligomycin addition; minimal respiration measured as OCR in the presence of oligomycin; and maximal respiration evaluated as OCR after FCCP addition. The so-called proton leak, which corresponds to the difference between the basal respiration and the respiration in the presence of oligomycin (minimal respiration), indicates the re-entry of H⁺ in the intermembrane space independently of the F₁F₀-ATP

synthase. The non-mitochondrial respiration, evaluated as OCR in the presence of rotenone plus antimycin A (respiratory chain inhibitors), was subtracted from all the above parameters. The ATP turnover or oligomycin-sensitive respiration was obtained from the difference between the basal respiration and the minimal respiration (OCR in presence of oligomycin). Finally, the difference between the maximal and the basal respiration provided the spare capacity, which represents the ability to respond to an increased energy demand and can be considered as a measure of the flexibility of the OXPHOS machinery (Bernardini et al., 2021).

The simultaneous measurement of mitochondrial respiration and glycolysis was carried out by the Cell Energy Phenotype Test under baseline and stressed conditions, the latter after simultaneous addition of oligomycin and FCCP. Oligomycin inhibits the mitochondrial ATP production by the F_1F_0 -ATP synthase and the cell compensates the failed OXPHOS by increasing the glycolysis rate, while the dissipation of the electrochemical gradient of H^+ in mitochondria by the ionophore FCCP drives the highest oxygen consumption (uncoupled respiration). The assay allows to evaluate two main parameters of cell energy metabolism, known as metabolic phenotypes (baseline and stressed phenotype) and metabolic potential. The baseline phenotype is featured by the OCR and ECAR values in cells under the starting condition in the presence of substrates. The stressed phenotype is shown by the OCR and ECAR values in cells after addition of stressor compounds (oligomycin plus FCCP). The metabolic potential is the ability to increase energy production *via* respiration and glycolysis and it is defined as the % increase of stressed phenotype over baseline phenotype of OCR and ECAR (Bernardini et al., 2021).

Statistical Analysis

Statistical analyses were performed by SIGMASTAT software. Each treatment was replicated three or eight times (viability test) in three independent experiments. Data were analyzed by the Student's *t*-test, or by one-way analysis of variance (ANOVA) followed by Students–Newman–Keuls test when *F* values indicated significance ($P \leq 0.05$) was applied. Percentage data were *arcsin*-transformed before statistical analyses to ensure normality.

RESULTS

Intracellular ATP Production

The cellular ATP level produced by OXPHOS and glycolysis in the presence of the different VK vitamers are shown in **Figure 2** by OCR and ECAR values, respectively, under basal metabolic conditions. The calculation of the mitoATP and glycoATP production rate (**Figure 2**), obtained by injecting oligomycin to inhibit mitochondrial ATP synthesis and then rotenone plus antimycin A to block mitochondrial respiration, highlight that IPEC-J2 cells are characterized by an oxidative metabolism. VK1 induces an increase in total ATP production at both the concentrations tested (5 and 10 μ M). This increase is due to a significant glycoATP production activation, whereas

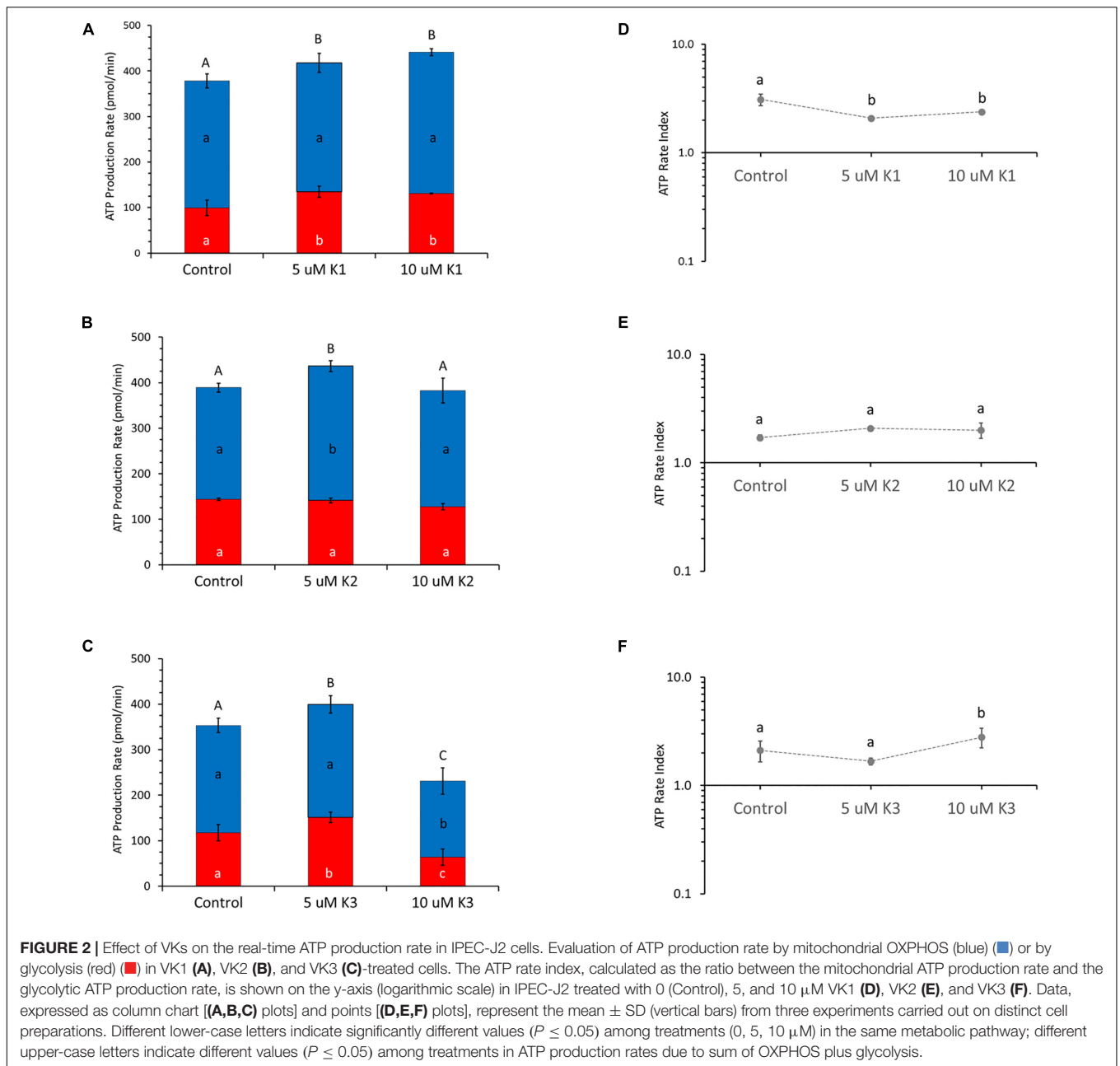
the mitoATP production is unaffected (**Figure 2A**). Conversely, VK2 does not affect the glycoATP production. The total ATP production is only 20% increased by 5 μ M VK2 with respect to the control, due to an enhanced mitochondrial ATP synthesis (**Figure 2B**). VK3 shows a concentration-dependent effect on intracellular ATP production by increasing the glycolysis by 30% without modifying the mitochondrial activity at 5 μ M, whereas at 10 μ M it reduces by 50% the glycoATP and the mitoATP synthesis by 30% (**Figure 2C**). Even if all the VK vitamers can modify ATP production, the results highlight that the ratio between mitoATP Production Rate and glycoATP Production Rate (ATP Rate Index) is always > 1 . In detail, 5 and 10 μ M VK1 decrease the propensity to produce mitoATP with respect to the control (**Figure 2D**), whereas this effect is not shown by VK2 which does not modify the ATP rate index (**Figure 2E**). In IPEC-J2 cells treated with 10 μ MVK3, the residual ATP production mainly relies on mitochondrial oxidative metabolism (**Figure 2F**).

Cellular Respiration

The profile and function of cell respiration of IPEC-J2 cells treated with VKs are shown in **Figure 3**. The key parameters of cell metabolism were obtained from functional metabolic data as detailed in the Materials and mMethods section. The results show that OCR values in the presence of both VK1 concentrations tested are not different from control ones (**Figures 3A,B**). VK1 does not modify the basal respiration and the proton leak; consequently, the calculated ATP turnover is not affected. Therefore, the coupling efficiency in the presence and in the absence of VK1 is about 0.80 a.u. (the maximal value of 1.0 a.u. is obtained when all the basal respiration is sensitive to oligomycin). The IPEC-J2 OCR in the presence of FCCP (maximal respiration) shows a twice higher value than basal OCR. The spare respiratory capacity, which defines the cell propensity to adjust cell bioenergetics to fulfill the increased energy demand, constantly attains a 50% OCR value of the FCCP-stimulated OCR, irrespective of the VK1 presence (**Figure 3B**).

VK2 has a concentration-dependent effect on the OCR (**Figure 3C**). Accordingly, 5 μ M VK2 increases the basal, maximal, and spare capacity OCR, as well as ATP turnover with respect to the control. Conversely, at 10 μ M VK2 the effect on the same parameters is inhibitory (**Figure 3D**). Even if the basal and ATP turnover is higher in presence of 5 μ M VK2 and lower at 10 μ M VK2, with respect to the control, the coupling efficiencies values in the presence of VK2 (0.77 a.u.) are not different from those of the control. Likewise, on comparing the maximal respiration and the spare respiratory capacity in the absence or in the presence of the two VK2 concentrations, significantly different OCR values are shown. However, the OCR values of the maximal respiration and spare respiratory capacity in all treatments (0.0, 5.0, and 10 μ M VK2) are of the same extent. In detail, the maximal respiration is always twice higher than the basal respiration, whereas for the latter the OCR activity is increased by 50% with FCCP (**Figure 3D**).

As shown in **Figure 3E**, the respiratory profile of IPEC-J2 cells decreases with increasing VK3 concentrations. Even if the basal respiration is apparently unaffected by VK3 (**Figure 3F**),



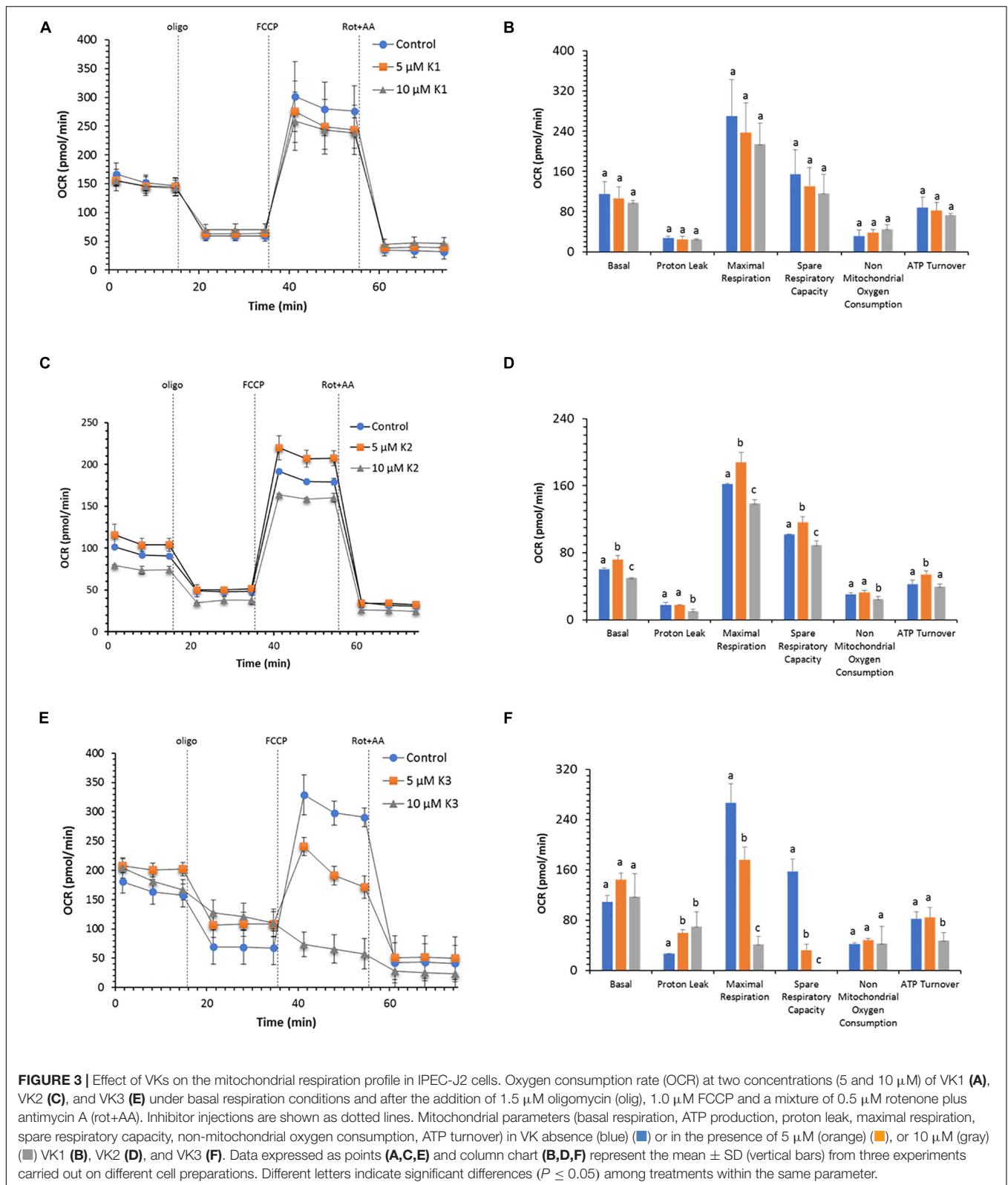
the coupling efficiency is halved by 10 μM VK3 as a result of an increase in proton leak. In addition, IPEC-J2 cells treated with 5 μM VK3 do not show any respiration stimulation by FCCP, while when these cells are treated with 10 μM VK3, not only do they not show any increase in OCR in response to FCCP, but also the OCR after FCCP addition is lower than the basal OCR. Consistently, a strong inhibition of respiration with strongly decreased or even abolished spare respiratory capacity is detected in the presence of 5 and 10 μM VK3, respectively.

Extracellular Acidification

The glycolytic function in IPEC-J2 cells evaluated as extracellular acidification rate (ECAR) does not show any change in the

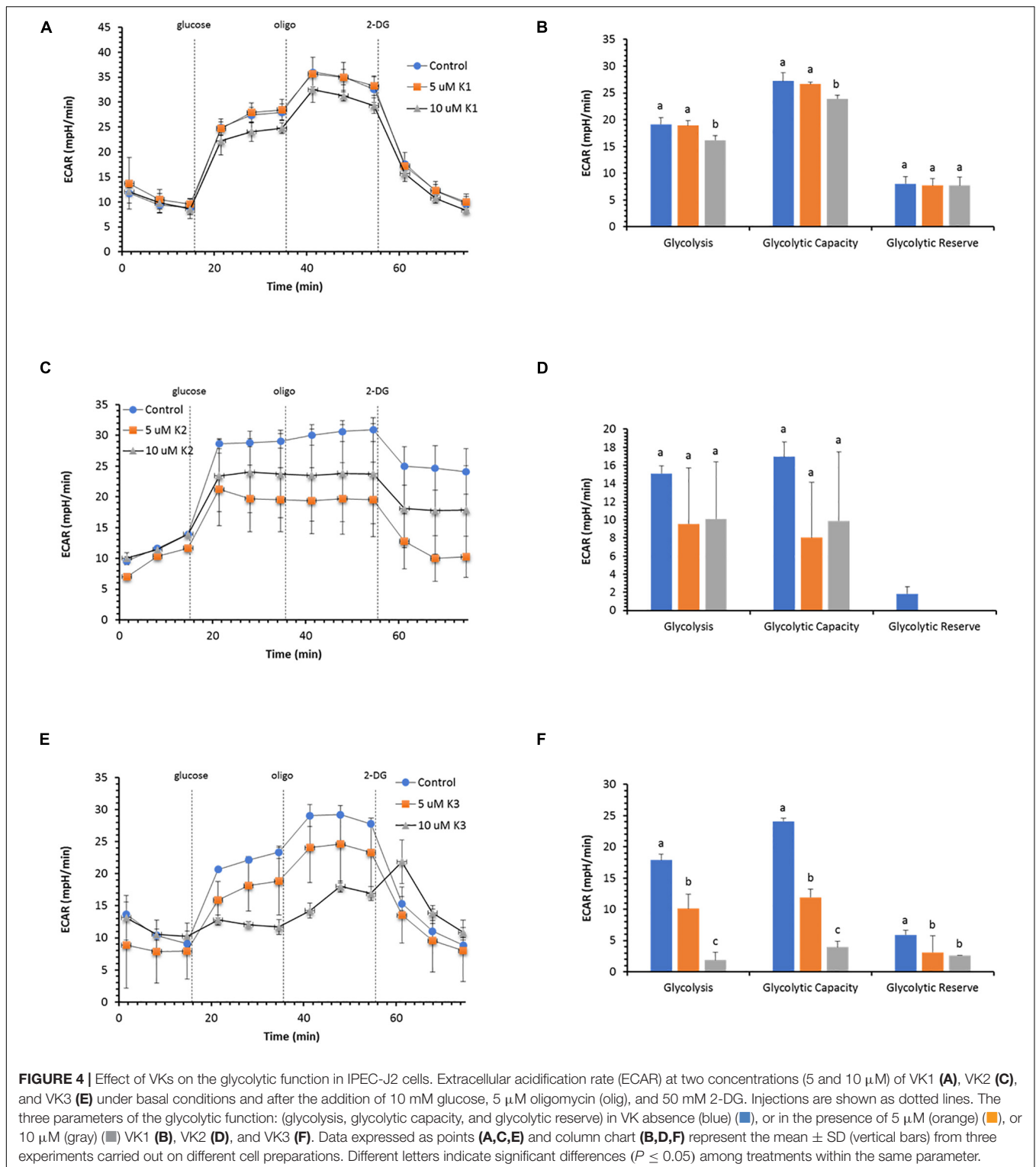
presence of the two VK1 concentrations tested (Figure 4A). The key parameters of glycolytic flux, i.e., Glycolysis and Glycolytic Capacity, attain the same value in the presence or in the absence of 5 μM VK. Conversely, 10 μM VK1 inhibits both parameters by 15% (Figure 4B). However, the Glycolytic Reserve, defined as the difference between Glycolytic Capacity and Glycolysis, is unaffected by 10 μM VK1, since the two parameters show a proportional decrease in ECAR with respect to the control (Figure 3B).

Also, VK2 does not substantially modify the glycolytic profile of IPEC-J2 cells (Figure 4C), but in this case the glycolytic reserve disappears, since the Glycolysis rate has the same ECAR value as the Glycolytic Capacity (Figure 4D).



VK3 shows an inhibitory action on ECAR with a concentration-dependent effect (Figure 4E). The Glycolysis and the Glycolytic Capacity are inhibited by 50 and 13% with 5

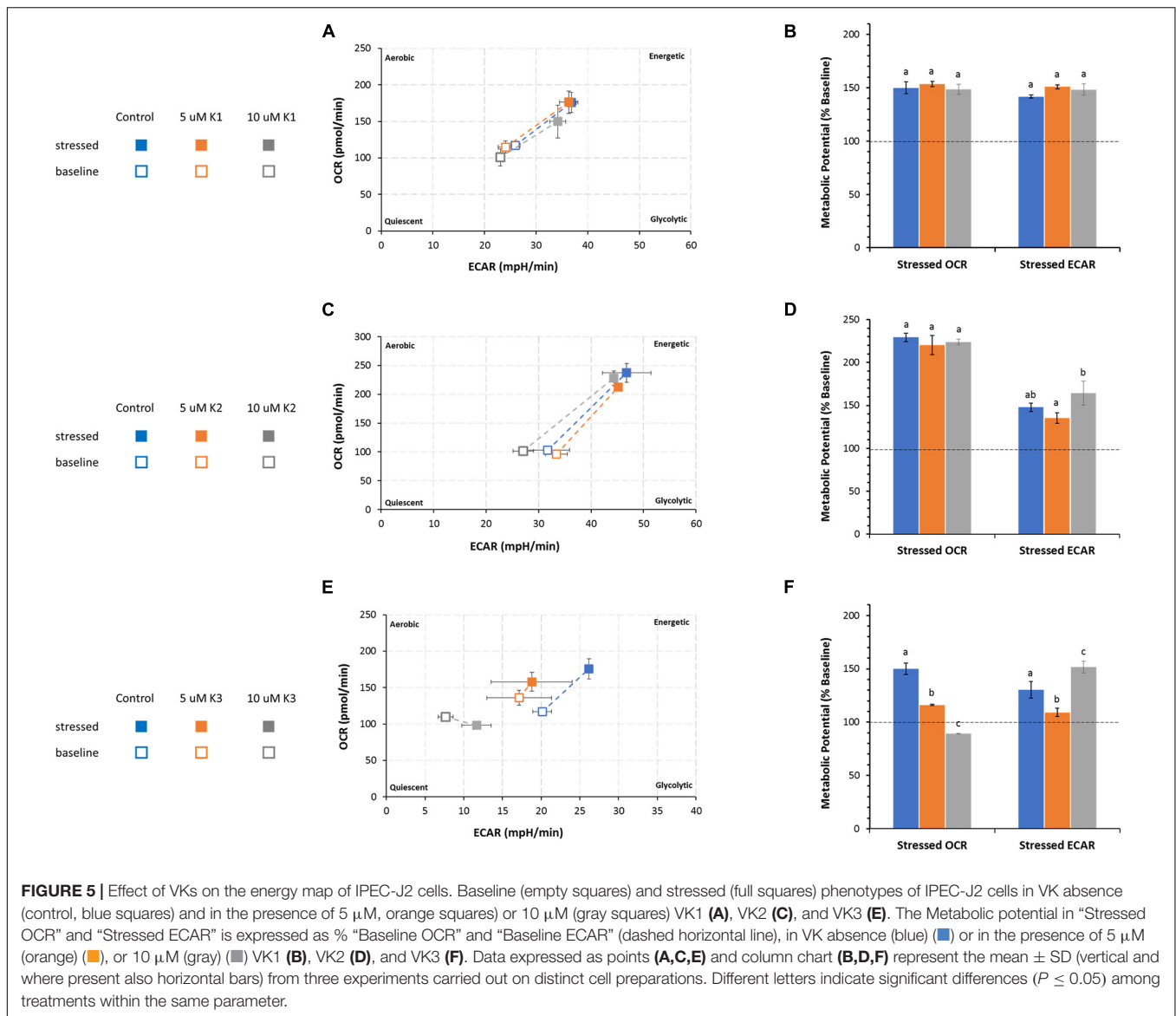
and 10 μM VK3, respectively. Conversely, the decrease in the Glycolytic Reserve is independent of the VK3 concentration tested (Figure 4F).



Bioenergetic Phenogram

The cell energy production of IPEC-J2 cells detected by OCR and ECAR in the presence or in the absence of VKs is shown as metabolic phenotype under normal (baseline) and stressed conditions (Figure 5). The treatment with

oligomycin and FCCP mixture, known as mitochondrial stressors, provides the phenogram which illustrates the relative baseline and stressed phenotype, and the response of the metabolic potential (expressed as % baseline) of IPEC-J2 cells after treatment with VKs.



According to the method adopted, the metabolic potential indicates the cell's ability to meet an energy demand by mitochondrial respiration and glycolysis.

Irrespective of the presence of VK1, IPEC-J2 cells show an increase in the utilization of both pathways (mitochondrial respiration and glycolysis) (Figure 5A) under stressed conditions without any significant difference in the metabolic potential in the presence or absence of VK1 (Figure 5B).

The IPEC-J2 phenogram under starting assay conditions (baseline phenotype) in the presence of substrates and without stressors (oligomycin plus FCCP) do not show any difference in the metabolic pathways between control and VK2 treated cells. The same results are detected under stressed conditions irrespective of the presence of VK2, even if in this case the cells undergo a metabolic switch toward an energetic phenotype (Figure 5C). The cell energy demand is satisfied by an increase in OCR. The metabolic potential primarily relies on an efficient

mitochondrial energy metabolism. No difference in OCR values between the VK2-treated IPEC-J2 cells and the control under stressed conditions is detectable (Figure 4D). The two VK2 concentrations tested do not modify the glycolytic activity stimulated by stressor compounds with respect to the control, even if the stressed ECAR, expressed as metabolic potential, in 5 μ M VK2-treated IPEC-J2 cells is lower than that in 10 μ M VK2-treated cells (Figure 5D).

VK3 affects the IPEC-J2 cells' energy production, highlighting an energy map which shows an inhibited aerobic metabolism (Figure 5E). Stressed OCR and ECAR in the 5 μ M VK3-treated IPEC-J2 cells are inhibited by 23 and 16%, respectively. The treatment with 10 μ M K3 makes IPEC-J2 cells shift their energy production mode from OXPHOS to glycolysis (Figure 5F). In these cells the stressed OCR is 11% lower than baseline OCR, whereas the metabolic potential of glycolysis (ECAR) increases by 50% when compared to baseline metabolism (Figure 5F).

However, the baseline OCR/ECAR ratio in VK3-treated IPEC-J2 cells is > 4 . This means that, other than acidification from glycolysis, the ECAR values in VK3-treated IPEC-J2 cells include the contribution of the mitochondrial acidification by CO_2 production by Krebs cycle. Accordingly, in aqueous media CO_2 forms the weak acid H_2CO_3 .

DISCUSSION

As far as we are aware, up to now the effect of the three VK vitamers on the bioenergetic metabolism of enterocytes has been poorly investigated. The IPEC-J2 cell line provides an excellent model to evaluate in detail the mechanism(s) involved in cell energy production. These cells also represent a good translational model to study fat-soluble vitamin effects on cellular metabolism in the gut. IPEC-J2 cells rely on oxidative metabolisms to supply the energy required by the physiological functions (Vaugelade et al., 1994; Bernardini et al., 2021).

The enhancement of ATP production by IPEC-J2 cells is the most relevant bioenergetic effect of VK1, which primarily contributes to stimulate the glycolytic pathway at both the concentrations tested. Indeed, the modification of ATP rate index highlights that VK1-treated IPEC-J2 cells switch to a less aerobic metabolism, namely glycolysis vs OXPHOS, with respect to the control, but without affecting the mitochondrial respiration and the glycolysis parameters. The ATP production of VK2-treated IPEC-J2 cells is only increased at the lower VK2 concentration tested, namely $5 \mu\text{M}$ VK2. Indeed, the effect is corroborated by the Mito Stress Test which shows that the mitochondrial parameters are improved at $5 \mu\text{M}$ VK2 concentration tested. The VK2 structure resembles that of the CoQ_{10} , a membrane-embedded electron carrier of mitochondrial electron transfer system (mETS) (Lenaz et al., 1999), even if it cannot substitute CoQ_{10} (Cerqua et al., 2019). VK2 can mimic the two structural components of CoQ_{10} which are crucial in OXPHOS, namely in the naphthoquinone core, which transfer electrons during the redox-cycle, and in the isoprenoid tail, which allows diffusion into the lipid bilayer. Recently both VK1 and VK2 were found to decrease the order and to increase fluidity in model membranes (Ausili et al., 2020). Therefore, these VKs may also act indirectly by facilitating the function of respiratory complexes through the inner mitochondrial membrane.

Short-chain quinones are known to be toxic, especially those containing 0–3 isoprene units, whereas CoQ_4 displays only minimal toxicity (Takahashi et al., 2018). During mitochondrial respiration the VK2 might transfer electrons from complex I or complex II directly or indirectly to cytochrome *c*, according to the diffusion mode of shuttling electrons along the respiratory chain (Nesci and Lenaz, 2021). This VK2 role as electron transporter in the respiratory chain (Colpa-Boonstra and Slater, 1958) is still controversial. Accordingly, in spite of reports which rule out this possibility (Cerqua et al., 2019), in an *in vitro* model VK2 enhanced respiratory chain efficiency and contributed to building the electrochemical proton gradient ($\Delta\mu\text{H}^+$) by respiratory complexes that are exploited to generate ATP, similarly to CoQ_{10} (Vos et al., 2012). Our

findings show that the effect on mitochondrial respiration could depend on VK2 concentration, namely the positive effect shown at $5 \mu\text{M}$ VK2 may become harmful at high concentrations. The VK2 structural properties are consistent with the stimulation of mitochondrial respiration without any effect on glycolysis. Consistently, low VK2 concentrations can favor an energy boost in IPEC-J2 cell activation, proliferation, and differentiation by increasing the OXPHOS capability to produce ATP.

Vitamer VK3 is the only one of the three forms of VK under study which exerts a negative effect on energy metabolism of IPEC-J2 cells. Accordingly, cell respiration is inhibited by both VK3 concentrations. The VK3-driven increase in H^+ leakage through the inner mitochondrial membrane leads to the decrease in the ATP synthesis. However, uncoupling agents such as FCCP can stimulate the mitochondrial respiration of VK3-treated IPEC-J2 cells. The increase in non-phosphorylating substrate oxidation is typical of a decrease in $\Delta\mu\text{H}^+$, accompanied by production of reactive oxygen species and increase in oxygen consumption (Zorov et al., 2020). Conversely, we also detected in VK3-treated IPEC-J2 cells an inhibited mitochondrial respiration, as it happens in the presence of excess of uncouplers. Moreover, the negative effect on cell metabolism is underscored by VK3-driven enhancement of the ECAR-insensitive glycolytic activity in IPEC-J2 cells. However, VK3-treated IPEC-J2 cells can only rely on the glycolytic pathway to supply the energy required when their energy production mode shifts upon induction of signaling pathways of stress (Hung and Calkins, 2016).

The present study points out that the different VK vitamers tested promote different effects on IPEC-J2 cell bioenergetics. Accordingly, the chemical structure of the sidechain of VKs is confirmed to be crucial to produce the effects.

New roles for VKs in reducing risk of certain chronic diseases have been proposed in the last decades (Shearer et al., 2012). Consistently, the present work which shows for the first time how different VK forms and concentrations differently act on the bioenergetics of IPEC-J2 cell line contributes to deepening the knowledge on the varied roles of VKs in enterocytes, of which the IPEC-J2 cell line constitutes a fascinating model. The swine is increasingly used in translational research and drug development (Monticello and Haschek, 2016). Therefore, the benefits of a VK stimulation of ATP production in enterocytes underlines and confirms the relevance of gut microbiota, as VK producer, in maintaining a healthy gut and, as a cascade, in the prevention and/or treatment of diseases of the intestinal tract. Interestingly, since the last century (Krasinski et al., 1985) certain chronic gastrointestinal disorders were associated with VK deficiency. At present this connection is established with Crohn's disease (Schoon et al., 2001), celiac disease (Djuric et al., 2007), and inflammatory bowel disease (Nowak et al., 2014). Pathological conditions are often associated with impaired mitochondrial bioenergetics (Nesci et al., 2021). Moreover, VK antagonists used in clinical therapy to prevent thromboembolism together with coadministration of other drugs can induce drug-drug interaction effects with VK malabsorption (Takada et al., 2015). Infants cannot obtain VK from the breast milk and have poor

intestinal adsorption due to immature gut flora. Therefore, VK oral administration is the best way to prevent Vitamin K deficiency bleeding in infancy (Araki and Shirahata, 2020). It seems likely to postulate that an insufficient ATP production by enterocytes, related to a poor VK availability, also due to antibiotic treatments (Shirakawa et al., 1990), may represent, or contribute to, the biochemical bases of some gut pathologies.

DATA AVAILABILITY STATEMENT

The raw data supporting the conclusions of this article will be made available by the authors, without undue reservation.

REFERENCES

- Araki, S., and Shirahata, A. (2020). Vitamin K deficiency bleeding in infancy. *Nutrients* 12:780. doi: 10.3390/nu12030780
- Ausili, A., Clemente, J., Pons-Belda, ÓD., de Godos, A., Corbalán-García, S., Torrecillas, A., et al. (2020). Interaction of vitamin K1 and vitamin K2 with dimyristoylphosphatidylcholine and their location in the membrane. *Langmuir* 36, 1062–1073. doi: 10.1021/acs.langmuir.9b03552
- Azuma, K., and Inoue, S. (2019). Multiple modes of vitamin K actions in aging-related musculoskeletal disorders. *Int. J. Mol. Sci.* 20:2844. doi: 10.3390/ijms20112844
- Bernardini, C., Algieri, C., La Mantia, D., Zannoni, A., Salaroli, R., Trombetti, F., et al. (2021). Relationship between serum concentration, functional parameters and cell bioenergetics in IPEC-J2 cell line. *Histochem. Cell Biol.* (in press). doi: 10.1007/s00418-021-01981-2
- Bórquez, J. C., Hidalgo, M., Rodríguez, J. M., Montaña, A., Porras, O., Troncoso, R., et al. (2020). Sucralose stimulates mitochondrial bioenergetics in Caco-2 cells. *Front. Nutr.* 7:585484. doi: 10.3389/fnut.2020.585484
- Cerqua, C., Casarin, A., Pierrel, F., Vazquez Fonseca, L., Viola, G., Salviati, L., et al. (2019). Vitamin K2 cannot substitute Coenzyme Q10 as electron carrier in the mitochondrial respiratory chain of mammalian cells. *Sci. Rep.* 9:6553. doi: 10.1038/s41598-019-43014-y
- Colpa-Boonstra, J. P., and Slater, E. C. (1958). The possible role of vitamin K in the respiratory chain. *Biochim. Biophys. Acta* 27, 122–133. doi: 10.1016/0006-3002(58)90298-1
- Djuric, Z., Zivic, S., and Katic, V. (2007). Celiac disease with diffuse cutaneous vitamin K-deficiency bleeding. *Adv. Ther.* 24, 1286–1289. doi: 10.1007/BF02877775
- Gordeladze, J. O. (ed.) (2017). *Vitamin K2 - Vital for Health and Wellbeing*. London: InTech, doi: 10.5772/61430
- Hung, K.-M., and Calkins, M. J. (2016). Mitochondrial homeostatic disruptions are sensitive indicators of stress in neurons with defective mitochondrial DNA transactions. *Mitochondrion* 31, 9–19. doi: 10.1016/j.mito.2016.08.015
- Ivanova, D., Zhelev, Z., Getsov, P., Nikolova, B., Aoki, I., Higashi, T., et al. (2018). Vitamin K: Redox-modulation, prevention of mitochondrial dysfunction and anticancer effect. *Redox Biol.* 16, 352–358. doi: 10.1016/j.redox.2018.03.013
- Krasinski, S. D., Russell, R. M., Furie, B. C., Kruger, S. F., Jacques, P. F., and Furie, B. (1985). The prevalence of vitamin K deficiency in chronic gastrointestinal disorders. *Am. J. Clin. Nutr.* 41, 639–643. doi: 10.1093/ajcn/41.3.639
- Lenaz, G., Fato, R., Di Bernardo, S., Jarreta, D., Costa, A., Genova, M. L., et al. (1999). Localization and mobility of coenzyme Q in lipid bilayers and membranes. *Biofactors* 9, 87–93. doi: 10.1002/biof.5520090202
- Marcocchia, R., Nesci, S., Merlo, B., Ballotta, G., Algieri, C., Pagliarini, A., et al. (2021). Biological characteristics and metabolic profile of canine mesenchymal stem cells isolated from adipose tissue and umbilical cord matrix. *PLoS One* 16:e0247567. doi: 10.1371/journal.pone.0247567
- Monticello, T. M., and Haschek, W. M. (2016). Swine in translational research and drug development. *Toxicol. Pathol.* 44, 297–298. doi: 10.1177/0192623316630838

AUTHOR CONTRIBUTIONS

CA and DLM performed the experiments. CA and CB analyzed the data. SN conceived the original idea. CB, MF, AP, and SN planned the experiments. SN supervised the project. AP and SN wrote the manuscript. CB, FT, and MF revised the text. MF acquired funding. All authors read and approved the manuscript.

FUNDING

This work was supported by University of Bologna, grant BIR2019 to MF.

- Nesci, S. (2017). Glucose and glutamine in the mitochondrial oxidative metabolism of stem cells. *Mitochondrion* 35, 11–12. doi: 10.1016/j.mito.2017.04.004
- Nesci, S., and Lenaz, G. (2021). The mitochondrial energy conversion involves cytochrome c diffusion into the respiratory supercomplexes. *Biochim. Biophys. Acta Bioenerg.* 1862:148394. doi: 10.1016/j.bbabi.2021.148394
- Nesci, S., Trombetti, F., Pagliarini, A., Ventrella, V., Algieri, C., Tioli, G., et al. (2021). Molecular and supramolecular structure of the mitochondrial oxidative phosphorylation system: implications for pathology. *Life* 11:242. doi: 10.3390/life11030242
- Nossol, C., Diesing, A.-K., Walk, N., Faber-Zuschratter, H., Hartig, R., Post, A., et al. (2011). Air-liquid interface cultures enhance the oxygen supply and trigger the structural and functional differentiation of intestinal porcine epithelial cells (IPEC). *Histochem. Cell Biol.* 136, 103–115. doi: 10.1007/s00418-011-0826-y
- Nowak, J. K., Grzybowska-Chlebowczyk, U., Landowski, P., Szaflarska-Poplawska, A., Klineciewicz, B., Adamczak, D., et al. (2014). Prevalence and correlates of vitamin K deficiency in children with inflammatory bowel disease. *Sci. Rep.* 4:4768. doi: 10.1038/srep04768
- Okano, T., Shimomura, Y., Yamano, M., Sahara, Y., Kamao, M., Sugiura, M., et al. (2008). Conversion of phyloquinone (Vitamin K1) into menaquinone-4 (Vitamin K2) in mice: two possible routes for menaquinone-4 accumulation in cerebra of mice. *J. Biol. Chem.* 283, 11270–11279. doi: 10.1074/jbc.M702971200
- Orlando, A., Linsalata, M., Tutino, V., D'Attoma, B., Notarnicola, M., and Russo, F. (2015). Vitamin K1 exerts antiproliferative effects and induces apoptosis in three differently graded human colon cancer cell lines. *Biomed. Res. Int.* 2015:296721. doi: 10.1155/2015/296721
- Schoon, E. J., Müller, M. C., Vermeer, C., Schurgers, L. J., Brummer, R. J., and Stockbrügger, R. W. (2001). Low serum and bone vitamin K status in patients with longstanding Crohn's disease: another pathogenetic factor of osteoporosis in Crohn's disease? *Gut* 48, 473–477. doi: 10.1136/gut.48.4.473
- Schwalfenberg, G. K. (2017). Vitamins K1 and K2: the emerging group of vitamins required for human health. *J. Nutr. Metab.* 2017:6254836. doi: 10.1155/2017/6254836
- Shearer, M. J., Fu, X., and Booth, S. L. (2012). Vitamin K nutrition, metabolism, and requirements: current concepts and future research. *Adv. Nutr.* 3, 182–195. doi: 10.3945/an.111.001800
- Shirakawa, H., Komai, M., and Kimura, S. (1990). Antibiotic-induced vitamin K deficiency and the role of the presence of intestinal flora. *Int. J. Vitam. Nutr. Res.* 60, 245–251.
- Suttie, J. W. (1985). Vitamin K-Dependent Carboxylase. *Annu. Rev. Biochem.* 54, 459–477. doi: 10.1146/annurev.bi.54.070185.002331
- Takada, T., Yamanashi, Y., Konishi, K., Yamamoto, T., Toyoda, Y., Masuo, Y., et al. (2015). NPC1L1 is a key regulator of intestinal vitamin K absorption and a modulator of warfarin therapy. *Sci. Transl. Med.* 7:275ra23. doi: 10.1126/scitranslmed.3010329
- Takahashi, T., Mine, Y., and Okamoto, T. (2018). Intracellular reduction of coenzyme Q homologues with a short isoprenoid side chain induces apoptosis of HeLa cells. *J. Biochem.* 163, 329–339. doi: 10.1093/jb/mvy002

- Tan, B., Xiao, H., Li, F., Zeng, L., and Yin, Y. (2015). The profiles of mitochondrial respiration and glycolysis using extracellular flux analysis in porcine enterocyte IPEC-J2. *Anim. Nutr.* 1, 239–243. doi: 10.1016/j.aninu.2015.08.004
- Tsugawa, N., and Shiraki, M. (2020). Vitamin K Nutrition and Bone Health. *Nutrients* 12, 1909. doi: 10.3390/nu12071909
- Vaugelade, P., Posho, L., Darcy-Vrillon, B., Bernard, F., Morel, M. T., and Duée, P. H. (1994). Intestinal oxygen uptake and glucose metabolism during nutrient absorption in the pig. *Proc. Soc. Exp. Biol. Med.* 207, 309–316. doi: 10.3181/00379727-207-43821
- Vergauwen, H. (2015). “The IPEC-J2 Cell Line,” in *The Impact of Food Bioactives on Health*, eds K. Verhoeckx, P. Cotter, I. López-Expósito, C. Kleiveland, T. Lea, A. Mackie, et al. (Cham: Springer International Publishing), 125–134. doi: 10.1007/978-3-319-16104-4_12
- Vos, M., Esposito, G., Edirisinghe, J. N., Vilain, S., Haddad, D. M., Slabbaert, J. R., et al. (2012). Vitamin K2 is a mitochondrial electron carrier that rescues pink1 deficiency. *Science* 336, 1306–1310. doi: 10.1126/science.1218632
- Wu, Z., Tan, B., Liu, Y., Dunn, J., Martorell Guerola, P., Tortajada, M., et al. (2019). Chemical composition and antioxidant properties of essential oils from peppermint, native spearmint and scotch spearmint. *Molecules* 24:2825. doi: 10.3390/molecules24152825
- Zorov, D. B., Andrianova, N. V., Babenko, V. A., Bakeeva, L. E., Zorov, S. D., Zorova, L. D., et al. (2020). Nonphosphorylating oxidation in mitochondria and related processes. *Biochemistry (Mosc)* 85, 1570–1577. doi: 10.1134/S0006297920120093

Conflict of Interest: The authors declare that the research was conducted in the absence of any commercial or financial relationships that could be construed as a potential conflict of interest.

Copyright © 2021 Bernardini, Algieri, La Mantia, Trombetti, Pagliarani, Forni and Nesci. This is an open-access article distributed under the terms of the Creative Commons Attribution License (CC BY). The use, distribution or reproduction in other forums is permitted, provided the original author(s) and the copyright owner(s) are credited and that the original publication in this journal is cited, in accordance with accepted academic practice. No use, distribution or reproduction is permitted which does not comply with these terms.



Yeast Cell-Based Transport Assay for the Functional Characterization of Human 4F2hc-LAT1 and -LAT2, and LAT1 and LAT2 Substrates and Inhibitors

Satish Kantipudi and Dimitrios Fotiadis*

Institute of Biochemistry and Molecular Medicine, University of Bern, Bern, Switzerland

OPEN ACCESS

Edited by:

Cesare Inciveri,
University of Calabria, Italy

Reviewed by:

Manuel Palacin,
Institute for Research in Biomedicine,
Spain
Andreas H. Engel,
University of Basel, Switzerland

*Correspondence:

Dimitrios Fotiadis
dimitrios.fotiadis@ibmm.unibe.ch

Specialty section:

This article was submitted to
Cellular Biochemistry,
a section of the journal
Frontiers in Molecular Biosciences

Received: 06 March 2021

Accepted: 06 May 2021

Published: 28 May 2021

Citation:

Kantipudi S and Fotiadis D (2021)
Yeast Cell-Based Transport Assay for
the Functional Characterization of
Human 4F2hc-LAT1 and -LAT2, and
LAT1 and LAT2 Substrates
and Inhibitors.
Front. Mol. Biosci. 8:676854.
doi: 10.3389/fmolb.2021.676854

In mammalian cells, the L-type amino acid transporters (LATs) LAT1 (SLC7A5) and LAT2 (SLC7A8) form heterodimeric amino acid transporters (HATs) with the ancillary protein 4F2hc and are involved in the cellular uptake of specific amino acids. The HAT 4F2hc-LAT1 is found upregulated in various cancer cell types, while 4F2hc-LAT2 is a transporter for non-cancer cells. Preclinical studies have highlighted that 4F2hc-LAT1 plays an important role in tumor progression representing a valid anticancer target. Consequently, current research is focusing on the development of potent and specific human 4F2hc-LAT1 inhibitors. On the other hand, 4F2hc-LAT2 is emerging as target of other diseases, thus also gaining clinical interest. To determine affinity and specificity of substrates and inhibitors for 4F2hc-LAT1 or 4F2hc-LAT2, robust transport cell assays are indispensable. We have optimized and validated a transport assay using cells of the methylotrophic yeast *Pichia pastoris* stably overexpressing the human HATs 4F2hc-LAT1 or -LAT2, and the LATs LAT1 or LAT2 alone. The radioligand [³H]L-leucine was used as reporter and the substrates L-leucine, triiodothyronine (T3) and thyroxine (T4) as well as the inhibitors BCH and JPH203 (KYT-0353) for assay validation. Obtained half-maximal inhibitory concentrations also provided new insights, e.g., into the LAT specificity of the potent inhibitor JPH203 and on the potency of the thyroid hormones T3 and T4 to inhibit transport through human 4F2hc-LAT2. The LAT1 and LAT2 assays are of particular interest to determine possible implications and influences of 4F2hc in ligand binding and transport. In summary, the presented assays are valuable for characterization of ligands, e.g., towards 4F2hc-LAT1 specificity, and can also be applied for compound screening. Finally, our established approach and assay would also be applicable to other HATs and LATs of interest.

Keywords: amino acid transporter, inhibitor, LAT1, LAT2, JPH203, *Pichia pastoris*, SLC7, Transport Assay

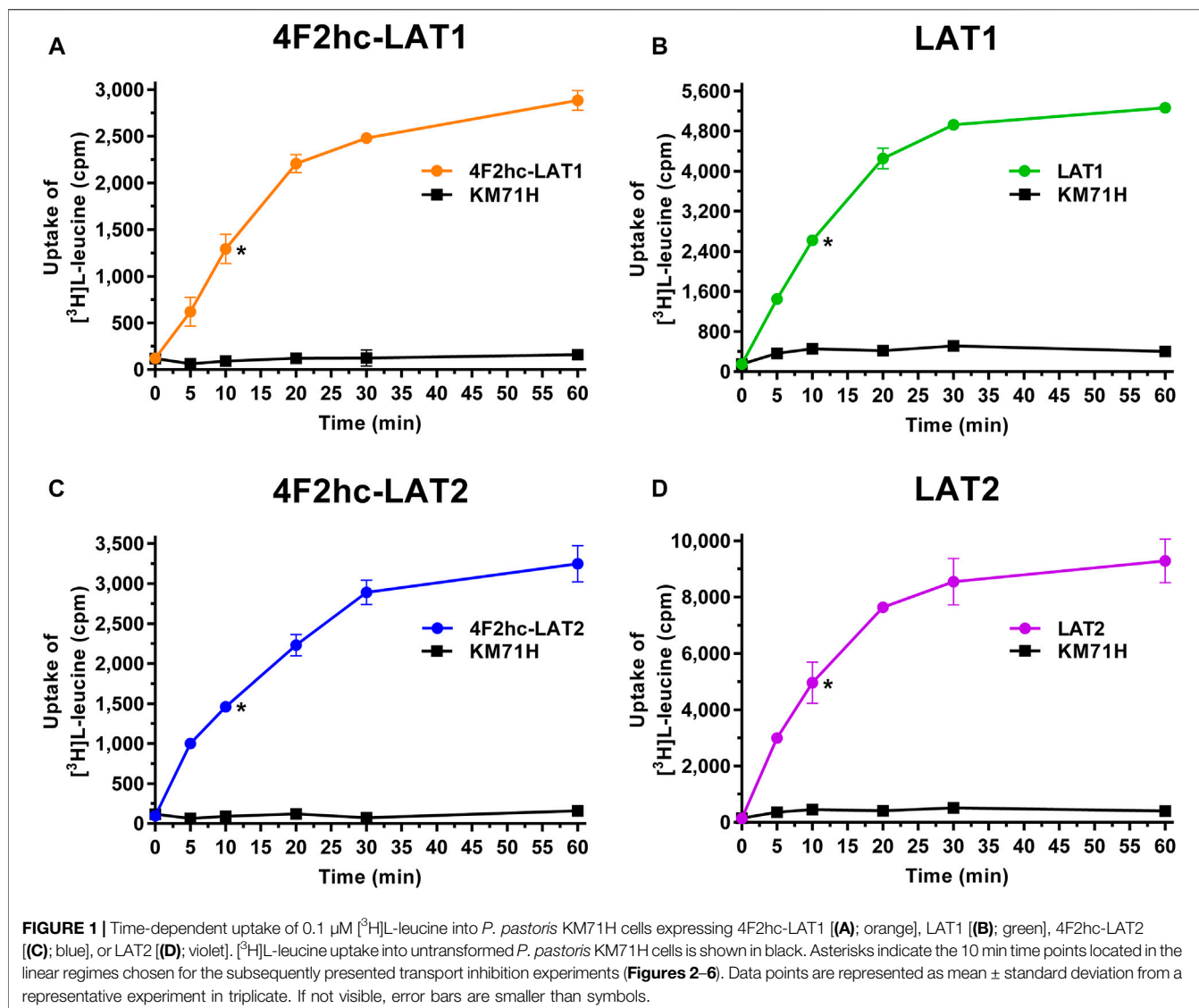
INTRODUCTION

Amino acids have diverse and essential roles in cell function, e.g., for protein synthesis, metabolism, signal transduction, neural transmission, and cellular growth and proliferation. Transport of amino acids across biological membranes is mediated by amino acid transporters, which are embedded in lipid bilayers of cells (Christensen, 1990; McGivan and Pastor-Anglada, 1994). Malfunction, absence or overexpression of amino acid transporters can affect homeostasis in the body leading to human diseases. The solute carrier (SLC) superfamily includes currently eleven families containing amino acid transporters (Kandasamy et al., 2018). The SLC7 family of amino acid transporters consists of fifteen genes and is split into two subgroups: the cationic amino acid transporters (CATs) and the L-type amino acid transporters (LATs) (Verrey et al., 2004; Fotiadis et al., 2013). CATs comprise the *SLC7A1-A4* and *SLC7A14* genes, and LATs the *SLC7A5-A11*, *Slc7a12*, *SLC7A13*, and *Slc7a15* genes (Fotiadis et al., 2013). In contrast to CATs, LATs are not glycosylated. For correct trafficking to the plasma membrane in mammalian cells, LATs associated with type II membrane N-glycoproteins from the SLC3 family, i.e., 4F2hc (SLC3A2; CD98) and rBAT (SLC3A1) (Palacin and Kanai, 2004). These ancillary proteins (the heavy chains) are covalently connected to the corresponding LATs (the light subunits) through a conserved disulfide bridge to form heterodimeric amino acid transporters (HATs) (Chillaron et al., 2001; Wagner et al., 2001; Palacin and Kanai, 2004; Verrey et al., 2004; Fotiadis et al., 2013). The light subunits are the catalytic subunits of HATs (Reig et al., 2002; Rosell et al., 2014; Napolitano et al., 2015).

LAT1 (SLC7A5) and LAT2 (SLC7A8) are isoforms of the system L of amino acid transporters requiring the heavy chain 4F2 (4F2hc) for functional expression at the plasma membrane (Kanai et al., 1998; Pineda et al., 1999; Segawa et al., 1999). Furthermore, we recently showed that 4F2hc can modulate the substrate affinity and specificity of the light chains LAT1 and LAT2 (Kantipudi et al., 2020). In addition to these two LAT specific functions, the ancillary protein 4F2hc has multifunctional roles such as in cell adhesion, cell fusion, integrin signaling and regulation of macrophage activation via galectin-3 (Fenczik et al., 1997; Tsurudome and Ito, 2000; Feral et al., 2005; MacKinnon et al., 2008). 4F2hc-LAT1 is expressed in different tissues and organs (e.g., brain, ovary, placenta and testis), and in relatively high levels at the blood-brain barrier and in several types of tumors (Fotiadis et al., 2013; Scalise et al., 2018; Häfliger and Charles, 2019). The location and high expression levels make 4F2hc-LAT1 an interesting vehicle for drug delivery into the brain and for cancer cell targeting (Häfliger and Charles, 2019; Puris et al., 2020). In cancer cells, 4F2hc-LAT1 provides neutral and essential amino acids for nutrition and regulation of the mTOR signaling pathway (Nicklin et al., 2009). Thus, inhibition of this HAT represents a valid approach to block migration and invasion of cancer cells, and to induce apoptosis. In contrast, 4F2hc-LAT2 is ubiquitously expressed in the human body and highly expressed in polarized epithelia suggesting a major role of this HAT in transepithelial transport of amino acids (Bröer, 2008; Fotiadis et al., 2013). Thus, both transporters have evolved towards specific functions, e.g., LAT1 for uptake of specific amino acids into growing cells, and LAT2 towards normal cell-type and transcellular amino acid transport.

LAT1 and LAT2 are sodium-independent transporters that exchange substrates across membranes with a one-to-one stoichiometry (Verrey et al., 2004; Fotiadis et al., 2013). The substrate specificities of both HATs are comparable, but 4F2hc-LAT2 accepts in addition to large neutral also small neutral amino acids (Pineda et al., 1999; Rossier et al., 1999; Meier et al., 2002). Other substrates of 4F2hc-LAT1 and -LAT2 represent amino acid derivatives such as the thyroid hormones T3 and T4 (Friesema et al., 2001; Zevenbergen et al., 2015). The compound 2-aminobicyclo-(2,2,1)-heptane-2-carboxylic acid (BCH) (Kim et al., 2008) was described as specific inhibitor of system L inhibiting both, 4F2hc-LAT1 and -LAT2 (Kanai et al., 1998; Segawa et al., 1999). On the other hand, the tyrosine-based JPH203 (KYT-0353) molecule was reported as a competitive, potent and highly specific 4F2hc-LAT1 inhibitor with strong inhibitory effects on the growth of different cancer cells (Oda et al., 2010; Yun et al., 2014; Häfliger et al., 2018). Therefore, transport inhibitors with high specificity towards 4F2hc-LAT1 but not -LAT2 represent promising drug candidates for cancer therapy and diagnosis. In crescentic glomerulonephritis pathogenesis, LAT2 was shown to be upregulated activating the mTORC1 pathway (Kurayama et al., 2011). Thus, LAT2-specific inhibitors might also be interesting and considered therapeutically for crescentic glomerulonephritis and other emerging LAT2-related diseases. Towards discovery of potent and selective inhibitors against 4F2hc-LAT1 or -LAT2, robust assays for ligand screening and functional characterization using cells overexpressing corresponding LATs separately are crucial. Establishment of mammalian cell lines for stable expression of 4F2hc-LAT1 and -LAT2 is not straightforward since most host cell lines express HATs endogenously. As a consequence, the activity of the exogenous LAT is difficult to distinguish from the endogenous one and the limited endogenous pool of 4F2hc is used for both, endogenous and exogenous LATs, thus introducing ambiguities in the assays. Khunweeraphong *et al.* reported the establishment of stable HEK293 cell lines expressing exogenous LAT1 or LAT2, and using endogenous 4F2hc of the cells to form HATs (Khunweeraphong et al., 2012). HEK293 cells indicated reduced backgrounds of amino acid transport, e.g., reduced contamination of endogenous LAT1 activity (Khunweeraphong et al., 2012), and other advantages compared to the murine S2 cells previously used in a similar endeavor (Morimoto et al., 2008).

The methylotrophic yeast *Pichia pastoris* represents a well-established system for the expression of recombinant human membrane proteins (Byrne, 2015). Cholesterol and derivatives thereof were shown to play an important role in function and stability of LATs (Meury et al., 2014; Dickens et al., 2017; Cosco et al., 2020). Yeasts such as *P. pastoris* produce ergosterol (Nes et al., 1978) providing a valuable cholesterol derivate for interaction with heterologously expressed membrane proteins. Towards establishment of a robust assay for ligand screening and functional characterization, we have optimized, applied and validated a previously reported radioligand assay using *P. pastoris* overexpressing human 4F2hc-LAT1 or -LAT2, and the substrate [³H]L-leucine as radioligand. In contrast to the previously reported HEK293 cell assay (Khunweeraphong et al., 2012), 4F2hc is co-expressed with LAT1 or LAT2 in the *Pichia*-based assay, thus not limiting 4F2hc availability and boosting expression of HATs (Costa et al., 2013; Rosell et al., 2014; Kantipudi et al., 2020). Interestingly,



and in absence of 4F2hc co-expression, *Pichia* is also able to express functionally the light subunits LAT1 and LAT2 alone (Costa et al., 2013; Rosell et al., 2014; Kantipudi et al., 2020). This allows evaluating possible contributions of the heavy chain 4F2hc on ligand binding and transport inhibition through selected substrates and inhibitors.

MATERIALS AND METHODS

Cloning and Expression in *P. pastoris* of Human 4F2hc-LAT1, LAT1, 4F2hc-LAT2 and LAT2

Cloning of the human HATs and LATs into the pPICZB vector (Thermo Fisher Scientific, Waltham, MA, United States), electrotransformation of competent *P. pastoris* strain KM71H cells (Thermo Fisher Scientific, Waltham, MA, United States) and selection of clones with high protein expression levels was

performed as described in detail previously: see for 4F2hc-LAT1 and LAT1 (Kantipudi et al., 2020), and for 4F2hc-LAT2 and LAT2 (Costa et al., 2013). Cell growth and expression conditions of *Pichia* clones overexpressing human 4F2hc-LAT1, LAT1, 4F2hc-LAT2 or LAT2, and untransformed *P. pastoris* KM71H cells (control) was conducted according to Kantipudi et al. (Kantipudi et al., 2020). Resulting cells were resuspended in transport buffer (150 mM choline chloride, 1 mM MgCl_2 , 1 mM CaCl_2 , 10 mM Tris-HEPES, pH 7.4) containing 50% (v/v) glycerol and the OD_{600} was adjusted to 40. Cells were stored at -18°C until further use.

[^3H]L-Leucine Radioligand Transport Assay

For transport studies, 1 ml of thawed *P. pastoris* cells (OD_{600} 40) expressing the corresponding transporter were diluted in 50 ml transport buffer and pelleted by centrifugation ($3,000 \times g$, 15 min, room temperature). The pellet was then washed by resuspending it in 50 mL transport buffer and by repeating the washing procedure

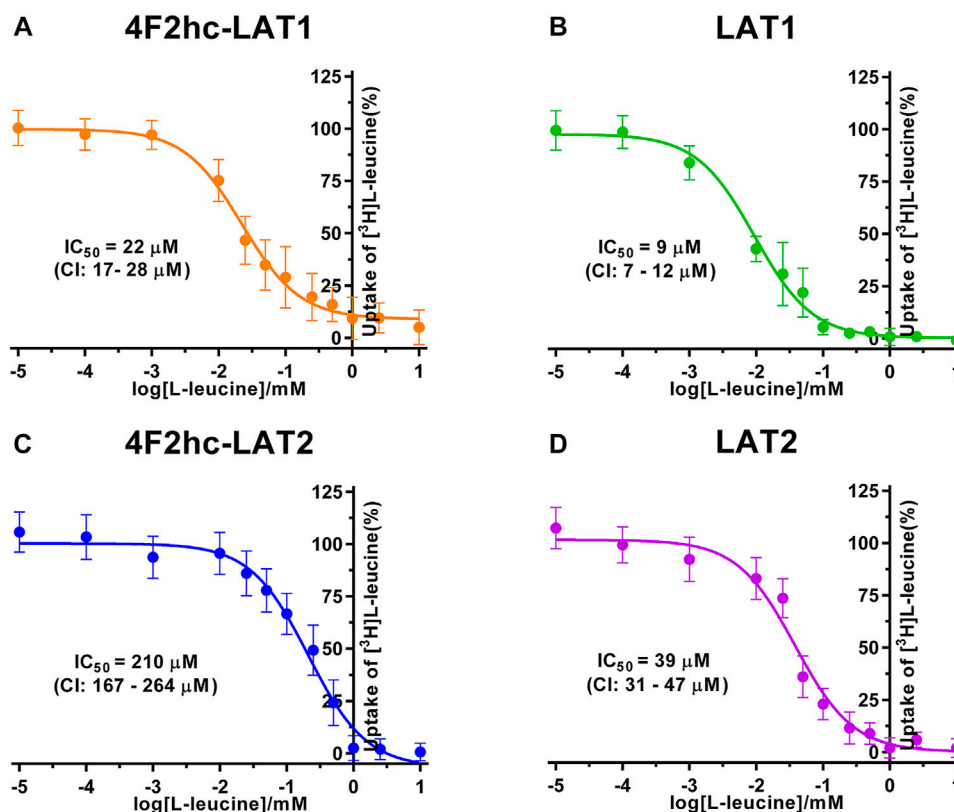
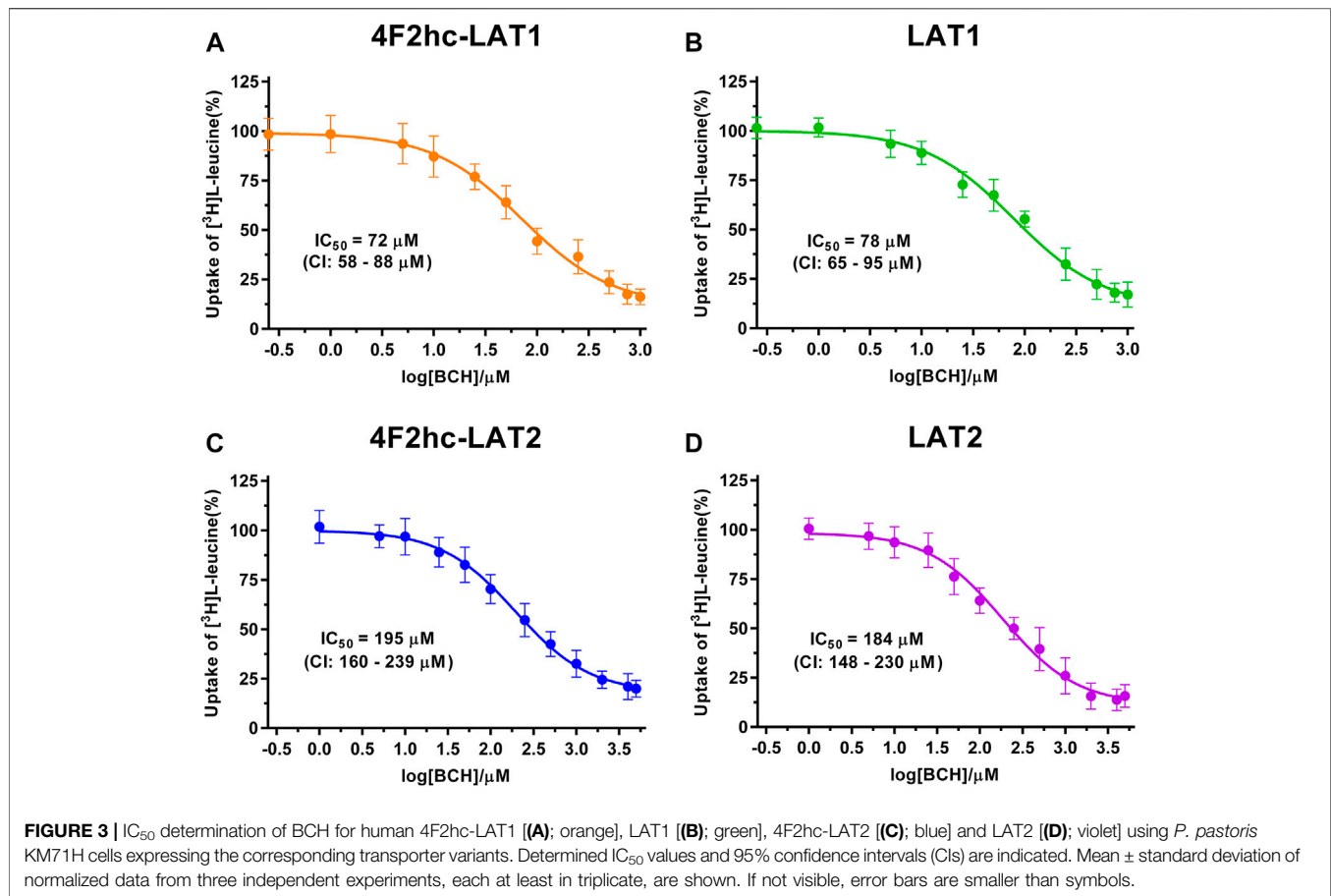


FIGURE 2 | IC_{50} determination of L-leucine for human 4F2hc-LAT1 [(A); orange], LAT1 [(B); green], 4F2hc-LAT2 [(C); blue] and LAT2 [(D); violet] using *P. pastoris* KM71H cells expressing the corresponding transporter variants. Determined IC_{50} values and 95% confidence intervals (CIs) are indicated. Mean \pm standard deviation of normalized data from three independent experiments, each at least in triplicate, are shown. If not visible, error bars are smaller than symbols.

(centrifugation and resuspension) two times. Finally, the cell pellet was resuspended in 2 ml of transport buffer and incubated for 20 min at 30°C under agitation (300 rpm, Multitron, Infors HT, Bottmingen, Switzerland). The yeast suspension density was adjusted with transport buffer to an OD_{600} of 1.875 (4F2hc-LAT1, LAT1, 4F2hc-LAT2 or LAT2, and untransformed *P. pastoris* KM71H cells). All transport experiments were performed in a reaction volume of 100 μ L. For time-dependent [3 H]L-leucine uptake experiments (Figure 1), the reaction mixture contained 40 μ L cell suspension and 60 μ L substrate master mix [0.167 μ M L-leucine spiked with [3 H]L-leucine (American Radiolabeled Chemicals, St. Louis, MO, United States)] with a specific activity of 20 Ci/mmol resulting in a final L-leucine concentration of 0.1 μ M. IC_{50} determinations of selected compounds for the transporters 4F2hc-LAT1, LAT1, 4F2hc-LAT2, or LAT2 were performed using 40 μ L cell suspension, 50 μ L of competitor solution at different concentrations and 10 μ L substrate master mix [1 μ M L-leucine spiked with [3 H]L-leucine (American Radiolabeled Chemicals, St. Louis, MO, United States)] with a specific activity of 20 Ci/mmol resulting in a final L-leucine concentration of 0.1 μ M. For L-leucine and BCH (2-aminobicyclo-(2,2,1)-heptane-2-carboxylic acid) IC_{50} experiments, the competitor solutions were at concentrations of 0.01–10,000 μ M L-leucine (4F2hc-LAT1, LAT1, 4F2hc-LAT2, and LAT2), and 0.25–1,000 μ M BCH (4F2hc-LAT1 and LAT1) and 1–5,000 μ M BCH (4F2hc-LAT2 and

LAT2)—see corresponding graphs in Figures 2, 3 for specific concentrations used. For determining the IC_{50} values of hydrophobic compounds such as JPH203 [(S)-2-amino-3-(4-((5-amino-2-phenylbenzo [d] oxazol-7-yl)-methoxy)-3,5-dichlorophenyl)-propanoic acid] also known as KYT-0353 (MedChemExpress, Monmouth Junction, NJ, United States), and the thyroid hormones T3 (triiodothyronine) and T4 (thyroxine) (Sigma, St. Louis, MO, United States), 40 μ L of cell suspension was incubated with 50 μ L of competitor solutions at different concentrations for 60 min at 25°C under agitation (500 rpm, Thermomixer compact, Eppendorf, Hamburg, Germany). The uptake was initiated by adding 10 μ L substrate master mix [1 μ M L-leucine spiked with [3 H]L-leucine (American Radiolabeled Chemicals, St. Louis, MO, United States)] with a specific activity of 20 Ci/mmol to the preincubated 90 μ L of reaction volume resulting in a final L-leucine concentration of 0.1 μ M. Final ligand concentrations in 100 μ L were 0.001–250 μ M (JPH203, T3, and T4). The competitors were prepared in 100% (v/v) DMSO. The final DMSO concentration was always 0.5% (v/v), independently of which final substrate or inhibitor concentration was used in the assay. Control samples contained the same concentration of DMSO. Final OD_{600} values in uptake experiments were 0.75 for all cells (4F2hc-LAT1, LAT1, 4F2hc-LAT2 or LAT2 expressing cells) and untransformed *P. pastoris* KM71H cells. All transport reactions were done in 2 ml reaction tubes



(Eppendorf, Hamburg, Germany) at 25°C under agitation (1,000 rpm, Thermomixer compact, Eppendorf, Hamburg, Germany). Uptakes were terminated after 10 min (uptake time) for all cells by adding 600 μ L of pre-chilled transport buffer. Cells were rapidly separated from the buffer by transferring the stopped reactions on a 96-well 0.66 mm glass fiber filter plate (Corning FiltrEX, Corning, NY, United States) and vacuum filtration. Each well was washed with 2 ml of ice-cold transport buffer to remove free radioligand. The plate was then dried overnight at 37°C, and the backside was sealed with a BackSeal (PerkinElmer, Waltham, MA, United States). The trapped radioligand was released by addition of 200 μ L scintillation cocktail (MicroScint 40, PerkinElmer, Waltham, MA, United States) to each well, and the plate topside was sealed with Topseal™-A Plus (PerkinElmer, Waltham, MA, United States), followed by incubation for 30 min at 25°C and 1,000 rpm (Thermomixer compact, Eppendorf, Hamburg, Germany). Counts were measured in each well for 2 min with a scintillation counter (TopCount NXT, PerkinElmer, Waltham, MA, United States).

Data Analysis, Curve Fitting and Statistics

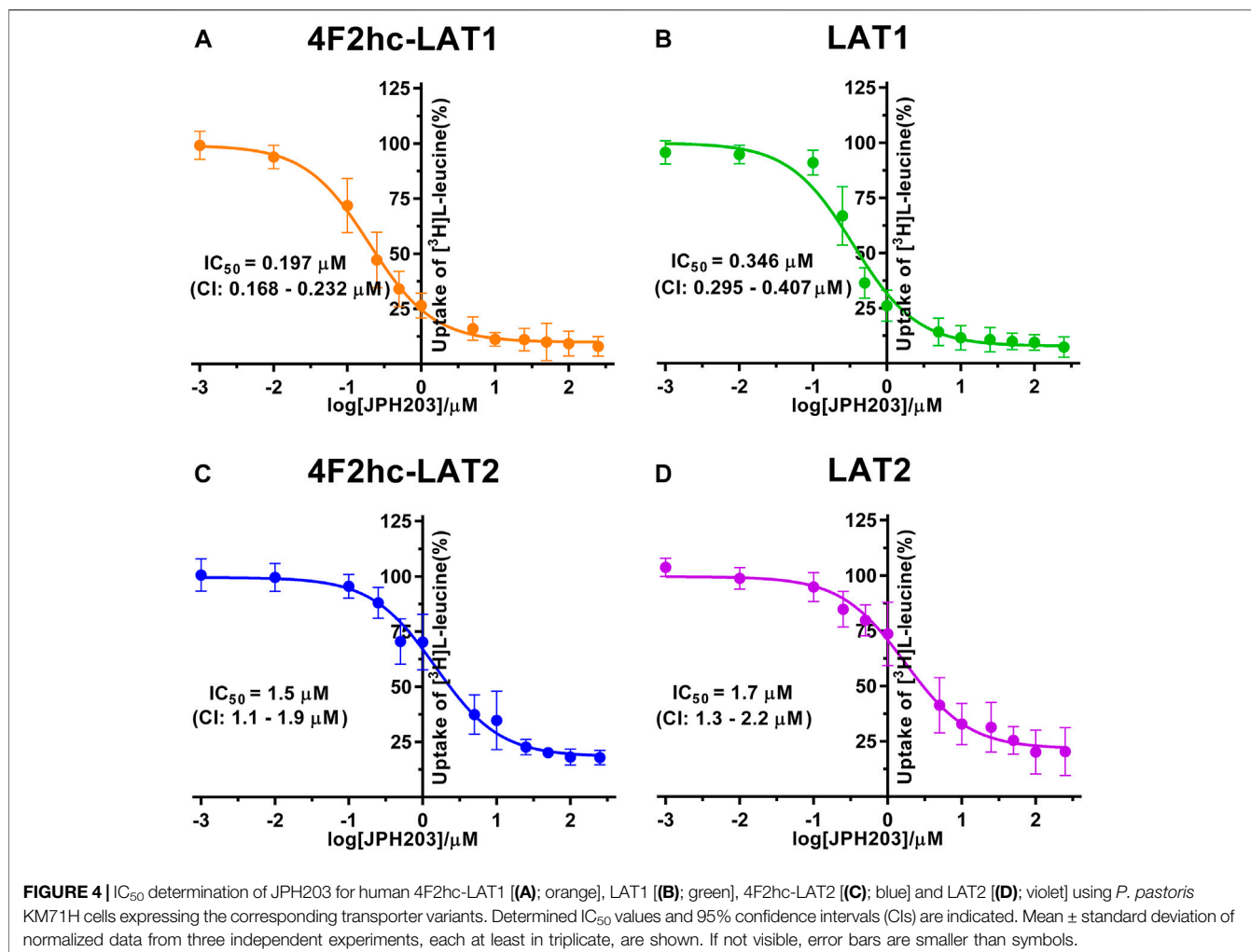
Experiments were performed at least in triplicate. For data analysis, the signal of the untransformed *P. pastoris* cells was subtracted from the transporter signal to obtain the net transport signal. Data from three independent experiments were taken. In each of these experiments, the net transport signals were averaged and the half

maximal inhibitory concentration (IC₅₀) values of homologous (L-leucine) and heterologous (BCH, JPH203, T3, and T4) L-leucine transport competition experiments were determined by fitting a sigmoidal model curve to these data. Every experimental data point was then individually normalized using the corresponding upper plateau values (i.e., the fitted upper plateau value that corresponds to 100%). Single, normalized data points from the three independent experiments were averaged and a sigmoidal model curve was fitted to the data in order to obtain the IC₅₀ values. Prism6 (GraphPad Software) was used for data analysis.

RESULTS

Human 4F2hc-LAT1, LAT1, 4F2hc-LAT2 or LAT2 were expressed in the methylotrophic yeast *P. pastoris*. We showed in previous reports that not only the HATs 4F2hc-LAT1 and -LAT2, but also the light subunits LAT1 and LAT2 in absence of ancillary protein are properly folded, correctly trafficked to the plasma membrane and functional in *P. pastoris* (Rosell et al., 2014; Kantipudi et al., 2020).

Transport activities were determined by measuring the uptake of the substrate [³H]L-leucine into *Pichia* cells at OD₆₀₀ 0.75 expressing the corresponding HAT or LAT. Time-course experiments showed clear HAT- and LAT-dependent transport activities, which were much higher than the [³H]L-leucine uptake into untransformed



host cells (Figure 1). In all cases, saturation of the transport process was observed. Differences in radioligand transport (Figure 1) are due to different expression levels of corresponding recombinant LATs as estimated from V_{max}/OD values using previously determined kinetic parameters (Kantipudi et al., 2020). Uptake assay times of 10 min (i.e., in the linear regimes—time points indicated by asterisks in Figure 1) and corresponding *Pichia* cells at OD₆₀₀ 0.75 were taken for the subsequently presented experiments with 4F2hc-LAT1, LAT1, 4F2hc-LAT2, and LAT2 (Figures 2–6).

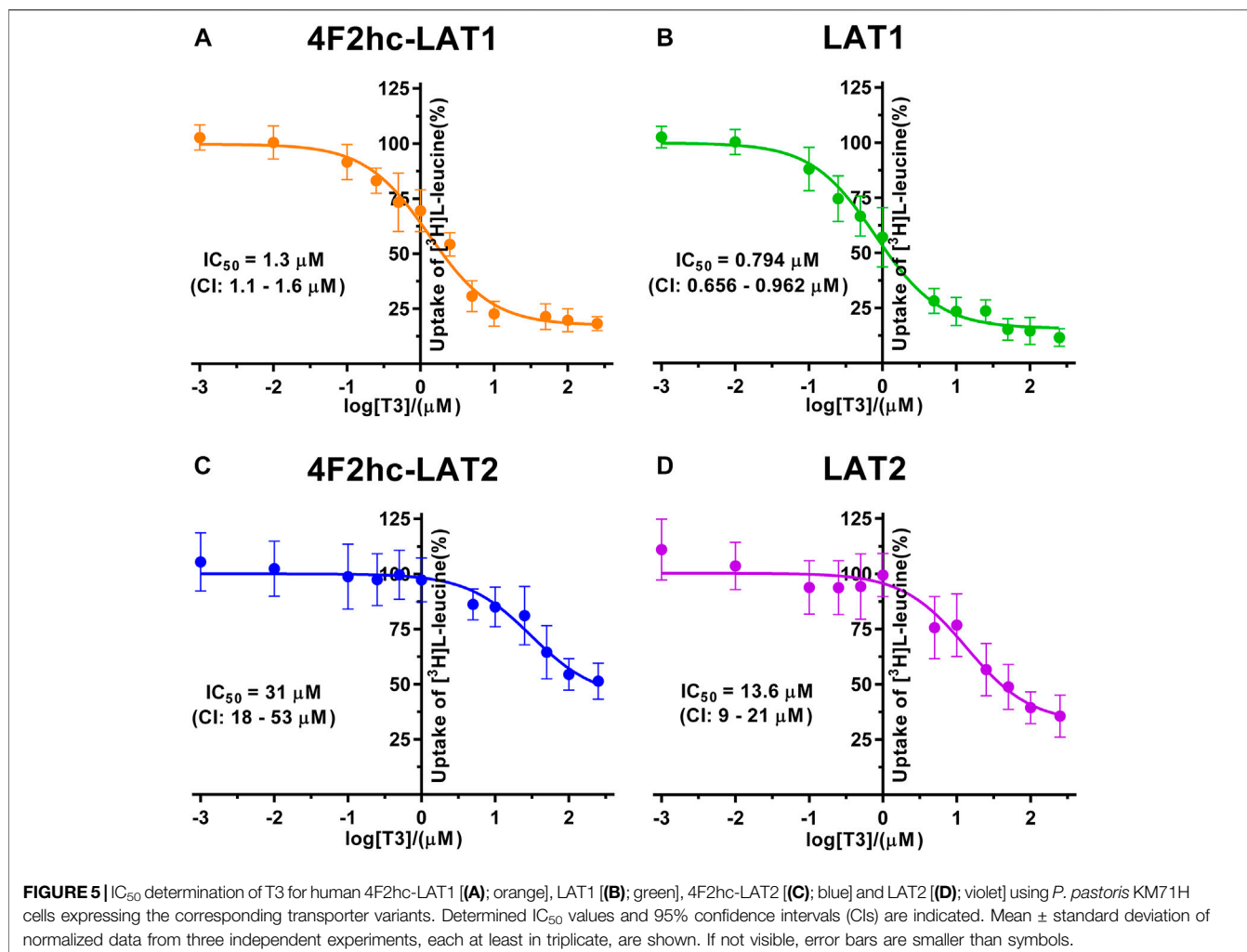
We determined the half-maximal inhibitory concentrations (IC₅₀s) of L-leucine by homologous competition for all four transporter variants. Obtained IC₅₀ values were 22 μM (4F2hc-LAT1), 9 μM (LAT1), 210 μM (4F2hc-LAT2), and 39 μM (LAT2) (Figure 2).

As previously reported (Kantipudi et al., 2020), comparison of IC₅₀s indicated a modulatory effect of the heavy subunit 4F2 on light subunits, which is most striking between 4F2hc-LAT2 and LAT2 (Figure 2). After validation of the yeast-cell based transport assay with the substrate L-leucine (Figures 1, 2), we pursued validation using the described system L transport inhibitor BCH (Kim et al., 2008) and the 4F2hc-LAT1 specific inhibitor JPH203 (Oda et al., 2010). We obtained IC₅₀ values of 72 μM (4F2hc-

LAT1), 78 μM (LAT1), 195 μM (4F2hc-LAT2), and 184 μM (LAT2) for BCH (Figure 3). These results indicated that the compound BCH inhibits both human HATs being about 2.7-fold more specific for 4F2hc-LAT1. Interestingly, and in contrast to L-leucine (Figure 2), LAT1 and LAT2 in absence of 4F2hc had comparable IC₅₀s as their heterodimeric forms (Figure 3) indicating no significant influence of the ancillary protein on BCH binding to LATs of HATs.

For the second inhibitor, i.e., JPH203, IC₅₀ values of 0.197 μM (4F2hc-LAT1), 0.346 μM (LAT1), 1.5 μM (4F2hc-LAT2) and 1.7 μM (LAT2) were obtained using our yeast cell-based assay (Figure 4). Clearly, the compound JPH203 is with its three-digit nanomolar IC₅₀ value potent and about 7.6-fold more specific for 4F2hc-LAT1 compared with 4F2hc-LAT2. As observed also with BCH, IC₅₀ values of JPH203 were comparable for 4F2hc-LAT1 and LAT1, and 4F2hc-LAT2 and LAT2, indicating no significant effect of the ancillary protein on inhibitor binding.

The thyroid hormones triiodothyronine (T3) and thyroxine (T4) represent substrates of 4F2hc-LAT1 and -LAT2 (Friesema et al., 2001; Zevenbergen et al., 2015). We selected these amino acid derivatives as substrates for further validation of our *P.*

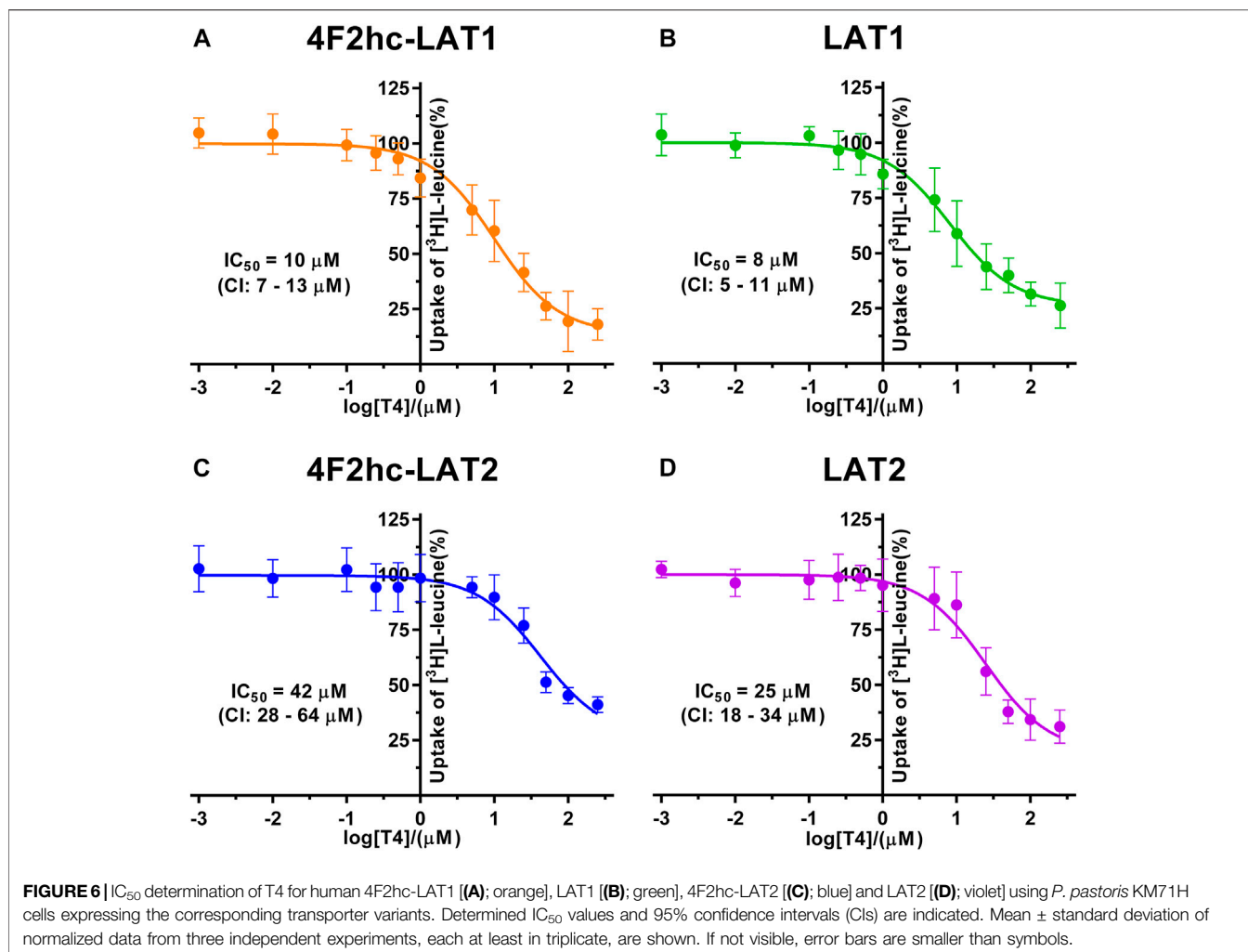


pastoris cell-based transport assay. For triiodothyronine, we obtained IC₅₀ values of 1.3 μM (4F2hc-LAT1), 0.794 μM (LAT1), 31 μM (4F2hc-LAT2), and 13.6 μM (LAT2) (Figure 5). The inhibitory effect of T3 was considerably more pronounced for 4F2hc-LAT1 and LAT1 compared with 4F2hc-LAT2 and LAT2, e.g., about 24-fold lower IC₅₀ value for 4F2hc-LAT1 in comparison with 4F2hc-LAT2.

Finally, we determined the IC₅₀s of the thyroid hormone thyroxine using our yeast cell-based transport assay and obtained IC₅₀ values of 10 μM (4F2hc-LAT1), 8 μM (LAT1), 42 μM (4F2hc-LAT2), and 25 μM (LAT2) (Figure 6). Similar to triiodothyronine, the thyroxine hormone also competed with [³H]L-leucine uptake through 4F2hc-LAT1, LAT1, 4F2hc-LAT2, and LAT2. The transport inhibitory effect and thus specificity of T4 was about four-times higher for 4F2hc-LAT1 compared with 4F2hc-LAT2. A comparable trend was observed for the light subunits LAT1 and LAT2. The presence of the heavy chain 4F2 had no marked or only a weak effect on the IC₅₀ values of 4F2hc-LAT1 (10 μM) and 4F2hc-LAT2 (42 μM) compared to the light subunits LAT1 (8 μM) and LAT1 (25 μM) alone.

DISCUSSION

A cell-based transport assay using the methylotrophic yeast *P. pastoris* overexpressing the human HATs 4F2hc-LAT1 or -LAT2, and LATs LAT1 or LAT2, and the radiolabeled substrate [³H]L-leucine was optimized and validated using selected substrates and inhibitors. In contrast to our previous study (Kantipudi et al., 2020), we adjusted uptake time and OD₆₀₀ for the four stably expressing *Pichia* clones to same conditions, i.e., to 10 min and OD₆₀₀ 0.75 (Figure 1). For comparison and validation of the adjusted uptake conditions, IC₅₀s were determined for the substrate L-leucine (Figure 2)—the here studied transporters have high affinities for L-leucine relative to the other proteinogenic amino acids (Kantipudi et al., 2020). The obtained IC₅₀s for L-leucine (Figure 2) were comparable to previously published values using oocytes (Kanai et al., 1998; Friesema et al., 2001; Yanagida et al., 2001), and *P. pastoris* cells at OD₆₀₀ 10 (4F2hc-LAT1, 4F2hc-LAT2, and LAT1) and OD₆₀₀ 3 (LAT2), and uptake times of 10 min (4F2hc-LAT1, 4F2hc-LAT2, and LAT1) and 2 min (LAT2) (Kantipudi et al., 2020). The modulatory effect of the heavy chain 4F2 on the L-leucine affinity of light subunits, this being most pronounced for 4F2hc-LAT2 and LAT2 (Figures 2C,D), was also



observed in line with our previous report (Kantipudi et al., 2020). Newly, we tested with the *P. pastoris* cell-based assay, described transport inhibitors, i.e., the system L and 4F2hc-LAT1 uptake inhibitors BCH (Kim et al., 2008) and JPH203 (Oda et al., 2010), respectively. The IC₅₀s of BCH for the two HATs were comparable with values from the literature (Table 1) and almost identical to the IC₅₀s from corresponding LATs in absence of 4F2hc (Figure 3). The latter indicated no contribution of the ancillary protein on BCH binding to light subunits. JPH203 was described as a competitive, potent and highly specific 4F2hc-LAT1 inhibitor (Endou et al., 2008; Oda et al., 2010). The authors of these two studies determined IC₅₀s of 0.14 μM (Oda et al., 2010), and 0.19 and 0.2 μM (Endou et al., 2008) for human LAT1 HATs expressed in S2 cells derived from mouse renal proximal tubules (Morimoto et al., 2008) (Table 1). The IC₅₀ of 0.197 μM for 4F2hc-LAT1 obtained with the here presented assay (Figure 4A) is similar to the values (0.14, 0.19, and 0.2 μM) determined for the same HAT using S2 cells (Table 1). Furthermore, most kinetic parameters for JPH203 and 4F2hc-LAT1 determined using other cell types than S2 cells were also in good agreement with the IC₅₀ value from *P. pastoris* cells (Table 1). However, a marked difference is found between the IC₅₀ of JPH203 determined for human 4F2hc-LAT2 using the *P. pastoris* (1.5 μM;

Figure 4C) and the S2 cell-based assays (>10 μM (Oda et al., 2010) and almost no inhibition at 10 μM (Endou et al., 2008)). Furthermore, Oda et al. indicated an IC₅₀(S2-LAT2)/IC₅₀(S2-LAT1) ratio of >500, which would be indicative of a high specificity of JPH203 towards human 4F2hc-LAT1 and not 4F2hc-LAT2 (Oda et al., 2010). In strong contrast, the IC₅₀(*Pichia*-4F2hc-LAT2)/IC₅₀(*Pichia*-4F2hc-LAT1) ratio was only about 7.6, indicating a significantly more moderate specificity of JPH203 towards 4F2hc-LAT1. This finding was further corroborated independently using *Pichia* cells expressing the light subunits alone, which yielded a comparable IC₅₀(*Pichia*-LAT2)/IC₅₀(*Pichia*-LAT1) ratio of about 4.9. Future studies on the specificity of JPH203 towards 4F2hc-LAT1 and -LAT2 will clarify this ambiguity. For further validation of our yeast cell-based transport assay, we tested amino acid derivatives, specifically the thyroid hormones T3 and T4, which are substrates of 4F2hc-LAT1 and -LAT2 (Friesema et al., 2001; Zevenbergen et al., 2015). For 4F2hc-LAT1, T3 reflected a higher potency in transport inhibition than T4 (Figures 5A, 6A) in line with previous studies (Table 1). No kinetic parameters were found in the literature for T3 and T4 with 4F2hc-LAT2 for comparison. Thus, our IC₅₀ for T3 and T4 represent first 4F2hc-LAT2 and LAT2 specific kinetic values (Figures 5C,D, 6C,D). Based on the obtained IC₅₀s, the ancillary protein 4F2hc did

TABLE 1 | Comparison of obtained with published 4F2hc-LAT1 and -LAT2 kinetic parameters.

Compound	4F2hc-LAT1 IC ₅₀ , K _M or K _i (μM) of L-leucine uptake			References
	This work (IC ₅₀)	Kinetic parameters	Host	
L-leucine	22	38 (IC ₅₀)	<i>Pichia pastoris</i>	Kantipudi et al. (2020)
		25 ± 3 (K _M)	Oocytes	
BCH	72	46 (K _M)	Saos2	Friesema et al. (2001)
		18.1 ± 3.4 (K _M)		Kanai et al. (1998)
		19.7 ± 4.1 (K _M)		Yanagida et al. (2001)
		72.17 ± 0.92 (IC ₅₀)		Choi et al. (2017)
		78.8 ± 3.5 (IC ₅₀)	Kim et al. (2008)	Kim et al. (2008)
		75.3 ± 6.7 (IC ₅₀)	KB cells	
		73.1 ± 4.5 (IC ₅₀)	C6 cells	
		92.6 ± 8.9 (IC ₅₀)	YD-38	
JPH203	0.197	78.3 ± 12.1 (IC ₅₀)	HEK293	Yun et al. (2014)
		132 ± 27.8 (IC ₅₀)	S2 cells	Khunweeraphong et al. (2012)
		1.31 ± 0.27 (IC ₅₀)	Saos2	Morimoto et al. (2008)
		0.14 (IC ₅₀)	S2 cells	Choi et al. (2017)
		0.19 and 0.20 (IC ₅₀)	S2 cells	Oda et al. (2010)
		0.79 ± 0.06 (IC ₅₀)	YD-38	Endou et al. (2008)
		0.134 (IC ₅₀)	HT-29	Yun et al. (2014)
		0.177 (IC ₅₀)	SW1736	Häfliger et al. (2018)
		0.120 (IC ₅₀)	8505c	
		0.20 ± 0.03 (IC ₅₀)	KKU-055	Yothaisong et al. (2017)
T3	1.3	0.12 ± 0.02 (IC ₅₀)	KKU-213	
		0.25 ± 0.04 (IC ₅₀)	KKU-100	
		0.8 (K _M)	Oocytes	Friesema et al. (2001)
T4	10	1.8 (K _M)	S2 cells	Ritchie et al. (1999)
		1.7 ± 0.1 (K _i)		Morimoto et al. (2008)
		7.9 (K _M)	Oocytes	Friesema et al. (2001)
JPH203	1.5	6.3 (K _M)	S2 cells	Ritchie et al. (1999)
		>10 (IC ₅₀)		
		115 ± 2.0 (K _i)		

Compound	4F2hc-LAT2 IC ₅₀ , K _M or K _i (μM) of L-leucine uptake			References
	This work (IC ₅₀)	Kinetic parameters	Host	
L-leucine	210	221 (IC ₅₀)	<i>Pichia pastoris</i>	Kantipudi et al. (2020)
BCH	195	249 ± 22 (K _M)	Oocytes	Pineda et al. (1999)
		220 (K _M)	S2 cells	Morimoto et al. (2008)
JPH203	1.5	315 ± 68.6 (IC ₅₀)	S2 cells	Oda et al. (2010)
		>10 (IC ₅₀)		

not have an important influence on the binding of the two hormones to the light subunits (Figures 5, 6).

CONCLUSION

We have provided a robust yeast cell-based transport assay for the functional characterization of human 4F2hc-LAT1 and -LAT2, and LAT1 and LAT2 substrates and inhibitors. *P. pastoris* cells expressing HATs are valuable for determining kinetic parameters of ligands, e.g., potency and selectivity of transport inhibitors towards 4F2hc-LAT1 and -LAT2. Such kinetic information will help evaluating the structure-activity relationship of new ligands. Moreover, assays performed with yeast cells expressing light subunits provide kinetic parameters that, when compared with those of corresponding HATs, are of interest towards identification of possible effects of the ancillary protein 4F2hc on ligand affinity and specificity. First kinetic parameters on T3 and T4 were successfully provided for human 4F2hc-LAT2 and LAT2 using the here presented yeast cell-based transport assay. Finally, the established approach and assay could also be used for compound screening and applied to other HATs and LATs of interest.

DATA AVAILABILITY STATEMENT

The raw data supporting the conclusions of this article will be made available by the authors, without undue reservation.

AUTHOR CONTRIBUTIONS

DF conceived and designed the study. SK performed the experiments, collected and analyzed the data. SK and DF wrote the manuscript. DF obtained the funding. SK and DF read, and approved the submitted version.

FUNDING

This research was funded by the University of Bern, the Swiss National Science Foundation and the Swiss National Centre of Competence in Research (NCCR) TransCure.

ACKNOWLEDGMENTS

We thank Sara Bonetti and Jean-Marc Jeckelmann for valuable feedback on the manuscript.

REFERENCES

- Brøer, S. (2008). Amino Acid Transport across Mammalian Intestinal and Renal Epithelia. *Physiol. Rev.* 88 (1), 249–286. doi:10.1152/physrev.00018.2006
- Byrne, B. (2015). *Pichia pastoris* as an Expression Host for Membrane Protein Structural Biology. *Curr. Opin. Struct. Biol.* 32, 9–17. doi:10.1016/j.sbi.2015.01.005
- Chillarón, J., Roca, R., Valencia, A., Zorzano, A., and Palacín, M. (2001). Heteromeric Amino Acid Transporters: Biochemistry, Genetics, and Physiology. *Am. J. Physiology-Renal Physiol.* 281, F995–F1018. doi:10.1152/ajprenal.2001.281.6.f995
- Choi, D. W., Kim, D. K., Kanai, Y., Wempe, M. F., Endou, H., and Kim, J.-K. (2017). JPH203, a Selective L-type Amino Acid Transporter 1 Inhibitor, Induces Mitochondria-dependent Apoptosis in Saos2 Human Osteosarcoma Cells. *Korean J. Physiol. Pharmacol.* 21 (6), 599–607. doi:10.4196/kjpp.2017.21.6.599
- Christensen, H. N. (1990). Role of Amino Acid Transport and Countertransport in Nutrition and Metabolism. *Physiol. Rev.* 70 (1), 43–77. doi:10.1152/physrev.1990.70.1.43
- Cosco, J., Scalise, M., Colas, C., Galluccio, M., Martini, R., Rovella, F., et al. (2020). ATP Modulates SLC7A5 (LAT1) Synergistically with Cholesterol. *Sci. Rep.* 10 (1), 16738. doi:10.1038/s41598-020-73757-y
- Costa, M., Rosell, A., Álvarez-Marimón, E., Zorzano, A., Fotiadis, D., and Palacín, M. (2013). Expression of Human Heteromeric Amino Acid Transporters in the Yeast *Pichia pastoris*. *Protein Expr. Purif.* 87 (1), 35–40. doi:10.1016/j.pep.2012.10.003
- Dickens, D., Chiduzu, G. N., Wright, G. S. A., Pirmohamed, M., Antonyuk, S. V., and Hasnain, S. S. (2017). Modulation of LAT1 (SLC7A5) Transporter Activity and Stability by Membrane Cholesterol. *Sci. Rep.* 7, 43580. doi:10.1038/srep43580
- Endou, H., Kanai, Y., Saito, K., and Oda, K. (2008). *Aromatic Amino Acid Derivative with LAT1 Inhibitory Activity, LAT1 Inhibitor Containing the Same and Method for Producing the Same*. Patent Publication No. WO2008081537 International Application No. PCT/JJP2006/326233.
- Fenczik, C. A., Sethi, T., Ramos, J. W., Hughes, P. E., and Ginsberg, M. H. (1997). Complementation of Dominant Suppression Implicates CD98 in Integrin Activation. *Nature* 390 (6655), 81–85. doi:10.1038/36349
- Feral, C. C., Nishiya, N., Fenczik, C. A., Stuhlmann, H., Slepak, M., and Ginsberg, M. H. (2005). CD98hc (SLC3A2) Mediates Integrin Signaling. *Proc. Natl. Acad. Sci.* 102 (2), 355–360. doi:10.1073/pnas.0404852102
- Fotiadis, D., Kanai, Y., and Palacín, M. (2013). The SLC3 and SLC7 Families of Amino Acid Transporters. *Mol. Aspects Med.* 34 (2–3), 139–158. doi:10.1016/j.mam.2012.10.007
- Friesema, E. C. H., Docter, R., Moerings, E. P. C. M., Verrey, F., Krenning, E. P., Hennemann, G., et al. (2001). Thyroid Hormone Transport by the Heterodimeric Human System L Amino Acid Transporter. *Endocrinology* 142 (10), 4339–4348. doi:10.1210/endo.142.10.8418
- Häfliger, P., and Charles, R.-P. (2019). The L-type Amino Acid Transporter LAT1—An Emerging Target in Cancer. *Ijms* 20 (10), 2428. doi:10.3390/ijms20102428
- Häfliger, P., Graff, J., Rubin, M., Stooss, A., Dettmer, M. S., Altmann, K.-H., et al. (2018). The LAT1 Inhibitor JPH203 Reduces Growth of Thyroid Carcinoma in a Fully Immunocompetent Mouse Model. *J. Exp. Clin. Cancer Res.* 37 (1), 234. doi:10.1186/s13046-018-0907-z
- Kanai, Y., Segawa, H., Miyamoto, K.-i., Uchino, H., Takeda, E., and Endou, H. (1998). Expression Cloning and Characterization of a Transporter for Large Neutral Amino Acids Activated by the Heavy Chain of 4F2 Antigen (CD98). *J. Biol. Chem.* 273 (37), 23629–23632. doi:10.1074/jbc.273.37.23629
- Kandasamy, P., Gyimesi, G., Kanai, Y., and Hediger, M. A. (2018). Amino Acid Transporters Revisited: New Views in Health and Disease. *Trends Biochem. Sci.* 43 (10), 752–789. doi:10.1016/j.tibs.2018.05.003
- Kantipudi, S., Jeckelmann, J.-M., Ucurum, Z., Bosshart, P. D., and Fotiadis, D. (2020). The Heavy Chain 4F2hc Modulates the Substrate Affinity and Specificity of the Light Chains LAT1 and LAT2. *Ijms* 21 (20), 7573. doi:10.3390/ijms21207573
- Khunweeraphong, N., Nagamori, S., Wiriyasermkul, P., Nishinaka, Y., Wongthai, P., Ohgaki, R., et al. (2012). Establishment of Stable Cell Lines with High Expression of Heterodimers of Human 4F2hc and Human Amino Acid Transporter LAT1 or LAT2 and Delineation of Their Differential Interaction with alpha-Alkyl Moieties. *J. Pharmacol. Sci.* 119 (4), 368–380. doi:10.1254/jphs.12124fp
- Kim, C. S., Cho, S.-H., Chun, H. S., Lee, S.-Y., Endou, H., Kanai, Y., et al. (2008). BCH, an Inhibitor of System L Amino Acid Transporters, Induces Apoptosis in Cancer Cells. *Biol. Pharm. Bull.* 31 (6), 1096–1100. doi:10.1248/bpb.31.1096
- Kurayama, R., Ito, N., Nishibori, Y., Fukuhara, D., Akimoto, Y., Higashihara, E., et al. (2011). Role of Amino Acid Transporter LAT2 in the Activation of mTORC1 Pathway and the Pathogenesis of Crescentic Glomerulonephritis. *Lab. Invest.* 91 (7), 992–1006. doi:10.1038/labinvest.2011.43
- MacKinnon, A. C., Farnworth, S. L., Hodkinson, P. S., Henderson, N. C., Atkinson, K. M., Leffler, H., et al. (2008). Regulation of Alternative Macrophage Activation by Galectin-3. *J. Immunol.* 180 (4), 2650–2658. doi:10.4049/jimmunol.180.4.2650
- McGivan, J. D., and Pastor-Anglada, M. (1994). Regulatory and Molecular Aspects of Mammalian Amino Acid Transport. *Biochem. J.* 299 (Pt 2), 321–334. doi:10.1042/bj2990321
- Meier, C., Ristic, Z., Klausner, S., and Verrey, F. (2002). Activation of System L Heterodimeric Amino Acid Exchangers by Intracellular Substrates. *EMBO J.* 21 (4), 580–589. doi:10.1093/emboj/21.4.580
- Meury, M., Costa, M., Harder, D., Stauffer, M., Jeckelmann, J.-M., Brühlmann, B., et al. (2014). Detergent-induced Stabilization and Improved 3D Map of the Human Heteromeric Amino Acid Transporter 4F2hc-LAT2. *PLoS ONE* 9, e109882. doi:10.1371/journal.pone.0109882
- Morimoto, E., Kanai, Y., Kim, D. K., Chairoungdua, A., Choi, H. W., Wempe, M. F., et al. (2008). Establishment and Characterization of Mammalian Cell Lines Stably Expressing Human L-type Amino Acid Transporters. *J. Pharmacol. Sci.* 108 (4), 505–516. doi:10.1254/jphs.08232fp
- Napolitano, L., Scalise, M., Galluccio, M., Pochini, L., Albanese, L. M., and Indiveri, C. (2015). LAT1 Is the Transport Competent Unit of the LAT1/CD98 Heterodimeric Amino Acid Transporter. *Int. J. Biochem. Cell Biol.* 67, 25–33. doi:10.1016/j.biocel.2015.08.004
- Nes, W. R., Sekula, B. C., Nes, W. D., and Adler, J. H. (1978). The Functional Importance of Structural Features of Ergosterol in Yeast. *J. Biol. Chem.* 253 (17), 6218–6225. doi:10.1016/s0021-9258(17)34602-1
- Nicklin, P., Bergman, P., Zhang, B., Triantafellow, E., Wang, H., Nyfeler, B., et al. (2009). Bidirectional Transport of Amino Acids Regulates mTOR and Autophagy. *Cell* 136 (3), 521–534. doi:10.1016/j.cell.2008.11.044
- Oda, K., Hosoda, N., Endo, H., Saito, K., Tsujihara, K., Yamamura, M., et al. (2010). L-type Amino Acid Transporter 1 Inhibitors Inhibit Tumor Cell Growth. *Cancer Sci.* 101 (2), 173–179. doi:10.1111/j.1349-7006.2009.01386.x
- Palacín, M., and Kanai, Y. (2004). The Ancillary Proteins of HATs: SLC3 Family of Amino Acid Transporters. *Pflugers Arch.* 447 (5), 490–494. doi:10.1007/s00424-003-1062-7
- Pineda, M., Fernández, E., Torrents, D., Estévez, R., López, C., Camps, M., et al. (1999). Identification of a Membrane Protein, LAT-2, that Co-expresses with 4F2 Heavy Chain, an L-type Amino Acid Transport Activity with Broad Specificity for Small and Large Zwitterionic Amino Acids. *J. Biol. Chem.* 274 (28), 19738–19744. doi:10.1074/jbc.274.28.19738
- Puris, E., Gynther, M., Auriola, S., and Huttunen, K. M. (2020). L-Type Amino Acid Transporter 1 as a Target for Drug Delivery. *Pharm. Res.* 37 (5), 88. doi:10.1007/s11095-020-02826-8
- Reig, N., Chillaron, J., Bartoccioni, P., Fernandez, E., Bendahan, A., Zorzano, A., et al. (2002). The Light Subunit of System Bo+ Is Fully Functional in the Absence of the Heavy Subunit. *EMBO J.* 21, 4906–4914. doi:10.1093/emboj/cdf500
- Ritchie, J., Peter, G., Shi, Y., and Taylor, P. (1999). Thyroid Hormone Transport by 4F2hc-IU12 Heterodimers Expressed in *Xenopus* Oocytes. *J. Endocrinol.* 163 (2), R5–R9. doi:10.1677/joe.0.163r005
- Rosell, A., Meury, M., Alvarez-Marimón, E., Costa, M., Perez-Cano, L., Zorzano, A., et al. (2014). Structural Bases for the Interaction and Stabilization of the Human Amino Acid Transporter LAT2 with its Ancillary Protein 4F2hc. *Proc. Natl. Acad. Sci.* 111 (8), 2966–2971. doi:10.1073/pnas.1323779111
- Rossier, G., Meier, C., Bauch, C., Summa, V., Sordat, B., Verrey, F., et al. (1999). LAT2, a New Basolateral 4F2hc/CD98-Associated Amino Acid Transporter of Kidney and Intestine. *J. Biol. Chem.* 274 (49), 34948–34954. doi:10.1074/jbc.274.49.34948
- Scalise, M., Galluccio, M., Console, L., Pochini, L., and Indiveri, C. (2018). The Human SLC7A5 (LAT1): The Intriguing Histidine/large Neutral Amino Acid

- Transporter and its Relevance to Human Health. *Front. Chem.* 6, 243. doi:10.3389/fchem.2018.00243
- Segawa, H., Fukasawa, Y., Miyamoto, K.-i., Takeda, E., Endou, H., and Kanai, Y. (1999). Identification and Functional Characterization of a Na⁺-independent Neutral Amino Acid Transporter with Broad Substrate Selectivity. *J. Biol. Chem.* 274 (28), 19745–19751. doi:10.1074/jbc.274.28.19745
- Tsurudome, M., and Ito, Y. (2000). Function of Fusion Regulatory Proteins (FRPs) in Immune Cells and Virus-Infected Cells. *Crit. Rev. Immunol.* 20 (3), 30–196. doi:10.1615/CritRevImmunol.v20.i3.10
- Verrey, F., Closs, E. I., Wagner, C. A., Palacin, M., Endou, H., and Kanai, Y. (2004). CATs and HATs: the SLC7 Family of Amino Acid Transporters. *Pflügers Archiv Eur. J. Physiol.* 447 (5), 532–542. doi:10.1007/s00424-003-1086-z
- Wagner, C. A., Lang, F., and Bröer, S. (2001). Function and Structure of Heterodimeric Amino Acid Transporters. *Am. J. Physiology-Cell Physiol.* 281 (4), C1077–C1093. doi:10.1152/ajpcell.2001.281.4.C1077
- Yanagida, O., Kanai, Y., Chairoungdua, A., Kim, D. K., Segawa, H., Nii, T., et al. (2001). Human L-type Amino Acid Transporter 1 (LAT1): Characterization of Function and Expression in Tumor Cell Lines. *Biochim. Biophys. Acta (Bba) - Biomembranes* 1514, 291–302. doi:10.1016/s0005-2736(01)00384-4
- Yothaisong, S., Dokduang, H., Anzai, N., Hayashi, K., Namwat, N., Yongvanit, P., et al. (2017). Inhibition of L-type Amino Acid Transporter 1 Activity as a New Therapeutic Target for Cholangiocarcinoma Treatment. *Tumour Biol.* 39 (3), 101042831769454. doi:10.1177/1010428317694545
- Yun, D.-W., Lee, S. A., Park, M.-G., Kim, J.-S., Yu, S.-K., Park, M.-R., et al. (2014). JPH203, an L-type Amino Acid Transporter 1-selective Compound, Induces Apoptosis of YD-38 Human Oral Cancer Cells. *J. Pharmacol. Sci.* 124 (2), 208–217. doi:10.1254/jphs.13154fp
- Zevenbergen, C., Meima, M. E., Lima De Souza, E. C., Peeters, R. P., Kinne, A., Krause, G., et al. (2015). Transport of Iodothyronines by Human L-type Amino Acid Transporters. *Endocrinology* 156 (11), 4345–4355. doi:10.1210/en.2015-1140

Conflict of Interest: The authors declare that the research was conducted in the absence of any commercial or financial relationships that could be construed as a potential conflict of interest.

Copyright © 2021 Kantipudi and Fotiadis. This is an open-access article distributed under the terms of the Creative Commons Attribution License (CC BY). The use, distribution or reproduction in other forums is permitted, provided the original author(s) and the copyright owner(s) are credited and that the original publication in this journal is cited, in accordance with accepted academic practice. No use, distribution or reproduction is permitted which does not comply with these terms.



Expression and Function of Organic Cation Transporter 2 in Pancreas

Sandra Schorn, Ann-Kristin Dicke, Ute Neugebauer, Rita Schröter, Maren Friedrich, Stefan Reuter and Giuliano Ciarimboli*

Experimental Nephrology, Medicine Clinic D, University Hospital Münster, Münster, Germany

OPEN ACCESS

Edited by:

Cesare Indiveri,
University of Calabria, Italy

Reviewed by:

Michele Visentin,
University Hospital Zurich, Switzerland
Annamaria Tonazzi,
National Research Council (CNR), Italy

*Correspondence:

Giuliano Ciarimboli
gciari@uni-muenster.de

Specialty section:

This article was submitted to
Cellular Biochemistry,
a section of the journal
Frontiers in Cell and Developmental
Biology

Received: 31 March 2021

Accepted: 30 April 2021

Published: 28 May 2021

Citation:

Schorn S, Dicke A-K,
Neugebauer U, Schröter R,
Friedrich M, Reuter S and
Ciarimboli G (2021) Expression
and Function of Organic Cation
Transporter 2 in Pancreas.
Front. Cell Dev. Biol. 9:688885.
doi: 10.3389/fcell.2021.688885

Organic cation transporters (OCT) play an important role in mediating cellular uptake of several pharmaceuticals, such as the antidiabetic drug metformin and the platinum-derived chemotherapeutics. Since these drugs can also affect the pancreas, here it was investigated whether these transporters are expressed in this organ. An interaction between OCT2 and the glucose transporter 2 (GLUT2), which is expressed with important functional consequences in the kidneys and in the pancreas, has already been demonstrated elsewhere. Therefore, here it was further investigated whether the two proteins have a functional relationship. It was demonstrated that OCT2 is expressed in pancreas, probably in β cells of Langerhans islets, together with GLUT2. However, a co-localization was only evident in a cell-line model of rat pancreatic β cells under incubation with high glucose concentration. High glucose stimulated OCT2 expression and activity. On the other side, studies conducted in human embryonic kidney cells stably expressing OCT2, showed that overexpression of GLUT2 decreased OCT2 activity. Unfortunately, pull-down experiments aimed to confirm a physical OCT2/GLUT2 interaction were not successful. Renal glucose excretion was reduced in mice with genetic deletion of OCT2. Nonetheless, in these mice no regulation of known kidney glucose transporters was measured. Therefore, it may be speculated that OCT2 may influence cellular trafficking of GLUT2, without changing its amount. OCT2 may play a role in drug uptake of the pancreas, and its activity may be regulated by glucose and GLUT2. Vice versa, GLUT2 activity may be regulated through an interaction with OCT2.

Keywords: organic cation transporters, glucose transporter, glucose, pancreas, metformin

INTRODUCTION

Metformin is a broadly used antidiabetic drug with glucose-lowering effects. It seems that metformin main mechanisms of action derive from inhibition of hepatic gluconeogenesis and improved glucose uptake in skeletal muscles (Pernicova and Korbonits, 2014). Metformin has also an effect on pancreas function restoring insulin secretion and protecting pancreatic β cells from lipotoxicity or glucotoxicity (Yang et al., 2017). Cellular metformin passage through the plasma membrane is mainly mediated by organic cation transporters (OCT) and multidrug and toxin extrusion proteins (MATEs) (Zhou et al., 2016). Polymorphisms of the genes encoding for these transporters may change cellular transport of metformin, despite that the question whether these mutations have a clinical significance is still debated (Zazuli et al., 2020). Interestingly, a mutation in the *Solute Carrier 2A2 (SLC2A2)* gene encoding for the glucose transporter 2

(GLUT2) has been demonstrated to have a clear clinical impact on metformin efficacy especially in obese patients (Zhou et al., 2016). GLUT2 is expressed in the central nervous system, in the liver, intestine, kidneys, and pancreatic islet β cells, where, at least in rodents, it is required for glucose-stimulated insulin secretion (Thorens, 2015). In enterocytes, hepatocytes, and in epithelial cells from the kidney proximal convoluted tubule epithelial cells, GLUT2 is expressed mainly in the basolateral membrane domain. However, in enterocytes after a sugar meal (Leturque et al., 2009) and in renal proximal tubules in dependence from increasing glucose concentrations (Marks et al., 2003), GLUT2 can translocate to the apical membrane. Using a mating-based split-ubiquitin-system (mbSUS), a protein-protein interaction between GLUT2 and the human OCT2 (hOCT2) was observed (Snieder et al., 2019). Because hOCT2 is a transporter for metformin (Song et al., 2008; Konig et al., 2011) and metformin also acts on pancreas (Yang et al., 2017), in this brief research report we investigated, whether OCT2 is expressed in pancreatic tissue and whether GLUT2 and glucose can regulate its activity.

MATERIALS AND METHODS

Cells

As a model for pancreatic β cells the INS-1 832-13 cells (Duke Molecular Physiology Institute, Duke University, Durham, NC, United States) (Hohmeier et al., 2000), which are cells isolated from X-ray induced rat-insulinoma and can secrete insulin, were used. The cells were cultured in Roswell Park Memorial Institute medium [RPMI 1640, Sigma-Aldrich, Taufkirchen, Germany (Hohmeier et al., 2000)] supplemented with 10% fetal calf serum (FCS), 1% penicillin/streptomycin, 10 mM HEPES, 1 mM glutamine, 2 mM Na^+ -pyruvate and 0.05 mM 2-mercaptoethanol. In some experiments, glucose concentration was increased from 9.8 to 14.8 mM. Osmolality in control cells was adjusted by mannose addition.

The effect of transfection with human GLUT2 (hGLUT2, a gift from RESOLUTE Consortium & Giulio Superti-Furga, Addgene plasmid #132126¹) cloned into a pcDNA DEST47 vector) was studied in human embryonic cells (HEK) stably over-expressing the human OCT2 [hOCT2, for a detailed description of these cells see Biermann et al. (2006)]. Transfection was performed using the calcium phosphate transfection method. 72 h after transfection with GLUT2 or the empty vector (EV), the cells were used for ASP^+ uptake measurements and western blot analysis, as described below.

Immunoprecipitation experiments with lysates from HEK cells transfected with hOCT2 tagged with green fluorescent protein (GFP) at the carboxy-terminus (hOCT2-GFP) (as described in Brast et al., 2012) and GLUT2 were performed using GFP trap agarose beads (ChromoTek, Planegg-Martinsried, Germany). Briefly, cells were lysed with Laemmli buffer [10% SDS, 20% (v/v) Glycerol, 125 mM Tris-HCl (pH 6.8)] containing 200 mM dithiothreitol and 0.004% bromophenol blue. Lysates were incubated 2.5 h at 4°C under rotation with GFP

trap agarose beads. The immunocomplexes bound to the beads were recovered by centrifugation, washed five times, resuspended in Laemmli buffer, denaturated at 95°C for 5 min, and loaded onto 4–20% SDS-polyacrylamide gels (Mini-Protean TGX gels, Bio-Rad, Hercules, CA, United States). For western blot analysis the proteins on the gel were transferred to a nitrocellulose membrane incubated with blocking reagent [3% milk powder and 1% bovine serum albumin (BSA) in Tris-buffered saline with Tween20 (TBST)]. After incubation with the primary antibody (1:500 rabbit-polyclonal antibody to hOCT2, Sigma-Aldrich, Munich, Germany, or 1:1000 rabbit-polyclonal antibody to hGLUT2 Proteintech, St. Leon-Rot, Germany, or 1:1000 rabbit antibody against α -actinin, Cell Signaling Technology, Frankfurt, Germany), membranes were incubated with anti-rabbit HRP-conjugate (1:10,000 Thermo Fisher Scientific, Waltham, MA, United States), then covered with Lumi-Light or Lumi-Light Plus (Roche, Mannheim, Germany) before exposure (c600 azure biosystem imager, Azure Biosystems, Dublin, CA, United States).

Fluorescence Measurements

The fluorescent organic cation ASP^+ was used as a tracer of OCT-mediated transport, as already described in detail (Wilde et al., 2009; Wittwer et al., 2013). Measurements were performed using a microplate fluorescence reader with excitation at 465 nm and emission at 590 nm (Infinite F200, Tecan, Switzerland) (Wilde et al., 2009). ASP^+ -concentration was 1 μM in experiments with hOCT2-expressing HEK cells and 5 μM for experiments with INS-1 cells.

PCR Analysis

For PCR analysis, total RNAs were isolated using the Qiagen RNeasy Minikit (Qiagen, Gilden, Germany) and reverse transcription was performed using the Superscript II system (Invitrogen, Carlsbad, CA, United States), both according to the manufacturer's recommendations. Standard PCR was performed using specific primer pairs as listed in **Supplementary Table 1**. The PCR products were separated using agarose gel electrophoresis. The bands were sequenced for confirmation of amplification product identity.

Animals

Male $\text{OCT2}^{-/-}$ mice (Prof. Schinkel, The Netherlands Cancer Institute, Amsterdam, Netherlands) on Bl6 background, and male Bl6 wild-type (WT) mice approximately 9 weeks old and weighing 25–30 g were used. Compared with WT animals, $\text{OCT2}^{-/-}$ mice display no obvious phenotypic abnormalities (Jonker et al., 2003). Experiments were approved by a governmental-committee on animal welfare (84-02.04.2014.A454) and were performed in accordance with national animal protection guidelines. Mice were placed in metabolic cages and 24 h urines were collected for the determinations of glucose excretion. Glucose was measured by the hexokinase method with a Roche Hitachi Modular automatic analyzer (Gluco-quant Glucose, Roche, Mannheim, Germany). In some experiments, pancreas tissues from mice and rats were collected. For immunofluorescence analysis, pancreas was removed and fixed with 4% neutral buffered formalin. Expression

¹<http://n2t.net/addgene:132126>

of OCT2 and GLUT2 in mouse pancreas was investigated using specific antibodies raised against mouse OCT2 (1:300, a generous gift from Prof. Koepsell) and against GLUT2 (1:50, Glut2 C19 SC-7580, Santa Cruz Biotechnology, Dallas, TX, United States). Five micrometer thick cryosections were prepared from mouse pancreas, which have been fixed in melting 2-methylbutane. Cryosections were incubated with 0.2% Triton in phosphate-buffered saline (PBS) for 5 min at room temperature, three times washed with PBS and then incubated 1 h with a 1:1 mix of 10% BSA and 10% normal human serum (NHS) in PBS. After this, sections were incubated overnight at 4°C with primary antibodies. After washing in PBS, the sections were incubated for 45 min at room temperature in the dark with PBS-diluted secondary antibodies (donkey Alexa Fluor 488 anti-goat -Ig, and Alexa Fluor 647 anti-rabbit -Ig Invitrogen, 1:1,000). Sections were rinsed with PBS, coverslipped with Fluoromount aqueous mounting medium (Sigma-Aldrich, München, Germany) and evaluated by epifluorescence microscopy (Observer Z1 with Apotome, Zeiss). Negative control slides were included without addition of primary antibody.

REAGENTS

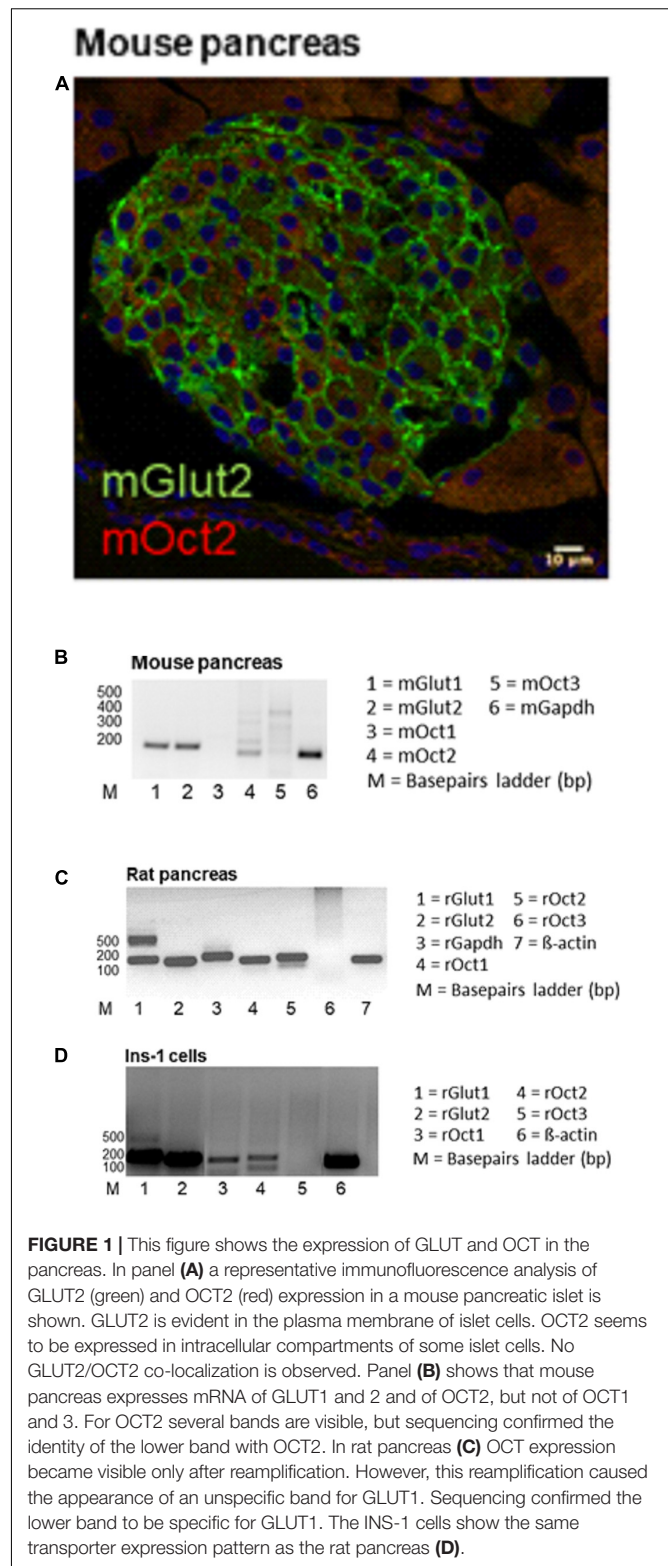
4-(4-dimethylaminostyryl)-N-methylpyridinium (ASP⁺) was purchased from Fischer Scientific. All other reagents were of the highest purity and obtained from Sigma-Aldrich (Sigma-Aldrich, Merck Chemicals, Darmstadt, Germany).

Statistical Analysis

Experimental data are presented as means \pm SEM, with *n* referring to the number of totally measured replicates obtained in at least three independent experiments. Significant differences were calculated using unpaired Student's *t*-test or ANOVA with Tukey's post-test for multiple comparisons. A *p*-value < 0.05 was considered statistically significant. Analyses were performed using GraphPad Prism, Version 5.3 (GraphPad Software, San Diego, CA, United States).

RESULTS

Expression of GLUT2 and OCT2 was studied in pancreas tissues from mice, rats and in the INS-1 cells (Figure 1). Immunofluorescence analysis of protein expression in mouse pancreas shows that islets express GLUT2 in the plasma membrane, while OCT2 is visible only in some cells in intracellular compartments (Figure 1A). No co-localization of the two proteins was evident. Mouse pancreas expresses mRNA for GLUT1, GLUT2, and OCT2 (Figure 1B). For OCT2 more bands were detected. The thicker lower one corresponds to mOCT2, as confirmed by sequencing (the identity of all PCR-products was confirmed by sequencing). No specific band for OCT1 and OCT3 was detected. In rat pancreas (Figure 1C) an expression of OCT1- and OCT2-, but not of OCT3-mRNA was evident only upon reamplification of the PCR-products, which produced a double band for



GLUT1. This suggests that OCT1- and 2-mRNA expression is relatively low. For GLUT1, only the lower band is specific. GLUT2-mRNA is also robustly expressed in rat pancreas. Since the INS1-cells show a similar transporter expression pattern

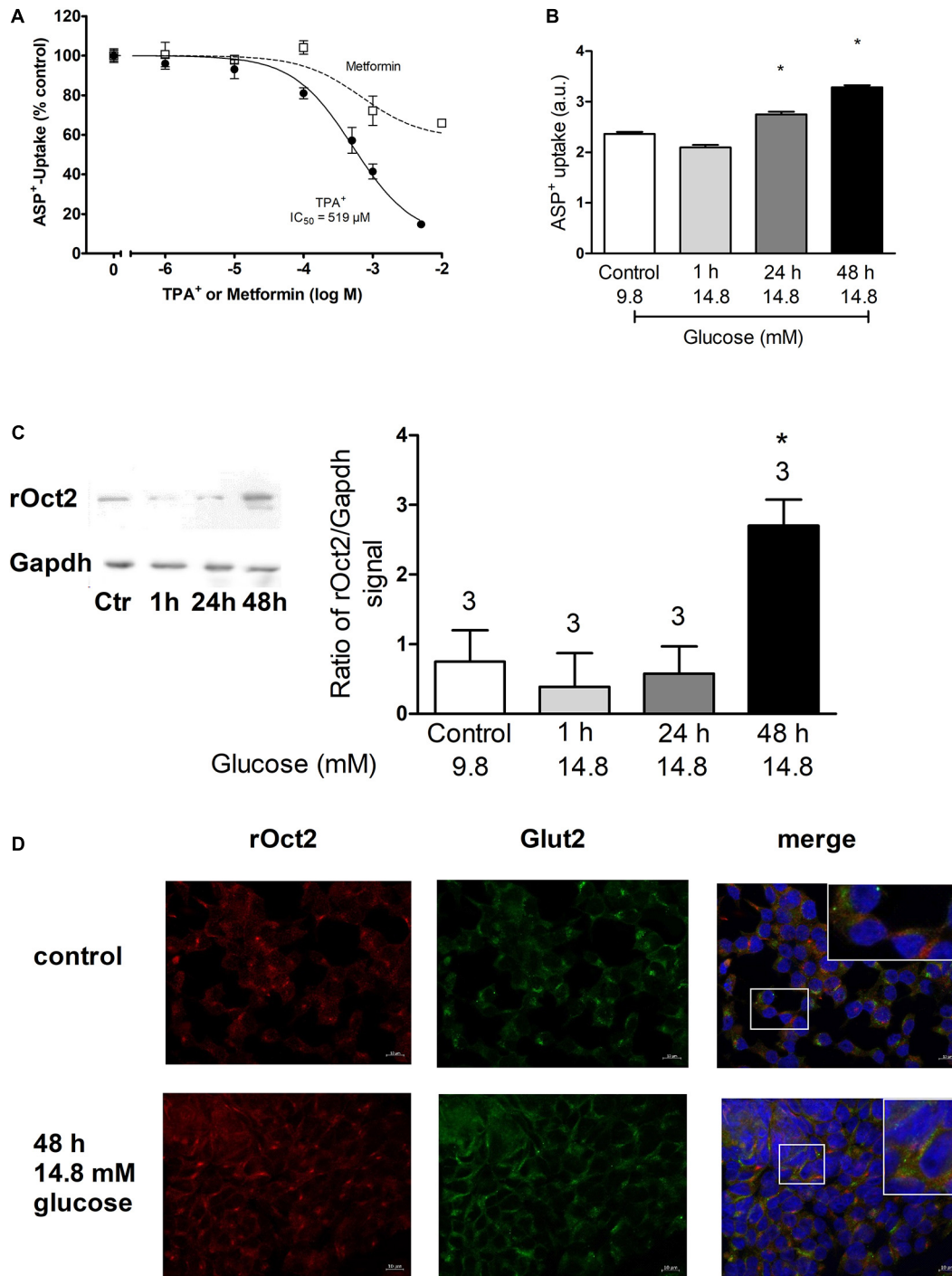


FIGURE 2 | This figure shows the ASP⁺ transport characteristics of INS-1 cells and the analysis of OCT2 and GLUT2 expression in dependence from glucose concentration. Panel **(A)** shows that TPA⁺ inhibits concentration-dependently the ASP⁺ uptake with an IC₅₀ of 519 μM. Inhibition of ASP⁺ uptake by metformin is also shown (at least six replicates for concentration measured in three independent experiments). Panel **(B)** shows the effect of incubation with 14.8 mM glucose for 1, 24, or 48 h on the ASP⁺ uptake in arbitrary units (a.u.) of INS-1 cells. Control experiments were performed with a glucose concentration of 9.8 mM. Osmolarity was adjusted in control experiments by adding mannose. High glucose significantly stimulated ASP⁺ uptake after incubation for 24 and 48 h (ANOVA with Tukey's post-test, nine replicates measured in four independent experiments). Panel **(C)** shows the evaluation of western blot analysis of OCT2 expression under incubation with high glucose. Only after 48 h incubation with 14.8 mM glucose a significant increase of OCT2 expression was observed (*, ANOVA with Tukey's post-test, three independent experiments). The insert on the left shows an example of the western blot analysis. Panel **(D)** shows the immunofluorescence analysis of OCT2 (red) and GLUT2 (green) expression in INS-1 cells after 48 h incubation with normal (9.8 mM) or high (14.8 mM) glucose. The labeling of nuclei with 4',6-diamidino-2-phenylindole (DAPI, blue) is also shown. In the upper right corners of the overlay picture a magnification of the field indicated by a box is shown.

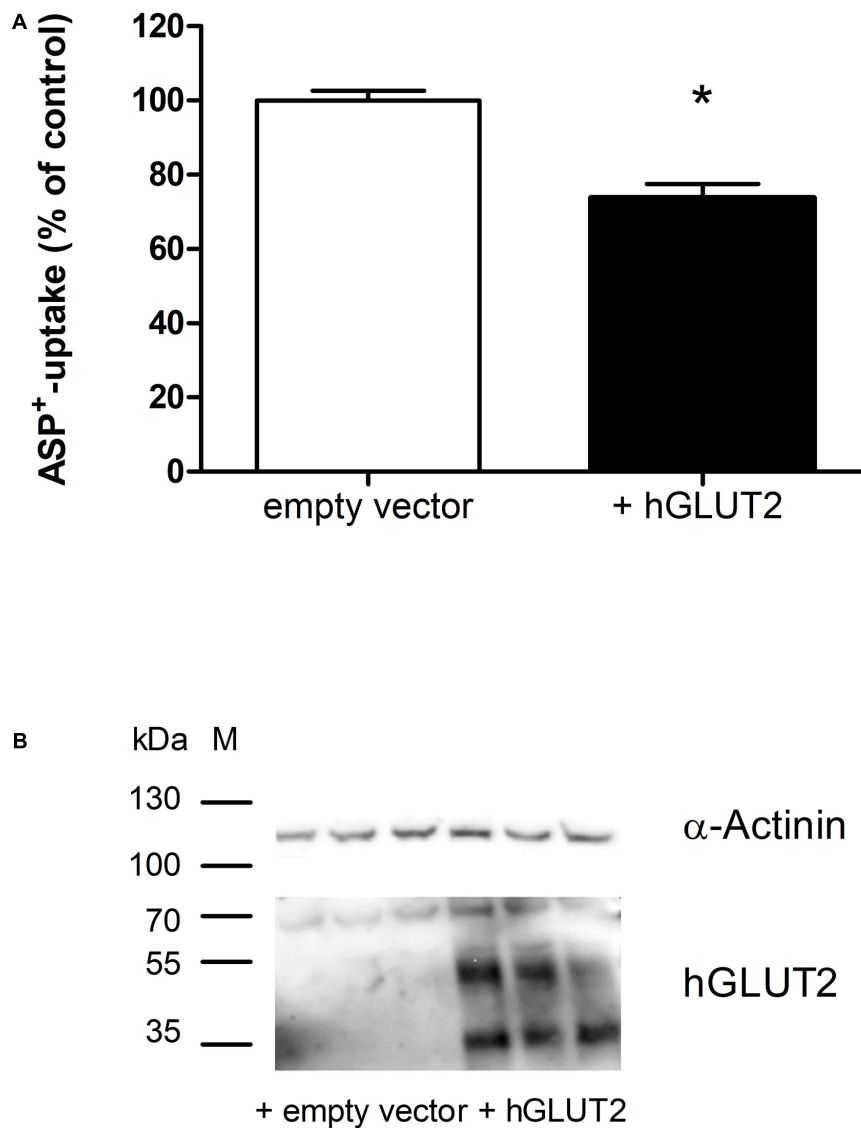


FIGURE 3 | Transfection of HEK cells stably expressing hOCT2 with GLUT2: effects on the ASP⁺ uptake. Panel **(A)** shows the uptake of 1 μ M ASP⁺ in HEK cells 72 h after transfection with GLUT2 or empty vector (EV). Overexpression of GLUT2 significantly inhibited ASP⁺ uptake (*, unpaired *t*-test, 27 replicates measured in three independent experiments). Panel **(B)** shows the western blot analysis of GLUT2 72 h after transfection. α -Actinin was used as loading marker. This antibody against hGLUT2 is known to detect mature glycosylated hGLUT2 at 60–70 kDa, non-glycosylated hGLUT2 at 38–45 kDa, and a hGLUT2 fragment at around 35 kDa (<https://www.ptglab.com/products/SLC2A2-Antibody-20436-1-AP.htm>). All these bands are visible in this western blot analysis, especially in HEK cells transfected with hGLUT2, confirming that transfection with hGLUT2 was successful. Bands corresponding to GLUT2 were observed mainly in transfected cells.

(**Figure 1D**, also here a reamplification was necessary to detect OCT1- and OCT2-mRNA, the thicker band was specific for the transporters as revealed by sequencing), it was investigated, whether these cells show any ASP⁺-transport. INS-1 cells are able to take up ASP⁺ (**Figure 2A**): this uptake was inhibited concentration-dependently by tetrapentylammonium (TPA⁺), a known OCT-inhibitor (Zhang et al., 1999; Wilde et al., 2009), with an apparent affinity (IC₅₀) of 519 μ M. Metformin, which is well known to interact with OCT, showed a lower but still significant inhibitory capacity than TPA⁺. Increasing glucose concentration from 9.8 to 14.8 mM resulted in an increased

uptake of ASP⁺ after 24 and 48 h incubation (**Figure 2B**). Osmolality was equilibrated by mannose addition. Western blot analysis of the cells showed that rat OCT2 protein expression significantly increased after 48 h incubation with high glucose (**Figure 2C**). Immunofluorescence analysis of INS-1 cells after 48 h incubation with 14.8 mM glucose suggests an increased cell proliferation (as already shown in Olson et al., 1998), and an increased expression of OCT2 and GLUT2, with augmented distribution to the plasma membrane (**Figure 2D**). In some cells, a partial co-localization of OCT2 and GLUT2 can be observed after 48 h incubation with 14.8 mM glucose (**Figure 2D**, merge).

Transfection of hGLUT2 in HEK cells overexpressing hOCT2 caused a significant inhibition ($-26 \pm 4\%$) of hOCT2 function measured as ASP⁺-uptake (**Figure 3A**). The transfection with hGLUT2 resulted in an evident GLUT2 protein expression (**Figure 3B**). The expression levels of hOCT2 were not changed (not shown). However, GLUT2 was not detectable in GFP-trap pull-down experiments (not shown).

The *in vitro* experiments suggest that high glucose and also GLUT2 protein expression can change OCT activity and cellular distribution. Since high amounts of GLUT2 and OCT2 are expressed in the basolateral plasma membrane domain of renal proximal tubules (Koepsell et al., 2007; Thorens, 2015), we tried to investigate whether OCT2 influences glucose kidney handling by comparing renal glucose excretion in WT- and OCT2^{-/-}-mice (**Figure 4**). A decreased glucose urinary secretion was measured in OCT2^{-/-}-compared to WT mice (**Figure 4**).

DISCUSSION

In this brief research report, it has been demonstrated that OCT1 and 2 are expressed in the pancreas. Previously, expression of OCT1 was demonstrated in human pancreatic stellate cells (Wu et al., 2018). Focusing on OCT2, it seems to be expressed in some cells of the Langerhans islets. From experiments with the INS-1 cells, which are able to release insulin and are a model for β cells, it can be speculated that OCT2 is expressed in the β -cells. Interestingly, a partial co-localization with GLUT2 was only detected under incubation with high glucose concentration, suggesting that probably in this cell system, a protein conformational change may be induced by high-glucose, which then facilitates OCT2-GLUT2 interaction. Increased OCT2 expression and function under incubation with high-glucose may facilitate metformin action under diabetic conditions. INS-1 cells can transport ASP⁺ and this transport can be inhibited by TPA⁺ with an apparent affinity, which is much

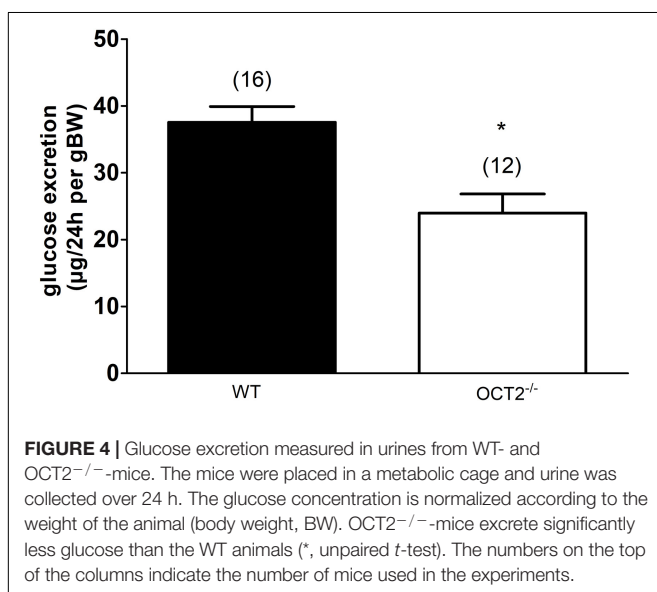
lower than that observed using rat OCT1 (rOCT1) (Ciarimboli et al., 2005) or rOCT2 (Wilde et al., 2009) in expression systems. This suggests that the apparent affinity can be changed by specific cellular regulation pathways (Ciarimboli et al., 2004). In INS-1 cells, a low but significant inhibition of ASP⁺ uptake by metformin was measured. This inhibition is lower than that measured using ASP⁺ with cloned OCT (see Frenzel et al., 2019), again suggesting an influence of cell specific factors in determining transport characteristics.

Transfection of GLUT2 decreases the transport activity of hOCT2 overexpressed in HEK cells, suggesting that the hOCT2-GLUT2 interaction detected using the mbSUS (Snieder et al., 2019) may have functional consequences. However, in pull-down experiments using GFP-trap and HEK cells transfected with hOCT2-GFP [the GFP tag is localized at the carboxy-terminus of the transporter and does not change its function, as already demonstrated in Brast et al. (2012)] it was not possible to confirm a direct hOCT2-GLUT2 interaction. It can be speculated, that the interaction domain is close to the carboxy-terminus, where hOCT2 bears the GFP-tag. The tag may change the conformation of this part of the protein, hindering the interaction with GLUT2.

Interestingly, genetic deletion of OCT2 in mice caused a significant lower excretion of glucose compared to WT animals. In a previous work, performing a proteomic analysis of kidneys from WT- and OCT1/2^{-/-} mice no different expression of proteins involved in glucose resorption [sodium glucose transporter (SGLT)1 and 2, GLUT1 and 2] was detected (Hucke et al., 2019), suggesting that the difference in glucose excretion is not due to changes in global protein amount. Perhaps the OCT2/GLUT2 interaction changes the transport characteristics of these proteins or modify their trafficking from/to the plasma membrane. For example, in the absence of OCT2, GLUT2 may increase its transport activity or/and may traffic to the apical plasma membrane, in both ways increasing renal glucose reabsorption. Unfortunately, we were not able to analyze these aspects in the kidneys.

Platinum derivatives such as the chemotherapeutic drugs cisplatin and oxaliplatin, are also substrates of OCT (Sprowl et al., 2013). Anticancer treatment with these drugs is well known to cause severe side-effects such as nephrotoxicity and peripheral neurotoxicity, which are probably mediated by OCT-mediated uptake (Hucke et al., 2019; Sprowl et al., 2013). There is also some evidence that cisplatin and oxaliplatin can cause pancreatic toxicity (Komdeur et al., 2007; Yadav, 2019). Therefore, it may be speculated that OCT2 may play a role also in this type of unwanted side-effect of platinum-based chemotherapy.

Organic cation transporters have a large binding pocket, with specific interaction domains for different substrates. Therefore, they are polyspecific, meaning that they can accept many different substances as substrate (Koepsell et al., 2007). For this reason, OCT can mediate the cellular uptake of many different drugs and can be involved in cellular drug toxicity. While the OCT-mediated drug toxicity in organs like the kidneys and the liver is well known (Motohashi and Inui, 2016), pancreatic drug toxicity has not yet been associated with OCT expression. Many medications, which are associated with pancreas toxicity (Jones et al., 2015) are substrates



of OCT, like prazosin, procainamide, ranitidine, and cimetidine (Koepsell, 2020).

CONCLUSION

In conclusion, here we demonstrated that OCT2 is expressed in the pancreas and that high-glucose stimulates its expression and co-localization with GLUT2. A possible functional role of this interaction is plausible, but we were not able to define the interaction mechanisms. Further studies are necessary to elucidate the characteristics of this interaction and whether it may have some functional implication.

DATA AVAILABILITY STATEMENT

The raw data supporting the conclusions of this article will be made available by the authors, without undue reservation.

ETHICS STATEMENT

The animal study was reviewed and approved by Landesamt für Natur, Umwelt und Verbraucherschutz Nordrhein-Westfalen.

REFERENCES

- Biermann, J., Lang, D., Gorboulev, V., Koepsell, H., Sindic, A., Schröter, R., et al. (2006). Characterization of regulatory mechanisms and states of human organic cation transporter 2. *Am. J. Physiol. Cell Physiol.* 290, C1521–C1531.
- Brast, S., Grabner, A., Sucic, S., Sitte, H. H., Hermann, E., Pavenstadt, H., et al. (2012). The cysteines of the extracellular loop are crucial for trafficking of human organic cation transporter 2 to the plasma membrane and are involved in oligomerization. *FASEB J.* 26, 976–986. doi: 10.1096/fj.11-180679
- Ciarimboli, G., Koepsell, H., Iordanova, M., Gorboulev, V., Dürner, B., Lang, D., et al. (2005). Individual PKC-phosphorylation sites in organic cation transporter 1 determine substrate selectivity and transport regulation. *J. Am. Soc. Nephrol.* 16, 1562–1570. doi: 10.1681/asn.2004040256
- Ciarimboli, G., Struwe, K., Arndt, P., Gorboulev, V., Koepsell, H., Schlatter, E., et al. (2004). Regulation of the human organic cation transporter hOCT1. *J. Cell Physiol.* 201, 420–428. doi: 10.1002/jcp.20081
- Frenzel, D., Koppen, C., Bauer, O. B., Karst, U., Schroter, R., Tzvetkov, M. V., et al. (2019). Effects of Single Nucleotide Polymorphism Ala270Ser (rs316019) on the Function and Regulation of hOCT2. *Biomolecules* 9:578. doi: 10.3390/biom9100578
- Hohmeier, H. E., Mulder, H., Chen, G., Henkel-Rieger, R., Prentki, M., and Newgard, C. B. (2000). Isolation of INS-1-derived cell lines with robust ATP-sensitive K⁺ channel-dependent and -independent glucose-stimulated insulin secretion. *Diabetes* 49, 424–430. doi: 10.2337/diabetes.49.3.424
- Hucke, A., Rinschen, M. M., Bauer, O. B., Sperling, M., Karst, U., Koppen, C., et al. (2019). An integrative approach to cisplatin chronic toxicities in mice reveals importance of organic cation-transporter-dependent protein networks for renoprotection. *Arch. Toxicol.* 93, 2835–2848. doi: 10.1007/s00204-019-02557-9
- Jones, M. R., Hall, O. M., Kaye, A. M., and Kaye, A. D. (2015). Drug-induced acute pancreatitis: a review. *Ochsner. J.* 15, 45–51.
- Jonker, J. W., Wagenaar, E., Van Eijl, S., and Schinkel, A. H. (2003). Deficiency in the organic cation transporters 1 and 2 (Oct1/Oct2 [Slc22a1/Slc22a2]) in mice abolishes renal secretion of organic cations. *Mol. Cell Biol.* 23, 7902–7908. doi: 10.1128/mcb.23.21.7902-7908.2003

AUTHOR CONTRIBUTIONS

SS, A-KD, UN, RS, MF, SR, and GC performed and evaluated the experiments. GC planned the study and wrote the manuscript. All authors contributed to the article and approved the submitted version.

FUNDING

This study was supported by the Deutsche Forschungsgemeinschaft (CI 107/11-1 to GC).

ACKNOWLEDGMENTS

The help of Christopher Newgard (Duke Molecular Physiology Institute, Duke University, Durham, NC, United States) for providing us with the INS-1 832/13 cells is acknowledged.

SUPPLEMENTARY MATERIAL

The Supplementary Material for this article can be found online at: <https://www.frontiersin.org/articles/10.3389/fcell.2021.688885/full#supplementary-material>

- Koepsell, H. (2020). Organic cation transporters in health and disease. *Pharmacol. Rev.* 72, 253–319. doi: 10.1124/pr.118.015578
- Koepsell, H., Lips, K., and Volk, C. (2007). Polyspecific organic cation transporters: structure, function, physiological roles, and biopharmaceutical implications. *Pharm. Res.* 24, 1227–1251. doi: 10.1007/s11095-007-9254-z
- Komdeur, R., Derksen, J., Legdeur, M. C., and Hylkema, B. S. (2007). Cisplatin-induced hyperglycemic hyperosmolar coma. *Neth. J. Med.* 65, 36–37.
- Konig, J., Zolk, O., Singer, K., Hoffmann, C., and Fromm, M. F. (2011). Double-transfected MDCK cells expressing human OCT1/MATE1 or OCT2/MATE1: determinants of uptake and transcellular translocation of organic cations. *Br. J. Pharmacol.* 163, 546–555. doi: 10.1111/j.1476-5381.2010.01052.x
- Leturque, A., Brot-Laroche, E., and Le, G. M. (2009). GLUT2 mutations, translocation, and receptor function in diet sugar managing. *Am. J. Physiol. Endocrinol. Metab.* 296, E985–E992.
- Marks, J., Carvou, N. J., Debnam, E. S., Srari, S. K., and Unwin, R. J. (2003). Diabetes increases facilitative glucose uptake and GLUT2 expression at the rat proximal tubule brush border membrane. *J. Physiol.* 553(Pt 1), 137–145. doi: 10.1113/jphysiol.2003.046268
- Motohashi, H., and Inui, K. (2016). “Pharmacological and toxicological significance of the organic cation transporters OCT and MATE: Drug disposition, interaction and toxicity,” in *Organic Cation Transporters*, eds G. Ciarimboli, S. Gautron, and E. Schlatter (Cham: Springer), 73–92. doi: 10.1007/978-3-319-23793-0_3
- Olson, L. K., Qian, J., and Poytout, V. (1998). Glucose rapidly and reversibly decreases INS-1 cell insulin gene transcription via decrements in STF-1 and C1 activator transcription factor activity. *Mol. Endocrinol.* 12, 207–219. doi: 10.1210/mend.12.2.0066
- Pernicova, I., and Korbonits, M. (2014). Metformin—mode of action and clinical implications for diabetes and cancer. *Nat. Rev. Endocrinol.* 10, 143–156. doi: 10.1038/nrendo.2013.256
- Snieder, B., Brast, S., Grabner, A., Buchholz, S., Schroter, R., Spoden, G. A., et al. (2019). Identification of the Tetraspanin CD9 as an interaction partner of organic cation transporters 1 and 2. *SLAS Discov.* 24, 904–914. doi: 10.1177/2472555219859837

- Song, I. S., Shin, H. J., and Shin, J. G. (2008). Genetic variants of organic cation transporter 2 (OCT2) significantly reduce metformin uptake in oocytes. *Xenobiotica* 38, 1252–1262. doi: 10.1080/00498250802130039
- Sprowl, J. A., Ciarimboli, G., Lancaster, C. S., Giovinazzo, H., Gibson, A. A., Du, G., et al. (2013). Oxaliplatin-induced neurotoxicity is dependent on the organic cation transporter OCT2. *Proc. Natl. Acad. Sci. U.S.A.* 110, 11199–11204. doi: 10.1073/pnas.1305321110
- Thorens, B. (2015). GLUT2, glucose sensing and glucose homeostasis. *Diabetologia* 58, 221–232. doi: 10.1007/s00125-014-3451-1
- Wilde, S., Schlatter, E., Koepsell, H., Edemir, B., Reuter, S., Pavenstädt, H., et al. (2009). Calmodulin-associated post-translational regulation of rat organic cation transporter 2 in the kidney is gender dependent. *Cell Mol. Life Sci.* 66, 1729–1740. doi: 10.1007/s00018-009-9145-z
- Wittwer, M. B., Zur, A. A., Khuri, N., Kido, Y., Kosaka, A., Zhang, X., et al. (2013). Discovery of potent, selective multidrug and toxin extrusion transporter 1 (MATE1, SLC47A1) inhibitors through prescription drug profiling and computational modeling. *J. Med. Chem.* 56, 781–795. doi: 10.1021/jm301302s
- Wu, C., Qiu, S., Zhu, X., Lin, H., and Li, L. (2018). OCT1-mediated metformin uptake regulates pancreatic stellate cell activity. *Cell Physiol. Biochem.* 47, 1711–1720. doi: 10.1159/000491003
- Yadav, Y. C. (2019). Effect of cisplatin on pancreas and testies in Wistar rats: biochemical parameters and histology. *Heliyon* 5:e02247. doi: 10.1016/j.heliyon.2019.e02247
- Yang, X., Xu, Z., Zhang, C., Cai, Z., and Zhang, J. (2017). Metformin, beyond an insulin sensitizer, targeting heart and pancreatic beta cells. *Biochim. Biophys. Acta Mol. Basis Dis.* 1863, 1984–1990. doi: 10.1016/j.bbadis.2016.09.019
- Zazuli, Z., Duin, N. J. C. B., Jansen, K., Vijverberg, S. J. H., Maitland-van der Zee, A. H., and Masereeuw, R. (2020). The impact of genetic polymorphisms in organic cation transporters on renal drug disposition. *Int. J. Mol. Sci.* 21:6627. doi: 10.3390/ijms21186627
- Zhang, L., Gorset, W., Dresser, M. J., and Giacomini, K. M. (1999). The interaction of n-tetraalkylammonium compounds with a human organic cation transporter, hOCT1. *J. Pharmacol. Exp. Ther.* 288, 1192–1198.
- Zhou, K., Yee, S. W., Seiser, E. L., van, L. N., Tavendale, R., Bennett, A. J., et al. (2016). Variation in the glucose transporter gene SLC2A2 is associated with glycemic response to metformin. *Nat. Genet.* 48, 1055–1059.

Conflict of Interest: The authors declare that the research was conducted in the absence of any commercial or financial relationships that could be construed as a potential conflict of interest.

Copyright © 2021 Schorn, Dicke, Neugebauer, Schröter, Friedrich, Reuter and Ciarimboli. This is an open-access article distributed under the terms of the Creative Commons Attribution License (CC BY). The use, distribution or reproduction in other forums is permitted, provided the original author(s) and the copyright owner(s) are credited and that the original publication in this journal is cited, in accordance with accepted academic practice. No use, distribution or reproduction is permitted which does not comply with these terms.



Mutational Analysis of the GXXXG/A Motifs in the Human Na⁺/Taurocholate Co-Transporting Polypeptide NTCP on Its Bile Acid Transport Function and Hepatitis B/D Virus Receptor Function

OPEN ACCESS

Massimo Palatini¹, Simon Franz Müller¹, Kira Alessandra Alicia Theresa Lowjaga¹, Saskia Noppes¹, Jörg Alber¹, Felix Lehmann², Nora Goldmann², Dieter Glebe² and Joachim Geyer^{1*}

Edited by:

Cesare Incliveri,
University of Calabria, Italy

Reviewed by:

Tiziano Verri,
University of Salento, Italy

Edwin Li,

Saint Joseph's University,
United States

*Correspondence:

Joachim Geyer
Joachim.M.Geyer@vetmed.uni-
giessen.de

Specialty section:

This article was submitted to
Cellular Biochemistry,
a section of the journal
Frontiers in Molecular Biosciences

Received: 23 April 2021

Accepted: 10 June 2021

Published: 22 June 2021

Citation:

Palatini M, Müller SF, Lowjaga KAAT, Noppes S, Alber J, Lehmann F, Goldmann N, Glebe D and Geyer J (2021) Mutational Analysis of the GXXXG/A Motifs in the Human Na⁺/Taurocholate Co-Transporting Polypeptide NTCP on Its Bile Acid Transport Function and Hepatitis B/D Virus Receptor Function. *Front. Mol. Biosci.* 8:699443. doi: 10.3389/fmolb.2021.699443

¹Institute of Pharmacology and Toxicology, Faculty of Veterinary Medicine, Justus Liebig University Giessen, Giessen, Germany, ²Institute of Medical Virology, National Reference Center for Hepatitis B and D Viruses, Justus Liebig University Giessen, Giessen, Germany

Homodimerization is essential for plasma membrane sorting of the liver bile acid transporter NTCP and its function as Hepatitis B/D Virus (HBV/HDV) receptor. However, the protein domains involved in NTCP dimerization are unknown. NTCP bears two potential GXXXG/A dimerization motifs in its transmembrane domains (TMDs) 2 and 7. The present study aimed to analyze the role of these GXXXG/A motifs for the sorting, function, and dimerization of NTCP. The NTCP mutants G₆₀LXXXA₆₄L (TMD2), G₂₃₃LXXXG₂₃₇L (TMD7) and a double mutant were generated and analyzed for their interaction with wild-type NTCP using a membrane-based yeast-two hybrid system (MYTH) and co-immunoprecipitation (co-IP). In the MYTH system, the TMD2 and TMD7 mutants showed significantly lower interaction with the wild-type NTCP. In transfected HEK293 cells, membrane expression and bile acid transport activity were slightly reduced for the TMD2 mutant but were completely abolished for the TMD7 and the TMD2/7 mutants, while co-IP experiments still showed intact protein-protein interactions. Susceptibility for *in vitro* HBV infection in transfected HepG2 cells was reduced to 50% for the TMD2 mutant, while the TMD7 mutant was not susceptible for HBV infection at all. We conclude that the GXXXG/A motifs in TMD2 and even more pronounced in TMD7 are important for proper folding and sorting of NTCP, and so indirectly affect glycosylation, homodimerization, and bile acid transport of NTCP, as well as its HBV/HDV receptor function.

Keywords: Na⁺/taurocholate co-transporting polypeptide, bile acid transport, dimerization, sorting, protein-protein interaction, hepatitis B virus, hepatitis D virus

INTRODUCTION

The Na⁺/taurocholate co-transporting polypeptide (NTCP, gene symbol *SLC10A1*) is the first of seven members of the solute carrier family SLC10 (Geyer et al., 2006) and plays, together with the apical sodium bile acid transporter (ASBT, gene symbol *SLC10A2*), a crucial role for the maintenance of the enterohepatic circulation of bile acids (Döring et al., 2012). While NTCP is dominantly expressed in hepatocytes and here is responsible for the re-uptake of bile acids from the portal blood (Stieger et al., 1994), ASBT, with its highest expression level in the apical brush border membrane of enterocytes of the terminal ileum, absorbs bile acids from the intestinal lumen for their return to the liver (Shneider, 1995). The identification of NTCP as the high-affinity binding and entry-receptor for the human Hepatitis B (HBV) and Hepatitis D (HDV) Viruses in 2012 made this carrier an attractive novel drug target for HBV/HDV entry inhibition (Yan et al., 2012; König et al., 2014; Kirstgen et al., 2020).

NTCP forms homodimers, in which the individual subunits are functionally active in transporting bile acids in a sodium-dependent manner (Bijmans et al., 2012; Noppes et al., 2019). NTCP homodimerization occurs early in the secretory pathway and persists after its sorting to the plasma membrane (Bijmans et al., 2012). In addition, NTCP dimerization seems to be essential for the entry of HBV/HDV virus particles into hepatocytes (Fukano et al., 2018). Interestingly, after co-expression of NTCP with the NTCP homolog *SLC10A4*, which has a vesicular expression pattern, wild-type NTCP is trapped in intracellular compartments and so plasma membrane expression and bile acid transport function of NTCP are hampered (Bijmans et al., 2012; Noppes et al., 2019). These data clearly point to functional homo- and heterodimerization of NTCP, but the protein domains responsible for this interaction have not been identified so far. Two GXXXG/A sequence motifs are present in transmembrane domains (TMDs) 2 and 7 of NTCP. Such motifs are well-known to be involved in protein-protein interactions of transmembrane proteins (Teese and Langosch, 2015). In the present study, we hypothesize that this sequence motif is involved in the dimerization of NTCP. In detail, this GXXXG/A motif, or more general (small)XXX(small) motif, is typically flanked by the small amino acid residues glycine, alanine or serine (Dawson et al., 2002). It was first described in the blood-based glycoprotein A (GPA), a transmembrane sialoglycoprotein in erythrocytes, as a key motif for homodimerization (Lemmon et al., 1992). Since then, this motif has been investigated in numerous other transmembrane proteins (Teese and Langosch, 2015). In addition, random sequence library screening of selected oligomerizing transmembrane domains by the TOXCAT *in vivo* selection system revealed dominant occurrence of the GXXXG motif in transmembrane helix-helix associations (Russ and Engelman, 2000), demonstrating the importance of this motif for transmembrane interactions. According to structure-based studies, the mode of action of this motif might be the enhancement of van der Waals forces and/or hydrogen bonds due to the close proximity of the small amino acid residues

(glycine, alanine, or serine) of this motif in the three-dimensional structure of an alpha helix (MacKenzie et al., 1997; Anderson et al., 2017). In addition to intermolecular protein-protein interactions, this (small)XXX(small) motif is also relevant for intramolecular interactions, which are important for proper protein folding and sorting (Eilers et al., 2000). Therefore, the present study aimed to analyze the role of the two GXXXG/A motifs of human NTCP for its transporter and virus receptor functions, sorting and dimerization. Mutation of these motifs in NTCP had significant impact on protein folding and sorting, and so indirectly affected homodimerization and bile acid transport of NTCP, as well as its HBV/HDV receptor function.

MATERIALS AND METHODS

Chemicals

All of the chemicals, unless otherwise stated, were bought from Sigma-Aldrich (St. Louis, MO, United States). Radio-labelled [³H]taurocholic acid ([³H]TC, 10 Ci/mmol) was purchased from PerkinElmer Life Sciences (Waltham, MA, United States).

Cell Lines and Transient Transfections

GripTite HEK293 MSR cells (Thermo Fisher Scientific), further referred to as HEK293 cells, were cultured in DMEM (Gibco, Carlsbad, United States) supplemented with 10% fetal calf serum (Pan-Biotech, Aidenbach, Germany), L-Glutamine (4 mM, anprotec, Bruckburg, Germany), penicillin (100 U/ml, anprotec), and streptomycin (100 µg/ml, anprotec) in a 5% CO₂ atmosphere at 37°C. Human hepatoma HepG2 Tet-On cells (BD Clontech, Heidelberg, Germany), further referred to as HepG2 cells, were maintained under the same conditions in DMEM with all supplements listed above. HEK293 cells were transiently transfected with Lipofectamine 2000 (Thermo Fisher Scientific) for co-localization as well as co-immunoprecipitation (co-IP) experiments following the manufacturer's protocol. HepG2 cells were transiently transfected using X-tremeGENE 9 (Roche Diagnostics, Basel, Germany) and used for HBV infection experiments.

Yeast-Two-Hybrid Membrane Protein System

The yeast-two-hybrid membrane protein system (MYTH) enables the identification of interactions between membranous proteins by utilizing the split-ubiquitin method (Stagljar et al., 1998). For this method the proteins of interest have to be fused with either the C-terminal part (C_{Ub}/bait construct) or the N-terminal part (N_{Ub}/prey construct) of ubiquitin, which allows the functional restoration of split-ubiquitin by interaction of the proteins of interest with each other (Johnsson and Varshavsky, 1994). Ubiquitin-specific proteases recognize and cleave the newly formed split-ubiquitin resulting in the separation of the transcriptional factor LexA-VP16 from the C_{Ub} construct, which subsequently activates certain reporter genes (Stagljar and Fields, 2002). All vectors and the reporter strain NMY51 (MATa his3Δ200 trp1-901 leu2-3,112 ade2

LYS2::(lexAop)4-HIS3 ura3::(lexAop)8-lacZ ade2::(lexAop)8-ADE2 GAL4) were purchased from DUALsystems Biotech AG (Schlieren, Switzerland). The bait vectors contain a kanamycin resistance gene for selection in chemical competent *E. coli* and a leucine synthesis gene for selection of the NMY51 yeast strain. In contrast, the prey vectors have an ampicillin resistance gene for selection in *E. coli* and a tryptophan synthesis gene for selection in yeast. For co-transformation control, the NMY51 yeast cells were grown on synthetically defined (SD) medium lacking leucine and tryptophan (SD-LW). For the protein interaction assays, the SD medium was deficient in adenine, histidine, leucine, and tryptophan (SD-AHLW). Cloning of the open reading frame of NTCP into the bait vector pBT3-STE and the prey vector pPR3-STE was reported before (Noppes et al., 2019).

Transformation of Bait and Prey Constructs Into NMY51

The NMY51 yeast strain was grown on YPAD plates containing 1% yeast extract (Roth, Karlsruhe, Germany), 2% tryptone/peptone ex casein (Roth), 2% glucose monohydrate (Roth), 2% agar-agar Kobe I (Roth), and 0.004% adenine sulfate. For transformation, several yeast colonies were inoculated in 50 ml YPAD medium, composed of the same contents as the YPAD plates, but without agar-agar, and grown overnight at 30°C under shaking at 180 rpm. The culture with an OD₆₀₀ of approximately 0.8 was then pelleted and re-suspended in 2.5 ml water. Co-transformations were carried out using 1.5 µg of each plasmid, 300 µl PEG/LiOAc master mix (composed of 2.4 ml 50% PEG 4000 (Roth), 360 µl 1 M lithium acetate (Roth), and 250 µl single stranded carrier DNA (ssDNA) for 10 reactions) and 100 µl of re-suspended yeast cells. Each reaction was incubated at 42°C for 45 min prior to pelleting and resuspending in 100 µl 0.9% NaCl. For single transformations, the resuspended yeast cells were plated on SD-L (bait constructs) or SD-W (prey constructs) plates, containing 0.7% yeast nitrogen base without amino acids (Roth), 0.1% yeast synthetic drop-out medium supplemented with the appropriate amino acids (Roth), 2% glucose monohydrate, and 2% agar-agar Kobe I, respectively. For co-transformations of bait and prey constructs, 4 µl of the yeast/NaCl-suspension were dropped onto SD-LW plates for transformation control and another 4 µl on SD-AHLW plates for interaction analysis. The residual suspension was completely plated on SD-AHLW plates for colony quantification. All plates were incubated at 30°C for 5 days.

Test for Non-specific Interactions of the Prey Constructs

To test the prey constructs for non-specific interactions, all prey constructs were co-transformed with the control bait construct pTSU2-APP, as described in the DUALmembrane pairwise interaction kit by DUALsystems Biotech AG. Expression of the pTSU2-APP construct leads to the expression of an apolipoprotein-precursor-C_{Ub}-LexA-VP16 fusion protein. After plating the transformed yeast cells on SD-AHLW, the plates were

incubated for 5 days at 30°C. In this assay, an absence of colonies indicates lack of non-specific interactions.

Expression Verification of the Prey Constructs

Protein expression of the mutated prey constructs was verified by western blot analysis. The NMY51 yeast strain was transformed with the prey constructs and grown overnight at 30°C under shaking in 10 ml SD-W medium. Membrane proteins were extracted as described (Karginov and Agaphonov, 2016). The samples were loaded onto a 12% SDS polyacrylamide gel and after separation transferred to Hybond electrochemiluminescence (ECL) nitrocellulose membrane (GE Healthcare, Little Chalfont, Buckinghamshire, United Kingdom). Blocking of the membranes was done with 5% low-fat powdered milk (Roth) in TBS-T [137 mM NaCl, 10 mM Tris (Roth), pH 8.0, 0.05% Tween-20 (Roth)] for 60 min prior to an overnight exposure with the primary antibody at 4°C in blocking solution. Detection of prey fusion proteins was performed using a mouse monoclonal anti-HA antibody (HA-Tag Monoclonal Antibody 5B1D10, 1:500, Thermo Fisher Scientific, Waltham, MA, United States, Cat #32-6700, Lot #QC215112). After three washing steps in TBS-T the membrane was incubated with a horseradish peroxidase (HRP)-labelled rabbit polyclonal anti-mouse antibody (anti-mouse IgG, 1:3000, Sigma-Aldrich, St. Louis, Missouri, United States, Cat #A9044, Lot #018M4899V). The western blot was visualized using the Intas ChemoStar and the Intas ChemoStar Imager software.

Site-Directed Mutagenesis

The mutated NTCP constructs were generated by site-directed mutagenesis as reported before (Bennien et al., 2018), using previously reported templates (König et al., 2014; Noppes et al., 2019) depending on the individual experiment, i.e., NTCP-prey construct, NTCP-bait construct, NTCP-GFP, NTCP-FLAG, and NTCP-V5-His, respectively. The GXXXG/A motifs in TMD2 and TMD7 were mutated into LXXXL using oligonucleotide primers synthesized from Metabion International AG (Planegg, Germany) (see Table 1). All mutated sequences were sequence-verified by Sanger sequencing (Microsynth AG, Balgach, Switzerland).

Colocalization in Transfected HEK293 Cells

For colocalization studies, GFP- and mScarlet-tagged NTCP constructs were transiently transfected into HEK293 cells as described (Müller et al., 2018). Cells were seeded into µ-Slide chambered coverslips (Ibidi, Martiensried, Germany) and transfected with 0.25 µg of each appropriate construct pDNA using Lipofectamine 2000 (Thermo Fisher Scientific). Finally, 50 µl of the Lipofectamine-pDNA-complex were added to the cells before incubation was started at 37°C for 2 days. Staining of the nuclei was performed with Hoechst33342 (1 µg/ml, Thermo Fisher Scientific). Fluorescence microscopy was performed on a Leica DMI6000 B fluorescence microscope (Leica, Wetzlar, Germany). All images were taken and analyzed with the Leica software LAS X.

TABLE 1 | Oligonucleotide primers used for site-directed mutagenesis of NTCP.

Primer	Sequence (5'–3')
NTCP_G60L_A64L_forward	gaagccta aa ctgctggccat ctc ctctggtggccacagatg
NTCP_G60L_A64L_reverse	catactgtgccaccag gag gatggccag cag tttaggcttc
NTCP_G233L_G237L_forward	coctgatgcctttt atc ttcttctgct ctt tatgtctctctg
NTCP_G233L_G237L_reverse	cagagagaacata aag cagcagaa gaga ataaaaggcatcaggg

Bold letters in the respective primer sequences indicate the codons changed for leucine.

Co-Immunoprecipitation and Western Blotting

HEK293 cells were transiently transfected with the respective mutants of the NTCP-V5-His and/or NTCP-FLAG constructs, being G₆₀LXXXA₆₄L (TMD2), G₂₃₃LXXXG₂₃₇L (TMD7), and the double mutant G₆₀LXXXA₆₄L/G₂₃₃LXXXG₂₃₇L. Six well plates were seeded with HEK293 cells and transfected with 1.2 µg of each pDNA of the respective constructs by Lipofectamine 2000 and incubated for 48 h at standard culture conditions. All following steps were performed at 4°C, if not otherwise indicated. Cells were washed with phosphate-buffered saline (PBS, containing 137 mM NaCl, 2.7 mM KCl (Roth), 1.5 mM KH₂PO₄ (Roth), 7.3 mM Na₂HPO₄ (Roth), pH 7.4, 37°C) prior to be harvested in 400 µl co-IP lysis buffer consisting of 20 mM Tris-HCl (Roth), 135 mM NaCl (Roth), 10% glycerol (Roth) and 1% Nonidet P40 (BioChemica). After centrifugation at 10,000 g for 10 min, the amount of protein in each sample was determined using the BCA Protein Assay Kit (Novagen, St. Louis, United States). Then, the samples were set to 500 µg of total protein. The samples were mixed with 30 µl of Pierce Anti-Flag Magnetic Agarose (Invitrogen, Carlsbad, CA, United States) and incubated overnight in a rotation stand. The agarose was washed three times using co-IP lysis buffer and then heated at 95°C for 10 min with Laemmli sample buffer containing 2% SDS (Roth), 10% glycerol (Roth), 0.002% bromophenol blue (Merck), 62.5 mM Tris-HCl (Roth) and 5% 2-mercaptoethanol (Roth). After cooling to room temperature, samples were loaded onto a 12% SDS polyacrylamide gel. Western blotting was performed as described above. The fusion proteins were detected using an anti-V5 rabbit polyclonal antibody (1:3000, Sigma-Aldrich, Cat #V8137, Lot #21160752) or an anti-FLAG rabbit polyclonal antibody (1:2000, Sigma-Aldrich, Cat #F7425, Lot #078M4886V). Glyceraldehyde 3-phosphate dehydrogenase (GAPDH) served as loading control and was detected using an anti-GAPDH polyclonal antibody (1:2000, Sigma-Aldrich, Cat #SAB2500450, Lot #6377C3). As secondary antibodies, a HRP-labelled goat polyclonal anti-rabbit antibody (Invitrogen, Cat #31460, Lot #UK293475) and a HRP-labelled rabbit polyclonal anti-goat antibody (Invitrogen, Cat #81-1620, Lot #VH308190) were used. The western blots were visualized using the Intas ChemoStar and the Intas ChemoStar Imager software. For quantification of the band intensities, the raw images of 10-min exposure time were used and the whole lane intensities were measured using ImageJ (Schneider et al., 2012). The

quotient of the intensities between the co-IP (anti-V5) and the lysate (anti-FLAG) bands was calculated and the quotient of wild-type NTCP was set to 100%.

Deglycosylation of Na⁺/Taurocholate Co-Transporting Polypeptide

HEK293 cells were mono-transfected with the mutated NTCP-FLAG constructs and lysed at 48 h post transfection as described above. After determination of the protein concentration, 10X Glycoprotein Denaturing Buffer containing 5% SDS and 0.4 M DTT (New England Biolabs, Massachusetts, United States, Cat #P0704S, Lot #0361002) were added to 50 µg of total protein. Samples were heated at 95°C for 10 min. Afterwards, each sample was mixed with a mastermix containing 10X G7 Reaction Buffer (composed of 0.5 M sodium phosphate, pH 7.5), 10% NP-40, and PNGase F (New England Biolabs, Massachusetts, United States, Cat #P0704S, Lot #0361002) followed by an incubation step at 37°C for 1 h. Glycosylated and deglycosylated NTCPs were visualized by western blotting using the Intas ChemoStar and the Intas ChemoStar Imager software. For quantification of the band intensities, the intensities of the area of interest between 50 and 60 kDa in the glycosylated NTCP samples were determined using ImageJ. The intensity of wild-type NTCP was set to 100%.

Binding Experiments With the Hepatitis B Virus/Hepatitis D Virus-Derived preS1₂₋₄₈ Peptide

HBV and HDV attach to NTCP via their myristoylated preS1-lipopeptide comprising the N-terminal amino acids 2-48 of the large HBV surface protein, briefly called preS1 (Glebe et al., 2005; Glebe and Bremer, 2013). The preS1-mediated HBV/HDV attachment to NTCP triggers virus entry into hepatocytes (Yan et al., 2015; Li and Urban, 2016). Therefore, preS1 peptide binding to NTCP not only indicates plasma membrane expression of NTCP, but also is used as a surrogate susceptibility parameter for *in vitro* HBV/HDV infection (Müller et al., 2018). Here, a preS1 peptide C-terminally labeled with the fluorescent dye AlexaFluor568 (further referred to as preS1-AF568, Biosynthesis, Lewisville, Texas, United States) was used for binding experiments on NTCP-transfected HEK293 cells as described before (König et al., 2014) in order to indicate plasma membrane expression of NTCP. HEK293 cells, expressing the green fluorescent wild-type or mutant NTCP-GFP fusion protein (see above) were incubated with 50 nM preS1-AF568 peptide in

DMEM for 20 min at 37°C. After intensive washing with PBS, GFP-derived green fluorescence as well as AF568-derived red fluorescence were analyzed on a Leica DMI6000 B fluorescent microscope.

Hepatitis B Virus Infection Experiments

HepG2 cells were inoculated with 50,000 genome equivalents of HBV particles per cell for 16 h. HBV was produced *in vitro* as reported before (König et al., 2014). For infection experiments, hepatocyte growth medium (HGM) was used, consisting of William's E Medium (Thermo Fisher Scientific) supplemented with 2% bovine serum albumin (Roth), 2 mM L-Glutamine (Thermo Fisher Scientific), 100 µg/ml gentamicin (Thermo Fisher Scientific), 10 nM dexamethasone (Sigma-Aldrich), 1 mM sodium pyruvate (Thermo Fisher Scientific), and 1X Insulin-Transferrin-Selen (Thermo Fisher Scientific). During the 16 h infection period, 2% DMSO (Merck, Darmstadt, Germany), 4% polyethylene glycol 8,000 (PEG; Sigma-Aldrich), a mix of antibiotics and antimycotics as well as 100 ng/ml human epidermal growth factor (EGF; Peprotech, Cranbury, New Jersey, United States) were added as reported (König et al., 2014; Müller et al., 2018). Cells were maintained with HGM lacking PEG and EGF. Medium was changed every three days until fixation at day 12 post infection with 3% paraformaldehyde (Sigma-Aldrich) in PBS for 30 min at room temperature (RT). 0.2% Triton X 100 (Roth) in PBS for 30 min at RT was utilized to permeabilize cells, followed by blocking unspecific epitopes with 5% bovine serum albumin (Roth) in PBS for 30 min at RT. For detection of HBV core (HBc) protein as an indicator of HBV infection, cells were incubated for 1 h at 37°C with a polyclonal guinea pig-HBcAg antiserum (1:1000 dilution) and thereafter with anti-guinea pig IgG AF568 (1:800 dilution, Thermo Fisher Scientific Cat# A-11075, Lot# 1885925) for 1 h at 37°C. Nuclei were stained with Hoechst33342 (1 µg/ml, Thermo Fisher Scientific).

Transport Function of the Na⁺/Taurocholate Co-Transporting Polypeptide GXXXG/A Mutants

Functional characterization of the mono- and co-expressed NTCP wild-type and mutant constructs was performed after transient transfection into HEK293 cells as described previously (Müller et al., 2018). HEK293 cells were cultured as described above and were plated into 24-well plates (Sarstedt, Nümbrecht, Germany) with 3×10^5 cells per well for the transport experiments. Cells were transfected with the indicated constructs with the identical absolute amount of 0.5 µg pDNA per well by Lipofectamine 2000. After 48 h of incubation, cells were washed three times with PBS. Then, cells were pre-incubated with transport buffer (142.9 mM NaCl, 4.7 mM KCl, 1.2 mM MgSO₄ (Roth), 1.2 mM KH₂PO₄, 1.8 mM CaCl₂ (Roth), and 20 mM HEPES (Roth), pH 7.4, 37°C) for 5 min. For uptake experiments, cells were incubated with 300 µl transport buffer containing 10 µM taurocholic acid (TC) spiked with [³H]TC for 10 min at 37°C. Uptake studies were terminated by removing the transport buffer followed by five

washing steps in PBS at 4°C. Afterwards, cells were lysed in 1 N NaOH (Roth) with 0.1% SDS and the cell-associated radioactivity of the lysate was determined by liquid scintillation counting. Additionally, protein content per well was determined for data normalization as described (Geyer et al., 2007).

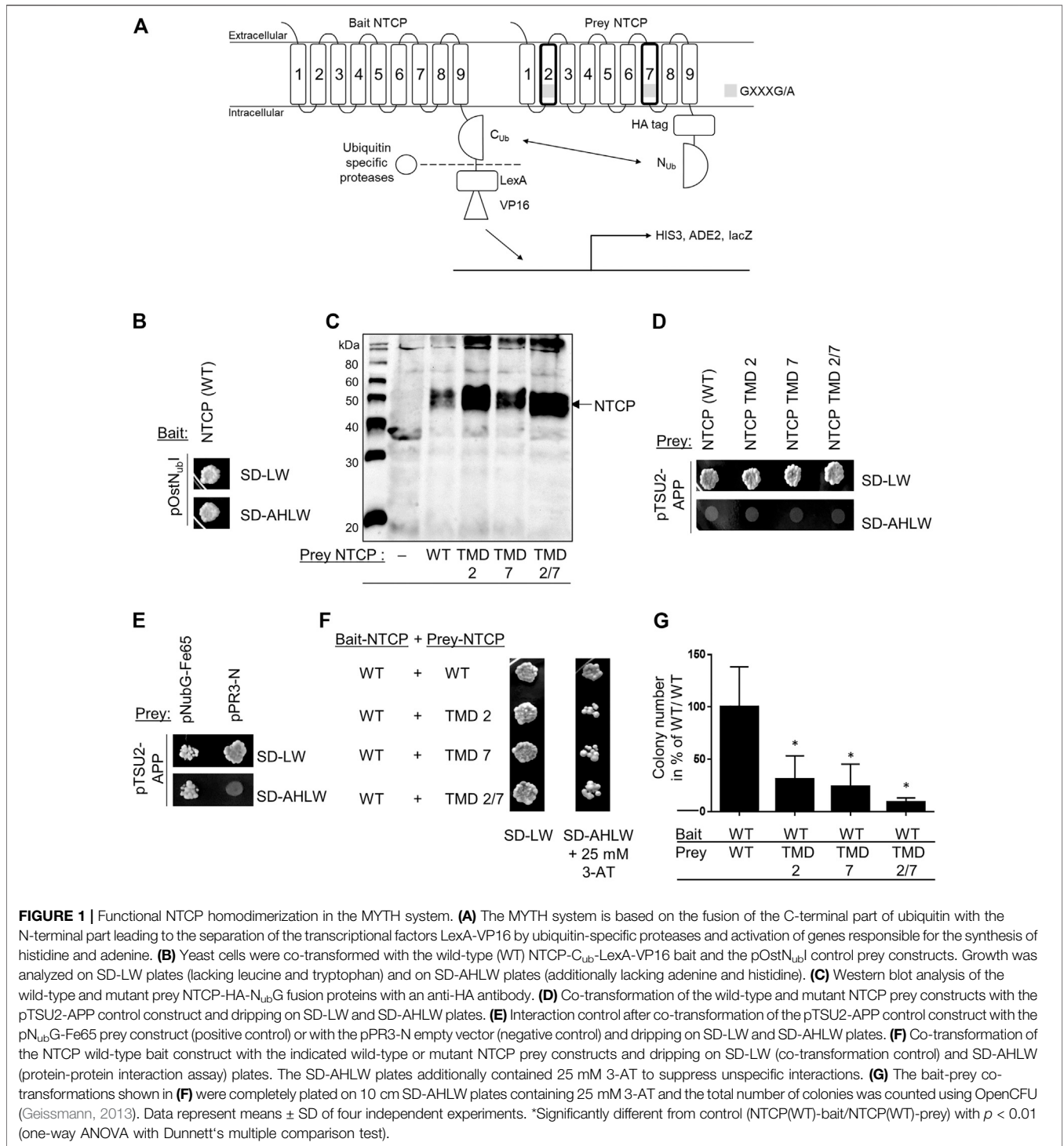
Homology Model of Human Na⁺/Taurocholate Co-Transporting Polypeptide

A 3D homology model of the human NTCP protein (GenBank accession No. NP_003040) was calculated with the SWISS-MODEL tool (<https://swissmodel.expasy.org/>) based on the crystal structure of the bacterial homolog ASBT from *Neisseria meningitidis* (PDB: 3zuy). Within this model the N-terminus of NTCP is oriented to the outside and the C-terminus to the intracellular site, according to experimental data (König et al., 2014). Amino acids 1–26 of the NTCP N-terminus as well as amino acids 309–349 of the C-terminus could not be included in the models, meaning that the NTCP homology model only covers amino acids 27–308, from TMD1 to TMD9.

RESULTS

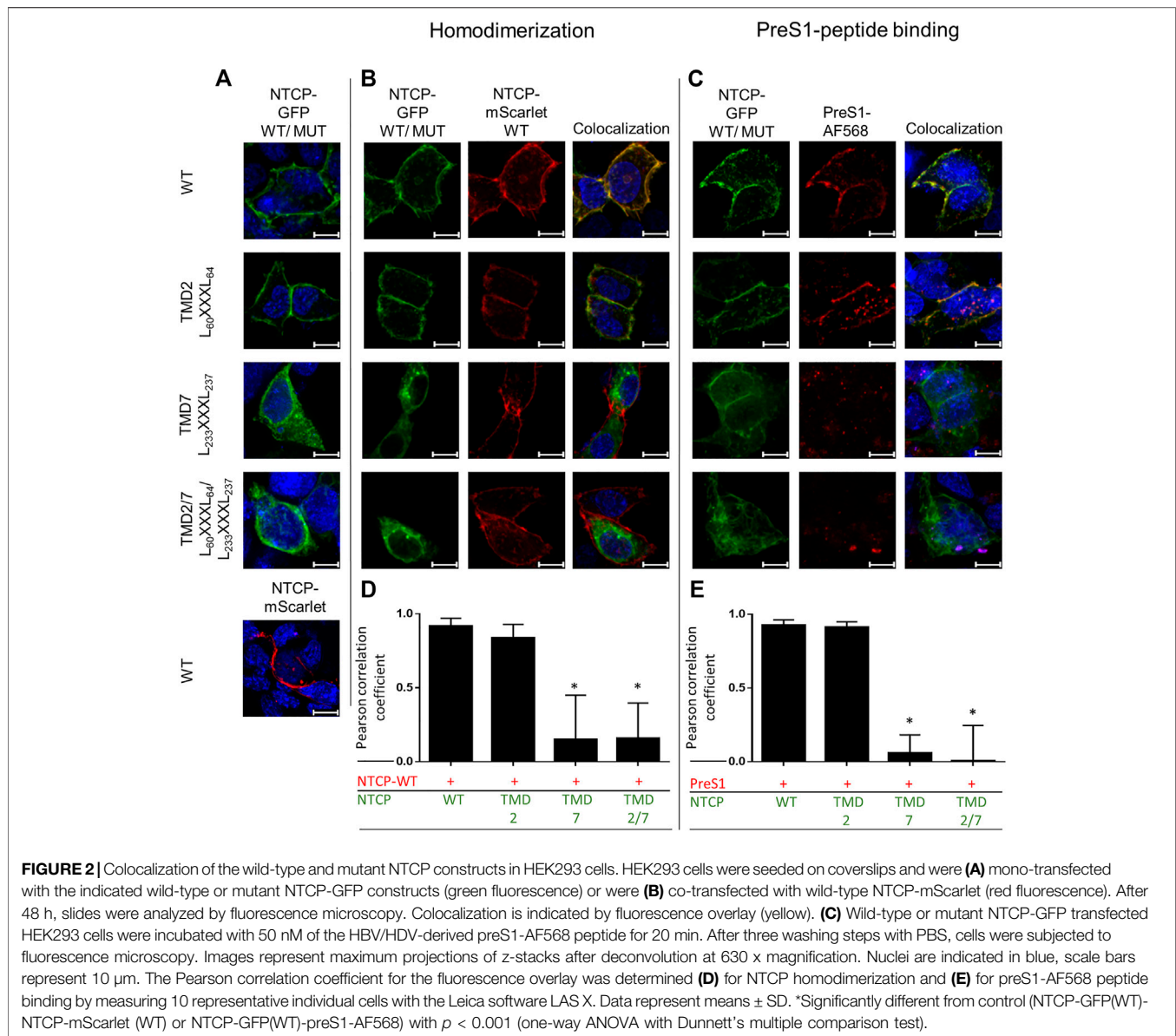
Na⁺/Taurocholate Co-Transporting Polypeptide Homodimerization in the Membrane-Based Yeast-Two Hybrid System

In order to analyze the role of the G₆₀XXXA₆₄ and G₂₃₃XXXG₂₃₇ sequence motifs for the dimerization of NTCP, the MYTH system was used to study dynamic protein-protein interactions of membrane proteins. Apart from the C-terminally C_{ub}-LexA-VP16-tagged bait and C-terminally HA-N_{ub}G-tagged prey wild-type NTCP constructs, the NTCP mutant prey constructs G₆₀LXXXA₆₄L (TMD2), G₂₃₃LXXXG₂₃₇L (TMD7), and G₆₀LXXXA₆₄L/G₂₃₃LXXXG₂₃₇L (TMD2/7) were generated by site-directed mutagenesis. Successful co-transformation of the yeasts with the wild-type bait and the mutant prey NTCP constructs was verified in all experiments by plating on SD-LW plates, lacking the amino acids leucine and tryptophan (Figure 1A). Expression of the NTCP-C_{ub}-LexA-VP16 bait construct was confirmed by co-transformation with the pOst-N_{ub}I control prey vector. In this assay, N_{ub}I expression together with NTCP-C_{ub} reconstitutes split-ubiquitin, and so enables yeast growth on the SD-LW (co-transformation control) and SD-AHLW plates (control interaction assay) as shown in Figure 1B. This control assay indirectly confirms expression of the NTCP-C_{ub}-LexA-VP16 fusion protein in the yeast cells. In addition, protein expression from the prey NTCP constructs was confirmed by western blot analysis (Figure 1C). Yeast cells were transformed with the respective wild-type or mutant prey NTCP constructs and the extracted proteins were subjected to sodium dodecyl sulfate-polyacrylamide gel electrophoresis (SDS-PAGE). The C-terminally HA-tagged proteins were detected by an anti-HA antibody. Next, non-specific interactions of the NTCP mutant prey constructs were analyzed. In this assay,



the NTCP prey constructs were co-transformed with the bait control vector pTSU2-APP, from which the amyloid precursor protein APP is expressed. None of NTCP constructs showed any unspecific interaction with APP in this assay on SD-AHLW plates, whereas co-transformation was confirmed by growth on SD-LW plates (Figure 1D). In contrast, co-transformation of the yeasts with pTSU2-APP and the prey control vector pN_{ub}G-Fe65

confirmed growth (positive interaction control) on the selective plates, whereas co-transformation of pTSU2-APP with the empty prey vector pPR3-N did not show any growth (negative interaction control) as expected (Figure 1E). Finally, the NTCP bait construct was co-transformed with the NTCP prey mutant constructs G₆₀LXXXA₆₄L (TMD2), G₂₃₃LXXXG₂₃₇L (TMD7), and G₆₀LXXXA₆₄L/G₂₃₃LXXXG₂₃₇L (TMD2/7), as



well as with the wild-type NTCP prey construct for control (Figure 1F). The necessary amount of 3-aminotriazole (3-AT) to suppress unspecific interactions was previously determined to 25 mM (Noppes et al., 2019) and was also used here. In this assay, homodimerization of the NTCP wild-type bait and prey constructs was used as the positive interaction control and the amount of yeast cells counted for this interaction was set to 100% (Figure 1G). Interestingly, all mutant NTCP prey constructs revealed growth on the SD-AHLW plates after co-transformation with wild-type bait NTCP in several independent dripping experiments. However, counting of the absolute number of yeast colonies on the SD-AHLW plates then revealed clear differences from the wild-type control (Figure 1G). The total number of colonies was significantly lower for the $G_{60}LXXXA_{64}L$ (TMD2) mutant and declined even more for the $G_{233}LXXXG_{237}L$ (TMD7) mutant and the

$G_{60}LXXXA_{64}L/G_{233}LXXXG_{237}L$ (TMD2/7) double mutant. As in the yeast system it can not be differentiated if this drop of interaction results from less efficient intermolecular protein-protein interaction or from intramolecular changes affecting protein folding and sorting, this effect was analyzed in more detail in cell culture.

Subcellular Localization and Sorting of Na^+ /Taurocholate Co-Transporting Polypeptide Mutants

First, the question of subcellular localization and sorting of the NTCP mutants was addressed by transfections of HEK293 cells. For these experiments, NTCP-GFP and NTCP-mScarlet constructs served as templates for site-directed mutagenesis to enable expression of green fluorescent wild-type, $G_{60}LXXXA_{64}L$

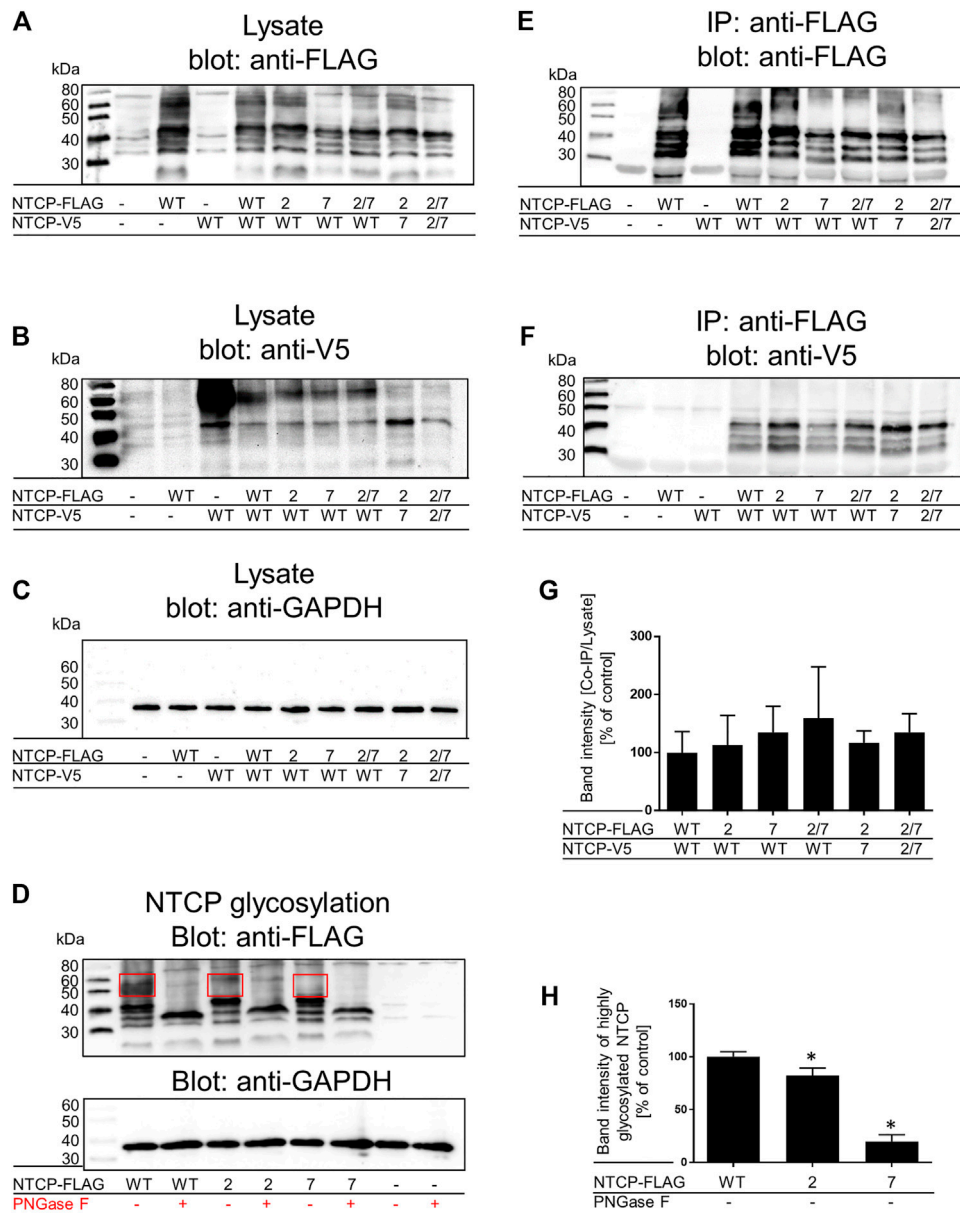


FIGURE 3 | Co-IP and glycosylation status of wild-type and mutant NTCPs. Wild-type and mutant NTCP-V5-His and NTCP-FLAG constructs were mono-transfected or co-transfected into HEK293 cells as indicated. Cell lysates were analyzed by western blotting with (A) an anti-FLAG antibody, (B) an anti-V5 antibody or (C) and anti-GAPDH antibody. Cell lysates from un-transfected cells were used as negative control, mono-transfected cells served as positive controls. In the figure legend the NTCP TMD2, TMD7 and TMD2/7 mutants are briefly indicated as “2”, “7” and “2/7”, respectively. These cell lysates were also used for IP with anti-FLAG agarose and then were processed for western blotting with (E) an anti-FLAG antibody or (F) an anti-V5 antibody. (G) Band intensities of three independent co-IP experiments were measured using ImageJ and signal intensities from the IP anti-V5 signals were normalized for the lysate anti-FLAG signals. Ratios were related to the NTCP(WT)-NTCP(WT) interaction, which was set to 100%. Data represent means ± SD of three independent experiments, one of which is representatively shown under (A–C), and (E, F). (D) Cell lysates of wild-type and mutant NTCP-FLAG mono-transfected HEK293 cells were subjected to deglycosylation with PNGaseF. The glycosylated and deglycosylated samples were visualized by western blotting with an anti-FLAG antibody and an anti-GAPDH antibody. (H) Band intensities of the highly glycosylated wild-type and mutant NTCPs (bands with apparent molecular weight of 50–60 kDa as indicated by frame) were quantified using ImageJ. The values were then compared to wild-type NTCP-FLAG, which was set to 100%. Data represent means ± SD of three independent experiments. *Significantly different from wild-type with $p < 0.05$ (one-way ANOVA with Dunnett’s multiple comparison test).

(TMD2), $G_{233}LXXXG_{237}L$ (TMD7), and $G_{60}LXXXA_{64}L/G_{233}LXXXG_{237}L$ (TMD2/7) NTCP-GFP fusion proteins. These constructs were either mono-transfected into HEK293 cells (Figure 2A) or were co-transfected with the red-fluorescent

wild-type NTCP-mScarlet fusion protein (Figure 2B). The wild-type NTCP-GFP construct showed nearly complete colocalization with NTCP-mScarlet in the plasma membrane (Figure 2D). This also applied for the NTCP- $G_{60}LXXXA_{64}L$ -GFP

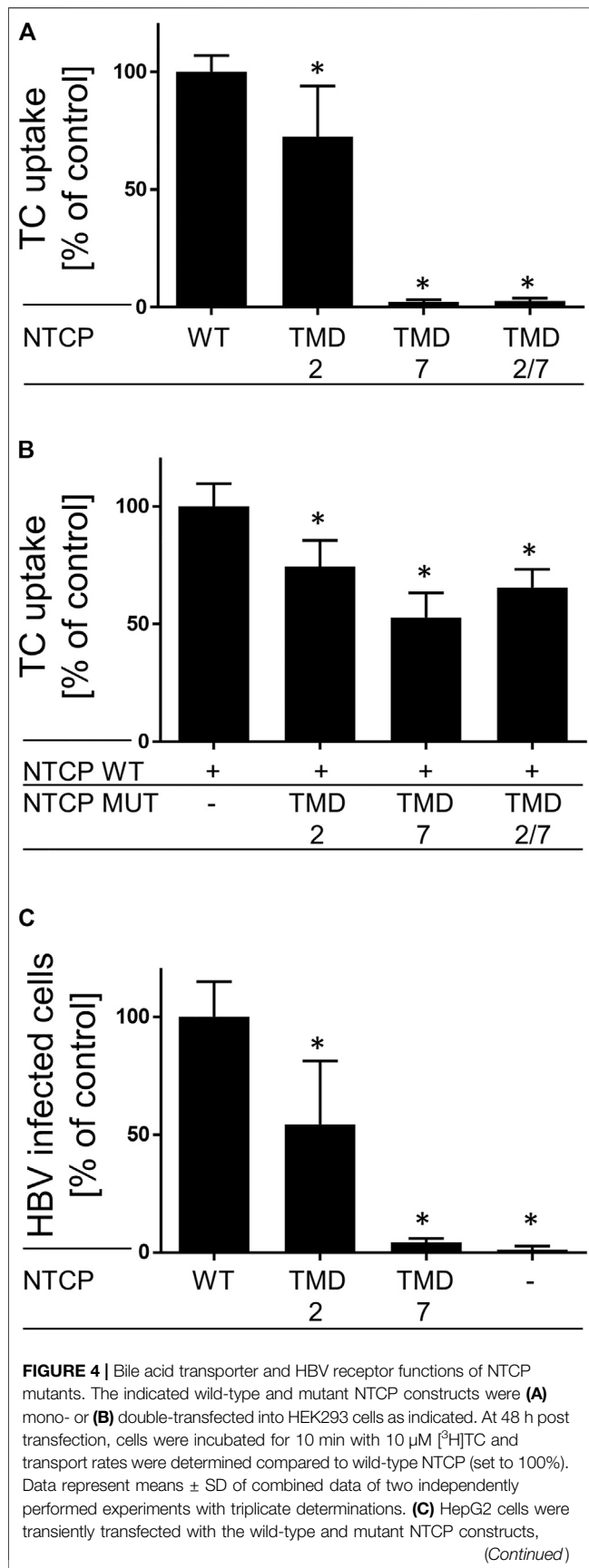


FIGURE 4 | respectively. Two days after transfection, cells were infected with HBV for 16 h. At 12 days post infection, cells were stained with an anti-HBc antibody. The numbers of HBV infected cells per well were counted using fluorescence microscopy. Data represents means \pm SD of two independent experiments each with triplicate determinations ($n = 6$). *Significantly lower compared with wild-type NTCP with $p < 0.05$ (one-way ANOVA with Dunnett's multiple comparison test).

TMD2 mutant, which closely co-localized with NTCP-mScarlet and showed only slightly reduced Pearson correlation coefficient compared to wild-type NTCP-GFP (Figure 2D). In addition, plasma membrane expression of NTCP-GFP and NTCP-G₆₀LXXXA₆₄L-GFP was confirmed by binding experiments with the HBV/HDV-derived red fluorescent preS1-AF568 peptide (Figure 2C). As the preS1 peptide is unable to penetrate the plasma membrane, it only binds to NTCP molecules which are expressed at the plasma membrane. As indicated in Figure 2C, preS1-AF568 peptide binding clearly highlights membrane expression of wild-type and TMD2 mutant NTCP-GFP as well as close overlay between the green and red fluorescence signals (Figure 2E). In contrast, the G₂₃₃LXXXG₂₃₇L (TMD7), and G₆₀LXXXA₆₄L/G₂₃₃LXXXG₂₃₇L (TMD2/7) NTCP-GFP mutant proteins seemed to be miss-sorted and did not appear in the plasma membrane. Therefore, neither colocalization with the NTCP-mScarlet protein (Figures 2B,D), nor with the preS1-AF568 peptide (Figures 2C,E) could be detected. These experiments clearly show that mutation of the GXXXG motif in TMD7 leads to retention of the respective NTCP-GFP protein in intracellular compartments.

Na⁺/Taurocholate Co-Transporting Polypeptide Homodimerization After Co-Immunoprecipitation

Next, the question of intermolecular protein-protein interactions was analyzed by co-IP experiments that were performed after co-expression of a wild-type NTCP-V5-His protein together with FLAG-tagged G₆₀LXXXA₆₄L (TMD2), G₂₃₃LXXXG₂₃₇L (TMD7), or G₆₀LXXXA₆₄L/G₂₃₃LXXXG₂₃₇L (TMD2/7) NTCP mutants in HEK293 cells (Figure 3). As indicated by the NTCP controls (A, lysate anti-FLAG; B, lysate anti-V5), wild-type (WT) and mutant NTCP-FLAG and NTCP-V5 proteins were expressed at comparable amounts and band pattern after co-transfection (Figures 3A,B). In addition, the loading control (Figure 3C, anti-GAPDH) showed equal protein amounts for all samples. The multiple NTCP bands most likely represent different degrees of glycosylation of NTCP, ranging from the unglycosylated form (with an apparent molecular weight of ~37 kDa), over less complex mannose glycosylated forms (at around 40 kDa), up to more complex glycosylated forms with molecular weights above 40 kDa (Figures 3A,B,D). After deglycosylation of the cell lysates with PNGase F, all these forms merged at a band with an apparent molecular weight of ~37 kDa (Figure 3D), most likely representing the unglycosylated full-length NTCP. Smaller bands that still appear after PNGase F treatment possibly represent N-terminally truncated non-glycosylated forms of

NTCP. Cell lysates of the double-transfected cells were subjected to IP with anti-FLAG agarose and the precipitates were analyzed by western blotting with anti-FLAG (IP, **Figure 3E**) or anti-V5 (co-IP, **Figure 3F**) antibodies. As indicated in **Figure 3F**, wild-type NTCP-FLAG as well as all NTCP-FLAG mutants co-precipitated the wild-type and mutant NTCP-V5 proteins to a certain degree. For quantification, the anti-V5 signals after co-IP were normalized for the anti-FLAG loading controls and data from three independent experiments are depicted in **Figure 3G**. No significant differences were observed between the NTCP wild-type and mutant co-IP signals. Of note, complex glycosylated forms of NTCP seemed not to be co-precipitated with NTCP-FLAG. At least no bands with apparent molecular weights above 40 kDa were detected with the anti-V5 antibody after co-IP (**Figure 3F**) in clear contrast to the loading control (**Figure 3B**). Appearance of these complex glycosylated forms of NTCP (apparent molecular weights of 50–60 kDa) were quantitatively analyzed for the wild-type NTCP as well as for TMD2 and TMD7 mutants. As shown in **Figures 3D,H**, under comparable protein amounts (loading control, anti-GAPDH) the TMD2 mutant showed slightly but significantly lower levels of complex glycosylated forms of NTCP, while in the TMD7 mutant these forms were almost completely absent.

GXXXG/A Mutation and Bile Acid Transporter/Virus Receptor Function of Na⁺/Taurocholate Co-Transporting Polypeptide

Finally, effects of GXXXG/A mutation on the bile acid transporter and virus receptor functions of NTCP were analyzed. To check if the physiological bile acid transport function of the NTCP mutants is still active, the respective constructs were transiently transfected into HEK293 cells for a subsequent measurement of taurocholate (TC) uptake. As shown in **Figure 4A**, the G₆₀LXXXA₆₄L (TMD2) mutant is still active in maintaining TC transport function at a level of about 75% compared to wild-type NTCP. In contrast, the TMD7 and TMD2/7 mutants, which do not reach the plasma membrane (see **Figure 2B**), were completely transport deficient (**Figure 4A**). Furthermore, it was investigated whether wild-type NTCP can be influenced in its transport behavior by co-expression and potential dimerization with one of these mutants. So, cells were co-transfected with wild-type NTCP and the respective mutant, and TC uptake was analyzed as before (**Figure 4B**). Co-expression of the G₆₀LXXXA₆₄L (TMD2) mutant with wild-type NTCP showed moderate reduction of TC uptake, similar to the mono-transfection condition (**Figure 4A**). In contrast, the G₂₃₃LXXXG₂₃₇L (TMD7) mutant maintained only about 50% of the transport rate of the wild-type NTCP (**Figure 4B**). Of note, formation of wild-type NTCP homodimers cannot be avoided here, so that transport rates are not expected to drop to zero in this experimental setup.

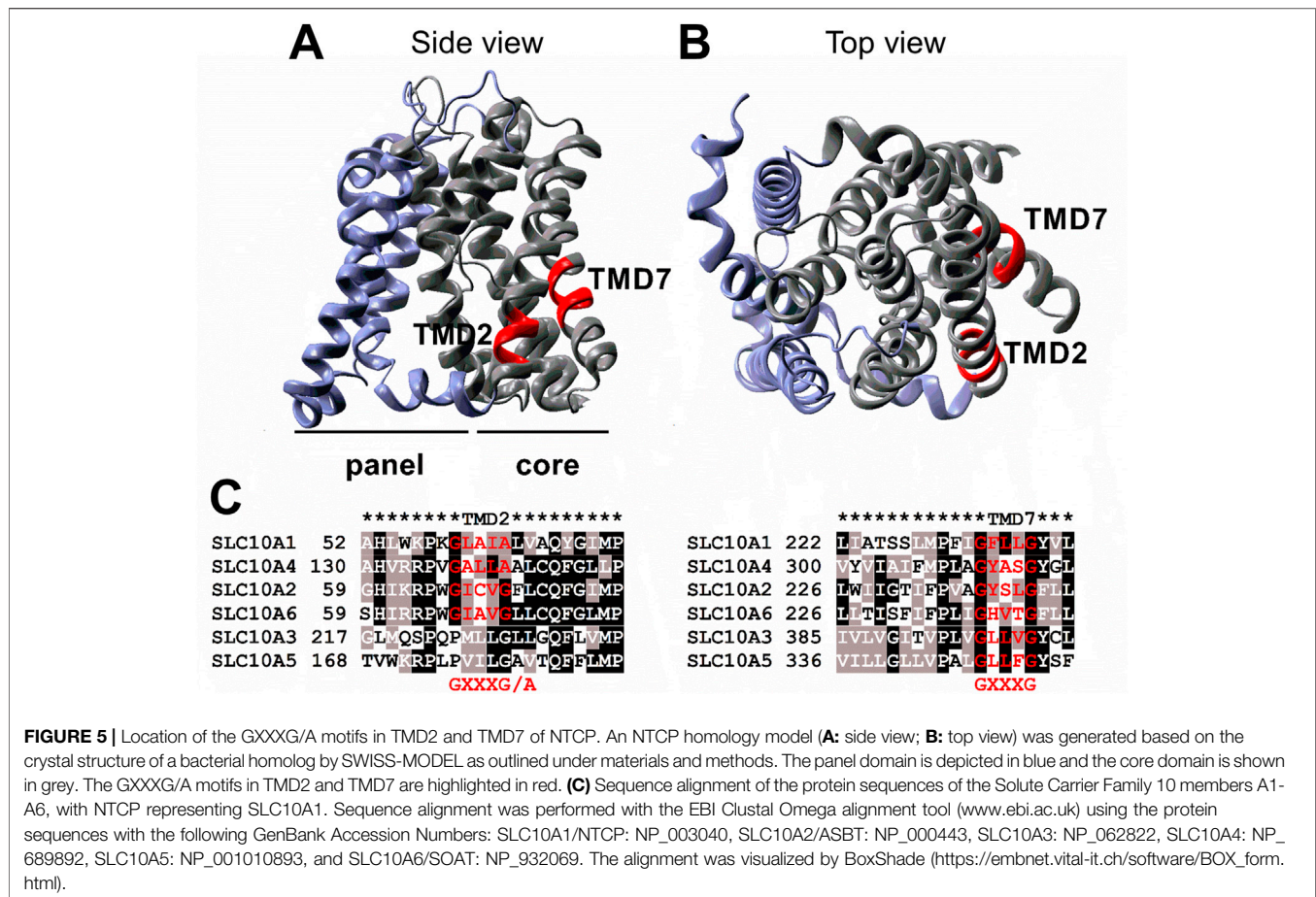
In order to analyze if mutation of the NTCP GXXXG/A motifs would have any effect on HBV susceptibility of the respective NTCP, wild-type and mutant NTCP constructs were transiently transfected into HepG2 cells and were used for *in vitro* HBV infection. At day 12 post infection, cells were subjected to fixation

and the HBV core protein was stained using a polyclonal guinea pig-HBcAg antiserum (**Figure 4C**). After expression of the TMD2 mutant the *in vitro* HBV infection rate dropped to about 50% compared with wild-type NTCP. Even more pronounced, HepG2 cells expressing the TMD7 NTCP mutants were completely insensitive against HBV infection.

DISCUSSION

Na⁺/Taurocholate Co-Transporting Polypeptide Dimerization and Hepatitis B Virus/Hepatitis D Virus Susceptibility

The aim of the present study was to analyze the molecular determinants and regulation of NTCP homodimerization. Homodimerization has been identified as a typical feature of NTCP (Bijsmans et al., 2012) and also other members of the SLC10 carrier family (Noppes et al., 2019), and more recently was also found to be relevant for the HBV/HDV virus receptor function of NTCP (Fukano et al., 2018). It was described that NTCP homodimerization is a prerequisite for cellular entry of the virus-NTCP complex and that the antidiabetic drug troglitazone is an appropriate inhibitor of this interaction. Since it was observed that the amount of preS1-peptide binding to NTCP dropped significantly when NTCP was kept in a monomeric state, this study claimed that blocking of NTCP homodimerization might be a novel strategy for HBV/HDV entry inhibition (Fukano et al., 2018). Furthermore, this study used NTCP peptide fragments, each displaying a length of 20 amino acids, which covered the whole NTCP sequence and investigated their role for NTCP dimerization and HBV/HDV susceptibility. The authors found that the peptide fragment derived from NTCP amino acids 221–240 prevented NTCP homodimerization and preS1-peptide binding. Interestingly, this peptide fragment covers the G₂₃₃XXXG₂₃₇ motif in TMD7 of NTCP that was closer analyzed in the present study. Therefore, it was hypothesized in the present study that this motif might be involved in NTCP homodimerization. In addition, a similar GXXXA motif in TMD2 was identified and analyzed. In order to investigate the role of these two sequence motifs of NTCP, different methods were applied that allowed investigation of NTCP sorting and homodimerization, as well as NTCP's functions as bile acid transporter and virus receptor. We used the MYTH system, which allows detection of dynamic protein-protein interactions in living cells (Stagljar et al., 1998) and co-IP as a method more focused on static protein-protein interactions in cell lysates (Phizicky and Fields, 1995). Moreover, we checked the mutants for bile acid transport function as well as for susceptibility to HBV infection and preS1 peptide binding (Glebe et al., 2005). Finally, the sorting behavior of the mutated NTCP constructs was analyzed by fluorescence microscopy. As protein dimerization of membrane proteins is a complex process that involves correct folding and assembly in the ER, trafficking to the plasma membrane and dynamic conformational changes within the plasma membrane, this question cannot be addressed just by a single method.



Furthermore, it has to be emphasized that all used methods direct quite different aspects of the dimerization and sorting process. This has to be considered when data seem not to be consistent between the different methods.

The GXXXG Motif in Sorting and Dimerization

Since its discovery in human GpA as a dimerization motif in 1992 (Lemmon et al., 1992), the role of the GXXXG motif for homodimerization has been analyzed in a variety of transmembrane proteins (Teese and Langosch, 2015). This motif has a particular prevalence in transmembrane helices (Senes et al., 2000) and is often conserved among families of membrane transporters (Liu et al., 2002), as it is also the case for the solute carrier family SLC10. One GXXXG/A motif is present in TMD2 of the members SLC10A1, A2, A4 and A6, whereas the GXXXG motif in TMD7 is present in the SLC10 carriers A1–A6 (Figures 5A–C). In the present study, both sequence motifs were only analyzed for human NTCP (SLC10A1), but this might also be representative for the other SLC10 carrier family members. However, it has to be considered that the GXXXG/A motifs analyzed in the present study are not found in the bacterial ASBT sequence from *Neisseria meningitidis*, which was used as template for the NTCP homology model depicted in Figures 5A,B.

The MYTH experiments allowed the investigation of dynamic protein-protein interactions in living cells. Expression of all NTCP wild-type and mutant proteins was confirmed in the yeast cells, but their sorting could not be experimentally analyzed. Most interestingly, co-expression of the wild-type NTCP protein as a bait together with the TMD2 and TMD7 mutants of NTCP as preys revealed a significant decline in functional protein-protein interactions when one of these motifs, or both of them were mutated (Figure 1). However, in the MYTH system it cannot be differentiated whether intermolecular protein-protein interactions are directly affected or if the NTCP mutants are not properly folded and sorted, and as a secondary effect abolish functional protein-protein interaction. In order to differentiate between these possible mechanisms, additional experiments were performed in HEK293 and HepG2 cells that addressed sorting, membrane expression, protein-protein interaction and functionality of NTCP.

Fluorescence microscopy of respective GFP- or mScarlet-tagged wild-type and mutant NTCP proteins as well as binding experiments with the preS1-AF568 peptide then revealed that the TMD2 mutant was correctly sorted to the plasma membrane, where NTCP normally fulfills its role as a bile acid transporter and HBV/HDV virus receptor (Figure 2). Accordingly, the bile acid transport function and preS1 binding capability were almost completely preserved in this mutant. In contrast, mutation of the GXXXG motif in TMD7

(G₂₃₃LXXXG₂₃₇L) led to an intracellular accumulation of the NTCP mutant protein in the ER and Golgi compartments, accompanied by a loss of transport function (Figure 4A) and preS1 binding (Figures 2C,E). Based on this data, it can be supposed that the G₂₃₃LXXXG₂₃₇ TMD7 sequence motif of NTCP is critical for correct protein folding or proper packing of the transmembrane segments that would be a prerequisite for its trafficking into the plasma membrane (Eilers et al., 2000). The incomplete glycosylation of the TMD7 mutant is an additional hint that protein folding and sorting are affected in this mutant, as only correctly folded proteins underwent complex glycosylation (Appelman et al., 2017). In contrast to these effects on protein folding and sorting, the TMD2 and TMD7 mutants showed no effect on co-IP together with the wild-type protein as indicated in Figures 3F,G. However, it is interesting to note that only apparently unglycosylated NTCP forms appear on the western blots after co-IP. This could mean that the co-IP experiments have limited validity for the complex glycosylated forms of NTCP that are expressed at the plasma membrane. The largely differing band pattern for the glycosylated forms of the NTCP-FLAG and NTCP-V5 proteins in these experiments most likely result from the different tags/plasmids used. Similar effects were also observed in previous studies (Bijmans et al., 2012; Donkers et al., 2019). Although the MYTH experiments indicated effects of TMD2 and TMD7 mutation on direct protein-protein interaction of NTCP, this could not be confirmed in the co-IP experiments. This data indicates that the protein-protein interaction in the yeast might have been indirectly affected by misfolding and/or miss-sorting. Finally, the effects of TMD2 and TMD7 mutation on the susceptibility of NTCP to mediate *in vitro* HBV infection were of interest. Whereas, in HepG2 cells transiently transfected with the TMD7 mutant NTCP protein almost no infection was detected, the infection rate dropped to 50% for the TMD2 mutant (Figure 4). As this effect of TMD2 mutation was much higher than expected from the completely preserved preS1-binding capability, it can be speculated that the G₆₀LXXXA₆₄ motif in TMD2 might be important for the conformational changes of the NTCP protein that occur after virus binding and that finally trigger the endocytosis of the virus-receptor complex. However, another explanation for this effect could be an uneven expression of wild-type and mutant NTCP after transient transfection of HepG2 cells. Anyhow, this effect needs further investigation in subsequent studies. The loss of HBV susceptibility for the TMD7 mutant can be explained by the localization of this protein in intracellular compartments (Figures 2A–C) making it impossible for the virus to bind to NTCP on the cell surface. Generally, it has to be considered that mutational studies on potential dimerization motifs only provide valuable and significant information, when the mutation does neither affect the folding and three-dimensional structure of the protein, nor its proper sorting. As both aspects seem to be affected in particular for the G₂₃₃LXXXG₂₃₇L TMD7 mutant, one only can conclude a role of this motif for folding and sorting of NTCP. However, a role of this motif for NTCP dimerization can not be completely excluded, as this would require experiments with a correctly folded and sorted protein, what can not be achieved by mutational analysis of NTCP. This is the major limitation of the present study.

Role of the GXXXG Motif for Sorting, Dimerization and Transport Function in Other Carriers

The results from the present study go in line with previous studies that also analyzed the role of GXXXG motifs on the sorting and dimerization of membrane proteins. As an example, a study on the ATP-binding cassette transporter ABCG2 showed that GXXXG motifs promote proper packing of the transmembrane segments and this is important to form functional ABCG2 homodimers (Polgar et al., 2004). Respective glycine to leucine mutants lost this function, whereas glycine to alanine mutants were not affected (Polgar et al., 2004). This supports the hypothesis that the tight packing of transmembrane helices during dimerization is impaired when bulky residues like leucine are present. This might also apply for the G₂₃₃LXXXG₂₃₇L NTCP mutation of the present study by just disturbing proper TMD packing and thereby preventing the sorting process into the plasma membrane. Other studies with GXXXG mutation point to a direct role of this motif for protein-protein interaction. As an example, another G₁₄₄LXXXG₁₄₈ motif of NTCP was analyzed in a previous study while searching for the interaction domain with the epidermal growth factor receptor (EGFR) that acts as an NTCP co-factor during internalization of the NTCP/virus receptor complex (Iwamoto et al., 2019). It was shown that G₁₄₄LXXXG₁₄₈A mutation strongly diminished the interaction between NTCP and EGFR, finally leading to decreased preS1-peptide binding and HBV/HDV infection rates in NTCP-transfected hepatoma cells (Iwamoto et al., 2019). Interestingly, the NTCP mutant G₆₀LXXXA₆₄L analyzed in the present study also showed a reduced susceptibility to *in vitro* HBV infection. However, in this case the signal of preS1-peptide did not differ from that of wild-type NTCP (Figure 2E). This data suggests that the G₆₀LXXXA₆₄ motif in TMD2 is not involved in preS1-peptide binding, but more likely in the internalization step of the virus/receptor complex.

The role of the GXXXG motif was also analyzed for drug carriers of the SLC22 family, such as organic anion transporter 1 (OAT1) (Duan et al., 2011). The authors showed that mutation of the GXXXG motif in TMD2 of OAT1 led to a complete loss of membrane expression and transport activity. Similar findings were also obtained for individual SLC17 carriers and for the mitochondrial oxoglutarate carrier (Cappello et al., 2007; Courville et al., 2010; Ruprecht and Kunji, 2020). These findings reflect quite well the properties of the NTCP G₂₃₃LXXXG₂₃₇L mutant observed in the present study and clearly indicate the important role of GXXXG motifs for proper folding and sorting of membrane carriers.

CONCLUSION

Prescreening of the TMD2 and TMD7 mutants of NTCP in the MYTH system revealed a clear drop in interactions after mutation of the respective GXXXG/A motifs. In the HEK293 cell model, membrane expression and bile acid transport activity were slightly reduced for the TMD2 mutant but were completely

abolished for the TMD7 and the TMD2/7 mutants, while co-IP experiments still showed intact protein-protein interactions. Susceptibility for *in vitro* HBV infection in transfected HepG2 cells was reduced to 50% for the TMD2 mutant, while the TMD7 mutant was not susceptible for HBV infection at all. We conclude that the GXXXG/A motif in TMD2 and even more pronounced that in TMD7 are important for proper folding and sorting of the NTCP protein, and so indirectly affect glycosylation, homodimerization, and bile acid transport of NTCP, as well as its HBV/HDV receptor function. So, against our initial hypothesis, the GXXXG/A motifs in TMDs 2 and 7 of NTCP seem not to be the primary sites for direct NTCP homodimerization, but might be part of a larger interaction domain that needs to be elucidated.

DATA AVAILABILITY STATEMENT

The original contributions presented in the study are included in the article/supplementary material, further inquiries can be directed to the corresponding author.

REFERENCES

- Anderson, S. M., Mueller, B. K., Lange, E. J., and Senes, A. (2017). Combination of Ca-H Hydrogen Bonds and van der Waals Packing Modulates the Stability of GxxxG-Mediated Dimers in Membranes. *J. Am. Chem. Soc.* 139 (44), 15774–15783. doi:10.1021/jacs.7b07505
- Appelman, M. D., Chakraborty, A., Protzer, U., McKeating, J. A., and van de Graaf, S. F. (2017). N-glycosylation of the Na⁺-Taurocholate Cotransporting Polypeptide (NTCP) Determines its Trafficking and Stability and Is Required for Hepatitis B Virus Infection. *PLoS One* 12 (1), e0170419. doi:10.1371/journal.pone.0170419
- Bennien, J., Fischer, T., and Geyer, J. (2018). Rare Genetic Variants in the Sodium-dependent Organic Anion Transporter SOAT (SLC10A6): Effects on Transport Function and Membrane Expression. *J. Steroid Biochem. Mol. Biol.* 179, 26–35. doi:10.1016/j.jsbmb.2017.09.004
- Bijsmans, I. T. G. W., Bouwmeester, R. A. M., Geyer, J., Faber, K. N., and van de Graaf, S. F. J. (2012). Homo- and Hetero-Dimeric Architecture of the Human Liver Na⁺-dependent Taurocholate Co-transporting Protein. *Biochem. J.* 441 (3), 1007–1016. doi:10.1042/bj20111234
- Cappello, A. R., Miniero, D. V., Curcio, R., Ludovico, A., Daddabbo, L., Stipani, I., et al. (2007). Functional and Structural Role of Amino Acid Residues in the Odd-Numbered Transmembrane α -Helices of the Bovine Mitochondrial Oxoglutarate Carrier. *J. Mol. Biol.* 369 (2), 400–412. doi:10.1016/j.jmb.2007.03.048
- Courville, P., Quick, M., and Reimer, R. J. (2010). Structure-function Studies of the SLC17 Transporter Sialin Identify Crucial Residues and Substrate-Induced Conformational Changes. *J. Biol. Chem.* 285 (25), 19316–19323. doi:10.1074/jbc.M110.130716
- Dawson, J. P., Weinger, J. S., and Engelman, D. M. (2002). Motifs of Serine and Threonine Can Drive Association of Transmembrane Helices. *J. Mol. Biol.* 316 (3), 799–805. doi:10.1006/jmbi.2001.5353
- Donkers, J. M., Appelman, M. D., and van de Graaf, S. F. J. (2019). Mechanistic Insights into the Inhibition of NTCP by Myrcludex B. *JHEP Rep.* 1 (4), 278–285. doi:10.1016/j.jhepr.2019.07.006
- Döring, B., Lütke, T., Geyer, J., and Petzinger, E. (2012). The SLC10 Carrier Family. *Curr. Top. Membr.* 70, 105–168. doi:10.1016/b978-0-12-394316-3.00004-1
- Duan, P., Wu, J., and You, G. (2011). Mutational Analysis of the Role of GxxxG Motif in the Function of Human Organic Anion Transporter 1 (hOAT1). *Int. J. Biochem. Mol. Biol.* 2 (1), 1–7.

AUTHOR CONTRIBUTIONS

MP, SM, KL, and JG conceived the experiments; MP, SM, and KL performed the experiments; MP, SM, KL, and JG analyzed and interpreted the results; SN, JA, NG, FL, and DG provided materials; MP, SM, KL, and JG wrote the manuscript. All authors reviewed and approved the manuscript.

FUNDING

This study was supported in part by the Deutsche Forschungsgemeinschaft (DFG, German Research Foundation) - Projektnummer 197785619 - SFB 1021.

ACKNOWLEDGMENTS

The authors thank Anita Neubauer, Regina Leidolf, and Silke Leiting for their excellent technical assistance and Dajana Gräfe for support regarding the yeast-two hybrid system.

- Eilers, M., Shekar, S. C., Shieh, T., Smith, S. O., and Fleming, P. J. (2000). Internal Packing of Helical Membrane Proteins. *Proc. Natl. Acad. Sci.* 97 (11), 5796–5801. doi:10.1073/pnas.97.11.5796
- Fukano, K., Tsukuda, S., Oshima, M., Suzuki, R., Aizaki, H., Ohki, M., et al. (2018). Troglitazone Impedes the Oligomerization of Sodium Taurocholate Cotransporting Polypeptide and Entry of Hepatitis B Virus into Hepatocytes. *Front. Microbiol.* 9, 3257. doi:10.3389/fmicb.2018.03257
- Geissmann, Q. (2013). OpenCFU, a New Free and Open-Source Software to Count Cell Colonies and Other Circular Objects. *PLoS One* 8 (2), e54072. doi:10.1371/journal.pone.0054072
- Geyer, J., Döring, B., Meerkamp, K., Ugele, B., Bakhiya, N., Fernandes, C. F., et al. (2007). Cloning and Functional Characterization of Human Sodium-dependent Organic Anion Transporter (SLC10A6). *J. Biol. Chem.* 282 (27), 19728–19741. doi:10.1074/jbc.M702663200
- Geyer, J., Wilke, T., and Petzinger, E. (2006). The Solute Carrier Family SLC10: More Than a Family of Bile Acid Transporters Regarding Function and Phylogenetic Relationships. *Naunyn-Schmied Arch. Pharmacol.* 372 (6), 413–431. doi:10.1007/s00210-006-0043-8
- Glebe, D., and Bremer, C. M. (2013). The Molecular Virology of Hepatitis B Virus. *Semin. Liver Dis.* 33 (2), 103–112. doi:10.1055/s-0033-1345717
- Glebe, D., Urban, S., Knoop, E. V., Çag, N., Krass, P., Grün, S., et al. (2005). Mapping of the Hepatitis B Virus Attachment Site by Use of Infection-Inhibiting preS1 Lipopeptides and tupaia Hepatocytes. *Gastroenterology* 129 (1), 234–245. doi:10.1053/j.gastro.2005.03.090
- Iwamoto, M., Saso, W., Sugiyama, R., Ishii, K., Ohki, M., Nagamori, S., et al. (2019). Epidermal Growth Factor Receptor Is a Host-Entry Cofactor Triggering Hepatitis B Virus Internalization. *Proc. Natl. Acad. Sci. USA* 116 (17), 8487–8492. doi:10.1073/pnas.1811064116
- Johnsson, N., and Varshavsky, A. (1994). Split Ubiquitin as a Sensor of Protein Interactions *In Vivo*. *Proc. Natl. Acad. Sci.* 91 (22), 10340–10344. doi:10.1073/pnas.91.22.10340
- Karginov, A., and Agaphonov, M. (2016). A Simple Enrichment Procedure Improves Detection of Membrane Proteins by Immunoblotting. *Biotechniques* 61 (5), 260–261. doi:10.2144/000114474
- Kirstgen, M., Lowjaga, K., Müller, S. F., Goldmann, N., Lehmann, F., Alakurtti, S., et al. (2020). Selective Hepatitis B and D Virus Entry Inhibitors from the Group of Pentacyclic Lupane-type Betulin-Derived Triterpenoids. *Sci. Rep.* 10 (1), 21772. doi:10.1038/s41598-020-78618-2
- König, A., Döring, B., Mohr, C., Geipel, A., Geyer, J., and Glebe, D. (2014). Kinetics of the Bile Acid Transporter and Hepatitis B Virus Receptor Na⁺/taurocholate

- Cotransporting Polypeptide (NTCP) in Hepatocytes. *J. Hepatol.* 61 (4), 867–875. doi:10.1016/j.jhep.2014.05.018
- Lemmon, M. A., Flanagan, J. M., Treutlein, H. R., Zhang, J., and Engelman, D. M. (1992). Sequence Specificity in the Dimerization of Transmembrane α -helices. *Biochemistry* 31 (51), 12719–12725. doi:10.1021/bi00166a002
- Li, W., and Urban, S. (2016). Entry of Hepatitis B and Hepatitis D Virus into Hepatocytes: Basic Insights and Clinical Implications. *J. Hepatol.* 64 (1 Suppl. 1), S32–S40. doi:10.1016/j.jhep.2016.02.011
- Liu, Y., Engelman, D. M., and Gerstein, M. (2002). Genomic Analysis of Membrane Protein Families: Abundance and Conserved Motifs. *Genome Biol.* 3 (10), research0054. doi:10.1186/gb-2002-3-10-research0054
- MacKenzie, K. R., Prestegard, J. H., and Engelman, D. M. (1997). A Transmembrane helix Dimer: Structure and Implications. *Science* 276 (5309), 131–133. doi:10.1126/science.276.5309.131
- Müller, S. F., König, A., Döring, B., Glebe, D., and Geyer, J. (2018). Characterisation of the Hepatitis B Virus Cross-Species Transmission Pattern via Na⁺/taurocholate Co-transporting Polypeptides from 11 New World and Old World Primate Species. *PLoS One* 13 (6), e0199200. doi:10.1371/journal.pone.0199200
- Noppes, S., Müller, S. F., Bennien, J., Holtemeyer, M., Palatini, M., Leidolf, R., et al. (2019). Homo- and Heterodimerization Is a Common Feature of the Solute Carrier Family SLC10 Members. *Biol. Chem.* 400(10), 1371–1384. doi:10.1515/hsz-2019-0148
- Phizicky, E. M., and Fields, S. (1995). Protein-protein Interactions: Methods for Detection and Analysis. *Microbiol. Rev.* 59 (1), 94–123. doi:10.1128/mr.59.1.94-123.1995
- Polgar, O., Robey, R. W., Morisaki, K., Dean, M., Michejda, C., Sauna, Z. E., et al. (2004). Mutational Analysis of ABCG2: Role of the GxxxG Motif. *Biochemistry* 43 (29), 9448–9456. doi:10.1021/bi0497953
- Ruprecht, J. J., and Kunji, E. R. S. (2020). The SLC25 Mitochondrial Carrier Family: Structure and Mechanism. *Trends Biochem. Sci.* 45 (3), 244–258. doi:10.1016/j.tibs.2019.11.001
- Russ, W. P., and Engelman, D. M. (2000). The GxxxG Motif: a Framework for Transmembrane helix-helix Association. *J. Mol. Biol.* 296 (3), 911–919. doi:10.1006/jmbi.1999.3489
- Schneider, C. A., Rasband, W. S., and Eliceiri, K. W. (2012). NIH Image to ImageJ: 25 Years of Image Analysis. *Nat. Methods* 9 (7), 671–675. doi:10.1038/nmeth.2089
- Senes, A., Gerstein, M., and Engelman, D. M. (2000). Statistical Analysis of Amino Acid Patterns in Transmembrane Helices: the GxxxG Motif Occurs Frequently and in Association with β -branched Residues at Neighboring Positions. *J. Mol. Biol.* 296 (3), 921–936. doi:10.1006/jmbi.1999.3488
- Shneider, B. L. (1995). Expression Cloning of the Ileal Sodium-dependent Bile Acid Transporter. *J. Pediatr. Gastroenterol. Nutr.* 20 (2), 233–234. doi:10.1097/00005176-199502000-00016
- Stagljari, I., and Fields, S. (2002). Analysis of Membrane Protein Interactions Using Yeast-Based Technologies. *Trends Biochem. Sci.* 27 (11), 559–563. doi:10.1016/s0968-0004(02)02197-7
- Stagljari, I., Korostensky, C., Johnsson, N., and te Heesen, S. (1998). A Genetic System Based on Split-Ubiquitin for the Analysis of Interactions between Membrane Proteins *In Vivo*. *Proc. Natl. Acad. Sci.* 95 (9), 5187–5192. doi:10.1073/pnas.95.9.5187
- Stieger, B., Hagenbuch, B., Landmann, L., Höchli, M., Schroeder, A., and Meier, P. J. (1994). *In Situ* localization of the Hepatocytic Na⁺/Taurocholate Cotransporting Polypeptide in Rat Liver. *Gastroenterology* 107 (6), 1781–1787. doi:10.1016/0016-5085(94)90821-4
- Teese, M. G., and Langosch, D. (2015). Role of GxxxG Motifs in Transmembrane Domain Interactions. *Biochemistry* 54 (33), 5125–5135. doi:10.1021/acs.biochem.5b00495
- Yan, H., Zhong, G., Xu, G., He, W., Jing, Z., Gao, Z., et al. (2012). Sodium Taurocholate Cotransporting Polypeptide Is a Functional Receptor for Human Hepatitis B and D Virus. *Elife* 1, e00049. doi:10.7554/elife.00049
- Yan, H., Liu, Y., Sui, J., and Li, W. (2015). NTCP Opens the Door for Hepatitis B Virus Infection. *Antiviral Res.* 121, 24–30. doi:10.1016/j.antiviral.2015.06.002

Conflict of Interest: The authors declare that the research was conducted in the absence of any commercial or financial relationships that could be construed as a potential conflict of interest.

Copyright © 2021 Palatini, Müller, Lowjaga, Noppes, Alber, Lehmann, Goldmann, Glebe and Geyer. This is an open-access article distributed under the terms of the Creative Commons Attribution License (CC BY). The use, distribution or reproduction in other forums is permitted, provided the original author(s) and the copyright owner(s) are credited and that the original publication in this journal is cited, in accordance with accepted academic practice. No use, distribution or reproduction is permitted which does not comply with these terms.

GLOSSARY

3-AT	3-aminotriazole	LiOAc	lithium acetate
ABCG2	ATP-binding cassette family G member 2	MUT	mutant
AF	Alexa Fluor	myr	myristoylated
APP	amyloid precursor protein	MYTH	membrane-based yeast-two hybrid
ASBT	apical sodium-dependent bile acid transporter	NTCP	Na ⁺ /taurocholate co-transporting polypeptide
BCA	bicinchoninic acid	N_{Ub}	N-terminal part of ubiquitin
C_{Ub}	C-terminal part of ubiquitin	OAT1	organic anion transporter 1
DMSO	dimethyl sulfoxide	OD	optical density
DTT	dithiothreitol	PBS	phosphate-buffered saline
EGF	epidermal growth factor	PEG	polyethylene glycol
EGFR	epidermal growth factor receptor	SD	synthetically defined
GPA	glycophorin A	SDS	sodium dodecyl sulfate
HBV	Hepatitis B Virus	SLC	solute carrier
HDV	Hepatitis D Virus	TBS	tris-buffered saline
HGM	hepatocyte growth medium	TC	taurocholic acid
HRP	horseradish peroxidase	TMD	transmembrane domain
IP	immunoprecipitation	WT	wild-type
		YPAD	yeast extract-peptone-adenine-dextrose



Selective Nutrient Transport in Bacteria: Multicomponent Transporter Systems Reign Supreme

James S. Davies^{1†}, Michael J. Currie^{1†}, Joshua D. Wright^{1†}, Michael C. Newton-Vesty¹, Rachel A. North², Peter D. Mace³, Jane R. Allison⁴ and Renwick C.J. Dobson^{1,5*}

¹Biomolecular Interaction Centre and School of Biological Sciences, University of Canterbury, Christchurch, New Zealand, ²Department of Biochemistry and Biophysics, Stockholm University, Stockholm, Sweden, ³Biochemistry Department, School of Biomedical Sciences, University of Otago, Dunedin, New Zealand, ⁴Maurice Wilkins Centre for Molecular Biodiscovery and School of Biological Sciences, Digital Life Institute, University of Auckland, Auckland, New Zealand, ⁵Department of Biochemistry and Molecular Biology, Bio21 Molecular Science and Biotechnology Institute, University of Melbourne, Parkville, VIC, Australia

Multicomponent transporters are used by bacteria to transport a wide range of nutrients. These systems use a substrate-binding protein to bind the nutrient with high affinity and then deliver it to a membrane-bound transporter for uptake. Nutrient uptake pathways are linked to the colonisation potential and pathogenicity of bacteria in humans and may be candidates for antimicrobial targeting. Here we review current research into bacterial multicomponent transport systems, with an emphasis on the interaction at the membrane, as well as new perspectives on the role of lipids and higher oligomers in these complex systems.

Keywords: protein-protein interaction, membrane proteins, transport mechanism, TRAP transporter, ABC transporter

INTRODUCTION

All bacteria must scavenge and take up nutrients from their environment to survive. The cellular repertoire of transporter proteins is responsible for both the uptake of essential nutrients such as carbohydrates, amino acids, and metals into the cell, as well as the efflux of toxins and antimicrobial agents out of the cell (Saier, 2000). Transporter proteins therefore play key roles in bacterial colonisation, pathogenesis, and antimicrobial resistance (Putman et al., 2000; Brown et al., 2008; Siegel and Weiser, 2015). In contrast to channel proteins, which catalyse the high-flux of molecules down a concentration gradient, transporters can couple uphill substrate translocation with the movement of ions down their electrochemical gradient (secondary active transporters), or by using processes such as ATP hydrolysis (primary active transporters). These processes enable bacteria to scavenge nutrients that may be scarce (Nikaido and Saier, 1992).

There are many different families of bacterial transporter proteins, with differing folds, substrate specificities, and mechanisms of transport. In this review, we focus on transporter systems that utilise a substrate-binding protein (SBP) to deliver nutrients to the membrane component. These types of transport systems are very substrate specific, which has been shown to provide a competitive advantage to pathogenic bacteria during colonisation and infection; for example, the uptake of carbohydrates such as sialic acid and fucose (Almagro-Moreno and Boyd, 2009; Ng et al., 2013), amino acids such as L-glutamate (Colicchio et al., 2009), and metal ions such as zinc (Nielubowicz et al., 2010) and iron (Perry et al., 2015). Multicomponent transporters are thought to be particularly advantageous in environments with low nutrient availability, and during different stages of infection where bacteria can upregulate transporters to suit their environments (Sanchez-Ortiz et al., 2021).

OPEN ACCESS

Edited by:

Piotr Koprowski,
Nencki Institute of Experimental
Biology (PAS), Poland

Reviewed by:

A. Sami Saribas,
Temple University, United States
Francesca Di Sole,
Des Moines University, United States

*Correspondence:

Renwick C.J. Dobson
renwick.dobson@canterbury.ac.nz

[†]These authors have contributed
equally to this work

Specialty section:

This article was submitted to
Cellular Biochemistry,
a section of the journal
Frontiers in Molecular Biosciences

Received: 23 April 2021

Accepted: 02 June 2021

Published: 29 June 2021

Citation:

Davies JS, Currie MJ, Wright JD,
Newton-Vesty MC, North RA,
Mace PD, Allison JR and Dobson RCJ
(2021) Selective Nutrient Transport in
Bacteria: Multicomponent Transporter
Systems Reign Supreme.
Front. Mol. Biosci. 8:699222.
doi: 10.3389/fmolb.2021.699222

Two important families of multicomponent active transporters are of particular interest: the widely studied ATP-binding cassette (ABC) transporters and the less understood tripartite ATP-independent periplasmic (TRAP) transporters. ABC transporters are found across all kingdoms of life, with many eukaryotic ABC transporters implicated in disease states (Gerlach et al., 1986; Gros et al., 1986; Hyde et al., 1990; Higgins, 1992; Borst and Elferink, 2002; Wolf et al., 2012). The role of ABC transporters in bacterial pathogenicity is well established (Tanaka et al., 2018), and ABC classes that lack homologs in eukaryotes have been explored as potential drug targets against Gram-positive bacteria (Counago et al., 2012). In contrast, TRAP transporters are not found in eukaryotes and are only present in bacteria and archaea (Forward et al., 1997; Kelly and Thomas, 2001; Fischer et al., 2010; Mulligan et al., 2011). Moreover, TRAP transporters are important for host colonisation and persistence by pathogenic bacteria (Severi et al., 2005; Almagro-Moreno and Boyd, 2009; Jenkins et al., 2010), thus representing an attractive therapeutic target. This link between transport by TRAPs and pathogenicity is comprehensively reviewed by Rosa et al. (2018).

ABC and TRAP transporters differ considerably in sequence, structure and mechanism of transport. ABC transporters are primary active transporters that use energy from ATP binding or hydrolysis to drive large structural rearrangements of the membrane domains—in particular, rearrangement between outward- and inward-facing orientations (Locher, 2016). The mechanism of TRAP transport is unresolved, but it is clear that they operate *via* a secondary active transport mechanism, coupling target molecule transport to the movement of cations down an electrochemical gradient (Mulligan et al., 2009). Common to both of these systems is the use of a high-affinity SBP to unload substrates to the integral membrane domain (Berntsson et al., 2010; Fischer et al., 2015). In ABC transporters, the general mechanism of substrate unloading involves distortion of the SBP upon docking at the membrane domain (Locher, 2016). This rearrangement lowers the affinity of the interaction between ligand and SBP, allowing substrate release for transport. It is not yet known if this is the same for TRAP transporters.

Given their link to the pathogenesis and survival strategy of bacteria, both ABC and TRAP transporters present as interesting targets for antimicrobial development. Inhibiting the SBP is an obvious strategy that has been shown to impede bacterial growth and pathogenesis *in vivo* (Ilari et al., 2016). Inhibiting substrate binding at the membrane components, or the protein-protein interaction at the membrane are strategies to be considered. Others have considered using the SBP in a “Trojan horse” mechanism to deliver bactericidal agents into the cell (Wilson et al., 2016). Understanding the structure-function relationships of these transporters is therefore key to chemical targeting and antimicrobial design (Scalise et al., 2020). Here we review the interplay of prokaryotic ABC and TRAP transporters with their cognate SBPs, as well as new perspectives on the structure and function of these systems.

Multicomponent Transporter Prevalence

The prevalence of multicomponent transporter genes in bacteria varies considerably. The micro-environment that the cell

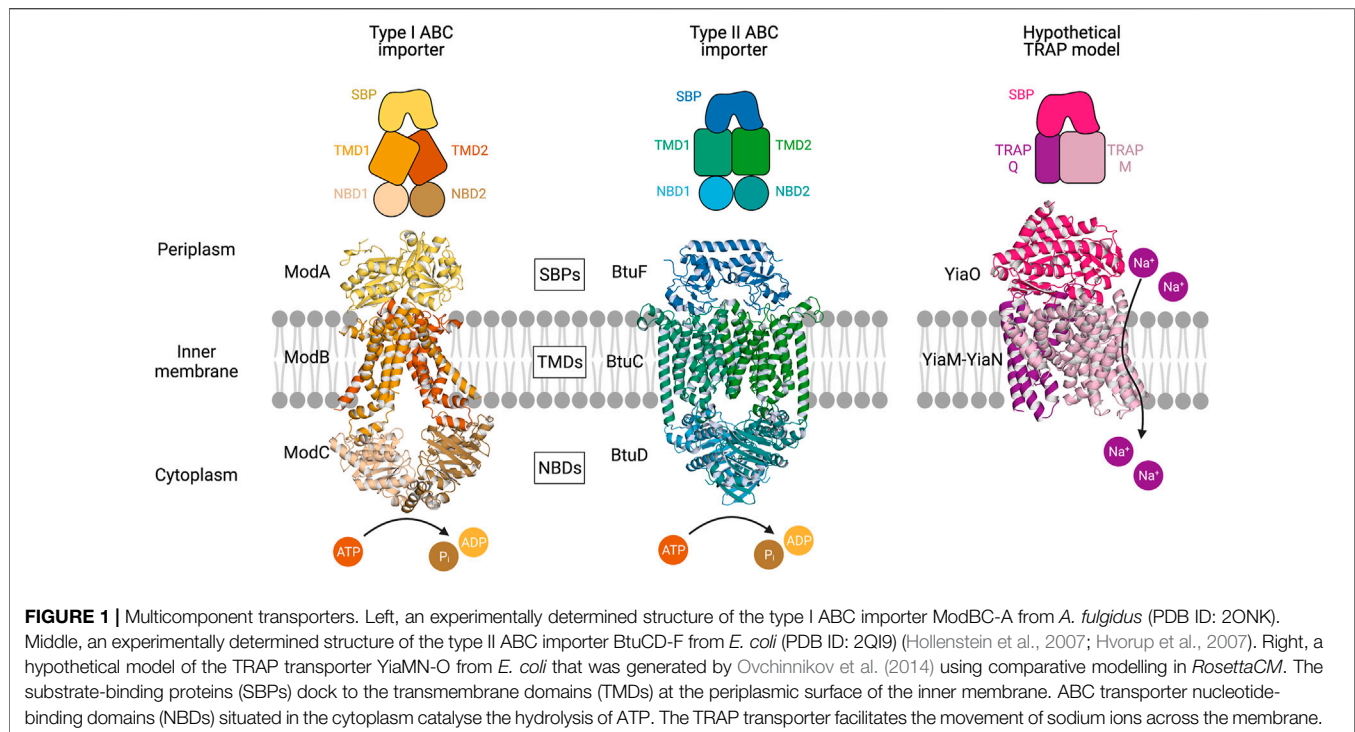
occupies is linked to the number and the type of transporter a bacterium may possess, with the number of transporters in the genome being generally proportional to genome size (Davidson et al., 2008). ABC transporter proteins are by far the most abundant of transporters, typically accounting for half of the transporters in a bacterial genome. *Escherichia coli* has a 4.6 Mb genome and encodes 78 ABC transporter systems, typical for a genome of this size. In contrast, *Mycobacterium tuberculosis* has a 4.4 Mb genome and encodes only 38 ABC systems, while *Agrobacterium tumefaciens* has a 5.7 Mb genome that encodes over 200 ABC systems (Davidson et al., 2008). *M. tuberculosis* lives a parasitic intracellular nutrient-rich lifestyle where the requirement to select nutrients that are low in abundance has been lost, whereas *A. tumefaciens* lives in the soil, a highly competitive environment. Recent comparative genomics of clinically significant pathogenic bacteria, such as *Salmonella enterica*, *E. coli* and species of *Bacteroides* show that ABC transporters are among the most commonly encoded transporter system, comprising 20–30% of all transporter proteins in the strains examined (Do et al., 2017; Zafar and Saier, 2018).

TRAP transporter prevalence in bacterial genomes is variable. The TransportDB 2.0 database (<http://www.membranetransport.org/transportDB2/index.html>) shows that out of the 2,722 prokaryotic genomes analysed in the database, 1,252 (46%) have at least one TRAP system in the genome. Some species have only one TRAP system (*E. coli* O42), others have over 20 (*Silicibacter pomeroyi* DSS-3 and *Chromohalobacter salexigens* DSM 3043) (Mulligan et al., 2007; Elbourne et al., 2017). Moreover, TRAP proteins appear more common in bacteria that live in saline environments (Mulligan et al., 2007). It seems likely that these species have adapted to exploit the high sodium concentration in their surrounding environments by utilising a sodium gradient to power transport as opposed to ATP. In addition, Bergauer et al. (2018) observed that TRAP transporters are more prevalent in bacteria that live at depths greater than 500 m compared to those between 0 and 500 m. The authors hypothesise that in deep sea oligotrophic conditions, TRAP transporters are more advantageous than ABC transporters as their transport is less energy-consuming due to a reduced requirement for ATP hydrolysis.

Multicomponent Transporter Architecture

Buried in the lipid membrane, transporter proteins are intrinsically hydrophobic and traditionally, they are difficult to isolate and characterise. Nonetheless, there have been significant improvements in membrane protein purification methodologies, particularly with the development of new detergents and membrane mimetics. Importantly, these improvements have led to an expansion in the number of membrane protein structures, although they are still under-represented in the PDB and notably, no TRAP transporter membrane protein structure has been experimentally determined.

ABC transporter structure: As of writing, 85 experimentally determined structures of ABC transporters have been deposited in the PDB, revealing wide structural diversity. Common to all ABC transporters is a dimeric membrane-bound component



(homo- or hetero-) that brings together two transmembrane domains (TMDs) and two nucleotide-binding domains (NBDs), otherwise known as ATP-binding cassettes (**Figure 1**). The NBDs, which in some cases may be fused to a TMD, hydrolyse ATP and drive conformational changes in the transmembrane domains that in turn allow for the substrate to pass through the membrane. Recent studies suggest that either the binding, or the hydrolysis of ATP provides the “power stroke” for transport, and this varies between systems (Mishra et al., 2014; Stefan et al., 2020). NBDs are highly conserved in structure and sequence, but the TMDs are less so, which reflects the diversity in transported substrates. Historically, ABC transporters have been classified by sequence alignments and substrate specificity, which has separated the transporters into three classes. However, a surge in the number of ABC transporter structures deposited in the PDB has led others to rethink this classification system—a seven class system where ABC transporters are classified based on their transmembrane domain fold is now suggested (Thomas et al., 2020).

The TMD monomer consists of anywhere between four and ten transmembrane helices (TMH), plus a small number of connecting and coupling α -helices. The number and topology of helices dictate the seven ABC transporter classes that are now proposed. Classically, ABC transporters that import using an SBP are categorised as either Type I (small), with five to eight TMH per subunit, or Type II (large), with ten TMH per subunit. A coupling helix on the cytoplasmic surface interacts tightly with the NBD. Each NBD consists of two sub-domains: a larger RecA-like domain and a smaller α -helical domain that is unique to ABC transporters. Several highly conserved motifs help identify NBDs,

including the Walker A and B motifs, and the signature ABC motif (Thomas and Tampé, 2020).

For Type I and Type II ABCs the periplasmic surface of the TMD serves as a docking interface for the SBP. All SBPs, including those from both ABC and TRAP systems, share a common architecture—two α/β domains linked by a hinge region about which the SBP can open and close around a ligand, which is likened to a “Venus flytrap” mechanism (Scheepers et al., 2016). Some experimental evidence favours induced-fit over conformational selection as the mechanism of substrate binding to the SBP (Gouridis et al., 2015), although it is unclear whether this is the case for all systems. This mechanism of conformational change and the conformational equilibria could both have implications for how the protein-protein interaction occurs, and the transport cycle overall.

TRAP transporter structure: TRAP transporters are a major class of secondary transporters used by both bacteria and archaea to import a range of carboxyl and sulfonate-containing molecules, including C4-dicarboxylates, α -keto acids, aromatic substrates, and amino acids (Rosa et al., 2018). TRAPs couple transport of these molecules to the movement of cations (Na^+) down an electrochemical gradient, and also utilise a high-affinity SBP. SBPs were previously thought to be unique to ABC transporters, until the discovery of the first TRAP transporter system, dctPQM, from *Rhodobacter capsulatus* (Forward et al., 1997). To date, there are no experimentally determined structures of the membrane domains of TRAP transporters, limiting our understanding. Unlike ABC systems, the TRAP membrane component is almost always heterodimeric. Typically, the

TRAP membrane domains are comprised of a large or “M” domain, estimated to be 12–14 TMH with a predicted $N_{\text{Out}}C_{\text{Out}}$ topology, and a small or “Q” domain made up of 4 TMH, with an experimentally determined $N_{\text{In}}C_{\text{In}}$ topology (Wyborn et al., 2001). Together with the SBP (or P domain), they make up the “tripartite” system (Figure 1).

A number of TRAP SBPs have been characterised structurally and biochemically (Muller et al., 2006; Johnston et al., 2008; Gangi Setty et al., 2014), generally showing the canonical SBP tertiary structure. Using a structural genomics approach, Vetting et al. (2015) solved 60 high-resolution crystal structures of SBPs (46 unique) greatly expanding the knowledge base for these transporter systems.

In a small proportion of TRAP transporters, the Q and the M domains are fused together and expressed as a single polypeptide. Rarer still are fusions of the Q domain to the P domain. For the majority of TRAP transporters, these domains are transcribed separately, and oligomerise *via* an unknown mechanism to form a functional transporter (Kelly and Thomas, 2001). The large membrane domain is predicted to form the translocation channel, and is a part of the ion transporter superfamily (Rabus et al., 1999). The function of the small membrane domain is unknown, but it is hypothesised that the small domain could function as a chaperone for the folding of the large domain, or act as a landing pad for the SBP (Mulligan et al., 2011).

The best-studied members of the TRAP transporter family are the non-fused *Vibrio cholerae* and the fused (Q and M domains) *Haemophilus influenzae* SiaPQM systems. These TRAPs transport sialic acids, a family of nine-carbon amino sugars, the most common of which is *N*-acetylneuraminic acid (North et al., 2018). The focus on these systems is due to the growing interest in the role of sialic acid as an important nutrient source for pathogenic bacteria *in vivo* (North et al., 2016; North et al., 2018; Wahlgren et al., 2018; Davies et al., 2019; Coombes et al., 2020; Horne et al., 2021). Electrochemical studies have been used to characterise the transport of sialic acid through the *H. influenzae* SiaPQM system (Mulligan et al., 2009). Proteoliposome assays identified that transport by SiaQM (membrane domains) is predominantly unidirectional. Efflux of sialic acid from the proteoliposome could only be achieved with an excess of unliganded SiaP (at conditions considered unlikely to be physiologically relevant). This study also identified that at least two Na^+ ions are coupled to the transport of sialic acid and that transport could not be driven by a pH gradient or membrane potential alone. These data strengthen the aforementioned argument that TRAP transporters have lower energetic costs in marine environments. More data is required to ascertain whether all TRAP transporters are Na^+ -dependent and have this coupling stoichiometry.

Current Models for Protein:Protein Interactions at the Membrane

Recently, it has been shown that SBPs can adopt a wide range of conformations that can activate transport and that both

transported and non-transported ligands can adopt similar conformations in solution. While the SBP is the primary specificity determinant for the target molecule, it is suggested that the fate of the transported ligand can also be determined by selectivity at the membrane domain, or by a slow opening of the SBP, preventing translocation (de Boer et al., 2019). In both situations, it is clear that the docking and allosteric interaction of these domains is key in the transport cycle. Whereas there is ample structural data to define this interaction in ABC systems, there is currently no experimentally determined structural data of the membrane components to guide our understanding of this interaction in the TRAP transporters (Figure 1).

For both ABC and TRAP transporters, docking of the SBP must trigger conformational changes in the membrane domains, and in the case of ABC transporters, catalytic transformations at the NBDs. How the soluble SBP and membrane-bound transporter interact is therefore key to understanding the transport cycle. Within the ABC transporter family, there is wide variation in how the SBP interacts with the transporter domain. The interactions have been well-characterised in the maltose-specific ABC MalFGK₂, where it was shown that the SBP MalE interacts with the periplasmic loops of MalFG. The crystal structure of ModB₂C₂A (PDB ID: 2ONK) shows both SBP lobes interacting with the TMDs (Figure 1), with six salt bridges per domain (Hollenstein et al., 2007). In comparison, the BtuCD-F structure (PDB ID: 2QI9) has a very different interacting surface that reflects the asymmetric structure of the SBP, and only one salt bridge per domain (Hvorup et al., 2007).

Vigonsky et al. (2013) examined this interaction with two different Type II ABC transporters with the same substrate specificity (molybdate and tungstate), and crucially found that the interaction at the membrane is completely different between the two systems. In one system, ModBC-A from *Archaeoglobus fulgidus*, the SBP appears to form a low-affinity, transient complex with the membrane domain that is stabilised by ligand binding. Contrastingly, the *H. influenzae* molybdate/tungstate ABC transporter has a high-affinity interaction that is destabilised by both ligand and nucleotide binding (Vigonsky et al., 2013). Mulligan et al. (2009) tested whether the *V. cholerae* TRAP SiaP could deliver substrate to the *H. influenzae* SiaQM membrane domains, but found no transport in a proteoliposome assay. These data together highlight the specificity of the interactions between the SBP and the membrane domains in these multicomponent systems.

Once the complex has formed, the substrate must pass to the membrane domain. The general model for this involves the disruption or distortion of the SBP high-affinity binding pocket by loops of the membrane domain. In ABC transporters, there is variation in the affinity for substrates within the membrane domain. Local concentrations of substrate are important to consider here, while the temporary binding pocket has only moderate affinity, with a K_d in the mM range—substrate concentration in the tunnel is thought to be at least two orders of magnitude greater than this. In Type II transporters, such as the well-studied *E. coli* vitamin B12 transporter BtuCD-F (PDB ID: 2QI9), there is no substrate binding pocket, and the substrate is released into a

hydrophobic pocket with no measurable affinity—likened to a “Teflon” cavity. The interactions within the BtuCD-F system, as well as the Type I ModBC-A transporter, have been studied using surface plasmon resonance and single-molecule fluorescence resonance energy transfer (FRET), and more recently by native mass spectrometry (Fiorentino et al., 2019). This variation in interaction perhaps reflects the diversity of both SBP folds and, as elaborated below, general mechanisms of transport.

Mechanisms of Transport

The alternating-access model is the dominant descriptor of substrate transport for ABC transporters (Locher, 2016). In its simplest form, this model involves conformational changes in the membrane domains that expose the substrate-binding site to either side of the membrane, which is achieved through an allosteric coupling of intracellular and extracellular gates within the transporter. The alternating-access model can be further divided into three distinct types: the rocker-switch, the rocking-bundle (or gated-pore) and the elevator model (Drew and Boudker, 2016). For descriptive purposes and in brief, if a typical transporter protein is described as two bundles (with an N- and a C-terminal domain), structurally similar bundles rearrange in a symmetrical fashion around a central substrate-binding site in the rocker-switch model; structurally dissimilar bundles rearrange asymmetrically around a central substrate-binding site in the rocking-bundle model; and in the elevator mechanism the two bundles are highly divergent, with one of them remaining fixed and immobile within the membrane, while the other moves against this bundle to physically translocate the substrate to the other side of the membrane in an elevator-type fashion (Drew et al., 2021).

A model of transport by TRAP transporters has been proposed and is based upon the alternating-mechanism seen in Type I ABC transporters (Mulligan et al., 2009). Recent work has started to uncover potential “scoop loops” in the membrane domains of TRAP transporters (Peter et al., 2021). Additionally, Darby et al. (2019) have found that disruption of the ordered waters within the binding cleft of an SBP can dramatically alter substrate binding affinity. They discovered that a mutation made on the surface of the protein was able to severely disrupt ligand binding at the distal (~4.7 Å) binding site. This may hint at how the membrane domains allosterically modulate the SBP—a subtle interaction at the surface of the binding protein may be all that is required to trigger the release of the substrate. This type of interaction fits with experiments performed by Marinelli et al. (2011), where the authors constructed an SBP mutant that is biased toward an open conformation, which in turn had a markedly lower affinity for substrate—providing some evidence that the binding affinity may be allosterically modulated. Recently, crystal structures of the *V. cholerae* SiaP, combined with single-molecule FRET experiments have shown that the conformational change is primarily substrate-induced (Glaenger et al., 2017). More experimental evidence is required to better understand the transport cycle, particularly how the loop regions of the TRAP transporter interact with the SBP, and in

general, how TRAP transporters function—this is a key knowledge gap in the field.

Co-Evolution and its Potential for Defining Substrate-Binding Protein:Membrane Protein Interactions

An emerging tool for understanding multicomponent transporter systems is the analysis of co-varying residues. In particular, new statistical methods now allow for an accurate prediction of co-varying residues, in turn thought to be co-evolving. These residue pairs are a very good predictor of spatial proximity (Marks et al., 2011; Jones et al., 2012; Kamisetty et al., 2013). This is of particular interest in the case of both ABC and TRAP transporters, where the subunits are functionally connected and appear to operate independently of other proteins (Juan et al., 2008). The abundance of sequences available for both families make them suitable for this kind of analysis.

Co-evolution has been successfully used to predict the SBP: TMD complex of an ABC transporter. Ovchinnikov et al. (2014) docked the SBP (MetQ) to the TMDs (MetI) of the *E. coli* methionine transporter MetNIQ using co-evolution restraints generated by the *GREMLIN* tool. At the time, the structure of the MetNIQ complex had not been determined, but has since been solved (PDB ID: 6CVL). Strikingly, a comparison of these two structures shows the remarkable accuracy of these predictions (Figure 2). The accuracy of this method was confirmed using a benchmark set, where nearly all identified co-varying residues were in contact in the already solved complex structure. Co-evolution analysis was used to both inform the building of a comparative model of the TRAP transporter Q and M domains using *Rosetta*, as well as the docking of the P domain (Figure 1) (Ovchinnikov et al., 2014). This model, although yet to be verified experimentally, gives us the first structural picture of the membrane domains, and may be of use to inform mechanistic experiments.

Importance of Lipids for Multicomponent Transporters

It is apparent that the lipid environment within which a membrane protein transporter is embedded plays an important role in modulating stability and activity. There are a wide variety of membrane mimetics currently available for transporter purification and characterisation, with different levels of similarity to the cell membrane. These include micelles, bicelles, peptidiscs, saposins, amphipols, styrene maleic acid lipid particles (SMALPs), nanodiscs, and liposomes (Chorev and Robinson, 2020). Each mimetic can result in substantially different transporter conformations and activities compared to the native environment of the protein. There are several examples of ABC transporters displaying significantly higher activity and/or stability when reconstituted into lipid environments, such as nanodiscs or liposomes, compared to their apparent activity when measured in detergent micelles. Examples of this include Wzm-Wzt, P-gp, and MalFGK₂ (O’Mara and Mark, 2012; Bao et al., 2013; Bi et al.,

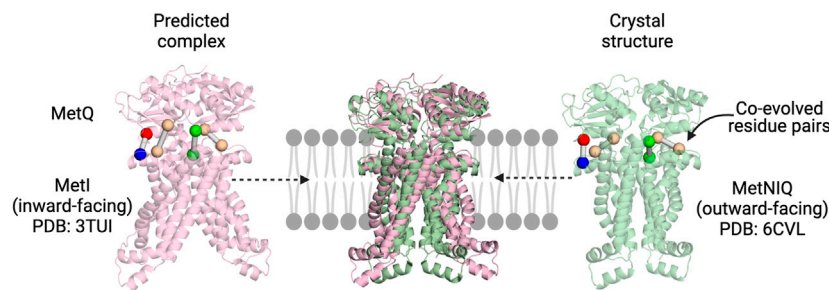


FIGURE 2 | Co-evolution analysis as a tool to explore SBP:TMD interactions in multicomponent systems. The predicted MetIQ structure (Ovchinnikov et al., 2014) maps well on to the MetNIQ crystal structure (MetN not displayed) (Nguyen et al., 2018). The top co-evolved residues between the two components are in similar positions, with the predicted complex correctly orienting the SBP.

2018). O'Mara and Mark (2012) carried out molecular dynamics simulations using the crystal structure of P-gp and found that this conformation of P-gp was stable, yet when inserted into model membranes the structure quickly deformed.

The bacterial ABC transporter MsbA, which can function both as a lipid flippase and a drug transporter, adopts a different conformation in lipid nanodiscs (*via* cryo-EM) than that observed when crystallised with detergent (Ward et al., 2007; Mi et al., 2017). Studies on MsbA comparing structure and activity in detergent to that in nanodiscs or liposomes observed the lowest activity in detergent (Kawai et al., 2011; Arana et al., 2019). MsbA is also significantly more stable in lipid carrier systems when compared MsbA in detergent or amphipol (Kehlenbeck et al., 2019). Although there is no substitute for native lipids, some detergents appear to be better at retaining functional activity, such as the maltose-neopentyl glycol (MNG) class. These are mild detergents that better mimic the classic two-tailed lipid structure, with a quaternary “linking” carbon that restricts the conformational flexibility of the molecule (Chae et al., 2010). Compared to another commonly used detergent, n-Dodecyl β -D-maltoside (DDM), MNG is predicted to pack more efficiently around the transmembrane region (Lee et al., 2020).

The composition of the lipid membrane varies between bacteria and can also change with their environment. Common lipids include phosphatidylglycerol (PG), cardiolipin (CL), phosphatidylethanolamine (PE) as well as methylated derivatives of PE such as phosphatidylcholine (PC) (Sohlenkamp and Geiger, 2016). Furthermore, the distribution of lipids within the bilayer is asymmetric. There are several studies comparing transporter activity in PC and PE lipids (Ahn et al., 2000; Gustot et al., 2010; Bao et al., 2013; Rice et al., 2014). One key observation here is that compared to the quaternary ammonium head groups of PC, the primary ammonium head groups of PE have greater hydrogen bonding potential and form specific interactions with transporter amino acid side chains (Immadisetty et al., 2019).

With the known importance of lipids for transporter function, it is essential that new methods are developed for their identification and for determining their role in transporter function. Native mass spectrometry is emerging as a valuable

technique to investigate protein-lipid interactions. Typical identification of required lipids and their interactions with transporters centre around *in vivo* studies, X-ray crystallography, and cryo-EM, which are challenging, time-consuming, and often low resolution, not allowing for proper tail and head identification (Bolla et al., 2019). High-energy native mass spectrometry has been gaining momentum in the field to identify lipids linked to function. Using a mild detergent for the purification of the ABC transporter TmrAB, successive delipidation, mass spectrometry, and ATPase assays showed a subset of closely associated lipids remain after detergent solubilisation. Critically, as more lipids were extracted from TmrAB, evidenced from the mass spectra, the corresponding ATPase activity decreased (Bechara et al., 2015).

The role of lipids in the assembly and function of the TRAP family is yet to be established but it is conceivable that interfacial lipids may play some role in the stability of the heterodimeric complex.

Oligomeric State and Implications for Function

Transporters, especially those that use an SBP, are typically functional as single transporter units. The possibility of larger assemblies occurring in the crowded environment of the membrane should be considered, where it is estimated that the protein composition may be as high as 30–55% of the membrane area (Linden et al., 2012). These assemblies may function independently of each other, or the conformational changes may be linked between protomers. Many studies do not take place in the membrane, or with measurement of oligomeric state in mind. There have been cases of higher-order ABC transporter oligomerisation (tetramers and above), but as most structural work is performed in detergents, physiologically relevant oligomerisation may be missed. Several biophysical techniques can accurately determine transporter oligomeric state in detergent, but in these experiments, it can be difficult to discriminate between cohabitation in the micelle and biologically relevant oligomerisation. Recently, the dicarboxylate transporter VcINDY from *V. cholerae* (which is of the divalent anion-sodium symporter family) has been shown

to form dimers, although transport *via* an elevator-type mechanism does not appear to be coupled between protomers (Mancusso et al., 2012; Mulligan et al., 2016). The biological relevance of this behaviour is not yet clear.

In ABC transporters, dimerisation of two subunits generates the active transporter core that binds the cognate SBP. Higher-order oligomers of the transporter core have been implicated in the function of several families of mammalian ABC transporters, but less is known about the oligomeric status in bacteria. One example is the *M. tuberculosis* ABC transporter Rv1747, which is important for *M. tuberculosis* growth in hosts and has recently been found to form higher-order assemblies termed “nanoclusters” at the membrane (Heinkel et al., 2019). Super-resolution microscopy was used to observe these clusters, where it appears the clustering is driven by oligomerisation and phase separation behaviour of a cytoplasmic regulatory module. The role of transporter oligomerisation in this clustering is unclear, although ABC transporter oligomerisation and subsequent colocalisation has been reported for human systems. Oligomerisation may conceivably improve transport efficiency *via* cooperativity, which has been seen in ABC transporters where an SBP is fused to the transport domain (Biemans-Oldehinkel and Poolman, 2003).

Recently, several ABC SBPs from the bacterium *Thermotoga maritima* have been identified to form homodimers that act as an allosteric switch (Li et al., 2017). These dimers dissociate into monomers upon ligand binding as a proposed form of transporter regulation. Another SBP from *T. maritima*, the arginine binding protein TmArgBP, is anchored to the membrane and forms a C-terminal helix-swapped dimer that could simultaneously interact with two ABC transporter cores (Ruggiero et al., 2014).

It is not known whether oligomerisation can occur with the integral membrane component of TRAP transporters (e.g., heterotetramers, where the heterodimer species oligomerise) as the structure is undetermined, although dimeric TRAP SBPs have been structurally characterised by crystallography (Gonin et al., 2007; Vetting et al., 2015). These dimeric SBPs (of which many homologs are predicted by sequence) have an extended C-terminal

helix away from the ligand-binding site that swaps over to form a dimer, positioning the binding sites in a back-to-back arrangement. Although it may be predicted, no cooperative binding was seen in the first example of these dimeric SBPs, TakP (Gonin et al., 2007). Any functional advantages of dimeric SBPs are still unknown, although dimerisation could conceivably increase transport efficiency, or be a part of the mechanism.

Our current examples of multicomponent transporters are functional without forming larger assemblies, but there are examples of SBP oligomerisation. This area has not expanded much over the last decade, potentially due to the difficulty of studying these systems. Examples could appear with future work in lipid systems such as nanodiscs.

CONCLUSION

Both the TRAP and ABC transporter systems enable bacteria to selectively import nutrients and are therefore important for colonisation and persistence. While much is known about ABC transporters, from how they bind and interact with substrate-binding proteins, to the conformational transitions of the membrane and nucleotide-binding domains, relatively little is known about TRAP transporters. It is clear that in ABC transporter systems there are a number of different mechanisms of transport, and it is not a case of one-size-fits-all. The current model of the TRAP transport cycle needs further experimental testing, with the key knowledge gap being that there are no experimentally determined structures of the membrane domains. Further research into how these transporter systems function in the membrane environment is also required.

AUTHOR CONTRIBUTIONS

JD coordinated the first draft of the article. JD, MC, JW, and MNV wrote sections of the article. All authors contributed to article revision, proof-read, and approved the submitted version.

REFERENCES

- Ahn, J., Wong, J. T., and Molday, R. S. (2000). The Effect of Lipid Environment and Retinoids on the ATPase Activity of ABCR, the Photoreceptor ABC Transporter Responsible for Stargardt Macular Dystrophy. *J. Biol. Chem.* 275, 20399–20405. doi:10.1074/jbc.m000555200
- Almagro-Moreno, S., and Boyd, E. F. (2009). Sialic Acid Catabolism Confers a Competitive Advantage to Pathogenic *Vibrio cholerae* in the Mouse Intestine. *Iai* 77, 3807–3816. doi:10.1128/iai.00279-09
- Arana, M. R., Fiori, M. C., and Altenberg, G. A. (2019). Functional and Structural Comparison of the ABC Exporter MsbA Studied in Detergent and Reconstituted in Nanodiscs. *Biochem. Biophysical Res. Commun.* 512, 448–452. doi:10.1016/j.bbrc.2019.03.069
- Bao, H., Dalal, K., Wang, V., Rouiller, I., and Duong, F. (2013). The Maltose ABC Transporter: Action of Membrane Lipids on the Transporter Stability, Coupling and ATPase Activity. *Biochim. Biophys. Acta (Bba) - Biomembranes* 1828, 1723–1730. doi:10.1016/j.bbmem.2013.03.024
- Bechara, C., Nöll, A., Morgner, N., Degiacomi, M. T., Tampé, R., and Robinson, C. V. (2015). A Subset of Annular Lipids Is Linked to the Flippase Activity of an ABC Transporter. *Nat. Chem* 7, 255–262. doi:10.1038/nchem.2172
- Bergauer, K., Fernandez-Guerra, A., Garcia, J. A. L., Sprenger, R. R., Stepanauskas, R., Pachiadaki, M. G., et al. (2018). Organic Matter Processing by Microbial Communities throughout the Atlantic Water Column as Revealed by Metaproteomics. *Proc. Natl. Acad. Sci. U.S.A.* 115, E400–E408. doi:10.1073/pnas.1708779115
- Berntsson, R. P.-A., Smits, S. H. J., Schmitt, L., Slotboom, D.-J., and Poolman, B. (2010). A Structural Classification of Substrate-Binding Proteins. *FEBS Lett.* 584, 2606–2617. doi:10.1016/j.febslet.2010.04.043
- Bi, Y., Mann, E., Whitfield, C., and Zimmer, J. (2018). Architecture of a Channel-Forming O-Antigen Polysaccharide ABC Transporter. *Nature* 553, 361–365. doi:10.1038/nature25190
- Biemans-Oldehinkel, E., and Poolman, B. (2003). On the Role of the two Extracytoplasmic Substrate-Binding Domains in the ABC Transporter OpuA. *EMBO J.* 22, 5983–5993.

- Bolla, J. R., Agasid, M. T., Mehmood, S., and Robinson, C. V. (2019). Membrane Protein-Lipid Interactions Probed Using Mass Spectrometry. *Annu. Rev. Biochem.* 88, 85–111. doi:10.1146/annurev-biochem-013118-111508
- Borst, P., and Elferink, R. O. (2002). Mammalian ABC Transporters in Health and Disease. *Annu. Rev. Biochem.* 71, 537–592. doi:10.1146/annurev.biochem.71.102301.093055
- Brown, S. A., Palmer, K. L., and Whiteley, M. (2008). Revisiting the Host as a Growth Medium. *Nat. Rev. Microbiol.* 6, 657–666. doi:10.1038/nrmicro1955
- Chae, P. S., Rasmussen, S. G. F., Rana, R. R., Gotfryd, K., Chandra, R., Goren, M. A., et al. (2010). Maltose-neopentyl Glycol (MNG) Amphiphiles for Solubilization, Stabilization and Crystallization of Membrane Proteins. *Nat. Methods* 7, 1003–1008. doi:10.1038/nmeth.1526
- Chorev, D. S., and Robinson, C. V. (2020). The Importance of the Membrane for Biophysical Measurements. *Nat. Chem. Biol.* 16, 1285–1292. doi:10.1038/s41589-020-0574-1
- Colicchio, R., Ricci, S., Lamberti, F., Pagliarulo, C., Pagliuca, C., Braione, V., et al. (2009). The Meningococcal ABC-type L-Glutamate Transporter GltT Is Necessary for the Development of Experimental Meningitis in Mice. *Iai* 77, 3578–3587. doi:10.1128/iai.01424-08
- Coombes, D., Davies, J. S., Newton-Vesty, M. C., Horne, C. R., Setty, T. G., Subramanian, R., et al. (2020). The Basis for Non-Canonical ROK Family Function in *N-acetylmannosamine* Kinase From the Pathogen *Staphylococcus aureus*. *J. Biol. Chem.* 295, 3301–3315. doi:10.1074/jbc.RA119.010526
- Couñago, R. M., Mcdevitt, C. A., Ween, M. P., and Kobe, B. (2012). Prokaryotic Substrate-Binding Proteins as Targets for Antimicrobial Therapies. *Curr. Drug Targets* 13, 1400–1410. doi:10.2174/138945012803530170
- Darby, J. F., Hopkins, A. P., Shimizu, S., Roberts, S. M., Brannigan, J. A., Turkenburg, J. P., et al. (2019). Water Networks Can Determine the Affinity of Ligand Binding to Proteins. *J. Am. Chem. Soc.* 141, 15818–15826. doi:10.1021/jacs.9b06275
- Davidson, A. L., Dassa, E., Orelle, C., and Chen, J. (2008). Structure, Function, and Evolution of Bacterial ATP-Binding Cassette Systems. *Microbiol. Mol. Biol. Rev.* 72, 317–364. doi:10.1128/mmb.00031-07
- Davies, J. S., Coombes, D., Horne, C. R., Pearce, F. G., Friemann, R., North, R. A., et al. (2019). Functional and Solution Structure Studies of Amino Sugar Deacetylase and Deaminase Enzymes from *Staphylococcus aureus*. *FEBS Lett.* 593, 52–66. doi:10.1002/1873-3468.13289
- De Boer, M., Gouridis, G., Vietrov, R., Begg, S. L., Schuurman-Wolters, G. K., Husada, F., et al. (2019). Conformational and Dynamic Plasticity in Substrate-Binding Proteins Underlies Selective Transport in ABC Importers. *Elife* 8, e44652. doi:10.7554/elif.44652.037
- Do, J., Zafar, H., and Saier, M. H., Jr (2017). Comparative Genomics of Transport Proteins in Probiotic and Pathogenic *Escherichia coli* and *Salmonella enterica* Strains. *Microb. Pathogenesis* 107, 106–115. doi:10.1016/j.micpath.2017.03.022
- Drew, D., and Boudker, O. (2016). Shared Molecular Mechanisms of Membrane Transporters. *Annu. Rev. Biochem.* 85, 543–572. doi:10.1146/annurev-biochem-060815-014520
- Drew, D., North, R. A., Nagarathinam, K., and Tanabe, M. (2021). Structures and General Transport Mechanisms by the Major Facilitator Superfamily (MFS). *Chem. Rev.* 121, 5289–5335. doi:10.1021/acs.chemrev.0c00983
- Elbourne, L. D. H., Tetu, S. G., Hassan, K. A., and Paulsen, I. T. (2017). TransportDB 2.0: a Database for Exploring Membrane Transporters in Sequenced Genomes from All Domains of Life. *Nucleic Acids Res.* 45, D320–D324. doi:10.1093/nar/gkw1068
- Fiorentino, F., Bolla, J. R., Mehmood, S., and Robinson, C. V. (2019). The Different Effects of Substrates and Nucleotides on the Complex Formation of ABC Transporters. *Structure* 27, 651–659. doi:10.1016/j.str.2019.01.010
- Fischer, M., Hopkins, A. P., Severi, E., Hawkhead, J., Bawdon, D., Watts, A. G., et al. (2015). Tripartite ATP-independent Periplasmic (TRAP) Transporters Use an Arginine-Mediated Selectivity Filter for High Affinity Substrate Binding. *J. Biol. Chem.* 290, 27113–27123. doi:10.1074/jbc.m115.656603
- Fischer, M., Zhang, Q. Y., Hubbard, R. E., and Thomas, G. H. (2010). Caught in a TRAP: Substrate-Binding Proteins in Secondary Transport. *Trends Microbiol.* 18, 471–478. doi:10.1016/j.tim.2010.06.009
- Forward, J. A., Behrendt, M. C., Wyborn, N. R., Cross, R., and Kelly, D. J. (1997). TRAP Transporters: a New Family of Periplasmic Solute Transport Systems Encoded by the dctPQM Genes of *Rhodobacter capsulatus* and by Homologs in Diverse Gram-Negative Bacteria. *J. Bacteriol.* 179, 5482–5493. doi:10.1128/jb.179.17.5482-5493.1997
- Gangi Setty, T., Cho, C., Govindappa, S., Apicella, M. A., and Ramaswamy, S. (2014). Bacterial Periplasmic Sialic Acid-Binding Proteins Exhibit a Conserved Binding Site. *Acta Cryst. D Biol. Crystallogr.* 70, 1801–1811. doi:10.1107/s139900471400830x
- Gerlach, J. H., Endicott, J. A., Juranka, P. F., Henderson, G., Sarangi, F., Deuchars, K. L., et al. (1986). Homology between P-Glycoprotein and a Bacterial Haemolysin Transport Protein Suggests a Model for Multidrug Resistance. *Nature* 324, 485–489. doi:10.1038/324485a0
- Glaenger, J., Peter, M. F., Thomas, G. H., and Hagelueken, G. (2017). PELDOR Spectroscopy Reveals Two Defined States of a Sialic Acid TRAP Transporter SBP in Solution. *Biophys. J.* 112, 109–120.
- Gonin, S., Arnoux, P., Pierru, B., Lavergne, J., Alonso, B., Sabaty, M., et al. (2007). Crystal Structures of an Extracytoplasmic Solute Receptor from a TRAP Transporter in its Open and Closed Forms Reveal a helix-swapped Dimer Requiring a Cation for α -keto Acid Binding. *BMC Struct. Biol.* 7, 11. doi:10.1186/1472-6807-7-11
- Gouridis, G., Schuurman-Wolters, G. K., Ploetz, E., Husada, F., Vietrov, R., De Boer, M., et al. (2015). Conformational Dynamics in Substrate-Binding Domains Influences Transport in the ABC Importer GlnPQ. *Nat. Struct. Mol. Biol.* 22, 57–64. doi:10.1038/nsmb.2929
- Gros, P., Croop, J., and Housman, D. (1986). Mammalian Multidrug Resistance Gene: Complete cDNA Sequence Indicates strong Homology to Bacterial Transport Proteins. *Cell* 47, 371–380. doi:10.1016/0092-8674(86)90594-5
- Gustot, A., Smriti, J.-M., Ruyschaert, H., and Govaerts, C. (2010). Lipid Composition Regulates the Orientation of Transmembrane Helices in HorA, an ABC Multidrug Transporter. *J. Biol. Chem.* 285, 14144–14151. doi:10.1074/jbc.m109.079673
- Heinkel, F., Abraham, L., Ko, M., Chao, J., Bach, H., Hui, L. T., et al. (2019). Phase Separation and Clustering of an ABC Transporter in *Mycobacterium tuberculosis*. *Proc. Natl. Acad. Sci. USA* 116, 16326–16331. doi:10.1073/pnas.1820683116
- Higgins, C. F. (1992). ABC Transporters: from Microorganisms to Man. *Annu. Rev. Cel. Biol.* 8, 67–113. doi:10.1146/annurev.cb.08.110192.000435
- Hollenstein, K., Frei, D. C., and Locher, K. P. (2007). Structure of an ABC Transporter in Complex with its Binding Protein. *Nature* 446, 213–216. doi:10.1038/nature05626
- Horne, C. R., Venugopal, H., Panjikar, S., Wood, D. M., Henrickson, A., Brookes, E., et al. (2021). Mechanism of NanR Gene Repression and Allosteric Induction of Bacterial Sialic Acid Metabolism. *Nat. Commun.* 12, 1988. doi:10.1038/s41467-021-22253-6
- Hvorup, R. N., Goetz, B. A., Niederer, M., Hollenstein, K., Perozo, E., and Locher, K. P. (2007). Asymmetry in the Structure of the ABC Transporter-Binding Protein Complex BtuCD-BtuF. *Science* 317, 1387–1390. doi:10.1126/science.1145950
- Hyde, S. C., Emsley, P., Hartshorn, M. J., Mimmack, M. M., Gileadi, U., Pearce, S. R., et al. (1990). Structural Model of ATP-Binding Protein Associated with Cystic Fibrosis, Multidrug Resistance and Bacterial Transport. *Nature* 346, 362–365. doi:10.1038/346362a0
- Ilari, A., Pescatori, L., Di Santo, R., Battistoni, A., Ammendola, S., Falconi, M., et al. (2016). *Salmonella enterica* Serovar Typhimurium Growth Is Inhibited by the Concomitant Binding of Zn(II) and a Pyrrolyl-Hydroxamate to ZnuA, the Soluble Component of the ZnuABC Transporter. *Biochim. Biophys. Acta (Bba) - Gen. Subjects* 1860, 534–541. doi:10.1016/j.bbagen.2015.12.006
- Immadisetty, K., Hettige, J., and Moradi, M. (2019). Lipid-Dependent Alternating Access Mechanism of a Bacterial Multidrug ABC Exporter. *ACS Cent. Sci.* 5, 43–56. doi:10.1021/acscentsci.8b00480
- Jenkins, G. A., Figueira, M., Kumar, G. A., Sweetman, W. A., Makepeace, K., Pelton, S. I., et al. (2010). Sialic Acid Mediated Transcriptional Modulation of a Highly Conserved Sialometabolism Gene Cluster in *Haemophilus influenzae* and its Effect on Virulence. *BMC Microbiol.* 10, 48. doi:10.1186/1471-2180-10-48
- Johnston, J. W., Coussens, N. P., Allen, S., Houtman, J. C. D., Turner, K. H., Zaleski, A., et al. (2008). Characterization of the *N*-Acetyl-5-Neuraminic Acid-Binding Site of the Extracytoplasmic Solute Receptor (SiaP) of Nontypeable *Haemophilus influenzae* Strain 2019. *J. Biol. Chem.* 283, 855–865. doi:10.1074/jbc.m706603200
- Jones, D. T., Buchan, D. W. A., Cozzetto, D., and Pontil, M. (2012). PSICOV: Precise Structural Contact Prediction Using Sparse Inverse Covariance

- Estimation on Large Multiple Sequence Alignments. *Bioinformatics* 28, 184–190. doi:10.1093/bioinformatics/btr638
- Juan, D., Pazos, F., and Valencia, A. (2008). High-confidence Prediction of Global Interactomes Based on Genome-wide Coevolutionary Networks. *Proc. Natl. Acad. Sci.* 105, 934–939. doi:10.1073/pnas.0709671105
- Kamisetty, H., Ovchinnikov, S., and Baker, D. (2013). Assessing the Utility of Coevolution-Based Residue-Residue Contact Predictions in a Sequence- and Structure-Rich Era. *Proc. Natl. Acad. Sci.* 110, 15674–15679. doi:10.1073/pnas.1314045110
- Kawai, T., Caaveiro, J. M. M., Abe, R., Katagiri, T., and Tsumoto, K. (2011). Catalytic Activity of MsbA Reconstituted in Nanodisc Particles Is Modulated by Remote Interactions with the Bilayer. *FEBS Lett.* 585, 3533–3537. doi:10.1016/j.febslet.2011.10.015
- Kehlenbeck, D.-M., Josts, I., Nitsche, J., Busch, S., Forsyth, V. T., and Tidow, H. (2019). Comparison of Lipidic Carrier Systems for Integral Membrane Proteins - MsbA as Case Study. *Biol. Chem.* 400, 1509–1518. doi:10.1515/hsz-2019-0171
- Kelly, D. J., and Thomas, G. H. (2001). The Tripartite ATP-independent Periplasmic (TRAP) Transporters of Bacteria and Archaea. *FEMS Microbiol. Rev.* 25, 405–424. doi:10.1111/j.1574-6976.2001.tb00584.x
- Lee, S., Ghosh, S., Jana, S., Robertson, N., Tate, C. G., and Vaidehi, N. (2020). How Do Branched Detergents Stabilize GPCRs in Micelles? *Biochemistry* 59, 2125–2134. doi:10.1021/acs.biochem.0c00183
- Li, L., Ghimire-Rijal, S., Lucas, S. L., Stanley, C. B., Wright, E., Agarwal, P. K., et al. (2017). Periplasmic Binding Protein Dimer Has a Second Allosteric Event Tied to Ligand Binding. *Biochemistry* 56, 5328–5337. doi:10.1021/acs.biochem.7b00657
- Lindén, M., Sens, P., and Phillips, R. (2012). Entropic Tension in Crowded Membranes. *Plos Comput. Biol.* 8, e1002431. doi:10.1371/journal.pcbi.1002431
- Locher, K. P. (2016). Mechanistic Diversity in ATP-Binding Cassette (ABC) Transporters. *Nat. Struct. Mol. Biol.* 23, 487–493. doi:10.1038/nsmb.3216
- Mancusso, R., Gregorio, G. G., Liu, Q., and Wang, D.-N. (2012). Structure and Mechanism of a Bacterial Sodium-dependent Dicarboxylate Transporter. *Nature* 491, 622–626. doi:10.1038/nature11542
- Marinelli, F., Kuhlmann, S. I., Grell, E., Kunte, H.-J., Ziegler, C., and Faraldo-Gomez, J. D. (2011). Evidence for an Allosteric Mechanism of Substrate Release from Membrane-Transporter Accessory Binding Proteins. *Proc. Natl. Acad. Sci.* 108, E1285–E1292. doi:10.1073/pnas.1112534108
- Marks, D. S., Colwell, L. J., Sheridan, R., Hopf, T. A., Pagnani, A., Zecchina, R., et al. (2011). Protein 3D Structure Computed from Evolutionary Sequence Variation. *PLoS One* 6, e28766. doi:10.1371/journal.pone.0028766
- Mi, W., Li, Y., Yoon, S. H., Ernst, R. K., Walz, T., and Liao, M. (2017). Structural Basis of MsbA-Mediated Lipopolysaccharide Transport. *Nature* 549, 233–237. doi:10.1038/nature23649
- Mishra, S., Verhalen, B., Stein, R. A., Wen, P. C., Tajkhorshid, E., and Mchaourab, H. S. (2014). Conformational Dynamics of the Nucleotide Binding Domains and the Power Stroke of a Heterodimeric ABC Transporter. *Elife* 3, e02740.
- Müller, A., Severi, E., Mulligan, C., Watts, A. G., Kelly, D. J., Wilson, K. S., et al. (2006). Conservation of Structure and Mechanism in Primary and Secondary Transporters Exemplified by SiaP, a Sialic Acid Binding Virulence Factor from *Haemophilus influenzae*. *J. Biol. Chem.* 281, 22212–22222. doi:10.1074/jbc.m603463200
- Mulligan, C., Fenollar-Ferrer, C., Fitzgerald, G. A., Vergara-Jaque, A., Kaufmann, D., Li, Y., et al. (2016). The Bacterial Dicarboxylate Transporter VcINDY Uses a Two-Domain Elevator-type Mechanism. *Nat. Struct. Mol. Biol.* 23, 256–263. doi:10.1038/nsmb.3166
- Mulligan, C., Fischer, M., and Thomas, G. H. (2011). Tripartite ATP-independent Periplasmic (TRAP) Transporters in Bacteria and Archaea. *FEMS Microbiol. Rev.* 35, 68–86. doi:10.1111/j.1574-6976.2010.00236.x
- Mulligan, C., Geertsma, E. R., Severi, E., Kelly, D. J., Poolman, B., and Thomas, G. H. (2009). The Substrate-Binding Protein Imposes Directionality on an Electrochemical Sodium Gradient-Driven TRAP Transporter. *Pnas* 106, 1778–1783. doi:10.1073/pnas.0809979106
- Mulligan, C., Kelly, D. J., and Thomas, G. H. (2007). Tripartite ATP-independent Periplasmic Transporters: Application of a Relational Database for Genome-wide Analysis of Transporter Gene Frequency and Organization. *J. Mol. Microbiol. Biotechnol.* 12, 218–226. doi:10.1159/000099643
- Ng, K. M., Ferreyra, J. A., Higginbottom, S. K., Lynch, J. B., Kashyap, P. C., Gopinath, S., et al. (2013). Microbiota-liberated Host Sugars Facilitate post-antibiotic Expansion of Enteric Pathogens. *Nature* 502, 96–99. doi:10.1038/nature12503
- Nguyen, P. T., Lai, J. Y., Lee, A. T., Kaiser, J. T., and Rees, D. C. (2018). Noncanonical Role for the Binding Protein in Substrate Uptake by the MetNI Methionine ATP Binding Cassette (ABC) Transporter. *Proc. Natl. Acad. Sci. U.S.A.* 115, E10596–E10604. doi:10.1073/pnas.1811003115
- Nielubowicz, G. R., Smith, S. N., and Mobley, H. L. T. (2010). Zinc Uptake Contributes to Motility and Provides a Competitive Advantage to *Proteus mirabilis* during Experimental Urinary Tract Infection. *Iai* 78, 2823–2833. doi:10.1128/iai.01220-09
- Nikaido, H., and Saier, M., Jr (1992). Transport Proteins in Bacteria: Common Themes in Their Design. *Science* 258, 936–942. doi:10.1126/science.1279804
- North, R. A., Horne, C. R., Davies, J. S., Remus, D. M., Muscroft-Taylor, A. C., Goyal, P., et al. (2018). "Just a Spoonful of sugar.": Import of Sialic Acid across Bacterial Cell Membranes. *Biophys. Rev.* 10, 219–227. doi:10.1007/s12551-017-0343-x
- North, R. A., Watson, A. J. A., Pearce, F. G., Muscroft-Taylor, A. C., Friemann, R., Fairbanks, A. J., et al. (2016). Structure and Inhibition of *N*-acetylneuraminase Lyase From Methicillin-Resistant *Staphylococcus aureus*. *FEBS Lett.* 590 (23), 4414–4428. doi:10.1002/1873-3468.12462
- O'Mara, M. L., and Mark, A. E. (2012). The Effect of Environment on the Structure of a Membrane Protein: P-Glycoprotein under Physiological Conditions. *J. Chem. Theor. Comput.* 8, 3964–3976. doi:10.1021/ct300254y
- Ovchinnikov, S., Kamisetty, H., and Baker, D. (2014). Robust and Accurate Prediction of Residue-Residue Interactions across Protein Interfaces Using Evolutionary Information. *eLife* 3. doi:10.7554/elife.02030.014
- Perry, R. D., Bobrov, A. G., and Fetherston, J. D. (2015). The Role of Transition Metal Transporters for Iron, Zinc, Manganese, and Copper in the Pathogenesis of *Yersinia pestis*. *Metallomics* 7, 965–978. doi:10.1039/c4mt00332b
- Peter, M. F., Gebhardt, C., Glaenger, J., Schneberger, N., De Boer, M., Thomas, G. H., et al. (2021). Triggering Closure of a Sialic Acid TRAP Transporter Substrate Binding Protein through Binding of Natural or Artificial Substrates. *J. Mol. Biol.* 433, 166756. doi:10.1016/j.jmb.2020.166756
- Putman, M., Van Veen, H. W., and Konings, W. N. (2000). Molecular Properties of Bacterial Multidrug Transporters. *Microbiol. Mol. Biol. Rev.* 64, 672–693. doi:10.1128/mmb.64.4.672-693.2000
- Rabus, R., Jack, D. L., Kelly, D. J., and Saier, M. H., Jr (1999). TRAP Transporters: an Ancient Family of Extracytoplasmic Solute-receptor-dependent Secondary Active Transporters. *Microbiology* 145 (Pt 12), 3431–3445. doi:10.1099/00221287-145-12-3431
- Rice, A. J., Alvarez, F. J., Davidson, A. L., and Pinkett, H. W. (2014). Effects of Lipid Environment on the Conformational Changes of an ABC Importer. *Channels* 8, 327–333. doi:10.4161/chan.29294
- Rosa, L. T., Bianconi, M. E., Thomas, G. H., and Kelly, D. J. (2018). Tripartite ATP-independent Periplasmic (TRAP) Transporters and Tripartite Tricarboxylate Transporters (TTT): From Uptake to Pathogenicity. *Front. Cel. Infect. Microbiol.* 8, 33. doi:10.3389/fcimb.2018.00033
- Ruggiero, A., Dattelbaum, J. D., Staiano, M., Berisio, R., D'auria, S., and Vitagliano, L. (2014). A Loose Domain Swapping Organization Confers a Remarkable Stability to the Dimeric Structure of the Arginine Binding Protein from *Thermotoga maritima*. *PLoS ONE* 9, e96560. doi:10.1371/journal.pone.0096560
- Saier, M. H., Jr (2000). A Functional-Phylogenetic Classification System for Transmembrane Solute Transporters. *Microbiol. Mol. Biol. Rev.* 64, 354–411. doi:10.1128/mmb.64.2.354-411.2000
- Sanchez-Ortiz, V. J., Domenzain, C., Poggio, S., Dreyfus, G., and Camarena, L. (2021). The Periplasmic Component of the DctPQM TRAP-Transporter Is Part of the DctS/DctR Sensory Pathway in *Rhodobacter sphaeroides*. *Microbiology* 167. doi:10.1099/mic.0.001037
- Scalise, M., Console, L., Galluccio, M., Pochini, L., and Indiveri, C. (2020). Chemical Targeting of Membrane Transporters: Insights into Structure/Function Relationships. *ACS Omega* 5, 2069–2080. doi:10.1021/acsomega.9b04078
- Scheepers, G. H., Lycklama, A. N. J. A., and Poolman, B. (2016). An Updated Structural Classification of Substrate-Binding Proteins. *FEBS Lett.* 590, 4393–4401. doi:10.1002/1873-3468.12445
- Severi, E., Randle, G., Kivlin, P., Whitfield, K., Young, R., Moxon, R., et al. (2005). Sialic Acid Transport in *Haemophilus influenzae* is Essential for Lipopolysaccharide Sialylation and Serum Resistance and Is Dependent on a

- Novel Tripartite ATP-independent Periplasmic Transporter. *Mol. Microbiol.* 58, 1173–1185. doi:10.1111/j.1365-2958.2005.04901.x
- Siegel, S. J., and Weiser, J. N. (2015). Mechanisms of Bacterial Colonization of the Respiratory Tract. *Annu. Rev. Microbiol.* 69, 425–444. doi:10.1146/annurev-micro-091014-104209
- Sohlenkamp, C., and Geiger, O. (2016). Bacterial Membrane Lipids: Diversity in Structures and Pathways. *FEMS Microbiol. Rev.* 40, 133–159. doi:10.1093/femsre/fuv008
- Stefan, E., Hofmann, S., and Tampe, R. (2020). A Single Power Stroke by ATP Binding Drives Substrate Translocation in a Heterodimeric ABC Transporter. *Elife* 9. doi:10.7554/elifesciences.55943.sa2
- Tanaka, K. J., Song, S., Mason, K., and Pinkett, H. W. (2018). Selective Substrate Uptake: The Role of ATP-Binding Cassette (ABC) Importers in Pathogenesis. *Biochim. Biophys. Acta (Bba) - Biomembranes* 1860, 868–877. doi:10.1016/j.bbame.2017.08.011
- Thomas, C., Aller, S. G., Beis, K., Carpenter, E. P., Chang, G., Chen, L., et al. (2020). Structural and Functional Diversity Calls for a New Classification of ABC Transporters. *FEBS Lett.* 594, 3767–3775. doi:10.1002/1873-3468.13935
- Thomas, C., and Tampé, R. (2020). Structural and Mechanistic Principles of ABC Transporters. *Annu. Rev. Biochem.* 89, 605–636. doi:10.1146/annurev-biochem-011520-105201
- Vetting, M. W., Al-Obaidi, N., Zhao, S., San Francisco, B., Kim, J., Wichelecki, D. J., et al. (2015). Experimental Strategies for Functional Annotation and Metabolism Discovery: Targeted Screening of Solute Binding Proteins and Unbiased Panning of Metabolomes. *Biochemistry* 54, 909–931. doi:10.1021/bi501388y
- Vigonsky, E., Ovcharenko, E., and Lewinson, O. (2013). Two Molybdate/tungstate ABC Transporters that Interact Very Differently with Their Substrate Binding Proteins. *Proc. Natl. Acad. Sci.* 110, 5440–5445. doi:10.1073/pnas.1213598110
- Wahlgren, W. Y., Dunevall, E., North, R. A., Paz, A., Scalise, M., Bisignano, P., et al. (2018). Substrate-bound Outward-Open Structure of a Na(+)-Coupled Sialic Acid Symporter Reveals a New Na(+) Site. *Nat. Commun.* 9, 1753. doi:10.1038/s41467-018-04045-7
- Ward, A., Reyes, C. L., Yu, J., Roth, C. B., and Chang, G. (2007). Flexibility in the ABC Transporter MsbA: Alternating Access with a Twist. *Proc. Natl. Acad. Sci.* 104, 19005–19010. doi:10.1073/pnas.0709388104
- Wilson, B. R., Bogdan, A. R., Miyazawa, M., Hashimoto, K., and Tsuji, Y. (2016). Siderophores in Iron Metabolism: from Mechanism to Therapy Potential. *Trends Mol. Med.* 22, 1077–1090. doi:10.1016/j.molmed.2016.10.005
- Wolf, A., Bauer, B., and Hartz, A. M. (2012). ABC Transporters and the Alzheimer's Disease Enigma. *Front. Psychiatry* 3, 54. doi:10.3389/fpsy.2012.00054
- Wyborn, N. R., Alderson, J., Andrews, S. C., and Kelly, D. J. (2001). Topological Analysis of DctQ, the Small Integral Membrane Protein of the C4-Dicarboxylate TRAP Transporter of *Rhodobacter capsulatus*. *FEMS Microbiol. Lett.* 194, 13–17. doi:10.1111/j.1574-6968.2001.tb09439.x
- Zafar, H., and Saier, M. H., Jr (2018). Comparative Genomics of Transport Proteins in Seven *Bacteroides* Species. *PLoS One* 13, e0208151.

Conflict of Interest: The authors declare that the research was conducted in the absence of any commercial or financial relationships that could be construed as a potential conflict of interest.

Copyright © 2021 Davies, Currie, Wright, Newton-Vesty, North, Mace, Allison and Dobson. This is an open-access article distributed under the terms of the Creative Commons Attribution License (CC BY). The use, distribution or reproduction in other forums is permitted, provided the original author(s) and the copyright owner(s) are credited and that the original publication in this journal is cited, in accordance with accepted academic practice. No use, distribution or reproduction is permitted which does not comply with these terms.



Role of Flavonoids in the Treatment of Iron Overload

Xiaomin Wang^{1†}, Ye Li^{1†}, Li Han², Jie Li³, Cun Liu¹ and Changgang Sun^{4,5*}

¹ College of First Clinical Medicine, Shandong University of Traditional Chinese Medicine, Jinan, China, ² Shandong Academy of Chinese Medicine, Jinan, China, ³ College of Traditional Chinese Medicine, Shandong University of Traditional Chinese Medicine, Jinan, China, ⁴ Department of Oncology, Weifang Traditional Chinese Hospital, Weifang, China, ⁵ Qingdao Academy of Chinese Medical Sciences, Shandong University of Traditional Chinese Medicine, Qingdao, China

Iron overload, a high risk factor for many diseases, is seen in almost all human chronic and common diseases. Iron chelating agents are often used for treatment but, at present, most of these have a narrow scope of application, obvious side effects, and other disadvantages. Recent studies have shown that flavonoids can affect iron status, reduce iron deposition, and inhibit the lipid peroxidation process caused by iron overload. Therefore, flavonoids with iron chelating and antioxidant activities may become potential complementary therapies. In this study, we not only reviewed the research progress of iron overload and the regulation mechanism of flavonoids, but also studied the structural basis and potential mechanism of their function. In addition, the advantages and disadvantages of flavonoids as plant iron chelating agents are discussed to provide a foundation for the prevention and treatment of iron homeostasis disorders using flavonoids.

Keywords: flavonoids, iron overload, iron metabolism, iron balance, plant iron chelator

OPEN ACCESS

Edited by:

Piotr Koprowski,
Nencki Institute of Experimental
Biology (PAS), Poland

Reviewed by:

Ming He,
Nanchang University, China
Joanna Izabela Lachowicz,
University of Cagliari, Italy

*Correspondence:

Changgang Sun
scgdoctor@126.com

[†]These authors have contributed
equally to this work and share first
authorship

Specialty section:

This article was submitted to
Cellular Biochemistry,
a section of the journal
Frontiers in Cell and Developmental
Biology

Received: 25 March 2021

Accepted: 10 June 2021

Published: 05 July 2021

Citation:

Wang X, Li Y, Han L, Li J, Liu C
and Sun C (2021) Role of Flavonoids
in the Treatment of Iron Overload.
Front. Cell Dev. Biol. 9:685364.
doi: 10.3389/fcell.2021.685364

INTRODUCTION

Iron overload is a long-standing problem that has aroused great interest in the field of chronic diseases (Fernández-Real and Manco, 2014). Iron, one of the essential metal elements, maintains normal physiological activities in human body, which is mainly involved in important physiological processes such as oxygen transport, electron transport, DNA synthesis, and many enzymatic reactions. Iron is absorbed through the gastrointestinal tract, delivered into the bloodstream, distributed throughout the body, and there are no physiological routes of excretion after absorption (Fleming and Ponka, 2012). When there is too much iron in the body, excess iron can be deposited in tissues and organs, produce lipid peroxidation, affects cell damage, which can lead to cancer, hematological diseases, and other chronic and commonly encountered diseases. In addition, iron overload is a characteristic of ferroptosis that is a form of regulated cell death, leading to accumulation of lethal levels of lipid hydroperoxides (Wu et al., 2021). The review of iron overload is helpful for us to better understand the occurrence and progress mechanism of ferroptosis.

Studies on iron overload mainly focus on liver fibrosis, liver cancer (Molina-Sánchez and Lujambio, 2019), atherosclerosis (Wunderer et al., 2020), and hematological diseases (Franke et al., 2020). Deferrioxamine, deferiprone, and deferasirox are usually used to treat iron overload as iron chelators, but they are prone to side effects. Flavonoids, with their special structure, maybe have good iron chelation, antioxidant properties and less toxic. Based on this, flavonoids have become a hot topic as plant iron chelators.

Recent researches on the treatment of iron overload by flavonoids mainly concentrated on the effect of animal or cell experiments of a single compound, and there was a lack of macroscopic summing up and sorting out from the same kind of compounds. The mechanisms involved in different studies are different or complicated, some of the experimental results are controversial and contradictory, and lack of systematic summary. In this paper, the research progress on the regulation mechanism of iron overload and flavonoids was reviewed, and the potential molecular cytological mechanism was generalized according to their structural basis. These findings provide a solid evidence base for flavonoids as plant iron chelating agents.

IRON OVERLOAD: AN IMBALANCE IRON METABOLISM THAT CAUSES CHRONIC AND COMMON DISEASES

Iron Metabolism of Iron Overload

Iron metabolism is a process in which iron is absorbed, regulated in the organism, and eventually excreted (**Figure 1A**). Fe^{3+} in the intestinal cavity is reduced to Fe^{2+} by duodenal cytochrome B, and then transported by divalent metal ion transporter 1 to the absorption cells of the intestinal mucosa epithelium. Some of this combines with apoferritin to form ferritin, which is stored in cells, and the remaining Fe^{2+} is released from the basal end of absorbing cells and enters the blood circulation, mediated by ferroportin (FPN), and is oxidized to Fe^{3+} by hephaestin. Excess ferritin is lost when cells are shed in the gut (Ramakrishnan et al., 2018). At the same time, the regulation of iron involves the combined action of various proteins and pathways. Among these, hepcidin plays a central regulatory role in the maintenance of iron homeostasis (Lee and Beutler, 2009).

Iron overload or iron deficiency are the mainly iron dyshomeostasis (Muñoz et al., 2011). Iron deficiency is the most common public nutrition problem worldwide (Pasricha et al., 2020), but less attention is paid to iron overload. Iron overload is a pathological phenomenon in which the supply of iron in the body exceeds the need for iron, which leads to an increase in iron storage in some tissues and organs (Sousa et al., 2020). The human body has many absorption, transport, and storage mechanisms for iron, but there is no mechanism for excretion of excessive iron. Excessive iron can also have toxic effects on the body. An increasing amount of studies have shown that iron overload is related to the occurrence and development of many diseases. With respect to iron metabolism in the case of iron overload (**Figure 1B**), free iron exceeds the binding limit of transferrin (Tf), and iron absorption efficiency decreases relatively, but absolute values increase. At the same time, hepcidin levels increase, thereby accelerating the degradation of FPN, closing the iron transport outlet to the blood, and reducing the transport of iron from small intestinal epithelial cells and macrophages to the blood (Yan et al., 2018). Iron overload in the body can stimulate the synthesis of ferritin and capture excessive iron (Pickart et al., 2014).

In addition, ferroptosis is closely related to iron metabolism under iron overload. Ferroptosis, as a kind of programmed apoptosis, is characterized by excessive accumulation of lipid peroxides and reactive oxygen species (Zhai et al., 2021). Ferroptosis, often accompanied with iron overload, caused the tissue damage mainly driven by iron overload and lipid peroxidation. At the same time, ferroptosis causes ferritin degradation, affects iron metabolism and leads to iron overload (Chen et al., 2021). The occurrence of ferroptosis leads to normal tissue and organ damage and loss of function, which is directly involved in the occurrence, development and prognosis of some chronic and common diseases (Mao et al., 2020).

Related Diseases and Mechanism of Iron Overload

When there is too much iron in the body, the body will mount a defensive response, but after excess iron exceeds the binding capacity of serum FPN, it becomes labile plasma iron (LPI), labile cellular iron (LCI), or non-transferrin bound iron (NTBI). Unbound free iron leads to the formation of dangerous free radicals, which lead to lipid peroxidation. The accumulation of unstable iron (LPI and LCI) and NTBI will inevitably lead to excessive iron deposition in tissues and organs, ultimately causing multiple target organ damage, seriously affecting the quality of life and survival time of patients. In addition, iron overload affects the electron transfer of oxygen (Ali-Rahmani et al., 2014). Tf continues to transport iron ions to cells, and this may eventually lead to aging, chronic anemia, or cancer (**Figure 2**).

Excessive iron is widely deposited in the parenchymal cells of some organs and tissues of the human body, resulting in multiple organ function damage. For example, iron ions cannot only act on the gastrointestinal mucosa, causing gastrointestinal damage, but also severely damage hepatocytes, causing lipid peroxidation, cell swelling, and tissue necrosis, leading to liver fibrosis or liver cancer (Jang et al., 2014). On the other hand, inhalation of oxide-containing iron can cause toxic reactions in the respiratory tract. Inhaled iron oxide particles gather in the lungs and are swallowed by macrophages, leading to siderosis (Kim and Wessling-Resnick, 2012). Excessive deposition in the pancreas can cause diabetes, in the heart it can cause cardiomyopathy and atherosclerosis, and in bones and joints it can cause osteoporosis and joint pain. These varied diseases may be due to the ability of different cells to synthesize antioxidants or ferritin. Phytochelators such as flavonoids bind to excess iron, decrease the concentration of iron ions in serum and, due to their antioxidant effects, might reduce iron deposits.

The most direct effect of iron overload on cell damage is caused by lipid peroxidation can triggered by free iron ions. In the presence of free iron ions, hydrogen peroxide (H_2O_2) and superoxide (O_2^-) produce OH (hydroxyl radicals) via the Fenton and Haber-Weiss reactions (Choi et al., 2020). OH produced *in vivo* is the most important chemical substance that initiates lipid peroxidation and causes DNA damage (Afsar et al., 2016). It can extract hydrogen from lipids to form lipid free radicals. Lipid free radicals react rapidly with oxygen at a high rate to form lipid peroxyl radicals. Lipid peroxides can continue to extract

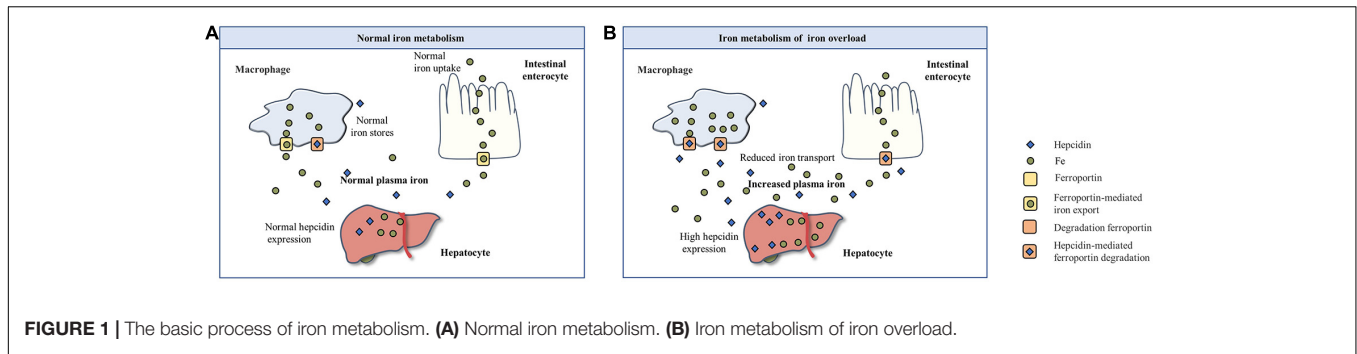


FIGURE 1 | The basic process of iron metabolism. **(A)** Normal iron metabolism. **(B)** Iron metabolism of iron overload.

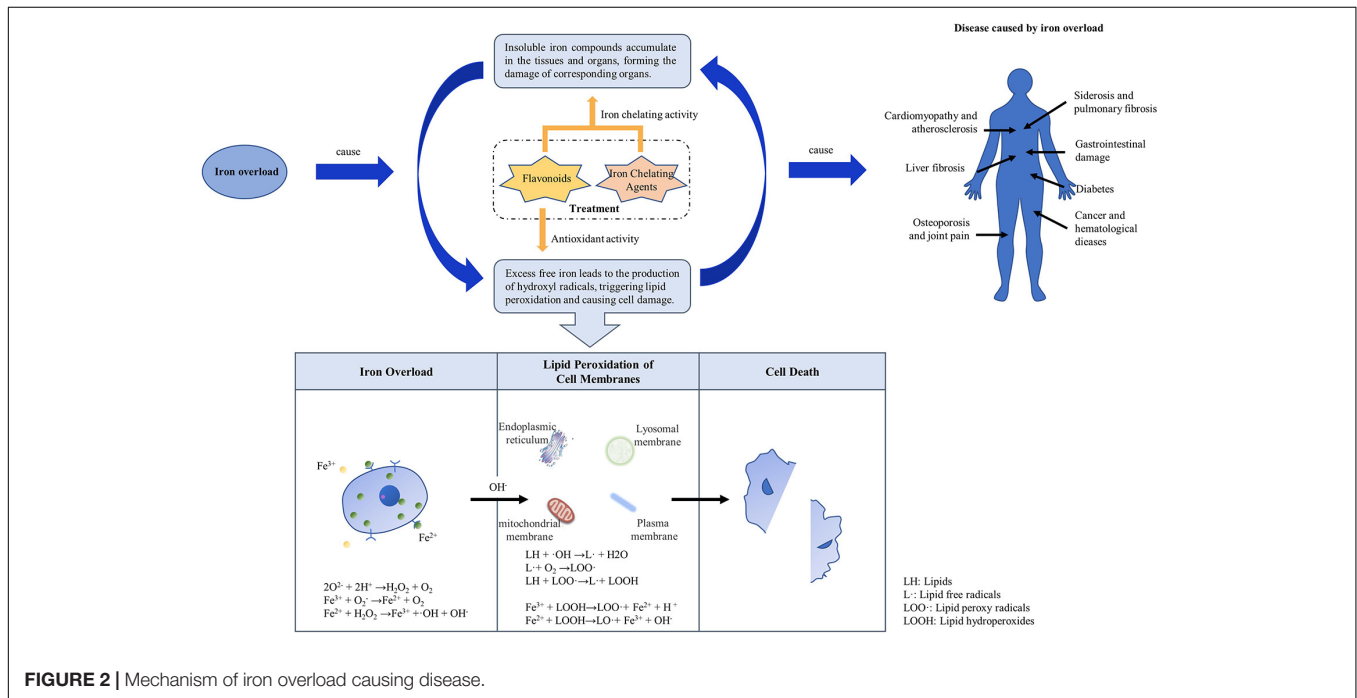


FIGURE 2 | Mechanism of iron overload causing disease.

hydrogen to form other lipid free radicals, which become lipid peroxides themselves, and a series of chain reactions ensues to form a large number of lipid peroxides (Chen et al., 2009). In the presence of Fe^{2+}/Fe^{3+} , iron ions near membrane lipids react with lipid peroxides to form new lipid peroxides and lipid oxygen free radicals, which further accelerate the chain reaction and eventually lead to cross-linking, polymerization, and inactivation of some lipids and functional macromolecular compounds (Choi et al., 2020). This results in damage to DNA, proteins, and lipids in cells, leading to cancer, hypertension, hyperlipidemia, or atherosclerosis. Antioxidants can block lipid chain autoxidation and provide hydrogen to free radicals, especially lipid peroxides, thus forming stable free radicals that do not initiate or induce further lipid oxidation (Ben Salah et al., 2019). The antioxidant properties of phytochemicals, such as flavonoids, may have a similar effect.

Treatment of Iron Overload

Iron chelating agents are the main treatment options for iron overload diseases. At present, three iron chelating agents,

deferrioxamine, deferiprone, and deferasirox, are mainly used in clinical practice (Yang et al., 2018). However, they are currently only used to treat thalassemia iron overload caused by excessive blood transfusions (Kontoghiorghes and Kontoghiorghes, 2020). In addition to the narrow scope of application, they also have some disadvantages, such as frequent use and high prices, obvious side effects, and poor patient compliance.

With the increased understanding of the pathways related to iron homeostasis in the human body, novel iron chelators have been widely studied. For example, hepcidin supplementation can reduce intestinal iron absorption (Swinkels and Drenth, 2008; Katsarou and Pantopoulos, 2018). Tf extracted from human serum, or genetically engineered (Bobik et al., 2019), can be used as a natural iron-chelating agent to treat iron overload in specific parts of the body. However, as far as current technology is concerned, these are difficult to obtain and have low yields and poor activity, which are sufficient for scientific research but not clinical application. The search for an ideal iron chelator has become a popular pursuit.

Flavonoids, which have the capacity to inhibit reactive oxygen species, scavenge free radicals and regulate iron homeostasis, are less expensive and have fewer side effects, and are promising novel iron chelators (Lesjak and Srail, 2019).

FLAVONOIDS: A PROMISING NATURAL COMPOUND FOR IRON OVERLOAD

Flavonoids are widely distributed in fruits, vegetables, tea, wine, seeds, and plant roots (Batiha et al., 2020). Many flavonoids have antitussive, expectorant, antiasthmatic, and antibacterial properties. In addition, flavonoids exert the same effect as phytoestrogens. They also have iron chelating and antioxidative properties. At present, iron overload is an important killer that endangers human health. Some phytochemicals, such as flavonoids, may provide a basis for new therapeutic approaches.

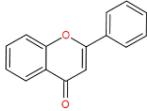
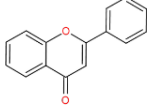
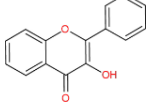
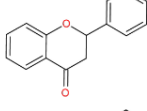
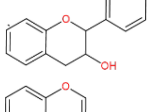
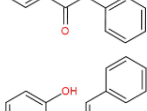
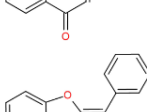
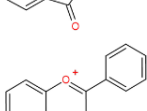
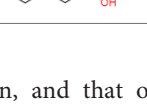
The Basic Structure of Flavonoids for Iron Overload

Flavonoids are a type of yellow pigment derived from two benzene rings with phenolic hydroxyl groups connected by three carbon atoms, that is, a series of compounds with C6-C3-C6 as the basic carbon structure. According to the different connection modes of the C3, flavonoids can be divided into several sub-types, including flavones, flavanones, flavonols, flavanols, isoflavones, chalcones, aurones, and anthocyanidins (Huynh et al., 2014; **Table 1**). Compared with other phytochemicals, flavonoids are highly iron chelation ability and reliable antioxidants. It is speculated that flavonoids can regulate iron metabolism and be used to treat iron overload. Two influential structures of flavonoids treating iron overload were presented as follows.

One is iron chelating properties of flavonoids. Studies have shown that flavonoids contain a variety of iron binding sites (**Table 2**), such as the 6, 7-dihydroxy structure, B ring catechol, and 2, 3-double bond. However, isolated ketone, hydroxyl, methoxy, or ortho-methoxy groups are not associated with the chelation of iron at all (Mladěnka et al., 2011). The 6, 7-dihydroxy structure is the most effective iron-binding site (Borges et al., 2016). Baicalein and baicalin, which have this structure, have strong iron-chelating properties. However, Vlachodimitropoulou et al. (2011) believe that the most effective is the catechin B ring catechol in quercetin and luteolin, but it may not play an important role in acidic conditions (Mladěnka et al., 2011). In addition, the chelation of metal ions generally requires the presence of 3- or 5-hydroxy groups. Rutin and quercetin contain these structures (Khalili et al., 2015). Furthermore, the 2, 3-double bonds of flavones and flavanols may also be important sites affecting iron binding (Braakhuis, 2019).

Another is antioxidant properties of flavonoids. As compounds containing two phenolic hydroxyl groups, flavonoids are effective antioxidants and free radical scavengers (Silva et al., 2020). The more phenolic hydroxyl groups there are, the more sites can be oxidized and the stronger the ability to scavenge oxygen free radicals (**Table 2**). For example, based on the structure, the oxidation resistance of luteolin is greater than

TABLE 1 | Classification of flavonoids.

Classification	Basic structure	Typical examples
Basic skeleton		—
Flavones		Baicalein, baicalin, apigenin, luteolin
Flavonols		quercetin, myricetin, kaempferol, rutin
Flavanones		Naringenin
Flavanols		Catechin
Isoflavones		Pururerarin, genistein
Chalcones		Corylifolinin
Aurones		Aureusidin
Anthocyanidins		Cyanidin, delphinidin

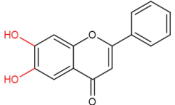
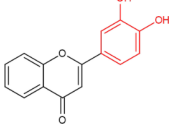
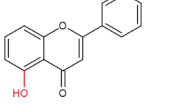
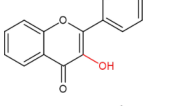
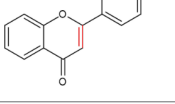
that of apigenin, and that of luteolin is less than quercetin (**Supplementary Figure 1**).

The Potential Molecular and Cellular Mechanism of Flavonoids for Iron Overload

Based on the previous research results, we summarized the underlying mechanisms of flavonoids for treating iron overload according to the following three mechanisms: amelioration of iron status by various proteins and pathways, chelation of iron to reduce iron deposition, and resistance to oxidation to reduce iron overload-induced oxidative damage (**Figure 3A**).

Flavonoids can ameliorate iron status by various proteins and pathways, which is an indirect way to reduce the saturation of iron (**Figure 3B**), such as ferritin, Tf, and hepcidin. The mechanism may involve inhibition of the expression of TfR1 and ferroportin 1, promoting the expression of divalent metal transporter 1, increasing hepcidin transcript levels and promoter activity.

TABLE 2 | Iron binding sites of flavonoids.

	Basic structure	Typical examples
6,7-dihydroxy		Baicalein, baicalin
B ring catechol		Quercetin, luteolin
5-hydroxyl		Rutin, quercetin
3-hydroxyl		Rutin, quercetin
2,3-double bond		Baicalein, baicalin, rutin, quercetin

Furthermore, the regulation of hepcidin and its regulatory elements by flavonoids is related to the STAT3-binding site.

Flavonoids can chelate iron to reduce iron accumulation, which is a direct way to reduce the saturation of iron. On account of flavonoids have iron-binding sites (Table 2) that are the structural basis of iron chelation. According to the relevant literature, baicalein, baicalin, quercetin, and rutin have the strongest iron chelating activity. When the bodily iron is overloaded, flavonoids inhibit the absorption and redistribution of iron in to some extent by chelating iron, thus reducing the iron content. In addition to inhibiting absorption, they can also increase excretion, and may combine with iron to form flavonoid-iron complexes that are excreted through feces.

Flavonoids can resist oxidation to reduce iron overload-induced oxidative damage. Flavonoids are a class of polyphenolic compounds, have strong reducibility, and can be used as antioxidants. The mechanism of action can be summarized in the following three stages: reaction with superoxide anion radical to prevent free radical trigger, inhibition of the Fenton reaction to prevent hydroxyl radical generation, and reaction with lipid peroxidation groups to prevent lipid peroxidation.

PROGRESS IN THE RESEARCH REGARDING FLAVONOIDS FOR THE TREATMENT OF IRON OVERLOAD

A number of *in vitro* and *in vivo* experiments have provided compelling evidence that flavonoids have iron chelating activity and strong antioxidant ability, which can reduce the damage caused by iron overload. These experiments indicate that flavonoids may subsequently be used as potential therapies for

iron overload syndromes. Herein, we focus on representative flavonoid compounds and summarize the experimental results regarding the treatment of iron overload-related diseases. We also discuss the related mechanisms of plant iron-chelating agents (Table 3).

Flavones

Flavones mostly form glycosides with sugars and are stored in plants. More than 30 types of glycoside belonging to the flavone group have been found, among which baicalein, baicalin, apigenin, and luteolin are widely distributed.

Baicalein

Baicalein and baicalin are the main compounds isolated from the roots of the traditional Chinese medicinal herb *Scutellaria baicalensis Georgi*, and can be present at the same time. Animal studies have shown that Baicalein is an antioxidant or iron chelator, and it can significantly reduce the oxidation levels of lipids and proteins (Czapski et al., 2012).

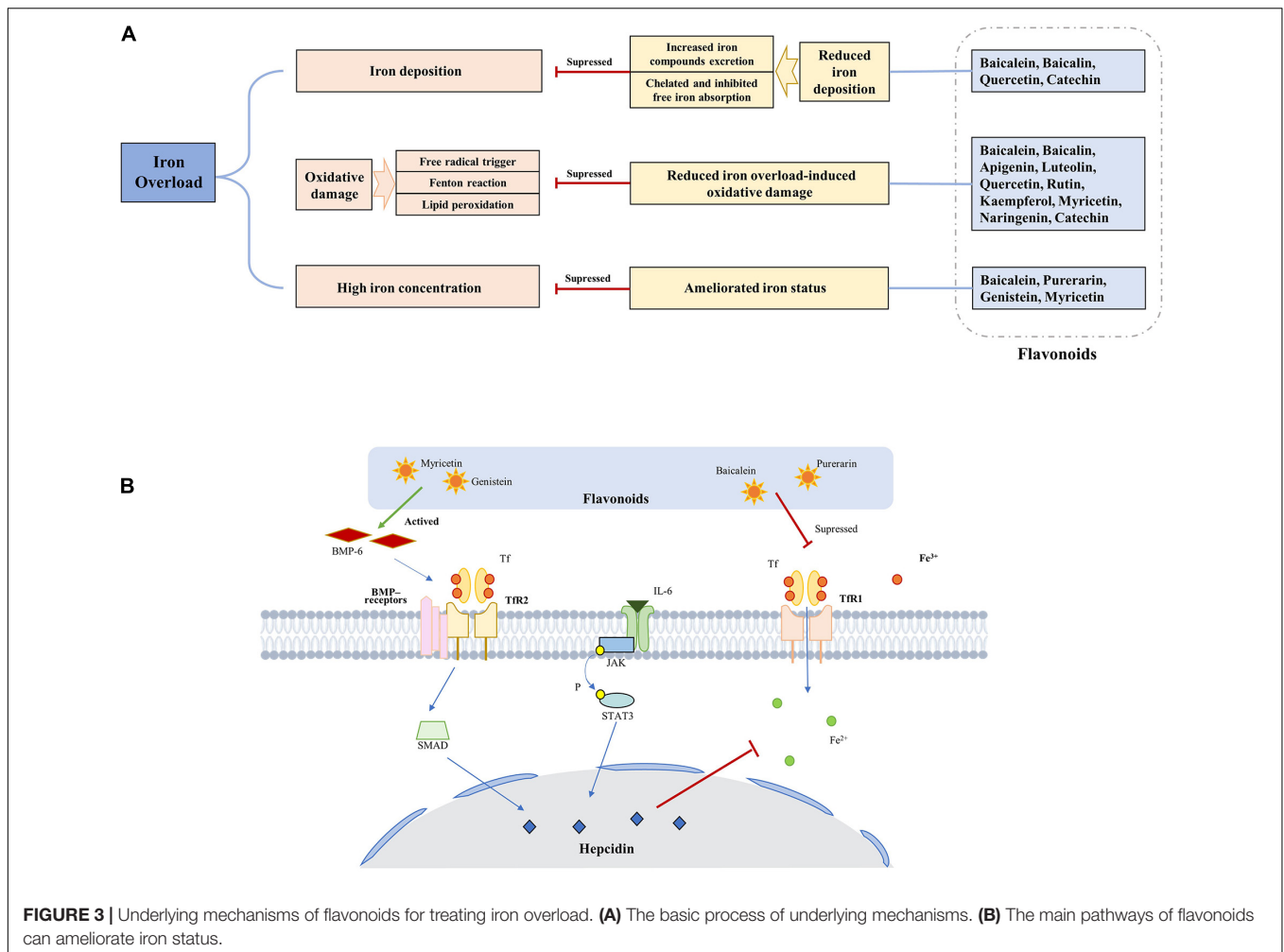
One study showed that baicalein could significantly improve white blood cells and hemoglobin in the bone marrow of anemic mice with regenerative disorder, and had a protective effect on apoptosis induced by iron overload. Baicalein had a limited effect on platelet recovery, which was better than deferoxamine; however, in reducing iron deposition, baicalein is superior to deferoxamine and its mechanism may be related to the up regulation of hepcidin and its regulators bone morphogenetic protein 6 (BMP-6), SMAD family member 4 (SMAD4), and transferrin receptor 2 (TfR2) at the protein and mRNA levels (Dijiong et al., 2019). Studies by Perez et al. (2009) suggested that baicalin strongly inhibits iron-promoted Fenton chemistry through a combination of chelation and free radical scavenging mechanisms, whereas baicalin only partially protects against free radical damage. Regulation of the metal dynamic balance and inhibition of Fenton chemistry may be two of the mechanisms of herbal medicine.

Baicalin

Baicalin is the 7-hydroxyl group of baicalein, followed by glucuronide. After entering the animal body, baicalein is rapidly transformed into baicalin and other metabolites in the blood. Baicalin is not easily absorbed orally and can be absorbed into the blood only after enzymatic hydrolysis into baicalein in the intestine, which is rapidly transformed into baicalin in the body. The structures of baicalin and baicalein are similar and have similar functions.

The results of Zhao et al. (2005) showed that baicalin has a protective effect on the liver of iron-overload mice, and its mechanism may be due to both the antioxidant and chelating iron activity. Xu et al. (2012) found that baicalin inhibits oxidative stress induced by the combination of alcohol and iron via iron chelation.

The antioxidation and iron chelation properties of baicalin may be related to the following reasons: baicalin promotes the transfer of electrons from Fe^{2+} to dissolved oxygen, so that most of the Fe^{2+} is transformed into Fe^{3+} , subsequently inhibiting the formation of hydroxyl radicals (Nishizaki and Iwahashi, 2015). In



addition, baicalin positively regulates the expression of divalent metal transporter 1 and negatively regulates the expression of ferroportin 1, which reduces the accumulation of iron in different brain regions (Xiong et al., 2012; Guo et al., 2014).

Apigenin

The main botanical sources of apigenin stem from *Chamomile*, *Petroselinum crispum*, and *Apium graveolens L.* have the ability to scavenge free radicals, chelate iron, and inhibit lipoxygenase. Compared with other flavonoids (quercetin and kaempferol), it has the characteristics of low toxicity and non-mutagenicity (Simunkova et al., 2019). Danciu et al. (2018) confirmed that apigenin has the ability to scavenge free radicals, chelate iron, and inhibit lipoxygenase. In addition, they found that apigenin from different sources had different apoptosis-promoting and immune-activating potentials.

Luteolin

Luteolin is found in various plants in the form of glycosides. These plants have a high content of *Capsicum annuum L.*, *Dendranthema indicum*, *Lonicera japonica Thunb.*, and *Perilla frutescens (L.) Britt.* Luteolin, which has various pharmacological

activities, reduces lipid oxidation of emulsions by scavenging radicals and chelating iron (Kim and Choe, 2018).

Flavonols

Flavonols include more than 60 types of aglycones, among which quercetin and kaempferol are widely distributed, although rutin and myricetin are also common.

Quercetin

Quercetin is a flavonoid that is widely distributed in the flowers, leaves, and fruits of plants and is found in large quantities in Chinese medicine, vegetables, fruits, and red wine. It has the ability to scavenge free radicals and chelate iron.

Gholampour et al. (Gholampour and Saki, 2019) found that quercetin could inhibit hepatorenal toxicity induced by ferrous sulfate and reduce the degree of liver and renal tissue injury in rats. Gleib et al. (2002) confirmed through experiments that quercetin might reduce the risk of colon cancer by protecting the oxidative damage to DNA induced by iron. Li et al. (2020) approved that quercetin lowered the iron level particularly in the islet in type 2 diabetes (T2DM) mice and abolished partially oxidative stress in pancreatic tissue. In addition, clinical

TABLE 3 | Progress in the research regarding flavonoids for the treatment of iron overload.

Classification	Compound	Model	Mechanism	Results	References	
Flavones	Baicalein	Male Wistar rats	Scavenged radical	Decreased the level of lipid and protein iron overload-induced oxidation	Czapski et al. (2012)	
		A mouse model of aplastic anemia with iron overload complication	Up-regulated hepcidin and its regulators (BMP-6, SMAD, and TFR2) at the protein and mRNA levels	Protected iron overload-induced apoptosis and reduced iron deposition	Dijing et al. (2019)	
		A model of UV/Visible spectroscopic studies	Modulation of metal homeostasis and the inhibition of Fenton chemistry	Ameliorated iron status and decreased iron overload-induced oxidation	Perez et al. (2009)	
	Baicalin	Male Kunming mice	Be capable of the antioxidant and iron chelation activities	Protected the liver of iron overload	Zhao et al. (2005)	
		Hepatocytes CYP2E1	Chelated iron	Decreased iron overload-induced oxidation	Xu et al. (2012)	
		A model of Electron Spin Resonance spectra	Facilitated the transfer of electrons from Fe(2+) to dissolved oxygen	Decreased iron overload-induced oxidation	Nishizaki and Iwahashi (2015)	
		C6 cells	Positively regulated divalent metal transporter 1 expression and negatively regulated ferroportin 1 expression	Down-regulated iron concentration and decreased iron deposition	Guo et al. (2014)	
	Apigenin	A375 human melanoma cell line and	Male Wistar rats	Chelated iron and reduced the loss of tyrosine hydroxylase-positive cells	Reduced iron deposition in different brain regions and protected dopaminergic neurons	Xiong et al. (2012)
			Chelated iron, scavenged radical and inhibited lipoxygenase	Decreased iron overload-induced oxidative damage	Danciu et al. (2018)	
			Chelated iron and scavenged radical	Decreased iron overload-induced lipid oxidation	Kim and Choe (2018)	
Flavonols	Quercetin	MDCK cells	Facilitated chelatable iron shuttling via glucose transport proteins in either direction across the cell membrane	Ameliorated iron status	Vlachodimitropoulou et al. (2011)	
		Male Wistar rats	Be capable of the antioxidant and iron chelation activities	Decreased iron overload-induced oxidative damage, hepatotoxicity and nephrotoxicity	Gholampour and Saki (2019)	
	Human colon carcinoma cell line HT29 clone 19A	Protected iron overload-induced DNA breaks and oxidized bases	Decreased iron overload-induced oxidative damage	Glei et al. (2002)		
		Male specific-pathogen-free C57BL/6J mice	Lowered the iron level particularly in the islet in T2DM mice and abolished partially oxidative stress in pancreatic tissue	Decreased iron overload-induced oxidative damage	Li et al. (2020)	
		β -thalassemia major patients	Reduced high sensitivity C-reactive protein, iron, ferritin, and transferrin saturation and increased transferrin	Ameliorated iron status	Sajadi Hezaveh et al. (2019)	
	HUVECs	Protected iron overload-induced mitochondrial dysfunction via ROS/ADMA/DDAHIII/eNOS/NO pathway	Decreased iron overload-induced cell damage	Chen et al. (2020)		

(Continued)

TABLE 3 | Continued

Classification	Compound	Model	Mechanism	Results	References
		Male Kunming mice	Inhibited iron overload-induced lipid peroxidation and protein oxidation of liver, decreased hepatic iron and hepatic collagen content, increased the serum non-heme iron level, released iron from liver and finally excrete it through feces	Decreased iron overload-induced oxidative damage, ameliorated iron status, and reduced iron deposition by excreting iron through feces	Kim and Choe (2018)
	Rutin	Male albino rats	Be capable of the antioxidant and iron chelation activities	Decreased iron overload-induced oxidative damage	Aziza et al. (2014)
	Kaempferol	HepG2 cells	Protected arachidonic acid and iron induced ROS	Decreased arachidonic acid and iron overload-induced oxidative damage	Cho et al. (2019)
	Myricetin	SH-SY5Y cells	Reduce iron contents may via inhibiting transferrin receptor 1 (TfR1) expression	Ameliorated iron status	Wang et al. (2017)
		Sprague Dawley male animals rat hepatocytes	Prevented both lipid peroxidation and accumulation of oxidation products in DNA via stimulation of DNA repair processes	Decreased iron overload-induced genotoxicity	Abalea et al. (1999)
Flavanones	Naringenin	Male Wistar rats	Improved antioxidant enzyme activities	Decreased iron overload-induced oxidative damage	Chtourou et al. (2014)
		Male Wistar rats	Scavenged radical	Restores iron overload-induced brain dysfunction	Chtourou et al. (2015)
Flavanols	Catechin	Male ICR mice	Chelated iron and Scavenged reactive oxygen active nitrogen	Decreased arachidonic acid and iron overload-induced oxidative damage	Yang et al. (2019)
		Male Swiss albino mice	Chelated iron and scavenged radical	Decreased iron overload-induced oxidative damage	Chaudhuri et al. (2015)
Isoflavones	Purerarin	Male Kunming mice and ARPE-19 cells	Be associated with regulation of iron-handling proteins, enhancement of the antioxidant capacity, and the inhibition of MAPK and STAT3 activation and the apoptotic pathways under iron overload condition	Decreased iron overload-induced retinal oxidative damage and reduced retinal iron deposition	Song et al. (2020)
		APP ^{swe} /PS1 Δ E9 transgenic mice	Decreased iron levels and malondialdehyde content, increased glutathione peroxidase and superoxide and reduced inflammatory response markers	Decreased iron overload-induced oxidative damage and inflammatory response markers	Zhang et al. (2018)
	Genistein	HepG2 cells	Be related to the BMP response element or the STAT3-binding site in the Hepcidin promoter	Increased Hepcidin transcript levels and promoter activity	Zhen et al. (2013)

experiments (Sajadi Hezaveh et al., 2019) indicated that quercetin could significantly reduce the saturation of high-sensitivity C-reactive protein, iron, ferritin, and Tf saturation, and increase Tf. Quercetin has also been shown to improve iron status.

The mechanism of quercetin in the treatment of iron overload mainly depends on its antioxidant properties, which reduce lipid peroxidation and iron chelation. In addition, quercetin may reduce iron overload-induced injury through the

ROS/ADMA/DDAH and II/eNOS/NO pathways (Chen et al., 2020). It also has the characteristic of iron-shuttling, and a quercetin concentration of $<1 \mu\text{M}$ can facilitate chelatable iron-shuttling through GLUT1 in any direction on the cell membrane (Vlachodimitropoulou et al., 2011). Quercetin and baicalin can release iron from the liver, which is eventually excreted through feces (Zhang et al., 2006).

These factors make it possible for quercetin to be effectively used in chelotherapy under conditions of iron overload. However, an experiment showed that, in contrast to the traditional antioxidant mechanism of quercetin, quercetin has dual effects on the hemoglobin (Hb) redox reaction *in vitro*. Quercetin significantly aggravates Hb-H₂O₂-induced protein oxidation at low concentrations and exhibits protective effects at high concentrations, which may provide new insights into the physiological and pharmacological implications of quercetin in iron overload diseases (Lu et al., 2013).

Rutin

Quercetin reacts with rutinose to form rutin. It is an effective component of the dried flowers and mature fruits of *Sophora japonica L.* Rutin is a well-known antioxidant and could be an efficient protective agent against iron overload (Aziza et al., 2014).

Aziza et al. (2014) found that the protective effect of rutin on the liver of iron-loaded rats might be related to its antioxidant and metal-chelating activities. One possible mechanism is that the formation of the iron-rutin complex cannot catalyze the conversion of superoxide ions to reactive hydroxyl radicals, which is the main process of the free radical-mediated toxicity of iron overload.

The fruit extract of *Prunus nepalensis Ser.* (Chaudhuri et al., 2015), *Drosera burmanni i* (Ghate et al., 2015), and *Pleurocybella porrigens* (Khalili et al., 2015) contain rutin and other phytochemicals and contribute to their free radical scavenging and iron chelation activity, potentially offering new natural alternatives to treat patients with iron overload. More studies are needed to determine which compounds are responsible for these biological activities.

Kaempferol

Kaempferol is mainly derived from the rhizome of *Kaempferia galanga L.* and widely exists in a variety of fruits, vegetables, and beverages. It has attracted attention because of its anti-cancer, anti-inflammatory, anti-oxidative, anti-viral, and other effects.

The relationship between kaempferol and iron absorption remains unclear. Some researchers believe that kaempferol inhibits iron absorption, while Hart and colleagues (Hart et al., 2015, 2020) believe that it promotes iron absorption. These inconsistencies may be related to the concentration of kaempferol and the pH of the environment. Kaempferol, as a plant iron-chelating agent for the treatment of iron overload-related diseases, requires further study.

However, kaempferol has good antioxidant activity. Cho et al. (2019) observed that kaempferol pretreatment could block the production of ROS induced by arachidonic acid and iron, reverse glutathione depletion, and reduce cell death.

Myricetin

Myricetin mainly comes from the extract of the leaves, bark, and roots of *Myrica rubra (Lour.)*, and it has been reported to have the biological functions of anti-oxidation, iron absorption inhibition, regulation of hepcidin, and chelation of iron ions.

Studies by Hart et al. (2015) showed that myricetin inhibits iron uptake by Caco-2 cells. Wang et al. (2017) suggested that myricetin reduces iron content by inhibiting the expression of TfR1. A study (Abalea et al., 1999) showed that myricetin antagonizes iron-induced genotoxicity by stimulating the process of DNA repair, preventing lipid peroxidation and the accumulation of oxidation products in DNA, in order to inhibit iron overload produced by liver cancer. In contrast, Mu et al. (2016) demonstrated that myricetin significantly inhibits hepcidin expression *in vitro* and *in vivo* by inhibiting the BMP/SMAD pathway and increasing the expression of FPN and the level of serum iron.

In addition, myricetin is generally shown to be an antioxidant, but sometimes may also be a pro-oxidant. In the presence of ascorbic acid, myricetin has antioxidative ability; in the absence of ascorbic acid, the pro-oxidative activity is dominant, and these two effects are enhanced when it forms a complex with iron (Chobot and Hadacek, 2011).

Although it is unclear whether myricetin can be used as an iron chelator, these results suggest that myricetin may play a key role in regulating iron homeostasis.

Flavanones

Flavanones are double-bonded hydrogenated derivatives of flavonoids at the C2-3 position, and most of these plant components have hydroxyl or methoxy groups. They exist in free form or in combined forms in the plant kingdom. The most common compound is naringenin.

Naringenin

Naringenin mainly originates from the buds of *Prunus yedoensis Mate* and the core and shell of *Anacardium occidentale*. It has antibacterial, anti-inflammatory, anti-cancer, antispasmodic, and chologenic effects.

Chtourou et al. (2014) suggested that naringenin could increase the activities of antioxidant enzymes and reduce the oxidative damage observed in the cerebral cortex of iron-treated rats. In addition, they also found that it could improve the angiogenic-like behavior impairment induced by excessive iron in rats, and emphasized that adding this flavonoid to the diet may prevent brain damage associated with iron load (Chtourou et al., 2015). These results suggest that naringenin has antioxidant and iron-chelating properties and can protect nerve tissues.

Flavanols

Flavanols are reduced from flavanonols and can be regarded as flavanonols after the removal of four carboxyl oxygen atoms. Catechin is a common flavanol.

Catechin

The derivatives of Flavan-3-ol is catechin, which is a type of active phenolic substance mainly extracted from tea and other

natural plants. The catechin in *Prunus nepalensis* Ser. (Steud) (Chaudhuri et al., 2015) and *Phyllostachys nigra* Bamboo stems (*henosis* variety) (Yang et al., 2019) have been studied, and it was suggested that iron-mediated oxidative stress could be improved, thereby increasing cell survival.

In addition, *Farsetia hamiltonii* Royle (Basu et al., 2019) and *Drosera burmannii* Vahl. (Ghate et al., 2015) catechin have good antioxidant activity, can remove a variety of reactive oxygen and nitrogen, and chelate iron. However, additional research is needed to determine whether catechins could be used to treat iron overload diseases.

Isoflavones

Isoflavones are a type of flavonoids mainly found in legumes. Daidzein is an isoflavone that has excellent antioxidant properties, although it has been proven unsuitable as a plant iron-chelating agent, as it does not chelate Fe³⁺ (Dowling et al., 2010). Puerarin and genistein may be potential iron chelating agents.

Puerarin

Puerarin is a crown-expanding isoflavone derivative separated from the roots of *Pueraria lobata* (Willd) Ohwi and *Pueraria thunbergiana* Benth.

Experimental data generated by Song et al. (2020) confirmed that puerarin reduces the retinal damage caused by iron overload. The possible mechanism might be associated with the regulation of iron-treated proteins, enhancement of antioxidant capacity (Zhang et al., 2018), inhibition of the activation and apoptosis of MAPK, and STAT3 under iron overload (Song et al., 2020).

Genistein

Genistein is derived from *Genista tinctoria* Linn. and *Sophora subprostrata* Chun et T. Chen root, which have antioxidant properties.

Zhen et al. (2013) confirmed that genistein treatment of HepG2 cells could increase both hepcidin promoter activity and transcript levels. This may be related to the BMP response element or the STAT3-binding site in the hepcidin promoter.

Other Flavonoids

There have been few studies on chalcones and aurones associated with iron overload and their basic mechanisms are still poorly understood.

DISCUSSION

Many flavonoids have specific metal binding sites, and the multiple phenolic hydroxyl structures they contain also have good oxygen reduction properties. Therefore, flavonoids can chelate iron to form iron complexes for excretion and reduce iron accumulation in tissues and organs. At the same time, they strongly inhibit active oxygen and scavenge free radicals, and can reduce lipid peroxidation caused by iron overload, which results in cell damage. Flavonoids

have the effect of regulating iron homeostasis and can be used as plant iron chelating agents. Compared with existing iron-chelating agents, they are very safe and inexpensive. In recent s, a large number of studies have shown that flavonoids can play an important role in the regulation of iron overload and are expected to be developed as natural drugs for the treatment of iron homeostasis disorders. Among them, baicalein, baicalin, quercetin, and rutin have shown outstanding results.

Researchers have made great efforts to explore the molecular mechanisms of flavonoids in iron overload. Although some progress has been made in the study of flavonoids in iron overload, research has mainly focused on *in vitro* studies and sufficient *in vivo* and clinical evidence is lacking, which are important considerations in evidence-based medicine. Furthermore, the use of flavonoids as iron-chelating agents requires risk and benefit assessment and comparison with existing treatments. In this respect, it is difficult to determine whether flavonoids have significant advantages.

It is also worth exploring whether flavonoids that chelate iron and inhibit lipid peroxidation can play an important role in ferroptosis. In addition, flavonoids also face a series of problems, such as low oral utilization rates and poor water solubility. New drug delivery approaches or dissolution methods for flavonoids have become a hot research topic. For example, the use of nanomaterials may be a viable solution strategy (Xia et al., 2011; Kang et al., 2019). The ability of flavonoids to chelate iron is affected by their concentration and environmental pH, and impacts the dosage and conditions of use. These factors should be the focus of subsequent studies (Abotaleb et al., 2018).

Iron overload can affect the clinical course of a variety of diseases and we suggest that patients with chronic and common diseases, such as cancer and hematological diseases, consume fruits, vegetables, and beverages that contain abundant flavonoids to prevent iron overload damage. Although the amount of flavonoids consumed in the diet for achieving a therapeutic effect remains to be determined, this field continues to hold much promise.

AUTHOR CONTRIBUTIONS

XW and YL: conceptualization, data curation, and writing – original draft preparation. LH: data curation and investigation. JL and CL: supervision, validation, and writing – review and editing. CS: conceptualization and writing – review and editing. All authors contributed to the article and approved the submitted version.

SUPPLEMENTARY MATERIAL

The Supplementary Material for this article can be found online at: <https://www.frontiersin.org/articles/10.3389/fcell.2021.685364/full#supplementary-material>

REFERENCES

- Abalea, V., Cillard, J., Dubos, M., Sergent, O., Cillard, P., and Morel, I. (1999). Repair of iron-induced DNA oxidation by the flavonoid myricetin in primary rat hepatocyte cultures. *Free Rad. Biol. Med.* 26, 1457–1466. doi: 10.1016/s0891-5849(99)00010-6
- Abotaleb, M., Samuel, S., Varghese, E., Varghese, S., Kubatka, P., Liskova, A., et al. (2018). Flavonoids in cancer and apoptosis. *Cancers* 11:28. doi: 10.3390/cancers11010028
- Afsar, T., Razak, S., Khan, M., Mawash, S., Almajwal, A., Shabir, M., et al. (2016). Evaluation of antioxidant, anti-hemolytic and anticancer activity of various solvent extracts of *Acacia hydasppica* R. Parker aerial parts. *BMC Complement. Altern. Med.* 16:258. doi: 10.1186/s12906-016-1240-8
- Ali-Rahmani, F., Schengrund, C., and Connor, J. (2014). HFE gene variants, iron, and lipids: a novel connection in Alzheimer's disease. *Front. Pharmacol.* 5:165. doi: 10.3389/fphar.2014.00165
- Aziza, S., Azab, M.-S., and El-Shall, S. (2014). Ameliorating role of rutin on oxidative stress induced by iron overload in hepatic tissue of rats. *Pak. J. Biol. Sci.* 17, 964–977. doi: 10.3923/pjbs.2014.964.977
- Basu, T., Kumar, B., Shendge, A., Panja, S., Chugh, H., Gautam, H., et al. (2019). An Indian desert shrub 'Hiran Chabba', *Farsetia hamiltonii* royle, exhibits potent antioxidant and hepatoprotective effect against iron- overload induced liver toxicity in Swiss albino mice. *Curr. Drug Discov. Technol.* 16, 210–222. doi: 10.2174/1570163815666180418150123
- Batiha, G., Beshbishy, A., Ikram, M., Mulla, Z., El-Hack, M., Taha, A., et al. (2020). The pharmacological activity, biochemical properties, and pharmacokinetics of the major natural Polyphenolic flavonoid: quercetin. *Foods* 9:374. doi: 10.3390/foods9030374
- Ben Salah, H., Smaoui, S., Abdennabi, R., and Allouche, N. (2019). LC-ESI-MS/MS phenolic profile of *Volutaria lippii* (L.) Cass. extracts and evaluation of their antioxidant, antiacetylcholinesterase, antidiabetic, and antibacterial activities. *Evid. Based Complement. Altern. Med.* 2019:9814537.
- Bobik, T., Popov, R., Aliev, T., Mokrushina, Y., Shamborant, O., Khurs, E., et al. (2019). Production of recombinant human transferrin in eukaryotic *Pichia pastoris* expression system. *Bull. Exp. Biol. Med.* 167, 335–338. doi: 10.1007/s10517-019-04521-0
- Borges, A., Abreu, A., Dias, C., Saavedra, M., Borges, F., and Simões, M. (2016). New perspectives on the use of phytochemicals as an emergent strategy to control bacterial infections including biofilms. *Molecules* 21:877. doi: 10.3390/molecules21070877
- Braakhuis, A. (2019). Evidence on the health benefits of supplemental propolis. *Nutrients* 11:2705. doi: 10.3390/nu11112705
- Chaudhuri, D., Ghate, N., Panja, S., Das, A., and Mandal, N. (2015). Wild edible fruit of *Prunus nepalensis* Ser. (Steud), a potential source of antioxidants, ameliorates iron overload-induced hepatotoxicity and liver fibrosis in mice. *PLoS One* 10:e0144280. doi: 10.1371/journal.pone.0144280
- Chen, B., Caballero, S., Seo, S., Grant, M., and Lewin, A. (2009). Delivery of antioxidant enzyme genes to protect against ischemia/reperfusion-induced injury to retinal microvasculature. *Invest. Ophthalmol. Vis. Sci.* 50, 5587–5595. doi: 10.1167/iops.09-3633
- Chen, X., Comish, P., Tang, D., and Kang, R. (2021). Characteristics and biomarkers of ferroptosis. *Front. Cell Dev. Biol.* 9:637162. doi: 10.3389/fcell.2021.637162
- Chen, X., Li, H., Wang, Z., Zhou, Q., Chen, S., Yang, B., et al. (2020). Quercetin protects the vascular endothelium against iron overload damages via ROS/ADMA/DDAH II/eNOS/NO pathway. *Eur. J. Pharmacol.* 868:172885. doi: 10.1016/j.ejphar.2019.172885
- Cho, S., Yang, J., Seo, K., Shin, S., Park, E., Cho, S., et al. (2019). Cudrania Tricuspidata extract and its major constituents inhibit oxidative stress-induced liver injury. *J. Med. Food* 22, 602–613. doi: 10.1089/jmf.2018.4322
- Chobot, V., and Hadacek, F. (2011). Exploration of pro-oxidant and antioxidant activities of the flavonoid myricetin. *Redox Rep.* 16, 242–247. doi: 10.1179/1351000211y.0000000015
- Choi, J., Min, K., Jeon, S., Kim, N., Pack, J., and Song, K. (2020). Continuous exposure to 1.7 GHz LTE electromagnetic fields increases intracellular reactive oxygen species to decrease human cell proliferation and induce senescence. *Sci. Rep.* 10:9238.
- Chtourou, Y., Fetoui, H., and Gdoura, R. (2014). Protective effects of naringenin on iron-overload-induced cerebral cortex neurotoxicity correlated with oxidative stress. *Biol. Trace Element Res.* 158, 376–383. doi: 10.1007/s12011-014-9948-0
- Chtourou, Y., Slima, A., Gdoura, R., and Fetoui, H. (2015). Naringenin mitigates iron-induced anxiety-like behavioral impairment, mitochondrial dysfunctions, Ectonucleotidases and Acetylcholinesterase alteration activities in rat Hippocampus. *Neurochem. Res.* 40, 1563–1575. doi: 10.1007/s11064-015-1627-9
- Czapski, G., Czubowicz, K., and Strosznajder, R. (2012). Evaluation of the antioxidative properties of lipoxygenase inhibitors. *Pharmacol. Rep.* 64, 1179–1188. doi: 10.1016/s1734-1140(12)70914-3
- Danciu, C., Zupko, I., Bor, A., Schwiebs, A., Radeke, H., Hancianu, M., et al. (2018). Botanical Therapeutics: phytochemical screening and biological assessment of chamomile, Parsley and celery extracts against A375 human melanoma and dendritic cells. *Int. J. Mol. Sci.* 19:3624. doi: 10.3390/ijms19113624
- Dijijong, W., Xiaowen, W., Linlong, X., Wenbin, L., Huijin, H., Baodong, Y., et al. (2019). Iron chelation effect of curcumin and baicalin on aplastic anemia mouse model with iron overload. *Iran. J. Basic Med. Sci.* 22, 660–668.
- Dowling, S., Regan, F., and Hughes, H. (2010). The characterisation of structural and antioxidant properties of isoflavone metal chelates. *J. Inorganic Biochem.* 104, 1091–1098. doi: 10.1016/j.jinorgbio.2010.06.007
- Fernández-Real, J., and Manco, M. (2014). Effects of iron overload on chronic metabolic diseases. *Lancet. Diabetes Endocrinol.* 2, 513–526. doi: 10.1016/s2213-8587(13)70174-8
- Fleming, R., and Ponka, P. (2012). Iron overload in human disease. *N. Engl. J. Med.* 366, 348–359.
- Franke, G., Kubasch, A., Cross, M., Vucinic, V., and Platzbecker, U. (2020). Iron overload and its impact on outcome of patients with hematological diseases. *Mol. Aspects Med.* 75:100868. doi: 10.1016/j.mam.2020.100868
- Ghate, N., Chaudhuri, D., Das, A., Panja, S., and Mandal, N. (2015). An antioxidant extract of the insectivorous plant *Drosera burmannii* Vahl. Alleviates iron-induced oxidative stress and hepatic injury in mice. *PLoS One* 10:e0128221. doi: 10.1371/journal.pone.0128221
- Gholampour, F., and Saki, N. (2019). Hepatic and renal protective effects of quercetin in ferrous sulfate-induced toxicity. *Gen. Physiol. Biophys.* 38, 27–38. doi: 10.4149/gpb_2018038
- Glei, M., Latunde-Dada, G., Klinder, A., Becker, T., Hermann, U., Voigt, K., et al. (2002). Iron-overload induces oxidative DNA damage in the human colon carcinoma cell line HT29 clone 19A. *Mutat. Res.* 519, 151–161. doi: 10.1016/s1383-5718(02)00135-3
- Guo, C., Chen, X., and Xiong, P. (2014). Baicalin suppresses iron accumulation after substantia nigra injury: relationship between iron concentration and transferrin expression. *Neural Regen. Res.* 9, 630–636. doi: 10.4103/1673-5374.130108
- Hart, J., Tako, E., Kochian, L., and Glahn, R. (2015). Identification of Black Bean (*Phaseolus vulgaris* L.) Polyphenols that inhibit and promote iron uptake by Caco-2 cells. *J. Agric. Food Chem.* 63, 5950–5956. doi: 10.1021/acs.jafc.5b00531
- Hart, J., Tako, E., Wiesinger, J., and Glahn, R. (2020). Polyphenolic profiles of yellow bean seed coats and their relationship with iron bioavailability. *J. Agric. Food Chem.* 68, 769–778. doi: 10.1021/acs.jafc.9b05663
- Huynh, N., Van Camp, J., Smaghe, G., and Raes, K. (2014). Improved release and metabolism of flavonoids by steered fermentation processes: a review. *Int. J. Mol. Sci.* 15, 19369–19388. doi: 10.3390/ijms151119369
- Jang, H., Do, G., Lee, H., Ok, H., Shin, J., and Kwon, O. (2014). Schisandra Chinensis Baillon regulates the gene expression of phase II antioxidant/detoxifying enzymes in hepatic damage induced rats. *Nutr. Res. Pract.* 8, 272–277. doi: 10.4162/nrp.2014.8.3.272
- Kang, H., Han, M., Xue, J., Baek, Y., Chang, J., Hu, S., et al. (2019). Renal clearable nanochelators for iron overload therapy. *Nat. Commun.* 10:5134.
- Katsarou, A., and Pantopoulos, K. (2018). Hepcidin therapeutics. *Pharmaceuticals* 11:127. doi: 10.3390/ph11040127
- Khalili, M., Ebrahimzadeh, M., and Kosaryan, M. (2015). In vivo iron-chelating activity and phenolic profiles of the Angel's wings mushroom, *Pleurotus porrigens* (Higher Basidiomycetes). *Int. J. Med. Mushr.* 17, 847–856. doi: 10.1615/intjmedmushrooms.v17.i9.50
- Kim, J., and Choe, E. (2018). Effect of the pH on the lipid oxidation and polyphenols of soybean oil-in-water emulsion with added peppermint (*Mentha*

- piperita* extract in the presence and absence of iron. *Food Sci. Biotechnol.* 27, 1285–1292. doi: 10.1007/s10068-018-0324-2
- Kim, J., and Wessling-Resnick, M. (2012). The role of iron metabolism in lung inflammation and injury. *J. Allergy Ther.* 3:004. doi: 10.4172/2155-6121.S4-004
- Kontoghiorghes, G., and Kontoghiorghes, C. (2020). Iron and chelation in biochemistry and medicine: new approaches to controlling iron metabolism and treating related diseases. *Cells* 9:1456. doi: 10.3390/cells9061456
- Lee, P., and Beutler, E. (2009). Regulation of hepcidin and iron-overload disease. *Ann. Rev. Pathol.* 4, 489–515. doi: 10.1146/annurev.pathol.4.110807.092205
- Lesjak, M., and Srai, S. K. S. (2019). Role of dietary flavonoids in iron homeostasis. *Pharmaceuticals* 12:119. doi: 10.3390/ph12030119
- Li, D., Jiang, C., Mei, G., Zhao, Y., Chen, L., Liu, J., et al. (2020). Quercetin alleviates ferroptosis of pancreatic β cells in Type 2 diabetes. *Nutrients* 12:2954. doi: 10.3390/nu12102954
- Lu, N., Chen, C., He, Y., Tian, R., Xiao, Q., and Peng, Y. (2013). Effects of quercetin on hemoglobin-dependent redox reactions: relationship to iron-overload rat liver injury. *J. Asian Nat. Products Res.* 15, 1265–1276. doi: 10.1080/10286020.2013.838952
- Mao, L., Zhao, T., Song, Y., Lin, L., Fan, X., Cui, B., et al. (2020). The emerging role of ferroptosis in non-cancer liver diseases: hype or increasing hope? *Cell Death Dis.* 11:518.
- Mladěnka, P., Macáková, K., Filipický, T., Zatloukalová, L., Jahodář, L., Bovicelli, P., et al. (2011). In vitro analysis of iron chelating activity of flavonoids. *J. Inorganic Biochem.* 105, 693–701. doi: 10.1016/j.jinorgbio.2011.02.003
- Molina-Sánchez, P., and Lujambio, A. (2019). Iron overload and liver cancer. *J. Exp. Med.* 216, 723–724. doi: 10.1084/jem.20190257
- Mu, M., An, P., Wu, Q., Shen, X., Shao, D., Wang, H., et al. (2016). The dietary flavonoid myricetin regulates iron homeostasis by suppressing hepcidin expression. *J. Nutr. Biochem.* 30, 53–61. doi: 10.1016/j.jnutbio.2015.10.015
- Muñoz, M., García-Erce, J., and Remacha, Á (2011). Disorders of iron metabolism. Part II: iron deficiency and iron overload. *J. Clin. Pathol.* 64, 287–296. doi: 10.1136/jcp.2010.086991
- Nishizaki, D., and Iwahashi, H. (2015). Baicalin inhibits the fenton reaction by enhancing electron transfer from Fe (2+) to dissolved oxygen. *Am. J. Chin. Med.* 43, 87–101. doi: 10.1142/s0192415x15500068
- Pasricha, S., Tye-Din, J., Muckenthaler, M., and Swinkels, D. (2020). Iron deficiency. *Lancet* 397, 233–248.
- Perez, C., Wei, Y., and Guo, M. (2009). Iron-binding and anti-Fenton properties of baicalin and baicalin. *J. Inorganic Biochem.* 103, 326–332. doi: 10.1016/j.jinorgbio.2008.11.003
- Pickart, L., Vasquez-Soltero, J., and Margolina, A. (2014). GHK and DNA: resetting the human genome to health. *Biomed. Res. Int.* 2014:151479.
- Ramakrishnan, L., Pedersen, S., Toe, Q., Quinlan, G., and Wort, S. (2018). Pulmonary arterial hypertension: iron matters. *Front. Physiol.* 9:641. doi: 10.3389/fphys.2018.00641
- Sajadi Hezaveh, Z., Azarkeivan, A., Janani, L., Hosseini, S., and Shidfar, F. (2019). The effect of quercetin on iron overload and inflammation in β -thalassemia major patients: a double-blind randomized clinical trial. *Complement. Ther. Med.* 46, 24–28. doi: 10.1016/j.ctim.2019.02.017
- Silva, T., Cavalcanti Filho, J., Barreto Fonsêca, M., Santos, N., Barbosa da Silva, A., Zagmignan, A., et al. (2020). Products derived *Buchenavia tetraphylla* from leaves have in vitro antioxidant activity and protect larvae against iron-induced injury. *Pharmaceuticals (Basel, Switzerland)* 13:46. doi: 10.3390/ph13030046
- Simunkova, M., Alwasel, S., Alhazza, I., Jomova, K., Kollar, V., Rusko, M., et al. (2019). Management of oxidative stress and other pathologies in Alzheimer's disease. *Arch. Toxicol.* 93, 2491–2513.
- Song, Q., Zhao, Y., Li, Q., Han, X., and Duan, J. (2020). Puerarin protects against iron overload-induced retinal injury through regulation of iron-handling proteins. *Biomed. Pharmacother.* 122:109690. doi: 10.1016/j.biopha.2019.109690
- Sousa, L., Oliveira, M., Pessôa, M., and Barbosa, L. (2020). Iron overload: effects on cellular biochemistry. *Clin. Chim. Acta* 504, 180–189. doi: 10.1016/j.cca.2019.11.029
- Swinkels, D., and Drenth, J. (2008). Hepcidin in the management of patients with mild non-hemochromatotic iron overload: fact or fiction? *J. Hepatol.* 49, 680–685. doi: 10.1016/j.jhep.2008.08.004
- Vlachodimitropoulou, E., Sharp, P., and Naftalin, R. (2011). Quercetin-iron chelates are transported via glucose transporters. *Free Rad. Biol. Med.* 50, 934–944. doi: 10.1016/j.freeradbiomed.2011.01.005
- Wang, B., Zhong, Y., Gao, C., and Li, J. (2017). Myricetin ameliorates scopolamine-induced memory impairment in mice via inhibiting acetylcholinesterase and down-regulating brain iron. *Biochem. Biophys. Res. Commun.* 490, 336–342. doi: 10.1016/j.bbrc.2017.06.045
- Wu, X., Li, Y., Zhang, S., and Zhou, X. (2021). Ferroptosis as a novel therapeutic target for cardiovascular disease. *Theranostics* 11, 3052–3059. doi: 10.7150/thno.54113
- Wunderer, F., Traeger, L., Sigurslid, H., Meybohm, P., Bloch, D., and Malhotra, R. (2020). The role of hepcidin and iron homeostasis in atherosclerosis. *Pharmacol. Res.* 153:104664. doi: 10.1016/j.phrs.2020.104664
- Xia, G., Chen, B., Ding, J., Gao, C., Lu, H., Shao, Z., et al. (2011). Effect of magnetic Fe₃O₄ nanoparticles with 2-methoxyestradiol on the cell-cycle progression and apoptosis of myelodysplastic syndrome cells. *Int. J. Nanomed.* 6, 1921–1927. doi: 10.2147/ijn.s24078
- Xiong, P., Chen, X., Guo, C., Zhang, N., and Ma, B. (2012). Baicalin and deferoxamine alleviate iron accumulation in different brain regions of Parkinson's disease rats. *Neural Regen. Res.* 7, 2092–2098.
- Xu, Y., Feng, Y., Li, H., and Gao, Z. (2012). Ferric citrate CYP2E1-independently promotes alcohol-induced apoptosis in HepG2 cells via oxidative/nitrative stress which is attenuated by pretreatment with baicalin. *Food Chem. Toxicol.* 50, 3264–3272. doi: 10.1016/j.fct.2012.05.061
- Yan, H., Liu, Z., Guan, Z., and Guo, C. (2018). Deferoxamine ameliorates adipocyte dysfunction by modulating iron metabolism in ob/ob mice. *Endocr. Connect.* 7, 604–616. doi: 10.1530/ec-18-0054
- Yang, J., Choi, M., Na, C., Cho, S., Kim, J., Ku, S., et al. (2019). Bamboo Stems (*Phyllostachys nigra variety henosis*) containing polyphenol mixtures activate Nrf2 and attenuate phenylhydrazine-induced oxidative stress and liver injury. *Nutrients* 11:114. doi: 10.3390/nu11010114
- Yang, J., Zhang, G., Dong, D., and Shang, P. (2018). Effects of iron overload and oxidative damage on the musculoskeletal system in the space environment: data from spaceflights and ground-based simulation models. *Int. J. Mol. Sci.* 19:2608. doi: 10.3390/ijms19092608
- Zhai, Z., Zou, P., Liu, F., Xia, Z., and Li, J. (2021). Ferroptosis is a potential novel diagnostic and therapeutic target for patients with cardiomyopathy. *Front. Cell Dev. Biol.* 9:649045. doi: 10.3389/fcell.2021.649045
- Zhang, Y., Kong, W., and Chai, X. (2018). Compound of icariin, astragalus, and puerarin mitigates iron overload in the cerebral cortex of Alzheimer's disease mice. *Neural Regen. Res.* 13, 731–736. doi: 10.4103/1673-5374.230302
- Zhang, Y., Li, H., Zhao, Y., and Gao, Z. (2006). Dietary supplementation of baicalin and quercetin attenuates iron overload induced mouse liver injury. *Eur. J. Pharmacol.* 535, 263–269. doi: 10.1016/j.ejphar.2006.01.067
- Zhao, Y., Li, H., Gao, Z., and Xu, H. (2005). Effects of dietary baicalin supplementation on iron overload-induced mouse liver oxidative injury. *Eur. J. Pharmacol.* 509, 195–200. doi: 10.1016/j.ejphar.2004.11.060
- Zhen, A., Nguyen, N., Gibert, Y., Motola, S., Buckett, P., Wessling-Resnick, M., et al. (2013). The small molecule, galein, increases hepcidin expression in human hepatocytes. *Hepatology (Baltimore, Md.)* 58, 1315–1325. doi: 10.1002/hep.26490

Conflict of Interest: The authors declare that the research was conducted in the absence of any commercial or financial relationships that could be construed as a potential conflict of interest.

Copyright © 2021 Wang, Li, Han, Li, Liu and Sun. This is an open-access article distributed under the terms of the Creative Commons Attribution License (CC BY). The use, distribution or reproduction in other forums is permitted, provided the original author(s) and the copyright owner(s) are credited and that the original publication in this journal is cited, in accordance with accepted academic practice. No use, distribution or reproduction is permitted which does not comply with these terms.

Advantages of publishing in Frontiers



OPEN ACCESS

Articles are free to read for greatest visibility and readership



FAST PUBLICATION

Around 90 days from submission to decision



HIGH QUALITY PEER-REVIEW

Rigorous, collaborative, and constructive peer-review



TRANSPARENT PEER-REVIEW

Editors and reviewers acknowledged by name on published articles

Frontiers

Avenue du Tribunal-Fédéral 34
1005 Lausanne | Switzerland

Visit us: www.frontiersin.org

Contact us: frontiersin.org/about/contact



REPRODUCIBILITY OF RESEARCH

Support open data and methods to enhance research reproducibility



DIGITAL PUBLISHING

Articles designed for optimal readership across devices



FOLLOW US

@frontiersin



IMPACT METRICS

Advanced article metrics track visibility across digital media



EXTENSIVE PROMOTION

Marketing and promotion of impactful research



LOOP RESEARCH NETWORK

Our network increases your article's readership